

Scuola Normale Superiore di Pisa

CLASSE DI SCIENZE

Corso di Perfezionamento in Fisica

PH. D. THESIS

Measurements of CP Asymmetries and Branching Fractions of Two-Body Charmless Decays of B^0 and B_s^0 Mesons

Candidate:
***Dr.* Michael Joseph Morello**

Advisor:
***Prof.* Giovanni Punzi**

19th December 2007

Contents

Introduction **1**

1 CP violation and charmless B decays **5**

1.1 Introduction . . . 5

1.2 CKM matrix and CP violation . . . 7

1.2.1 Phase Structure of the CKM Matrix . . . 8

1.2.2 Further Requirements for CP Violation . . . 9

1.2.3 Experimental Information on $|V_{\rm CKM}|$ . . . 10

1.2.4 Wolfenstein Parameterization of the CKM Matrix . . . 10

1.2.5 Unitarity Triangles of the CKM Matrix . . . 12

1.3 Non-leptonic decays of B mesons . . . 14

1.3.1 Factorization of Hadronic Matrix Elements . . . 16

1.4 Direct CP Violation . . . 18

1.5 Neutral B mesons . . . 19

1.5.1 Mixing Parameters . . . 20

1.5.2 Time-Dependent Decay Rates . . . 22

1.5.3 "Untagged" Rates . . . 22

1.5.4 CP Asymmetries . . . 23

1.6 How could new physics enter? . . . 24

1.7 Phenomenology of $B^0_{(s)} \to h^+ h'^-$ modes . . . 25

1.7.1 Amplitude relations from U-spin flavor symmetry . . . 26

1.7.2 $B^0 \to \pi^+\pi^-$ . . . 28

1.7.3 $B^0 \to K^+\pi^-$ . . . 29

1.7.4 $B^0 \to K^+K^-$ . . . 31

1.7.5 $B^0_s \to K^-\pi^+$ . . . 31

1.7.6 $B^0_s \to K^+K^-$ . . . 32

1.7.7 $B^0_s \to \pi^+\pi^-$ . . . 35

2 The experimental apparatus **37**
2.1 The Tevatron collider . . . 37
2.1.1 Proton beam . . . 39
2.1.2 Antiproton beam . . . 39
2.1.3 The collision . . . 40
2.1.4 Tevatron Status . . . 41
2.2 The CDF II detector . . . 41
2.2.1 Coordinates and notation . . . 41
2.2.2 Overview . . . 43
2.2.3 Tracking system . . . 44
2.2.4 Tracking performance . . . 48
2.3 Other CDF II subdetectors . . . 50
2.3.1 Time of Flight detector . . . 50
2.3.2 Calorimeters . . . 50
2.3.3 Muon systems . . . 53
2.3.4 Cherenkov Luminosity Counters . . . 53
2.4 Trigger and Data Acquisition system . . . 54
2.4.1 Silicon Vertex Trigger (SVT) . . . 56
2.5 Operations and data quality . . . 59

3 Sample selection and signal extraction **61**
3.1 $B^0_{(s)} \to h^+h'^-$ decays at CDF . . . 61
3.2 Displaced-Tracks Trigger . . . 63
3.2.1 The `B_PIPI` and `B_PIPI_HIGHPT` path . . . 64
3.2.2 Other Displaced-Tracks Triggers . . . 65
3.2.3 Trigger performance . . . 66
3.3 Extraction of the $B^0_{(s)} \to h^+h'^-$ signal . . . 67
3.3.1 Tracks . . . 67
3.3.2 Trigger confirmation . . . 68
3.3.3 Reconstruction of $B^0_{(s)} \to h^+h'^-$ candidates . . . 68
3.4 Further variables . . . 69
3.5 Final selections . . . 71

4 Separation of individual $B^0_{(s)} \to h^+h'^-$ modes **75**
4.1 CDF II simulation . . . 75
4.1.1 Monte Carlo validation . . . 77
4.2 $B^0_{(s)} \to h^+h'^-$ modes . . . 82
4.3 Kinematic separation . . . 83

4.4 Particle Identification (PID) . . . 91
4.4.1 dE/dx calibration samples . . . 92
4.4.2 dE/dx residual . . . 93
4.4.3 Separation power . . . 94
4.4.4 Correlations . . . 95
4.4.5 Model of the dE/dx distributions . . . 99
4.4.6 Sample dependence of correlation . . . 103
4.4.7 PID observable: kaonness . . . 105

5 Mass templates **109**
5.1 Introduction . . . 109
5.2 Invariant mass distribution from CDF II simulation . . . 110
5.3 Fast Monte Carlo Simulation (FMC) . . . 113
5.3.1 Smearing of curvature k . . . 113
5.3.2 Smearing of λ and φ_0 . . . 117
5.3.3 Smearing of the impact parameter d_0 . . . 118
5.3.4 Comparison FMC vs MC . . . 119
5.4 Final State Radiation . . . 121
5.4.1 QED calculations . . . 121
5.4.2 Putting everything together . . . 124
5.5 Testing the model with real data . . . 125

6 Fit of composition **133**
6.1 Discriminating observables . . . 133
6.2 Likelihood function . . . 134
6.3 Probability density function of the signal mass term . . . 135
6.4 Probability density function of the background mass term . . . 142
6.4.1 Combinatorial background (E) . . . 143
6.4.2 Physics background (A) . . . 144
6.5 Probability density function of the momentum term . . . 145
6.5.1 Signal momentum term . . . 145
6.5.2 Background momentum term . . . 147
6.6 Probability density function of the PID term . . . 148
6.6.1 Signal PID term . . . 148
6.6.2 Background PID term . . . 149
6.6.3 $B^0_{(s)} \to h^+ h^{'-}$ correlation . . . 150

7 Isolation of B^0 and B^0_s mesons **151**

7.1 Isolation . . . 151
7.2 Choice of the control samples . . . 152
7.3 Measurement of the isolation efficiency . . . 154
7.3.1 Probability density functions . . . 156
7.3.2 Likelihood fit . . . 156
7.4 p_{T}-dependent effects . . . 160
7.4.1 Fit of the reweighted $B^0_{(s)} \to J/\psi X$ samples . . . 162
7.4.2 Isolation efficiency ratio $\frac{\varepsilon_{\mathrm{iso}}(B^0)}{\varepsilon_{\mathrm{iso}}(B^0_s)}$ . . . 165
7.4.3 $p_{\mathrm{T}}(B)$ dependence of the isolation . . . 165
7.4.4 Isolation efficiency vs I_{cut} . . . 168

8 Fit-based cuts optimization **171**
8.1 Unbiased selection optimization . . . 171
8.2 Minimum Variance Bound . . . 171
8.3 Gaussian peak (S) over a flat background (B) . . . 172
8.3.1 Search for a rare decay ($S \to 0$) over a flat background (B) . . . 174
8.4 Optimization for $B^0_{(s)} \to h^+h^{'-}$ . . . 177
8.5 Optimized selection . . . 179
8.6 Performance of the optimization procedure . . . 180

9 Fit results and cross-checks **183**
9.1 Fit results . . . 183
9.2 Correlation matrix . . . 188
9.3 Fit projections . . . 189
9.4 Checks . . . 196
9.4.1 Pulls . . . 196
9.4.2 Probability ratio plots . . . 199
9.4.3 Additional fits . . . 202

10 Relative efficiency corrections **205**
10.1 Definitions . . . 205
10.2 Kinematic efficiencies . . . 206
10.2.1 Lifetimes in the Monte Carlo . . . 207
10.2.2 Kinematic efficiency corrections . . . 208
10.2.3 Trigger bias corrections . . . 209
10.2.4 FSR correction . . . 210
10.3 Results (not involving isolation efficiency and charge asymmetry correction) . . . 211
10.3.1 Ratio $\mathcal{B}(B^0 \to \pi^+\pi^-)/\mathcal{B}(B^0 \to K^+\pi^-)$ . . . 211

10.3.2 Ratio $\mathcal{B}(B^0 \to K^+K^-)/\mathcal{B}(B^0 \to K^+\pi^-)$ . . . 212
10.3.3 Ratio $\mathcal{B}(\Lambda_b^0 \to p\pi^-)/\mathcal{B}(\Lambda_b^0 \to pK^-)$ . . . 212
10.4 Efficiency of the B-isolation cut . . . 212
10.5 Results (involving isolation efficiency) . . . 212
10.5.1 Ratio $(f_s/f_d) \times \mathcal{B}(B_s^0 \to K^-\pi^+)/\mathcal{B}(B^0 \to K^+\pi^-)$ . . . 213
10.5.2 Ratio $(f_s/f_d) \times \mathcal{B}(B_s^0 \to K^+K^-)/\mathcal{B}(B^0 \to K^+\pi^-)$ . . . 213
10.5.3 Ratio $(f_s/f_d) \times \mathcal{B}(B_s^0 \to \pi^+\pi^-)/\mathcal{B}(B^0 \to K^+\pi^-)$ . . . 213
10.6 Further considerations . . . 213

11 Charge asymmetry **215**
11.1 Introduction . . . 215
11.2 Reconstruction of the prompt $D^0 \to h^+h^{'-}$ sample . . . 216
11.2.1 Checking the content of non-prompt D^0 . . . 219
11.3 Measurement of the charge asymmetry . . . 220
11.3.1 Probability density function of the signal mass term . . . 221
11.3.2 Probability density function of the background mass term . . . 222
11.3.3 Probability density function of the momentum term . . . 224
11.4 Fit results . . . 224
11.4.1 Fit projections . . . 225
11.5 Cross-check: PID-only fit . . . 227
11.5.1 Fit results for the dE/dx-only fit . . . 227
11.6 Charge asymmetry . . . 229
11.6.1 Momentum correction . . . 230
11.7 Results (involving charge asymmetry correction) . . . 230
11.7.1 Direct CP asymmetry in the $B^0 \to K^+\pi^-$ and $B_s^0 \to K^-\pi^+$ decay . . . 230
11.7.2 Ratio $\frac{f_d}{f_s} \times \frac{\Gamma(\overline{B}^0 \to K^-\pi^+) - \Gamma(B^0 \to K^+\pi^-)}{\Gamma(\overline{B}_s^0 \to K^+\pi^-) - \Gamma(B_s^0 \to K^-\pi^+)}$ . . . 230

12 Systematic uncertainties and significance **233**
12.1 Systematic uncertainties . . . 233
12.2 Uncertainty on the global mass scale (mass scale) . . . 234
12.3 Uncertainty on the nominal b-hadron masses (nominal masses) . . . 234
12.4 Charge asymmetries of momentum p.d.f. (asymm. $\wp^p$) . . . 235
12.5 Momentum p.d.f. of background ($\wp^p_{\text{bck}}$ model) . . . 235
12.6 Uncertainty on the combinatorial background mass term ($\wp^m_E$ model) . . . 236
12.7 dE/dx related systematics (dE/dx) . . . 238
12.8 Efficiency-related systematic effects . . . 240
12.8.1 Effect of Poisson fluctuations in simulated samples (MC stat.) . . . 240
12.8.2 Uncertainty on the XFT-bias correction (XFT bias) . . . 241

12.8.3 Uncertainty on the B-isolation efficiency (B-isol.) . . . 241
12.8.4 Charge asymmetry correction (charge asymmetry) . . . 241
12.9 Lifetime-related systematic effects . . . 241
12.9.1 Uncertainty on the nominal $B^0_{(s)}$ meson lifetimes ($B^0_{(s)}$ lifetime) . . . 241
12.9.2 Uncertainty on $\Delta\Gamma_s/\Gamma_s$ ($\Delta\Gamma_s/\Gamma_s$) . . . 242
12.10Total systematic uncertainties . . . 242
12.11Significance of the rare modes . . . 250

13 Results and discussion **255**
13.1 Final results . . . 255
13.2 Search for rare decay modes . . . 255
13.2.1 $B^0_s \to K^-\pi^+$ . . . 256
13.2.2 $B^0_s \to \pi^+\pi^-$ . . . 257
13.2.3 $B^0 \to K^+K^-$ . . . 258
13.2.4 $\Lambda^0_b \to pK^-$ and $\Lambda^0_b \to p\pi^-$ . . . 259
13.3 CP asymmetries . . . 259
13.3.1 Direct CP asymmetry of $B^0 \to K^+\pi^-$ . . . 259
13.3.2 Direct CP asymmetry of $B^0_s \to K^-\pi^+$ . . . 261
13.4 Precision branching fractions . . . 263
13.4.1 $B^0 \to \pi^+\pi^-$ . . . 263
13.4.2 $B^0_s \to K^+K^-$ . . . 265
13.5 U-spin-breaking effects . . . 269
13.5.1 $B^0 \to K^+\pi^-$ vs $B^0_s \to K^-\pi^+$ again . . . 270
13.5.2 Ratio of branching fractions and SU(3) . . . 271
13.6 Conclusions . . . 272

Bibliography **275**

List of Figures

1.1 CP-conjugate charged-current quark-level interaction processes in the Standard Model 8
1.2 Hierarchy of the quark transitions mediated through charged-current processes 11
1.3 The two non-squashed unitarity triangles of the CKM matrix 13
1.4 Feynman diagrams of the topologies characterizing non-leptonic B decays 15
1.5 Box diagrams contributing to B^0_q-$\overline{B}^0_q$ flavor mixing 19
1.6 Tree diagrams contributing to $B^0_{(s)} \to h^+h^{'-}$ decays 26
1.7 QCD-penguin diagram contributing to $B^0_{(s)} \to h^+h^{'-}$ decays 26
1.8 Electroweak penguin diagrams contributing to $B^0_{(s)} \to h^+h^{'-}$ decays 27
1.9 W-exchange and penguin-annihilation diagrams contributing to $B^0_{(s)} \to h^+h^{'-}$ decays 27

2.1 Illustration of the Fermilab Tevatron collider 38
2.2 Integrated and initial instantaneous luminosity as a function of the time 39
2.3 Elevation view of one half of the CDF II detector 42
2.4 Elevation view of one quadrant of the CDF II tracking volume 44
2.5 Schematic illustration of the SVXII barrels 46
2.6 A 1/6 section of the COT end-plate and a cross-section of three drift-cells 48
2.7 Schematic illustration of the central and plug electromagnetic calorimeter 52
2.8 Diagram of the CDF II trigger and data acquisition system 56
2.9 Distribution of the SVT impact parameter 59

3.1 Illustration of a $p\bar{p}$ event containing a $B^0_{(s)} \to h^+h^{'-}$ decay 62
3.2 Signal-to-background ratio as a function of the selection requirements 66
3.3 Invariant $\pi\pi$-mass distribution obtained by applying off-line the trigger confirmation selection 70
3.4 Invariant $\pi\pi$-mass distribution of the events passing the final selections 71

4.1 Check on real data of a purely `B_PIPI` topology 76
4.2 Background-subtracted $p_{\rm T}(B)$-distribution in $B^0_{(s)} \to h^+h^{'-}$ decays without isolation requirement 77

4.3 Background-subtracted $p_{\mathrm{T}}(B)$-distribution in $B^0_{(s)} \to h^+h^{'-}$ decays and reweighting functions . . . 79
4.4 Comparison of background-subtracted distributions in $B^0_{(s)} \to h^+h^{'-}$ decays and equivalent Monte Carlo distributions . . . 80
4.5 Comparison of background-subtracted distributions in $B^0_{(s)} \to h^+h^{'-}$ decays and equivalent Monte Carlo distributions . . . 81
4.6 Invariant $\pi\pi$-mass distribution of the simulated $B^0_{(s)} \to h^+h^{'-}$ decay modes . . . 82
4.7 Invariant $\pi\pi$-mass of the simulated $B^0_{(s)} \to h^+h^{'-}$ and $\Lambda^0_b \to ph^-$ decays as a function of α. . . . 87
4.8 Invariant $\pi\pi$-mass of the simulated $B^0_{(s)} \to h^+h^{'-}$ and $\Lambda^0_b \to ph^-$ decays as a function of α. . . . 88
4.9 Profile plots of the invariant $\pi\pi$-mass as a function of signed momentum imbalance for all simulated signal modes . . . 89
4.10 Universal curves . . . 92
4.11 Invariant mass of the $D^0 \to K^-\pi^+$ and $\Lambda^0 \to p\pi^-$ decays . . . 94
4.12 Distribution of dE/dx around the average pion response for pions, kaons . . . 95
4.13 Residual for pions versus dE/dx residual for kaons (protons) . . . 96
4.14 Distributions of the sum and difference of residuals . . . 98
4.15 Distribution of the observed residuals and resulting models . . . 100
4.16 dE/dx residuals templates . . . 101
4.17 Distributions of the sum and difference of the residuals and resulting model . . . 102
4.18 Correlation probability density functions . . . 103
4.19 κ observables . . . 105
4.20 Probability density function $\wp(\kappa_1, \kappa_2)$ for the $B^0_{(s)} \to h^+h^{'-}$ decays . . . 106
4.21 Probability density function $\wp(\kappa_1, \kappa_2)$ for the $\Lambda^0_b \to ph^-$ decays . . . 107
4.22 Probability density function $\wp(\kappa_1, \kappa_2)$ for the $B^0_{(s)} \to h^+h^{'-}$ decays . . . 108

5.1 Invariant mass of the simulated $B^0_{(s)} \to h^+h^{'-}$ signals . . . 110
5.2 Curvature residual as a function of the true curvature of the simulated events . . . 114
5.3 Curvature uncertainty as a function of the true curvature for simulated events . . . 115
5.4 Resolution function of the rescaled curvature of the simulated events . . . 116
5.5 λ and φ_0 resolution as a function of the true curvature of the simulated events . . . 117
5.6 d_0 resolution as a function of the true curvature of the simulated events . . . 118
5.7 Comparison between the official CDF Monte Carlo (MC) and the Fast Monte Carlo simulation (FMC) . . . 119
5.8 Comparison between Fast Monte Carlo simulation and the official CDF Monte Carlo simulation . . . 120
5.9 Radiative processes: real photon in the final state . . . 121

5.10 Radiative processes: virtual photon . . . 121
5.11 Differential decay rate for the *bremsstrahlung* process $H^0 \to P_1^+ P_2^- \gamma$ . . . 123
5.12 Illustration of the $D^{*+} \to D^0\pi^+ \to [K^-\pi^+]\pi^+$ decay chain . . . 125
5.13 Invariant $K\pi$-mass distribution of simulated $D^0 \to h^+h^{'-}$ . . . 127
5.14 Mass template of the $D^0 \to K^-\pi^+$ decays . . . 128
5.15 Check of the mass line shape template on $D^0 \to K^-\pi^+$ data sample . . . 131

6.1 Invariant mass of the simulated $B^0_{(s)} \to h^+h^{'-}$ signals . . . 136
6.2 Invariant mass of the simulated $B^0 \to h^+h^{'-}$ signals . . . 137
6.3 Invariant mass of the simulated $B^0_s \to h^+h^{'-}$ signals . . . 138
6.4 Invariant mass of the simulated $\Lambda^0_b \to ph^-$ signals . . . 139
6.5 Dependence of the mass resolution on the momentum observables . . . 142
6.6 Invariant $m_{\pi\pi}$-mass distribution of combinatorial background . . . 143
6.7 Invariant $\pi\pi$-mass distribution of simulated $B \to \rho\pi/\rho K$ decay modes . . . 144
6.8 $p_{\rm tot}$ versus α distribution for simulated $B^0_{(s)} \to h^+h^{'-}$ decays . . . 146
6.9 $p_{\rm tot}$ versus α distribution for background . . . 147

7.1 Illustration of the isolation cone . . . 152
7.2 Background-subtracted $p_{\rm T}(B)$-distributions of $B^0_{(s)} \to J/\psi X$ . . . 153
7.3 Illustration of the $B^0_{(s)} \to J/\psi X$ decay topologies . . . 154
7.4 Invariant mass distributions of $B^0_{(s)} \to J/\psi X$ candidates . . . 155
7.5 Mass distributions of $B^0_{(s)} \to J/\psi X$ candidates with $I(B) > 0.5$ and with $I(B) < 0.5$ . . . 157
7.6 Fit of the $B^0_{(s)} \to J/\psi X$ samples with $I(B) > 0.5$ and with $I(B) < 0.5$ . . . 158
7.7 Fit of the $B^0_{(s)} \to J/\psi X$ samples with $I(B) > 0.525$ and with $I(B) < 0.525$ . . . 159
7.8 Background-subtracted $p_{\rm T}(B)$-distribution of $B^0_{(s)} \to h^+h^{'-}$ and of $B^0_{(s)} \to J/\psi X$ decays and reweighting function . . . 161
7.9 Fit of the $B^0_{(s)} \to J/\psi X$ samples with $I(B) > 0.5$ and with $I(B) < 0.5$. $p_{\rm T}(B)$-spectrum reweighted . . . 163
7.10 Fit of the $B^0_{(s)} \to J/\psi X$ samples with $I(B) > 0.525$ and with $I(B) < 0.525$. $p_{\rm T}(B)$-spectrum reweighted . . . 164
7.11 Background-subtracted $p_{\rm T}(B)$-distribution in $B^0_{(s)} \to h^+h^{'-}$ decays with and without isolation requirement . . . 166
7.12 Background-subtracted $p_{\rm T}(B)$-distribution in $B^0_{(s)} \to J/\psi X$ decays . . . 166
7.13 Isolation efficiency as a function of $p_{\rm T}(B)$ . . . 167
7.14 Background-subtracted $p_{\rm T}(B)$-distribution in $B^0_{(s)} \to h^+h^{'-}$ decays with isolation requirements . . . 168
7.15 Isolation efficiency as function of the isolation cut . . . 169

8.1 Illustration of a Gaussian signal peak over a flat background . . . 173

8.2 Score functions for the $B^0_{(s)} \to h^+h'^-$ case 178

9.1 Fit projections onto the variable $m_{\pi\pi}$ 190
9.2 Fit projections onto the variables α, $p_{\rm tot}$, κ_1 191
9.3 Fit projections onto the variables κ_2, $\kappa_1+\kappa_2$, $\kappa_1 - id_2$ 192
9.4 Fit projections onto the variables α, $p_{\rm tot}$, κ_1 193
9.5 Fit projections onto the variables κ_2, $\kappa_1+\kappa_2$, $\kappa_1-\kappa_2$ 194
9.6 Fit projections onto the variables α, $p_{\rm tot}$, κ_1, κ_2, $\kappa_1+\kappa_2$, $\kappa_1-\kappa_2$ 195
9.7 Distribution of the pulls of the most relevant fit parameters 198
9.8 Distribution of the probability ratio 200
9.9 Distribution of the probability ratio 201

10.1 XFT efficiency as a function of $1/p_{\rm T}$ 210

11.1 Invariant $\pi\pi$-mass and KK-mass distribution of prompt $D^0 \to h^+h'^-$ 218
11.2 Invariant $\pi\pi$-mass distribution of prompt $D^0 \to h^+h'^-$ with the additional requirements: $m_{KK} > 1.93$ GeV/c^2 and $m_{\pi\pi} < 1.82$ GeV/c^2 219
11.3 Impact parameter distribution of D^0 candidates 220
11.4 Invariant D^0-mass distribution of simulated $D^0 \to K^-\pi^+$ decays with the additional requirement $m_{KK} > 1.93$ GeV/c^2 222
11.5 Invariant $\pi\pi$-mass distribution for a sample of simulated prompt $D^0 \to h^+h'^-$ decays as a function of momentum imbalance α 223
11.6 $p_{\rm tot}$ versus α distribution for simulated $D^0 \to K^-\pi^+$ decays and background 224
11.7 Fit projection onto $m_{\pi\pi}$, α and $p_{\rm tot}$ variables for different subsamples 226

12.1 Alternative $p_{\rm tot}$ versus α distribution for background 236
12.2 Invariant $\pi\pi$-mass distribution of the events passing the loose selection 237
12.3 Invariant $\pi\pi$-mass distribution of the events passing the tight selection 238
12.4 Distribution of observed residuals and systematic uncertainty 239
12.5 Pie-chart of systematic uncertainties I 247
12.6 Pie-chart of systematic uncertainties II 248
12.7 Pie-chart of systematic uncertainties III 249
12.8 Likelihood ratio distribution for each rare mode 252
12.9 Distribution of the number of events for the rare modes from pseudo-experiments . . . 253

13.1 Current measurements of $\mathcal{A}_{\rm CP}(B^0 \to K^+\pi^-)$ reported on HFAG 260
13.2 Expectation for $\mathcal{A}_{\rm CP}(B^0_s \to K^-\pi^+)$ 264
13.3 Current measurements of $\mathcal{B}(B^0 \to \pi^+\pi^-)$ reported on HFAG 265
13.4 Contours in the γ–d plane 267

List of Tables

1.1 Summary of branching fractions of $B^0_{(s)} \to h^+h^{'-}$ 29
1.2 The CP-averaged branching ratios ($\times 10^{-6}$) of $B^0_{(s)} \to h^+h^{'-}$ decays and the direct CP asymmetry (in %) of the $B^0 \to K^+\pi^-$ and $B^0_s \to K^-\pi^+$ decays 33

3.1 Summary of the trigger requirements 66
3.2 Off-line trigger confirmation selection 69
3.3 Summary of the optimized selections 72

4.1 $\mathcal{M}^2(\alpha, p_{\rm tot})$ for $B^0_{(s)} \to h^+h^{'-}$ and $\Lambda^0_b \to ph^-$ decays 86
4.2 Off-line selection for $\Lambda^0 \to p\pi^-$ 94

5.1 Fit results on the invariant mass distribution of the simulated modes 111
5.2 Summary of the input masses in the simulation 111
5.3 Mean value $\hat{\mu}$ of the invariant mass in simulated events 112
5.4 The $D^{*+} \to D^0\pi^+ \to [K^-\pi^+]\pi^+$ selection 126
5.5 Parameterization of the invariant $K\pi$-mass of the $D^0 \to K^-\pi^+$ simulated events . . . 128
5.6 Check on data $D^0 \to K^-\pi^+$ 129

7.1 The $B^0_{(s)} \to J/\psi X$ selection 154
7.2 Fit results ($I(B) > 0.5$ and $I(B) > 0.525$) in the $B^0_{(s)} \to J/\psi X$ sample 160
7.3 Isolation efficiency as $p_{\rm T}(B)$ function. 160
7.4 Isolation efficiencies ($I(B) > 0.5$ and $I(B) > 0.525$) of the $B^0_{(s)} \to J/\psi X$ sample. $p_{\rm T}(B)$-spectrum reweighted 162
7.5 Isolation efficiency as $p_{\rm T}(B)$ function. 167
7.6 Isolation efficiency for different requirements $I(B) > I_{\rm cut}$. 169

8.1 Quantities used in the optimization and results 180

9.1 Results of fit of composition 185
9.2 Physics observables 186

9.3 Fit yields . . . 187
9.4 Results of the Gaussian fit of the pull distributions . . . 196
9.5 Additional fits . . . 202

10.1 Summary of the input lifetimes in the simulation . . . 208

11.1 Summary of selection for $D^0 \to h^+h'^-$ decays . . . 217
11.2 $\mathcal{M}^2(\alpha, p_{\rm tot})$ for $D^0 \to h^+h'^-$ decays . . . 223
11.3 Results of kinematic-only fits on prompt $D^0 \to K^-\pi^+$ . . . 225
11.4 Results of PID-only fits on prompt $D^0 \to K^-\pi^+$ . . . 228

12.1 Summary of the systematic uncertainties for observables extracted using the loose selection . . . 243
12.2 Summary of the systematic uncertainties for observables related to $B_s^0 \to K^-\pi^+$ mode 244
12.3 Summary of the systematic uncertainties for observables related to other rare modes extracted using the tight selection . . . 245
12.4 Summary of the systematic uncertainties for the yield measurements of rare modes . . 246
12.5 Significance of the rare modes with statistical approach . . . 250
12.6 Significance of the rare modes . . . 251

13.1 Results . . . 256

Introduction

Non-leptonic two-body charmless decays of neutral B mesons ($B^0_{(s)} \to h^+h^{'-}$, where h is a charged pion or kaon) are very interesting for the understanding of flavor physics and CP violation mechanism in the b-meson sector. Their rich phenomenology offers several opportunities to explore and constrain the parameters of the quark-mixing matrix (i. e., Cabibbo-Kobayashi-Maskawa, CKM). These processes allow to access the phase of the V_{ub} element of the CKM matrix (γ angle), and to test the reliability of the Standard Model and hadronic calculations. The presence of New Physics can be revealed by its impact on their decay amplitudes, where new particles may enter in penguin diagrams. The $B^0 \to K^+\pi^-$ is the first process involving the b quark where direct CP violation has been observed.

The measurements obtained at e^+e^- colliders (ARGUS, CLEO, LEP, and more recently, *BABAR* and Belle experiments) already provided a wealth of results for B^0 and B^+ mesons.

The upgraded Collider Detector at the Fermilab Tevatron (CDF II), with its large production of b-hadrons is in principle an ideal environment for studying these rare modes. In addition to providing further large samples of B^0 and B^+ mesons in a different experimental environment, it provides the exciting opportunity of studying the charmless decays of other b-hadrons that are unaccessible (or much less accessible) in other experiments. A variety of techniques have been proposed to constrain the CKM parameters or probe effects of New Physics [5, 6, 7, 8] exploiting a combination of observables from B^0_s and B^0 , B^+ mesons.

The $B^0_s \to K^+K^-$ decay, observed for the first time in the previous version of the analysis presented in this thesis [1], offers several and interesting strategies to extract useful information from the comparison between its observables and those of its U-spin related partner $B^0 \to \pi^+\pi^-$ [5]. By combining the information from measurements of rates of $B^0 \to \pi^+\pi^-$ and $B^0_s \to K^+K^-$ decays it is possible to constrain the hadronic uncertainty to determine the phase γ. It will be very interesting to compare this measurement, where the contribution of penguin amplitudes is large, to a theoretically cleaner (tree level) determination of γ from the $B \to DK$ decays [9, 10]. A significant discrepancy would be an hint of New Physics contribution in penguin amplitudes. The power of this technique will increase considerably when the comparison will be performed between the time-dependent CP violating asymmetries.

Another interesting example in this category consists of combining the information of rates and direct CP asymmetries of U-spin–related decays $B^0 \to K^+\pi^-$ and $B^0_s \to K^-\pi^+$ [7, 8]. This allows a stringent test of the Standard Model origin of the $\mathcal{O}(10\%)$ direct CP asymmetry observed in $B^0 \to K^+\pi^-$ [11], which is not matched by a similar effect in the $B^+ \to K^+\pi^0$ decay, which differs only by the spectator quark. This raised discussions about a possible exotic source for the CP vi-

olation in the $B^0 \to K^+\pi^-$ decay [12, 13, 14]. Any significant disagreement between the measured partial rate asymmetries of strange and non-strange b-meson $K\pi$ decays should be strong indication of New Physics.

The $B_s^0 \to K^-\pi^+$ is still unobserved and the current experimental upper limit $\mathcal{B}(B_s^0 \to K^-\pi^+) < 5.6 \times 10^{-6}$ @ 90% CL [1] from CDF is very close to (sometimes lower than) the current theoretical expectations [15, 16, 17]. The comparison of this branching fraction, sensitive to CKM angle values of α and γ [19], with theoretical predictions provides valuable information for tuning the phenomenological models of hadronic $B_{(s)}^0$ meson decays and for optimizing the choice of their input parameters. Therefore, in this context the measurement of the decay rate of the $B_s^0 \to K^-\pi^+$ and the measurement of its direct CP asymmetry becomes crucial.

The amplitudes of penguin-annihilation and exchange diagrams, in which all initial-state quarks undergo a transition, are difficult to predict with current phenomenological models. In general they may carry different CP-violating and CP-conserving phases with respect to the leading processes, thereby influencing the determination of CKM-related parameters. The $B^0 \to K^+K^-$ and $B_s^0 \to \pi^+\pi^-$ decays proceed only through these kinds of diagrams. A simultaneous measurement of their decay rates (or improved constraints on them) would provide valuable estimates of the magnitude of these contributions [18].

Simultaneous measurements of $B_{(s)}^0 \to h^+h^{'-}$ observables, in most cases, exploit the U-spin symmetries to partially cancel out or constrain hadronic uncertainties and probe the electroweak and QCD structure. U-spin symmetry is not exactly conserved in the Standard Model and the magnitude of its violation is not precisely known but most authors estimate a $\mathcal{O}(10\%)$ effect. The $B_{(s)}^0 \to h^+h^{'-}$ system is a privileged laboratory since it offers the simultaneous opportunities of using U-spin assumptions and, at the same time, of checking their validity by measuring the symmetry breaking-size, from the interplaying of several U-spin–related observables.

This rich set of measurements requires however to overcome several experimental difficulties: reconstruction of rare signals ($\mathcal{B}(B_{(s)}^0 \to h^+h^{'-}) \sim \mathcal{O}(10^{-5})$) hidden by an enormous background; separation of different overlapping decay modes with similar kinematics based on limited particle identification capabilities; and accurate control of efficiencies of complex event selections. The techniques to deal with these experimental issues are the main subject of this thesis. This thesis describes how these issues have been solved in the analysis of a sample of $B_{(s)}^0 \to h^+h^{'-}$ decays collected by CDF experiment, corresponding to an integrated luminosity of 1 fb^{-1}. This work required substantial refinements with respect to the early $B_{(s)}^0 \to h^+h^{'-}$ analysis based on $\int \mathcal{L}dt = 180$ pb^{-1}[1] and provides a significantly improved precision and many new results. The precision achieved in the B^0 sector now matches the best existing measurements, while the new results obtained in the B_s^0 sector are unique to this work, and represent significant steps into a previously unexplored territory.

The main results are:

- A precise measurement of direct CP asymmetry in the $B^0 \to K^+\pi^-$ decays and of relative branching fraction of $B^0 \to \pi^+\pi^-$ decays.
- A precise measurement of the $B_s^0 \to K^+K^-$ relative branching fraction, which provides one the first experimental insight on the magnitude of the SU(3) breaking. This is a necessary test and ingredient for the U-spin–based method of extracting the CKM parameters, like γ angle [5, 20].

- First observation of the $B_s^0 \to K^-\pi^+$ decay mode and measurement of its relative branching fraction and direct CP-violating asymmetry allowing the first test of [7, 8].
- First observation of the $\Lambda_b^0 \to pK^-$ and $\Lambda_b^0 \to p\pi^-$ decay mode, which were included in the analysis as possible physics backgrounds to the other channels. The branching fractions and direct CP asymmetries of these modes will also provide useful information in the future.
- Improved upper limits on the relative branching fractions of $B^0 \to K^+K^-$ and $B_s^0 \to \pi^+\pi^-$ modes, which receive contribution from penguin-annihilation amplitudes. These measurements have implications for both the knowledge of CKM sector of the Standard Model and the phenomenology of non-perturbative hadronic contributions in non-leptonic $B_{(s)}^0$ meson decays.

The thesis is organized as follows.

Chapter 1 describes the theoretical framework of non-leptonic $B_{(s)}^0 \to h^+h'^-$ decays, with a simple overview of the CP violation mechanism within the Standard Model and of the most used phenomenological approaches in the evaluation of strong interaction contributions. The chapter contains also a review of the theoretical expectations and the current experimental measurements along with a discussion about the importance of studying such decays.

Chapter 2 contains a general description of the Tevatron collider and of the CDF II detector.

Chapter 3 is devoted to the description of the data sample used for the measurement and the method used in extracting the signal from the background. Particular attention is dedicated to the on-line trigger selection, which is crucial to collect a sample enriched in $B_{(s)}^0 \to h^+h'^-$ decays.

Chapter 4 shows how the information from kinematics and particle identification was used to achieve a statistical discrimination amongst modes to extract individual measurements. The available resolutions in mass or in particle identification are separately insufficient for an event-by-event separation of $B_{(s)}^0 \to h^+h'^-$ modes. The choice of observables and the technique used to combine them is an important and innovative aspect of the analysis described in this thesis.

Chapter 5 is devoted to the accurate determination of the invariant mass lineshape. This is a crucial ingredient for resolving overlapping mass peaks. This chapter details all resolution effects with particular attention at the tails due to the emission of low-energy photons from charged kaons and pions in the final state (FSR). For the first time the effect of FSR has been accurately accounted for in a CDF analysis.

Chapter 6 describes how kinematic and PID information, discussed in *chap. 4* and *chap. 5* were combined in a maximum Likelihood fit to statistically determine the composition of the $B_{(s)}^0 \to h^+h'^-$ sample. This kinematics-PID combined fit has been developed and performed for the first time at CDF in the analysis presented in this thesis and this methodology was later inherited by several other analyses.

Chapter 7 is devoted to the study of the isolation variable, which is a crucial handle to enhance the signal-to-background ratio in the off-line selection. It exploits the property that the b-hadrons tend to carry a larger fraction of the transverse momentum of the particles produced in the fragmentation, with respect to lighter hadrons. Since the simulators do not accurately reproduce the fragmentation processes, this chapter is devoted to the study of the control data sample of $B_{(s)}^0 \to J/\psi X$ decays to probe the characteristics of this variable.

Chapter 8 describes an innovative procedure used to optimize the selection to minimize the statistical uncertainty on the quantities one wishes to measure. The procedure is based on the fit of composition described in *chap. 6*.

Chapter 9 reports the results of the fit of composition described in *chap. 6* and the cross-checks performed to verify the goodness of the fit of composition.

In order to translate the parameters returned from the fit into physics measurements the relative efficiency corrections between the various decay modes need to be applied. *Chapter 10* is devoted to the description of these corrections.

Chapter 11 describes the measurement of the detector-induced charge asymmetry between positively and negatively charged kaons and pions, due to their different probability of strong interaction in the tracker material using the real data. This allows to extract the acceptance correction factor for the CP asymmetries measurement without any external inputs from the simulation, and to perform a powerful check of whole analysis.

Chapter 12 describes the main sources of systematic uncertainties and the method used to evaluate the significance of the results on rare modes. The final results of the measurements and their interpretation are discussed in *chap. 13*.

I personally presented the results of this thesis for the first time at "*The 11th International Conference on B-Physics at Hadron Machines*" (BEAUTY 2006) held to Oxford (UK) from September $25 - 29^{th}$, 2006 (published in Nuclear Physics **B** (Proc. Suppl.) [2][1]). They are currently under internal CDF review for publication.

[1]The measurements quoted in [2] are slightly outdated with respect to those presented in this thesis.

Chapter 1

CP violation and charmless B decays

In this chapter we focus our attention on the theoretical frame. In particular we discuss the connections between CP violation in the Standard Model and the charmless two body B decays $B^0_{(s)} \to h^+h'^-$ where h is a charged pion or kaon [21]. These decays are a privileged laboratory to improve our understanding of the CP violation mechanism in the Standard Model and, simultaneously, to probe possible effects of New Physics.

1.1 Introduction

The CP violation, i.e. the non-invariance of the weak interactions with respect to a combined charge-conjugation (C) and parity (P) transformation, dates back to year 1964, when this phenomenon was discovered through the observation of $K_{\rm L} \to \pi^+\pi^-$ decays [22], which exhibit a branching ratio at the 10^{-3} level. This surprising effect is a manifestation of *indirect* CP violation, which arises from the fact that the mass eigenstates $K_{\rm L,S}$ of the neutral kaon system, which shows mixing, are not eigenstates of the CP operator. The $K_{\rm L}$ state is governed by the CP-odd eigenstate, but also contains a small fraction of the CP-even eigenstate, which may decay through CP-conserving interactions into the $\pi^+\pi^-$ final state. These CP-violating effects are described by the observable:

$$\varepsilon_K = (2.280 \pm 0.013) \times 10^{-3} \times e^{i\pi/4}. \tag{1.1}$$

CP-violating effects may also arise at the decay-amplitude level, thereby yielding *direct* CP violation. This phenomenon, which leads to a non-vanishing value of the quantity $\mathrm{Re}(\varepsilon'_K/\varepsilon_K)$, was established in 1999 by the NA48 (CERN) and KTeV (FNAL) collaborations [23]; the measured values are:

$$\mathrm{Re}(\varepsilon'_K/\varepsilon_K) = \begin{cases} (14.7 \pm 2.2) \times 10^{-4} & \text{(NA48 [24])} \\ (20.7 \pm 2.8) \times 10^{-4} & \text{(KTeV [25]).} \end{cases} \tag{1.2}$$

The understanding of CP violation, and therefore of flavour physics, is particularly interesting since "New Physics", i.e. physics lying beyond the Standard Model, typically leads to new sources of flavour

and CP violation. Furthermore, the origin of the fermion masses, flavour mixing, CP violation etc. lies completely in the dark and is expected to involve New Physics, too. Interestingly, CP violation offers also a link to cosmology. One of the key features of our Universe is the cosmological baryon asymmetry of $\mathcal{O}(10^{-10})$. As was pointed out by Sakharov [26], the necessary conditions for the generation of such an asymmetry include also the requirement that elementary interactions violate CP (and C). Model calculations of the baryon asymmetry indicate, however, that the CP violation present in the Standard Model seems to be too small to generate the observed asymmetry. On the one hand, the required new sources of CP violation could be associated with very high energy scales, as in "leptogenesis", where new CP-violating effects appear in decays of heavy Majorana neutrinos. On the other hand, new sources of CP violation could also be accessible in the laboratory, as they arise naturally when going beyond the Standard Model.

Before searching for New Physics, it is essential to understand first the picture of flavour physics and CP violation arising in the framework of the Standard Model, where the Cabibbo–Kobayashi–Maskawa (CKM) matrix – the quark-mixing matrix – plays a key rôle [27, 28]. The corresponding phenomenology is extremely rich. In this decade, there are huge experimental efforts to further explore CP violation and the quark-flavour sector of the Standard Model. In these studies, the main actor is the B-meson system, characterized by the following valence-quark contents:

$$\begin{array}{llll} B^+ \sim u\bar{b}, & B_c^+ \sim c\bar{b}, & B_d^0 \sim d\bar{b}, & B_s^0 \sim s\bar{b}, \\ B^- \sim \bar{u}b, & B_c^- \sim \bar{c}b, & \overline{B}{}_d^0 \sim \bar{d}b, & \overline{B}{}_s^0 \sim \bar{s}b. \end{array} \tag{1.3}$$

In contrast to the charged B mesons, their neutral counterparts B_q^0 ($q \in \{d, s\}$) show – in analogy to K^0–$\bar{K}^0$ mixing – the phenomenon of B_q^0–$\overline{B}{}_q^0$ mixing. The subscript d in the B_d^0 and $\overline{B}{}_d^0$ is often omitted ($B^0 \equiv B_d^0$ and $\overline{B}{}^0 \equiv \overline{B}{}_d^0$) through this thesis. In 2001, CP-violating effects were discovered in B decays with the help of $B^0 \to J/\psi K_{\rm S}$ modes by the *BABAR* and Belle Collaborations [29], representing the first observation of CP violation outside the kaon system. This particular kind of CP violation, which is by now well established, originates from the interference between B^0–$\overline{B}{}^0$ mixing and $B^0 \to J/\psi K_{\rm S}$, $\overline{B}{}^0 \to J/\psi K_{\rm S}$ decay processes, and is referred to as "mixing-induced" CP violation. In the summer of 2004, also direct CP violation was observed in the $B^0 \to K^+\pi^-$ decay [11], thereby complementing the measurement of a non-zero value of $\mathrm{Re}(\varepsilon'_K/\varepsilon_K)$ [24, 25].

In general, the key problem for the theoretical interpretation is related to strong interactions, i.e. to "hadronic" uncertainties. In the B-meson system, there are various strategies to eliminate the hadronic uncertainties in the exploration of CP violation (simply speaking, there are many B decays). Moreover, we may also search for relations and/or correlations that hold in the Standard Model but could well be spoiled by New Physics.

In this chapter we will focus our attention on the privileged laboratory provided by the $B_{(s)}^0 \to h^+h'^-$ decays. When the distinction between the different decay modes ($B^0 \to \pi^+\pi^-$, $B^0 \to K^+\pi^-$, $B_s^0 \to K^-\pi^+$, $B_s^0 \to K^+K^-$, etc.) is not relevant, the expression $B_{(s)}^0 \to h^+h'^-$ (h, $h' = \pi$ or K) is used to collectively indicate all of them [1]. Unless otherwise stated, throughout this thesis, C-conjugate modes are implied and branching fractions ($\mathcal{B}$) indicate CP-averages, that is,

$$\mathcal{B}(B \to f) \equiv \frac{\Gamma(B \to f) + \Gamma(\overline{B} \to \overline{f})}{2\Gamma_B},$$

[1] The same assumption is valid for the $\Lambda_b^0 \to ph^-$ decays (h, $h' = \pi$ or K).

where $\Gamma(B \to f)$ is the partial decay-width of a particle B into a final state f, Γ_B represents the natural width.

1.2 CKM matrix and CP violation

In the framework of the Standard Model of electroweak interactions, which is based on the spontaneously broken gauge group

$$SU(2)_{\rm L} \times U(1)_{\rm Y} \xrightarrow{\rm SSB} U(1)_{\rm em}, \tag{1.4}$$

CP-violating effects originate from the charged-current interactions of quarks, having the structure

$$D \to U W^- . \tag{1.5}$$

Here $D \in \{d, s, b\}$ and $U \in \{u, c, t\}$ denote down- and up-type quark flavours, respectively, whereas the W^- is the usual $SU(2)_{\rm L}$ gauge boson. From a phenomenological point of view, it is convenient to collect the generic "coupling strengths" V_{UD} of the charged-current processes in eq. (1.5) in the Cabibbo–Kobayashi–Maskawa (CKM) matrix [27, 28]:

$$\hat{V}_{\rm CKM} = \begin{pmatrix} V_{ud} & V_{us} & V_{ub} \\ V_{cd} & V_{cs} & V_{cb} \\ V_{td} & V_{ts} & V_{tb} \end{pmatrix} . \tag{1.6}$$

From a theoretical point of view, this matrix connects the electroweak states (d', s', b') of the down, strange and bottom quarks with their mass eigenstates (d, s, b) through the following unitary transformation:

$$\begin{pmatrix} d' \\ s' \\ b' \end{pmatrix} = \begin{pmatrix} V_{ud} & V_{us} & V_{ub} \\ V_{cd} & V_{cs} & V_{cb} \\ V_{td} & V_{ts} & V_{tb} \end{pmatrix} \cdot \begin{pmatrix} d \\ s \\ b \end{pmatrix} . \tag{1.7}$$

$\hat{V}_{\rm CKM}$ is a *unitary* matrix. This feature ensures the absence of flavour-changing neutral-current (FCNC) processes at the tree level in the Standard Model, and is hence at the basis of the famous Glashow–Iliopoulos–Maiani (GIM) mechanism [30]. If we express the non-leptonic charged-current interaction Lagrangian in terms of the mass eigenstates appearing in (1.7), we arrive at

$$\mathcal{L}_{\rm int}^{\rm CC} = -\frac{g_2}{\sqrt{2}} \begin{pmatrix} \bar{u}_{\rm L}, & \bar{c}_{\rm L}, & \bar{t}_{\rm L} \end{pmatrix} \gamma^\mu \, \hat{V}_{\rm CKM} \begin{pmatrix} d_{\rm L} \\ s_{\rm L} \\ b_{\rm L} \end{pmatrix} W_\mu^\dagger \; + \; \text{h.c.}, \tag{1.8}$$

where the gauge coupling g_2 is related to the gauge group $SU(2)_{\rm L}$, and the $W_\mu^{(\dagger)}$ field corresponds to the charged W bosons. Looking at the interaction vertices following from eq. (1.8), we observe that the elements of the CKM matrix describe the generic strengths of the associated charged-current processes, as we have noted above.

Figure 1.1 shows the $D \to U W^-$ vertex and its CP conjugate. Since the corresponding CP transformation involves the replacement

$$V_{UD} \xrightarrow{\mathcal{CP}} V_{UD}^* , \tag{1.9}$$

CP violation could – in principle – be accommodated in the Standard Model through complex phases in the CKM matrix. The crucial question in this context is, whether we may actually have physical complex phases in that matrix.

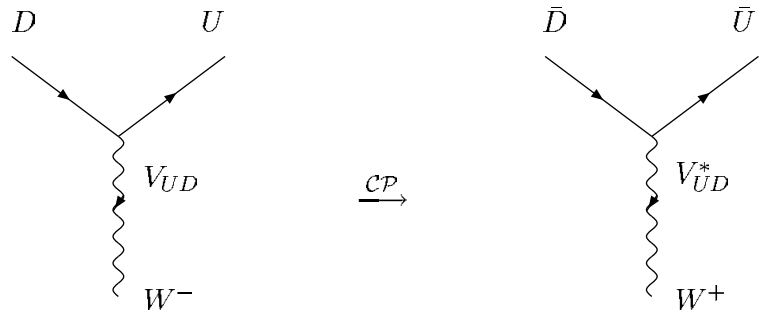


Figure 1.1: CP-conjugate charged-current quark-level interaction processes in the Standard Model.

1.2.1 Phase Structure of the CKM Matrix

We have the freedom to redefine the up- and down-type quark fields in the following manner:

$$U \to \exp(i\xi_U)U, \quad D \to \exp(i\xi_D)D. \tag{1.10}$$

If we apply such transformations to eq. (1.8), the invariance of the charged-current interaction Lagrangian implies the following phase transformations of the CKM matrix elements:

$$V_{UD} \to \exp(i\xi_U)V_{UD}\exp(-i\xi_D). \tag{1.11}$$

Using these transformations to eliminate unphysical phases, it can be shown that the parametrization of the general $N \times N$ quark-mixing matrix, where N denotes the number of fermion generations, involves the following parameters:

$$\underbrace{\frac{1}{2}N(N-1)}_{\text{Euler angles}} + \underbrace{\frac{1}{2}(N-1)(N-2)}_{\text{complex phases}} = (N-1)^2. \tag{1.12}$$

If we apply this expression to the case of $N = 2$ generations, we observe that only one rotation angle – the Cabibbo angle $\theta_{\rm C}$ [27] – is required for the parametrization of the 2×2 quark-mixing matrix, which can be written in the following form:

$$\hat{V}_{\rm C} = \begin{pmatrix} \cos\theta_{\rm C} & \sin\theta_{\rm C} \\ -\sin\theta_{\rm C} & \cos\theta_{\rm C} \end{pmatrix}, \tag{1.13}$$

where $\sin\theta_{\rm C} = 0.22$ can be determined from $K \to \pi\ell\bar{\nu}$ decays. On the other hand, for $N = 3$ generations, the parameterization of the corresponding 3×3 quark-mixing matrix involves three Euler-type angles and one *complex* phase. This complex phase allows to accommodate CP violation

in the Standard Model, as was pointed out by Kobayashi and Maskawa in 1973 [28]. The corresponding picture is referred to as the Kobayashi–Maskawa (KM) mechanism of CP violation.

A "standard parametrization" for the three-generation CKM matrix takes the following form:

$$\hat{V}_{\rm CKM} = \begin{pmatrix} c_{12}c_{13} & s_{12}c_{13} & s_{13}e^{-i\delta_{13}} \\ -s_{12}c_{23} - c_{12}s_{23}s_{13}e^{i\delta_{13}} & c_{12}c_{23} - s_{12}s_{23}s_{13}e^{i\delta_{13}} & s_{23}c_{13} \\ s_{12}s_{23} - c_{12}c_{23}s_{13}e^{i\delta_{13}} & -c_{12}s_{23} - s_{12}c_{23}s_{13}e^{i\delta_{13}} & c_{23}c_{13} \end{pmatrix}, \tag{1.14}$$

where $c_{ij} \equiv \cos\theta_{ij}$ and $s_{ij} \equiv \sin\theta_{ij}$. Performing appropriate redefinitions of the quark-field phases, the real angles θ_{12}, θ_{23} and θ_{13} can all be made to lie in the first quadrant. The advantage of this parametrization is that the generation labels $i, j = 1, 2, 3$ are introduced in such a manner that the mixing between two chosen generations vanishes if the corresponding mixing angle θ_{ij} is set to zero. In particular, for $\theta_{23} = \theta_{13} = 0$, the third generation decouples, and the 2×2 submatrix describing the mixing between the first and second generations takes the same form as (1.13).

1.2.2 Further Requirements for CP Violation

As we have just seen, in order to accommodate CP violation within the Standard Model framework through a complex phase in the CKM matrix, at least three generations of quarks are required. However, this feature is not sufficient for observable CP-violating effects. To this end, further conditions have to be satisfied, which can be summarized as follows [31]:

$$(m_t^2 - m_c^2)(m_t^2 - m_u^2)(m_c^2 - m_u^2)(m_b^2 - m_s^2)(m_b^2 - m_d^2)(m_s^2 - m_d^2) \times J_{\rm CP} \neq 0, \tag{1.15}$$

where

$$J_{\rm CP} = |{\rm Im}(V_{i\alpha}V_{j\beta}V_{i\beta}^*V_{j\alpha}^*)| \quad (i \neq j,\, \alpha \neq \beta)\,. \tag{1.16}$$

The mass factors in eq. (1.15) are related to the fact that the CP-violating CKM phase could be eliminated through an appropriate unitary transformation of the quark fields if any two quarks with the same charge had the same mass. Consequently, the origin of CP violation is closely related to the "flavour problem" in elementary particle physics, and it cannot be understood in a deeper way, unless we have fundamental insights into the hierarchy of quark masses and the number of fermion generations.

The second element of eq. (1.15), the "Jarlskog parameter" $J_{\rm CP}$ [31], can be interpreted as a measure of the strength of CP violation in the Standard Model. It does not depend on the chosen quark-field parametrization, i.e. it is invariant under (1.11), and the unitarity of the CKM matrix implies that all the combinations $|{\rm Im}(V_{i\alpha}V_{j\beta}V_{i\beta}^*V_{j\alpha}^*)|$ are equal to one another. Using the standard parameterization of the CKM matrix introduced in (1.14), we obtain

$$J_{\rm CP} = s_{12}s_{13}s_{23}c_{12}c_{23}c_{13}^2 \sin\delta_{13}. \tag{1.17}$$

The experimental information on the CKM parameters implies $J_{\rm CP} = \mathcal{O}(10^{-5})$, so that CP-violating phenomena are hard to observe. However, new complex couplings are typically present in scenarios for New Physics. Such additional sources for CP violation could be detected through flavour experiments.

1.2.3 Experimental Information on $|V_{\rm CKM}|$

In order to determine the magnitudes $|V_{ij}|$ of the elements of the CKM matrix, we can use the following tree-level processes:

- Nuclear beta decays, neutron decays $\Rightarrow |V_{ud}|$.
- $K \to \pi \ell \bar{\nu}$ decays $\Rightarrow |V_{us}|$.
- ν production of charm off valence d quarks $\Rightarrow |V_{cd}|$.
- Charm-tagged W decays (as well as ν production and semileptonic D decays) $\Rightarrow |V_{cs}|$.
- Exclusive and inclusive $b \to c \ell \bar{\nu}$ decays $\Rightarrow |V_{cb}|$.
- Exclusive and inclusive $b \to u \ell \bar{\nu}$ decays $\Rightarrow |V_{ub}|$.
- $\bar{t} \to \bar{b} \ell \bar{\nu}$ processes $\Rightarrow$ (crude direct determination of) $|V_{tb}|$.

If we use the corresponding experimental information, together with the CKM unitarity condition, and we assume that there are only three generations, we obtain the following 90% C.L. limits for the $|V_{ij}|$ elements [32]:

$$|\hat{V}_{\rm CKM}| = \begin{pmatrix} 0.9739\text{–}0.9751 & 0.221\text{–}0.227 & 0.0029\text{–}0.0045 \\ 0.221\text{–}0.227 & 0.9730\text{–}0.9744 & 0.039\text{–}0.044 \\ 0.0048\text{–}0.014 & 0.037\text{–}0.043 & 0.9990\text{–}0.9992 \end{pmatrix}. \tag{1.18}$$

Figure 1.2 illustrates the resulting hierarchy of the strengths of the charged-current quark-level processes: transitions within the same generation are governed by the CKM matrix elements of $\mathcal{O}(1)$, those between the first and the second generation are suppressed by CKM factors of $\mathcal{O}(10^{-1})$, those between the second and the third generation are suppressed by $\mathcal{O}(10^{-2})$, and the transitions between the first and the third generation are even suppressed by CKM factors of $\mathcal{O}(10^{-3})$. In the standard parameterization (1.14), this hierarchy is reflected by

$$s_{12} = 0.22 \gg s_{23} = \mathcal{O}(10^{-2}) \gg s_{13} = \mathcal{O}(10^{-3}). \tag{1.19}$$

1.2.4 Wolfenstein Parameterization of the CKM Matrix

For phenomenological applications, it would be useful to have a parameterization of the CKM matrix that makes the hierarchy arising in (1.18) – and illustrated in fig. 1.2 – explicit [33]. In order to derive such a parameterization, we introduce a set of new parameters, λ, A, ρ and η, by imposing the following relations:

$$s_{12} \equiv \lambda = 0.22, \quad s_{23} \equiv A\lambda^2, \quad s_{13} e^{-i\delta_{13}} \equiv A\lambda^3(\rho - i\eta). \tag{1.20}$$

If we now go back to the standard parameterization (1.14), we obtain a parameterization of the CKM matrix as a function of λ (and A, ρ, η), which allows to expand each CKM element in powers of the

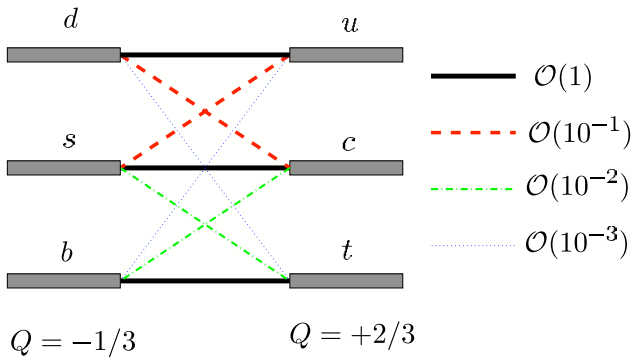


Figure 1.2: Hierarchy of the quark transitions mediated through charged-current processes.

small parameter λ. If we neglect terms of $\mathcal{O}(\lambda^4)$, we obtain the famous "Wolfenstein parameterization" [33]:

$$\hat{V}_{\rm CKM} = \begin{pmatrix} 1-\frac{1}{2}\lambda^2 & \lambda & A\lambda^3(\rho - i\eta) \\ -\lambda & 1-\frac{1}{2}\lambda^2 & A\lambda^2 \\ A\lambda^3(1-\rho-i\eta) & -A\lambda^2 & 1 \end{pmatrix} + \mathcal{O}(\lambda^4), \tag{1.21}$$

which makes the hierarchical structure of the CKM matrix very transparent and is an important tool for phenomenological considerations.

For several applications, next-to-leading order corrections in λ play an important rôle. Using the exact parameterization following from (1.14) and (1.20), they can be calculated straightforwardly by expanding each CKM element to the desired accuracy in λ:

$$\begin{gathered} V_{ud} = 1 - \frac{1}{2}\lambda^2 - \frac{1}{8}\lambda^4 + \mathcal{O}(\lambda^6), \quad V_{us} = \lambda + \mathcal{O}(\lambda^7), \quad V_{ub} = A\lambda^3(\rho - i\,\eta), \\ V_{cd} = -\lambda + \frac{1}{2}A^2\lambda^5\left[1 - 2(\rho + i\eta)\right] + \mathcal{O}(\lambda^7), \\ V_{cs} = 1 - \frac{1}{2}\lambda^2 - \frac{1}{8}\lambda^4(1 + 4A^2) + \mathcal{O}(\lambda^6), \\ V_{cb} = A\lambda^2 + \mathcal{O}(\lambda^8), \quad V_{td} = A\lambda^3\left[1 - (\rho + i\eta)\left(1 - \frac{1}{2}\lambda^2\right)\right] + \mathcal{O}(\lambda^7), \\ V_{ts} = -A\lambda^2 + \frac{1}{2}A(1 - 2\rho)\lambda^4 - i\eta A\lambda^4 + \mathcal{O}(\lambda^6), \quad V_{tb} = 1 - \frac{1}{2}A^2\lambda^4 + \mathcal{O}(\lambda^6). \end{gathered} \tag{1.22}$$

It should be noted that

$$V_{ub} \equiv A\lambda^3(\rho - i\eta) \tag{1.23}$$

receives *by definition* no power corrections in λ within this prescription. If we introduce the generalized Wolfenstein parameters

$$\bar{\rho} \equiv \rho\left(1 - \frac{1}{2}\lambda^2\right), \quad \bar{\eta} \equiv \eta\left(1 - \frac{1}{2}\lambda^2\right), \tag{1.24}$$

we may simply write, up to corrections of $\mathcal{O}(\lambda^7)$,

$$V_{td} = A\lambda^3(1 - \bar{\rho} - i\,\bar{\eta}). \tag{1.25}$$

Moreover, we have to an excellent accuracy

$$V_{us} = \lambda \quad \text{and} \quad V_{cb} = A\lambda^2, \tag{1.26}$$

as these quantities receive, respectively, only corrections at the λ^7 and λ^8 level.In comparison with other generalizations of the Wolfenstein parameterization found in the literature, the advantage of (1.22) is the absence of relevant corrections to V_{us} and V_{cb}, and that V_{ub} and V_{td} take forms similar to those in (1.21). As far as the Jarlskog parameter introduced in (1.16) is concerned, we obtain the simple expression

$$J_{\rm CP} = \lambda^6 A^2 \eta, \tag{1.27}$$

which should be compared with (1.17).

1.2.5 Unitarity Triangles of the CKM Matrix

The unitarity of the CKM matrix, which is described by

$$\hat{V}_{\rm CKM}^{\dagger} \cdot \hat{V}_{\rm CKM} = \hat{1} = \hat{V}_{\rm CKM} \cdot \hat{V}_{\rm CKM}^{\dagger}, \tag{1.28}$$

leads to a set of 12 equations, consisting of 6 normalization and 6 orthogonality relations. The latter can be represented as 6 triangles in the complex plane, all having the same area, $2A_\Delta = J_{\rm CP}$. Let us now have a closer look at these relations: those describing the orthogonality of different columns of the CKM matrix are given by

$$\underbrace{V_{ud}V_{us}^*}_{\mathcal{O}(\lambda)} + \underbrace{V_{cd}V_{cs}^*}_{\mathcal{O}(\lambda)} + \underbrace{V_{td}V_{ts}^*}_{\mathcal{O}(\lambda^5)} = 0 \tag{1.29}$$

$$\underbrace{V_{us}V_{ub}^*}_{\mathcal{O}(\lambda^4)} + \underbrace{V_{cs}V_{cb}^*}_{\mathcal{O}(\lambda^2)} + \underbrace{V_{ts}V_{tb}^*}_{\mathcal{O}(\lambda^2)} = 0 \tag{1.30}$$

$$\underbrace{V_{ud}V_{ub}^*}_{(\rho+i\eta)A\lambda^3} + \underbrace{V_{cd}V_{cb}^*}_{-A\lambda^3} + \underbrace{V_{td}V_{tb}^*}_{(1-\rho-i\eta)A\lambda^3} = 0, \tag{1.31}$$

whereas those associated with the orthogonality of different rows take the following form:

$$\underbrace{V_{ud}^*V_{cd}}_{\mathcal{O}(\lambda)} + \underbrace{V_{us}^*V_{cs}}_{\mathcal{O}(\lambda)} + \underbrace{V_{ub}^*V_{cb}}_{\mathcal{O}(\lambda^5)} = 0 \tag{1.32}$$

$$\underbrace{V_{cd}^*V_{td}}_{\mathcal{O}(\lambda^4)} + \underbrace{V_{cs}^*V_{ts}}_{\mathcal{O}(\lambda^2)} + \underbrace{V_{cb}^*V_{tb}}_{\mathcal{O}(\lambda^2)} = 0 \tag{1.33}$$

$$\underbrace{V_{ud}^*V_{td}}_{(1-\rho-i\eta)A\lambda^3} + \underbrace{V_{us}^*V_{ts}}_{-A\lambda^3} + \underbrace{V_{ub}^*V_{tb}}_{(\rho+i\eta)A\lambda^3} = 0. \tag{1.34}$$

Here we have also indicated the structures that arise if we apply the Wolfenstein parameterization by keeping just the leading, non-vanishing terms. We observe that only in eq. (1.31) and eq. (1.34), which describe the orthogonality of the first and third columns and of the first and third rows, respectively, all three sides are of comparable magnitude, $\mathcal{O}(\lambda^3)$, while in the remaining relations, one side is suppressed with respect to the others by factors of $\mathcal{O}(\lambda^2)$ or $\mathcal{O}(\lambda^4)$. Consequently, we have to deal with only *two* non-squashed unitarity triangles in the complex plane. However, as we have already

indicated in eq. (1.31) and eq. (1.34), the corresponding orthogonality relations agree with each other at the λ^3 level, yielding

$$[(\rho + i\eta) + (-1) + (1 - \rho - i\eta)]\, A\lambda^3 = 0. \tag{1.35}$$

Consequently, they describe the same triangle, which is usually referred to as *the* unitarity triangle of the CKM matrix.

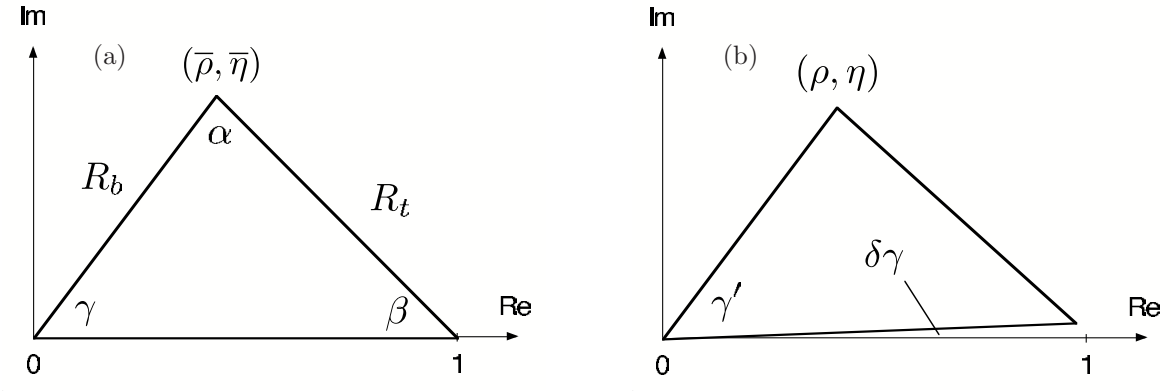


Figure 1.3: The two non-squashed unitarity triangles of the CKM matrix: (a) and (b) correspond to the orthogonality relations (1.31) and (1.34), respectively. In Asia, the notation $\phi_1 \equiv \beta$, $\phi_2 \equiv \alpha$ and $\phi_3 \equiv \gamma$ is used for the angles of the triangle shown in (a).

If we take the next-to-leading order terms of the Wolfenstein expansion into account, we will have to distinguish between the unitarity triangles following from eq. (1.31) and eq. (1.34). Let us first have a closer look at the former relation. Including terms of $\mathcal{O}(\lambda^5)$, we obtain the following generalization of (1.35):

$$[(\bar{\rho} + i\bar{\eta}) + (-1) + (1 - \bar{\rho} - i\bar{\eta})]\, A\lambda^3 + \mathcal{O}(\lambda^7) = 0, \tag{1.36}$$

where $\bar{\rho}$ and $\bar{\eta}$ are as defined in (1.24). If we divide this relation by the overall normalization factor $A\lambda^3$, and introduce

$$R_b \equiv \sqrt{\overline{\rho}^2 + \overline{\eta}^2} = \left(1 - \frac{\lambda^2}{2}\right) \frac{1}{\lambda} \left|\frac{V_{ub}}{V_{cb}}\right| \tag{1.37}$$

$$R_t \equiv \sqrt{(1 - \overline{\rho})^2 + \overline{\eta}^2} = \frac{1}{\lambda} \left|\frac{V_{td}}{V_{cb}}\right|, \tag{1.38}$$

we arrive at the unitarity triangle illustrated in fig. 1.3(a). It is a straightforward generalization of the leading-order case described by (1.35): instead of (ρ, η), the apex is now simply given by $(\bar{\rho}, \bar{\eta})$. The two sides R_b and R_t, as well as the three angles α, β and γ, will show up at several places throughout these thesis. Moreover, the relations

$$V_{ub} = A\lambda^3 \left(\frac{R_b}{1 - \lambda^2/2}\right) e^{-i\gamma}, \quad V_{td} = A\lambda^3 R_t e^{-i\beta} \tag{1.39}$$

are also useful for phenomenological applications, since they make the dependences of γ and β explicit; they correspond to the phase convention chosen both in the standard parameterization (1.14) and in

the generalized Wolfenstein parameterization (1.22). Finally, if we take also (1.20) into account, we obtain

$$\delta_{13} = \gamma. \tag{1.40}$$

Let us now turn to eq. (1.34). Here we arrive at an expression more complicated than (1.36):

$$\left[\left\{1 - \frac{\lambda^2}{2} - (1-\lambda^2)\rho - i(1-\lambda^2)\eta\right\} + \left\{-1 + \left(\frac{1}{2} - \rho\right)\lambda^2 - i\eta\lambda^2\right\} + \{\rho + i\eta\}\right] A\lambda^3 + \mathcal{O}(\lambda^7) = 0. \tag{1.41}$$

If we divide again by $A\lambda^3$, we obtain the unitarity triangle sketched in fig. 1.3(b), where the apex is given by (ρ, η) and *not* by $(\bar{\rho}, \bar{\eta})$. On the other hand, we find a tiny angle

$$\delta\gamma \equiv \lambda^2\eta = \mathcal{O}(1^\circ) \tag{1.42}$$

between the real axis and the basis of the triangle, which satisfies

$$\gamma = \gamma' + \delta\gamma, \tag{1.43}$$

where γ coincides with the corresponding angle in fig. 1.3a.

Whenever we will refer to a "unitarity triangle" (UT) in the following, we mean the one illustrated in fig. 1.3(a), which is the generic generalization of the leading-order case described by (1.35). As we will see below, the UT is the central target of the experimental tests of the Standard Model description of CP violation. Interestingly, also the tiny angle $\delta\gamma$ can be probed directly through certain CP-violating effects that can be explored at hadron colliders, in particular at CDF and LHC*b*.

1.3 Non-leptonic decays of B mesons

The B-meson system consists of charged and neutral B mesons, characterized by the valence quark contents in (1.3). The characteristic feature of the neutral B_q ($q \in \{d, s\}$) mesons is the phenomenon of B_q^0–$\bar{B}_q^0$ mixing, which will be discussed in sec. 1.5. As far as the weak decays of B mesons are concerned, we distinguish between leptonic, semileptonic and non-leptonic transitions. The $B_{(s)}^0 \to h^+h'^-$ charmless decays belong to the non-leptonic transitions.

The most complicated B decays are the non-leptonic transitions, which are mediated by $b \to q_1\,\bar{q}_2\,d\,(s)$ quark-level processes, with $q_1, q_2 \in \{u, d, c, s\}$. There are two kinds of topologies contributing to such decays: tree and penguin diagrams topologies. The latter consist of gluonic (QCD) and electroweak (EW) penguins. In fig. 1.4, the corresponding leading-order Feynman diagrams are shown. Depending on the flavour content of their final states, we may classify $b \to q_1\,\bar{q}_2\,d\,(s)$ decays as follows:

- $q_1 \neq q_2 \in \{u, c\}$: *only* tree diagrams contribute;
- $q_1 = q_2 \in \{u, c\}$: tree *and* penguin diagrams contribute;
- $q_1 = q_2 \in \{d, s\}$: *only* penguin diagrams contribute.

In order to analyse the non-leptonic B decays, one uses low-energy effective Hamiltonians, which are calculated by making use of the "Operator Product Expansion", yielding transition matrix elements

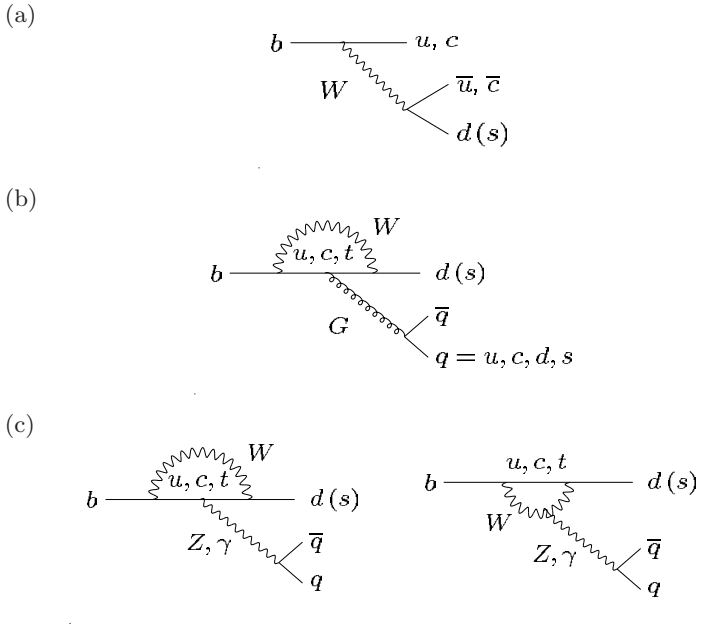


Figure 1.4: Feynman diagrams of the topologies characterizing non-leptonic B decays: trees (a), QCD penguins (b), and electroweak penguins (c).

with the following structure:

$$\langle f|\mathcal{H}_{\text{eff}}|i\rangle = \frac{G_{\text{F}}}{\sqrt{2}}\lambda_{\text{CKM}}\sum_k C_k(\mu)\langle f|Q_k(\mu)|i\rangle\,. \tag{1.44}$$

The technique of the operator product expansion allows to separate the short-distance contributions to this transition amplitude from the long-distance ones, described by perturbative quantities $C_k(\mu)$ ("Wilson coefficient functions") and by non-perturbative quantities $\langle f|Q_k(\mu)|i\rangle$ ("hadronic matrix elements"), respectively. As before, G_{F} is the Fermi constant, whereas λ_{CKM} is a CKM factor and μ denotes an appropriate renormalization scale. The Q_k are local operators, which are generated by electroweak interactions and QCD, and govern "effectively" the decay in question. The Wilson coefficients $C_k(\mu)$ can be considered as scale-dependent couplings related to the vertices described by the Q_k.

For the exploration of CP violation, the class of non-leptonic B decays that receives contributions both from tree and from penguin topologies plays a key rôle. In this important case, the operator basis is much larger than the case where a pure "tree" decay is considered. If we apply the relation

$$V_{ur}^* V_{ub} + V_{cr}^* V_{cb} + V_{tr}^* V_{tb} = 0 \quad (r \in \{d, s\}), \tag{1.45}$$

which follows from the unitarity of the CKM matrix, and "integrate out" the top quark (which enters through the penguin loop processes) and the W boson, we may write

$$\mathcal{H}_{\text{eff}} = \frac{G_{\text{F}}}{\sqrt{2}}\left[\sum_{j=u,c} V_{jr}^* V_{jb}\left\{\sum_{k=1}^{2} C_k(\mu)\, Q_k^{jr} + \sum_{k=3}^{10} C_k(\mu)\, Q_k^{r}\right\}\right]. \tag{1.46}$$

Here we have introduced another quark-flavour label $j \in \{u, c\}$, and the Q_k^{jr} can be divided as follows:

- Current–current operators:

$$\begin{array}{rcl} Q_1^{jr} & = & (\bar{r}_\alpha j_\beta)_{\text{V–A}} (\bar{j}_\beta b_\alpha)_{\text{V–A}} \\ Q_2^{jr} & = & (\bar{r}_\alpha j_\alpha)_{\text{V–A}} (\bar{j}_\beta b_\beta)_{\text{V–A}} . \end{array} \tag{1.47}$$

- QCD penguin operators:

$$\begin{array}{rcl} Q_3^r & = & (\bar{r}_\alpha b_\alpha)_{\text{V–A}} \sum_{q'} (\bar{q}'_\beta q'_\beta)_{\text{V–A}} \\ Q_4^r & = & (\bar{r}_\alpha b_\beta)_{\text{V–A}} \sum_{q'} (\bar{q}'_\beta q'_\alpha)_{\text{V–A}} \\ Q_5^r & = & (\bar{r}_\alpha b_\alpha)_{\text{V–A}} \sum_{q'} (\bar{q}'_\beta q'_\beta)_{\text{V+A}} \\ Q_6^r & = & (\bar{r}_\alpha b_\beta)_{\text{V–A}} \sum_{q'} (\bar{q}'_\beta q'_\alpha)_{\text{V+A}} . \end{array} \tag{1.48}$$

- EW penguin operators (the $e_{q'}$ denote the electrical quark charges):

$$\begin{array}{rcl} Q_7^r & = & \frac{3}{2} (\bar{r}_\alpha b_\alpha)_{\text{V–A}} \sum_{q'} e_{q'} (\bar{q}'_\beta q'_\beta)_{\text{V+A}} \\ Q_8^r & = & \frac{3}{2} (\bar{r}_\alpha b_\beta)_{\text{V–A}} \sum_{q'} e_{q'} (\bar{q}'_\beta q'_\alpha)_{\text{V+A}} \\ Q_9^r & = & \frac{3}{2} (\bar{r}_\alpha b_\alpha)_{\text{V–A}} \sum_{q'} e_{q'} (\bar{q}'_\beta q'_\beta)_{\text{V–A}} \\ Q_{10}^r & = & \frac{3}{2} (\bar{r}_\alpha b_\beta)_{\text{V–A}} \sum_{q'} e_{q'} (\bar{q}'_\beta q'_\alpha)_{\text{V–A}} . \end{array} \tag{1.49}$$

The current–current, QCD and EW penguin operators are related to the tree, QCD and EW penguin processes shown in fig. 1.4. At the renormalization scale $\mu = \mathcal{O}(m_b)$, the Wilson coefficients of the current–current operators are $C_1(\mu) = \mathcal{O}(10^{-1})$ and $C_2(\mu) = \mathcal{O}(1)$, whereas those of the penguin operators are $\mathcal{O}(10^{-2})$ [34, 35]. Note that penguin topologies with internal charm- and up-quark exchanges are described in this framework by penguin-like matrix elements of the corresponding current–current operators, and may also have important phenomenological consequences [36, 37].

Since the ratio $\alpha/\alpha_s = \mathcal{O}(10^{-2})$ of the QED and QCD couplings is very small, we would expect naïvely that EW penguins should play a minor rôle in comparison with QCD penguins. This would actually be the case if the top quark were not "heavy". However, since the Wilson coefficient C_9 increases strongly with m_t, we obtain interesting EW penguin effects in several B decays. EW penguins have an important impact on the $B \to K\pi$ system [38].

The low-energy effective Hamiltonians discussed above apply to all B decays that are generated by the same quark-level transition, i.e. they are "universal". Consequently, the differences between the various exclusive modes of a given decay class arise within this formalism only through the hadronic matrix elements of the relevant four-quark operators. Unfortunately, the evaluation of such matrix elements is associated with large uncertainties and is a very challenging task. In this context, "factorization" is a widely used concept.

1.3.1 Factorization of Hadronic Matrix Elements

The concept of factorization of the hadronic matrix elements of four-quark operators into the product of hadronic matrix elements of quark currents has a long history [39]. Interesting recent developments are the following:

- "QCD factorization" [15], which is in agreement with the old picture that factorization should hold for certain decays in the limit of $m_b \gg \Lambda_{\rm QCD}$ [40], provides a formalism to calculate the relevant amplitudes at the leading order of a $\Lambda_{\rm QCD}/m_b$ expansion.

- Another QCD approach to deal with non-leptonic B-meson decays – the "perturbative hard-scattering approach " (pQCD) – was developed independently in [41], and differs from the QCD factorization formalism in some technical aspects.

- An interesting technique for "factorization proofs" is provided by the framework of the "soft collinear effective theory" (SCET) [42], which has received a lot of attention in the recent literature and led to various applications.

- Non-leptonic B decays can also be studied within the QCD light-cone sum-rule approaches [43].

A detailed description of these topics would be very technical and is beyond the scope of this thesis. However, for the discussion of the CP-violating effects in the B-meson system, we must only be familiar with the general structure of the non-leptonic B decay amplitudes and not with the details of the techniques necessary to deal with the corresponding hadronic matrix elements. The data will establish how well factorization and the concepts sketched above are actually working.

An alternative approach that has been pursued extensively is to use *flavor symmetries* to extract hadronic matrix elements from experimental data and then use them to predict flavor symmetries-related channels principle. In this way it is possible to eliminate all the uncertainties connected to factorization and the infinite mass limit.

SU(2) isospin symmetry – Use of isospin relations is based on expansions in $m_{u,d}/\Lambda \sim 0.03 \ll 1$. Several methods proposed for determining α and γ rely on the isospin symmetry, which is conserved to a few percent accuracy. However, in $B^0_{(s)} \to h^+ h'^-$ decays, the effectiveness of this approach is currently limited by the number of unknown isospin parameters. Even with a more complete experimental information, it would still be important to complement this strategy with information on amplitudes from SU(3) or factorization. Otherwise, the possible presence of new physics effects may remain undetected in full fits of SU(2) amplitudes [44].

SU(3) symmetry – SU(3)-based amplitude relations are obtained by combining the $m_s/\Lambda \sim 0.3 \ll 1$ expansion parameter with those of the SU(2) symmetry. Several Standard Model strategies based on SU(3) symmetry have been proposed to cancel out the hadronic uncertainties. Still, the limited number of currently precise measurements available makes it necessary to introduce additional "dynamical assumptions" to further reduce the number of hadronic parameters. These assumptions usually rely on the additional knowledge of the strong matrix elements from the factorization approach.

1.4 Direct CP Violation

Let us consider a non-leptonic decay $\bar{B} \to \bar{f}$ that is described by the low-energy effective Hamiltonian in (1.46). The corresponding decay amplitude is given as follows:

$$\begin{aligned} A(\bar{B} \to \bar{f}) &= \langle \bar{f}|\mathcal{H}_{\rm eff}|\bar{B}\rangle \\ &= \frac{G_{\rm F}}{\sqrt{2}}\left[\sum_{j=u,c} V_{jr}^* V_{jb}\left\{\sum_{k=1}^{2} C_k(\mu)\langle \bar{f}|Q_k^{jr}(\mu)|\bar{B}\rangle + \sum_{k=3}^{10} C_k(\mu)\langle \bar{f}|Q_k^{r}(\mu)|\bar{B}\rangle\right\}\right]. \end{aligned} \tag{1.50}$$

For the CP-conjugate process $B \to f$, we have

$$\begin{aligned} A(B \to f) &= \langle f|\mathcal{H}_{\rm eff}^\dagger|B\rangle \\ &= \frac{G_{\rm F}}{\sqrt{2}}\left[\sum_{j=u,c} V_{jr} V_{jb}^*\left\{\sum_{k=1}^{2} C_k(\mu)\langle f|Q_k^{jr\dagger}(\mu)|B\rangle + \sum_{k=3}^{10} C_k(\mu)\langle f|Q_k^{r\dagger}(\mu)|B\rangle\right\}\right]. \end{aligned} \tag{1.51}$$

If we now use that strong interactions are invariant under CP transformations, insert $(\mathcal{CP})^\dagger(\mathcal{CP}) = \hat{1}$ both after the $\langle f|$ and in front of the $|B\rangle$, and take the relation

$$(\mathcal{CP})Q_k^{jr\dagger}(\mathcal{CP})^\dagger = Q_k^{jr} \tag{1.52}$$

into account, we arrive at

$$\begin{aligned} A(B \to f) &= e^{i[\phi_{\rm CP}(B)-\phi_{\rm CP}(f)]} \\ &\times \frac{G_{\rm F}}{\sqrt{2}}\left[\sum_{j=u,c} V_{jr} V_{jb}^*\left\{\sum_{k=1}^{2} C_k(\mu)\langle \bar{f}|Q_k^{jr}(\mu)|\bar{B}\rangle + \sum_{k=3}^{10} C_k(\mu)\langle \bar{f}|Q_k^{r}(\mu)|\bar{B}\rangle\right\}\right], \end{aligned} \tag{1.53}$$

where the convention-dependent phases $\phi_{\rm CP}(B)$ and $\phi_{\rm CP}(f)$ are defined through the relations

$$(\mathcal{CP})|B\rangle = e^{i\phi_{\rm CP}(B)}|\bar{B}\rangle, \quad (\mathcal{CP})|f\rangle = e^{i\phi_{\rm CP}(f)}|\bar{f}\rangle. \tag{1.54}$$

Consequently, we may write

$$A(\bar{B} \to \bar{f}) = e^{+i\varphi_1}|A_1|e^{i\delta_1} + e^{+i\varphi_2}|A_2|e^{i\delta_2} \tag{1.55}$$

$$A(B \to f) = e^{i[\phi_{\rm CP}(B)-\phi_{\rm CP}(f)]}\left[e^{-i\varphi_1}|A_1|e^{i\delta_1} + e^{-i\varphi_2}|A_2|e^{i\delta_2}\right]. \tag{1.56}$$

Here the CP-violating phases $\varphi_{1,2}$ originate from the CKM factors $V_{jr}^* V_{jb}$, and the CP-conserving "strong" amplitudes $|A_{1,2}|e^{i\delta_{1,2}}$ involve the hadronic matrix elements of the four-quark operators. In fact, these expressions are the most general forms of any non-leptonic B-decay amplitude in the Standard Model, i.e. they do not only refer to the $\Delta C = \Delta U = 0$ case described by (1.46). Using (1.55) and (1.56), we obtain the following CP asymmetry:

$$\begin{aligned} \mathcal{A}_{\rm CP} &\equiv \frac{\Gamma(\bar{B} \to \bar{f}) - \Gamma(B \to f)}{\Gamma(\bar{B} \to \bar{f}) + \Gamma(B \to f)} = \frac{|A(\bar{B} \to \bar{f})|^2 - |A(B \to f)|^2}{|A(\bar{B} \to \bar{f})|^2 + |A(B \to f)|^2} \\ &= -\frac{2|A_1||A_2|\sin(\delta_1-\delta_2)\sin(\varphi_1-\varphi_2)}{|A_1|^2 + 2|A_1||A_2|\cos(\delta_1-\delta_2)\cos(\varphi_1-\varphi_2) + |A_2|^2}. \end{aligned} \tag{1.57}$$

We observe that a non-vanishing value can be generated through the interference between the two weak amplitudes, provided both a non-trivial weak phase difference $\varphi_1 - \varphi_2$ and a non-trivial strong phase difference $\delta_1 - \delta_2$ are present. This kind of CP violation is referred to as "direct" CP violation, as it originates directly at the amplitude level of the considered decay. It is the B-meson counterpart of the effects probed through $\mathrm{Re}(\varepsilon'/\varepsilon)$ in the neutral kaon system, and recently established only in the $B^0 \to K^+\pi^-$ decay [11].

Since $\varphi_1 - \varphi_2$ is in general given by one of the UT angles – usually γ – the goal is to extract this quantity from the measured value of $\mathcal{A}_{\mathrm{CP}}$. Unfortunately, hadronic uncertainties affect this determination through the poorly known hadronic matrix elements present in (1.50). In order to deal with this problem, we may proceed along one of the following two avenues:

(i) Amplitude relations can be used to eliminate the hadronic matrix elements. We distinguish between exact relations, using pure "tree" decays of the kind $B^+ \to K^+D$ [9, 10] or $B_c^+ \to D_s^+D$ [45], and relations which follow from the flavour symmetries of strong interactions, i.e. isospin or $SU(3)_{\mathrm{F}}$, and involve $B_{(s)} \to \pi\pi, \pi K, KK$ modes [46].

(ii) In decays of the neutral B_q^0 mesons, interference effects between B_q^0–$\bar{B}_q^0$ mixing and decay processes may cause "mixing-induced CP violation" (see sec. 1.5.4). If a single CKM amplitude governs the decay, the hadronic matrix elements cancel in the corresponding CP asymmetries; otherwise we have to use again amplitude relations. The most important example is the decay $B_d^0 \to J/\psi K_{\mathrm{S}}$ [47] (see sec. 1.5.4).

1.5 Neutral B mesons

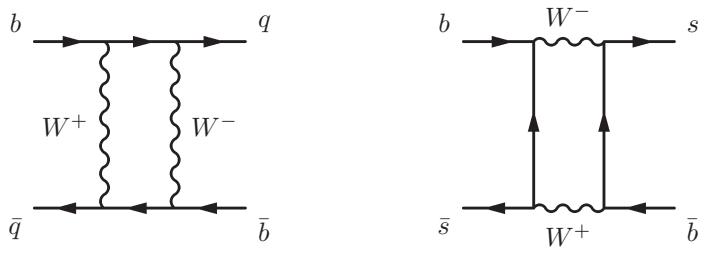


Figure 1.5: Box diagrams contributing to B_q^0-$\overline{B}_q^0$ flavor mixing.

Within the Standard Model, B_q^0–$\bar{B}_q^0$ mixing ($q \in \{d, s\}$) arises from the box diagrams shown in Fig. 1.5. Because of this phenomenon, an initially, i.e. at time $t = 0$, present B_q^0-meson state evolves into a time-dependent linear combination of B_q^0 and $\bar{B}_q^0$ states:

$$|B_q(t)\rangle = a(t)|B_q^0\rangle + b(t)|\bar{B}_q^0\rangle, \tag{1.58}$$

where $a(t)$ and $b(t)$ are governed by a Schrödinger equation of the following form:

$$i\,\frac{\mathrm{d}}{\mathrm{d}t}\begin{pmatrix} a(t) \\ b(t) \end{pmatrix} = H\cdot\begin{pmatrix} a(t) \\ b(t) \end{pmatrix} \equiv \Bigg[\underbrace{\begin{pmatrix} M_0^{(q)} & M_{12}^{(q)} \\ M_{12}^{(q)*} & M_0^{(q)} \end{pmatrix}}_{\text{mass matrix}} - \frac{i}{2}\underbrace{\begin{pmatrix} \Gamma_0^{(q)} & \Gamma_{12}^{(q)} \\ \Gamma_{12}^{(q)*} & \Gamma_0^{(q)} \end{pmatrix}}_{\text{decay matrix}}\Bigg]\cdot\begin{pmatrix} a(t) \\ b(t) \end{pmatrix}.$$

The special form $H_{11} = H_{22}$ of the Hamiltonian H is an implication of the CPT theorem, i.e. of the invariance under combined CP and time-reversal (T) transformations.

It is straightforward to calculate the eigenstates $|B_\pm^{(q)}\rangle$ and eigenvalues $\lambda_\pm^{(q)}$ of (1.59):

$$|B_\pm^{(q)}\rangle = \frac{1}{\sqrt{1+|\alpha_q|^2}}\left(|B_q^0\rangle \pm \alpha_q|\bar{B}_q^0\rangle\right) \tag{1.59}$$

$$\lambda_\pm^{(q)} = \left(M_0^{(q)} - \frac{i}{2}\Gamma_0^{(q)}\right) \pm \left(M_{12}^{(q)} - \frac{i}{2}\Gamma_{12}^{(q)}\right)\alpha_q, \tag{1.60}$$

where

$$\alpha_q e^{+i\left(\Theta_{\Gamma_{12}}^{(q)}+n'\pi\right)} = \sqrt{\frac{4|M_{12}^{(q)}|^2 e^{-i2\delta\Theta_{M/\Gamma}^{(q)}} + |\Gamma_{12}^{(q)}|^2}{4|M_{12}^{(q)}|^2 + |\Gamma_{12}^{(q)}|^2 - 4|M_{12}^{(q)}||\Gamma_{12}^{(q)}|\sin\delta\Theta_{M/\Gamma}^{(q)}}}. \tag{1.61}$$

Here we have written

$$M_{12}^{(q)} \equiv e^{i\Theta_{M_{12}}^{(q)}}|M_{12}^{(q)}|, \quad \Gamma_{12}^{(q)} \equiv e^{i\Theta_{\Gamma_{12}}^{(q)}}|\Gamma_{12}^{(q)}|, \quad \delta\Theta_{M/\Gamma}^{(q)} \equiv \Theta_{M_{12}}^{(q)} - \Theta_{\Gamma_{12}}^{(q)}, \tag{1.62}$$

and have introduced the quantity $n' \in \{0,1\}$ to parametrize the sign of the square root in (1.61).

Analytical (QCD sum-rules) and numerical (lattice simulation) calculations of mixing amplitudes allow estimating values of the mass and decay matrix elements:

$$M_{12}^{(q)} \propto (V_{tq}^* V_{tb})^2 e^{i\left[\pi - \phi_{\mathrm{CP}}(B_q^0)\right]} \tag{1.63}$$

where $\phi_{\mathrm{CP}}(B_q)$ is a convention-dependent phase, defined in analogy to (1.54). It is found that $\Gamma_{12}^{(q)}/M_{12}^{(q)} \approx \mathcal{O}(m_b^2/m_t^2) \ll 1$. Consequently, the expansion of (1.61) at first order yields

$$\alpha_q = \left[1 + \frac{1}{2}\left|\frac{\Gamma_{12}^{(q)}}{M_{12}^{(q)}}\right|\sin\left(\Theta_{M_{12}}^{(q)} - \Theta_{\Gamma_{12}}^{(q)}\right)\right] e^{-i\left(\Theta_{\Gamma_{12}}^{(q)}+n'\pi\right)}. \tag{1.64}$$

The deviation of $|\alpha_q|$ from unit measures the CP violation in the *mixing* transition. The expected magnitude of the corresponding asymmetry, $\frac{|\alpha_q|^4-1}{|\alpha_q|^4+1} = \mathcal{O}(10^{-4})$ is strongly suppressed in the Standard Model. It is difficult to measure, but represents also an interesting probe of New Physics, that may significantly enhance the asymmetry.

1.5.1 Mixing Parameters

From an experimental point of view it is interesting to define some parameters related to the time evolution process mentioned in the previous section. The masses of the eigenstates of (1.59) are indicated with $M_{\mathrm{H}}^{(q)}$ ("heavy") and $M_{\mathrm{L}}^{(q)}$ ("light"). It is then useful to introduce

$$M_q \equiv \frac{M_{\mathrm{H}}^{(q)} + M_{\mathrm{L}}^{(q)}}{2} = M_0^{(q)}, \tag{1.65}$$

as well as the mass difference

$$\Delta M_q \equiv M_{\rm H}^{(q)} - M_{\rm L}^{(q)} = 2|M_{12}^{(q)}| > 0, \tag{1.66}$$

which is by definition *positive*. While B_d^0–$\bar{B}_d^0$ mixing is well established and

$$\Delta M_d = (0.507 \pm 0.004)\,{\rm ps}^{-1} \tag{1.67}$$

known with impressive experimental accuracy [48], only lower bounds on ΔM_s were available, for many years, from the LEP (CERN) experiments and SLD (SLAC) [49]. In the fall of 2006, CDF collaboration reported the observation of B_s^0-$\overline{B}_s^0$oscillations from a time-dependent measurement of the oscillation frequency:

$$\Delta M_s = [17.77 \pm 0.10({\rm stat}) \pm 0.07({\rm syst})]\,{\rm ps}^{-1}. \tag{1.68}$$

The decay widths $\Gamma_{\rm H}^{(q)}$ and $\Gamma_{\rm L}^{(q)}$ of the mass eigenstates, which correspond to $M_{\rm H}^{(q)}$ and $M_{\rm L}^{(q)}$, respectively, satisfy

$$\Delta\Gamma_q \equiv \Gamma_{\rm H}^{(q)} - \Gamma_{\rm L}^{(q)} = \frac{4\,{\rm Re}\left[M_{12}^{(q)}\Gamma_{12}^{(q)*}\right]}{\Delta M_q}, \tag{1.69}$$

whereas

$$\Gamma_q \equiv \frac{\Gamma_{\rm H}^{(q)} + \Gamma_{\rm L}^{(q)}}{2} = \Gamma_0^{(q)}. \tag{1.70}$$

There is the following interesting relation:

$$\frac{\Delta\Gamma_q}{\Gamma_q} \approx -\frac{3\pi}{2S_0(x_t)}\left(\frac{m_b^2}{M_W^2}\right) x_q = -\mathcal{O}(10^{-2}) \times x_q, \tag{1.71}$$

where $S_0(x_t \equiv m_t^2/M_W^2)$ [50] is the "Inami–Lim" function, which can be written – to a good approximation – in the Standard Model as [51]

$$S_0(x_t) = 2.40 \times \left[\frac{m_t}{167\,{\rm GeV}}\right]^{1.52}, \tag{1.72}$$

and where

$$x_q \equiv \frac{\Delta M_q}{\Gamma_q} = \begin{cases} 0.771 \pm 0.012 & (q = d) \\ \mathcal{O}(20) & (q = s) \end{cases} \tag{1.73}$$

is often referred to as *the* B_q^0–$\bar{B}_q^0$ "mixing parameter".[2] Consequently, $\Delta\Gamma_d/\Gamma_d \sim 10^{-2}$ is negligibly small, while $\Delta\Gamma_s/\Gamma_s \sim 10^{-1}$ may be sizeable. As was reviewed in Ref. [52], the state of the art of calculations of these quantities is given as follows:

$$\frac{|\Delta\Gamma_d|}{\Gamma_d} = (3 \pm 1.2) \times 10^{-3}, \quad \frac{|\Delta\Gamma_s|}{\Gamma_s} = 0.12 \pm 0.05. \tag{1.74}$$

Recently, the first results for $\Delta\Gamma_s$ were reported from the Tevatron, using the $B_s^0 \to J/\psi\phi$ channel:

$$\frac{|\Delta\Gamma_s|}{\Gamma_s} = \begin{cases} 0.12 \pm 0.09 & ({\rm CDF}\ [53]) \\ 0.18 \pm 0.14 & ({\rm D0}\ [54]). \end{cases} \tag{1.75}$$

[2] Note that $\Delta\Gamma_q/\Gamma_q$ is negative in the Standard Model because of the minus sign in (1.71).

1.5.2 Time-Dependent Decay Rates

The time evolution of initially, i.e. at $t = 0$, pure B_q^0- and $\bar{B}_q^0$-meson states is given by

$$|B_q^0(t)\rangle = f_+^{(q)}(t)|B_q^0\rangle + \alpha_q f_-^{(q)}(t)|\bar{B}_q^0\rangle \tag{1.76}$$

and

$$|\bar{B}_q^0(t)\rangle = \frac{1}{\alpha_q} f_-^{(q)}(t)|B_q^0\rangle + f_+^{(q)}(t)|\bar{B}_q^0\rangle, \tag{1.77}$$

respectively, with

$$f_\pm^{(q)}(t) = \frac{1}{2}\left[e^{-i\lambda_+^{(q)}t} \pm e^{-i\lambda_-^{(q)}t}\right]. \tag{1.78}$$

These time-dependent state vectors allow the calculation of the corresponding transition rates. To this end, it is useful to introduce

$$|g_\pm^{(q)}(t)|^2 = \frac{1}{4}\left[e^{-\Gamma_{\rm L}^{(q)}t} + e^{-\Gamma_{\rm H}^{(q)}t} \pm 2\,e^{-\Gamma_q t}\cos(\Delta M_q t)\right] \tag{1.79}$$

$$g_-^{(q)}(t)\,g_+^{(q)}(t)^* = \frac{1}{4}\left[e^{-\Gamma_{\rm L}^{(q)}t} - e^{-\Gamma_{\rm H}^{(q)}t} + 2\,i\,e^{-\Gamma_q t}\sin(\Delta M_q t)\right], \tag{1.80}$$

as well as

$$\xi_f^{(q)} = e^{-i\Theta_{M_{12}}^{(q)}}\frac{A(\bar{B}_q^0 \to f)}{A(B_q^0 \to f)}, \quad \xi_{\bar{f}}^{(q)} = e^{-i\Theta_{M_{12}}^{(q)}}\frac{A(\bar{B}_q^0 \to \bar{f})}{A(B_q^0 \to \bar{f})}. \tag{1.81}$$

Looking at (1.63), we find

$$\Theta_{M_{12}}^{(q)} = \pi + 2\arg(V_{tq}^* V_{tb}) - \phi_{\rm CP}(B_q), \tag{1.82}$$

and observe that this phase depends on the chosen CKM and CP phase conventions specified in (1.11) and (1.54), respectively. However, these dependences are canceled through the amplitude ratios in (1.81), so that $\xi_f^{(q)}$ and $\xi_{\bar{f}}^{(q)}$ are *convention-independent* observables. Whereas n' enters the functions in (1.78) through (1.60), the dependence on this parameter is canceled in (1.79) and (1.80) through the introduction of the *positive* mass difference ΔM_q (see (1.66)). Combining the formulas listed above, we eventually arrive at the following transition rates for decays of initially present B_q^0 or $\bar{B}_q^0$ mesons, i.e. at $t = 0$:

$$\Gamma(\overset{(-)}{B}{}_q^0(t) \to f) = \left[|g_\mp^{(q)}(t)|^2 + |\xi_f^{(q)}|^2|g_\pm^{(q)}(t)|^2 - 2\,{\rm Re}\left\{\xi_f^{(q)} g_\pm^{(q)}(t) g_\mp^{(q)}(t)^*\right\}\right]\tilde{\Gamma}_f, \tag{1.83}$$

where the time-independent rate $\tilde{\Gamma}_f$ corresponds to the "unevolved" decay amplitude $A(B_q^0 \to f)$, and can be calculated by performing the usual phase-space integrations. The rates into the CP-conjugate final state $\bar{f}$ can straightforwardly be obtained from (1.83) by making the substitutions

$$\tilde{\Gamma}_f \;\to\; \tilde{\Gamma}_{\bar{f}}, \quad \xi_f^{(q)} \;\to\; \xi_{\bar{f}}^{(q)}. \tag{1.84}$$

1.5.3 "Untagged" Rates

The expected sizeable width difference $\Delta\Gamma_s$ may provide interesting studies of CP violation through "untagged" B_s rates (see Ref. [55] and [56]–[57]), defined as

$$\langle\Gamma(B_s(t) \to f)\rangle \equiv \Gamma(B_s^0(t) \to f) + \Gamma(\bar{B}_s^0(t) \to f), \tag{1.85}$$

and are characterized by the feature that we do not distinguish between B_s^0 or $\bar{B}_s^0$ mesons. If we consider a final state f to which both a B_s^0 and a $\bar{B}_s^0$ may decay, and use the expressions in (1.83), we find

$$\langle \Gamma(B_s(t) \to f) \rangle \propto [\cosh(\Delta\Gamma_s t/2) - \mathcal{A}_{\Delta\Gamma}(B_s \to f) \sinh(\Delta\Gamma_s t/2)]\, e^{-\Gamma_s t}, \tag{1.86}$$

with

$$\mathcal{A}_{\Delta\Gamma}(B_s \to f) \equiv \frac{2\,\mathrm{Re}\,\xi_f^{(s)}}{1 + \left|\xi_f^{(s)}\right|^2}. \tag{1.87}$$

We observe that the rapidly oscillating $\Delta M_s t$ terms cancel, and that we may obtain information about the phase structure of the observable $\xi_f^{(s)}$, thereby providing valuable insights into CP violation.

1.5.4 CP Asymmetries

A particularly simple – but also very interesting – situation arises if we restrict ourselves to decays of neutral B_q mesons into final states f that are eigenstates of the CP operator, i.e. satisfy the relation

$$(\mathcal{CP})|f\rangle = \pm|f\rangle. \tag{1.88}$$

Consequently, we have $\xi_f^{(q)} = \xi_{\bar{f}}^{(q)}$ in this case, as can be seen in (1.81). Using the decay rates in (1.83), we find that the corresponding time-dependent CP asymmetry is given by

$$\begin{aligned} \mathcal{A}_{\mathrm{CP}}(t) &\equiv \frac{\Gamma(\bar{B}_q^0(t) \to f) - \Gamma(B_q^0(t) \to f)}{\Gamma(\bar{B}_q^0(t) \to f) + \Gamma(B_q^0(t) \to f)} \\ &= \left[\frac{\mathcal{A}_{\mathrm{CP}}^{\mathrm{dir}}(B_q \to f)\, \cos(\Delta M_q t) + \mathcal{A}_{\mathrm{CP}}^{\mathrm{mix}}(B_q \to f)\, \sin(\Delta M_q t)}{\cosh(\Delta\Gamma_q t/2) - \mathcal{A}_{\Delta\Gamma}(B_q \to f)\, \sinh(\Delta\Gamma_q t/2)}\right], \end{aligned} \tag{1.89}$$

with

$$\mathcal{A}_{\mathrm{CP}}^{\mathrm{dir}}(B_q \to f) \equiv \frac{1 - \left|\xi_f^{(q)}\right|^2}{1 + \left|\xi_f^{(q)}\right|^2}, \qquad \mathcal{A}_{\mathrm{CP}}^{\mathrm{mix}}(B_q \to f) \equiv \frac{2\,\mathrm{Im}\,\xi_f^{(q)}}{1 + \left|\xi_f^{(q)}\right|^2}. \tag{1.90}$$

Because of the relation

$$\mathcal{A}_{\mathrm{CP}}^{\mathrm{dir}}(B_q \to f) = \frac{|A(\bar{B}_q^0 \to \bar{f})|^2 - |A(B_q^0 \to f)|^2}{|A(\bar{B}_q^0 \to \bar{f})|^2 + |A(B_q^0 \to f)|^2}, \tag{1.91}$$

this observable measures the direct CP violation in the decay $B_q \to f$, which originates from the interference between different weak amplitudes, as in eq. (1.57). On the other hand, the interesting *new* aspect of (1.89) is due to $\mathcal{A}_{\mathrm{CP}}^{\mathrm{mix}}(B_q \to f)$, which originates from interference effects between B_q^0–$\bar{B}_q^0$ mixing and decay processes, and describes "mixing-induced" CP violation. Finally, the width difference $\Delta\Gamma_q$, which may be sizeable in the B_s-meson system, provides access to $\mathcal{A}_{\Delta\Gamma}(B_q \to f)$ introduced in (1.87). However, this observable is not independent from $\mathcal{A}_{\mathrm{CP}}^{\mathrm{dir}}(B_q \to f)$ and $\mathcal{A}_{\mathrm{CP}}^{\mathrm{mix}}(B_q \to f)$, satisfying

$$\left[\mathcal{A}_{\mathrm{CP}}^{\mathrm{dir}}(B_q \to f)\right]^2 + \left[\mathcal{A}_{\mathrm{CP}}^{\mathrm{mix}}(B_q \to f)\right]^2 + \left[\mathcal{A}_{\Delta\Gamma}(B_q \to f)\right]^2 = 1. \tag{1.92}$$

In order to calculate $\xi_f^{(q)}$, we use the general expressions (1.55) and (1.56), where $e^{-i\phi_{\mathrm{CP}}(f)} = \pm 1$ because of (1.88), and $\phi_{\mathrm{CP}}(B) = \phi_{\mathrm{CP}}(B_q)$. If we insert these amplitude parameterizations into (1.81)

and take (1.82) into account, we observe that the phase-convention-dependent quantity $\phi_{\rm CP}(B_q)$ cancels, and finally arrive at

$$\xi_f^{(q)} = \mp e^{-i\phi_q}\left[\frac{e^{+i\varphi_1}|A_1|e^{i\delta_1} + e^{+i\varphi_2}|A_2|e^{i\delta_2}}{e^{-i\varphi_1}|A_1|e^{i\delta_1} + e^{-i\varphi_2}|A_2|e^{i\delta_2}}\right], \tag{1.93}$$

where

$$\phi_q \equiv 2\arg(V_{tq}^* V_{tb}) = \begin{cases} +2\beta & (q=d) \\ -2\delta\gamma & (q=s) \end{cases} \tag{1.94}$$

is associated with the CP-violating weak B_q^0–$\bar{B}_q^0$ mixing phase arising in the Standard Model; β and $\delta\gamma$ refer to the corresponding angles in the unitarity triangles shown in Fig. 1.3.

In analogy to eq. (1.57), the calculation of $\xi_f^{(q)}$ is also affected by large hadronic uncertainties. However, if one CKM amplitude plays the dominant rôle in the $B_q \to f$ transition, we obtain

$$\xi_f^{(q)} = \mp e^{-i\phi_q}\left[\frac{e^{+i\phi_f/2}|M_f|e^{i\delta_f}}{e^{-i\phi_f/2}|M_f|e^{i\delta_f}}\right] = \mp e^{-i(\phi_q-\phi_f)}, \tag{1.95}$$

and observe that the hadronic matrix element $|M_f|e^{i\delta_f}$ cancels in this expression. Since the requirements for direct CP violation discussed above are no longer satisfied, direct CP violation vanishes in this important special case, i.e. $\mathcal{A}_{\rm CP}^{\rm dir}(B_q \to f) = 0$. On the other hand, this is *not* the case for the mixing-induced CP asymmetry. In particular,

$$\mathcal{A}_{\rm CP}^{\rm mix}(B_q \to f) = \pm\sin\phi \tag{1.96}$$

is now governed by the CP-violating weak phase difference $\phi \equiv \phi_q - \phi_f$ and is not affected by hadronic uncertainties. The corresponding time-dependent CP asymmetry takes then the simple form

$$\left.\frac{\Gamma(B_q^0(t)\to f) - \Gamma(\bar{B}_q^0(t)\to \bar{f})}{\Gamma(B_q^0(t)\to f) + \Gamma(\bar{B}_q^0(t)\to \bar{f})}\right|_{\Delta\Gamma_q=0} = \pm\sin\phi\,\sin(\Delta M_q t), \tag{1.97}$$

and allows an elegant determination of $\sin\phi$.

1.6 How could new physics enter?

Using the concept of low-energy effective Hamiltonians introduced in sec. 1.3, we may address this important question in a systematic manner [58]:

- New Physics may modify the "strength" of the Standard Model operators through new short-distance functions which depend on the New Physics parameters, such as the masses of charginos, squarks, charged Higgs particles and $\tan\bar{\beta} \equiv v_2/v_1$ in the "minimal supersymmetric Standard Model" (MSSM). The New Physics particles may enter in box and penguin topologies, and are "integrated out" as the W boson and top quark in the Standard Model.

- It should be emphasized that the New Physics may also involve new CP-violating phases which are *not* related to the CKM matrix.

- New Physics may enhance the operator basis, so that operators which are not present (or strongly suppressed) in the Standard Model may actually play an important rôle. In this case, we encounter, in general, also new sources for flavour– and CP–violation.

The B-meson system offers a variety of processes and strategies for the exploration of CP violation. There are processes with a very *different* dynamics that are – in the Standard Model – sensitive to the *same* angles of the UT. In the presence of New Physics contributions, the subtle interplay between the different processes could well be disturbed. New Physics could enter through the exchange of new particles in the box diagrams, or through new contributions at the tree level (B^0_q–$\bar{B}^0_q$ mixing). On other hand New Physics has typically a small effect when Standard Model tree processes play the dominant rôle. However, New Physics could well have a significant impact on the decay amplitudes where new particles may enter in penguin diagrams.

Just in this context charmless hadronic two body decays $B^0_{(s)} \to h^+h'^-$ constitute both a probe of electroweak structure of Standard Model as well as a testing ground for our understanding of QCD dynamics and then a powerful probe to investigate New Physics effects.

1.7 Phenomenology of $B^0_{(s)} \to h^+h'^-$ modes

Non-leptonic two-body charmless decays are the most interesting processes to study flavor physics in the b-meson sector. The large mass of the b-meson allows for a plethora of open channels, which provide multiple ways for testing the consistency of the Standard Model interpretation of CP violation. For each channel, observables include the CP-averaged branching fractions, the direct CP-violating asymmetries and, for certain decays of neutral mesons, the mixing-induced CP-violating asymmetry.

In the years 1998–2000, the CLEO experiment established the relevant role of penguin amplitudes measuring for the first time $\mathcal{B}(B^0 \to K^+\pi^-)/\mathcal{B}(B^0 \to \pi^+\pi^-) \simeq 4$ whereas if only tree processes were to contribute, $\mathcal{B}(B^0 \to K^+\pi^-)/\mathcal{B}(B^0 \to \pi^+\pi^-) \propto |V_{us}|^2/|V_{ud}|^2 \approx \mathcal{O}(\lambda^2) \approx 0.05$ was expected. Today, it is common to think of penguin amplitudes as an opportunity to be exploited rather than as a limitation, because the increased complexity implies also an enriched phenomenology: higher-order penguin processes may provide access for New Physics phases, induced by virtual contributions of new particles in the loops. The $B^0_{(s)} \to h^+h'^-$ decays can be used to determine the values of the CKM-related quantities, which may differ from the ones extracted from other tree-level dominated processes, possibly indicating non-Standard Model CP-violating phases. In addition, the $B^0_{(s)} \to h^+h'^-$ decays can provide valuable information on low-energy strong dynamics in $B^0_{(s)}$ meson decays.

The phenomenology of non-leptonic charmless two-body decays of b-mesons offers rich opportunities for increasing our understanding of the CP violation, and the precise measurements obtained recently at dedicated e^+e^- colliders already provided demonstration of the central role of these decay modes. While rich experimental data are available for B^0 and B^+ mesons from the ARGUS, CLEO, and LEP experiments, and, more recently, from the *BABAR* and Belle experiments, no hadronic charmless decays of B^0_s mesons into pions or kaons are accessible at these facilities.[3] The upgraded Collider Detector at the Fermilab Tevatron (CDF II) is an ideal environment to study hadronic charmless

[3] ARGUS stands for "A Russian German US" Collaboration, LEP for Large Electron Positron collider.

decays of B_s^0 (along with B^0 and B^+) mesons into charged final states and to exploit the very promising physics potential of the B_s system. Consequently, B_s physics is in some sense the "El Dorado" for B experiments at hadron colliders. In fact only simultaneous measurement of B^0, B^+ and B_s^0 observables can fully exploit U-spin symmetries to cancel out hadronic uncertainties and probe the electroweak and QCD structure.

Amplitudes of $B^0_{(s)} \to h^+h^{'-}$ decays are dominated by $\bar{b} \to \bar{u}$ (tree-type) and $\bar{b} \to \bar{s}(\bar{d})$ (penguin-type) quark transitions (see figs. 1.6–1.9). The observed decay-rates are $\mathcal{O}(10^{-5})$ and smaller because the former processes involve leading-order diagrams that are CKM suppressed ($|V_{ub}| \ll |V_{cb}|$), while the latter involves higher-order diagrams.

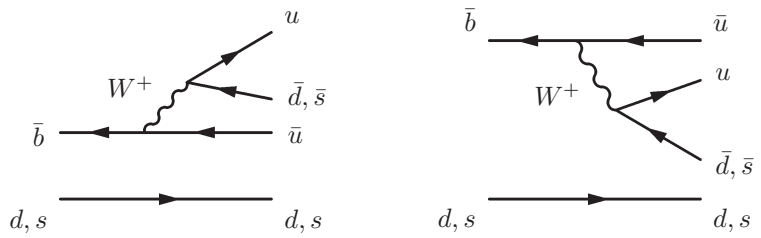


Figure 1.6: Color-allowed (left panel) and color-suppressed (right panel) tree (T) diagram contributing to $B^0_{(s)} \to h^+h^{'-}$ decays.

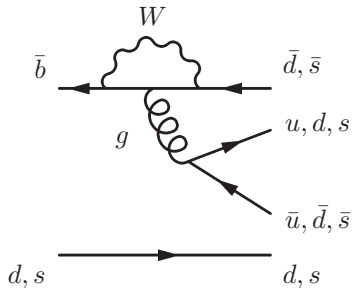


Figure 1.7: QCD-penguin (P) diagram contributing to $B^0_{(s)} \to h^+h^{'-}$ decays.

Several strategies based on flavor symmetries were proposed to control the hadronic uncertainties in the predictions of $B^0_{(s)} \to h^+h^{'-}$ amplitudes. In the following, we first focus the discussion on the U-spin flavor-symmetry because it has a specific interest in the context of this analysis and second we study the phenomenology of individual $B^0_{(s)} \to h^+h^{'-}$ mode.

1.7.1 Amplitude relations from U-spin flavor symmetry

The U-spin symmetry is a sub-group of the SU(3) flavor symmetry under which d quarks transform into s quarks. The $B^0 \to \pi^+\pi^-$ and the $B_s^0 \to K^+K^-$ decays are an example of completely U-spin-symmetric channels. Relations (1.98)–(1.101) show an extended set of U-spin-symmetric decay modes

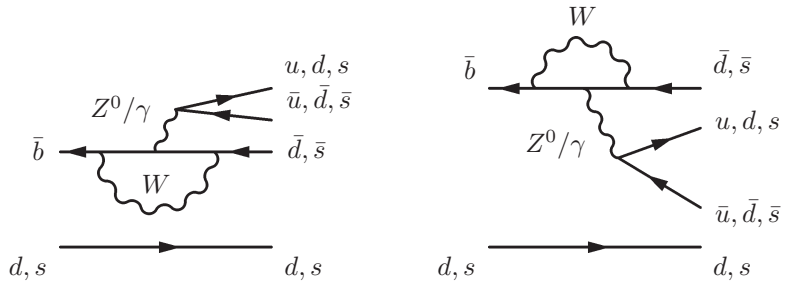


Figure 1.8: Color-allowed ($\mathrm{P_{EW}}$, left panel) and color suppressed ($\mathrm{P^C_{EW}}$, right panel) electroweak penguin diagram contributing to $B^0_{(s)} \to h^+h'^-$ decays.

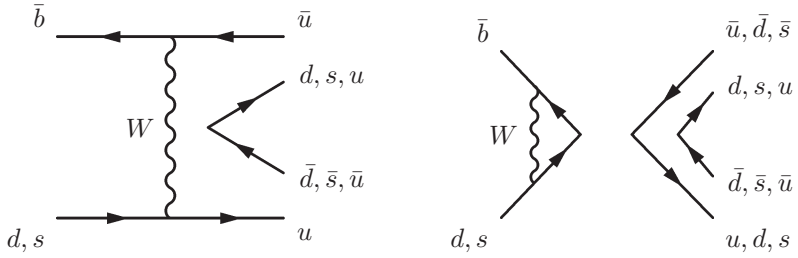


Figure 1.9: W-exchange (E, left panel) and penguin-annihilation (PA, right panel) diagram contributing to $B^0_{(s)} \to h^+h'^-$ decays.

along with their amplitudes (indicated following the classification of figs. 1.6–1.9)

$$\underbrace{B^0 \to \pi^+\pi^-}_{\mathrm{T+P+\frac{2}{3}P^C_{EW}+PA+E}} \quad d \longleftrightarrow s \quad \underbrace{B^0_s \to K^+K^-}_{\mathrm{T+P+\frac{2}{3}P^C_{EW}+PA+E}} \tag{1.98}$$

$$\underbrace{B^0 \to K^+\pi^-}_{\mathrm{T+P+\frac{2}{3}P^C_{EW}}} \quad d \longleftrightarrow s \quad \underbrace{B^0_s \to K^-\pi^+}_{\mathrm{T+P+\frac{2}{3}P^C_{EW}}} \tag{1.99}$$

$$\underbrace{B^0 \to K^+\pi^-}_{\mathrm{T+P+\frac{2}{3}P^C_{EW}}} \quad d \overset{\text{spect.}}{\longleftrightarrow} s \quad \underbrace{B^0_s \to K^+K^-}_{\mathrm{T+P+\frac{2}{3}P^C_{EW}+PA+E}} \tag{1.100}$$

$$\underbrace{B^0 \to \pi^+\pi^-}_{\mathrm{T+P+\frac{2}{3}P^C_{EW}+PA+E}} \quad d \overset{\text{spect.}}{\longleftrightarrow} s \quad \underbrace{B^0_s \to K^-\pi^+}_{\mathrm{T+P+\frac{2}{3}P^C_{EW}}} \tag{1.101}$$

The "spect." superscript labels relations in which U-spin-symmetry is applied only to the "spectator" quark, i. e., the valence quark of the $B^0_{(s)}$ meson that does *not* participate to the weak, quark-level process governing the decay. In these cases, where the U-spin transformation regards only the spectator quark, two decay modes can be treated as U-spin partners only if the effect of annihilation and exchange diagrams (see fig. 1.9), in which *both* quarks of the $B^0_{(s)}$ meson participate to the weak transition, is assumed negligible. This assumption can be verified experimentally by measuring the rates of other $B^0_{(s)} \to h^+h'^-$ decays (see sec. 1.7.7).

U-spin symmetry is not exactly conserved in the Standard Model. The magnitude of its violation, due to both factorizable and non-factorizable hadronic matrix elements, is not precisely known but most authors estimate a $\mathcal{O}(10\%)$ effect. The factorizable part of the violation can be calculated from QCD methods, such as light-cone sum-rules [59]; the full violation, however, that includes non-factorizable components, can only be inferred from data, by comparing amplitudes of U-spin-related modes.

1.7.2 $B^0 \to \pi^+\pi^-$

This decay is a transition into a CP eigenstate with eigenvalue +1, and originates from $\bar{b} \to \bar{u}u\bar{d}$ processes. Its decay amplitude can be written as follows [5]:

$$A(B_d^0 \to \pi^+\pi^-) = \lambda_u^{(d)}\,(A_{\rm T}^u + A_{\rm P}^u) + \lambda_c^{(d)} A_{\rm P}^c + \lambda_t^{(d)} A_{\rm P}^t. \tag{1.102}$$

where $A_{\rm T}^u$ is due to current–current contributions, and the amplitudes $A_{\rm P}^j$ describe penguin topologies with internal j quarks ($j \in \{u, c, t\}$). These penguin amplitudes take into account both QCD and electroweak penguin contributions. The quantities

$$\lambda_j^{(d)} \equiv V_{jd} V_{jb}^* \tag{1.103}$$

are the usual CKM factors. If we make use of the unitarity of the CKM matrix (eq. (1.45)) and apply the Wolfenstein parameterization, generalized to include non-leading terms in λ, we obtain:

$$A(B_d^0 \to \pi^+\pi^-) = \mathcal{C}\left[e^{i\gamma} - de^{i\theta}\right], \tag{1.104}$$

where the overall normalization $\mathcal{C}$ and

$$de^{i\theta} \equiv \frac{1}{R_b}\left[\frac{A_{\rm P}^c - A_{\rm P}^t}{A_{\rm T}^u + A_{\rm P}^u - A_{\rm P}^t}\right] \tag{1.105}$$

are hadronic parameters. The formalism discussed in sec. 1.5.4 then implies

$$\xi_{\pi^+\pi^-}^{(d)} = -e^{-i\phi_d}\left[\frac{e^{-i\gamma} - de^{i\theta}}{e^{+i\gamma} - de^{i\theta}}\right]. \tag{1.106}$$

The hadronic parameter $de^{i\theta}$, which suffers from large theoretical uncertainties, does *not* enter (eq. (1.106)) in a doubly Cabibbo-suppressed way. This feature is at the basis of the famous "penguin problem" in $B^0 \to \pi^+\pi^-$, which was addressed in many papers (see, for instance, Ref. [60]). If the penguin contributions to this channel were negligible, i.e. $d = 0$, its CP asymmetries were simply given by

$$\mathcal{A}_{\rm CP}^{\rm dir}(B_d \to \pi^+\pi^-) = 0 \tag{1.107}$$

$$\mathcal{A}_{\rm CP}^{\rm mix}(B_d \to \pi^+\pi^-) = \sin(\phi_d + 2\gamma) \stackrel{\rm SM}{=} \sin(\underbrace{2\beta + 2\gamma}_{2\pi - 2\alpha}) = -\sin 2\alpha. \tag{1.108}$$

Consequently, $\mathcal{A}_{\rm CP}^{\rm mix}(B_d \to \pi^+\pi^-)$ would allow us to determine α. However, in the general case, we obtain expressions with the help of eq. (1.90) and eq. (1.106) of the form

$$\mathcal{A}_{\rm CP}^{\rm dir}(B_d \to \pi^+\pi^-) = G_1(d, \theta; \gamma) \tag{1.109}$$

$$\mathcal{A}_{\rm CP}^{\rm mix}(B_d \to \pi^+\pi^-) = G_2(d, \theta; \gamma, \phi_d); \tag{1.110}$$

for explicit formulas, see Ref. [5]. We observe that actually the phases ϕ_d and γ enter directly in the $B_d \to \pi^+\pi^-$ observables, and not α. Consequently, since ϕ_d can be fixed through the mixing-induced CP violation in the "golden" mode $B_d \to J/\psi K_{\rm S}$, we may use $B_d \to \pi^+\pi^-$ to probe γ.

The branching fraction of the $B^0 \to \pi^+\pi^-$ mode was measured and the values are reported in tab. 1.1. The B-Factories also measured the time-dependent CP asymmetries The current measurements are given as follows:

$$\mathcal{A}_{\rm CP}^{\rm dir}(B^0 \to \pi^+\pi^-) = \begin{cases} +0.21 \pm 0.09 \pm 0.02 & (\textit{BABAR}\ [61]) \\ +0.55 \pm 0.08 \pm 0.05 & (\text{Belle}\ [62]) \end{cases} \tag{1.111}$$

$$\mathcal{A}_{\rm CP}^{\rm mix}(B^0 \to \pi^+\pi^-) = \begin{cases} -0.60 \pm 0.11 \pm 0.03 & (\textit{BABAR}\ [61]) \\ -0.61 \pm 0.10 \pm 0.04 & (\text{Belle}\ [62]). \end{cases} \tag{1.112}$$

The *BABAR* and Belle results are not fully consistent with each other, although the experiments are now in better agreement. In Ref. [48], the following averages were obtained:

$$\mathcal{A}_{\rm CP}^{\rm dir}(B^0 \to \pi^+\pi^-) = +0.38 \pm 0.07 \tag{1.113}$$

$$\mathcal{A}_{\rm CP}^{\rm mix}(B^0 \to \pi^+\pi^-) = -0.61 \pm 0.08. \tag{1.114}$$

The central values of these averages are remarkably stable with time. Direct CP violation at this level would require large penguin contributions with large CP-conserving strong phases, thereby indicating large non-factorizable effects.

From an experimental point of view a third measurement of the time-dependent CP asymmetries of the $B^0 \to \pi^+\pi^-$ would be desirable to solve the the B-Factories discrepancy.

	BABAR	Belle	CLEO	CDF
$\mathcal{B}(B^0 \to \pi^+\pi^-)$	$5.5 \pm 0.4 \pm 0.3$	$5.1 \pm 0.2 \pm 0.2$	$4.5^{+1.4+0.5}_{-1.2-0.4}$	$3.9 \pm 1.0 \pm 0.6$
$\mathcal{B}(B^0 \to K^+\pi^-)$	$19.1 \pm 0.6 \pm 0.6$	$19.9 \pm 0.4 \pm 0.8$	$18.0^{+2.3+1.2}_{-2.1-0.9}$	–
$\mathcal{B}(B^0 \to K^+K^-)$	< 0.5 @ 90%CL	< 0.41 @ 90%CL	< 0.8 @ 90%CL	< 1.8 @ 90%CL
$\mathcal{B}(B^0_s \to \pi^+\pi^-)$	–	–	–	< 1.7 @ 90%CL
$\mathcal{B}(B^0_s \to K^-\pi^+)$	–	–	–	< 5.6 @ 90%CL
$\mathcal{B}(B^0_s \to K^+K^-)$	–	–	–	$33 \pm 6 \pm 7$

Table 1.1: Summary of branching fractions in unit 10^{-6} of $B^0_{(s)} \to h^+h'^-$ decays for *BABAR* [63], Belle [64, 65], CLEO [66], CDF [1].

1.7.3 $B^0 \to K^+\pi^-$

The $B^0 \to K^+\pi^-$ decay channel receives contributions both from tree and from penguin topologies. Since this decay originates from a $\bar{b} \to \bar{s}$ transition, the tree amplitude is suppressed by a CKM factor $\lambda^2 R_b \sim 0.02$ with respect to the penguin amplitude. Consequently, $B^0 \to K^+\pi^-$ is governed by QCD penguins; the tree topologies contribute only at the 20% level to the decay amplitude. The diagrams contributing to $B^0 \to K^+\pi^-$ can straightforwardly be obtained by just replacing the anti-down quark emerging from the W boson through an anti-strange quark of the diagram of the $B^0 \to \pi^+\pi^-$. The

hadronic matrix elements entering $B^0 \to \pi^+\pi^-$ and $B^0 \to K^+\pi^-$ can be related through the SU(3) flavour symmetry of strong interactions and the additional assumption that the penguin annihilation and exchange topologies contributing to $B^0 \to \pi^+\pi^-$, which have no counterpart in $B^0 \to K^+\pi^-$ and involve the "spectator" down quark, play actually a negligible rôle [67]. Following these lines, we obtain the following relation in the Standard Model:

$$H_{\mathcal{B}} \equiv \frac{1}{\epsilon}\left(\frac{f_K}{f_\pi}\right)^2\left[\frac{\mathcal{B}(B^0 \to \pi^+\pi^-)}{\mathcal{B}(B^0 \to K^+\pi^-)}\right] = -\frac{1}{\epsilon}\left[\frac{\mathcal{A}_{\rm CP}^{\rm dir}(B^0 \to \pi^+\pi^-)}{\mathcal{A}_{\rm CP}^{\rm dir}(B^0 \to \pi^+\pi^-)}\right] \equiv H_{\mathcal{A}_{\rm CP}^{\rm dir}}, \tag{1.115}$$

where

$$\epsilon \equiv \frac{\lambda^2}{1-\lambda^2} = 0.053, \tag{1.116}$$

and the ratio $f_K/f_\pi = 160/131$ of the kaon and pion decay constants describes factorizable SU(3)-breaking corrections. The quantities $H_{\mathcal{B}}$ and $H_{\mathcal{A}_{\rm CP}^{\rm dir}}$ introduced in this relation can be written as follows:

$$H_{\mathcal{B}} = G_3(d,\theta;\gamma) = H_{\mathcal{A}_{\rm CP}^{\rm dir}}. \tag{1.117}$$

where we have sufficient information to determine γ, as well as (d,θ) [5, 67, 68] from the interplay of the observables of the $B^0 \to \pi^+\pi^-$ and $B^0 \to K^+\pi^-$ (the time dependent CP asymmetries for the $B^0 \to \pi^+\pi^-$ are currently experimentally accessible to the B-Factories [48], see sec. 1.7.2). In Ref. [69], the results following from $H_{\mathcal{B}}$ and $H_{\mathcal{A}_{\rm CP}^{\rm dir}}$ give results that are in good agreement with one another.

Another interesting example of interplaying between separate experimental information to probe New Physics effects is given by the comparison between the direct CP asymmetry of $B^0 \to K^+\pi^-$ and that of its U-spin partner $B^+ \to K^+\pi^0$. In the $B^0 \to K^+\pi^-$ and $B^+ \to K^+\pi^0$ decays, EW penguins contribute in color-suppressed form and are hence expected to play a minor rôle. In this limit, of vanishing color-suppressed tree and EW penguin topologies, CP asymmetry of the $B^+ \to K^+\pi^0$ is expected to be equal to the direct CP asymmetry of the $B^0 \to K^+\pi^-$ modes [12, 13, 14]. Since the experimental values of both asymmetries can be accessed and they do not agree [48]

$$\mathcal{A}_{\rm CP}^{\rm dir}(B^+ \to K^+\pi^0) = +0.047 \pm 0.026 \tag{1.118}$$

$$\mathcal{A}_{\rm CP}^{\rm dir}(B^0 \to K^+\pi^-) = -0.095 \pm 0.013 \tag{1.119}$$

the direct CP violation in $B^+ \to K^+\pi^0$ has also received a lot of attention. The lifted color suppression could, in principle, be responsible for a non-vanishing difference:

$$\Delta A \equiv \mathcal{A}_{\rm CP}^{\rm dir}(B^+ \to K^+\pi^0) - \mathcal{A}_{\rm CP}^{\rm dir}(B^0 \to K^+\pi^-) \stackrel{\rm exp}{=} +0.14 \pm 0.03. \tag{1.120}$$

ΔA shows a deviation of 4.7σ from 0. While it has been argued in the past that the asymmetries in these two modes should be equal in the standard model due to isospin symmetry, this is not anymore considered a reliable test [70, 71, 72]. In view of the large uncertainties, no more stringent test is provided at this point. Nevertheless, it is tempting to play a bit with the CP asymmetries of the $B^+ \to K^+\pi^0$ and $B^0 \to \pi^0 K_{\rm S}$ decays and in particular the measurement on its ideal partner $B_s^0 \to K^-\pi^+$ can shed light on the source of the direct CP violation in the $B^0 \to K^+\pi^-$ counterpart and solve the puzzling above described.

1.7.4 $B^0 \to K^+K^-$

The $B^0 \to K^+K^-$ mode receives contributions from penguin-annihilation and exchange diagrams, in which all initial-state quarks undergo a transition. These diagrams are difficult to predict with current phenomenological models. Since this decay is similar to the $B^0_s \to \pi^+\pi^-$ we will infer on both in sec. 1.7.7. Here we anticipate that this decay has not yet been observed and the experimental upper limits at 90% CL are reported in tab. 1.1.

1.7.5 $B^0_s \to K^-\pi^+$

The $B^0_s \to K^-\pi^+$ decay, which is the U-spin partner of the $B^0 \to K^+\pi^-$ decay, has been indicated by several authors as a source of rich opportunities of investigation.

In 2000 Gronau and Rosner proposed an SU(3)-based strategy to measure the CKM phase γ [73, 74] with the help of the $B^0_s \to K^-\pi^+$ mode. Experimentally, their proposal is accessible since it involves only time-integrated measurements of partial rates of untagged $B^0_{(s)}$ and B^+ decays into kaons and pions. But, from the theoretical stand-point, it needs some unknown corrections, due to rescattering effects and $\mathrm{P}^{\mathrm{C}}_{\mathrm{EW}}$ contributions. Gronau and Rosner indicated the $B^0_s \to K^-\pi^+$ mode as the key to reduce one of the major sources of theoretical uncertainty, i. e., the parameter associated to the ratio between tree and penguin amplitudes (P/T) [74]. Using the spectator-U-spin symmetry, which transforms the U-spin partners decays $B^0_s \to K^-\pi^+$ and $B^0 \to K^+\pi^-$ into another pair of U-spin partners, $B^0_s \to K^+K^-$ and $B^0 \to \pi^+\pi^-$, the authors devise a method to precisely measure P/T, provided separate measurement of $B^0_s \to K^-\pi^+$ and $\overline{B}^0_s \to K^+\pi^-$ decay rates are made.

The $B^0_s \to K^-\pi^+$ is still unobserved. The expectations for its branching fraction and direct CP asymmetry are reported in tab. 1.2. Regarding the decay rate the different theoretical approaches are in agreement within the large uncertainties associated. Only the SCET gives a lower central value more in agreement with the current experimental upper limit $\mathcal{B}(B^0_s \to K^-\pi^+) < 5.6 \times 10^{-6}$ @ 90% CL [1] from CDF. Also the expectations for the direct CP asymmetry varies in a large range as a function of the approach used and also in this case the theoretical uncertainties are very large. Without entering the details of the calculations details we note that they depend on several hadronic parameters and on the element of UT like α and γ.

In this context the measurement of the decay rate of the $B^0_s \to K^-\pi^+$ decay and the measurement of its direct CP asymmetry becomes crucial. It is important to note that the CP asymmetry of this mode may be large, so it may be the second mode after the $B^0 \to K^+\pi^-$ where it is possible observe direct CP violation effects in the B-mesons system. In 2005 in Ref. [8] Lipkin, inspired by an earlier work of Gronau [7] in 2000, pointed out an interesting model independent relation between the direct CP asymmetry of the $B^0_s \to K^-\pi^+$ and that one of the $B^0 \to K^+\pi^-$ decay, which may verify is the $\mathcal{A}_{\mathrm{CP}}(B^0 \to K^+\pi^-)$ is described by the Standard Model or is due to New Physics effects.

The observation of a $\mathcal{O}(10\%)$ direct CP violation in the $B^0 \to K^+\pi^-$ decay [11] is not supported by an expected similar effect in the $B^+ \to K^+\pi^0$ decay, which differs only by the spectator quark (see sec. 1.7.3). This raised interpretations about this disagreement being a possible indication of New Physics (see section sec. 1.7.3). Lipkin suggests that partial decay-rates in $B^0_s \to K^-\pi^+$ provide a stringent test that necessarily confirms or rules out the presence of New Physics involved in

$B^0 \to K^+\pi^-$ amplitudes. This approach exploits an accidental cancellation between CKM factors involved in $B^0 \to K^+\pi^-$ and $B_s^0 \to K^-\pi^+$ decays, which yields *equal* expected direct CP asymmetries in these decays. In fact, penguin (tree) amplitudes dominate the $B^0 \to K^+\pi^-$ ($B_s^0 \to K^-\pi^+$) process; in the B_s^0 decay, the penguin amplitude is suppressed, with respect to its B^0 counterpart, by exactly the same factor that enhances the amplitude of the interfering tree amplitude. This accidental correspondence is valid only within the framework of the Standard Model, thereby any significant disagreement between the measured partial rate asymmetries of strange and non-strange b-meson $K\pi$ decays is strong convincing indication of New Physics.

Gronau and Lipkin predict that:

$$|A(B_s^0 \to K^-\pi^+)|^2 - |A(\overline{B}_s^0 \to K^+\pi^-)|^2 = |A(\overline{B}^0 \to K^-\pi^+)|^2 - |A(B^0 \to K^+\pi^-)|^2 \qquad (1.121)$$

where A is the decay amplitude. In terms of decay width the relation (1.121) becomes:

$$\Gamma(B_s^0 \to K^-\pi^+) - \Gamma(\overline{B}_s^0 \to K^+\pi^-) = \Gamma(\overline{B}^0 \to K^-\pi^+) - \Gamma(B^0 \to K^+\pi^-). \qquad (1.122)$$

All these transitions involve the product of a pion form factor and a kaon form factor. These form factors are all equal in the U-spin symmetry limit and differences arising from symmetry breaking have been analyzed [7]. The tree-penguin interference term relevant to direct CP violation is proportional to the product of four form factors, one of which is a point-like form factor of the meson created from a $q\bar{q}$ pair produced at the weak vertex of the tree diagram and the other three are hadronic. The dominant symmetry-breaking in these products between B_d and B_s decays is in the difference between the products of a point-like kaon and a hadronic pion form factor for B_d decay and of a point-like pion and a hadronic kaon form factor for B_s decay. This symmetry-breaking was neglected here, but note that the error introduced is expected to be real and not change the relative phase of diagrams which is crucial for CP violation. The error can also be estimated from simple models or determined from other experiments[7]. Since the individual tree and penguin contributions to U-spin conjugate B_d and B_s decays are very different and their branching ratios and lifetimes are different, the equality of eq. (1.121) does not apply to the expressions $\mathcal{A}_{\rm CP}$ commonly used to express CP violation. Instead we have

$$\mathcal{A}_{\rm CP}(B_s^0 \to K^-\pi^+) = -\mathcal{A}_{\rm CP}(B^0 \to K^+\pi^-) \times \frac{\mathcal{B}(B^0 \to K^+\pi^-)}{\mathcal{B}(B_s^0 \to K^-\pi^+)} \times \frac{\tau(B_s^0)}{\tau(B^0)} \qquad (1.123)$$

where $\mathcal{B}$ denotes branching ratio and τ denotes lifetime.

The relevance of this test resides in its nearly complete independence of models. No flavor symmetry are required, but only charge-conjugation invariance for all final state rescattering. In addition, the large asymmetries expected in the $B_s^0 \to K^-\pi^+$ decay make this test relatively easy, from an experimental point of view, once $B_s^0 \to K^-\pi^+$ decays will be observed.

All these observables can be measured simultaneously by hadronic machine experiment, with no external experimental information, so this makes it the best place to explore the origin of direct CP violation.

1.7.6 $B_s^0 \to K^+K^-$

The $B_s^0 \to K^+K^-$ decay is a $\bar{b} \to \bar{s}$ transition, and it involves tree and penguin amplitudes, as the $B^0 \to \pi^+\pi^-$ decay mode [5]. However, because of the different CKM structure, the latter topologies

	QCDF	SCET	pQCD
$\mathcal{B}(B^0 \to \pi^+\pi^-)$	$8.9^{+4.0+3.6+0.6+1.2}_{-3.4-3.0-1.0-0.8}$	$5.4 \pm 1.3 \pm 1.4 \pm 0.4$	$6.5^{+6.7}_{-3.8}$
$\mathcal{B}(B^0 \to K^+\pi^-)$	$16.3^{+2.6+9.6+1.4+11.4}_{-2.3-6.5-1.4-4.8}$	$20.1 \pm 7.4 \pm 1.3 \pm 0.6$	$20.4^{+16.1}_{-8.4}$
$\mathcal{B}(B^0 \to K^+K^-)$	$0.013^{+0.005+0.008+0.000+0.087}_{-0.005-0.005-0.000-0.011}$	—	—
$\mathcal{A}_{\rm CP}(B^0 \to K^+\pi^-)$	$+4.5^{+1.1+2.2+0.5+8.7}_{-1.1-2.5-0.6-9.5}$	$-0.06 \pm 0.05 \pm 0.06 \pm 0.02$	$-0.10^{+0.7}_{-0.8}$
$\mathcal{B}(B^0_s \to \pi^+\pi^-)$	$0.024^{+0.003+0.025+0.000+0.163}_{-0.003-0.012-0.000-0.021}$	—	$0.57^{+0.16+0.09+0.01}_{-0.13-0.10-0.00}$
$\mathcal{B}(B^0_s \to K^-\pi^+)$	$10.2^{+4.5+3.8+0.7+0.8}_{-3.9-3.2-1.2-0.7}$	$4.9 \pm 1.2 \pm 1.3 \pm 0.3$	$7.6^{+3.2+0.7+0.5}_{-2.3-0.7-0.5}$
$\mathcal{B}(B^0_s \to K^+K^-)$	$22.7^{+3.5+12.7+2.0+24.1}_{-3.2-\ 8.4-2.0-\ 9.1}$	$18.2 \pm 6.7 \pm 1.1 \pm 0.5$	$13.6^{+4.2+7.5+0.7}_{-3.2-4.1-0.2}$
$\mathcal{A}_{\rm CP}(B^0_s \to K^-\pi^+)$	$-6.7^{+2.2+2.9+0.4+15.2}_{-2.1-3.1-0.2-15.5}$	$+20 \pm 17 \pm 19 \pm 5$	$+24.1^{+3.6+3.0+1.2}_{-3.9-3.3-2.3}$

Table 1.2: The CP-averaged branching ratios ($\times 10^{-6}$) of $B^0_{(s)} \to h^+h^{'-}$ decays and the direct CP asymmetry (in %) of the $B^0 \to K^+\pi^-$ and $B^0_s \to K^-\pi^+$ decays obtained from QCDF [15], pQCD [16, 71], SCET [17] approach. The errors for these entries correspond to the uncertainties in the input hadronic quantities, from the scale-dependence, and the CKM matrix elements, respectively.

play actually the dominant rôle in the $B^0_s \to K^+K^-$ channel. In analogy to eq. (1.104), we may write

$$A(B^0_s \to K^+K^-) = \sqrt{\epsilon}\, \mathcal{C}' \left[e^{i\gamma} + \frac{1}{\epsilon}\, d' e^{i\theta'} \right], \tag{1.124}$$

where ϵ was introduced in eq. (1.116), and the CP-conserving hadronic parameters $\mathcal{C}'$ and $d'e^{i\theta'}$ correspond to $\mathcal{C}$ and $de^{i\theta}$, respectively. The corresponding observables take then the following generic form:

$$\mathcal{A}^{\rm dir}_{\rm CP}(B_s \to K^+K^-) = G'_1(d', \theta'; \gamma) \tag{1.125}$$

$$\mathcal{A}^{\rm mix}_{\rm CP}(B_s \to K^+K^-) = G'_2(d', \theta'; \gamma, \phi_s), \tag{1.126}$$

in analogy to the expressions for the CP-violating $B^0 \to \pi^+\pi^-$ asymmetries in eq. (1.109) and eq. (1.110). Since $\phi_d = 2\beta$ is already well measured and ϕ_s is negligibly small in the Standard Model – or can be determined through $B^0_s \to J/\psi\phi$ should CP-violating New Physics contributions to B^0_s–$\bar{B}^0_s$ mixing make it sizeable – we may convert the measured values of $\mathcal{A}^{\rm dir}_{\rm CP}(B_d \to \pi^+\pi^-)$, $\mathcal{A}^{\rm mix}_{\rm CP}(B_d \to \pi^+\pi^-)$ and $\mathcal{A}^{\rm dir}_{\rm CP}(B_s \to K^+K^-)$, $\mathcal{A}^{\rm mix}_{\rm CP}(B_s \to K^+K^-)$ into *theoretically clean* contours in the γ–d and γ–d' planes, respectively.

The $B^0 \to \pi^+\pi^-$ decay is actually related to $B^0_s \to K^+K^-$ through the interchange of *all* down and strange quarks. Consequently, each decay topology contributing to $B^0 \to \pi^+\pi^-$ has a counterpart in $B^0_s \to K^+K^-$, and the corresponding hadronic parameters can be related to each other with the help of the U-spin flavour symmetry of strong interactions, implying the following relations [5]:

$$d' = d, \quad \theta' = \theta. \tag{1.127}$$

Applying the former, we may extract γ and d through the intersections of the theoretically clean γ–d and γ–d' contours. As discussed in Ref. [5], it is also possible to resolve the twofold ambiguity for (γ, d), thereby leaving us with the solution of γ. Moreover, we may determine θ and θ', which allow an interesting internal consistency check of the second U-spin relation in eq. (1.127). An alternative

avenue is provided if we eliminate d and d' through the CP-violating $B_d \to \pi^+\pi^-$ and $B_s \to K^+K^-$ observables, respectively, and extract then these parameters and γ through the U-spin relation $\theta' = \theta$.

This strategy is very promising for the hadronic machines experiments, where it is possible to access simultaneously the $B^0 \to \pi^+\pi^-$ and $B_s^0 \to K^+K^-$ observables. As far as possible U-spin-breaking corrections to $d' = d$ are concerned, they enter the determination of γ through a relative shift of the γ–d and γ–d' contours; their impact on the extracted value of γ therefore depends on the form of these curves, which is fixed through the measured observables. The extracted value of γ would be very stable under such effects. Let us also note that the U-spin relations in eq. (1.127) are particularly robust since they involve only ratios of hadronic amplitudes, where all $SU(3)$-breaking decay constants and form factors cancel in factorization and also chirally enhanced terms would not lead to U-spin-breaking corrections [5]. On the other hand, the ratio $|\mathcal{C}'/\mathcal{C}|$, which equals 1 in the strict U-spin limit and enters the U-spin relation

$$\frac{\mathcal{A}_{\rm CP}^{\rm mix}(B_s \to K^+K^-)}{\mathcal{A}_{\rm CP}^{\rm dir}(B_d \to \pi^+\pi^-)} = -\left|\frac{\mathcal{C}'}{\mathcal{C}}\right|^2 \left[\frac{\mathcal{B}(B_d \to \pi^+\pi^-)}{\mathcal{B}(B_s \to K^+K^-)}\right] \frac{\tau_{B_s}}{\tau_{B_d}}, \tag{1.128}$$

is affected by U-spin-breaking effects within factorization. An estimate of the corresponding form factors was performed in Ref. [59] with the help of QCD sum rules $|\mathcal{C}'/\mathcal{C}| = 1.76^{+0.15}_{-0.17}$, which is an important ingredient for a Standard Model prediction of the CP-averaged $B_s^0 \to K^+K^-$ branching ratio [18]. Following these lines, the prediction

$$\mathcal{B}(B_s \to K^+K^-) = (35 \pm 7) \times 10^{-6} \tag{1.129}$$

was obtained in Refs. [18, 75] from the CP-averaged $B^0 \to K^+\pi^-$ branching ratio. This prediction has to be compared with the current experimental measurement from CDF [1]:

$$\mathcal{B}(B_s^0 \to K^+K^-) = (33 \pm 5.7 \pm 6.7) \times 10^{-6}, \tag{1.130}$$

and the other theoretical expectations reported in tab. 1.2.

Descotes-Genon, Matias, and Virto recently proposed a new approach to the calculation of $\mathcal{B}(B_s^0 \to K^+K^-)$ that complements the benefits of the QCD factorization expansion (QCDF) with those of the SU(3) symmetry relations to control the $1/m_b$ corrections [76]. The measured rate of the $B^0 \to K^0\bar{K}^0$ process [77] is connected to the $B_s^0 \to K^+K^-$ rate, using a combination of U-spin and isospin arguments and fully evaluating SU(3) breaking within QCDF. The resulting prediction for the branching fraction is $\mathcal{B}(B_s^0 \to K^+K^-) = (20 \pm 9) \times 10^{-6}$ within the Standard Model. The uncertainty of this method is dominated by the experimental uncertainty on $\mathcal{B}(B^0 \to K^0\bar{K}^0)$, which is expected to be further reduced with future measurements from the B-Factories.

The experimental accuracy is still too poor for a statistically significant discrimination between the hypotheses of large U-spin violation or exact U-spin validity. However, the current $B_s^0 \to K^+K^-$ decay rate exceeds the predictions of Khodjamirian et al., suggesting large U-spin breaking in this process. A more precise measurement of this branching fraction becomes crucial to shed light on the size of U-spin-breaking.

The $B_s^0 \to K^+K^-$ mode is also a golden mode to extract $\Delta\Gamma_s$. In the Standard Model the $B_s^0 \to K^+K^-$ channel is predicted to be a 95% CP even decay [68, 52], this means that the measurement of the $B_s^0 \to K^+K^-$ lifetime provides in a very straightforward way the lifetime of the

light mass eigenstate $c\tau(B^0_s \to K^+K^-) = 1/\Gamma^{(s)}_{\rm L}$. By the comparison of this measurement with other independent measurements (for example $\Gamma^{(s)}_{\rm H}$ and $\Gamma^{(s)}_{\rm L}$ from angular analysis of $B^0_s \to J/\psi\phi$ mode) and the theoretical expectations [52] it is possible check the Standard Model predictions and to probe New Physics. A preliminary measurement of the lifetime of $B^0_s \to K^+K^-$ mode was already performed by CDF [78]:

$$\tau_{\rm L} = 1.53 \pm 0.18 \pm 0.02 \text{ ps}, \tag{1.131}$$

which, combined with the world average flavor-specific B^0_s meson lifetime [48], yielded the following measurement of the width-difference in the B^0_s-system for CP-eigenstates:

$$\frac{\Delta\Gamma^{\rm CP}_{(s)}}{\Gamma^{\rm CP}_{(s)}} = -0.08 \pm 0.23 \pm 0.03. \tag{1.132}$$

This measurement is still limited by statistical uncertainty therefore a more precise estimate of this parameter is desirable to probe inside this field.

1.7.7 $B^0_s \to \pi^+\pi^-$

Amplitudes of penguin-annihilation and exchange diagrams, in which all initial-state quarks undergo a transition, are difficult to predict with current phenomenological models. Their contribution needs to be neglected, for instance, when assuming spectator-U-spin relations (e. g., $B^0 \to K^+\pi^- \longleftrightarrow B^0_s \to K^-\pi^+$). And QCDF predictions are also affected by extremely large uncertainties due to the empirical corrections necessary to control soft end-point divergences. But, in general, PA and E topologies may carry different CP-violating and CP-conserving phases with respect to the leading processes, thereby influencing the determination of CKM-related parameters from widely-used decays as $B^0 \to \pi^+\pi^-$.

In the Standard Model, the decays $B^0 \to K^+K^-$ and $B^0_s \to \pi^+\pi^-$ proceed only through PA and E diagrams. A measurement of their decay rates (or improved constraints on them) would thereby provide valuable estimates of the magnitude of PA and E contributions. Theoretical predictions estimate the branching fractions of $B^0 \to K^+K^-$ and $B^0_s \to \pi^+\pi^-$ modes in the 10^{-7}–10^{-8} range are reported in [79, 80, 81] and in tab. 1.2. While the $B^0 \to K^+K^-$ mode is reconstructible also at the B-Factories, currently only CDF has access to the $B^0_s \to \pi^+\pi^-$ decay mode. This is a big opportunity for hadronic machines since only a simultaneously measurement of strength of both processes allows to extract the hadronic parameters entering in this diagrams [18]. The current upper limit from CDF [1] are: $\mathcal{B}(B^0 \to K^+K^-) < 1.8 \times 10^{-6}$ @ 90% CL reported also in tab. 1.2, and $\mathcal{B}(B^0_s \to \pi^+\pi^-) < 1.7 \times 10^{-6}$ @ 90% CL. Additional experimental information on their magnitude is, therefore, particularly desirable.

Chapter 2

The experimental apparatus

This chapter briefly describes the Tevatron collider accelerator and the CDF II detector, focusing on the subsystems most important for b-physics such as the tracking system. For an exhaustive description of the experimental apparatus, refer to Ref. [83].

2.1 The Tevatron collider

The Fermilab Tevatron collider is the last and highest energy accelerating stage located at Fermi National Accelerator Laboratory (a.k.a FNAL or Fermilab), about 50 km West from Chicago (IL) in the US. The Tevatron is a circular proton synchrotron 1 km in radius. While operating in collider mode, it collides bunches of protons circulating clockwise against antiprotons accelerated counter-clockwise, both at energies of 980 GeV. The energy available in the centre-of-mass after the collision is thus $\sqrt{s}$ =1.96 TeV, currently the highest in the world.
The Tevatron produced its first $p\bar{p}$ collisions in 1985 and since then has undergone extensive upgrades and improvements. The performance of the Tevatron collider is evaluated in terms of two key parameters: the available center-of-mass energy, $\sqrt{s}$, and the instantaneous luminosity, $\mathcal{L}$. The former defines the accessible phase-space for the production of resonances in the final states. The latter is the coefficient of proportionality between the rate of a given process and its cross-section σ:

$$\text{rate [events s}^{-1}] = \mathcal{L}\ [\text{cm}^{-2}\text{s}^{-1}]\ \times\ \sigma\ [\text{cm}^2].$$

The time-integral of the luminosity (integrated luminosity) is therefore a measure of the expected number of events, n, produced in a finite time T:

$$n(T) = \int_0^T \mathcal{L}\sigma dt. \tag{2.1}$$

Assuming an ideal head-on $p\bar{p}$ collision with no crossing angle between the beams, the instantaneous luminosity is defined as

$$\mathcal{L} = 10^{-5}\frac{N_p N_{\bar{p}} B f \beta\gamma}{2\pi\beta^*\sqrt{(\epsilon_p+\epsilon_{\bar{p}})_x(\epsilon_p+\epsilon_{\bar{p}})_y}}\mathcal{H}(\sigma_z/\beta^*) \qquad [10^{30}\text{cm}^{-2}\text{s}^{-1}]. \tag{2.2}$$

$\mathcal{L}$ depends on the following Tevatron parameters: the number of circulating bunches in the ring ($B = 36$), the revolution frequency ($f = 47.713$ kHz), the Lorentz relativistic factor (boost, $\beta\gamma = 1045.8$ at 980 GeV), the average numbers of protons ($N_p \approx 250 \times 10^9$) and antiprotons ($N_{\bar{p}} \approx 25 \times 10^9$) in a bunch, an empiric "hourglass" factor ($\mathcal{H} = 0.6$–0.7), which is a function of the ratio between the longitudinal r.m.s. width of the bunch ($\sigma_z \approx 60$ cm) and the "beta function" calculated at the interaction point ($\beta^* \approx 31$ cm), and the 95% normalized emittances of the beams ($\epsilon_p \approx 18\pi$ mm mrad and $\epsilon_{\bar{p}} \approx 13\pi$ mm mrad after injection).[1]

At the Tevatron the limiting factor of the luminosity is the availability of antiprotons because it is difficult to produce and to compact them into bunches and to transfer them efficiently through the subsequent accelerator stages. The Tevatron provides beams for experiments in different modes

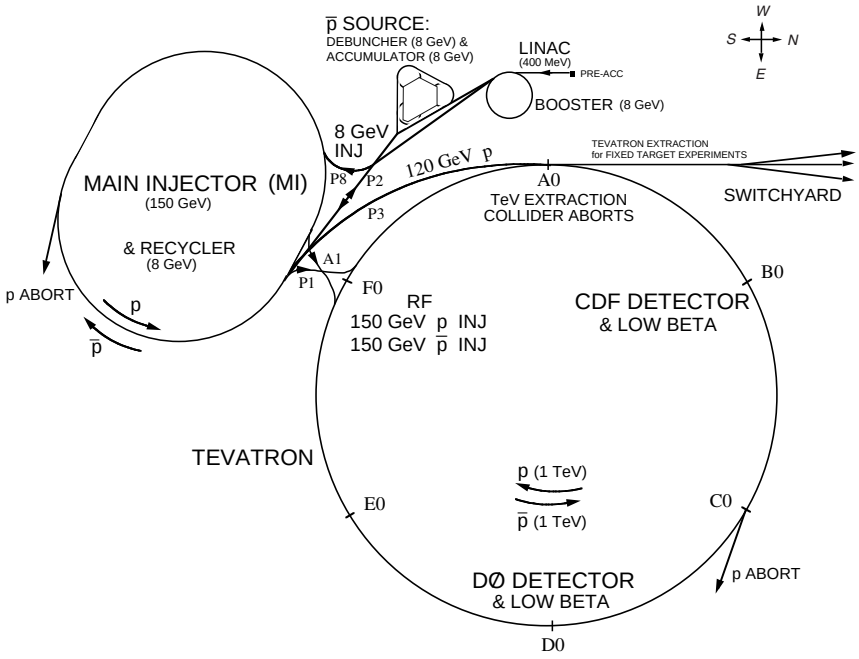


Figure 2.1: Illustration of the Fermilab Tevatron collider.

(fixed-target, collider, etc.). For the purpose of the present analysis, we will describe the procedure for obtaining a continuous period of collider operation using the same collection of protons and antiprotons, called a *store*. Further details can be found in Ref. [84].

[1]The hourglass factor is a parameterization of the longitudinal profile of the beams in the collision region, which assumes the shape of an horizontal hourglass centered in the interaction region. The beta function is a parameter convenient for solving the equation of motion of a particle through an arbitrary beam transport system. The emittance ϵ measures the phase-space occupied by the particles of the beam. Three independent two-dimensional emittances are defined. The quantity $\sqrt{\beta\epsilon}$ is proportional to the r.m.s. width of the beam in the corresponding phase plane. On-line measurements of the transverse emittances are performed at the Tevatron with various methods, including flying through the beam a 7 μm wire and by measuring the cascade of losses, which is proportional to the beam intensity, or detecting the synchrotron light radiated by the particles at the edge of a dipole magnet.

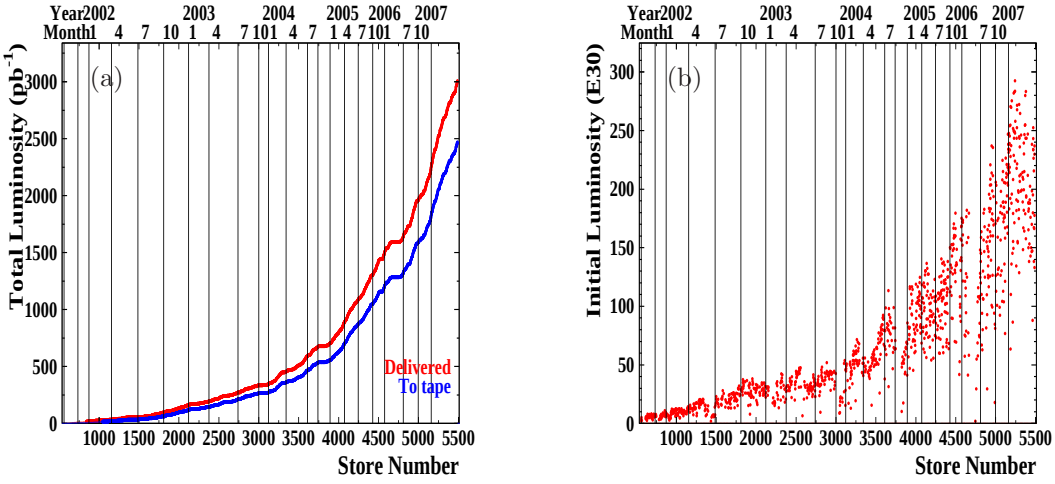


Figure 2.2: Integrated luminosity as a function of the time (or store number) (a). Initial luminosity as a function of the time (or store number) (b).

2.1.1 Proton beam

H^- ions are produced by ionization of gaseous hydrogen and boosted to 750 keV by a commercial Cockroft-Walton accelerator. Then they are injected in a 150 m long linear accelerator *Linac* which increases their energy to 400 MeV. A carbon foil is used to strip the electrons from the H^- before the resulting protons are injected to the *Booster*. The Booster (see fig. 2.1) is a rapid cycling synchrotron (radius of 75.5 m) that accelerates the protons up to 8 GeV and compacts them into bunches. The protons are then transfered to a synchrotron, called the *Main Injector*, which brings their energy to 150 GeV: this is the beginning of the process of final injection into the Tevatron called *'shot'*. Inside the Main Injector several bunches are coalesced into one for Tevatron injection. The last stage of the process is the transfer to the Tevatron, a synchrotron which employs superconducting Nb-Ti alloy filaments embedded in copper as magnet coils. The magnetic field of 5.7 T keeps the protons on an approximately circular orbit while they reach the final energy of 980 GeV.

2.1.2 Antiproton beam

While the energy of the protons bunches circulating in the Main Injector reaches 120 GeV, they are slammed to a rotating 7 cm thick nickel or copper target. Spatially wide-spread antiprotons are produced and focused into a beam via a cylindrical lithium lens which separates $\bar{p}$ from other charged interaction products. The emerging antiprotons have a bunch structure similar to that of the incident protons and are stored in a *Debuncher*. It is a storage ring where the momentum spread of the $\bar{p}$ is reduced while maintaining a constant energy of 8 GeV, via stochastic cooling stations. Many cycles of Debuncher cause the destruction of the bunch structure which results in a continuous beam of antiprotons. At the end of the process the monochromatic antiprotons are stored in the *Accumulator* (see fig. 2.1) which is a triangle-shaped storage ring where they are further cooled and stored until

the cycles of the Debuncher are completed. When a current sufficient to create 36 bunches with the required density is available, the $\bar{p}$ are injected into the Main Injector. Here their energy is raised to 150 GeV and they are transferred to the Tevatron where 36 bunches of protons are already circulating in opposite direction.

2.1.3 The collision

When 36 bunches of both protons and antiprotons are circulating in the Tevatron, the energy of the machine is increased in about 10 seconds from 150 to 980 GeV and the collisions begin at the two interaction points: DØ (where the homonym detector is located) and BØ (home of CDF II). Special quadrupole magnets (*low-β squeezers*) located at both extremities of the detectors along the beam pipe "squeeze" the beam to maximize luminosity inside the detectors. A roughly Gaussian distribution of the interaction region along the beam axis is achieved ($\sigma_z \approx 28$ cm) and its center is shifted on the nominal interaction point by the fine tuning of squeezers. The transverse shape of the interaction region has an almost circular spatial distribution with a diameter of $\sigma_{\mathrm{T}} \approx 30$ μm. Luminosity lifetime is increased by using electrostatic separators which separate transversely the proton and antiproton bunches except at the collision regions. Then the *'scraping'* takes place, a procedure which shapes the beam transverse profile to its optimized configuration, in order to avoid detector damages due to the tails of the $p(\bar{p})$ distributions entering the active volumes. The scraping is done by moving iron plates which act as collimators in the transverse plane toward the beam and sweep away the transverse beam halo. When the beam profile is narrow enough and the conditions are safely stable the detectors are powered and the data taking starts. This is the end of the injection procedure called *'shot'*.
The inter-bunch crossing is 396 ns and this defines an overall time constant which influences the whole detector design: on this parameter depends the choice of the active parts, the design of the readout electronics, the structure of the trigger etc.. The number of overlapping interactions N for each bunch crossing is a Poisson-distributed variable dependent on the instantaneous luminosity and on the number of colliding bunches. At Tevatron peak luminosities of $\mathcal{L} \approx 10 \times 10^{31}$ cm^{-2}s^{-1} $\bar{N}$ is approximately 2.
Each time that at least one of the CDF II triggers fires, an *event* is labeled with an increasing number. Events are grouped into *'runs'*; a run is a period of continuous[2] operation of the CDF II Data Acquisition. Most parameter of the CDF II operations (e. g., the position of the beam) are stored in the database on a run-averaged format.
While collisions are taking place the luminosity decreases exponentially[3] because of the beam-gas and beam-halo interactions. In the meantime, antiproton production and storage continues. When the antiproton stack is sufficiently large ($\simeq 10^{12}$ antiprotons) and the circulating beams are degraded (~ 14 hours) the detector high-voltages are switched off and the store is dumped. The beam is extracted via a switch-yard and sent to an absorption zone. Beam abortion can occur also accidentally when the temperature of a superconducting magnet shift above the critical value and the magnet quenches destroying the orbit of the beams. The typical time between the end of a store and the beginning of collisions of the next one is typically 2 hr. During this time CDF II usually performs calibrations of

[2]Many different cases can require the DAQ to be stopped and restarted including the need to enable or disable a subdetector, a change in the trigger Table, a problem in the trigger/DAQ chain etc..

[3]The decrease is about a factor of 2.5-5 for a store ($\sim$ 10-20 hrs), depending from the initial luminosity also.

the sub-detectors and test runs with cosmics.

2.1.4 Tevatron Status

The stated goal of Tevatron Run II was (1996) the accumulation of 2 fb^{-1} at $\sqrt{s} = 2$ TeV with instantaneous luminosity peaks up to 2×10^{32} $\text{cm}^{-2}\text{s}^{-1}$. The current performance is well beyond these expectations. The centre-of-mass energy is 1.96 TeV, the peak luminosity exceeds regularly 2×10^{32} $\text{cm}^{-2}\text{s}^{-1}$ (with a record of 2.85×10^{32} $\text{cm}^{-2}\text{s}^{-1}$, 18 February 2007) and the crossing time is equal to 396 ns. From February 2002 to March 2006, ≈ 1.2 fb^{-1} were recorded on tape but the most stringent data quality requirements shrank the sample to 1 fb^{-1} to be used for this analysis. Tevatron delivered until today about ≈ 3 fb^{-1} (on tape ≈ 2.5 fb^{-1}).

2.2 The CDF II detector

The CDF II detector is a large multi-purpose solenoidal magnetic spectrometer surrounded by 4π fast, projective calorimeters and fine-grained muon detectors. It is installed at the BØ interaction point of the Tevatron (see fig. 2.1) to determine energy, momentum and, whenever possible, the identity of a broad range of particles produced in 1.96 TeV $p\bar{p}$ collisions. Several upgrades modified the design of the original facility commissioned in 1985.[4] The most extensive upgrade started in 1995 and led to the current detector whose operation is generally referred to as Run II.

2.2.1 Coordinates and notation

CDF II employs a right-handed Cartesian coordinates system with the origin in the B0 interaction point, assumed coincident with the center of the drift chamber. The positive z-axis lies along the nominal beam-line pointing toward the proton direction (east). The (x, y) plane is therefore perpendicular to either beams, with positive y-axis pointing vertically upward and positive x-axis in the horizontal plane of the Tevatron, pointing radially outward with respect to the center of the ring.

Since the colliding beams of the Tevatron are unpolarized, the resulting physical observations are invariant under rotations around the beam line axis. Thus, a cylindrical (r, ϕ, z) coordinates system is particularly convenient to describe the detector geometry. Throughout this thesis, *longitudinal* means parallel to the proton beam direction (i.e., to the z-axis), and *transverse* means perpendicular to the proton direction, i.e., in the $(x, y) \equiv (r, \phi)$ plane.

Since the protons and antiprotons are composite particles, the actual interaction occurs between individuals partons (valence or sea quarks and gluons) contained within them. Each parton carries a varying fraction of the (anti)proton momentum, not known on a event-by-event basis. As a consequence of the possible imbalance in the longitudinal components of the momenta of interacting partons, possible large velocities along $\hat{z}$ for the center-of-mass of the parton-level interaction may occur. In the hadron collisions environment, it is customary to use a variable invariant under $\hat{z}$ boosts

[4] Originally, the CDF acronym was meant for Collider Detector Facility.

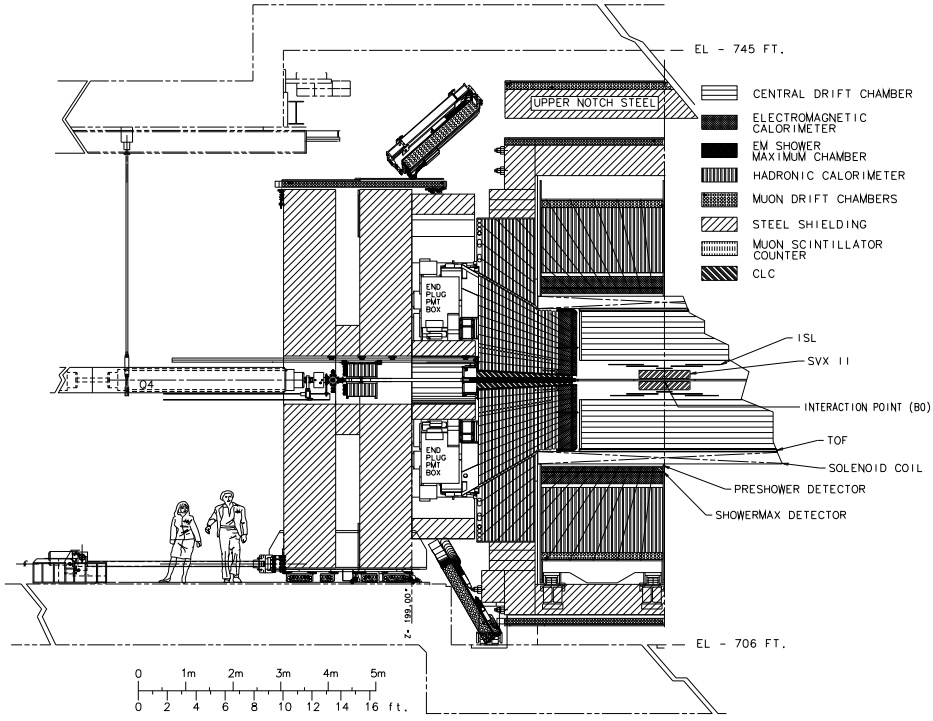


Figure 2.3: Elevation view of one half of the CDF II detector.

as an unit of relativistic phase-space, instead of the polar angle θ. This variable is the *rapidity* defined as

$$Y = \frac{1}{2}\ln\left[\frac{\mathrm{E} + \mathrm{pcos}(\theta)}{\mathrm{E} - \mathrm{pcos}(\theta)}\right], \tag{2.3}$$

where $(E, \vec{p})$ is the energy-momentum four-vector of the particle. Under a $\hat{z}$ boost to an inertial frame with velocity β, the rapidity of a particle transforms linearly, according to $Y \rightarrow Y' \equiv Y + \tanh^{-1}(\beta)$, therefore Y is invariant since $dY \equiv dY'$. However, a measurement of rapidity still requires a detector with accurate identification capabilities because of the mass term entering E. Thus, for practical reasons, it is often preferred to substitute Y with its approximate expression η in the ultra-relativistic limit ($p >> m$), usually valid for products of high-energy collisions:

$$Y \rightarrow \eta + \mathcal{O}(m^2/p^2), \tag{2.4}$$

where the *pseudo-rapidity* $\eta \equiv -\ln[\tan(\theta/2)]$ is only function of the momenta. As the event-by-event longitudinal position of the actual interaction is distributed around the nominal interaction point with

30 cm r.m.s width, it is useful to distinguish the *detector pseudo-rapidity*, $\eta_{\rm det}$, measured with respect to the (0,0,0) nominal interaction point, from the *particle pseudo-rapidity*, η, measured with respect to the z_0 position of the real vertex where the particle originated[5].

Other convenient variables are the transverse component of the momentum with respect to the beam axis ($p_{\rm T}$), the "transverse energy" ($E_{\rm T}$), and the approximately Lorentz-invariant angular distance ΔR, defined as

$$\vec{p}_{\rm T} \equiv (p_x, p_y) \rightarrow p_{\rm T} \equiv p\sin(\theta), \quad E_{\rm T} \equiv E\sin(\theta), \quad \text{and} \quad \Delta R \equiv \sqrt{\eta^2 + \phi^2}. \tag{2.5}$$

2.2.2 Overview

CDF II is designed for measurements of a broad range of final states in $p\bar{p}$ collisions at high energy. A comprehensive description of the CDF II detector and its subsystems is given in Ref. [83].
CDF II (see fig. 2.3) is a three-story, 5000-ton approximately cylindric assembly of sub-detectors, ~ 15 m in length, ~ 15 m in diameter. The flow of final state particles in energetic hadronic collisions is well described by quantities of (pseudo)rapidity, transverse component of the momentum with respect to the beam axis and azimuthal angle around this axis. Consequently CDF II detector was designed and constructed with an approximately cylindrically symmetric layout both in the azimuthal plane and in the *"forward"* ($z > 0$) - *"backward"* ($z < 0$) directions with spatial segmentation of its subcomponents roughly uniform in pseudorapidity and azimuth.
CDF II is composed of several specialized sub-systems each one designed to perform a different task. Its capabilities include high resolution charged particle tracking, electron and muon identification, low momentum π/K separation, precise secondary vertices proper time measurements, finely segmented sampling of energy flow coming from final state hadrons, electrons or photons, identification of ν's via transverse energy imbalance.
A 1.4116 T solenoidal magnetic field is maintained in the region $r < 150$ cm $|z| < 250$ cm by circulating a 4650 A current through 1164 turns of a Nb-Ti/Cu superconducting coil. The field is oriented along the positive $\hat{z}$ direction and is uniform at the 0.1% level in the $|z| < 150$ cm volume where tracking measurements are made (see fig. 2.4). The tiny non-uniformities, mapped out during detector construction, are treated as a small perturbation within the track fitting software. The field is continuously monitored via NMR probes during data taking and any deviation from the mapped values is applied as a correction to measured track momenta. The threshold to escape radially the magnetic field for a particle is $p_{\rm T} > 0.3$ GeV/c while the trajectory of a $p_{\rm T} = 30$ GeV/c particle deviates only 1.6 cm from a straight path of 150 cm. The solenoid is 4.8 m in length, 1.5 m in radius, 0.85 X_0 in radial thickness[6] and is cooled by forced flow of two-phase helium. Outside the coil the field flux is returned through a steel yoke to avoid having the fields interfere with the proper operations of the calorimeter's PMTs.
The detector is divided conventionally into two main polar regions. In the following we shall refer to the detector volume contained in the $|\eta_{det}| < 1$ as the *central region*, while the *forward region* indicates the detector volume comprised in $1 < |\eta_{det}| < 3.6$.

[5] An idea of the difference is given by considering that $\eta_{\rm det} \approx \eta \pm 0.2$ if the particle was produced a $z = 60$ cm from the nominal interaction point

[6] This has to be intended for normally incident particles.

2.2.3 Tracking system

Three-dimensional charged particle tracking is achieved through an integrated system consisting of three silicon inner subdetectors and a large outer drift-chamber, all contained in a superconducting solenoid. The 1.41 T magnetic field and the 130 cm total lever arm provide an excellent tracking performance (see fig. 2.4).

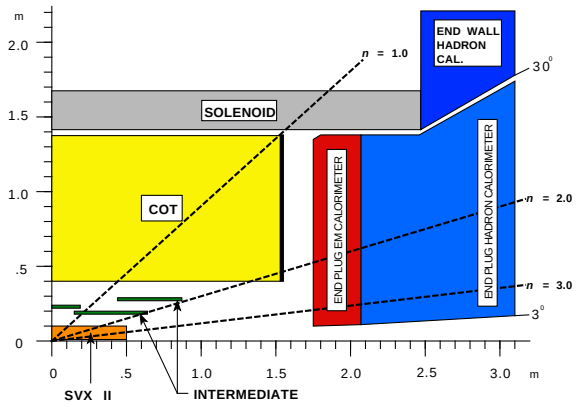


Figure 2.4: Elevation view of one quadrant of the inner portion of the CDF II detector showing the tracking volume surrounded by the solenoid and the forward calorimeters.

In the central region ($|\eta_{\rm det}| \lesssim 1$), 7 silicon samplings (one in the (r,ϕ) view plus six in the (r,ϕ,z) view), and 96 chamber samplings (48 (r,ϕ) plus 48 (r,z)) are available between 1.6 and 132 cm. In the forward and backward regions ($1 \lesssim |\eta_{\rm det}| \lesssim 2$), 8 silicon samplings (one in the (r,ϕ) view plus seven in the (r,ϕ,z) view) are available between 1.6 and 29 cm, along with partial information from the chamber.

The high number of samplings over the 88 cm lever arm of the chamber ensure precise determination of curvature, azimuth, and pseudo-rapidity of the tracks in the central region. The chamber provides also track seeds for pattern-recognition in silicon.

The core of the silicon detector is the Silicon VerteX detector (SVXII). It provides five three-dimensional measurements that extend the lever arm by 41.5 cm toward the beam thus allowing more precise determination of the trajectories and identification of decay-vertices displaced from the beam-line. The SVXII has an outer and an inner extension.

The outer extension, i. e., the Intermediate Silicon Layers (ISL), provides a single (double) three-dimensional silicon measurement in the central (forward-backward) region, at intermediate radial distance from the chamber. The ISL allows efficient linking between tracks reconstructed in the chamber and hits detected in the SVXII, and extends the track finding at pseudo-rapidities $1 \lesssim |\eta_{\rm det}| \lesssim 2$, where the chamber coverage is marginal.

The inner extension, i. e., the Layer ØØ (LØØ), is a light-weight silicon layer placed on the beam-pipe. It recovers the degradation in resolution of the reconstructed vertex position due to multiple scattering on the SVXII read-out electronics and cooling system, installed within the tracking

volume. The LØØis made of state-of-the-art radiation-tolerant sensors, and it will extend the lifetime of the whole system when the effects of radiation damage will degrade the performance of the inner SVXII layers. The integrated design of the tracking system allowed commonality of components among subdetectors (read-out chip, support structures, etc.) thus simplifying the construction and the operation.

The total amount of material in the silicon system, averaged over ϕ and z, varies roughly as $\frac{0.1X_0}{\sin(\theta)}$ in the $|\eta_{\rm det}| \lesssim 1$ region, and roughly doubles in $1 \lesssim |\eta_{\rm det}| \lesssim 2$ because of the presence of cables, cooling bulk-heads, and portions of the support frame.[7] The average amount of energy loss for a charged particle is roughly 9 MeV. The total heat load of the silicon system is approximately 4 kW. To prevent thermal expansion, relative detector motion, increased leakage-current, and chip failure due to thermal heating, the silicon detectors and the associated front-end electronics are held at roughly constant temperature ranging from -6°C to -10°C for LØØ and SVXII, and around 10°C for ISL, by an under-pressurized water and ethylene-glycol coolant flowing in aluminum pipes integrated in the supporting structures.[8]

Layer ØØ (LØØ)

Layer ØØ (LØØ) is the innermost layer of the microvertex silicon detector [85]. It consists of one layer of single sided AC-coupled silicon sensors which covers the beryllium beam pipe along 80 cm longitudinally. The state-of-the-art 7.85 cm long silicon sensors of LØØ can be biased to very high ($\mathcal{O}$(500 V)) voltages allowing to maintain a good signal-to-noise ratio even after high integrated radiation dose ($\mathcal{O}$(5 MRad)). The radiation hardness of such sensors allowed their installation at radii of 1.35 and 1.62 cm supported by a mechanical structure in direct contact with the beam pipe. The LØØ strips are parallel to the beam axis allowing the first sampling of the track within the $r-\phi$ plane, the inter-strip pitch is 25 μm but the read-out strip are alternated with floating ones resulting in 50 μm of readout pitch.
The signals of the 13,824 channels are fed via special optical fiber cables to the front-end electronic which is placed in a region separated from the sensors and less exposed to the radiation. The operation temperature of this device is around 0^oC maintained by a forced flux of under-pressurized[9] gas through tiny aluminum pipes installed in between the sensor and the beam-pipe. The cooling circuit increases the total mass of the LØØ which is about $1\%X_0$ where pass the cooling pipes and reduces to $0.6\%X_0$ where only sensors contribute.

Silicon VerteX detector II (SVXII)

The Silicon VerteX detector II (SVXII) [86] is a fine resolution silicon microstrip vertex detector which provides five 3D samplings of a track between 2.45 and 10.6 cm of radial distance from the beam (see fig. 2.4). Its cylindrical geometry coaxial with the beam is segmented along z into three *'mechanical barrels'* for a total length of 96 cm which provides complete geometrical coverage within $|\eta_{\rm det}| < 2$ (see

[7] The symbol X_0 indicates the radiation length.
[8] The pressure of the cooling fluid is maintained under the atmospheric pressure to prevent leaks in case of damaged cooling pipes.
[9] The pressure of the cooling fluid is maintained under the atmospheric pressure to avoid dangerous leaks of fluid in case of damaged cooling pipe.

fig. 2.5(a)). Each barrel consists of twelve azimuthal wedges each of which subtends approximately[10] 30^o. One wedge of a given barrel comprises 5 concentric and equally spaced layers of silicon sensors installed at radii 2.45 (3.0), 4.1 (4.6), 6.5 (7.0), 8.2 (8.7), and 10.1 (10.6) cm from the beam as shown in (see fig. 2.5(b)).

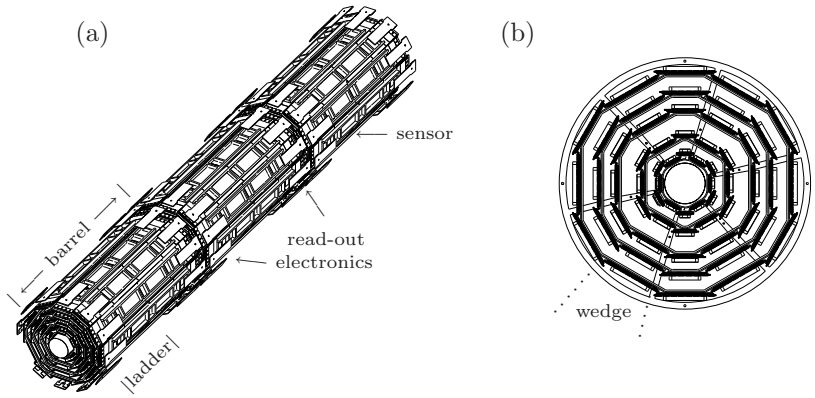


Figure 2.5: Schematic illustration of the three instrumented mechanical barrels of SVXII (a) and of the cross-section of a SVXII barrel in the (r, ϕ) plane (b).

Sensors in a layer are arranged into independent readout units, called *'ladders'* (or electrical barrels). The ladder components are two double sided rectangular 7.5 cm long sensors and the *hybrid* which is a multilayer board where all the front end electronics, biasing circuits and fan-out are allocated. The two silicon sensors, accurately aligned along their major axis, are glued end-to-end on a carbon-fiber support, with wirebonds connections joining the strips on one sensor to the strips of the next. It results in strips with an effective length of 15 cm in turn wirebonded to the front-end electronics of the hybrid which is mounted at one end of the carbon fiber support. Two ladders are longitudinally juxtaposed head-to-head within a barrel's layer, in order to leave the two hybrids at the two outside extremities of the barrel.
The active surface consists of double-sided, AC-coupled silicon sensors having microstrips implanted on a 300 μm thick, high resistivity bulk. Bias is applied through integrated polysilicon resistors. There are three different possible sort of strip orientations in each sensor's side: $r - \phi$ (axial) strips oriented parallel to the beam axis, small angle stereo (SAS) strips whose orientation is tilted by 1.2^o with respect to the beam axis and the 90^o stereo strips which lie in the transverse plane. All the five layers have axial strips on one side, three of the other sides have 90^o stereo and two have SAS strips. The charge pulse from each strip flows to a channel of SVX3D, the radiation-hard front-end chip [87]. SVX3D operates readout in "sparse-mode" which means that only signals above a threshold are processed. SVX3D samples the pedestal event-by-event and subtracts it from the signal. The discriminated differential pulse from each one of the 405,504 channels is preamplified, ADC-converted to a digital string and fed through neighbor-logic[11] to the DAQ chain. The measured average signal-

[10] There is a small overlap between the edges of two adjacent wedges, which helps in wedge-to-wedge alignment.
[11] In presence of a channel over threshold also the signal of the neighbor channels is accepted allowing clustering of the hits.

to-noise ratio is S/N $\geq$ 10, with a single hit efficiency greater than 99%.
To prevent thermal expansion, relative detector motion, increased leakage current and chip failure due to thermal heating the SVX II is held at roughly constant temperature of 10-15^{o}C through the operation of a water-glycol cooling system whose pipes run all below the detector. The average material of SVX II corresponds to 5%X_0.

Intermediate Silicon Layers (ISL)

The Intermediate Silicon Layer [88] detector is a silicon tracker placed at intermediate radial distance between the SVXII and the drift chamber (see fig. 2.4). The polar coverage extends to $|\eta_{\rm det}| < 2$. In the central region ISL consist of a single layer of silicon installed over a cylindrical barrel at radius of 22 cm. In the forward region, two layers of silicon are placed on concentric barrels at radii of 20 and 28 cm. Each silicon layer is azimuthally divided into a 30^o wedge structure matching that of SVXII. The basic readout unit is the ISL *ladder* which is similar to the SVXII ladder but consists of three, instead of two, sensors wirebonded in series resulting in a total active length of 25 cm.
ISL employs 5.7$\times$ 7.5 cm^2 double sided AC-coupled 300 μm thick sensors. Each sensor has axial strips on one side and SAS strips on the other. As in SVXII, signals from the 303,104 channels are read by SVX3D chips. Average mass of the detector is 2%X_0 for normally incident particles.

Central Outer Tracker (COT)

The outermost tracking volume [89] of CDF II is a large open cell drift chamber called the Central Outer Tracker (COT).
The COT has a coaxial bi-cylindrical geometry and extends, within the central region, from 44 to 132 cm radially from the beam axis. The chamber contains 96 radial layers of 0.40 μm diameter gold-plated tungsten sense (anode) wires arranged into 8 *"superlayers"*. Each superlayer samples the path of a charged particle at 12 radii (spaced 0.762 cm apart) where sense wires are strung. Four superlayers have their constituent sense wires oriented parallel to the beam axis in order to measure the hit coordinates in the $r-\phi$ plane. These are radially interleaved with four *stereo* superlayers having wires canted at angles of either $+3^o$ or -3^o with respect to the beamline. Combined readout of stereo and axial superlayers allows the measurement of the $r-z$ hit coordinates.
Each superlayer is azimuthally segmented into open drift cells. A drift cell, as shown in fig. 2.6, contains a row of 12 sense wires alternating with thirteen 0.40 μm diameter gold-plated tungsten potential wires which control the gain on the sense wires, optimizing the electric field intensity. The cathode of the detection circuit is the *field panel* which closes the cell along the azimuthal direction. It is made of gold on a 0.25 mm thick Mylar sheet and defines the fiducial volume of a cell. The electric field strength is 2.5 kV/cm. Innermost and outermost radial extremities of a cell are closed both mechanically and electrostatically by the *shaper panels*, which are Mylar strips carrying field-shaping wires attached. The architecture of the cell allows the containment of a possible broken wire inside only one cell and its dimensions bound to 0.9 cm the maximum drift distance.
Wire planes are not aligned with $\hat{r}$. A 35^o azimuthal tilt is provided in order to offset the Lorentz angle of the drift paths which results from the combined effect of crossed electrical and magnetic field and the characteristics of the gas mixture. Moreover the tilted-cell geometry helps in the drift-velocity

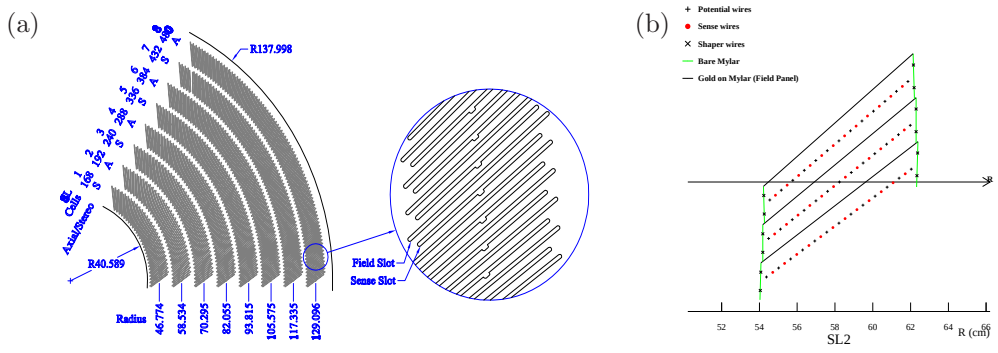


Figure 2.6: A 1/6 section of the COT end-plate (a). For each super-layer is given the total number of cells, the wire orientation (axial or stereo), and the average radius [cm]. The enlargement shows in details the slot were wire planes (sense) and field sheet (field) are installed. Sketch of an axial cross-section of three cells in super-layer 2, (b). The arrow shows the radial direction.

calibration as every high-p_{T} (radial) track samples the full range of drift distances within each super-layer. Further benefit of the tilt is that the left-right ambiguity[12] is cleared-up for track coming from the origin since the ghost track in each superlayer appears rotated of a large azimuthal angle becoming unfittable by pattern recognition. The volume of the COT is filled with a Ar(50%)/Ethane(50%) gas mixture. Drift electrons follow approximately azimuthal trajectories at speed $v \approx 100$ μm/ns. The resulting maximum drift time is about 100 ns, well smaller than the inter-bunch spacing 396 ns, providing the read-out and processing of the COT data available for the Level 1 trigger.
The analog pulses from the 30,240 sense wires flow to preamplifiers where are amplified and shaped. The discriminated differential output encodes charge information in its width to be used for dE/dx measures and is fed to a TDC which records leading and trailing edge of the signals in 1 ns bins. COT has 99% efficiency on tracks with measured single hit resolution $\sigma_{\mathrm{hit}} \simeq 175$ μm and p_{T} resolution is $\sigma_{p_{\mathrm{T}}}/p_{\mathrm{T}}^2 \simeq 0.13\%$ GeV/c^{-1}. The material of the COT is about 1.6% X_0 for tracks at normal incidence.

2.2.4 Tracking performance

The only physics objects used in this analysis are the tracks. Within an uniform axial magnetic field in vacuum, the trajectory of a charged particle produced with non-zero initial velocity in the bending plane of the magnet is described by an helix. The arc of an helix described by a charged particle in the magnetic volume of CDF is parameterized using three transverse, and two longitudinal parameters:

$\boldsymbol{C}$ – signed helix (half)-curvature, defined as $C \equiv \frac{q}{2R}$, where R is the radius of the helix. This is directly related to the transverse momentum: $p_{\mathrm{T}} = \frac{cB}{2|C|}$;

$\boldsymbol{\varphi_0}$ – ϕ direction of the particle at the point of closest approach to the z-axis;

[12] Each pulse on a given wire has a two fold ambiguity corresponding to the two incoming azimuthal drift trajectories. The signals from a group of nearby radially wires will satisfy the configuration for two tracks, one from the actual particle trajectory and another "ghost track" originated by the two fold ambiguity.

$\boldsymbol{d_0}$ – signed impact parameter, i. e., the distance of closest approach to the z-axis, defined as $d_0 \equiv q(\sqrt{x_c^2 + y_c^2} - R)$, where (x_c, y_c) are the coordinates of the center-guide;

$\boldsymbol{\lambda}$ – the helix pitch, i. e., $\cot(\theta)$, where θ is the polar direction of the particle at the point of its closest approach to the z-axis. This is directly related to the longitudinal component of the momentum: $p_z = p_{\mathrm{T}} \cot(\theta)$;

$\boldsymbol{z_0}$ – the z coordinate of the point of closest approach to the z-axis.

The trajectory of a charged particle satisfies the following equations [90]:

$$x = r\sin(\varphi) - (r + d_0)\sin(\varphi_0) \tag{2.6}$$

$$y = -r\cos(\varphi) + (r + d_0)\cos(\varphi_0) \tag{2.7}$$

$$z = z_0 + s\lambda, \tag{2.8}$$

where s is the projected length along the track, $r = 1/2C$, and $\varphi = 2Cs + \varphi_0$. The reconstruction of a charged-particle trajectory consists of determining the above parameters through an helical fit of a set of spatial measurements ("hits") reconstructed in the tracking detectors by clustering and pattern-recognition algorithms. The helical fit takes into account field non-uniformities and scattering in the detector material.

For this analysis, only COT-seeded silicon tracks were used, because the pattern recognition algorithms that use stand-alone silicon information would have given marginal contribution for two reasons. First, the impact of silicon stand-alone tracking becomes important in the region $1 \lesssim |\eta| \lesssim 2$ where the COT coverage is incomplete. This region of acceptance is already excluded in our analysis, since the trigger that collects $B^0_{(s)} \to h^+ h^{'-}$ events uses the COT information (see sec. 3.2). Secondly, the algorithms for silicon stand-alone tracking were not yet optimized as of this analysis.

All tracks were first fit in the COT and then extrapolated inward to the silicon. This approach guarantees fast and efficient tracking with high track purities. The greater radial distance of the COT with respect to the silicon tracker results in a lower track density and consequent fewer accidental combination of hits in the track reconstruction. A concise overview of the tracking algorithms is given in the following, see Ref. [91] for more details.

COT performance

All the channels of the COT are properly working. Its efficiency for tracks is typically 99%. The single-hit resolution is 140 μm, including a 75 μm contribution from the ≈ 0.5 ns uncertainty on the measurement of the $p\bar{p}$ interaction time. Internal alignments of the COT cells are maintained within 10 μm using cosmic rays. Curvatures effects from gravitational and electrostatic sagging are under control within 0.5% by equalizing the difference of E/p between electrons and positrons as a function of $\cot(\theta)$. The typical resolutions on track parameters are: $\sigma_{p_{\mathrm{T}}}/p_{\mathrm{T}}^2 \approx 0.0015$ $(\mathrm{GeV}/c)^{-1}$, $\sigma_{\varphi_0} \approx 0.035^\circ$, $\sigma_{d_0} \approx 250$ μm, $\sigma_\theta \approx 0.17^\circ$, and $\sigma_{z_0} \approx 0.3$ cm for tracks fit with no silicon information or beam constraint.

Performance of the silicon detectors

The silicon information improves the impact parameter resolution of tracks which, depending on the number (and radial distance) of the silicon hits, may reach $\sigma_{d_0} \approx 20$ μm (not including the transverse beam size). This value, combined with the $\sigma_{\mathrm{T}} \approx 30$ μm transverse beam size, is sufficiently small with respect to the typical transverse decay-lengths of heavy flavors (a few hundred microns) to allow separation of their decay-vertices from production vertices. The silicon tracker improves also the stereo resolutions up to $\sigma_\theta \approx 0.06°$, and $\sigma_{z_0} \approx 70$ μm, while the transverse momentum and the azimuthal resolutions remain approximately the same of COT-only tracks.

2.3 Other CDF II subdetectors

In this section the subdetectors not used in this analysis are briefly discussed.

2.3.1 Time of Flight detector

The Time of Flight detector (TOF) is a cylindrical array made of 216 scintillating bars [92] and it is located between the external surface of the COT and the cryostat containing the superconducting solenoid. Bars are 280 cm long and oriented along the beam axis all around the inner cryostat surface at an average radial distance of 138 cm. Both longitudinal sides of the bars collect the light pulse into PMT and measure accurately the timing of the two pulses. The time between the bunch crossing and the scintillation signal in these bars defines the β of the charged particle while the momentum is provided by the tracking. PID information is available through the combination of TOF information and tracking measurements. The measured mean time resolution is now 110 ps. This guarantees a separation between charged pions and kaons with $p_{\mathrm{T}} \lesssim 1.6$ GeV/c equivalent to 2σ, assuming Gaussian distributions. Unfortunately, in high ($\mathcal{L} \gtrsim 5 \times 10^{31}$ cm^{-2}s^{-1}) luminosity conditions, the occupancy of the single bars determines a degradation in efficiency, which is about 60% per track.

2.3.2 Calorimeters

Outside the solenoid, scintillator-based calorimetry covers the region $\eta_{\mathrm{det}} \leq 3.6$, and is devoted to the measurement of the net energy deposition of photons, electrons and hadrons using the *shower sampling* technique.

The basic structure consists of alternating layers of passive absorber and plastic scintillator. Neutral particles and charged particles with a transverse momentum greater than about 350 MeV/c are likely to escape the solenoid's magnetic field and penetrate into the CDF II calorimeters. Here particles undergo energy loss, striking the absorber material, and produce daughter particles which also interact in a cascade process, giving rise to a *shower* of particles. Showers propagate through many layers of absorber before they exhaust their energy generating a detectable signal, roughly proportional to the number of particles in the shower, within the active scintillator layers. The sum of the signals collected by all the sampling active layers is proportional to the energy of the incident particle.

The CDF II calorimeters are finely segmented in solid angle around the nominal collision point,

and coarsely segmented radially outward from the collision point (in-depth segmentation.) Angular segmentation is organized in projective *towers*. Each tower has a truncated-pyramidal architecture having the imaginary vertex pointing to the nominal interaction point and the base is a rectangular cell in the ($\eta_{\rm det},\ \phi$) space. Radial segmentation of each tower instead consists of two compartments, the inner (closer to the beam) devoted to the measure of the electromagnetic component of the shower, and the outer devoted to the measure of the hadronic fraction of energy. These two compartments are read independently through separated electronics channels.
A different fraction of energy release in the two compartments distinguishes photons and electrons from hadronic particles. CDF II calorimetry is divided in several independent subsystems presented in the following subsections.

Central region: CEM, CHA, WHA

The radial extension of the calorimeters in the central region is 1.73 $m < r < 3.5\ m$. The Central ElectroMagnetic calorimeter (CEM) [93] is constructed as four azimuthal arches (NE, NW, SE, SW) each of which subtends 180^o and is divided into twelve 15^o wedges. A wedge consists of 31 layers of 5 mm thick polystyrene scintillator interleaved with 30 aluminum-clad lead 3.2 mm thick sheets, divided along $\eta_{\rm det}$ into ten towers ($\Delta\eta_{\rm det} \approx 0.11$ per tower). To maintain a constant thickness in X_0, compensating the $\sin(\theta)$ variation between towers, some lead layers are replaced with increasing amounts of acrylic as a function of $\eta_{\rm det}$[13]. Light from each tower is collected by sheets of acrylic wavelength shifter at both azimuthal tower boundaries and guided to two phototubes per tower. The spatial resolution of the CEM is about 2 mm. The outer two towers in one wedge (known as *chimney towers*) are missing to allow solenoid access, for a resulting total number of 478 instrumented towers. At a radial depth of $5.9X_0$, which is approximately the depth corresponding to the peak of shower development, the CEntral Strip multi-wire proportional chambers (CES) measure the transverse shower shape with $\sim$ 1.5 cm segmentation. A further set of multi-wire proportional chambers, the Central Pre-Radiator (CPR) [94] is located in the gap between outer surface of the solenoid and the CEM. It monitors eventual photon conversions started before the first CEM layer. Phototube gains are calibrated once per store using an automated system of Xenon or LED light flashers.
The hadronic compartment is the combination of two sub-systems: the Central HAdronic (CHA) and Wall HAdronic (WHA) [95] calorimeters. Analogously as in the CEM, in both systems four "C"-shaped arches contain 48 wedges. Each CHA wedge is segmented into 9 $\eta_{\rm det}$ towers matching in size and position the CEM towers. The WHA wedge instead consists of 6 towers of which three are matching CHA towers. Radially a CHA tower is constructed of 32 layers of 2.5 thick steel absorber alternating with 1.0 cm thick acrylic scintillator. WHA towers structure is similar but there are only 15 layers of absorber which is 5.1 cm thick.

The total thickness of the electromagnetic section corresponds to approximately $19X_0$ ($1\lambda_{\rm int}$, where $\lambda_{\rm int}$ is the pion nuclear absorption length in units of g cm^{-2}), for a relative energy resolution $\sigma_E/E = 13.5\%/\sqrt{E\sin(\theta)} \oplus 2\%$.[14] The total thickness of the hadronic section corresponds to approximately

[13] The number of lead layers varies from 30 in the innermost ($|\eta_{\rm det}| \approx 0.06$) tower to 20 in the outermost ($|\eta_{\rm det}| \approx 1.0$).
[14] The first term is called the "stochastic" term and derives from the intrinsic fluctuations of the shower sampling process and of the PMT photo-electron yield. The second term, added in quadrature, depends on the calorimeter non-uniformities and on the uncertainty on the calibrations. All energies are in GeV.

$4.5\lambda_{\rm int}$, for an energy resolution of $\sigma_E/E = 50\%/\sqrt{E\sin(\theta)} \oplus 3\%$ for the central, and $\sigma_E/E = 75\%/\sqrt{E\sin(\theta)} \oplus 4\%$ for the end-wall.

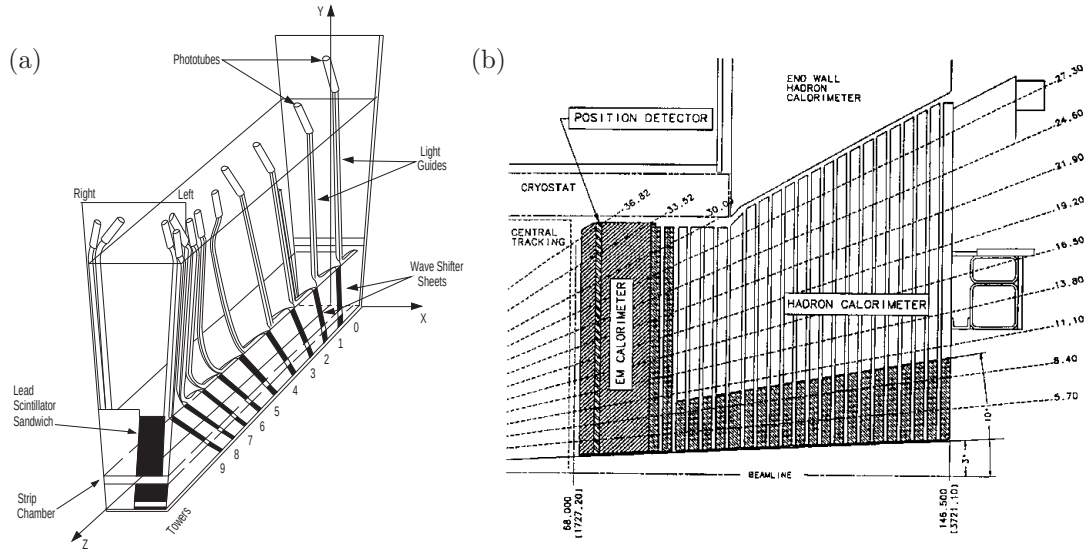


Figure 2.7: Schematic illustration of an azimuthal sector of the central electromagnetic calorimeter (a). Elevation view of one quarter of the plug calorimeter (b).

Forward region: PEM, PHA

The coverage of the $1.1 \leq |\eta_{\rm det}| \leq 3.6$ region relies on the scintillating tile *Plug* calorimeter [96] which is composed of two identical devices, one installed in $\eta_{\rm det} > 0$ region and the other in the $\eta_{\rm det} < 0$. Each of these two halves has electromagnetic and hadronic compartments (see fig. 2.7(b)).
In each half the absorber of the Plug ElectroMagnetic calorimeter (PEM) consists in 23 *"doughnuts"*-shaped lead plates, 2.77 m in outer diameter, which have a central hole where the beam pipe is allocated. Each plate is made out of 4.5 mm thick calcium-tin-lead sandwiched between two 0.5 mm thick stainless-steel sheets. Between the absorber plates are inserted the 4 mm thick scintillator *tiles* organized azimuthally in 15^o triangularly-shaped wedges. The signal of each tile is collected independently by embedded wavelength-shifter fibers which guide it to the photomultipliers. A preshower detector consist of a thicker (10 mm) amount of scintillator installed in the first layer of PEM, while shower maximum sampling is performed at radial depth of $\sim 6X_0$ by two tilted layers of scintillator strips (pitch 5 mm).
Each half of the hadronic compartment, Plug HAdronic calorimeter (PHA), is azimuthally subdivided in 12 wedge-shaped modules each subtending 30^o. In depth each module consists of 23 layers of 5 cm thick iron absorber alternated with 6 mm scintillator layers. Within each sampling layer the scintillator is arranged in tiles similar to those used in the PEM.

The total thickness of the electromagnetic section corresponds to approximately $21X_0$ ($1\lambda_{\rm int}$), for

an energy resolution of $\sigma_E/E = 16\%/\sqrt{E\sin(\theta)} \oplus 1\%$.[15] The total thickness of the hadronic section corresponds to approximately $7\lambda_{\rm int}$, for an energy resolution of $\sigma_E/E = 74\%/\sqrt{E\sin(\theta)} \oplus 4\%$.

2.3.3 Muon systems

CDF II is equipped with scintillating counters and drift tubes [97] installed at various radial distances from the beam to detect muons and shielded by the iron structure of the inner detector. Scintillators serve as trigger and vetoes while the drift chambers measure the ϕ coordinate using the absolute difference of drift electrons arrival time between two cells, and the z coordinate by charge division.
These systems cover the whole range of pseudorapidity $|\eta_{\rm det}| < 2$ and are used only to identify the penetrating muon reconstructing a small segment of their path (*stub*) sampled by the chambers. The momentum measurement is performed by pointing back the stub to the corresponding, track in the COT. The shield is constituted by the iron of the calorimeter, the return yoke and further steel walls intended to filter out the punch-through of hadrons. Different muon sub-systems cover different geometrical regions. In the $|\eta_{\rm det}| < 0.6$ region moving outward from the beam we encounter the inner CMU (Central MUon detector) chambers at radial distance of 3.5 m. Approximately $5.4\lambda_{\rm int}(\pi)$ of material[16] separate the luminous region from the CMU resulting in about 1/220 high energy hadrons traversing the calorimeter unchecked. In order to recognize and discard them, the CMP (Central Muon uPgrade) chambers lie in the same $\eta_{\rm det}$ region separated radially from the CMU by a 60 cm thick wall of steel achieving a rejection of 95% of the fake muons.
The muon coverage in the $0.6 < |\eta_{\rm det}| < 1$ volume is ensured by the CMX (Central Muon eXtension) chambers, embedded in scintillator counters and placed at radius of 3.5 m. The Intermediate MUon (IMU) detectors are instead drift tubes covering the pseudorapidity range of $1 < |\eta_{\rm det}| < 2.0$.
CDF II triggers on muons only emerging at $|\eta_{\rm det}| < 1.5$ where the muon coverage is segmented with sufficient granularity to survive high occupancies. The granularity of muon devices in the forward regions is less fine and not adequate for triggering, but sufficient for offline muon assignation to high $p_{\rm T}$ tracks going through that region.

2.3.4 Cherenkov Luminosity Counters

The luminosity ($\mathcal{L}$) is inferred from the average number of inelastic interactions per bunch crossing ($\overline{N}$) according to $\overline{N} \times f_{\rm b.c.} = \sigma_{\rm p\bar{p}-in.} \times \varepsilon \times \mathcal{L}$, where the bunch-crossing frequency ($f_{\rm b.c.}$) is precisely known from the Tevatron RF, $\sigma_{\rm p\bar{p}-in.} = 59.3 \pm 2.3$ mb is the inelastic $p\bar{p}$ cross-section resulting from the averaged CDF and E811 luminosity-independent measurements at $\sqrt{s} = 1.8$ TeV [98], and extrapolated to $\sqrt{s} = 1.96$ TeV, and ε is the efficiency to detect an inelastic scattering.

The Cherenkov Luminosity Counters (CLC) are two separate modules, covering the $3.7 \lesssim |\eta_{\rm det}| \lesssim 4.7$ range symmetrically in the forward and backward regions [99]. Each module consists of 48 thin, 110–180 cm long, conical, isobutane-filled Cherenkov counters. They are arranged around the beam-pipe in three concentric layers and point to the nominal interaction region. The base of each cone, 6–8 cm in diameter and located at the furthest extremity from the interaction region, contains a

[15] See footnote at pag. 51 for an explanation of terms.
[16] This defines also a $p_{\rm T}$ threshold for muons reaching the CMU which is approximately 1.4 GeV/c.

conical mirror that collects the light into a PMT, partially shielded from the solenoidal magnetic field. Isobutane guarantees high refraction index and good transparency for ultraviolet photons. With a Cherenkov angle $\theta_C = 3.4°$, the momentum thresholds for light emission are 9.3 MeV/c for electrons and 2.6 GeV/c for charged pions. Prompt charged particles from the $p\bar{p}$ interaction are likely to traverse the full counter length, thus generating large signals and allowing discrimination from the smaller signals of particles emitter at the same angle due to the beam halo or to secondary interactions. In addition, the signal amplitude distribution shows distinct peaks for different particle multiplicities entering the counters. This allows a measurement of $\overline{N}$ with 4.4% relative uncertainty in the luminosity range $10^{31} \lesssim \mathcal{L} \lesssim 10^{32}$ cm^{-2}s^{-1}. This accuracy, combined with the 4% relative uncertainty on the inelastic $p\bar{p}$ cross-section, results in an instantaneous luminosity measured with 5.9% relative uncertainty. This uncertainty does not affect the results of this analysis since ratios of branching fractions, instead of absolute branching fractions, are measured.

2.4 Trigger and Data Acquisition system

Since the interaction rate at the Tevatron collider is well beyond the current maximum storage rate, the task of separating the great majority[17] of background events from the tiny fraction of interesting events is of crucial importance. This goal is achieved by the trigger system which evaluates the partial information provided by the detector in real time and discards the uninteresting events.
The Tevatron running at 396 ns of interbunch spacing has a collision rate of about 2.53 MHz. The writing of events on permanent memories cannot proceed faster than 100 Hz. For practical reasons the CDF II trigger has been designed as a multi-stage system in order to reduce the acquisition rate allowing to record only the events with a physical interest. Its architecture is modular and divided into three levels, represented in fig. 2.8. Each level receives the data event from the previous one and, provided with more accurate detector information and more time for processing, chooses to discard it or to send it to the next level. Level-1 receives the data directly from the detector front end electronics. Events passing the Level-3 are stored to permanent memory.

Since the read-out of the entire detector needs about 2 ms on average, after the acquisition of one event, another approximately 5,000 interactions would occur and remain unrecorded. The percentage of events rejected solely because the trigger is busy processing previous events is referred to as trigger *deadtime*.

Level-1

A trigger divided in three stages does not remove the problem to deal with the Tevatron crossing rate of more than 2.53 MHz, the problem is now re-routed to the Level-1 stage. In order to avoid deadtime caused by the trigger processing time, the Level-1 has to sustain the clock of the Tevatron. In a complex detector as CDF II, it is unconceivable an effective trigger architecture able to process data and make a decision in less than 396 ns. The *impasse* is overcome with a fully pipelined front-end electronics for the whole detector. The signal of each channel is stored, every 396 ns, in a buffer of a

[17] The b production cross section is, for example $\sim$ 1,000 times smaller than the generic $p\bar{p}$ inelastic one. High p_{T} physics as vector bosons or *top* physics suffers even smaller signal-to-background ratios at production.

42-cell long pipeline. This means that the Level-1 has 396×42 ns $\simeq$ 16 μs to make its decision before the content of the buffer is deleted. The actual latency of the Level-1 is 5.5 μs, as was designed for a crossing time of 132 ns.

At Level-1, a synchronous system of custom-designed hardware process a simplified subset of data in three parallel streams to reconstruct coarse information from the calorimeters (total energy and presence of single towers over threshold), the COT (two-dimensional tracks in the transverse plane), and the muon system (muon stubs in the CMU, CMX, and CMP chambers). A decision stage combines the information from these low-resolution physics objects, called "primitives", into more sophisticated objects, e. g., track primitives are matched with muon stubs, or tower primitives, to form muon, electron, or jet objects, which are subjected to basic selections.[18]

The eXtremely Fast Tracker (XFT) is a custom processor that identifies two-dimensional tracks in the (r, ϕ) view of the COT (transverse plane) in time with the Level-1 decision. It uses pattern matching to first identify short segments of tracks and then to link them into full-length tracks [100]. If a coincidence between segments crossing four super-layers is found, two-dimensional XFT-tracks are reconstructed by linking the segments. The segments are compared with a set of about 2,400 predetermined patterns corresponding to all tracks with $p_{\rm T} \gtrsim 1.5$ GeV/c originating from the beam line. The track-finding efficiency and the fake-rate with respect to the off-line tracks depend on the instantaneous luminosity, and were measured to be $\varepsilon \approx 96\%$, and 3%, respectively, for tracks with $p_{\rm T} \gtrsim$ 1.5 GeV/c at $\mathcal{L} \simeq 10^{31}$ cm^{-2}s^{-1}. The observed momentum resolution is $\sigma_{p_{\rm T}}/p_{\rm T}^2 \approx 0.017(\text{GeV}/c)^{-1}$, and the azimuthal resolution is $\sigma_{\varphi_6} \approx 0.3^\circ$, where φ_6 is the azimuthal angle of the track measured at the sixth COT super-layer, located at 106 cm radius from the beam line.

Currently are implemented about 56 different Level-1 different combinations of requirements with an output rate of 18 KHz.

Level-2

The Level-2 trigger performs two subsequent operations. The *Event building* produces in output the event as reconstructed with Level-2 detector information, and the *Decision* combines outputs from Level-1 and Level-2 to evaluate whether to flag or not the event for Level-3 processing.

The Event building process is done in parallel. Calorimetric information is used to perform clustering and identification of hadronic jets. Simultaneously, the Silicon Vertex Trigger (SVT), a dedicated processor, combines XFT track informations with SVXII hits. It measures 2D track parameters with almost offline level quality for tracks with $p_{\rm T} > 2$ GeV/c. The key improvement of the SVT track with respect to the XFT track is the measurement of the track impact parameter. The event building has 10 μs to complete its task.

In the Decision stage some selection algorithms, customized for each different combinations of requirement, run on four dedicated CPUs and process the available information from Level-1 and Level-2 in less than 10 μs.

The maximum latency of Level-2 is 20 μs for each event. The current number of different combinations of requirements at Level-2 are about 116 and the output rate is about 300 Hz.

[18] A particle jet is a flow of observable secondary particles produced in a spatially collimated form, as a consequence of the hadronization of partons produced in the hard collision.

Level-3

This stage is implemented exclusively by software. About 400 commercial processors running in parallel reconstruct the event provided by Level-2 at full detector resolution. Level-3 codes are very similar to the offline reconstruction codes. About 140 trigger paths are implemented at Level-3. Moreover Level-3 distributes the information to on-line monitoring consumers and data logger programs. The Level-3 decision to write on tape happens after the full reconstruction of the event is completed and the integrity of its data is checked in less than 10 ms. Typical size for an event is 150 kbyte. Maximum storage rate is about 20 Mbyte/s. At Level-3 the number of different combinations of requirements is about 185. The available output rate passed from 75 Hz (40% tracking, 30% jet and photon, and 30% lepton).

The trigger deadtime never exceeded 5%, and its integrated value in the data used for this analysis was below 1%.

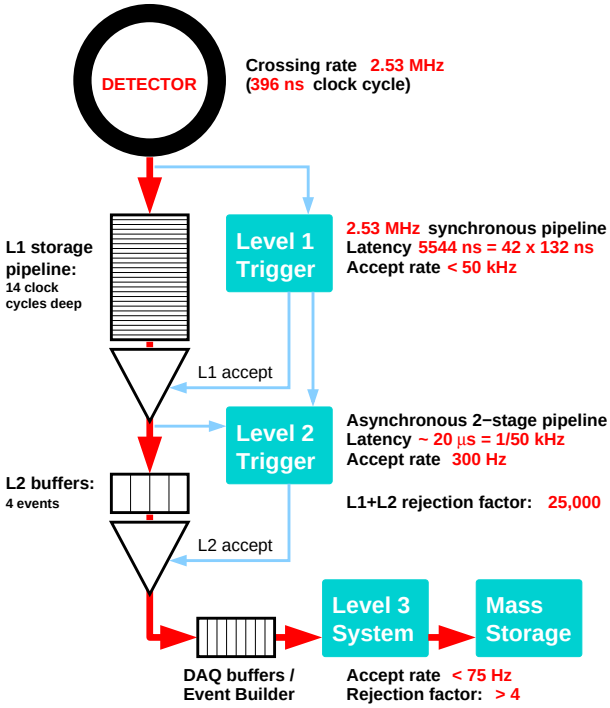


Figure 2.8: Functional block diagram of the CDF II trigger and data acquisition system.

2.4.1 Silicon Vertex Trigger (SVT)

The main advantage of investigating B physics in an hadronic environment like the Tevatron is the very large ($\mathcal{O}(50\ \mu\text{b})$ [111], to be compared with $\mathcal{O}(\text{nb})$) b-flavour production cross section at the e^+e^- machines. However the large b-cross-section has to be compared with the total inelastic $p\bar{p}$ cross

section which is about 1,000 times larger. This means that b events are overwhelmed by an amount of uninteresting background events larger by three orders of magnitude. A further complication is that the b production cross section is a steep exponentially decreasing function of the p_{T} of the produced B. This results in b events populating mainly the *soft* region of the p_{T} spectrum (4-5 GeV/c) which is the region where also most of the background is distributed. In the CDF II case, this problem is enhanced by the characteristics of the detector which was originally designed to optimize its performances in the central region where high-p_{T} decay products of particles such as $W^{\pm}$, Z^0, *top* are searched.
The task of improving the unfavorable ratio between b events and background is two-fold. An on-line selection is in charge to select samples enriched on b-flavours. Once this is done, sophisticated off-line algorithms allow to further purify the sample from the background events.
CDF trigger strategy in Run I was to take advantage of the excellent lepton identification capabilities to implement lepton-based triggers able to select semileptonic B decays and $B \to J/\psi{+}X \to [l^+l^-]{+}X$ decays[19]. At off-line level CDF used the silicon vertices detector to reconstruct secondary vertexes allowing further skimming of b-enriched samples. This was possible because b-hadrons produced at Tevatron have enough high p_{T} to travel several hundredths of microns ($\sim$ 450 μm for a B meson) through the detector before the decay. It results in large mean valued distributions of their impact parameters with respect to the beam axis. However such a lepton based trigger is not very efficient and excludes a whole bunch of *rarer* hadronic decays, such as $B^0_{(s)} \to h^+h^{'-}$, $B^0_{(s)} \to D^-_{(s)}\pi^+$, etc. which are among the most promising for CP violation measurements.
The basic purpose of SVT is to anticipate the step of secondary vertexes identification from the off-line to the trigger level. This allows the on-line selection of b-events over the short-lived background with larger yield than by using only the leptonic triggers. In order to achieve this it is necessary to measure the impact parameter on-line. SVT performs this task, reaching a resolution on fitted track parameter comparable to the off-line resolution, with a time constraint of less than 10 μs which is the maximum time allowed at Level-2 event building. A brief description of the SVT architecture follows in order to explain how this task is achieved [101].

SVT at work

Reconstructing decay vertices on-line is technically challenging and it requires the reconstruction of high resolution tracks at high event-rates. SVT measures the impact parameters of the charged particles, which is faster than reconstructing their decay vertices, and provides also information on the lifetime of the decaying particle. The COT tracks are not measured with the desired resolution, therefore SVT needs SVX II data to be available. Due to this need, its natural location within the trigger chain is at Level-2. At this stage, the 2D COT tracks previously reconstructed by XFT are available and the event rate is sufficiently low to allow the readout of the silicon detector. XFT tracks are provided together with the silicon hit information coming from SVX II front-end electronics. The design of a silicon front-end electronics capable to readout the more than 400,000 SVXII channels within the time constraint of the Level-2 trigger was a challenging task which turned to be successful. In fact one of the main impediments to the realization of an SVT-like system in Run I was the too readout of the silicon detector.

[19]The mentioned decays are a fraction of about the 20% of the total B width.

The output of SVXII is fed to the *Hit Finder*. This set of processors reconstructs the clusters on SVXII layers and calculates the coordinates of the charge-barycenter in each cluster. Hit Finder processing speed sustains the output rate of the SVXII front-end and calculated hit coordinates are sent in parallel to the *Hit Buffer* and to the *Associative Memory* (AM). Simultaneously, XFT track parameters are transmitted both to the Hit Buffer and the Associative Memory.

AM is the device devoted to pattern recognition. The Level-2 latency time does not allow SVT to adopt the off-line-like pattern recognition strategy based upon solving the whole system of constrained equations. AM uses instead a technique based on highly parallelized comparison between XFT-SVXII data and preselected patterns. The channels of each silicon layer are grouped into *superstrips*. A typical superstrip size is $\sim$ 250 μm, while the detector typical full resolution is about 25 μm. The task of the AM is then reduced to perform pattern recognition using a coarser spatial resolution. This reduces combinatorics to combination of hits within the same superstrip. A *road* is defined as one possible combination of excited superstrips (one per layer) through the silicon layers.
In principle, it would be possible to store in the AM all possible roads for whatever configuration of real tracks, then compare them to the sequence of hits coming from the Hit Finder and to the 2D tracks reconstructed by XFT. An SVT track would be identified when the matching of a pre-stored road with the XFT track together with the hit list occurs. In practice, an efficiency $\epsilon \sim 95\%$ is achieved storing in the AM only a subset ($\sim 33,000$ roads) of the all possible patterns. This allows the AM to operate the comparison in parallel remaining within the Level-2 time constraints. The maximum output of the AM is 64 roads per event, each one having a maximum of 8 hits per superstrip.

This Hit Buffer device is a buffer which stores the XFT track and the Hit Finder information during the AM processing. When AM comparison is completed the Hit Buffer sends to the *Track Fitters* only the stored data corresponding to the roads matched by the AM.

The Track Fitters are a system of processors operating in parallel devoted to fit tracks with final resolution. Each processor receives the roads found by the AM, the hit coordinates and the XFT parameters from the Hit Buffer. It combines the information and reconstructs one or more tracks within the same road by a linearized fit procedure.

The SVT outputs are the reconstructed parameters of the two-dimensional tracks in the transverse plane: φ_0, p_{T}, and the impact parameter, d_0. The list of parameters for all found tracks is sent to Level-2 for trigger decision.

The SVT measures the impact parameter with $\sigma_{d_0,\mathrm{SVT}} \approx 35$ μm r.m.s. width, with an average latency of 24 μs, 9 μs of which being spent waiting for the start of the read-out of silicon data. This resolution is comparable with the off-line performance for tracks not using LØØ hits, and yields a distribution of impact parameter of prompt tracks with respect to the z axis with $\sigma_{d_0} \approx 47$ μm (see fig. 2.9) when combined with the transverse beam-spot size.[20] The SVT efficiency is higher than 85%. This efficiency is defined as the ratio between the number of tracks reconstructed by SVT and all XFT-matched off-line silicon tracks that are of physics analysis quality.

[20] Prompt tracks are those associated to particles produced in the hard $p\bar{p}$ interaction.

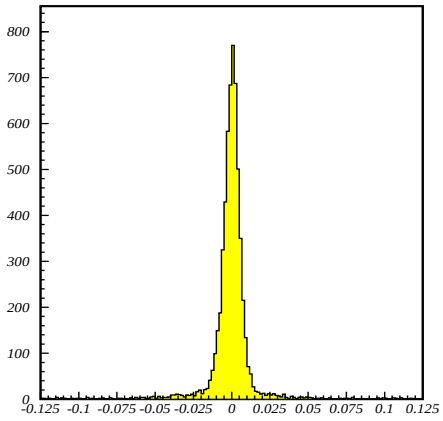


Figure 2.9: Impact parameter distribution as measured by the SVT.

2.5 Operations and data quality

The proper operation of the detector and the quality of the on-line data-taking is continuously ensured by "crews" of five members of the CDF Collaboration plus one technician who alternate on duty with eight-hours shifts, plus several subdetector experts available on request. The on-line crew, in communication with the Tevatron crew, ensures smooth data-acquisition, monitors the crucial parameters of all subdetector, and intervenes in case of malfunctions. The average data-taking efficiency is 85%. The inefficiency is approximately equally shared in a 5% arising at the beginning of the store, when the detector is not powered while waiting for stable beam conditions, a 5% due to trigger deadtime, and a 5% due to unexpected detector or DAQ problems.

When no beam is present, cosmic-rays runs are taken, or calibrations of the subdetector are done. During the Tevatron shut-down periods, the crew coordinates and helps the work of experts that directly access the detector.

Each time that at least one of the trigger paths fires, an "event" is labeled with a progressive number. Events are grouped into runs, i. e., periods of continuous data-taking in constant configurations of trigger table, set of active subdetectors and so forth.[21] Several parameters of the operations (e. g., beam-line position and slope, set of calibrations, etc.) are stored in the database on a run-averaged format.

All data manipulations occurring some time after the data are written to permanent memories are referred to as *off-line* processes, as opposed to the on-line operations which take place in real time, during the data-taking. The most important off-line operation is the processing with a centralized *production* analysis that generates collections of high-level physics objects suitable for analysis, such as tracks, vertices, muons, electrons, jets, etc. from low-level information such as hits in the tracking

[21] The data acquisition might need to be interrupted and recovered for several motivations, including the need for enabling or disabling a subdetector, the need for a change in the trigger table, a problem in the DAQ chain and so forth.

subdetectors, muon stubs, fired calorimeter towers, etc. [102]. During the production, more precise information about the detector conditions (e. g., calibrations, beam-line positions, alignment constants, masks of malfunctioning detector-channels, etc.) and more sophisticated algorithms are used than those available at the Level-3 of the trigger. The production may be repeated when improved detector information or reconstruction algorithms become available: this typically occurs once or twice every year. The reprocessing uses large farms of commercial processors that reconstruct approximately 10^7 events per day employing approximately 2–5 s per event with 1 GHz CPU.[22] The added information increases the event size by typically 20% after production.

To ensure homogeneous data-taking conditions, each run undergoes a quality inspection. On-line shift operators, off-line production operators, and subdetector experts certify in what fraction of data the running conditions for all relevant subdetectors are compliant to physics-quality standards.

When detectable problems of the detector occur, the data-taking is quickly stopped, so very short runs are likely to contain corrupted data. Runs with fewer than 10^8 live Tevatron clock-cycles, or fewer than 10^4 (10^3) Level-1 (Level-2) accepts, or containing data corresponding to an integrated luminosity $\int \mathcal{L}dt < 1$ nb^{-1} are excluded from physics analysis. On-line shift operators further exclude the runs in which temporary or test trigger tables were used.[23] Runs whose data underwent problems or software crashes during the production are excluded off-line.

Accurate integrated luminosity measurements are ensured in physics-quality data by requiring the CLC to be operative during the data-taking and by verifying that a set of luminosity and beam-monitor probe quantities are within the expected ranges. Shift operators ensure that Level-1 and Level-2 trigger operate correctly and that the rate of SVXII data corruption errors is smaller than 1%.[24] SVT experts verify that the on-line fit and subtraction of the beam position is done correctly and that the SVT occupancy is within the expected limits. In addition, higher level quantities, such as event yields of $J/\psi \to \mu^+\mu^-$, $D^0 \to K^-\pi^+$, and $D^{*+} \to D^0\pi^+$ decays are monitored on-line and are required to be within the expected ranges. For analyses that use COT information, the minimum integrated luminosity required is 10 nb^{-1} and the fraction of noisy COT channels is required to be below 1%.

[22] The event size, and the processing-time increase roughly linearly with the instantaneous luminosity.

[23] It is sometimes necessary to test new configurations of the trigger selections in a real data-taking condition to monitor trigger rates, performance and so on.

[24] The read-out of the silicon detector and the proper integration of the information in the on-line infrastructure is a complex operation which, occasionally, leads to a certain fraction of data to be improperly processed.

Chapter 3

Sample selection and signal extraction

This chapter describes the main stages of the process used to extract the $B^0_{(s)} \to h^+h^{'-}$ decays (referred to as 'signal') from other events ('background'). First we describe the on-line trigger selection which is crucial to collect events most likely containing $B^0_{(s)} \to h^+h^{'-}$ decays. Second we describe a simple off-line improvement of this trigger selection to extract a visible $B^0_{(s)} \to h^+h^{'-}$ signal (referred to as 'baseline selection') and finally we describe the optimized selection. This last step is aimed at obtaining the sample such that the statistical uncertainties on the quantities one wishes to measure are minimized. This chapter report only the final results of the last step (final sets of cuts used in this analysis) since the optimization procedure uses the fit of composition, described in chap. 6. An exhaustive description of the selection optimization process is described in chapter chap. 8.

3.1 $B^0_{(s)} \to h^+h^{'-}$ decays at CDF

The analysis uses the data collected between February 2002 (run 138809) and March 2006 (run 212133). After the application of the standard CDF data-quality requirements (see sec. 2.5), the sample size corresponds to an integrated luminosity of $\int \mathcal{L}dt \simeq 1$ fb^{-1}.

The topology of a $B^0_{(s)} \to h^+h^{'-}$ decay is very simple. Two charged pseudo-scalar mesons ($\pi^+\pi^-$, $K^+\pi^-$, $K^-\pi^+$, K^+K^-) or a proton/anti-proton plus a pseudo-scalar meson ($\bar{p}\pi^+$, $p\pi^-$, $\bar{p}K^+$, pK^-) from the decay of a long-lived $B^0_{(s)}$ meson or Λ^0_b baryon generate two oppositely-curved tracks intersecting in a space-point a few hundreds microns away from the location of the $p\bar{p}$ interaction where the $B^0_{(s)}$ meson or Λ^0_b meson was produced.

Such a simple topology poses a first experimental challenge: rare ($\mathcal{B} \approx 10^{-5}$) processes, confused in a background $\mathcal{O}(10^9)$ times larger, need to be selected on-line, relying uniquely on tracking resources, since the trigger bandwidth available at CDF II it is not sufficient to record all events. The signature of $B^0_{(s)} \to h^+h^{'-}$ decays lacks the most used discriminating features. No leptons are present to exploit the good CDF muon and electron identification capability, nor narrow intermediate resonances (e.g.,

a ϕ meson) can be used to provide additional kinematics constraints.

The $B^0_{(s)} \to h^+h^{'-}$ final states contain only pions and kaons which, unfortunately, are also the most common particles present in the background. However, if the momentum of the $B^0_{(s)}$ meson has sufficiently large component in the plane transverse to the beam-line, the displacement between production and decay positions of the $B^0_{(s)}$ meson can be measured with the silicon tracker. This provides a highly discriminating quantity for background rejection.

Prior to discussing the details of trigger and off-line selection, it is useful to define some relevant quantities used in the analysis. All quantities are calculated in the laboratory frame, and are illustrated in fig. 3.1. For the present description we neglect the curvature of particles with momentum $\mathcal{O}(\mathrm{GeV}/c)$.

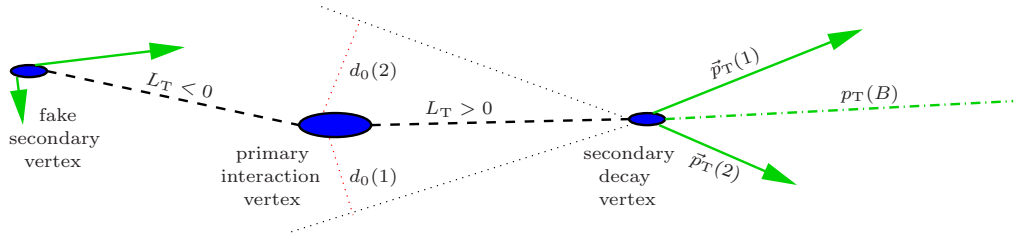


Figure 3.1: Illustration of a $p\bar{p}$ event containing a $B^0_{(s)} \to h^+h^{'-}$ decay, projected into the transverse plane. Ellipses indicate vertices, arrows indicate the transverse momenta (i. e., the direction) of charged particles. Nothing is to scale.

Transverse plane – the plane perpendicular to the proton beam direction, in which the profile region is approximately Gaussian with r.m.s. $\sigma_{p_T} \approx 30\ \mu m$

Transverse momentum ($\vec{p}_T$) – the projection of the momentum vector onto the transverse plane. This quantity is the simplest discriminant between heavy-flavor signals and background because, in $p\bar{p}$ collisions, charged particles from b-hadron decays have average transverse momenta higher than particles from generic QCD-backgrounds. Another useful quantity used in the selection is the scalar sum of the transverse momenta of the two particles $\Sigma p_T \equiv p_T(1) + p_T(2)$.

Primary vertex – the space-point of the reconstructed primary $p\bar{p}$ interaction, where the b-quark, once produced, quickly hadronizes to a b-hadron pair.

Secondary vertex – the space point in which the decay of a long-lived particles occurs. The components of its displacement with respect to the primary vertex in the transverse plane are indicated by the vector $\vec{x}_v = \vec{\beta}_T \gamma ct = (\vec{p}_T/m)ct$, for a particle of mass m and momentum p that decays at time t after its production.

Transverse decay-length (L_T)– the displacement of the secondary vertex with respect to the primary one, projected onto the transverse momentum vector of the decaying particle ($\vec{p}_T(B)$). The transverse displacement of the secondary vertex ($\vec{x}_v$) may not be collinear with $\vec{p}_T(B)$

because of the measurement uncertainties. Thus, the transverse decay-length,

$$L_{\mathrm{T}} \equiv \frac{\vec{p}_{\mathrm{T}} \cdot \vec{x}_v}{p_{\mathrm{T}}}, \tag{3.1}$$

is usually preferred to $\vec{x}_v$ as an estimator of transverse decay-length travelled before decay. This quantity is typically positive for a true long-lived decays, while it is negative or positive with almost equal probability for decays from a fake secondary vertex or for combinations of prompt tracks, although in the latter case its value is comparable with its resolution.

Impact parameter (d_0) – the component of the distance of closest approach between a track and the primary vertex in the transverse plane. This is a signed quantity defined as

$$d_0 \equiv \frac{\hat{z} \cdot (\vec{p}_{\mathrm{T}} \wedge \vec{x}_v)}{p_{\mathrm{T}}}, \tag{3.2}$$

where the scalar product with the unit vector pointing toward the proton direction ($\hat{z}$) determines its sign and the symbol "$\wedge$" indicates the cross product. The impact parameter is typically different from zero for products of long-lived decays, while it is comparable with the convolution of its resolution and the transverse size of the beam for particles produced in the vicinity of the primary vertex (prompt background).

Azimuthal opening angle ($\Delta\varphi_0$) – the opening angle between the two outgoing particles projected in the transverse plane. The distribution of this quantity in $B^0_{(s)} \to h^+h^{'-}$ decays depends on the distributions in impact parameter and transverse momentum. However, it has generally a slowly-varying shape for signal candidates, while it shows two enhancements around 0° and 180° for background candidates. Pairs of quasi-collinear tracks are found in hadronic jets, due to light-quark fragmentation, or in highly occupied regions of the detector, due to combinations of fake tracks; pairs of azimuthally-opposed tracks are found in back-to-back jets of generic QCD background.

3.2 Displaced-Tracks Trigger

The data have been collected with the Displaced-Tracks Trigger. The Displaced-Tracks Trigger is composed by several trigger *paths*. A trigger path is a well defined sequence of Level-1, Level-2, Level-3 requirements. The specific trigger paths used for this analysis can be grouped, due to their similar kinematic requirements, in two main groups: `B_PIPI` and `B_PIPI_HIGHPT`.
The `B_PIPI_HIGHPT` has higher thresholds on the transverse momentum than the `B_PIPI` trigger path. The purpose of having two separate triggers with different transverse momentum requirements is to keep alive the triggers as much as possible at high instantaneous luminosities. At luminosities $\mathcal{L} \simeq 50 \times 10^{30}$ cm^{-2}s^{-1}, the Level-1 of the Displaced-Tracks Trigger causes a trigger dead-time larger than the design limit of 5%. The introduction of trigger paths like `B_PIPI_HIGHPT`, with higher momentum thresholds, are required to avoid saturation of the bandwidth available.
The Tevatron instantaneous luminosity increased thanks to improvements of the accelerator complex performance, achieving values $\mathcal{L} \simeq 170 \times 10^{30}$ cm^{-2}s^{-1} in the last part of data collected for this analysis, close to the design value of 200×10^{30} cm^{-2}s^{-1}. It has been necessary to further reduce the

trigger accept-rates by applying a *prescale factor*. Prescaling a trigger by a factor N means accepting 1 event every N valid events. To better use the trigger bandwidth, a *dynamic prescale* (DPS) has been added to particularly high trigger accept-rates. The DPS adjusts the prescale factor N according to the instantaneous luminosity, since the instantaneous luminosity of the store decreases with time. This is due to the interactions of the proton and anti-proton bunches with the residual gas in the beam-pipe and due to the degradation process of the transverse section of bunches in many hours of collisions. The dynamic prescale factor decreases along the store to keep the trigger bandwidth fully occupied.

In the following, we outline just the trigger requirements for the `B_PIPI` and `B_PIPI_HIGHPT` trigger paths.

3.2.1 The `B_PIPI` and `B_PIPI_HIGHPT` path

Level-1

At Level-1 the only tracking data available comes from the XFT. XFT measures the p_{T}, φ_6 and charge q of each track (2D). The azimuthal angle is measured at a radial distance corresponding to the super-layer 6 of the COT and it is labeled φ_6. These are the only handles available at Level-1 to disentangle the signal from the background. Two XFT tracks having p_{T} larger than 2.04 GeV/c are required. A natural request is also the opposite sign of the two XFT tracks: $q(1) \cdot q(2) < 0$. In addition, track pairs due to light-quark fragmentation in back-to-back jets are rejected with the $0° < \Delta\varphi_6 < 135°$ requirement on the azimuthal opening angle between tracks. The requirement $\Delta\varphi_6 > 0$ is forced because of the `B_PIPI` path at Level-1 is shared with other hadronic trigger paths which require a small azimuthal opening angle (see sec. 3.2.2). Further conditions on transverse momenta of the tracks has to be imposed to reduce the Level-1 accept-rate. The solution is to leave the individual thresholds at 2.04 GeV/c but constrain the scalar sum $\sum p_{\mathrm{T}}$ of the transverse momenta to be larger than 5.5 GeV/c. The `B_PIPI` rate at $\mathcal{L} \simeq 60 \times 10^{30}$ cm^{-2}s^{-1} is 25 kHz at Level-1.

Level-2

At Level-2, the azimuthal opening-angle requirement is further tightened with respect to the previous trigger stage to $20° < \Delta\varphi_0 < 135°$, to reduce the fraction of events with light-quark background. At Level-2 the SVX II hits are available and SVT receives the XFT track and refit them in the silicon providing impact parameter information. The `B_PIPI` trigger requires a pair of oppositely-curved SVT tracks that satisfy a minimal linearized-fit quality requirement: $\chi^2_{\mathrm{SVT}} < 25$ [104].[1] A lower threshold in impact parameter d_0 is required to enrich the sample in b-decays, which exhibit typical values of $d_0 \sim 150$ μm. An upper threshold is dictated by hardware constraints, then the trigger requirement is: $100\ \mu\mathrm{m} <\mid d_0 \mid < 1000\ \mu\mathrm{m}$. The impact parameter requirement is the single most selective requirement. It reduces the trigger accept-rate by a factor ~ 100, while still keeping $\sim 50\%$ efficiency on signal. The spatial resolution of SVT in identifying secondary vertices is further exploited: positive decay-length of the $B^0_{(s)}$ candidate is required, $L_{\mathrm{T}}(B) > 200$ μm, along with a $|d_0(B)| < 140$ μm requirement on its impact parameter. The latter imposes that the candidate originates from the primary vertex,

[1] The efficiency of the $\chi^2_{\mathrm{SVT}} < 25$ requirement on unbiased samples is approximately 97%.

rejecting sequential $B \to DX \to h^+h^{'-}X$ decays. Events with $L_{\rm T}(B) < -200$ μm are retained as well for background studies. The B_PIPI rate at $\mathcal{L} \simeq 60 \times 10^{30}$ cm^{-2}s^{-1} is 25 Hz at Level-2.

Level-3

The Level-1 and Level-2 criteria are reapplied on Level-3 tracks. In addition, a requirement on the longitudinal separation between the two tracks at the point of their minimum distance from the beam is applied: $|\Delta z_0| < 5$ cm. This significantly reduces the fraction of combinations of two tracks descending from particles produced in distinct primary vertices (pile-up events). A $|\eta| < 1.2$ requirement on tracks excludes events with particles outside the XFT fiducial acceptance. The Level-3 mass-resolution, comparable with the off-line resolution, allows a loose $4.0 < m_{\pi\pi} < 6.0$ GeV/c^2 requirement on the reconstructed invariant $\pi\pi$-mass of the particle pair. This is adequate for reducing the Level-3 accept-rate, while keeping events populating a sufficiently wide mass-spectrum for signal and background studies. The B_PIPI rate at $\mathcal{L} \simeq 60 \times 10^{30}$ cm^{-2}s^{-1} is 0.7 Hz at Level-3.

The B_PIPI_HIGHPT trigger path applies the same requirements of the B_PIPI, but tightening few of them. At Level-1 it requires both tracks to have $p_{\rm T} > 2.46$ GeV/c and scalar sum of the transverse momenta $\sum p_{\rm T} > 6.5$ GeV/c. At Level-2 it confirms, on SVT tracks, the scalar sum of the transverse momenta $\sum p_{\rm T} > 6.5$ GeV/c and tightens the transverse momentum requirement to $p_{\rm T} > 2.5$ GeV/c. At Level-3 has exactly the same requirements as B_PIPI.
The B_PIPI_HIGHPT accept-rate at $\mathcal{L} \simeq 100 \times 10^{30}$ cm^{-2}s^{-1} is 14 kHz, 10 Hz, 0.2 Hz at Level-1, Level-2, Level-3, respectively.

The overall acceptance of the B_PIPI trigger selection is $\simeq 2\%$ for $B^0_{(s)} \to h^+h^{'-}$ decays in which the $B^0_{(s)}$ meson has transverse momentum $p_{\rm T} > 4$ GeV/c.

3.2.2 Other Displaced-Tracks Triggers

This is a concise description of the B_CHARM path, implemented to efficiently collect multi-body heavy-flavor decays, such as $B^0_{(s)} \to D^-_{(s)}\pi^+$, $D^{*+} \to D^0\pi^+$ and prompt $D^0 \to h^+h^{'-}$ used as control samples for the present measurement. At Level-1 the B_CHARM and B_PIPI paths share common requirements; this explains why, in the B_PIPI path, the $\Delta\varphi_0 > 20^\circ$ requirement was applied only at Level-2, although the information needed for this requirement was available since Level-1. At subsequent levels, the B_CHARM selection is similar to the B_PIPI one but it has different thresholds on the impact parameter of the SVT tracks ($|d_0| > 120$ μm), on the azimuthal opening angle ($2^\circ < \Delta\varphi_0 < 90^\circ$), and it does not contain any requirement on the impact parameter of the B candidate. Like in the B_PIPI case, the dynamic prescale and the introduction of additional trigger paths (B_CHARM_HIGHPT trigger), was required to cope larger luminosities. This is similar to the B_PIPI_HIGHPT path respectively, it has tighter requirements on the transverse momenta of XFT tracks ($p_{\rm T} > 2.46$ GeV/c), and on their scalar sum ($\sum p_{\rm T} > 6.5$ GeV/c) at Level-1.

Quantity	Units	B_PIPI	B_PIPI_HIGHPT
$p_{\rm T}(1),\ p_{\rm T}(2)$	GeV/c	> 2.0	> 2.5
$\Delta\varphi_0$	Degrees	$[20°, 135°]$	$[20°, 135°]$
$\sum p_{\rm T}$	GeV/c	> 5.5	> 6.5
$\lvert d_0(1)\rvert,\ \lvert d_0(2)\rvert$	μm	$[100,\ 1000]$	$[100,\ 1000]$
$\lvert d_0(B)\rvert$	μm	< 140	< 140
$\lvert L_{\rm T}(B)\rvert$	μm	> 200	> 200
$\lvert\eta(1)\rvert,\ \lvert\eta(2)\rvert$	–	< 1.2	< 1.2
$m_{\pi\pi}$	GeV/c^2	$[4.0, 7.0]$	$[4.0, 7.0]$

Table 3.1: Summary of the most relevant trigger requirements.

3.2.3 Trigger performance

An illustration of the impact of the trigger selection on the signal-to-background ratio for $B^0_{(s)} \to h^+h^{'-}$ decays is shown in fig. 3.2. A production cross-section times branching fraction $\sigma_{p\bar{p}\to B^0_{(s)}+X} \times \mathcal{B}(B^0_{(s)} \to h^+h^{'-}) \approx 30\ \mu\text{b} \times 3 \times 10^{-5} \approx 1$ nb is assumed for the signal, and a total inelastic $p\bar{p}$ cross-section $\sigma_{p\bar{p}} = 60$ mb at $\sqrt{s} = 1.96$ TeV. The illustration points out the key rôle of SVT at Level-2 of

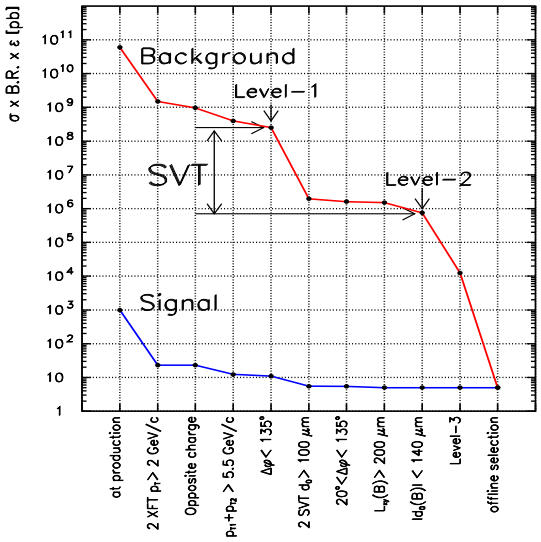


Figure 3.2: Cross-section times branching-fraction times detection efficiency for $B^0_{(s)} \to h^+h^{'-}$ decays compared with the cross-section times efficiency for generic inelastic $p\bar{p}$ background, as a function of the selection requirements.

the trigger chain. Thanks to the on-line requirements on impact parameter, decay transverse length, impact parameter of B candidate etc., SVT improves the signal-to-noise ratio of about two orders of magnitude and it allows to collect (*to write on tape*) events most likely containing $B^0_{(s)} \to h^+h^{'-}$

decays. This is essential to obtain at off-line level a rich sample of $B^0_{(s)} \to h^+h^{'-}$ decays.

3.3 Extraction of the $B^0_{(s)} \to h^+h^{'-}$ signal

The first step of the off-line analysis consists in applying a baseline selection to the events collected by the `B_PIPI` and `B_PIPI_HIGHPT` trigger paths. Trigger requirements are reapplied using high-resolution off-line quantities to remove the $B^0_{(s)} \to h^+h^{'-}$ candidates not satisfying the trigger selection.

3.3.1 Tracks

This analysis is based on tracks. Tracks are reconstructed by the standard CDF II production executable using LØØ, SVXII, ISL and COT hits, the detailed magnetic map of the tracking volume, and taking into account the measured angular and translation mis-alignments among LØØ, SVXII, ISL, COT and the beam-line. Since the measurements described in this thesis are not a lifetime-based, but they are decay rate measurements and since the lifetime information enters only in the selection (see sec. 3.5) through the cuts on impact parameter and decay transverse length the improvement due to the LØØ hits is marginal. This was verified repeating the analysis including/removing the LØØ silicon hits from the reconstruction. We found an improvement on the statistical uncertainty of desired physics observables of $\approx$ few%, due to a small improvement of the signal-to-noise ratio when the LØØ silicon hits are included in the reconstruction. At the time of this thesis, the SVXII and ISL detector simulation was validated and extensively tested in many CDF analyses, while the LØØ simulation was not well understood yet. We therefore used only tracks whose reconstruction included silicon hits of SVXII, ISL. Mis-alignments and noise hits in the silicon detectors and in the COT cause a contamination of fake or mis-reconstructed tracks. The fraction of such undesirable tracks was reduced by applying a set of standard criteria: we selected tracks reconstructed using at least 5 hits in at least two axial and two stereo COT super-layers. Each track was also required to be associated to hits in at least 3 $r-\phi$ SVX layers and to result from a converged helix-fit with a positive error matrix.

The default 3-D silicon tracking code uses a stepwise fit that starts from a COT track pointing to the silicon detector fiducial volume and progressively adds hits within the search road[2] as the fit moves from the outer silicon radii to the inner radii. The tracking algorithms which provide the standard CDF track collections are named OI, OIS, OIZ. The OI (Outside In) tracking algorithm starts from the COT precursor tracks and only $r-\phi$ silicon hits are added by the progressive track fit. If three or more $r-\phi$ hits are found silicon tracking proceeds toward the more complex algorithms OIS (Outside In Stereo) and OIZ (Outside In Z). Starting from the COT track and $r-\phi$ hits found by the OI tracking, the OIS algorithm adds only SAS $r-z$ (Small Angle Stereo) hits as the fit progresses from outer to inner radii. If SAS hits and at least two $90^\circ z$ $r-z$ hits are added simultaneously to the OI tracks we obtain the third type of tracks named OIZ tracks. The standard CDF prescriptions require to use the collections tracks OI, OIS, OIZ, but in the present analysis only the OIZ track collections are used since they have a better resolution on $r-z$-plane with respect to the other tracks collections.

[2]Silicon hits are searched in a 4σ-wide extrapolation of the COT track in the silicon layers, where σ are the uncertainties on the estimated track parameters.

The requirement of tracks with sufficient $r-z$ information reduces the contamination from those coming from two distinct heavy-flavors in the event, which have sizable impact parameter but are separated along the z direction. This additional requirement has a $\sim 90\%$ efficiency on signal yield while it reduces the background by a factor $\simeq 2$.

The error matrix of the track fit in the COT is estimated by default disregarding the effect of multiple scattering in the COT. According to the standard CDF prescriptions, we compensated for this approximation by refitting the tracks, after rescaling the covariance matrix of the COT track with an appropriate set of empirical scale factors. The rescaled COT track is used to seed the refit of the combined COT-SVXII tracks. The refitting uses the algorithm based on the Kalman filtering [105] and includes energy-loss corrections for kaons, pions and protons, according to the chosen mass assignment for each particle. The refitting procedure, the tracking alignments, and the GEANT description of the detector material have been carefully studied and validated by independent analyses for the measurement of b-hadron masses [106].

3.3.2 Trigger confirmation

Since SVT tracks are reconstructed with a different fitting algorithm with respect to the off-line tracks, the sample selected by the off-line analysis may contain candidates which did not satisfy the trigger selection ("volunteers"). Since the Monte Carlo does not reproduce volunteers, we need to exclude them also from data. They were excluded by requiring the matching[3] between the off-line track pair forming the $B^0_{(s)} \to h^+h^{'-}$ candidate and two SVT tracks in each event; then the complete set of trigger requirements was applied to the SVT quantities of the matched tracks, thus repeating the real trigger decision in the off-line analysis.

3.3.3 Reconstruction of $B^0_{(s)} \to h^+h^{'-}$ candidates

Fully reconstructed decays of b-hadrons are expected to appear as peaking structures on an otherwise smooth invariant mass spectrum. The off-line reconstruction of $B^0_{(s)} \to h^+h^{'-}$ candidates was solely based on tracking, disregarding any form of particle identification. In each event, the two particle invariant mass was computed for all possible pairs of oppositely-curved tracks satisfying the criteria described in sec. 3.3.1 and 3.3.2. We used the measured momenta and we arbitrarily assigned the charged-pion mass to both tracks. The two tracks were constrained by the vertex fit algorithm to originate from a common vertex in the 3-D space. In case of a converged vertex-fit with satisfactory quality, the pair was promoted to a $B^0_{(s)} \to h^+h^{'-}$ candidate, and retained for further processing, if its invariant $\pi\pi$-mass is within the interval $4.0 < M_{\pi\pi} < 7.0$ GeV/c^2. During reconstruction, we applied a baseline selection, reapplying the trigger selection on off-line quantities (see tab. 3.2). In addition, we rejected tracks reconstructed outside the SVT fiducial acceptance ($|\eta| \leq 1$), and pairs with a positive product of impact parameters. The invariant $\pi\pi$-mass distribution of the resulting sample is shown in fig. 3.3. A bump appears at masses around the nominal $B^0_{(s)}$ meson masses. A simple binned χ^2-fit of the distribution to a Gaussian function for the signal, over a negative exponential plus a constant function for the background, provides an estimate of $\sim 14,500$ signal events. The signal is centered

[3] The algorithm required proximity in curvature and azimuthal opening angle between SVT tracks and off-line tracks.

at about 5.25 GeV/c^2, with about 35 MeV/c^2 r.m.s. deviation, and ≈ 0.2 signal-to-background ratio at the peak.

The distribution in fig. 3.3 is an important achievement at an hadron collider. $B^0_{(s)} \to h^+h'^-$ decays, with $\mathcal{O}(10^{-5})$ branching fractions, are reconstructed, and this is made possible even at level of trigger selection by the SVT. This is the largest total number of events in the world, but a tighter selection is needed for the analysis.

Quantity of the track	Units	Requirement
Axial Si hits	–	≥ 3
Axial COT SL (hits/SL)	–	≥ 2 (≥ 5)
Stereo COT SL (hits/SL)	–	≥ 2 (≥ 5)
Reco. algorithm	–	OI,OIS,OIZ
p_{T}	GeV/c	> 2.0
$\lvert\eta\rvert$	–	< 1.0
$\lvert d_0\rvert$	μm	[100, 1000]
Quantity of the candidate		
$q(1) \times q(2)$	e^2	-1
$d_0(1) \times d_0(2)$	μm^2	< 0
L_{T}	μm	> 300
$\sum p_{\mathrm{T}}$	GeV/c	> 5.5
$\lvert d_0\rvert$	μm	< 140
$\Delta\varphi_0$	Degrees	[20°, 135°]
$m_{\pi\pi}$	GeV/c^2	[4.0, 7.0]

Table 3.2: Summary of the off-line trigger confirmation selection.

3.4 Further variables

In the off-line analysis, the discriminating power of the $B^0_{(s)}$ meson isolation and of the information provided by the 3D reconstruction capability of the CDF tracking was used, allowing a great improvement in the signal purity.

Isolation of the B meson ($I(B)$)

One of the useful variable used to discriminate the $B^0_{(s)} \to h^+h'^-$ signals from the background in the off-line selection is the "isolation". Given their hard fragmentation, b-hadrons tend to carry a larger fraction of the transverse momentum of the particles produced in the fragmentation, with respect to lighter hadrons [108]. We used an estimator of the fraction of momentum carried by the b-meson:

$$I|_{R=1}(B) = \frac{p_{\mathrm{T}}(B)}{p_{\mathrm{T}}(B) + \sum\limits_{i\neq j : B \to j}^{R} p_{\mathrm{T}}(i)}, \tag{3.3}$$

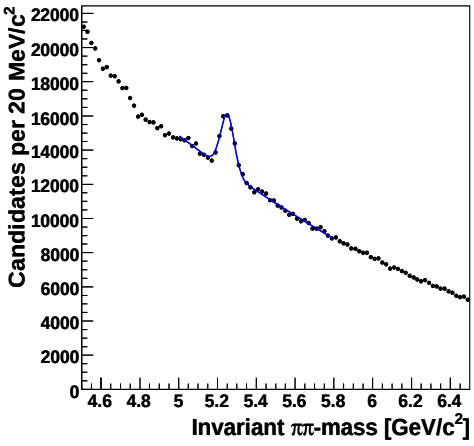


Figure 3.3: Invariant $\pi\pi$-mass distribution obtained by applying off-line the trigger confirmation selection. A Gaussian (signal) plus exponential (background) fit function is overlaid.

where the sum in the right-hand term of the denominator runs over all fragmentation tracks, identified as tracks (other than those of the B candidate decay-chain) satisfying standard track-quality requirements and found in a local region around the flight direction of the B candidate. Such region is parameterized as a cone in the $(\eta - \phi)$ space, unitary in radius ($R = \sqrt{\phi^2 + \eta^2} = 1$), whose apex is the primary vertex and the axis collinear with $\vec{p}_{\rm T}(B)$ (see fig. 7.1). When the decay products of the b-meson are contained in the cone, $I(B)$ is just the fraction of transverse momentum within the cone carried by the b-meson.[4] Candidates with large isolation are more likely to be b-mesons than candidates with low isolation.

The introduction of the isolation adds further complexity in the analysis: its distribution depends on the mechanism of hadronization of the b-quark, which is not described by the signal-only simulation discussed in sec. 4.1. We therefore uses real data to characterize this new observable (see chap. 7).

3-D vertex quality (χ^2_{3D})

Vertexing includes a large amount of information and it is sensitive to many issues, including alignments, geometry and track parameter errors. A quantity that summarizes all information of the three-dimensional vertex fit quality is the χ^2 of the vertex fit. The χ^2_{3D} is the minimum χ^2 resulting from the vertex fit minimization, when in the minimization all 3-D tracking information from the drift chamber and silicon detectors is used. This variable rejects a large amount of combinatorial background with an high efficiency for the signal.

[4]Since we use $R = 1$ all through this thesis, we henceforth simply wirite $I(B) \equiv I|_{R=1}(B)$.

3.5 Final selections

In this section we report the final results of the selection optimization process described in detail in chap. 8. The cuts optimization procedure is based on the fitter described in the following chapters and then for a better understanding we postpone its description after a full explanation of the technique developed to disentangle the different $B^0_{(s)} \to h^+h'^-$ signals.

We chose the selection with the aim to optimize the expected statistical uncertainty individually for each observables that we want to measure. In the present analysis we use two different selections: "*loose selection or loose cuts*" optimized to minimize the statistical uncertainty on the measurement of the direct CP-asymmetry $\mathcal{A}_{\rm CP}(B^0 \to K^+\pi^-)$ and "*tight selection or tight cuts*" optimized to improve the probability of discovery and limit setting of the $B^0_s \to K^-\pi^+$ mode. The adjectives loose and tight refer to the fact that the selection optimized to observe the rare $B^0_s \to K^-\pi^+$ mode is tighter than that one optimized to measure the direct CP-asymmetry in the $B^0 \to K^+\pi^-$ mode. For simplicity in this thesis we refer to these selections, using simply these two adjectives. The loose selection is also well suited to measure all the observables related to the large-yield modes ($B^0 \to \pi^+\pi^-$, $B^0_s \to K^+K^-$), while the tight selection is well-suited to measure all the observables related to rare modes ($B^0_s \to \pi^+\pi^-$, $B^0 \to K^+K^-$, $\Lambda^0_b \to p\pi^-$, $\Lambda^0_b \to pK^-$).

In the optimization process entered the following variables: the transverse decay length of the B candidate ($L_{\rm T}$), the impact parameter of the B candidate ($d_0(B)$), the impact parameter of both tracks (d_0), the isolation of the B candidate ($I(B)$) and the 3-D vertex quality ($\chi^2_{3D}(B)$).

The final selections are reported in tab. 3.3. Both final samples contain just one $B^0_{(s)} \to h^+h'^-$ candidate per event. The invariant mass distributions of the candidates (with the pion mass assigned to both tracks) are shown in fig. 3.4.

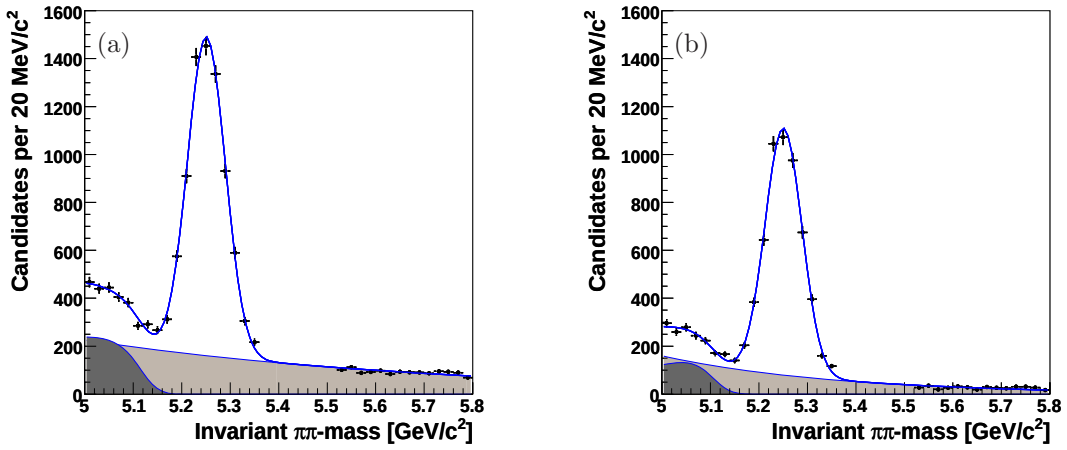


Figure 3.4: Invariant $\pi\pi$-mass distribution of the events passing the loose selection (a) and the tight selection (b). A Gaussian (signal) plus exponential (combinatoric background, light grey) plus a smeared Argus (physics background, dark grey) fit function is overlaid. For Argus function definition see text or Ref. [109].

Quantity of the track	Units	Loose	Tight
Axial Si hits	–	≥ 3	≥ 3
$90^\circ - z$ Si hits	–	≥ 2	≥ 2
Axial COT SL (hits/SL)	–	≥ 2 (≥ 5)	≥ 2 (≥ 5)
Stereo COT SL (hits/SL)	–	≥ 2 (≥ 5)	≥ 2 (≥ 5)
Total COT hits	–	≥ 42	≥ 42
Reco. algorithm	–	OIZ	OIZ
p_{T}	GeV/c	> 2.0	> 2.0
$\lvert\eta\rvert$	–	< 1.0	< 1.0
$\lvert d_0\rvert$	μm	[100, 1000]	[120, 1000]
Quantity of the candidate			
$q(1) \times q(2)$	e^2	-1	-1
$d_0(1) \times d_0(2)$	$\mu\mathrm{m}^2$	< 0	< 0
L_{T}	μm	> 300	> 350
$\sum p_{\mathrm{T}}$	GeV/c	> 5.5	> 5.5
$\lvert d_0\rvert$	μm	< 80	< 60
I	–	> 0.5	> 0.525
χ^2_{3D}	–	< 7	< 5
$\lvert\eta\rvert$	–	< 1.0	< 1.0
$\Delta\varphi_0$	Degrees	[20°, 135°]	[20°, 135°]
$m_{\pi\pi}$	GeV/c^2	[4.0, 7.0]	[4.0, 7.0]

Table 3.3: Summary of the optimized selections

Owing to the extremely selective criteria used to isolate the final sample, a detailed understanding of the background is challenging. Contributions to the background include an unknown mixture of rare events from heavy-flavors, light-quarks, resolution tails and so forth. A detailed simulation would require prohibitive amounts of CPU. However, the invariant $\pi\pi$-mass distribution already provides a first insight on the background composition. There are two different kinds of backgrounds:

combinatorial background – it is mostly composed of random pairs of charged particles, displaced from the beam-line, accidentally satisfying the selection requirements. Its dominant sources include generic QCD background of light-quark decays, lepton pairs from Drell-Yan processes, pairs of mis-measured tracks, combinations of a mis-measured track with a track from an heavy-flavor decay, or combinations of two tracks originated from two independent heavy-flavor decays of the event ($b\bar{b}$ and $c\bar{c}$ production). This is consistent with the smooth, slowly decreasing invariant $\pi\pi$-mass distribution in the signal sample for masses above 5.5 GeV/c. In this region, as well as in the signal region, the combinatorial component is the prominent source of background.

Partially-reconstructed heavy-flavor decays – (referred as "physics background") a change in the slope of the mass distribution of the signal sample, at masses just smaller than the signal mass, indicates the presence of an additional background source. This contribution is readily interpreted as mis-reconstructed b-hadron decays. These are multi-body b-hadron decays (e. g.,

$B^0 \to \rho^{\mp}\pi^{\pm}$, $B^0 \to \rho^- K^+$, $B_s^0 \to \rho^{\mp}\pi^{\pm}$, $B_s^0 \to \rho^+ K^-$ and many others), in which only two tracks were reconstructed, resulting in the typical shoulder-shape, that is suppressed around 5.15 GeV/c^2, because their contribution is kinematically limited to the $m_{\pi\pi} < m_{B^0_{(s)}}$ region.

To give a rough estimate of the signal yield and of the purity of these samples, two simple χ^2-binned fits were performed. A Gaussian shape was assumed to parametrize the "signal" peak, while two different distributions were used to parameterize the distinct background components: an exponential for the combinatorial background and an *Argus* function[5] convoluted with a Gaussian distribution centered at zero with a width equal to the mass resolution (≈ 22 MeV/c^2) for the physics background component.

We estimate a yield of 6509 ± 159 $B^0_{(s)} \to h^+h^{'-}$ events with a standard deviation $\sigma = 39.0 \pm 0.8$ MeV/c^2, and a purity $S/B \approx 8.3$ at the peak, for the loose cuts, while we estimate a yield of 4918 ± 209 $B^0_{(s)} \to h^+h^{'-}$ events with a standard deviation $\sigma = 38 \pm 1$ MeV/c^2, and a purity $S/B \approx 13$ at the peak, for the tight cuts. The observed width of the $B^0_{(s)} \to h^+h^{'-}$ signal is approximately 38 MeV/c^2, much larger than what expected from the simulation for a single (e.g.,$B^0 \to \pi^+\pi^-$ or $B^0 \to K^+\pi^-$) decay $\approx$ 22 MeV/c^2. This indicates that the $B^0_{(s)} \to h^+h^{'-}$ signal is the overlap of signals from different B^0 and B^0_s decay modes with unknown proportions. Theoretical and experimental knowledge at the time of this analysis (see tabs. 1.1 and 1.2) predicts sizable contributions for $B^0 \to \pi^+\pi^-$, $B^0 \to K^+\pi^-$ and $B^0_s \to K^+K^-$mode, and five, as yet unobserved modes $B^0 \to K^+K^-$, $B^0_s \to \pi^+\pi^-$ $B^0_s \to K^-\pi^+$, $\Lambda^0_b \to p\pi^-$and $\Lambda^0_b \to pK^-$. Since the theoretical expected branching frations of the rare signals $B^0_s \to K^-\pi^+$, $\Lambda^0_b \to p\pi^-$, $\Lambda^0_b \to pK^-$ modes are large enough, we expect to observe for the first time these three modes. These are located in the right tail of the $B^0_{(s)} \to h^+h^{'-}$ signal peak, in the mass region $5.38 < m_{\pi\pi} < 5.52$ GeV/c^2. The analysis was performed following a blind procedure, where all significant plots and physical numbers were hidden until the analysis was approved officially by the Collaboration. For these reasons the mass region $5.38 < m_{\pi\pi} < 5.52$ GeV/c^2 was excluded from the fit of fig. 3.4. However this one-dimensional binned fit is only a qualitative tool to estimate the yield and the purity of the final optimized samples in a quick way. The Gaussian distribution to describe the total signal peak is inadequate to describe the overlapping of the different signals.

In order to obtain the desired branching fraction measurements, it is necessary to separate the contributions of the different signal components. The measurement of the composition of the $B^0_{(s)} \to h^+h^{'-}$ signal is the goal of this analysis, and it is described in this thesis. In chap. 4, we see that a separation on an event-by-event basis is not possible, and we introduce the statistical approach that combines information from PID and kinematics into an unbinned multivariate likelihood fit to determine the contribution of each mode. It includes also the choice of the kinematic observables and the description of the achieved PID performance.

[5] $\text{Argus}(x; c, m) = \frac{1}{\text{Norm}} \cdot [xe^{-c(\frac{x}{m})^2}\sqrt{1-(\frac{x}{m})^2}]$ if $x \leq m$, $\text{Argus}(x; c, m) = 0$ if $x > m$. See Ref. [109].

Chapter 4

Separation of individual $B^0_{(s)} \to h^+h^{'-}$ modes

The reconstructed $B^0_{(s)} \to h^+h^{'-}$ signal contains several B^0 and B^0_s meson decay-modes. We need to discriminate each contribution to extract the measurements of branching fractions. The available resolution in mass and in particle identification is insufficient for an event-by-event separation. This chapter is devoted to the description of how the information from kinematics and particle identification was used to achieve a statistical discrimination amongst the individual modes.

4.1 CDF II simulation

We used the official CDF II simulation to study the features of the two body charmless $B^0_{(s)} \to h^+h^{'-}$ decays. This simulation is used in several parts of the analysis and it is a crucial tool of our analysis. Here, we summarize only the general features of the standard CDF II simulation, without technical details. For a better understanding, we prefer to describe them in the chapters where they are actually used.

We used the BGENERATOR package to generate large samples of b-hadron decays [110]. BGENERATOR simulates the production and the decay of b-hadrons only: no fragmentation products, collision remnants, or pile-up events are present in the simulated data. This package provides less complex events, particularly suited for a fast processing with the detector simulation, but no information about QCD backgrounds or fragmentation can be extracted from the simulated samples. Conversely this information is available in full $p\bar{p}$ interaction generators, like PYTHIA, but its use in precision measurements would require extensive checking and likely complex tuning. Furthermore, a huge amount of computing power would be needed to generate background samples of adequate size for this analysis, with $\mathcal{O}(10^9)$ rejection factors of background. Hence we chose the simpler, and more reliable, approach of using Monte Carlo simulation for the signal, while extracting the information on background from collision data.

We simulated $B^0_{(s)} \to h^+h'^-$ decays taking into account varying detector and trigger configuration during the data-taking period: changes of the silicon coverage, of the XFT and the SVT configurations, as well as of the Two-Track Trigger trigger selection. The average prescale factors (see sec. 3.2) for the B_PIPI and B_PIPI_HIGHPT trigger paths are approximately equal in the period in which our data were collected, and since the B_PIPI_HIGHPT data are a subsample of those collected with the B_PIPI path, the kinematics of the decay can be considered as a purely B_PIPI topology. We verified directly on data that our decays are actually distributed with a purely B_PIPI kinematics. Figure 4.1 shows the data distribution of the scalar sum of momenta $\sum p_{\rm T}$ (a) and transverse momentum of both tracks $p_{\rm T}$ (b) obtained removing all requirements. No discontinuity at the values $\sum p_{\rm T} = 6.5$ GeV/c and $p_{\rm T}$(track) = 2.5 GeV/c is visible from this distributions in spite of the huge statistics in these plots. It is only visible a change of slope in the distribution of $\sum p_{\rm T}$ (fig. 4.1(b)) at the value

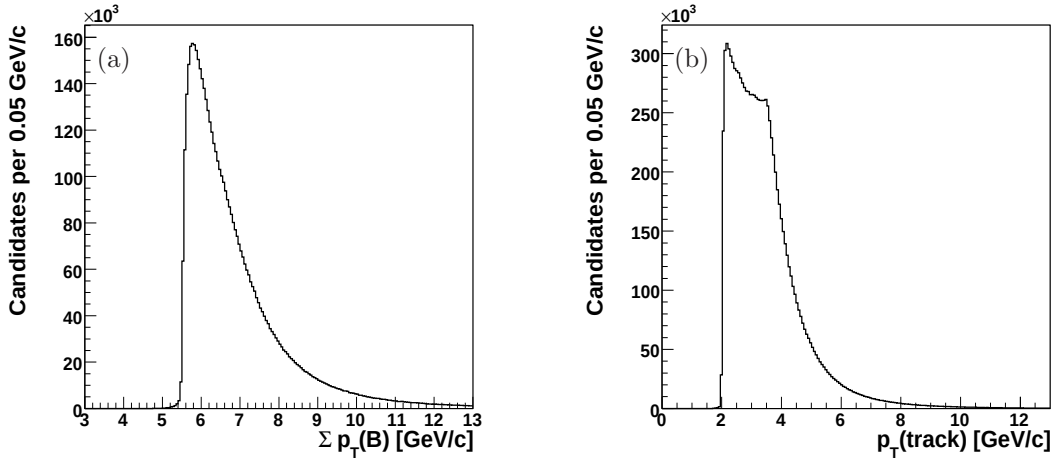


Figure 4.1: Check on real data of a purely B_PIPI topology, removing all off-line requirements. Distribution of the scalar sum of momenta $\sum p_{\rm T}$ (a), and transverse momentum of both tracks $p_{\rm T}$ (b). See text.

$\sum p_{\rm T} = 3.5$ GeV/c. This results by the combination of the trigger cuts: $p_{\rm T} > 2$ GeV/c for both tracks and $\sum p_{\rm T} > 5.5$ GeV/c (see sec. 3.2.1).

The beam-line, the detector and the trigger performance corresponding to the configuration of each run are simulated in the Monte Carlo. We generated 10 million events for each of the following decays $B^0 \to \pi^+\pi^-$, $B^0 \to K^+\pi^-$, $B^0_s \to K^-\pi^+$, and $B^0_s \to K^+K^-$, for each of the rare modes ($B^0 \to K^+K^-$, $B^0_s \to \pi^+\pi^-$), the baryonic backgrounds ($\Lambda^-_b \to p\pi^-$, $\Lambda^0_b \to pK^-$) and the partially heavy flavors decays ($B^0 \to \rho^\mp\pi^\pm$, $B^0 \to \rho^-K^+$, $B^0_s \to \rho^\mp\pi^\pm$, $B^0_s \to \rho^+K^-$ and $B^+ \to \rho^-\pi^+$, $B^+ \to \rho^0K^+$).

We generated single B^+, B^0, B^0_s and Λ^0_b mesons with a flat rapidity distribution in the range $|y(B)| < 1.3$, while the $p_{\rm T}(B)$ input distribution was taken from an external histogram containing a smooth fit to the data published in CDF Run II measurement [111], according to the standard CDF prescription. The $p_{\rm T}$ input spectrum of Λ^0_b was assumed equal to the B-meson spectrum.

Fragmentation was turned off. Decays were forced to $B^0_{(s)} \to h^+h'^-$ using the EVTGEN package [112]; $B-\overline{B}$ oscillations were inhibited ($\Delta m_d = \Delta m_s = 0$), and the lifetime difference in the B^0_s system was set to zero ($\Delta\Gamma_s/\Gamma_s = 0$). The generated sample was processed with the realistic trigger and GEANT simulation, and then reconstructed using the same executable used for real data.

4.1.1 Monte Carlo validation

In order to evaluate whether the Monte Carlo simulation describes the data reliably, we performed a comparison between real data and the Monte Carlo. To extract unbiased distributions of the signal quantities, we made a background subtraction: for each quantity, we subtracted the distributions for *background* candidates from the distributions for *signal plus background* candidates. The signal plus background candidates are defined as those found in the invariant-mass range $|m_{\pi\pi} - \mu| < 2\sigma$ where $\mu = 5251.0$ MeV/c^2 and $\sigma = 38$ MeV/c^2 are respectively the parameters returned from the simple fit performed in sec. 3.5. For the background candidates, we assumed that their contribution below the signal peak is dominated by pairs of random tracks satisfying the selection requirements (combinatorial background). We sampled this component using candidates at masses higher with respect to the signal peak since candidates at lower masses may include partially reconstructed $B^0_{(s)}$ meson decays, such as $B^0 \to \rho^+\pi^- \to [\pi^+\gamma]\pi^-$, which are kinematically excluded from the signal region;[1] we therefore used, as background candidates, those in the mass range $|m_{\pi\pi} - (\mu + 10\sigma)| < 2\sigma$. The distribution of background candidates was rescaled to the number of background events expected below the signal. In the simulation, each $B^0_{(s)} \to h^+h'^-$ contribution is weighted according to the measured branching fractions of the already observed modes and the theoretical expectations for those not yet observed.

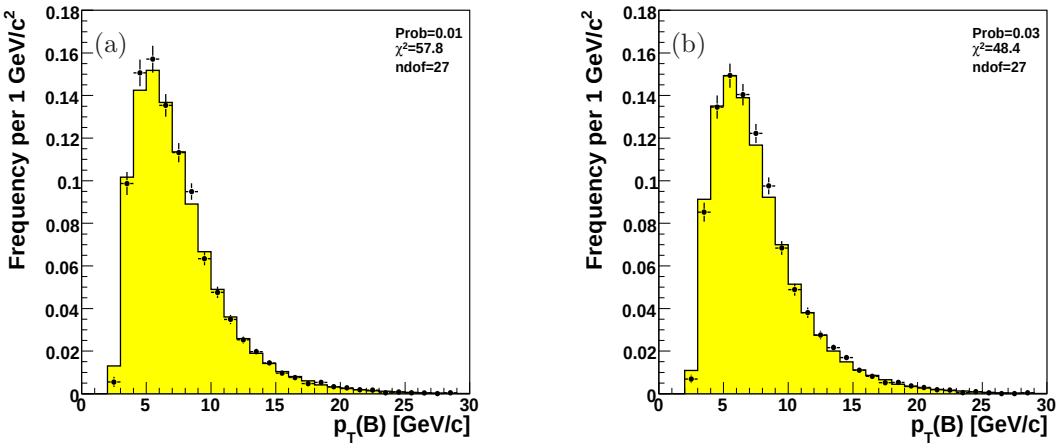


Figure 4.2: Background-subtracted $p_{\rm T}(B)$-distribution in $B^0_{(s)} \to h^+h'^-$ decays. Data (points with error bars) are compared with Monte Carlo simulation (filled histogram). Selection optimized to measure $\mathcal{A}_{\rm CP}(B^0 \to K^+\pi^-)$ (a), to observe $B^0_s \to K^-\pi^+$ mode (b) (see tab. 3.3). No isolation requirement was applied.

[1] See sec. 3.5 and sec. 6.4 for further details on the background composition.

We compared the distributions of several observables of the two outgoing particles (transverse momentum, and impact parameter), and of the candidate (transverse momentum, sum of transverse momenta of outgoing particles, azimuthal opening angle, transverse decay-length, impact parameter, three dimensional vertex quality). We used the selections described in tab. 3.3 without the isolation requirement since the simulation does not reproduce the fragmentation processes (see chap. 3). The agreement between simulation and data is satisfactory for all the observables, indicating that the simulated sample describes the data with good accuracy. Figure 4.2 shows an example of the comparison.

The final selections (see tab. 3.3) used in this analysis have the additional requirement of the isolation cut. The isolation distribution depends strongly on $p_{\rm T}(B)$ (see chap. 7), therefore a requirement on this variable sculpts the $p_{\rm T}(B)$ distribution. Figures 4.3(a) and (b) and fig. 4.4 show the comparison between the simulation (without the isolation cut) and the data selected using all requirements (included isolation) for the $p_{\rm T}(B)$ distribution, respectively for the sample selected with loose cuts (with $I > 0.5$) and tight cuts (with $I > 0.525$). The discrepancy is due to the isolation requirement as we show in chap. 7, where the isolation features are studied accurately. To not introduce any bias in the Monte Carlo distributions, the $p_{\rm T}(B)$ spectrum of the simulation was reweighted to the $p_{\rm T}(B)$ spectrum observed in the data. The reweighting functions were extracted by the comparison between the data distributions with the isolation requirement and the simulated distributions without the isolation requirement. We parameterized the histogram ratio with the following function $\mathcal{F}$ (see figs. 4.3(c) and (d)):

$$\mathcal{F}(p_{\rm T}(B); a_0, a_1, a_2, a_3) = a_0 \cdot {\rm Erf}(a_1(p_{\rm T}(B) - a_2)) + a_3 \tag{4.1}$$

where a_0, a_1, a_2, a_3 are free parameters in the fit and ${\rm Erf}(x) = \frac{2}{\sqrt{\pi}} \int_0^x e^{-t^2} dt$. After the reweighting the agreement between data and the simulated distributions is satisfactory. Figure 4.5 shows the comparison between the $p_{\rm T}(B)$ reweighted Monte Carlo distributions and the data distributions for different variables.

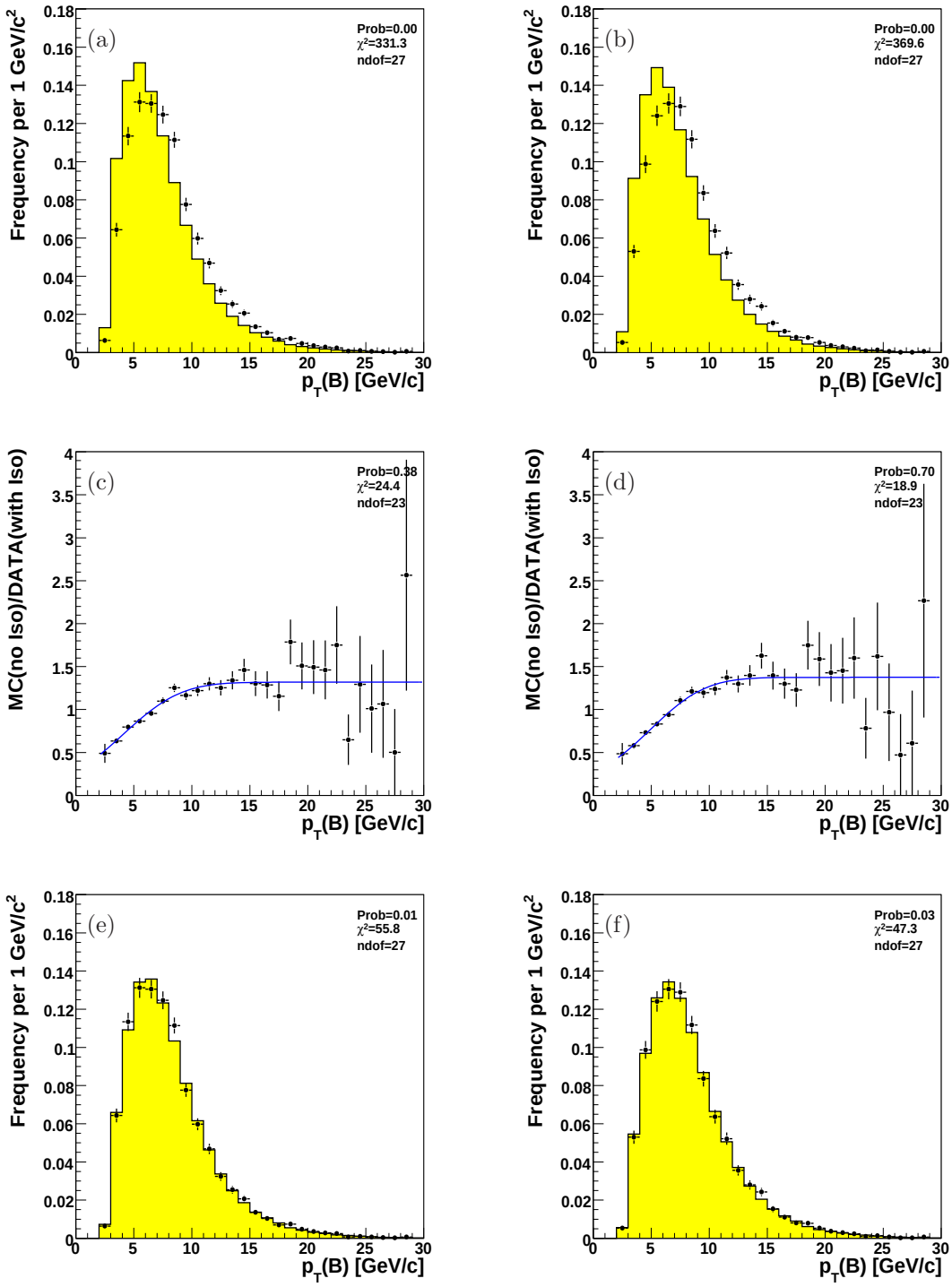


Figure 4.3: Background-subtracted $p_{\mathrm{T}}(B)$-distribution in $B^0_{(s)} \to h^+h'^-$ decays. Data (points with error bars) with isolation requirement are compared with Monte Carlo simulation (filled histogram) without isolation requirement (a,b). Ratio between data histogram with the isolation requirement and Monte Carlo histogram without isolation requirement is shown in (c,d). Data (points with error bars) with isolation requirement are compared with the reweighted Monte Carlo distribution (filled histogram) to keep into account the isolation sculpting (e,f). Loose (a,c,e) and tight (b,d,f) selection. In (c,d) the fit function is overlaid.

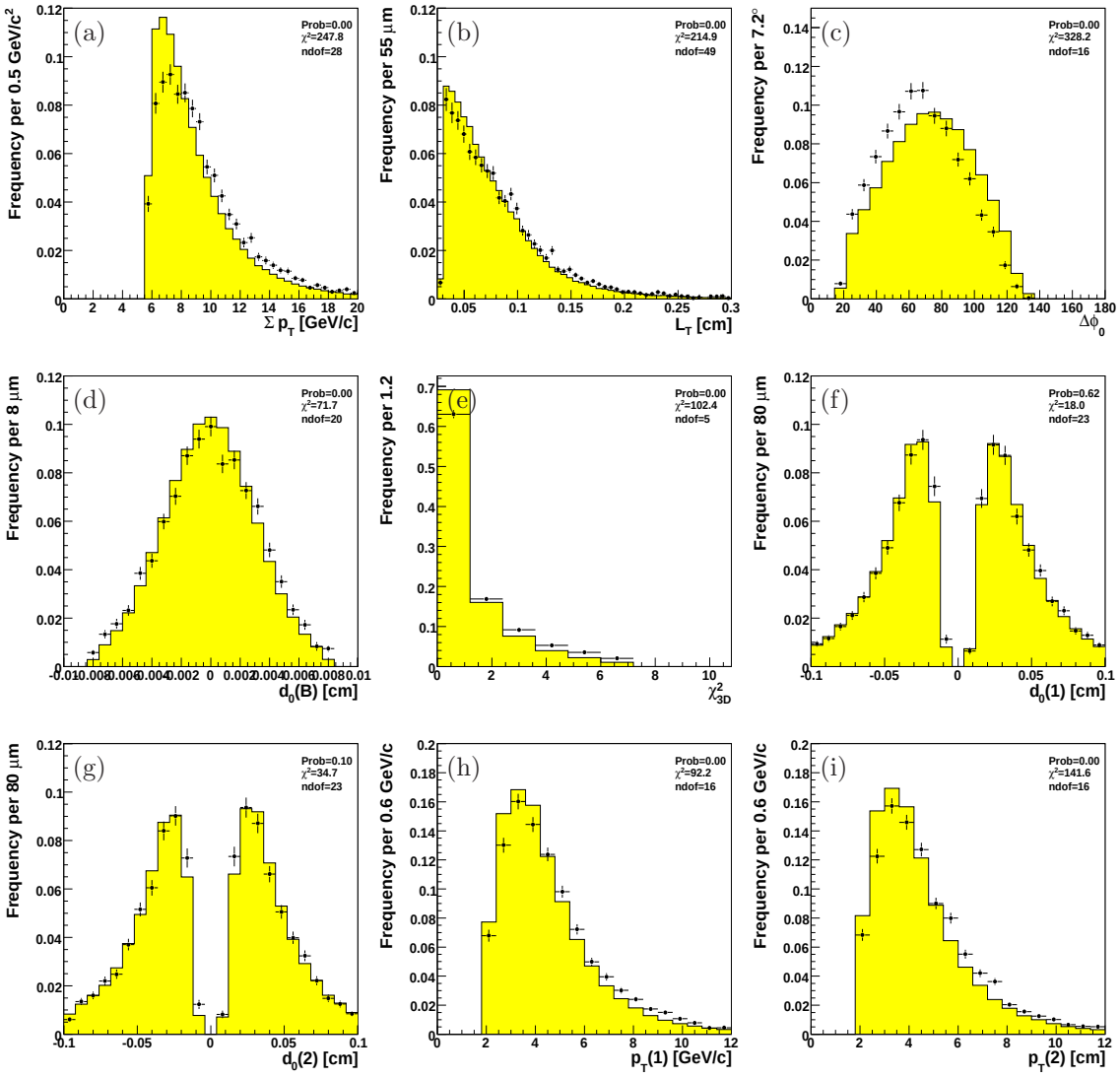


Figure 4.4: Comparison of background-subtracted distributions in $B^0_{(s)} \to h^+h'^-$ decays and equivalent Monte Carlo distributions $\sum p_{\mathrm{T}}$ (a), L_{T} (b), $\Delta\varphi_0$ (c), $d_0(B)$ (d), χ^2_{3D} (e), $d_0(1)$ (f), $d_0(2)$ (g), $p_{\mathrm{T}}(1)$ (h), $p_{\mathrm{T}}(2)$ (i). Data with the isolation requirement (points with error bars) are compared with Monte Carlo simulation without isolation requirement (filled histogram). These plots refer to the loose selection. Similar disagreement is observed for the tight selection.

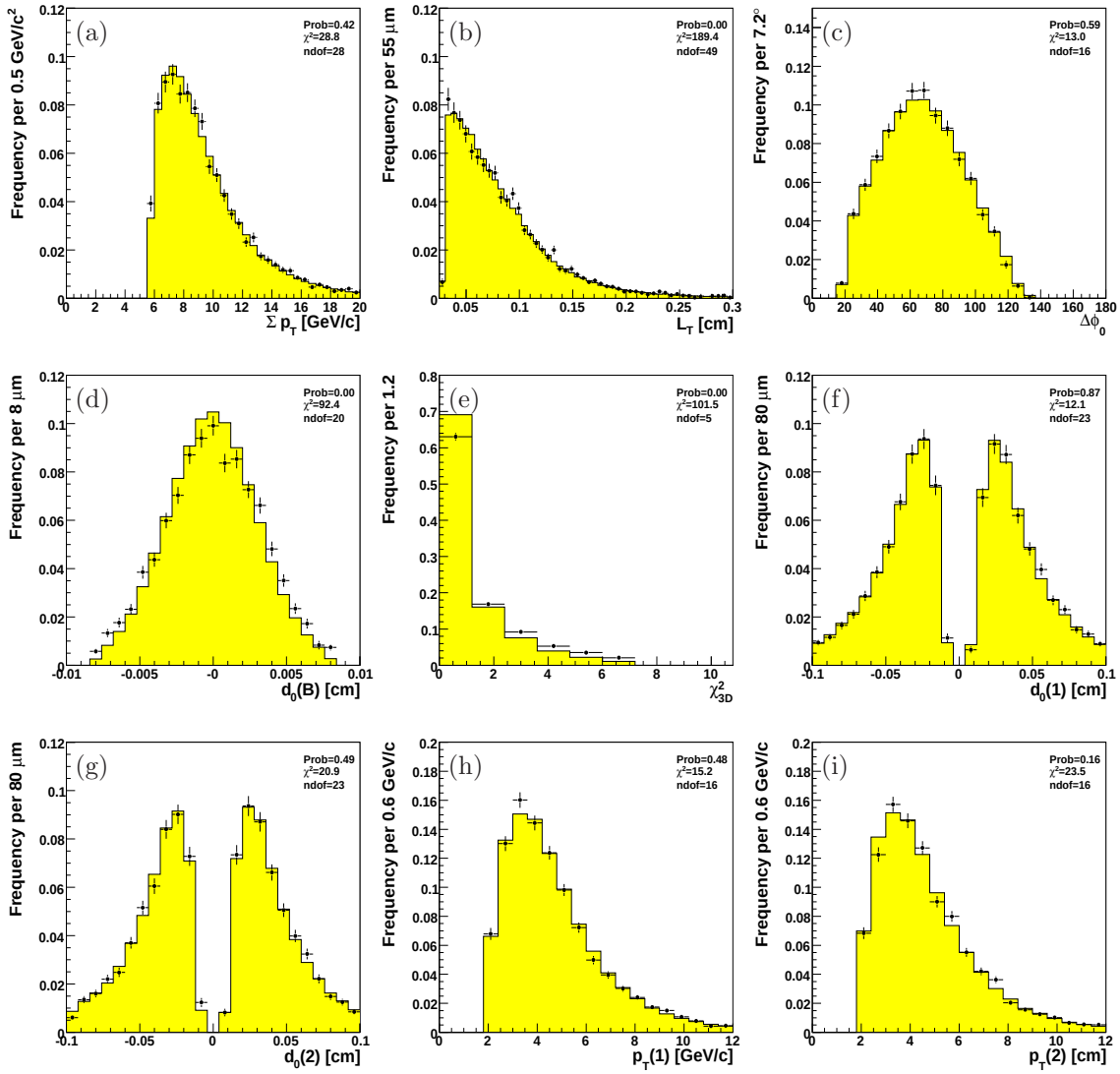


Figure 4.5: Comparison of background-subtracted distributions in $B^0_{(s)} \to h^+h^{'-}$ decays and equivalent Monte Carlo distributions $\sum p_{\rm T}$ (a), $L_{\rm T}$ (b), $\Delta\varphi_0$ (c), $d_0(B)$ (d), χ^2_{3D} (e), $d_0(1)$ (f), $d_0(2)$ (g), $p_{\rm T}(1)$ (h), $p_{\rm T}(2)$ (i). Data (points with error bars) are compared with reweighted Monte Carlo simulation (filled histogram). These plots refer to the loose selection. Similar agreement is observed for the tight selection.

4.2 $B^0_{(s)} \to h^+h'^-$ modes

In spite of the excellent CDF II mass-resolution, the $B^0_{(s)} \to h^+h'^-$ decay-modes are too closely spaced in mass to be resolved; they overlap in a single peak ($\sigma \approx 38$ MeV/c^2), broader than the expected mass resolution for an individual decay ($\sigma \approx 22$ MeV/c^2). Only the momenta of charged particles are measured, while their masses are arbitrarily assigned to compute the invariant mass of the track pair. Unfortunately, whatever mass assignment we choose (a single one for all modes), the invariant-mass distributions of modes with mis-assigned masses are inevitably broadened. Even with an infinitely precise mass resolution, their reconstructed invariant-mass would vary as a function of the momenta of the outgoing particles. We chose the charged pion mass for both outgoing particles. Figure 4.6 shows the expected invariant $\pi\pi$-mass distribution of the $B^0_{(s)} \to h^+h'^-$ decay-modes, resulting from the Monte Carlo simulation of each mode normalized using the branching fractions derived from the current experimental knowledge and theoretical predictions. The mis-assigned invariant $\pi\pi$-mass of the $B^0 \to K^+\pi^-$ mode peaks at about 45 MeV/c^2 lower than the nominal B^0 meson mass, while the invariant $\pi\pi$-mass of the $B^0_s \to K^-\pi^+$ mode peaks at a value about 45 MeV/c^2 higher, although 45 MeV/c^2 lower than the nominal B^0_s meson mass. The mis-reconstructed $B^0_s \to K^+K^-$ decays centers at the B^0 meson mass, because the B^0-B^0_s mass difference approximately compensates the effect of mis-identifying both kaons. While the mass r.m.s. width is approximately 22 MeV/c^2 for the properly reconstructed $B^0 \to \pi^+\pi^-$ mode, the widths of other modes appear larger (about 30 MeV/c^2), as a consequence of wrong mass assignment.

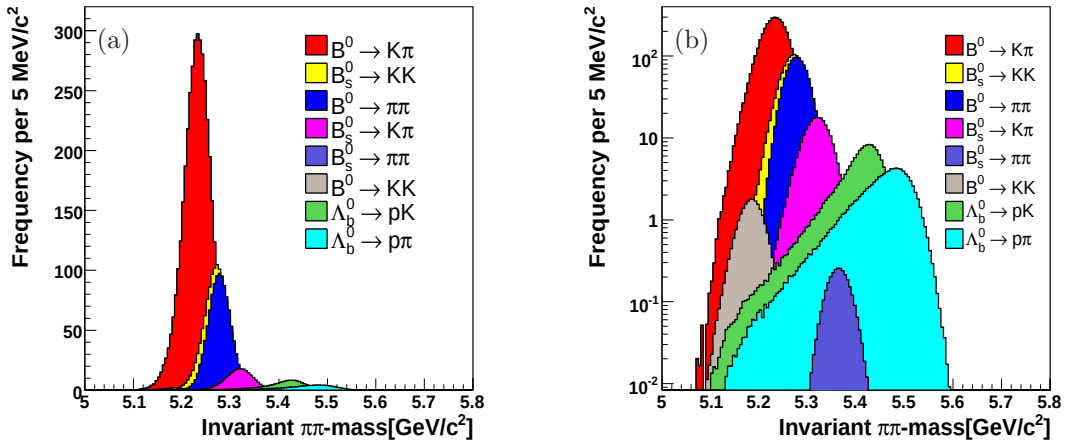


Figure 4.6: Invariant $\pi\pi$-mass distribution of the simulated $B^0_{(s)} \to h^+h'^-$ decay modes.

The simulated invariant $\pi\pi$-mass distribution of each mode shows the difficulty of the measurements of the deacay rates. We need to disentangle the contribution of each involved process, making sure to exploit all the available information provided by the detector. The following sections of this chapter are devoted to the description of how we can use the kinematic information to disentangle the $B^0_{(s)} \to h^+h'^-$ modes and to the description of the CDF II capabilities in the identification of charged

particles in the final states.

4.3 Kinematic separation

We exploit the kinematic differences to discriminate amongst decay modes. These differences are small, since the ≈ 90 MeV/c^2 difference between B_s^0 and B^0 masses, and the ≈ 350 MeV/c^2 difference between kaon and pion masses are small, compared with the typical energy of each outgoing particle in the decay rest-frame ($E \approx 2.5$ GeV).

Evaluating the different invariant masses resulting from all possible mass assignments to the particle pair (i. e., $\pi^+\pi^-$, $K^+\pi^-$, π^+K^-, and K^+K^-) for each event, induces unavoidable and large correlations between the Likelihood terms, with complications for their description and use in the fitting procedure [113]. In addition, this choice would considerably increase the number of observables needed in the Likelihood function. If the contributions from the other modes (e. g., $\Lambda_b^0 \to p\pi^-$) are considered, additional observables add up to the set of fit observables. On the other hand, choosing a single mass-assignment capable of discriminating the modes better than other assignments is disadvantageous. The resulting separation power remains limited whatever assignment is chosen, because not all the available kinematic information is efficiently exploited.

In a decay of a particle into two bodies of momenta $\vec{p}_1$ and $\vec{p}_2$ and masses $\overline{m}_1$ and $\overline{m}_2$, the invariant mass of the decaying particle satisfies the following relation:

$$m^2_{\overline{m}_1\overline{m}_2} = \left(\sqrt{\overline{m}_1^2 + p_1^2} + \sqrt{\overline{m}_2^2 + p_2^2}\right)^2 - (\vec{p}_1 + \vec{p}_2)^2. \tag{4.2}$$

Similarly, the invariant mass of the pair resulting from a different mass assignment to the outgoing particles is

$$m^2_{m_1 m_2} = \left(\sqrt{m_1^2 + p_1^2} + \sqrt{m_2^2 + p_2^2}\right)^2 - (\vec{p}_1 + \vec{p}_2)^2, \tag{4.3}$$

where the incorrect mass m_1 (m_2) is assigned to the particle with momentum $\vec{p}_1$ ($\vec{p}_2$) with, in general, $m_1 \neq m_2 \neq \overline{m}_1 \neq \overline{m}_2$. The difference between the mis-reconstructed and the true mass of the pair can be written as:

$$m^2_{m_1 m_2} - m^2_{\overline{m}_1\overline{m}_2} = (m_1^2 + m_2^2) - (\overline{m}_1^2 + \overline{m}_2^2) + 2 \cdot \left(\sqrt{p_1^2 + m_1^2} \cdot \sqrt{p_2^2 + m_2^2} - \sqrt{p_1^2 + \overline{m}_1^2} \cdot \sqrt{p_2^2 + \overline{m}_2^2}\right) \tag{4.4}$$

The relation (4.4) allows writing the invariant mass of the decay, $m^2_{m_1 m_2}$, for any mass assignment to the outgoing particles (m_1, m_2), as a function of three variables: an invariant mass $m^2_{\overline{m}_1\overline{m}_2}$ obtained from a single arbitrary choice of mass assignment, and the momenta of the outgoing particles p_1 and p_2. After choosing a single mass-assignment for all events, thus obtaining the observable $m^2_{m_1 m_2}$, of which the p.d.f. is function, the Likelihood term corresponding to a given decay-mode is easily written in terms of the nominal B^0, B_s^0 or Λ_b^0 mass (i. e., the value of $m_{\overline{m}_1\overline{m}_2}$ obtained with the correct mass assignment for the given mode), and of the momenta of outgoing particles p_1 and p_2. Our choice of the charged-pion mass (m_π) for the two particles yields

$$m^2_{\pi\pi} = m^2_{\overline{m}_1\overline{m}_2} + (m_\pi^2 + m_\pi^2) - (\overline{m}_1^2 + \overline{m}_2^2) + 2 \cdot \left(\sqrt{p_1^2 + m_\pi^2} \cdot \sqrt{p_2^2 + m_\pi^2} - \sqrt{p_1^2 + \overline{m}_1^2} \cdot \sqrt{p_2^2 + \overline{m}_2^2}\right) \tag{4.5}$$

For each event (i. e., for each set of observed $m_{m_1m_2} = m_{\pi\pi}$ and p_1 and p_2), eq. (4.5) takes different forms, depending on the decay mode one is referring to. For the $B^0 \to K^+\pi^-$ mode, for instance, $\overline{m}_1 = m_{K^+}$, $\overline{m}_2 = m_{\pi^-}$ or viceversa by construction, hence $m^2_{\overline{m}_1\overline{m}_2} = m_{B^0}$.

The dedicated $B^0_{(s)} \to h^+h^{'-}$ trigger selects particles with transverse momenta larger than 2 GeV/c. In this regime, the limit of relativistic decay-products is sufficiently accurate, $m^2_{1,2}, \overline{m}^2_{1,2} \ll p^2_{1,2}$, thus eq. (4.5) can be expanded in the Taylor series up to $\mathcal{O}(m^2/p^2)$:

$$m^2_{\pi\pi} \approx m^2_{\overline{m}_1\overline{m}_2} + \left(1 + \frac{p_1}{p_2}\right)\left(m^2_\pi - \overline{m}^2_2\right) + \left(1 + \frac{p_2}{p_1}\right)\left(m^2_\pi - \overline{m}^2_1\right). \tag{4.6}$$

Neglecting terms of order $\mathcal{O}(m^2/p^2)$, eq. (4.5) is function only of the ratio of p_1/p_2 and not of the individual momenta p_1 and p_2. For this reason it is convenient to write eq. (4.5) as a function of the "momentum imbalance" p_1/p_2 and of a second variable such that p_1 and p_2 are univocally determined once the momentum imbalance and this variable are known. The ideal candidate is the scalar sum of momenta of the particles, $p_{\rm tot} = p_1 + p_2$. In this way the momentum imbalance appears explicitly in the relation and the momentum information is summarized using a set of quantities $(p_1/p_2, p_{\rm tot})$ less correlated than (p_1, p_2). In principle one could use the approximated eq. (4.6) instead of the exact eq. (4.5) and describe the kinematic of the decays using only two variables $(m_{\pi\pi}, p_1/p_2)$. However, when the contributions from $\Lambda^0_b \to ph^-$ decays are not negligible, the relativistic approximation is less accurate. In case of the proton the terms $\mathcal{O}(m^2/p^2)$ cannot be neglected. For example in Ref. [1], where the contribution from $\Lambda^0_b \to ph^-$ decays was negligible, the relation (4.6) was used to describe the kinematics of the $B^0_{(s)} \to h^+h^{'-}$ decays, using only two variables $(m_{\pi\pi}, p_1/p_2)$.

The advantage of this approach consists in the fact that all kinematic information is summarized in just three, loosely correlated, variables ($m_{\pi\pi}$, p_1/p_2 and $p_{\rm tot}$), while a larger number of strongly-correlated variables would have been needed if all mass assignments had been used in the Likelihood. Also, eq. (4.6) means that $m^2_{\pi\pi}$ is determined mainly by p_1/p_2, with only a small correction related to $p_{\rm tot}$.

Charge-kinematics flavor tagging

By combining charge information with kinematic information, one can gain separation power between $K^+\pi^-$ and $K^-\pi^+$ (also between ph^- and $\bar{p}h^+$) final states.

We label the outgoing particles according to the increasing magnitude of their momenta, index "1" labels the charge (q_1), mass (m_1), and momentum ($\vec{p}_1$) of the lower momentum particle in the decay, index "2" labels the corresponding quantities of the higher momentum particle. Then we define a "signed momentum-imbalance" as

$$\alpha = \left(1 - \frac{p_1}{p_2}\right) \times q_1, \tag{4.7}$$

which takes values in the finite interval $[-1, 1]$. Equation (4.5) can be rewritten in terms of α and $p_{\rm tot}$

as:

$$\begin{aligned} m^2_{\pi\pi} &= m^2_{\overline{m}_1\overline{m}_2} + 2m^2_\pi - (\overline{m}^2_1 + \overline{m}^2_2) \\ &+ 2\sqrt{\left(\frac{1-|\alpha|}{2-|\alpha|}p_{\rm tot}\right)^2 + m^2_\pi} \cdot \sqrt{\left(\frac{1}{2-|\alpha|}p_{\rm tot}\right)^2 + m^2_\pi} \\ &- 2\sqrt{\left(\frac{1-|\alpha|}{2-|\alpha|}p_{\rm tot}\right)^2 + \overline{m}^2_1} \cdot \sqrt{\left(\frac{1}{2-|\alpha|}p_{\rm tot}\right)^2 + \overline{m}^2_2} \end{aligned} \tag{4.8}$$

where $\overline{m}_1$ ($\overline{m}_2$) is the mass of the lower (higher) momentum particle and where

$$p_1 = \frac{1-|\alpha|}{2-|\alpha|}p_{\rm tot} \tag{4.9}$$

$$p_2 = \frac{1}{2-|\alpha|}p_{\rm tot} \tag{4.10}$$

Table 4.1 reports the analytical expressions for the average invariant $\pi\pi$-mass of the decay, as a function of the signed momentum imbalance α and the scalar sum of momenta of the particles $p_{\rm tot}$, for each specific mode. The formulas are obtained by solving eq. (4.8) for $m_{\pi\pi}$, and replacing all masses with the nominal values appropriate to each decay mode. For each mode, and for every value of α and $p_{\rm tot}$, the observed $\pi\pi$-invariant mass is distributed as the mass resolution templates extracted in sec. 6.3, owing to the detector resolution smearing of the natural width of the $B^0_{(s)}$ meson. The mean of the distribution is labeled as $\mathcal{M}^2(\alpha, p_{\rm tot}) \equiv E[m^2_{\pi\pi}(\alpha, p_{\rm tot})]$, where $E[x]$ indicates the expectation value of the random variable x (see tab. 4.1). The mean of the invariant-mass distribution, $\mathcal{M}(\alpha, p_{\rm tot})$, shifts as a function of the signed momentum imbalance and the scalar sum of particles momenta. The gain in information due to this mass-momentum correlation over the simpler invariant mass information comes from the differences among shifting patterns amongst the different modes. The distributions of invariant $\pi\pi$-mass as a function of the signed momentum-imbalance for simulated $B^0_{(s)} \to h^+h^{'-}$ decays are shown in figs. 4.7 and 4.8. In spite of the smearing effect of the mass resolution, the different trends of the different modes are visible. Differences between $B^0 \to K^+\pi^-$ and $\overline{B}^0 \to K^-\pi^+$ decays, between $B^0_s \to K^-\pi^+$ and $\overline{B}^0_s \to K^+\pi^-$ decays and between $\Lambda^0_b \to p\pi^-(\Lambda^0_b \to pK^-)$ and $\overline{\Lambda}^0_b \to \overline{p}\pi^+(\overline{\Lambda}^0_b \to \overline{p}K^+)$ are also visible. The latter are used to measure the CP-violating decay-rate asymmetry in these modes. The shape of the $B^0 \to \pi^+\pi^-(B^0_s \to \pi^+\pi^-)$ mode is obviously a straight line centered at the $B^0(B^0_s)$ meson mass, since the chosen mass assignment is correct for this mode. A small kinematic separation is expected between $B^0 \to \pi^+\pi^-$ and $B^0_s \to K^+K^-$ modes, because the $B^0_s \to K^+K^-$ curve is also approximately constant, and it overlaps the $B^0 \to \pi^+\pi^-$curve. However, an increased separation between these two modes is provided by the PID information, since both particles in final states are different.

The separation power among the modes given by the $p_{\rm tot}$ variable is small, order $\mathcal{O}(m/p)$, and since it is not possible to visualize in a three-dimensional space a four-dimensions surface ($m_{\pi\pi}, \alpha, p_{\rm tot}$ and $z-$axis), in the illustrations only the correlations between the invariant $\pi\pi$-mass and α are plotted. $p_{\rm tot}$ has a limited separation power for the signal modes, but it provides a mild discrimination between all signals and background (see sec. 6.5) and in combination with α, it gives an univocal determination of (p_1, p_2) necessary to exploit the PID information (see sec. 6.6).

mode	$\mathcal{M}^2[p_1(\alpha, p_{\rm tot}), p_2(\alpha, p_{\rm tot})] \quad \alpha < 0$
$B^0 \to \pi^- K^+$	$m^2_{B^0} + (m^2_\pi - m^2_K) + 2 \cdot \sqrt{p_1^2 + m^2_\pi} \cdot \left(\sqrt{p_2^2 + m^2_\pi} - \sqrt{p_2^2 + m^2_K} \right)$
$\overline{B}^0 \to K^- \pi^+$	$m^2_{B^0} + (m^2_\pi - m^2_K) + 2 \cdot \sqrt{p_2^2 + m^2_\pi} \cdot \left(\sqrt{p_1^2 + m^2_\pi} - \sqrt{p_1^2 + m^2_K} \right)$
$B^0/\overline{B}^0 \to K^- K^+$	$m^2_{B^0} + 2 \cdot (m^2_\pi - m^2_K) + 2 \cdot \left(\sqrt{p_1^2 + m^2_\pi} \cdot \sqrt{p_2^2 + m^2_\pi} - \sqrt{p_1^2 + m^2_K} \cdot \sqrt{p_2^2 + m^2_K} \right)$
$B^0/\overline{B}^0 \to \pi^- \pi^+$	$m^2_{B^0}$
$\overline{B}^0_s \to \pi^- K^+$	$m^2_{B^0_s} + (m^2_\pi - m^2_K) + 2 \cdot \sqrt{p_1^2 + m^2_\pi} \cdot \left(\sqrt{p_2^2 + m^2_\pi} - \sqrt{p_2^2 + m^2_K} \right)$
$B^0_s \to K^- \pi^+$	$m^2_{B^0_s} + (m^2_\pi - m^2_K) + 2 \cdot \sqrt{p_2^2 + m^2_\pi} \cdot \left(\sqrt{p_1^2 + m^2_\pi} - \sqrt{p_1^2 + m^2_K} \right)$
$B^0_s/\overline{B}^0_s \to K^- K^+$	$m^2_{B^0_s} + 2 \cdot (m^2_\pi - m^2_K) + 2 \cdot \left(\sqrt{p_1^2 + m^2_\pi} \cdot \sqrt{p_2^2 + m^2_\pi} - \sqrt{p_1^2 + m^2_K} \cdot \sqrt{p_2^2 + m^2_K} \right)$
$B^0_s/\overline{B}^0_s \to \pi^- \pi^+$	$m^2_{B^0_s}$
$\Lambda^0_b \to \pi^- p$	$m^2_{\Lambda^0_b} + (m^2_\pi - m^2_p) + 2 \cdot \sqrt{p_1^2 + m^2_\pi} \cdot \left(\sqrt{p_2^2 + m^2_\pi} - \sqrt{p_2^2 + m^2_p} \right)$
$\overline{\Lambda}^0_b \to \overline{p} \pi^+$	$m^2_{\Lambda^0_b} + (m^2_\pi - m^2_p) + 2 \cdot \sqrt{p_2^2 + m^2_\pi} \cdot \left(\sqrt{p_1^2 + m^2_\pi} - \sqrt{p_1^2 + m^2_p} \right)$
$\Lambda^0_b \to K^- p$	$m^2_{\Lambda^0_b} + 2m^2_\pi - (m^2_K + m^2_p) + 2 \cdot \left(\sqrt{p_1^2 + m^2_\pi} \cdot \sqrt{p_2^2 + m^2_\pi} - \sqrt{p_1^2 + m^2_K} \cdot \sqrt{p_2^2 + m^2_p} \right)$
$\overline{\Lambda}^0_b \to \overline{p} K^+$	$m^2_{\Lambda^0_b} + 2m^2_\pi - (m^2_p + m^2_K) + 2 \cdot \left(\sqrt{p_1^2 + m^2_\pi} \cdot \sqrt{p_2^2 + m^2_\pi} - \sqrt{p_1^2 + m^2_p} \cdot \sqrt{p_2^2 + m^2_K} \right)$
mode	$\mathcal{M}^2[p_1(\alpha, p_{\rm tot}), p_2(\alpha, p_{\rm tot})] \quad \alpha > 0$
$\overline{B}^0 \to \pi^+ K^-$	$m^2_{B^0} + (m^2_\pi - m^2_K) + 2 \cdot \sqrt{p_1^2 + m^2_\pi} \cdot \left(\sqrt{p_2^2 + m^2_\pi} - \sqrt{p_2^2 + m^2_K} \right)$
$B^0 \to K^+ \pi^-$	$m^2_{B^0} + (m^2_\pi - m^2_K) + 2 \cdot \sqrt{p_2^2 + m^2_\pi} \cdot \left(\sqrt{p_1^2 + m^2_\pi} - \sqrt{p_1^2 + m^2_K} \right)$
$B^0/\overline{B}^0 \to K^+ K^-$	$m^2_{B^0} + 2 \cdot (m^2_\pi - m^2_K) + 2 \cdot \left(\sqrt{p_1^2 + m^2_\pi} \cdot \sqrt{p_2^2 + m^2_\pi} - \sqrt{p_1^2 + m^2_K} \cdot \sqrt{p_2^2 + m^2_K} \right)$
$B^0/\overline{B}^0 \to \pi^+ \pi^-$	$m^2_{B^0}$
$B^0_s \to \pi^+ K^-$	$m^2_{B^0_s} + (m^2_\pi - m^2_K) + 2 \cdot \sqrt{p_1^2 + m^2_\pi} \cdot \left(\sqrt{p_2^2 + m^2_\pi} - \sqrt{p_2^2 + m^2_K} \right)$
$\overline{B}^0_s \to K^+ \pi^-$	$m^2_{B^0_s} + (m^2_\pi - m^2_K) + 2 \cdot \sqrt{p_2^2 + m^2_\pi} \cdot \left(\sqrt{p_1^2 + m^2_\pi} - \sqrt{p_1^2 + m^2_K} \right)$
$B^0_s/\overline{B}^0_s \to K^+ K^-$	$m^2_{B^0_s} + 2 \cdot (m^2_\pi - m^2_K) + 2 \cdot \left(\sqrt{p_1^2 + m^2_\pi} \cdot \sqrt{p_2^2 + m^2_\pi} - \sqrt{p_1^2 + m^2_K} \cdot \sqrt{p_2^2 + m^2_K} \right)$
$B^0_s/\overline{B}^0_s \to \pi^+ \pi^-$	$m^2_{B^0_s}$
$\overline{\Lambda}^0_b \to \pi^+ \overline{p}$	$m^2_{\Lambda^0_b} + (m^2_\pi - m^2_p) + 2 \cdot \sqrt{p_1^2 + m^2_\pi} \cdot \left(\sqrt{p_2^2 + m^2_\pi} - \sqrt{p_2^2 + m^2_p} \right)$
$\Lambda^0_b \to p \pi^-$	$m^2_{\Lambda^0_b} + (m^2_\pi - m^2_p) + 2 \cdot \sqrt{p_2^2 + m^2_\pi} \cdot \left(\sqrt{p_1^2 + m^2_\pi} - \sqrt{p_1^2 + m^2_p} \right)$
$\overline{\Lambda}^0_b \to K^+ \overline{p}$	$m^2_{\Lambda^0_b} + 2m^2_\pi - (m^2_K + m^2_p) + 2 \cdot \left(\sqrt{p_1^2 + m^2_\pi} \cdot \sqrt{p_2^2 + m^2_\pi} - \sqrt{p_1^2 + m^2_K} \cdot \sqrt{p_2^2 + m^2_p} \right)$
$\Lambda^0_b \to p K^-$	$m^2_{\Lambda^0_b} + 2m^2_\pi - (m^2_p + m^2_K) + 2 \cdot \left(\sqrt{p_1^2 + m^2_\pi} \cdot \sqrt{p_2^2 + m^2_\pi} - \sqrt{p_1^2 + m^2_p} \cdot \sqrt{p_2^2 + m^2_K} \right)$

Table 4.1: Upper table: $\mathcal{M}^2(\alpha, p_{\rm tot})$ for $\alpha < 0$ (i.e. the negative particle carries smaller momentum). Lower table: $\alpha > 0$ (i.e. the positive particle carries smaller momentum). For simplicity, the formulas in the tables are written as functions of p_1 and p_2, instead of α and $p_{\rm tot}$.

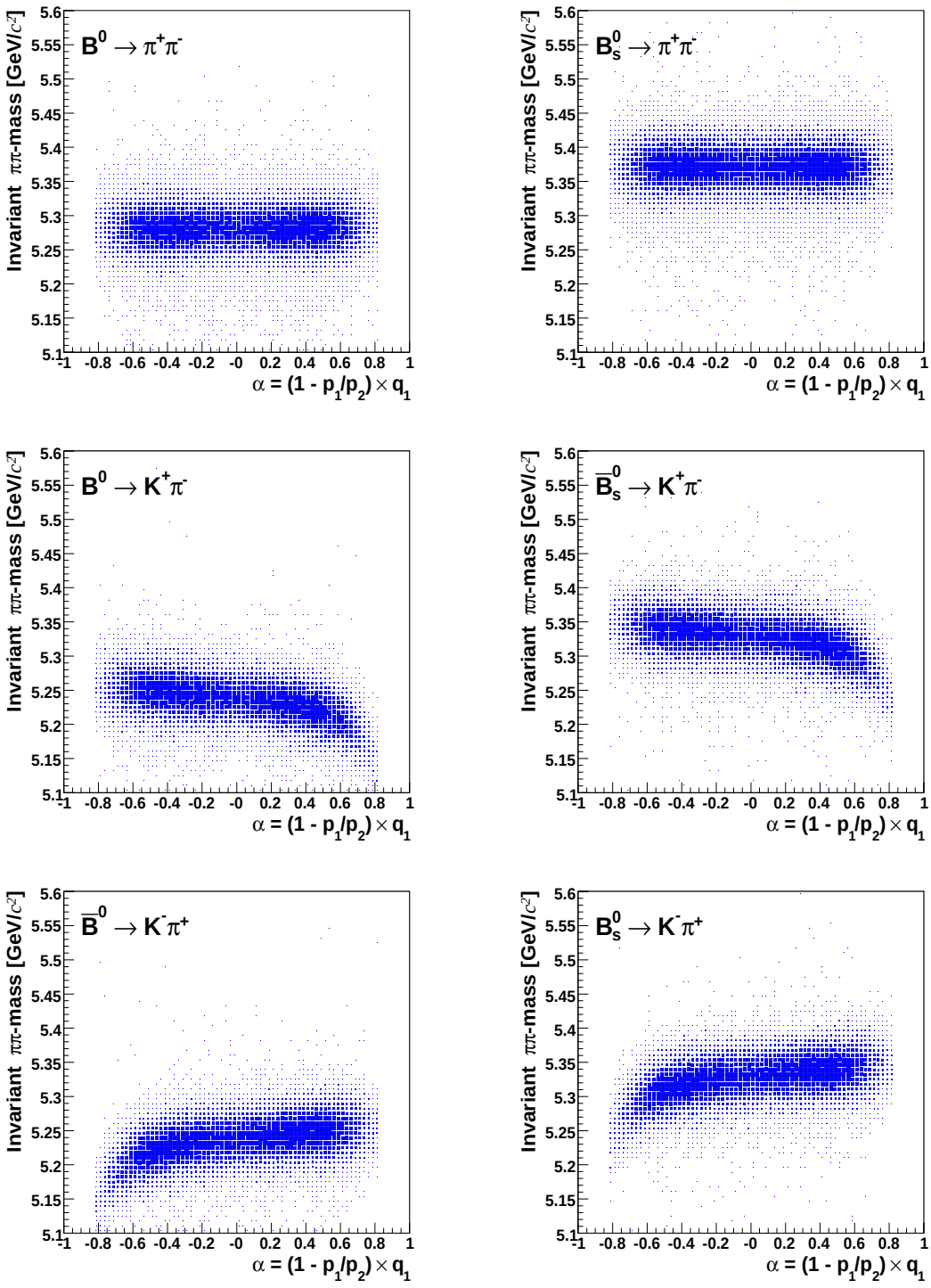


Figure 4.7: Invariant $\pi\pi$-mass of the simulated $B^0_{(s)} \to h^+h'^-$ and $\Lambda^0_b \to ph^-$ decays as a function of α.

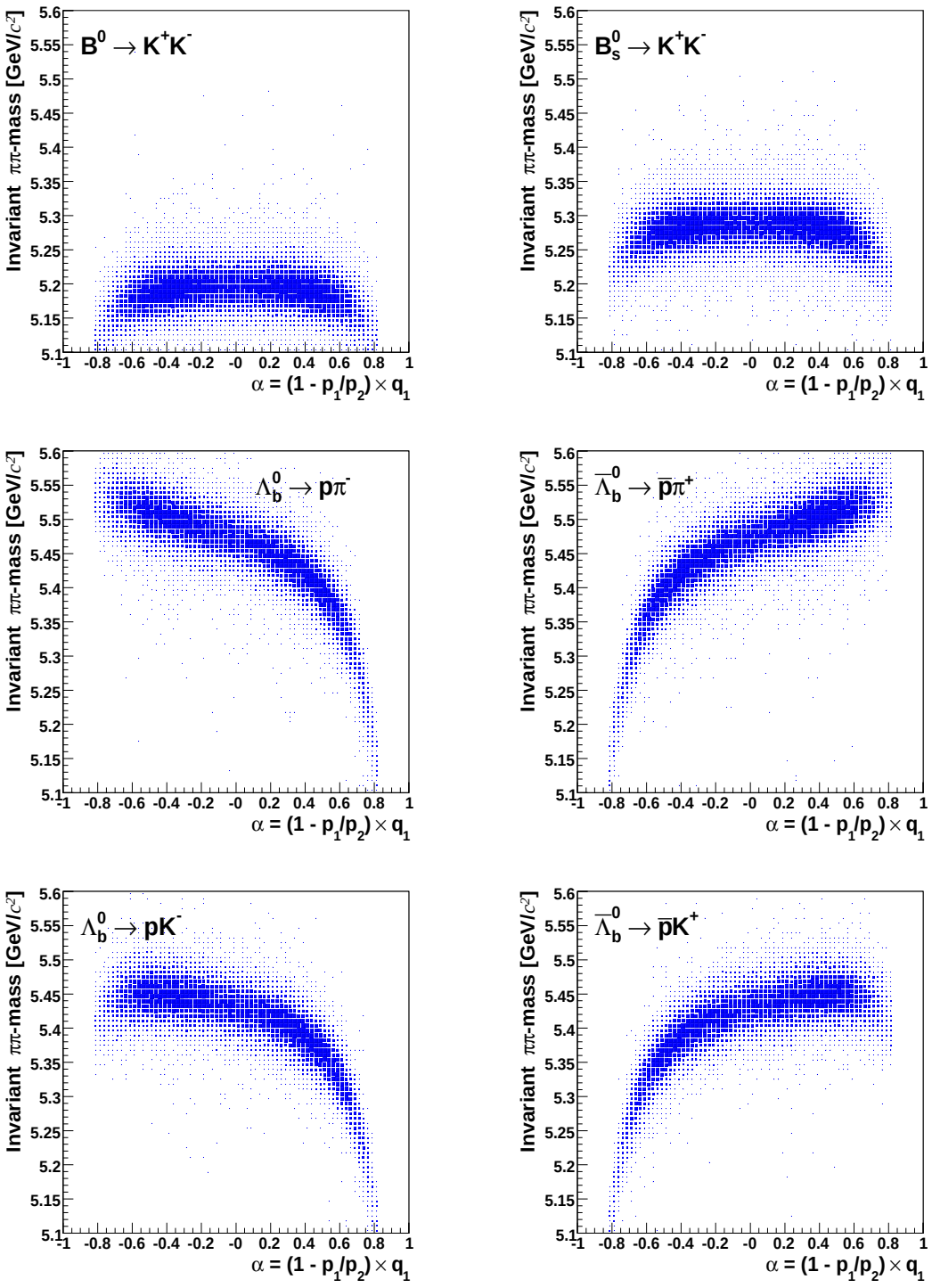


Figure 4.8: Invariant $\pi\pi$-mass of the simulated $B^0_{(s)} \to h^+h'^-$ and $\Lambda^0_b \to ph^-$ decays as a function of α.

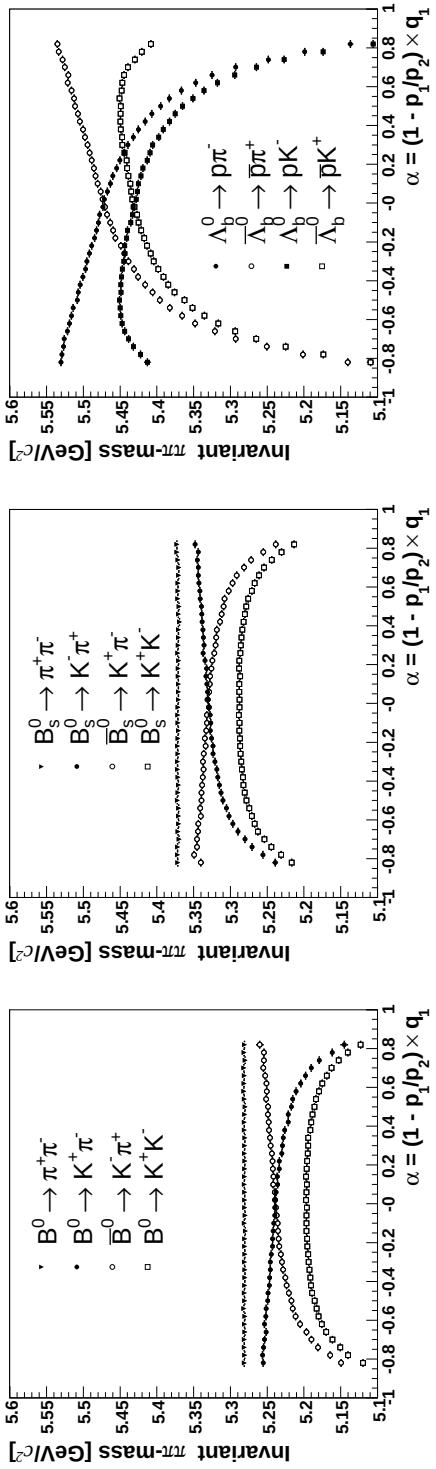


Figure 4.9: Profile plots of the invariant $\pi\pi$-mass as a function of signed momentum imbalance for all simulated signal modes.

The same features are more evident in fig. 4.9, where the distributions of figs. 4.7 and 4.8 are $m_{\pi\pi}$-averaged within each bin (profile plots) to remove the effect of mass-resolution smearing. A general feature of these plots is that slopes are enhanced at the boundaries of the α domain ($|\alpha| \approx 1$), suggesting that the kinematic separation is more effective in the decays where the momenta of the final particles are strongly unbalanced.

4.4 Particle Identification (PID)

Hadron identification is difficult at CDF II, since the detector was designed for high-p_{T} physics measurements [114]. The TOF is the only detector entirely devoted to this function, but its performance is marginal for particles with momenta greater than 2.0 GeV/c. Similarly, specific ionization from the silicon tracker is of little help, because its identification power is only effective for particles with $p_{\mathrm{T}} \lesssim 800$ MeV/c.[2] For charged particles with $p_{\mathrm{T}} \gtrsim 2$ GeV/c, a reasonably effective separation can be obtained from the rate of energy loss through ionization (dE/dx) in the gas that fills the active volume of the drift chamber.

The average total energy-loss per unit length of a particle (heavier than the electron) of charge q traversing a gas volume with velocity $c\beta$ is approximated by the Bethe-Bloch formula [115]

$$\left\langle \frac{dE}{dx} \right\rangle = \frac{4\pi N e^4}{m_e c^2 \beta^2} q^2 \left[\ln\left(\frac{2 m_e c^2 \beta^2 \gamma^2}{I} \right) - \beta^2 - \frac{\delta(\beta)}{2} \right], \tag{4.11}$$

where N is the electron density in the medium, m_e (e) is the electron mass (charge), I is the mean excitation energy of the medium atoms, and $\delta(\beta)$ is the correction that accounts for the density effect at high velocities. To a good approximation, the most probable dE/dx value of a charged particle is a function of its velocity. If the momentum of the particle is measured, the mass can also be determined. In the COT, the signal induced on each sense-wire depends on the amount of ionization charge produced by the passage of the charged particle near the wire. It is measured in nanoseconds because it is encoded as the digital pulse-width between the leading and the trailing-edge time of the hit. Multiple samplings along the trajectory of the charged particle allow a more reliable estimation of dE/dx, which has usually a broad distribution. The COT samples a maximum of 96 dE/dx measurements per track, from which a 80% truncated mean is calculated to avoid the adverse effect of long positive tails in the estimation of the average dE/dx.

The empirical equation that better models the COT average energy-loss as a function of velocity is the following variant of the Bethe-Bloch curve:

$$\left\langle \frac{dE}{dx} \right\rangle = \frac{1}{\beta^2} \left[c_1 \ln\left(\frac{\beta\gamma}{b + \beta\gamma} \right) + c_0 \right] + a_1(\beta - 1) + a_2(\beta - 1)^2 + C, \tag{4.12}$$

with a_i, b, c_j, and C parameters extracted from data. The above function has all the features that are present in the Bethe-Bloch curve (eq. (4.11)). The parameters c_0 and c_1 represent the intensities of the $1/\beta^2$ fall and of the relativistic rise. The parameter b is associated with the COT gas properties, e. g., mean excitation energy of the gas atoms, etc.. The parameters a_1 and a_2 provide a further adjustment, especially in the low $\beta\gamma$ region.

The individual charge collections output by the COT are subject to several corrections (*hit-level* corrections), applied in the off-line production (sec. 2.5), to eliminate a number of detector related conditions: hit merging, electronic pedestal subtraction, path-length correction high-voltage correction, z correction, angle and drift distance corrections, wire correction, super-layer correction, and pressure correction. An exhaustive description of these corrections can be found in [4, 116] In addition to the hit-level corrections [116] an accurate calibration of the uniformity of the dE/dx response in time

[2] A separation equivalent to the one between two equal Gaussian distributions spaced by one standard deviation apart is obtained for kaons and pions at this momentum.

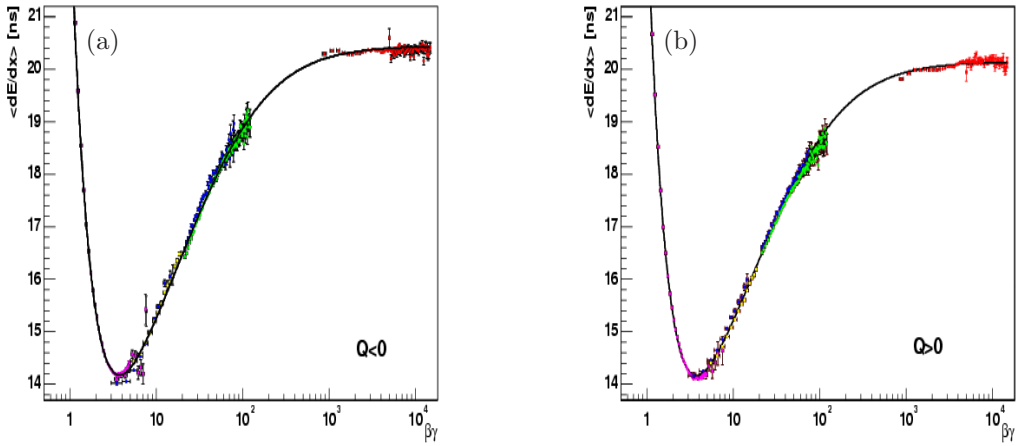


Figure 4.10: Experimental dE/dx as a function of $\beta\gamma$. The fit function eq. (4.12) is overlaid (continuous line). Negative particles (a), positive particles (b). The electrons are in red, the muons are in green, the kaons in yellow, the pions in blue and the protons in magenta.

and over the chamber volume was required. These were determined using track-oriented parameters (like φ_0, η, hit multiplicity and time) which allowed complementary corrections accounting for some "macroscopic" effects (i.e. the track length dependence). This improved the PID performance in terms of *separation power* to distinguish different classes of particles and reduced the effects due to the *correlations* between the dE/dx response of tracks. Understanding the dE/dx correlations is crucial to avoid bias in the estimate of physical observables.

The details of the calibration procedure are reported in [4], in the next sections we will describe only the relevant results: the dE/dx performance and the templates used to model the dE/dx response [119], and what we needed to change for the purpose of the present analysis.

4.4.1 dE/dx calibration samples

To perform the calibration and to parameterize the templates to model the dE/dx response of each particle, the real data were used, exploiting the rich available control samples. In order to describe correctly the signal and the background we need a model for all particle types.

pions and kaons – For pions and kaons an huge sample of $\simeq 1.5 \times 10^6$ $D^0 \to K^-\pi^+$ decays from the decay chain $D^{*+} \to D^0\pi^+ \to [K^-\pi^+]\pi^+$ was used. This sample was described in sec. 5.5 since it was used as control sample in the parameterization of the invariant mass distribution. In this context it is even more important, in fact the final states of $B^0_{(s)} \to h^+h^{'-}$ modes and of the dominant backgrounds contain charged kaons and pions, therefore this copious and pure sample is ideal for calibration and parameterization. Moreover, this sample was collected by the `B_CHARM(B_CHARM_HIGHPT)` triggers (see sec. 3.2.2), a path belonging, along with the `B_PIPI(B_PIPI_HIGHPT)` path, to the Displaced-Tracks Trigger. A large fraction of trigger re-

quirements is common to these two paths. Most trigger-dependent effects on the dE/dx of $B^0_{(s)} \to h^+h^{'-}$ final states are automatically accounted for the calibration and for the templates parameterization.

protons – A sample of $\Lambda^0 \to p\pi^-$ decays was used to calibrate the proton response. These two-body decays were reconstructed with the same prescription of the $B^0_{(s)} \to h^+h^{'-}$ decays, (see sec. 3.3) and were collected using the same `B_PIPI`(`B_PIPI_HIGHPT`) trigger path (see sec. 3.2). It is important to notice that the $\Lambda^0 \to p\pi^-$ decays are *volunteers* in the `B_PIPI`(`B_PIPI_HIGHPT`) trigger path, because one of two tracks in the final state (in most of cases the pion) does not satisfy the trigger requirements. This is due to the small energy available in the Λ^0 rest frame ($m_{\Lambda^0} - m_p - m_\pi \simeq 38$ MeV/c^2) and because of $m_{B^0} \approx 5m_{\Lambda^0}$. The trigger requirements on the transverse momentum of the particle $p_{\rm T} > 2$ GeV/c, on the scalar sum of the transverse momenta of the particles $\sum p_{\rm T} > 5.5$ GeV/c and on the invariant $\pi\pi$-mass requirement $4 < m_{\pi\pi} < 7$ GeV/c^2 suppress almost totally the signal. For these reasons, the trigger cuts confirmation was required only for the proton.

The invariant $p\pi$-mass distribution of the resulting samples selected with the requirement summarized in tab. 4.2 are shown in fig. 4.11. A simple binned χ^2-fit of the distribution to a double Gaussian function for the signal, over a straight line function for the background, provides an estimate of about 124,000 signal events. The signal is centered at about 1115.79 GeV/c^2, with about 1.19 MeV/c^2 average r.m.s. deviation, and ≈ 70 signal-to-background ratio at the peak. The kinematics allows a total separation between $\Lambda^0 \to p\pi^-$ and $\overline{\Lambda}^0 \to \overline{p}\pi^+$.

electrons and muons – We used a sample of electrons coming from γ conversions to parameterize the dE/dx templates. A small fraction of electrons in the $B^0_{(s)} \to h^+h^{'-}$ background is expected from semileptonic decays of heavy flavors. For particles with transverse momentum greater than 2 GeV/c and with the available dE/dx response the muons can be considered indistinguishable from pions. This assumption was verified complementing the sample of pions, kaons and protons with a sample of muons from a sample of $J/\psi \to \mu^+\mu^-$ decays. For this reason and since a large fraction of muons is unlikely, the background of muons and pions in this analysis will be considered as an unique background of pions.

4.4.2 dE/dx residual

The dE/dx residual (in m_A mass hypothesis) of a charged particle with momentum p and observed specific energy-loss $dE/dx_{\rm obs}$, is defined as

$$\delta_A = \frac{dE}{dx}_{\rm obs} - \frac{dE}{dx}_A, \tag{4.13}$$

where dE/dx_A is the expected dE/dx, determined from the function eq. (4.12) evaluated at $\beta\gamma = p/m_A$.

Quantity of the track	Units	Requirement
$p_{\mathrm{T}}(\mathrm{p})$	GeV/c	> 2.0
$\lvert\eta(p)\rvert$	–	< 1.0
$\lvert d_0(p)\rvert$	μm	[100, 1000]
Quantity of the candidate		
$q(p) \times q(\pi)$	e^2	-1
$d_0(p) \times d_0(\pi)$	$\mu\mathrm{m}^2$	< 0
$\mathrm{corr}((d_0(p), d_0(\pi)))$	μm	< 51
L_{T}	cm	> 0.85
$\sum p_{\mathrm{T}}$	GeV/c	> 1.1
$\lvert d_0\rvert$	μm	< 70
$\lvert z_0(p) - z_0(\pi)\rvert$	cm	< 2
χ^2_{T}	–	< 10
$m_{\pi\pi}$	GeV/c^2	[0.1, 1.5]

Table 4.2: Summary of the off-line selection used to reconstruct the $\Lambda^0 \to p\pi^-$ decays. $\mathrm{corr}((d_0(p), d_0(\pi)))$ is a variable related to the correlation between the proton and the pion impact parameters. It selects a region in the two-dimensional space $((d_0(p), d_0(\pi)))$, for more details see [119, 120].

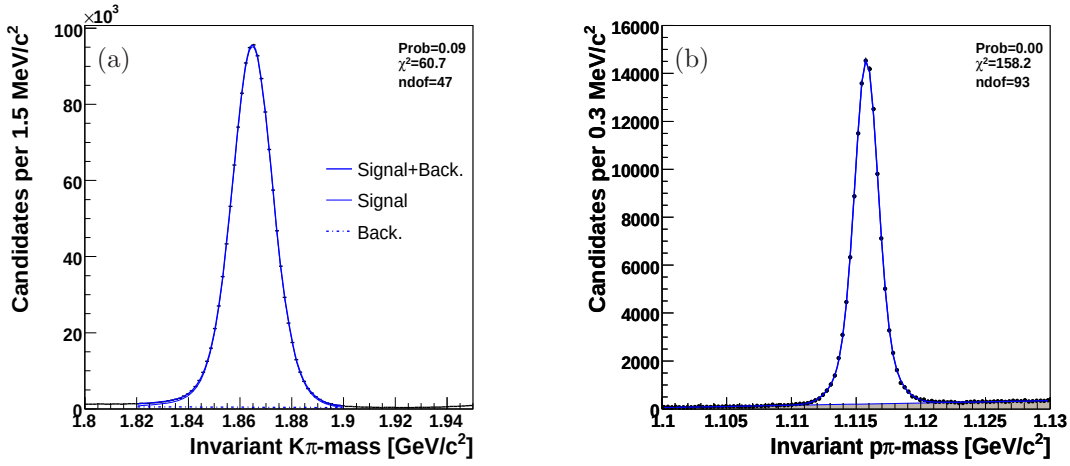


Figure 4.11: Invariant $K\pi$-mass of the $D^0 \to K^-\pi^+$ reconstructed from $D^{*+} \to D^0\pi^+ \to [K^-\pi^+]\pi^+$ decays passing the selection summarized in tab. 5.4 (a). Invariant $p\pi$-mass for the $\Lambda^0 \to p\pi^-$ decays passing the selection summarized in tab. 4.2 (b).

4.4.3 Separation power

Given a PID-related observable, (the dE/dx residual, for instance) the identification performance relies on the difference in the distributions of the chosen observable between the classes of events to be

identified. Such difference is generally expressed in terms of a *separation* between those distributions. The achieved separation power depends on the variable used to measure it, and a wise choice of the variable (or set of variables) may enhance the actual separation. To find the optimal variable, we checked a few combinations of observed dE/dx, expected dE/dx, and dE/dx resolutions. We chose to use dE/dx residuals with pion mass hypothesis, δ_π, since no significant enhancements in separation were found by using other variables.

We evaluated the separation using the sample of kaons and pions from candidates with mass within $\pm 2\sigma$ from the nominal D^0 mass. Following the approach described in Ref. [121], the resulting

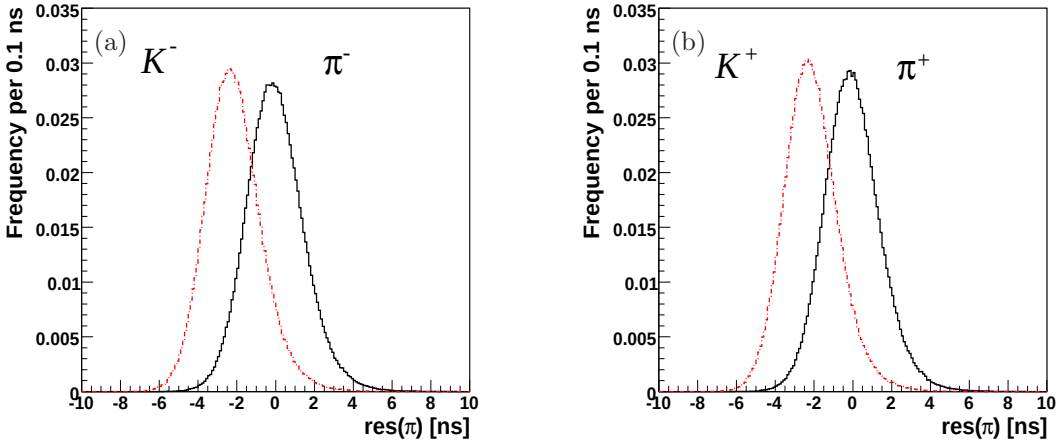


Figure 4.12: Distribution of dE/dx around the average pion response for negatively (a) and positively-charged (b) particles. Pions (continuous black line) and kaons (dashed red line) from $D^0 \to K^-\pi^+$ decays.

separation between pions and kaons from the $D^0 \to K^-\pi^+$ decays is 1.53σ for positively-charged particles, and 1.50σ for negatively-charged particles, approximately constant in the momentum range of interest $2 \lesssim p \lesssim 20$ GeV/c. Since the separation power depends on the specific proportions among classes of events present in the sample, the above values hold only for samples with approximately equal contributions from pions and kaons.

4.4.4 Correlations

Figure 4.13 shows the distribution of the residual for kaons (with kaon hypothesis) as a function of the residual for pions (with pion hypothesis) and the same two-dimensional distribution of the residual for protons (with proton hypothesis) as a function of the residual for pions (with pions hypothesis). A non-zero, positive correlation is visible from the shape of the distributions, corresponding to a correlation coefficient $\rho \simeq 6.6\%$ for kaons and pions from $D^0 \to K^-\pi^+$ decays and $\rho \simeq 7.9\%$ for

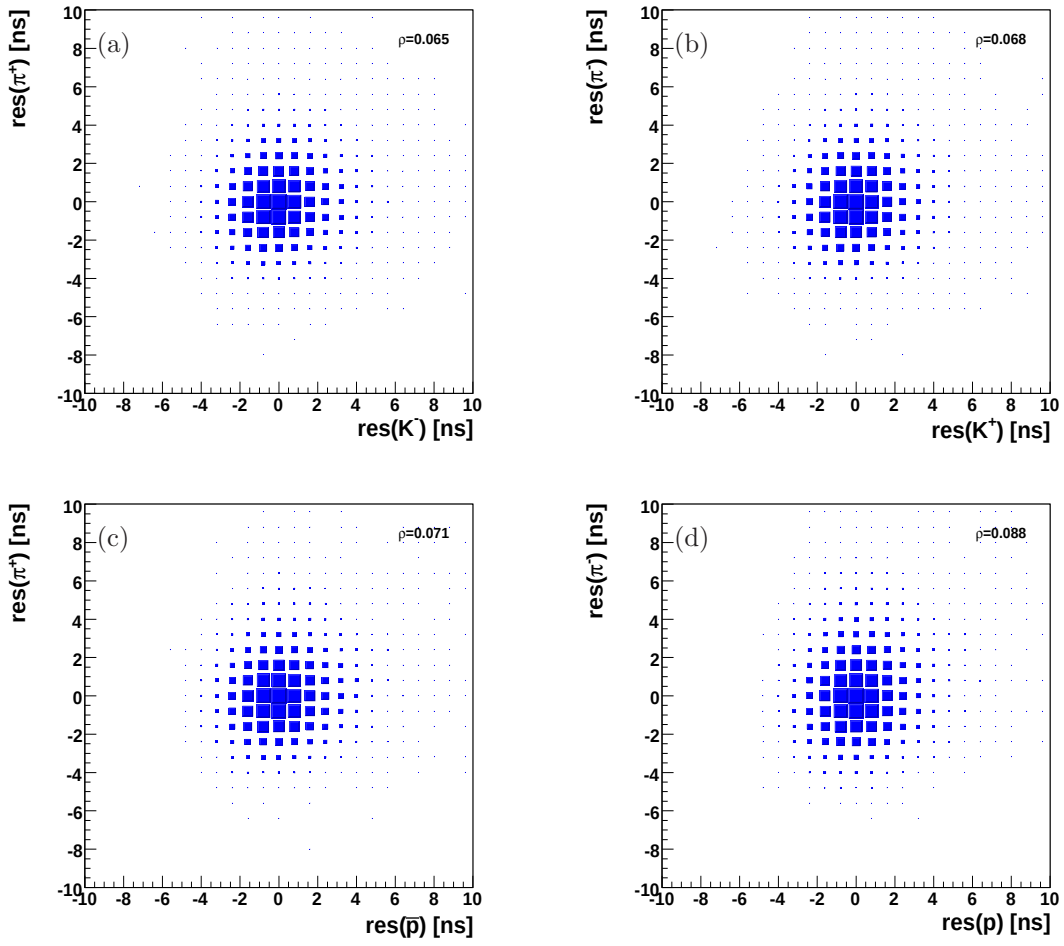


Figure 4.13: Residual for pions (with pion hypothesis) as a function of the residual for kaons (with kaon hypothesis) (a,b). Residual for pions (with pion hypothesis) as a function of the residual for protons (with proton hypothesis) (c,d).

protons and pions from $\Lambda^0 \to p\pi^-$ decays.[3] This correlation is dangerous for the present analysis. While a small separation power only degrades the statistical uncertainty on the relative fractions of the different signal modes, a large correlation strongly biases the central values. Therefore this effect was carefully studied and parameterized.

With an ideal PID detector, no correlation is expected between independent measurements. A non-vanishing correlation indicates the presence of residual dE/dx gain variations from event to event. An uncorrected gain variation would induce a correlation between the observed ionizations of distinct particles, through the inevitable correlations present in the calibration sample. The sources of correlation

[3]The correlation coefficient in this case is $\rho = \frac{E[\delta_\pi \times \delta_{K(p)}] - E[\delta_\pi] \times E[\delta_{K(p)}]}{\sigma_{\delta_\pi} \times \sigma_{\delta_{K(p)}}}$, in which $E[x]$ indicates the expected value of x, and σ are sample standard-deviations.

can be divided into two groupes:

Global effects – these are all the effects unrelated to the kinematics. Suppose the dE/dx shows gain variations as a function of the instantaneous luminosity: $\frac{dE}{dx} = \frac{dE}{dx}(\beta\gamma, \mathcal{L})$. Then, since the kaon and the pion from a D^0 decay are reconstructed in the same event (e. g., in the same conditions of luminosity), their observed dE/dx would appear correlated by the common dependence on luminosity. This may apply to a variety of global variables, such as time, pressure or temperature of the gas, and so forth.

Local effects – these are all effects related to kinematics. Suppose that the dE/dx shows gain variations as a function of the azimuthal angle of emission of the particle: $\frac{dE}{dx} = \frac{dE}{dx}(\beta\gamma, \varphi_0)$. Then, since the azimuthal angle of a kaon and a pion from a D^0 decay are correlated by the kinematic of the decay and by the selection cuts, their observed dE/dx would become correlated. This may apply to a variety of local variables, such as η, z_0, hit multiplicity, etc.

We investigated the combined effect of all possible residual gain variations by allowing for a generic, time-dependent common-mode fluctuation $c(t)$ that affects and correlates the observed dE/dx values of the tracks in the event. In particular, we extracted the variance (σ_c^2) of the distribution of the common mode, as an estimator of the size of the correlation. We denote the probability distribution of the dE/dx residual for pions (with pion mass-hypothesis) as $\wp_\pi(\delta_\pi)$, with standard deviation σ_π. A similar notation is used for kaons. If δ_π and δ_K were independent variables, the probability distribution of their sum $(\delta_K + \delta_\pi)$ would satisfy

$$\wp(\delta_\pi + \delta_K) = \wp_\pi(\delta_\pi) * \wp_K(\delta_K), \tag{4.14}$$

in which the symbol $*$ indicates the Fourier convolution product.[4] Similarly, their difference $\delta_\pi - \delta_K$ would be distributed as

$$\wp(\delta_\pi - \delta_K) = \wp_\pi(\delta_\pi) * \wp_{-K}(-\delta_K), \tag{4.15}$$

where $\wp_{-K}(-\delta_K)$ is the distribution of the negative residual for kaons ($\frac{dE}{dx}_K - \frac{dE}{dx}_{\rm obs}$), whose variance satisfies the condition $\sigma_K^2 = \sigma_{-K}^2$. Since the variance of a convolution product is the sum of variances of the convoluted distributions, the standard deviations of the distributions of sum and difference are equal:

$$\sigma_{\pi+K} = \sigma_{\pi-K} = \sqrt{\sigma_\pi^2 + \sigma_K^2}. \tag{4.16}$$

On the other hand, if the two residuals are correlated by a common-mode fluctuation, the observed residual ($\delta^{\rm obs}$) is written as the sum of the intrinsic, uncorrelated residual with the common-mode shift:

$$\delta_\pi^{\rm obs} = \delta_\pi + c \quad \text{and} \quad \delta_K^{\rm obs} = \delta_K + c. \tag{4.17}$$

Therefore, the sum of the observed residuals, $\delta_\pi^{\rm obs} + \delta_K^{\rm obs} = \delta_\pi + \delta_K + 2c$, is distributed as

$$\wp(\delta_\pi^{\rm obs} + \delta_K^{\rm obs}) = \wp_\pi(\delta_\pi) * \wp_K(\delta_K) * \wp_c(2c), \tag{4.18}$$

whereas their difference, $\delta_\pi^{\rm obs} - \delta_K^{\rm obs} = \delta_\pi + c - \delta_K - c = \delta_\pi - \delta_K$, is distributed as

$$\wp(\delta_\pi^{\rm obs} - \delta_K^{\rm obs}) = \wp_\pi(\delta_\pi) * \wp_{-K}(-\delta_K). \tag{4.19}$$

[4] Henceforth, "convolution" always denote the Fourier convolution product.

Equations (4.18) and (4.19) show that, in presence of a common mode, the sum of residuals has greater variance than their difference, $\sigma^2_{\pi+K} > \sigma^2_{K-\pi}$. The standard deviation of the correlation is easily obtained:

$$\sigma_c = \frac{1}{2}\sqrt{\sigma^2_{\pi+K} - \sigma^2_{\pi-K}}. \tag{4.20}$$

Following eq. (4.20), we used the distributions of sum and difference of the observed residual to estimate the magnitude of time-dependent common modes. For $\Lambda^0 \to p\pi^-$ decays, the standard deviation of the time-dependent common-mode is:

$$\sigma_c = \frac{1}{2}\sqrt{\sigma^2_{\pi+p} - \sigma^2_{\pi-p}}. \tag{4.21}$$

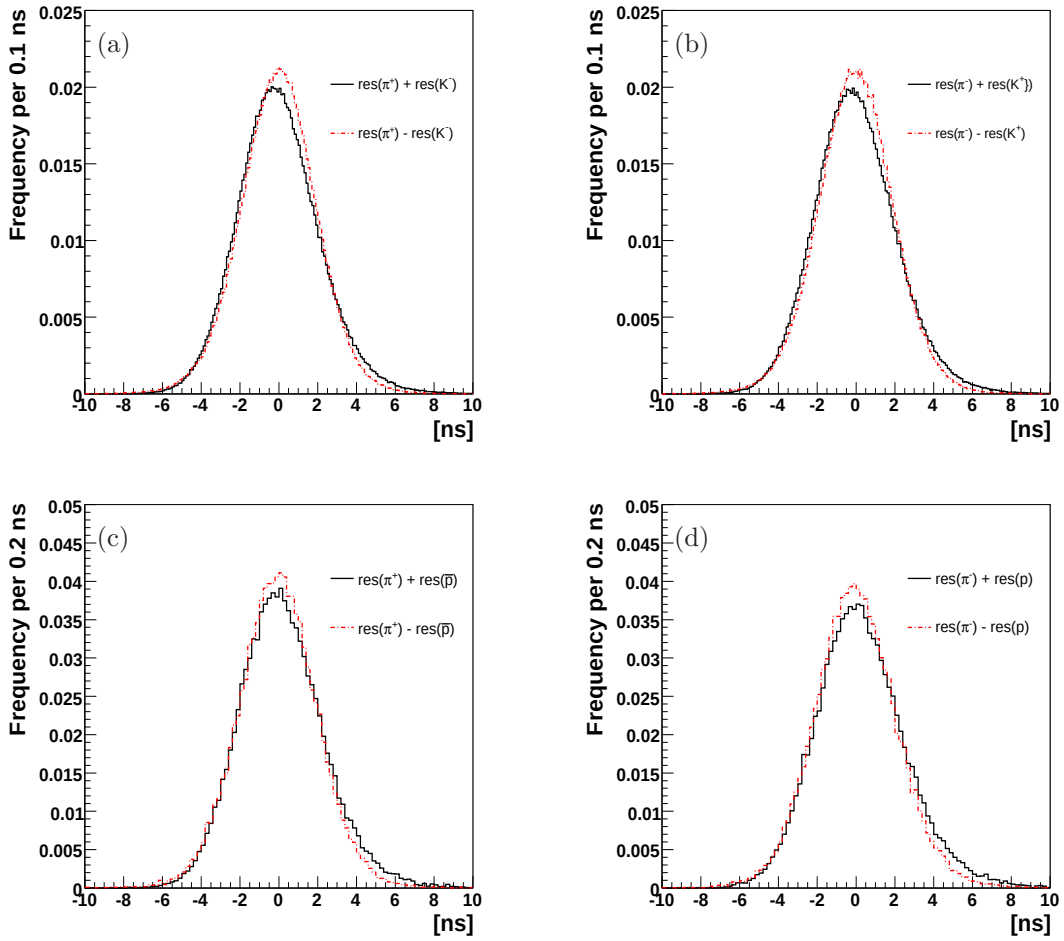


Figure 4.14: Distribution of the sum (black continuous line) and difference (red dashed line) of residuals for a kaon (in kaon hypothesis) and a pion (in pion hypothesis) from a D^0 decay.

4.4.5 Model of the dE/dx distributions

Using the dE/dx information in a Likelihood fit requires modeling the distributions of the desired observables. It is convenient to stress the difference between *observed* dE/dx quantities, i. e., those affected by common-mode fluctuations, and *intrinsic* quantities, the quantities which would have been observed if the correlations were not present. Since the intrinsic residuals and the correlation are, by construction, independent variables (see eq. (4.17)), the (known) distribution of the observed residuals is the convolution of their unknown distributions:

$$\wp(\delta^{\rm obs}) = \wp(\delta + c) = \wp(\delta) * \wp(c). \tag{4.22}$$

The model of the intrinsic residuals, $\wp(\delta)$, and of the correlations, $\wp(c)$, were extracted from the distributions of the observed residuals, $\wp(\delta^{\rm obs})$, of pions and kaons from D^0 decays. We expanded each term of the right-hand side of eq. (4.22) in sum of Gaussian distributions, and we fit the distributions of the observed residuals to extract the unknown parameters. In practice, the first three terms of the expansion were sufficient to model accurately the intrinsic residuals and correlations:

$$\wp_K(\delta_K) = q' \cdot \mathscr{G}_{K'}(\delta_K) + q'' \cdot \mathscr{G}_{K''}(\delta_K) + (1 - q' - q'') \cdot \mathscr{G}_{K'''}(\delta_K) \tag{4.23}$$

$$\wp_\pi(\delta_\pi) = p' \cdot \mathscr{G}_{\pi''}(\delta_\pi) + p'' \cdot \mathscr{G}_{\pi''}(\delta_\pi) + (1 - p' - p'') \cdot \mathscr{G}_{\pi'''}(\delta_\pi) \tag{4.24}$$

$$\wp_c(c) = r \cdot \mathscr{G}_{c'}(c) + (1 - r) \cdot \mathscr{G}_{c''}(c) \tag{4.25}$$

where we used the following notation for the Gaussian distribution:

$$\mathscr{G}_s(x) = \mathscr{G}(x; \mu_s, \sigma_s) = \frac{1}{\sigma_s\sqrt{2\pi}} e^{-\frac{(x-\mu_s)^2}{2\sigma_s^2}}.$$

Independent parameterizations were assumed for the distributions of intrinsic residuals for positively and negatively-charged particles. Mean (μ), variance (σ^2) and fraction of each Gaussian were determined with a simultaneous, binned ML fit of the following combinations of observed residuals:

$$\wp_K(\delta_K^{\rm obs}) = \wp(\delta_K) * \wp(c) = (\mathscr{G}_{K'} + \mathscr{G}_{K''} + \mathscr{G}_{K'''}) * (\mathscr{G}_{c'} + \mathscr{G}_{c''}) \tag{4.26}$$

$$\wp_\pi(\delta_\pi^{\rm obs}) = \wp(\delta_\pi) * \wp(c) = (\mathscr{G}_{\pi'} + \mathscr{G}_{\pi''} + \mathscr{G}_{\pi'''}) * (\mathscr{G}_{c'} + \mathscr{G}_{c''}) \tag{4.27}$$

$$\wp(\delta_\pi^{\rm obs} + \delta_K^{\rm obs}) = (\mathscr{G}_{\pi'} + \mathscr{G}_{\pi''} + \mathscr{G}_{\pi'''}) * (\mathscr{G}_{K'} + \mathscr{G}_{K''} + \mathscr{G}_{K'''}) * (\mathscr{G}_{2c'} + \mathscr{G}_{2c''}) \tag{4.28}$$

$$\wp(\delta_\pi^{\rm obs} - \delta_K^{\rm obs}) = (\mathscr{G}_{\pi'} + \mathscr{G}_{\pi''} + \mathscr{G}_{\pi'''}) * (\mathscr{G}_{-K'} + \mathscr{G}_{-K''} + \mathscr{G}_{-K'''}), \tag{4.29}$$

where the relative normalization factors (p, q, r) were included in the fit, but omitted above for a clearer notation. If in the equations above (eqs. (4.23)–(4.29)) we replace the kaon index (K) with the proton index (p) we obtain the equivalent relations to model the probability density functions of protons and pions from $\Lambda^0 \to p\pi^-$ decay. In this case we parameterized a different correlation function with respect to the $D^0 \to K^-\pi^+$ case since we used a different sample.

The technique used to extract the parameters of the dE/dx templates, of the intrinsic residuals and correlation, is based on an iterative method of one-dimensional binned fits of the distributions of $\delta_\pi^{\rm obs}$, $\delta_K^{\rm obs}$, $\delta_\pi^{\rm obs} + \delta_K^{\rm obs}$ and $\delta_\pi^{\rm obs} - \delta_K^{\rm obs}$. The details of the parameterization can be found in [117, 118, 4, 119].

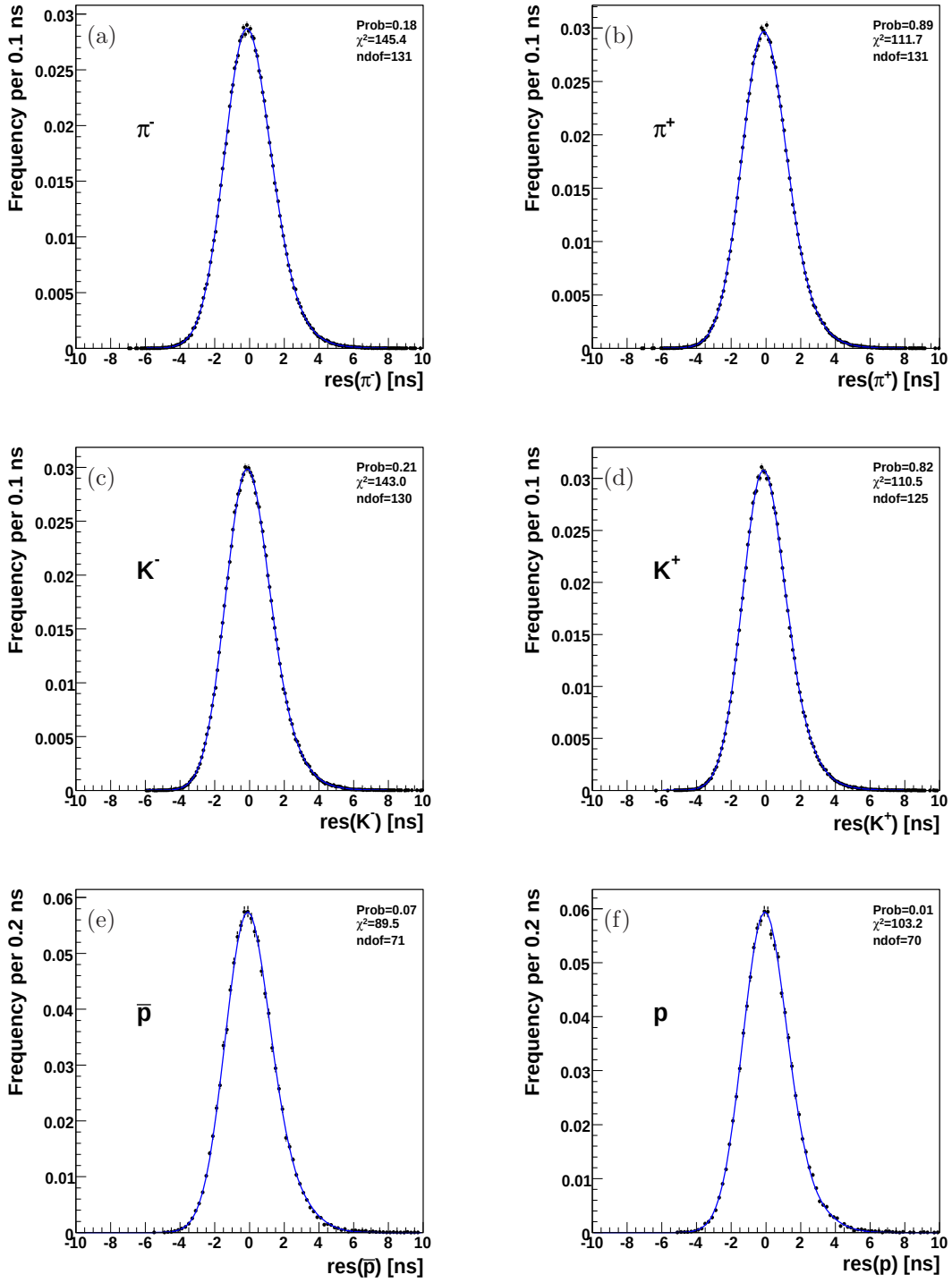


Figure 4.15: Distribution of observed dE/dx residual ($\wp(\delta^{\text{obs}}) = \wp(\delta + c) = \wp(\delta) * \wp(c)$), for pions (with pion mass hypothesis) (a,b), for kaons (with kaon mass hypothesis) (c,d) and for protons (with proton mass hypothesis) (e,f). The results of the fit to the functions in eq. (4.27) and eq. (4.26) are overlaid (blue, solid line).

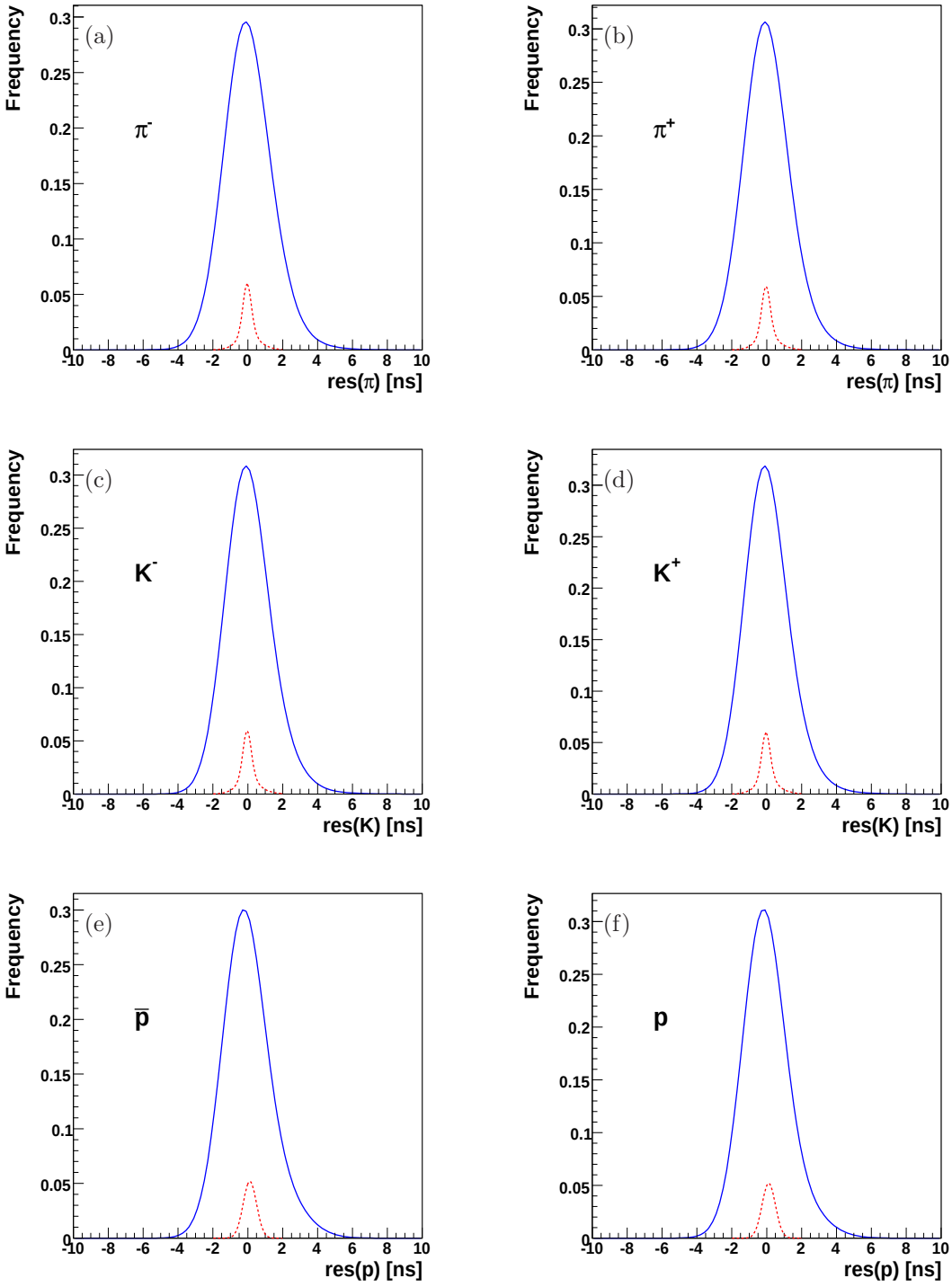


Figure 4.16: dE/dx probability density for the intrinsic residuals $\wp(\delta)$ (blue solid line) and the correlation $\wp(c)$ (dashed red line) for pions (with pion mass hypothesis) (a,b), for kaons (with kaon mass hypothesis) (c,d) and for protons (with proton mass hypothesis) (e,f). In the illustration $\wp(\delta)$ is correctly normalized to 1, while $\wp(c)$ is normalized to 1/20.

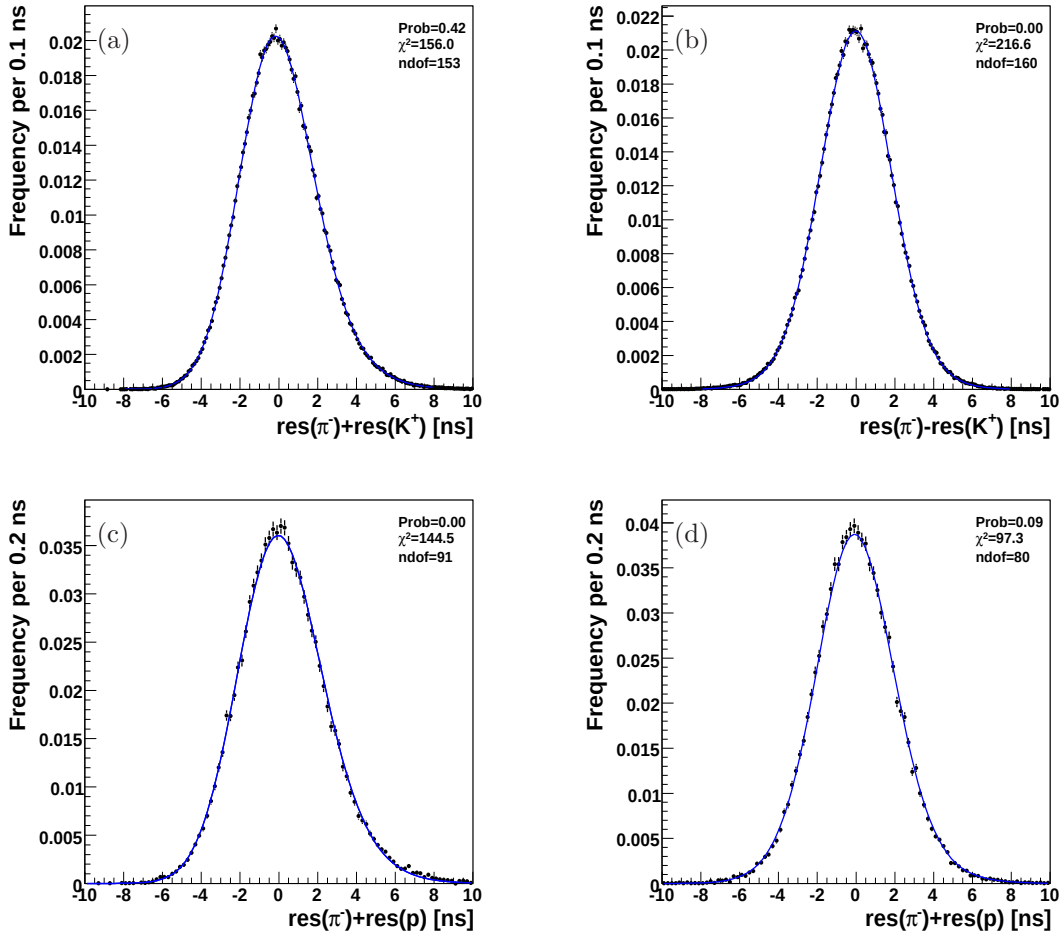


Figure 4.17: Distribution of the sum (a,b) and the difference (b,d) of the residuals for a kaon (in kaon hypothesis) and a pion (in pion hypothesis) from $D^0 \to K^-\pi^+$ decay and of residuals for a proton (in proton hypothesis) and a pion (in pion hypothesis) from $\Lambda^0 \to p\pi^-$ decay. The results of the fit to the functions in eq. (4.28) and eq. (4.29) are overlaid (blue, solid line).

Figures 4.15 and 4.17 show a satisfactory agreement between the chosen model and the distributions of the observed residuals and correlations. Although we allowed for independent residual distributions for kaons, pions and protons (negative and positive particles) the extracted shapes are similar, all showing non-Gaussian positive tails. The differences between the residuals of positively and negatively-charged particles are tiny. These small differences between kaons and pions and between positively and negatively-charged particles have been ascribed to a systematic dependence of the dE/dx response on track curvature, caused by the geometric and electrostatic asymmetry of the COT drift-cells. For a given Lorentz boost, the trajectories of charged particles with different masses or charge have different curvatures, and are sensitive to the systematic effects in the efficiency of charge-collection of the COT sense-wires.

Figure 4.16 shows the extracted probability density functions for the intrinsic residuals and for correlation. We extracted two models for the correlation function: one from the $D^0 \to K^-\pi^+$ sample and the other one from the $\Lambda^0 \to p\pi^-$ sample. Both models show a non negligible correlation, as expected from the distributions of the sum and the difference of the residuals. These correlation functions show small differences. The correlation function extracted from pions and kaons from $D^0 \to K^-\pi^+$ decays has a tighter RMS than the correlation extracted from protons and pions from $\Lambda^0 \to p\pi^-$ decays. The core of the distribution is centered at zero for $D^0 \to K^-\pi^+$ decays, while it is shifted by ≈ 0.06 ns for $\Lambda^0 \to p\pi^-$ decays (see fig. 4.18).

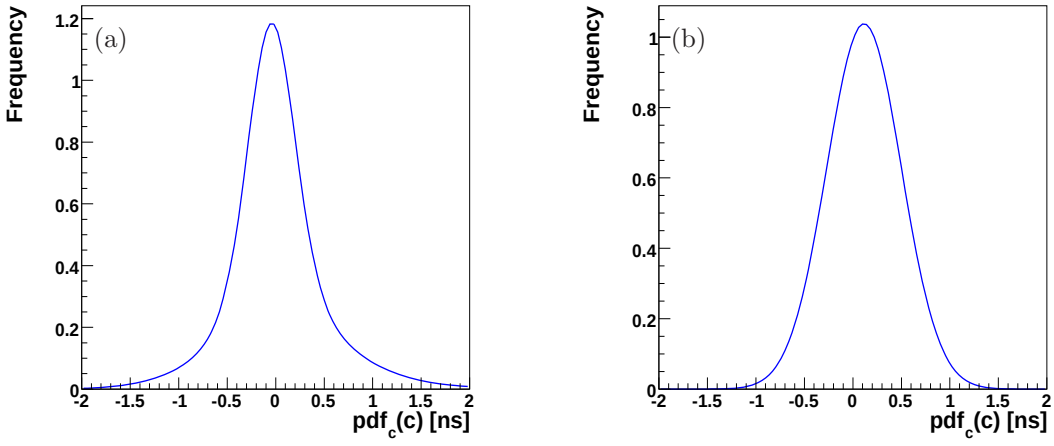


Figure 4.18: Correlation probability density functions for pions and kaons from $D^0 \to K^-\pi^+$ decays (a), for pions and protons from $\Lambda^0 \to p\pi^-$ decays (b).

4.4.6 Sample dependence of correlation

The correlation was introduced in the previous section by allowing a generic, time-dependent common-mode fluctuation that affects and correlates the dE/dx values in the event. We saw that the correlation can originate from either "global effects" and "local effects" (see sec. 4.4.4). We want point out that the correlation shape depends on the sample used to extract its parameterization, while the intrinsic residuals are independent of the sample.

We know that the correlation can be sample dependent, because it is due to the local effects related to the kinematics of the process (for example the azimuthal opening angle ($\Delta\varphi_0$) distribution is different for the $B^0_{(s)} \to h^+h'^-$, $D^0 \to K^-\pi^+$and $\Lambda^0 \to p\pi^-$ decays), but the gain variations of the dE/dx response due to the kinematics differences are reduced greatly by the track-based corrections and then we expect very small differences due to the different kinematics of the processes.

It is important to notice that the correlation shape is different if we consider two or more sub-samples of the same kinematic process. This is due to the fact that the correlation is the parameterization of a time-dependent common-mode fluctuation and it is extracted by averaging over the whole

data sample, in our case the $D^0 \to K^-\pi^+$ and $\Lambda^0 \to p\pi^-$ decays in 1 fb^{-1} of integrated luminosity. For this reason if we take two different samples, for example the $D^0 \to K^-\pi^+$ decays and the $B^0_{(s)} \to h^+h^{'-}$ decays in 1 fb^{-1} of integrated luminosity, and if we assume that the correlation due to the different kinematics is negligible, we expect to find the same correlation only if the efficiency ratio of data collection for two samples is a constant over time. Although the calibration sample ($D^0 \to K^-\pi^+$ decays) used to calibrate and to model the dE/dx response of pions and kaons and the $B^0_{(s)} \to h^+h^{'-}$ decays was collected using two very similar configuration of the Displaced-Tracks Trigger (see sec. 3.2), `B_CHARM` (`B_CHARM_HIGHPT`) for $D^0 \to K^-\pi^+$ and `B_PIPI` (`B_PIPI_HIGHPT`) for $B^0_{(s)} \to h^+h^{'-}$ decays, the efficiency ratio is not perfectly constant during the time.

The entire procedure to extract the dE/dx probability density functions is finalized to parameterize the intrinsic residuals for pions, kaons and protons and the probability density functions of the correlation in the different calibration samples. Since the correlation shape has some small but non-negligible variations due to the sample dependence while the intrinsic residuals is independent of the sample, in the fit of composition (see chap. 6) to separate the individual channels we will use the $\wp$ of the intrinsic residuals while we will fit the correlation shape to be insensitive to these sample variations.

4.4.7 PID observable: kaonness

Particle identification information was summarized in a single observable for each charged particle, the "kaonness" κ, defined as

$$\kappa = \frac{dE/dx_{\text{obs}} - dE/dx_{\pi}}{dE/dx_{K} - dE/dx_{\pi}}. \tag{4.30}$$

The average of this quantity is, by construction, zero for pions and one for kaons, with almost momentum-independent distribution for both types of particles (see fig. 4.19). This is particularly convenient in our case, since all $B^0_{(s)} \to h^+h^{'-}$ modes have only pions and kaons in their final states, and also the background composition is expected to be dominated by these particles.

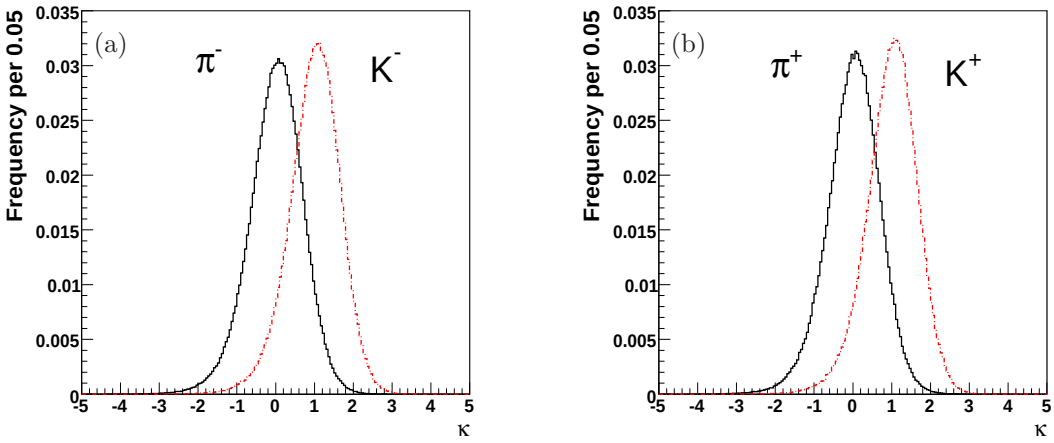


Figure 4.19: The kaonness κ for pion and kaons from $D^0 \to K^-\pi^+$ decays reconstructed from $D^{*+} \to D^0\pi^+ \to [K^-\pi^+]\pi^+$ decays. Negative particles (a), positive particles (b).

To appreciate the separation power of the dE/dx response among the signal modes we simulated the $B^0_{(s)} \to h^+h^{'-}$ and $\Lambda^0_b \to ph^-$ decays in agreement with the dE/dx p.d.f. extracted in the previous section and the momenta distributions extracted from the Monte Carlo for both particles. Following the same notation of sec. 4.3 where we labeled the outgoing particles according to increasing momenta, index "1" labels the charge (q_1), mass (m_1), momentum ($\vec{p}_1$) and kaonness (κ_1) of the lower momentum particle in the decay, index "2" labels the corresponding quantities of the higher momentum particle, we can look at the two-dimensional probability density function $\wp(\kappa_1, \kappa_2)$. According with charge-kinematics flavor tagging (see tab. 4.1) we divided the decays in two categories: $\alpha > 0$ (namely $q_1 > 0$) and $\alpha < 0$ (namely $q_1 < 0$). Figures 4.20 and 4.21 show the probability density function $\wp(\kappa_1, \kappa_2)$ for the $B^0_{(s)} \to h^+h^{'-}$ and $\Lambda^0_b \to ph^-$ decays in the space $\alpha > 0$. To obtain the equivalent distribution for $\alpha < 0$ it is sufficient to invert $\kappa_1 \leftrightarrow \kappa_2$.

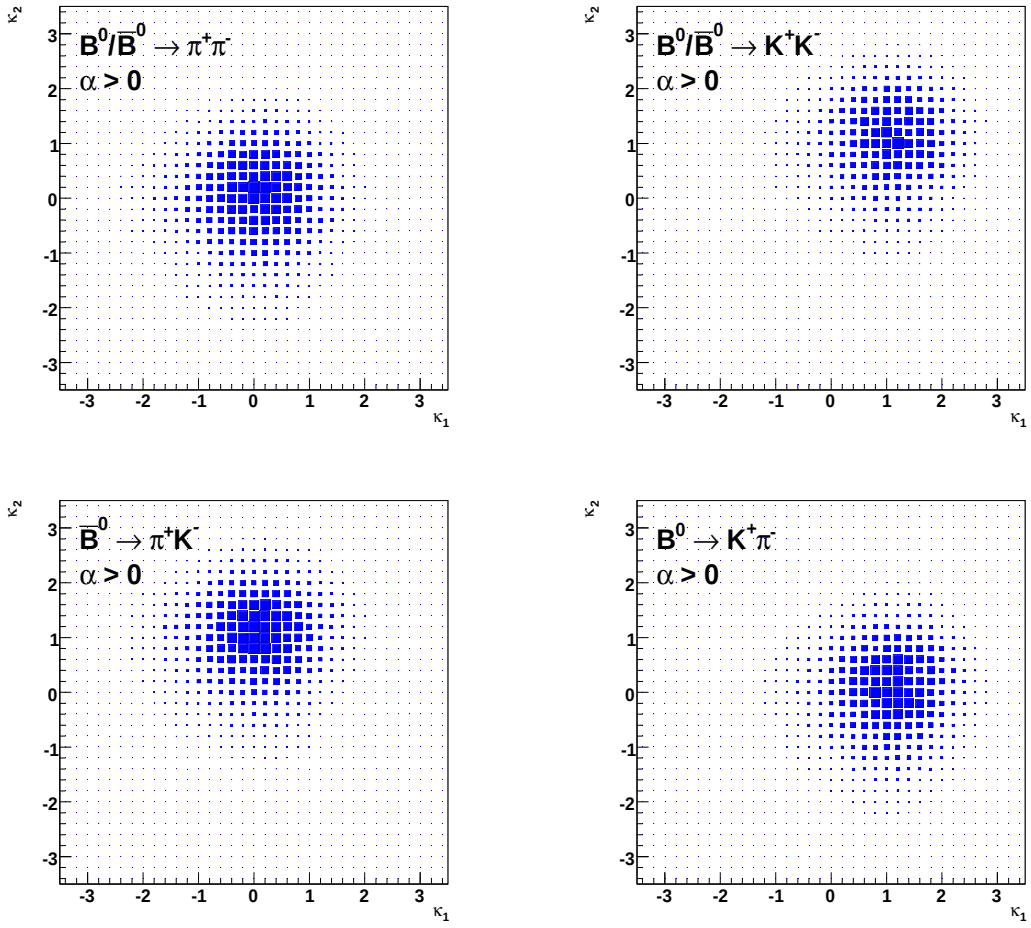


Figure 4.20: Probability density function $\wp(\kappa_1, \kappa_2)$ for the $B^0 \to h^+h^{'-}$ decays in the space $\alpha > 0$. To obtain the equivalent distribution for $\alpha < 0$ it is sufficient to invert $\kappa_1 \leftrightarrow \kappa_2$. Similar probability density functions are obtained for B^0_s meson meson decys.

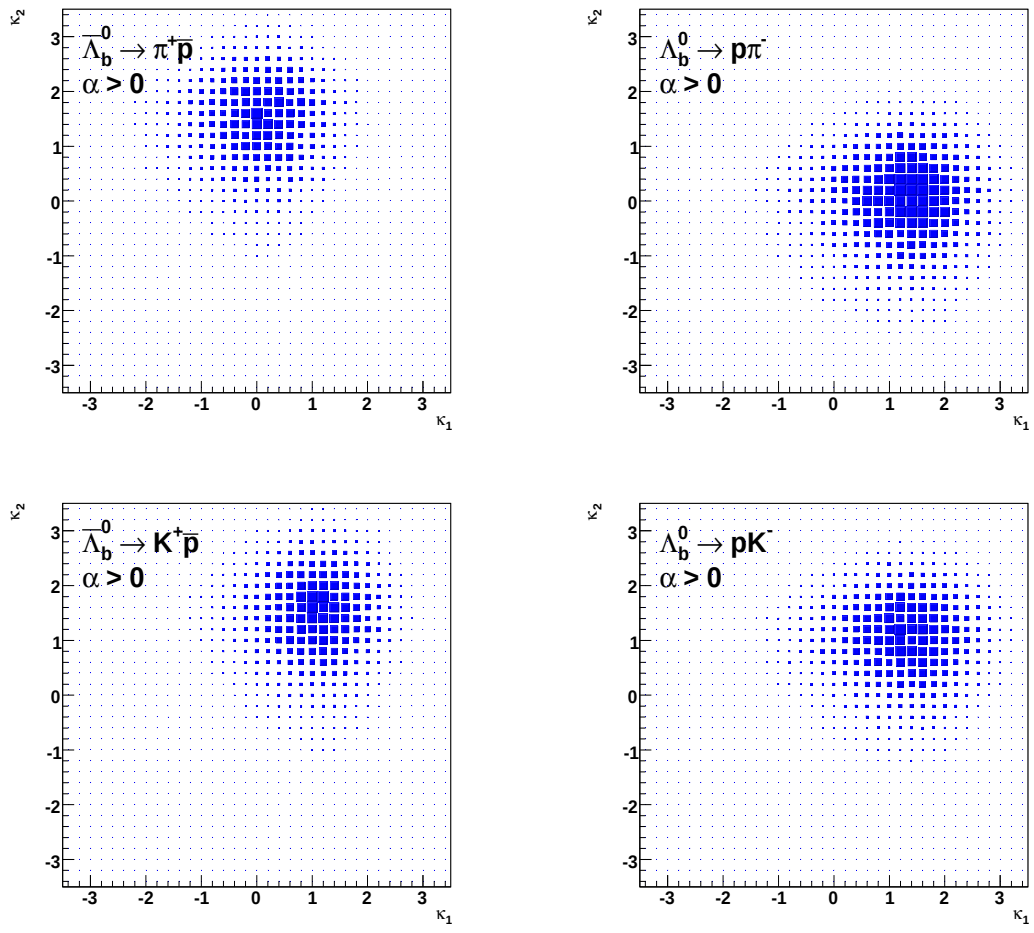


Figure 4.21: Probability density function $\wp(\kappa_1, \kappa_2)$ for the $\Lambda_b^0 \to ph^-$ decays in the space $\alpha > 0$. To obtain the equivalent distribution for $\alpha < 0$ it is sufficient to invert $\kappa_1 \leftrightarrow \kappa_2$.

The effective separation among final states consisting in particle pairs, like in our case (between $\pi^+\pi^-$ and K^+K^-, between π^+K^- and $K^+\pi-$) corresponds to $1.5\sigma \cdot \sqrt{2} \simeq 2.1\sigma$. This achievement is important. In particular if we consider that the kinematics and the dE/dx are perfectly complementary and they allow a very good separation among the individual modes. For example the kinematic separation power between the $B^0 \to \pi^+\pi^-$ and $B^0_s \to K^+K^-$ modes is almost null (see figs. 4.7 and 4.8), while the dE/dx power separation is maximum , about 2σ (see fig. 4.22). In the chap. 6 we will

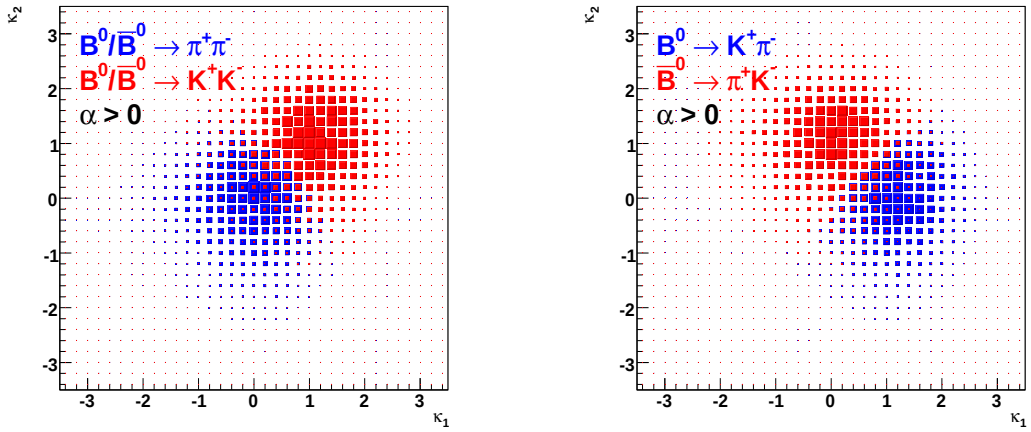


Figure 4.22: Probability density function $\wp(\kappa_1, \kappa_2)$ for the $B^0_{(s)} \to h^+h^{'-}$ decays in the space $\alpha > 0$. To obtain the equivalent distribution for $\alpha < 0$ it is sufficient to invert $\kappa_1 \leftrightarrow \kappa_2$.

describe the fit of composition: all the available information from kinematic and PID observables will be condensed in a Likelihood function to exploit the global separation power between each modes. Before describing the fit of composition, in chap. 5 we will discuss a crucial ingredient to disentangle the different decay modes: the invariant mass line shape.

Chapter 5

Mass templates

This chapter is devoted to the accurate determination of the invariant mass line shape. This is a crucial ingredient for extracting the physical observables of interest, in particular, when there are two or more closely spaced signals to be separated like in our case. Therefore we studied in detail all the resolution effects with particular attention to the tails at low masses due to the emission of low-energy photons from charged kaons and pions in the final state (Final State Radiation, FSR). We developed our own Fast Monte Carlo as a way to include the most recent QED calculations and to allow easy tuning of the finer details of the mass line shape.

5.1 Introduction

An important ingredient of kinematic fits of samples containing one or more decay modes is the accurate knowledge of the invariant mass distribution of each signal mode. This is particularly important when there are two or more closely spaced signals to be separated. The results may strongly depend on the detailed shape on the invariant mass distribution, thus an accurate description of the mass line shape, including the tails, is crucial to obtain correct results. This is just the case of the rare $B_s^0 \to K^-\pi^+$ decay mode, expected to appear on the tail of more abundant decay modes as $B^0 \to K^+\pi^-$, $B^0 \to \pi^+\pi^-$ and $B_s^0 \to K^+K^-$.

Past studies comparing the CDF Monte Carlo mass resolution to real data found only approximate agreement, with data showing somewhat worse resolution and larger tails [1, 122]. Some kind of tuning of the simulation was required to reproduce the data. The issue is complicated by the emission of low-energy photons from charged particles in the final state (Final State Radiation, FSR), which distorts the distributions of kinematic variables due of the unreconstructed photon momentum. This effect modifies the distribution of the invariant mass of each signal mode, generating a tail at low masses.

In this chapter we describe the software tool we developed to obtain reliable line shapes of invariant mass peaks at least in the simplest and most common cases. The first ingredient is a simple Monte Carlo describing the kinematics of the decay; the second a detailed parameterization of the resolution functions of individual track parameters; the third ingredient is the simulation of FSR based on accurate formulas from recent QED calculations [123, 124, 125]. These formulas are the same used

in measuring precision branching fractions for two–body $B^0 \to h^+h'^-$ modes in a recent *BABAR* publication [63]. These QED formulas are claimed to be more accurate [124], for the applicable decays, than currently available simulations packages like PHOTOS [126]. The idea is to use this Monte Carlo program to generate distributions of mass and other kinematic variables for resonances for which large samples of real data are available. By comparing the results with a few real data samples, we can fit for the parameters of the resolution functions of individual track parameters until we get a good description of the data.

This approach is expected to be more reliable than the methods used in the past [1, 3, 4], based on tuning the mass distribution itself on some reference signal, and then trying to extrapolate the results to a different signal. The present approach, instead, is based on tuning the resolution track quantities (e. g., track curvature) and it is independent from the reference signal chosen. In particular this approach guarantees an easy and safe extrapolation of the mass line shape of interest since the invariant mass resolution depends directly on these quantities in the same way for each decay mode given the momentum distribution and the mass of mother particle.

Using a standalone code in place of a full simulation makes it easy to keep it up to date.

5.2 Invariant mass distribution from CDF II simulation

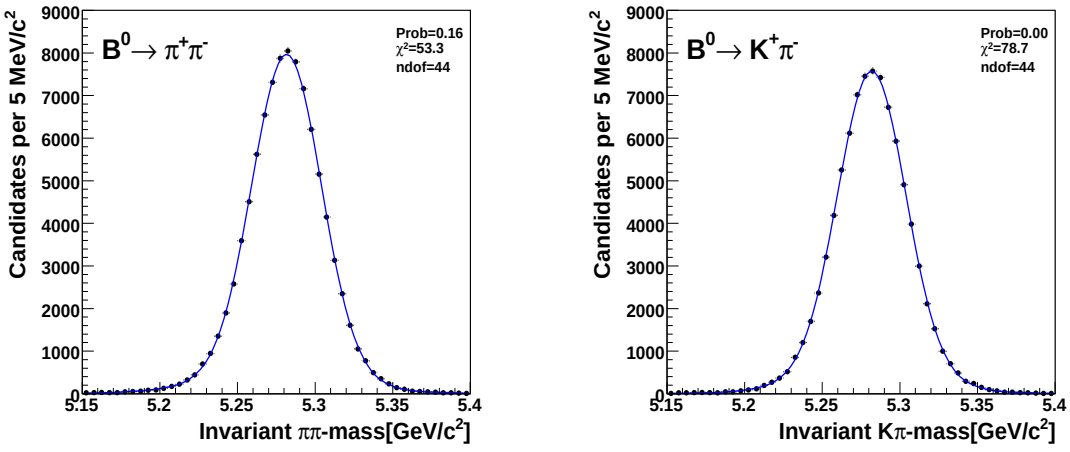


Figure 5.1: Invariant mass of the simulated $B^0 \to \pi^+\pi^-$ and $B^0 \to K^+\pi^-$ signals without FSR effects. Fit function is overlaid. A similar distribution is obtained for all signal modes.

The invariant mass distribution returned from CDF II simulation for $B^0_{(s)} \to h^+h'^-$ decays represents the initial step of the accurate study of the mass line shape described in this chapter. The FSR has not been introduced in the CDF II simulation, since the currently available simulation packages like PHOTOS [126] are not reliable for B and D hadronic decays.

Figure 5.1 shows the simulated invariant mass distribution of a single signal mode, computed assigning the correct mass hypothesis to both particles in the final state ($\pi\pi, K\pi, KK, pK, p\pi$). These

distributions are fitted using a sum of two Gaussians:

$$\wp(m; N, f_1, \mu_1, \sigma_1, \mu_2, \sigma_2) = N \cdot \left[f_1 \frac{1}{\sqrt{2\pi}\sigma_1} e^{-\frac{1}{2}\left(\frac{m-\mu_1}{\sigma_1}\right)^2} + (1-f_1)\frac{1}{\sqrt{2\pi}\sigma_2} e^{-\frac{1}{2}\left(\frac{m-\mu_2}{\sigma_2}\right)^2} \right] \tag{5.1}$$

where the means of the two Gaussians, μ_1 and μ_2, the standard deviations, σ_1 and σ_2, the relative fraction of the first Gaussian with respect to the second one, f_1, and the absolute normalization N, are determined by the fit. Table 5.1 summarizes the results of the fit. The model parameterizes accurately the resolution shape. We obtained a dominant Gaussian component ($f_1 \approx 89\%$) with a width of about 22 MeV/c^2 and a second wider Gaussian component ($f_2 = 1 - f_1 \approx 11\%$) with a width of about $44 - 45$ MeV/c^2. The distributions do not show any relevant non-Gaussian asymmetric tails since the FSR effects are not included in the simulation.

mode	f_1 [%]	μ_1 [MeV/c^2]	σ_1 [MeV/c^2]	μ_2 [MeV/c^2]	σ_2 [MeV/c^2]	$\hat{\mu}$ [MeV/c^2]
$B^0 \to \pi^+\pi^-$	89.3 ± 0.8	5281.7 ± 0.1	21.8 ± 0.1	5274.5 ± 0.7	44.6 ± 1.1	5280.9 ± 0.1
$B^0 \to K^+\pi^-$	89.3 ± 1.2	5281.9 ± 0.1	21.6 ± 0.2	5277.8 ± 0.8	41.7 ± 1.3	5281.5 ± 0.1
$B^0 \to K^+K^-$	89.6 ± 1.2	5282.1 ± 0.1	21.1 ± 0.2	5282.8 ± 0.7	39.3 ± 1.2	5282.2 ± 0.1
$B_s^0 \to \pi^+\pi^-$	89.1 ± 0.9	5371.9 ± 0.1	22.2 ± 0.1	5364.9 ± 0.8	44.8 ± 1.2	5371.1 ± 0.1
$B_s^0 \to K^-\pi^+$	88.0 ± 1.2	5372.3 ± 0.1	21.8 ± 0.2	5369.4 ± 0.7	40.6 ± 1.1	5372.0 ± 0.1
$B_s^0 \to K^+K^-$	89.8 ± 1.2	5372.3 ± 0.1	21.6 ± 0.2	5372.6 ± 0.7	40.7 ± 1.3	5372.3 ± 0.1
$\Lambda_b^0 \to p\pi^-$	90.4 ± 0.9	5624.9 ± 0.1	22.1 ± 0.1	5623.4 ± 0.7	44.9 ± 1.4	5626.2 ± 0.1
$\Lambda_b^0 \to pK^-$	89.3 ± 1.3	5626.8 ± 0.1	21.7 ± 0.2	5627.6 ± 0.7	40.2 ± 1.3	5626.8 ± 0.1

Table 5.1: Fit results on the invariant mass distribution of the simulated modes computed with the correct mass assignment to both particles. Every loss correction was performed using the pion hypothesis for both tracks.

Since we fitted μ_1 and μ_2 as two separate parameters, and since the returned value for μ_2 is slightly different from μ_1, we quoted the average value $\hat{\mu} = f_1\mu_1 + (1 - f_2)\mu_2$, reported in the last column of tab. 5.1, to estimate the average of the invariant mass distribution for each signal mode. From the comparison between $\hat{\mu}$ and the input mass values reported in tab. 5.2 of the simulation, we observed a slight (but non negligible) discrepancy. Such a discrepancy, $\mathcal{O}(2 - 3$ MeV/$c^2)$, is expected. In fact,

mode	m [MeV/c^2]
B^+	5279.0
B^0	5279.4
$B_s^0 \to \pi^+\pi^-$	5369.6
$B_s^0 \to K^-\pi^+$	5369.6
$B_s^0 \to K^+K^-$	5369.6
Λ_b^0	5624.0

Table 5.2: Summary of the input masses in the simulation.

the simulation is done in two steps. In the first step, the events are generated and are processed to simulate the transit of the particles in the detector material. All the silicon layers, all the wires in

the drift chamber and every part of the detector are simulated accurately. In the second step, the simulated events are reconstructed, like real data, by the off-line reconstruction code. This off-line code applies a track by track correction for the energy lost in the material, according to a chosen mass assignment (see sec. 3.3.1). When analyzing real data, at reconstruction time, we did not know what kind of particles we have, so we assigned arbitrarily the pion mass to all tracks. Thus for all modes in which the final state is different from the $\pi\pi$ case, we introduced an artificial shift in the invariant mass distribution of our signals, both for simulation and data, because of the wrong mass hypothesis. This bias can be measured by reprocessing the simulated events with the correct mass hypothesis for both tracks (see tab. 5.3), as, in this case, we know event by event the correct particle assignment. From the difference between the simulated events processed, first with the pion mass hypothesis for both tracks (like the real data), and second with the exact mass hypothesis for both tracks, we obtain the mass shift due to this effect. This information will be used in the fit of composition (see chap. 6) to cancel the bias on the mass difference among signals (the global mass scale is treated separately, see sec. 9.4.3 and 12.2).

mode	$\pi\pi$ (a)	correct (b)	$\delta_{\rm Kal}$ (c)
$B^0 \to \pi^+\pi^-$	5280.9 ± 0.1	5280.9 ± 0.1	–
$B^0 \to K^+\pi^-$	5281.5 ± 0.1	5280.4 ± 0.1	1.1
$B^0 \to K^+K^-$	5282.2 ± 0.1	5280.1 ± 0.1	2.1
$B_s^0 \to \pi^+\pi^-$	5371.1 ± 0.1	5371.1 ± 0.1	–
$B_s^0 \to K^-\pi^+$	5372.0 ± 0.1	5370.9 ± 0.1	1.1
$B_s^0 \to K^+K^-$	5372.3 ± 0.1	5370.2 ± 0.1	2.1
$\Lambda_b^0 \to p\pi^-$	5626.2 ± 0.1	5624.5 ± 0.1	1.7
$\Lambda_b^0 \to pK^-$	5626.8 ± 0.1	5624.2 ± 0.1	2.6

Table 5.3: Mean value $\hat{\mu}$ of the invariant mass in simulated events. All the masses in the table are computed using the correct mass hypothesis for both tracks. Both tracks are processed with pion mass assignment (a), with the correct mass assignment to compensate the energy losses in the material (b). Invariant mass shift $\delta_{\rm Kal}$ due to the uncorrected mass assignment in the refitting (c)=(a)-(b). The unit is MeV/c^2.

Even when tracks are refitted using the correct mass hypothesis and the energy losses are compensated correctly (see column (c) of tab. 5.3), an additional residual shift from the input values still remains. This residual shift depends on several factors. This appears only in the simulated samples but not when we process real data. The compensation of energy losses in the material was tuned accurately using large sample of real data $K_s^0 \to \pi^+\pi^-$, $B^\pm \to J/\psi K^\pm$, $J/\psi \to \mu^+\mu^-$ and $\Upsilon(4S) \to \mu^+\mu^-$ decays [106, 107], so that the absolute mass scale in the data is reproduced accurately. When, instead, we process the simulated events, using the off-line code tuned on real data, we put in evidence that the energy losses in the material are not reproduced within the precision level obtained with real data. The corrections do not compensate perfectly the simulated energy losses. This discrepancy depends on the particle mass. In fact it is about ≈ 2 MeV/c^2 for the $B^0 \to \pi^+\pi^-$ mode and it becomes ≈ 0.2 MeV/c^2 for the $\Lambda_b^0 \to pK^-$ mode.

This residual discrepancy does not affect the fit of composition of real data (see sec. 6.3) and we

will not apply any correction. In fact, for the $B^0_{(s)}$ mesons and Λ^0_b baryon, we will use as input masses the masses measured by CDF in Run II [106]. Using the masses measured with the same apparatus and reconstruction code as for $B^0_{(s)} \to h^+h^{'-}$ events allows the cancellation of common systematic uncertainties due to a possible overall shift of the CDF II mass scale.

5.3 Fast Monte Carlo Simulation (FMC)

We wrote a *Fast Monte Carlo Simulation* (FMC) specifically for this work based on the official CDF Monte Carlo (MC). The FMC consists in a C++ code which generates the decays of a generic $B(D)$ meson (indicated by the letter H), into two scalar or pseudo-scalar mesons P_1P_2 ($H \to P_1P_2$) [1]. The particle H is decayed in its rest frame. Then the three-dimensional momenta of decay products $\vec{p}^*_1$ and $\vec{p}^*_2$ are boosted to obtain the corresponding quantities in the laboratory frame ($\vec{p}_1$ and $\vec{p}_2$) according to the two-dimensional distribution of rapidity and transverse momentum of the particle H in the laboratory frame. In the case of the b-meson we used a flat rapidity distribution in the range $|y(B)| < 1.3$, while the $p_{\rm T}(B)$ input distribution was taken from an external histogram containing a smooth fit to the data published by CDF Run II measurement [111]. This is the same procedure adopted by the the official CDF Monte Carlo.

The track parameters in the laboratory frame have to be smeared according to the resolution functions that we extract from the official CDF simulation and if necessary tuned with real data. The strategy consists of: 1) tuning the resolution functions of FMC using the information from the CDF Monte Carlo; 2) implementing the FSR into the FMC; 3) comparing the FMC with some reference signal from real data (e. g., $D^0 \to K^-\pi^+$ decays); 4) in case of discrepancy between FMC and this reference signal, performing a finer tuning of resolution functions with real data.

5.3.1 Smearing of curvature k

The trajectory of a particle with momentum p and charge Ze in a constant magnetic field $\vec{B}$ is a helix, with radius of curvature R and pitch angle θ ($\lambda = \cot\theta$)[2]. The radius of curvature and the momentum component perpendicular to $\vec{B}$ are related by:

$$p\sin(\theta) = 0.3ZBR, \tag{5.2}$$

where p is GeV/c, B is in Tesla and R in meters. If the distribution of the measurements of the curvature $k \equiv 1/R$ is approximately Gaussian, the curvature error for a large number of uniformly spaced measurements on the trajectory of the charged particle in a uniform magnetic field can be approximately by

$$(\delta k)^2 = (\delta k_{\rm res})^2 + (\delta k_{\rm ms})^2, \tag{5.3}$$

where δk is the total curvature uncertainty, $\delta k_{\rm res}$ is the curvature uncertainty due to the finite measurement resolution and $\delta k_{\rm ms}$ is the curvature uncertainty due to multiple scattering.

[1] $\Lambda^0_b \to ph^-$ decays do not belong to the class of $H \to P_1P_2$ decays and they will be treated in a different way.

[2] $\lambda = \cot(\theta)$ is the helix pitch, where θ is the polar direction of the particle at the point of its closest approach to the z-axis. This is directly related to the longitudinal component of the momentum: $p_z = p_{\rm T}\cot(\theta)$

If many (≥ 10) uniformly spaced position measurements are made along the trajectory in a uniform medium [32]

$$\delta k_{\rm res} = \frac{\epsilon}{L'^2}\sqrt{\frac{720}{N+4}} \propto \text{constant}, \tag{5.4}$$

where N is the number of points measured along track, L' is the projected length of the track into the bending plane and ϵ is the measurement error for each point, perpendicular to the trajectory. If a vertex constraint is applied at the origin of the track, the coefficient under the square root becomes 320. $\delta k_{\rm res}$ is independent of the curvature.

The contribution to the resolution due to the multiple scattering is approximately [32]

$$\delta k_{\rm ms} \approx \frac{(0.16)(\text{GeV}/c)Z}{Lp\beta\ \sin^2\theta}\sqrt{\frac{L}{X_0}} \propto \frac{k}{\beta\sin\theta}, \tag{5.5}$$

where p is the momentum in GeV/c, Z is the charge of the incident particle in units of e, L is the total track length, X_0 is the radiation length of the scattering medium (in units of length) and β is the kinematic variable v/c. $\delta k_{\rm ms}$ can be considered approximately proportional to the curvature k, since for pions and kaons with transverse momentum greater than 2 GeV/c, β is assumed equal to one, and since the pseudo-rapidity of both tracks is $|\eta| < 1$, namely $\sin\theta > 0.648$ with $< \sin\theta >= 0.91$. Then the contribution due to multiple scattering is approximated as:

$$\delta k_{\rm ms} \approx \text{constant} \cdot \text{k}. \tag{5.6}$$

Therefore, in our sample, the curvature uncertainty can be parameterized by the approximate formula:

$$\delta k \approx A \cdot \sqrt{1 + B \cdot k^2}. \tag{5.7}$$

where A and B are parameters to be determined.

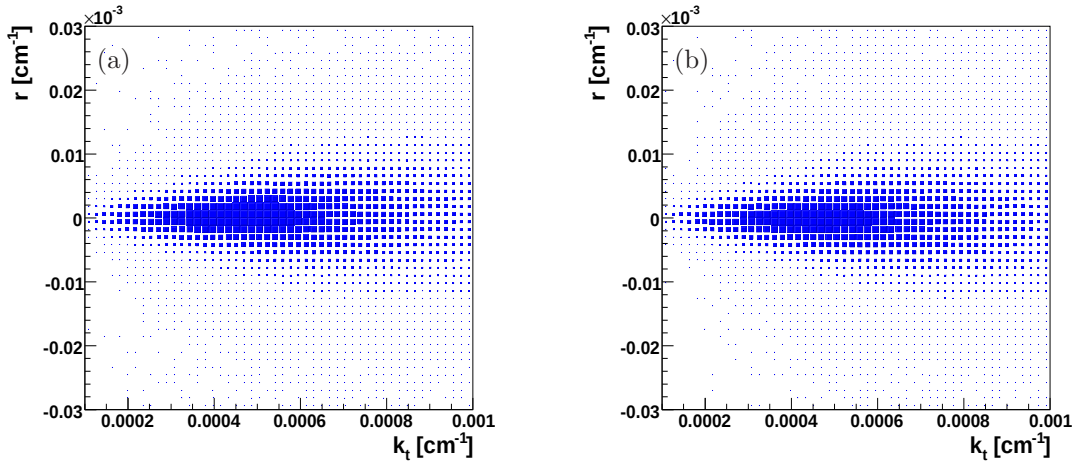


Figure 5.2: Curvature residual as a function of the true curvature of the simulated events for $B^0 \to \pi^+\pi^-$, $B^0 \to K^+\pi^-$ and $B^0 \to K^+K^-$ modes. Negative tracks (a), positive tracks (b).

Using the MC we can access simultaneously the distributions of the smeared quantities after the full simulation chain of the detector and the "true" quantities before the experimental smearing. We used a sample of 10M generated events of $B^0 \to \pi^+\pi^-$, $B^0 \to K^+\pi^-$ and $B^0 \to K^+K^-$ modes (see sec. 4.1), yielding about 80,000 events of each mode after the selections (trigger and off-line reconstruction). The specific decay has no particular relevance in this context, and we used the whole sample of tracks as a single sample. Figure 5.2 shows the curvature residual $r = k - k_t$, where k is the smeared curvature and k_t is the true curvature, as a function of k_t for negative (a) and positive tracks (b). The curvature resolution depends on the curvature value, and we fitted the distribution of the variable r in 10 k_t slices using a single Gaussian distribution:

$$N_k \cdot \mathscr{G}(r; \mu_k, \sigma_k) = N_k \cdot \frac{1}{\sqrt{2\pi}\sigma_k} \; e^{-\frac{1}{2}\left(\frac{r-\mu_k}{\sigma_k}\right)^2}, \tag{5.8}$$

where N_k is the absolute normalization, μ_k and σ_k are respectively the mean and the standard deviation of the Gaussian. The resulting values of σ_k are reported in fig. 5.3 respectively for negative (a) and positive tracks (b) and are fitted with the function described in eq. (5.7) as a function of k_t. A and B are extracted from these fits separately for negative and positive tracks. The values $\chi^2/\text{ndof} = 12.4/8$ and $\chi^2/\text{ndof} = 8.2/8$ demonstrate the goodness of our model.

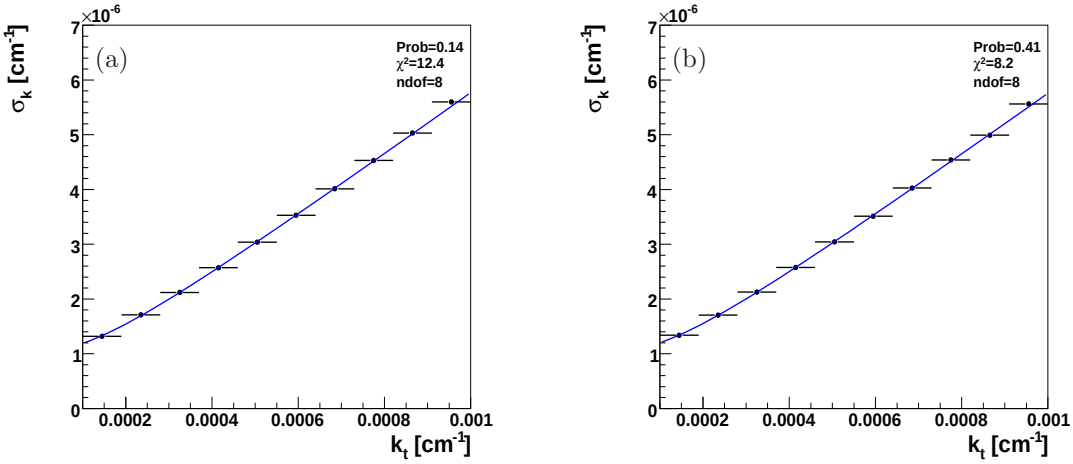


Figure 5.3: Curvature uncertainty as a function of the true curvature for simulated events of $B^0 \to \pi^+\pi^-$, $B^0 \to K^+\pi^-$ and $B^0 \to K^+K^-$ modes. Negative tracks (a), positive tracks (b).

The model with a single Gaussian is sufficient to reproduce the relationship between the δk and k but it is not sensitive to possible non-Gaussian deviations of the curvature resolution function. From tab. 5.1 we expect a deviation of the order of 10%. Although we have a large statistics in the MC, it is not sufficient to show this effect in each curvature slice with sufficient precision, especially for large values of curvature. Therefore, to parameterize accurately the deviation from the Gaussian model, we used the rescaled variable r'

$$r' = \frac{k - k_t}{\sigma_k(k_t)} = \frac{r}{\sigma_k(k_t)}. \tag{5.9}$$

r' by definition is independent on the curvature k_t and it allows to parameterize the non-Gaussian effects with a single fit. Figure 5.4 reports the distribution of the r' variable. Three Gaussians were necessary to achieve a good parameterization:

$$N'_k \cdot [f_1 \, \mathscr{G}(r'; \mu'_{k1}, \sigma'_{k1}) + f_2 \, \mathscr{G}(r'; \mu'_{k2}, \sigma'_{k2}) + (1 - f_1 - f_2) \, \mathscr{G}(r'; \mu'_{k3}, \sigma'_{k3})] \, . \tag{5.10}$$

N'_k is the absolute normalization, $f_{1(2)}$ is the relative fraction of the first (second) Gaussian and μ'_{ki} and σ'_{ki} are respectively the mean and the standard deviation of the i^{th} Gaussian.

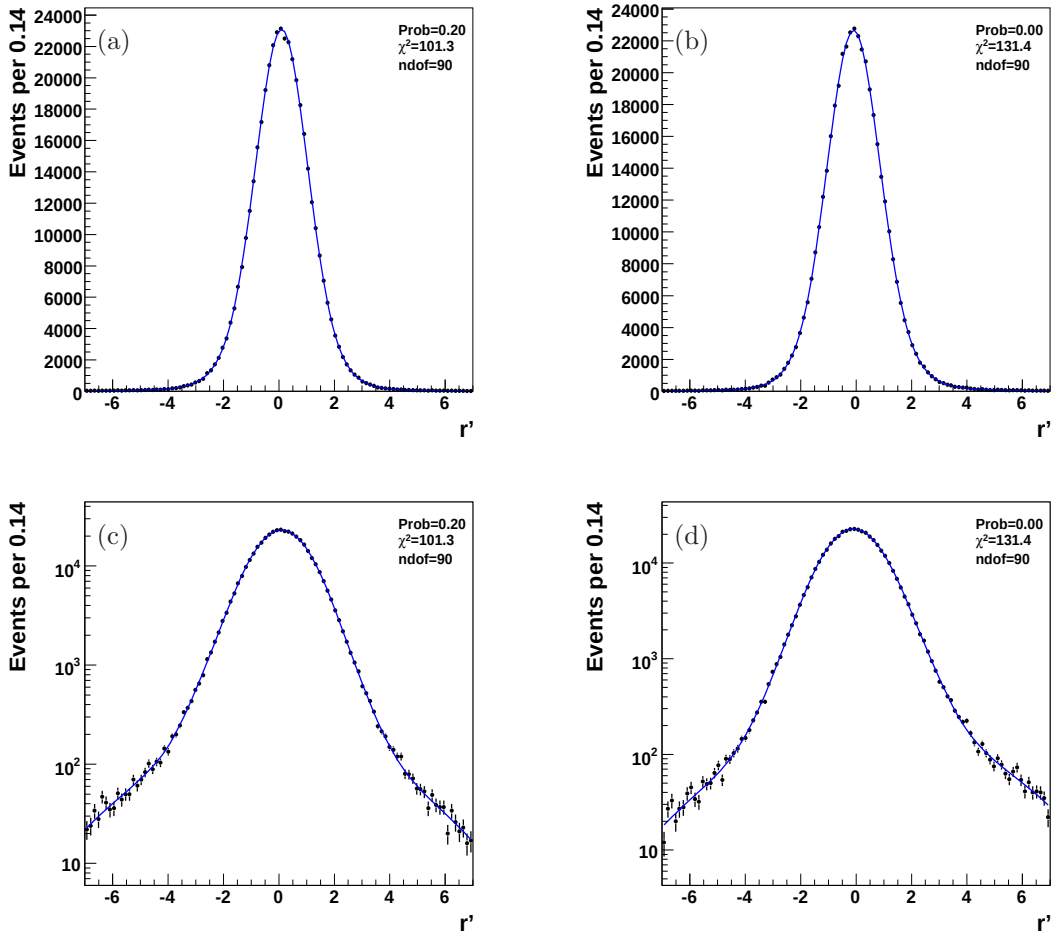


Figure 5.4: Resolution function of the rescaled curvature $r' = (k - k_t)/\sigma_k(k_t)$ of simulated events for $B^0 \to \pi^+\pi^-$, $B^0 \to K^+\pi^-$ and $B^0 \to K^+K^-$ modes. Negative tracks (a,c), positive tracks (b,d). Liner scale (a,b) and logarithmic scale (c,d).

In our FMC simulation, we first smeared the r' variable according to the parameters f_i, μ_{ki} and σ_{ki} of the triple Gaussian extracted, and then changed variable $r' \to r$ to obtain the smeared curvature k. We performed two independent smearings for negative and positive tracks.

We verified that the curvature resolution depends mainly on the curvature k and that the effect of λ and φ_0 dependences are much smaller. They have a negligible influence on the invariant mass distribution, thus their effect on the curvature resolution was neglected.

5.3.2 Smearing of λ and φ_0

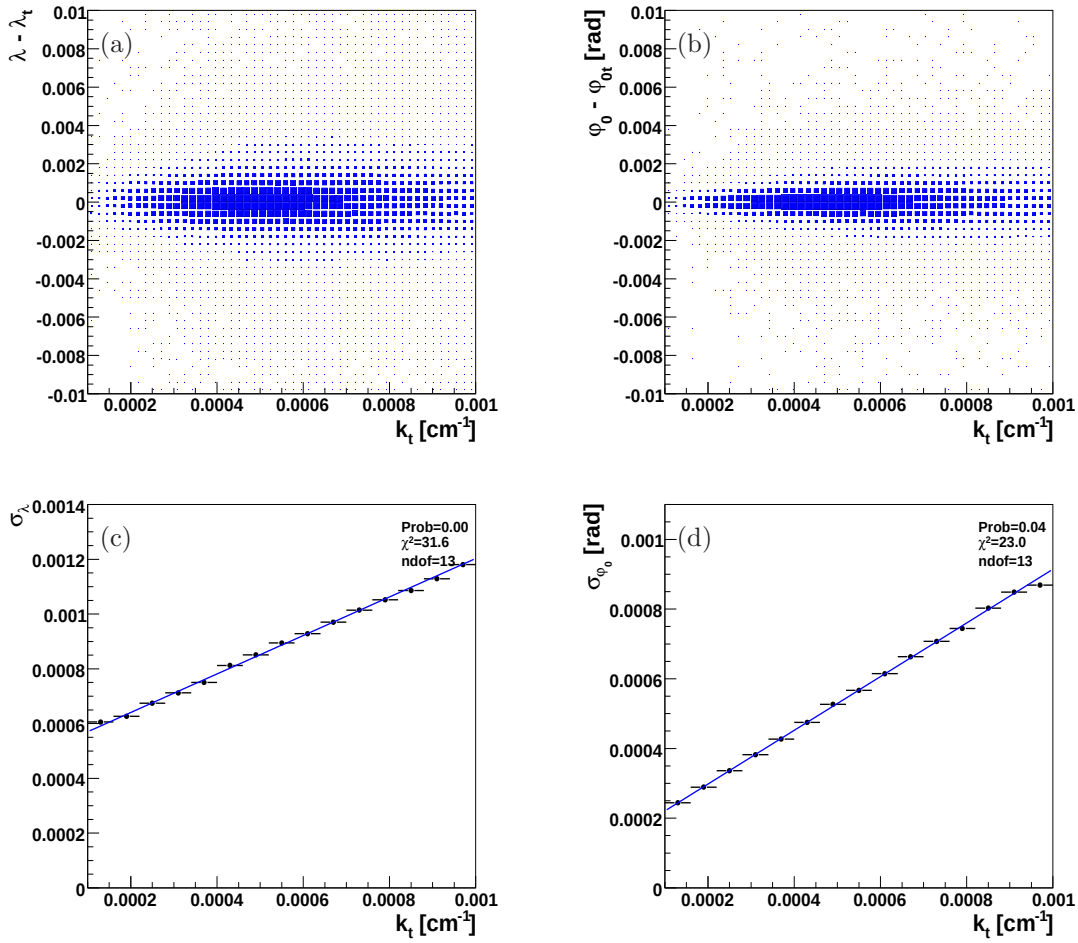


Figure 5.5: λ (a) and φ_0 (b) residual as a function of the true curvature of the simulated events. λ (c) and φ_0 (d) resolution as a function of the true curvature of the simulated events, the fit function is overlaid.

In order to simulate the measurement of the helix pitch $\lambda \equiv \cot\theta$, and of the azimuthal angle φ_0 we parameterized the resolution σ_λ and σ_{φ_0} as a function of curvature using the same technique described in the previous section. We verified that the tails of these distributions have a negligible effect on the invariant mass distribution and we therefore ignored them in our model. Also in this case the dependences of the resolution on λ and φ_0 were neglected as they are much smaller effects.

In case of λ and φ_0 smearing, no difference in charge was found and to further increase the statistics, negative and positive tracks were added up.

Figures 5.5(a) and (b) show the residuals $\lambda - \lambda_t$ and $\varphi_0 - \varphi_{0t}$, where λ and φ_0 are the smeared quantities and λ_t and φ_{0t} are the true quantities in the MC, as a function of the true curvature k_t. We fitted the residual distributions in 15 k_t slices using a single Gaussian distribution. The fitted values of σ_λ and σ_{φ_0} are reported in figs. 5.5(c) and (d) respectively and we empirically parameterized them with linear functions:

$$\sigma_\lambda(k_t) = a_0 + a_1\ k_t \quad \text{and} \quad \sigma_{\varphi_0}(k_t) = b_0 + b_1\ k_t. \tag{5.11}$$

$a_0(b_0)$, $a_1(b_1)$ are free parameters in the fit. The quality of the fit is slightly worse than in the curvature case that was derived from a physical model but it is still satisfactory for our purpose.

5.3.3 Smearing of the impact parameter d_0

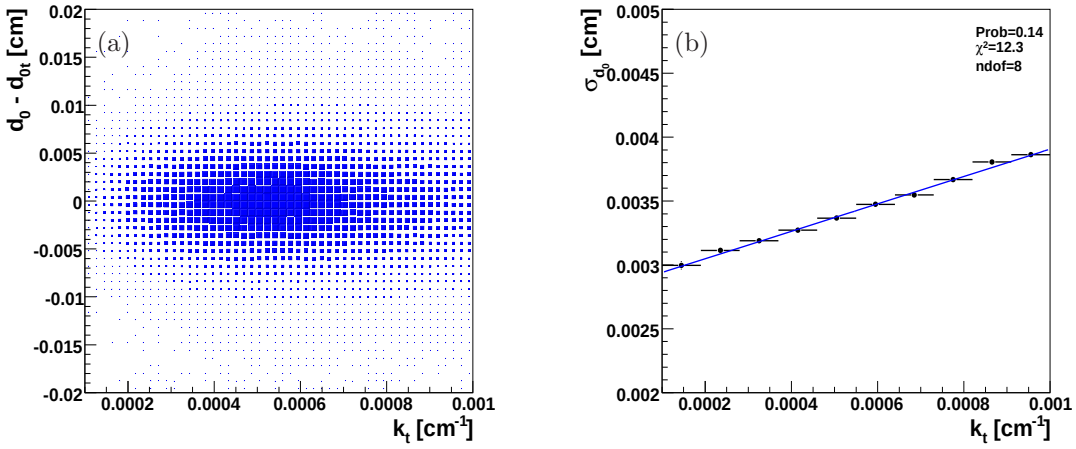


Figure 5.6: d_0 residual as a function of the true curvature of the simulated events (a). d_0 resolution as a function of the true curvature of the simulated events (b), the fit function is overlaid.

In addition to smearing the track parameters k, λ and φ_0, we also needed to smear the impact parameter d_0. While d_0 is not important variable of direct interest here, it is important because of its correlation with the other kinematic variables. Most heavy flavor samples are selected using cuts on d_0 or related quantities, so it is necessary to have an appropriate simulation of the d_0 distributions.

To smear the impact parameter we followed the same procedure used for λ and φ_0. Figure 5.6 shows the residual distribution of $d_0 - d_{0t}$ as a function of the true curvature k_t (a) and the parameterization of σ_{d_0} in curvature slices with a linear function (b).

5.3.4 Comparison FMC vs MC

In order to check if the FMC simulation reproduces all the features of the MC, a comparison of the most relevant kinematic distributions (mass, $p_{\mathrm{T}}(B)$, $\sum p_{\mathrm{T}}$, L_{T}, $\Delta\varphi_0$, $d_0(B)$, $d_0(1)$, $d_0(2)$, $p_{\mathrm{T}}(1)$, $p_{\mathrm{T}}(2)$) was performed. For this check we used the decay mode $B^0 \to \pi^+\pi^-$.

FMC events have been reweighted to match the observed p_{T} distribution of the B–meson in the full MC. This is done to avoid the need of a precisely matching the p_{T} dependence on the detector acceptance, since the mass line shape is sensitive to small changes of the $p_{\mathrm{T}}(B)$ spectra.

Figure 5.7 shows this comparison for the invariant mass distribution and the value $\chi^2/\mathrm{ndof} = 87.5/49$ indicates a good agreement between the two distributions. This confirms that the invariant mass resolution shape is determined by the tracks parameters uncertainty, and that possible correlations between two tracks can be neglected. This is important for our purpose, because we want to calibrate on a mass peak ($D^0 \to K^-\pi^+$) and export the calibration to the $B^0_{(s)} \to h^+h^{'-}$ via the single track resolutions. The results show that the source of the observed 10% non–Gaussian tails of the invariant mass distribution is the tail of the curvature resolution function. Comparison of other

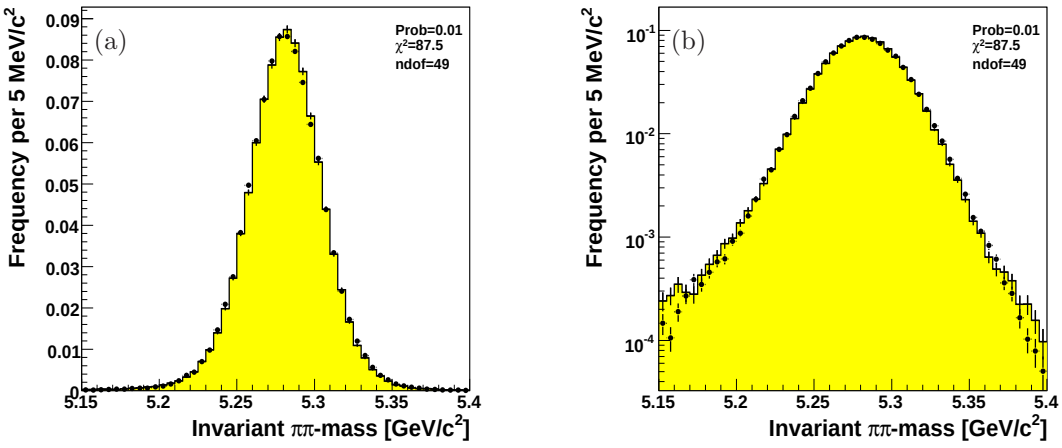


Figure 5.7: Comparison between the invariant mass distribution of the $B^0 \to \pi^+\pi^-$ events simulated with the the official CDF Monte Carlo (filled yellow histogram) and with the Fast Monte Carlo simulation (points with error bars). Linear scale (a), logarithmic scale (b).

kinematics variables (see fig. 5.8) also show a satisfactory agreement.

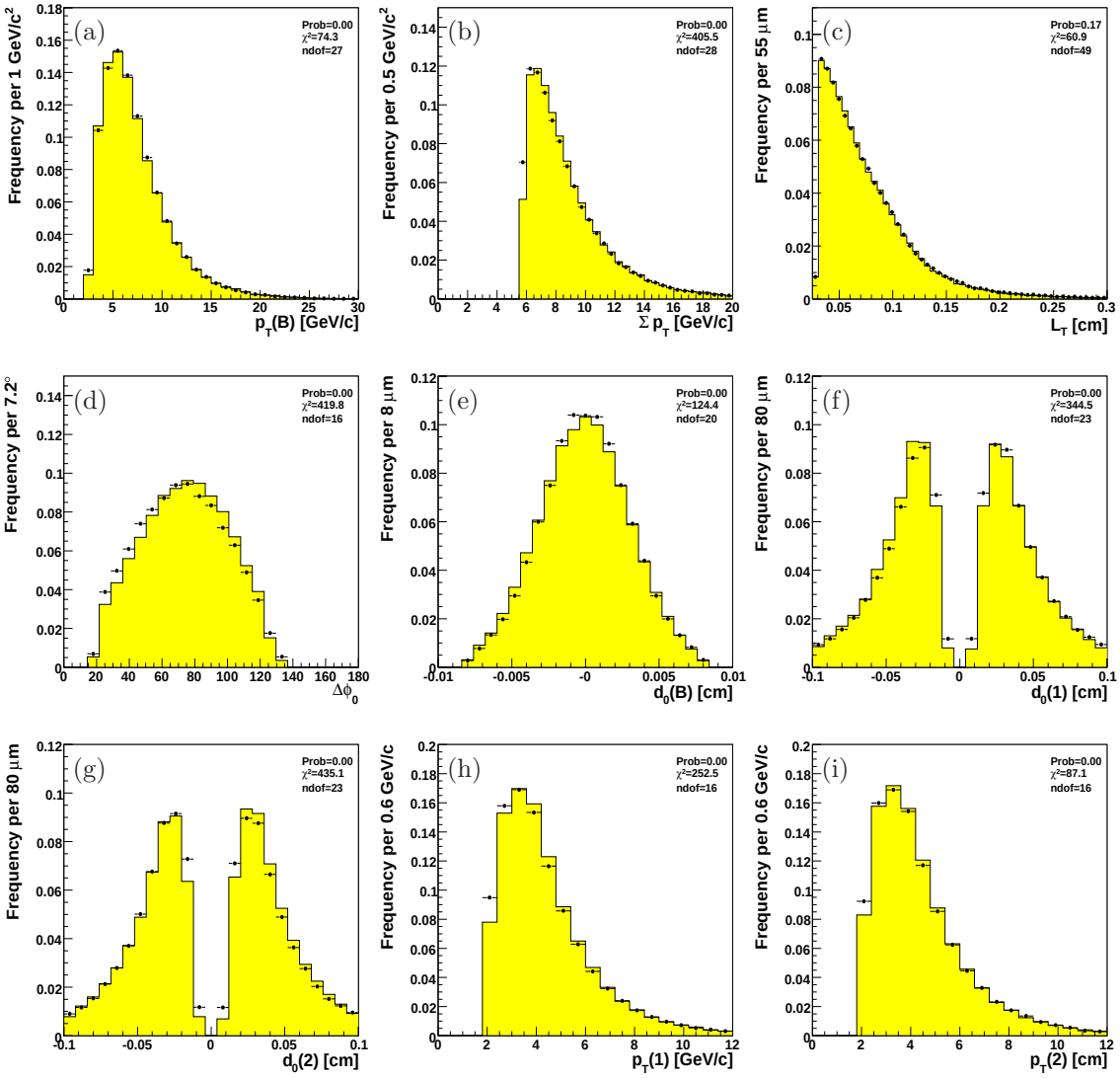


Figure 5.8: Comparison of the distributions of the single mode $B^0 \to \pi^+\pi^-$ simulated with the Fast Monte Carlo Simulation (points with error bars) and the official CDF Monte Carlo simulation (filled histogram). $p_{\mathrm{T}}(B)$ (a) $\sum p_{\mathrm{T}}$ (b), L_{T} (c), $\Delta\varphi_0$ (d), $d_0(B)$ (e), $d_0(1)$ (f), $d_0(2)$ (g), $p_{\mathrm{T}}(1)$ (h), $p_{\mathrm{T}}(2)$ (i).

5.4 Final State Radiation

We simulated the soft photon emission in our FMC, using the QED calculations described in Ref. [124]. We summarize here the main formulas used.

5.4.1 QED calculations

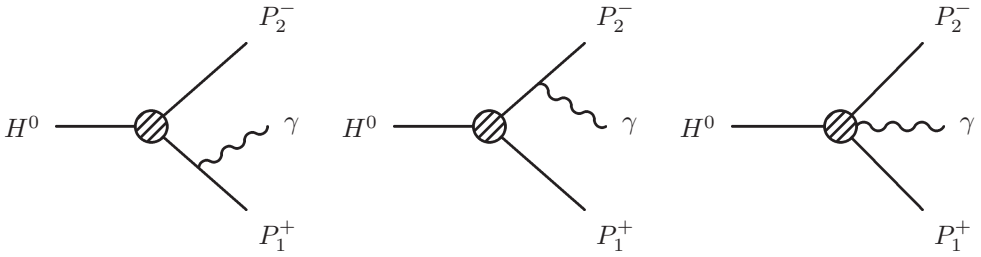


Figure 5.9: Illustration of electromagnetic contributions to the $H^0 \to P_1^+ P_2^-$ process with a real photon in the final state: *bremsstrahlung*.

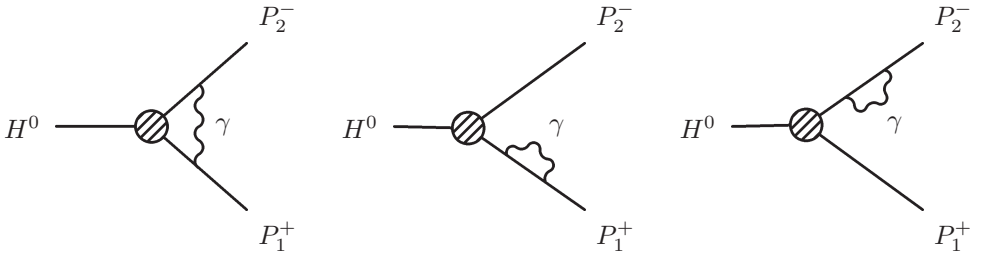


Figure 5.10: Illustration of electromagnetic contributions to the $H^0 \to P_1^+ P_2^-$ process with a virtual photon: one-loop vertex correction and $P_{1(2)}$ self-energy.

The most convenient infrared-safe observable related to the process $H^0 \to P_1^+ P_2^-$, where H^0 is a pseudo-scalar meson (B^0 or D^0) and $P_{1(2)}^{+(-)}$ are scalar or pseudo-scalar particles, is the photon-inclusive width

$$\Gamma_{12}^{\rm incl}(E^{\rm max}) = \Gamma(H^0 \to P_1^+ P_2^- + n\gamma)\,\big|_{\sum E_\gamma < E^{\rm max}} \tag{5.12}$$

namely the width of the process $H^0 \to P_1^+ P_2^-$ accompanied by any number of (undetected) photons, with total missing energy $\sum E_\gamma$ less or equal to $E^{\rm max}$ in the H^0 meson rest frame. At any order in perturbation theory $\Gamma_{12}^{\rm incl}$ can be factorized into two theoretical quantities: the so-called non-radiative width, Γ_{12}^0, and the corresponding energy-dependent e.m. correction factor $G_{12}(E^{\rm max})$,

$$\Gamma_{12}^{\rm incl}(E^{\rm max}) = \Gamma_{12}^0\; G_{12}(E^{\rm max})\;. \tag{5.13}$$

The energy dependence of $G_{12}(E)$ is unambiguous and universal (i.e. independent on the short-distance dynamics which generate the decay) up to terms which vanish in the limit $E \to 0$. On the contrary, the normalization of $G_{12}(E)$ is arbitrary: it is always possible to move part of the finite (energy-independent) electromagnetic corrections from Γ_{12}^0 to $G_{12}(E)$. Only the product in eq. (5.13) corresponds to an observable quantity.

From the purely experimental point of view, the only relevant aspect of the $G_{12}(E)$ factors is their energy dependence. This allows to evaluate the missing-energy distribution, or the soft-photon spectrum, $d\Gamma_{12}^{\rm incl}(E)/dE$. The $E \to 0$ singularity of this distribution is not integrable if evaluated at any fixed order in perturbation theory; however, the all–order resummation of the leading infrared singularities leads to an integrable distribution [124]. In our case, the differential decay rate of the process $H^0 \to P_1^+ P_2^- + n\gamma$ with respect to the total photons energy E can be written as:

$$\frac{d\Gamma_{12}^{\rm incl}(E)}{dE} \;=\; \frac{2\alpha}{\pi}\,\frac{|b_{12}|\Gamma_{12}^0}{E}\left(\frac{2E}{m_{H^0}}\right)^{\frac{2\alpha}{\pi}|b_{12}|}\left[1+\mathcal{O}\left(\frac{E}{m_{H^0}},\frac{\alpha}{\pi}\right)\right] \tag{5.14}$$

where α is fine structure constant and β and b_{12} are the coefficients defined as:

$$\beta^2 \;=\; \left[1-(r_1+r_2)^2\right]\left[1-(r_1-r_2)^2\right]\;, \qquad r_i \;=\; \frac{m_i}{m_{H^0}}\;, \tag{5.15}$$

$$b_{12} \;=\; \frac{1}{2}-\frac{4-\Delta_1^2-\Delta_2^2+2\beta^2}{8\beta}\,\ln\left(\frac{\Delta_1+\beta}{\Delta_1-\beta}\right) \quad + \quad (1\to 2)\;, \tag{5.16}$$

where $\Delta_{1(2)} = 1 + r_{1(2)}^2 - r_{2(1)}^2$, and m_{H^0}, m_1, m_2 are respectively the masses of H^0, P_1^+ and P_2^-.

Concerning the angular distribution of the *bremsstrahlung* photons (see fig. 5.9), the differential decay rate up to $\mathcal{O}(\alpha)$ terms can be written:

$$\frac{d^2\Gamma(H^0\to P_1^+P_2^-\gamma)}{dE_\gamma\; d\cos\theta_\gamma} = \frac{\alpha}{2\pi}\;\frac{1}{\beta}\;\frac{\Gamma_{12}^0}{E_\gamma}\;R_{12} \tag{5.17}$$

where E_γ and θ_γ denote, respectively, the photon energy and the angle between photon and P_1^+ momenta in the H^0 meson rest frame, and in this case β has a different definition:

$$\beta^2 \;=\; \left[1-\frac{(r_1+r_2)^2}{1-2z}\right]\left[1-\frac{(r_1-r_2)^2}{1-2z}\right]\;, \qquad z \;=\; \frac{E_\gamma}{m_{H^0}}\;. \tag{5.18}$$

The R_{12} coefficients assume the following explicit form

$$R_{12} \;=\; \frac{1-r_1^2-r_2^2-2z}{t_1 t_2}-\frac{r_1^2}{t_1^2}-\frac{r_2^2}{t_2^2} \tag{5.19}$$

in terms of the kinematic variables

$$t_{1,2} = \frac{1}{2}\left[1+\frac{r_{1,2}^2}{1-2z}\mp\cos\theta_\gamma\right]\;. \tag{5.20}$$

Figure 5.11 (a,b,c) shows the distribution of eq. (5.17) for the emission of a real photon respectively for the $B^0\to\pi^+\pi^-$, $B^0\to K^+\pi^-$, and $B^0\to K^+K^-$ modes. The photon direction is, mostly, nearly collinear or anti-collinear to the direction of P_1^+ momentum in H^0 rest frame. The differential decay rate is invariant under the transformation $\cos\theta_\gamma \to -\cos\theta_\gamma$ for symmetrical final states like $\pi^+\pi^-$ or K^+K^-. This implies that the probability of a photon to be emitted in the same direction of P_1^+ (namely $\cos\theta_\gamma > 0$) is equal to the probability of being emitted in the opposite direction (namely $\cos\theta_\gamma < 0$). Instead, in final states with different kind of particles, like $B^0 \to K^+\pi^-$, the photon

has a larger probability to be emitted in the direction of the lighter particle (in our case the pion) as fig. 5.11(b) shows. The size of this asymmetry is related to the mass difference $m_1 - m_2$ relative to the mass m_{H^0}, through the coefficients R_{12}.

Equation (5.17) is divergent for $E_\gamma \to 0$ and for $\cos\theta_\gamma \to \pm 1$, and its integral is also divergent and cannot be integrated in both energy and angular domains. The first singularity is due to the infrared divergence, since the eq. (5.17) was calculated only for real contributions (*bremsstrahlung* photons, see fig. 5.9), while the second divergence is due to the relativistic conservation of four-momentum. The photon has zero mass and therefore it cannot be emitted exactly collinear or anti-collinear to the direction of the emitting particle.

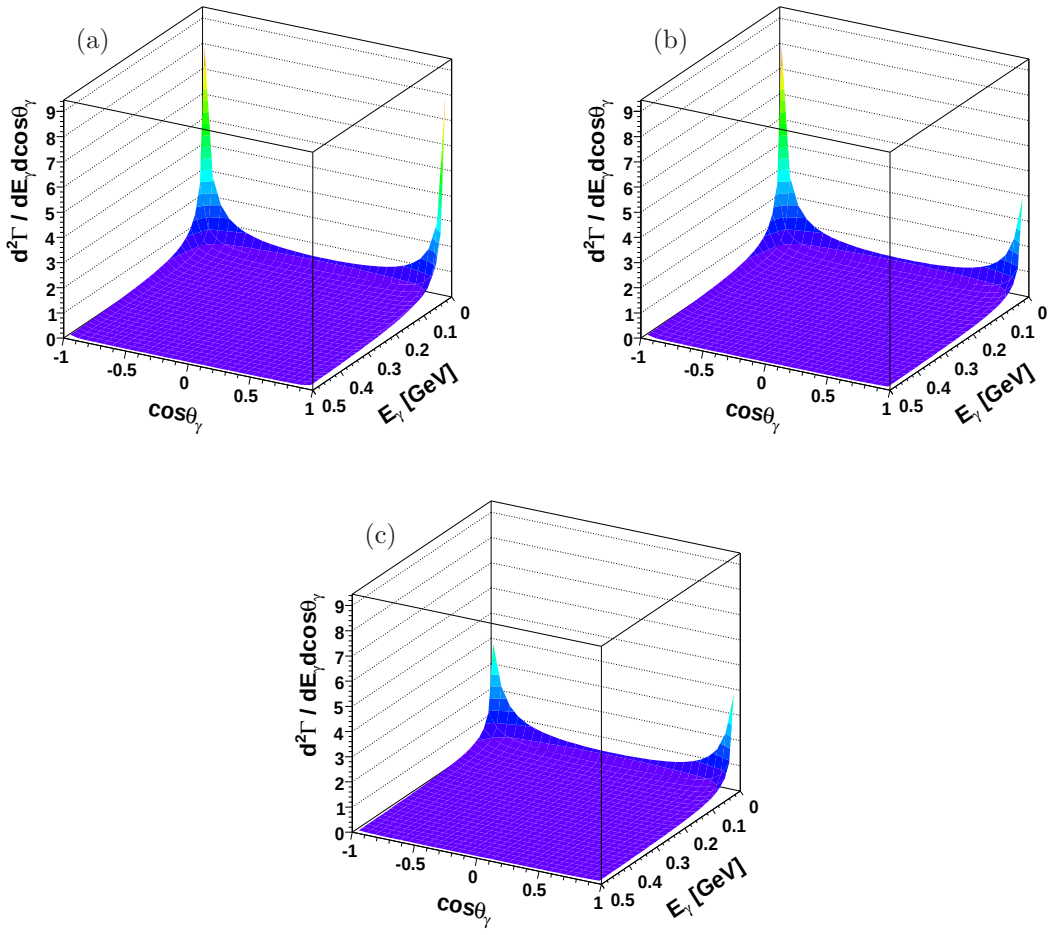


Figure 5.11: Differential decay rate for the *bremsstrahlung* process $H^0 \to P_1^+ P_2^- \gamma$ with respect to the photon energy E_γ and the cosine of angle between photon and P_1^+ momenta in the H^0 meson rest frame. $B^0 \to \pi^+\pi^-$ (a), $B^0 \to K^+\pi^-$ (b), $B^0 \to K^+K^-$ (c).

Equation (5.14) is the soft-photon spectrum $d\Gamma_{12}^{\text{incl}}(E)/dE$, and although it has a singularity for

$E \to 0$ it is integrable, since it was evaluated by all-order resummation of the leading infrared singularities (*bremsstrahlung* plus virtual photons , see figs. 5.9 and 5.10).

From the phenomenological point of view both equations (eq. (5.17) and eq. (5.14)) only make sense if the information on detection threshold for photons (or maximum missing energy) $E_{\max}$ is available. Without this information, an unambiguous comparison between theory and experiments, and also the combination of different experimental results, cannot be performed. For this reason eq. (5.14) is well defined only in a determined integration domain $[0, E_{\max}]$. In practice, in our case of relative branching fractions measurements, it is sufficient to make sure that the cut–off $E_{\max}$ is set large enough to have effects only outside of the mass window used in the analysis.

5.4.2 Putting everything together

Our FMC simulates a generic $H^0 \to P_1^+ P_2^-$ decay in the rest frame of the H^0 meson and then it boosts in the laboratory frame the momentum of the $P_{1(2)}^{+(-)}$ particle (see sec. 5.3). For simplicity we used the same notation of sec. 5.4.1. We indicate with $(E^*_{1(2)}, \vec{p}^{\,*}_{1(2)})$ the four-momentum of the decay product $P_{1(2)}^{+(-)}$ in the rest frame of the meson H^0 while the same quantities in the laboratory frame will be indicated by $(E_{1(2)}, \vec{p}_{1(2)})$. Regarding the photon, we used only the quantities in the rest frame of H^0 meson and they are indicated without the star: E is the total missing energy of the undetected photons defined in eq. (5.14). E_γ and $\cos\theta_\gamma$ are respectively the energy of the *bremsstrahlung* photon and the cosine of the angle between himself and P_1^+ momentum defined in eq. (5.17).

To include the FSR in the FMC we made the following approximations.

- Emission of a single leading photon, $E = E_\gamma$. Processes with $n\gamma > 1$ are suppressed by factor of α.

- We used the eq. (5.14) $\frac{d\Gamma_{12}^{\rm incl}(E_\gamma)}{dE_\gamma} = \frac{2\alpha}{\pi} \frac{|b_{12}|\Gamma_{12}^0}{E_\gamma} \left(\frac{2E_\gamma}{m_{H^0}}\right)^{\frac{2\alpha}{\pi}|b_{12}|}$ to generate the energy spectrum of the soft photon, integrating the distribution between $E_\gamma \to 0$ and $E_\gamma = E_{\max}$. The cut-off $E_{\max}$ depends on the decay mode we want to analyse and its choice is motivated by the acceptance fit interval in the invariant mass distribution.
  The fit of composition (described chap. 6) is performed in the invariant mass region $5.0 < m_{\pi\pi} < 5.8$ GeV/c. The inclusion of the soft photon emission produces a long lower-mass tail in the invariant mass distribution and this must be well–defined within this range. We chose a cut-off $E_{\max} = 0.5$ GeV, large enough so that the radiative tail is well defined in the mass interval, but still smaller than the kinematic energy cut-off $m_{B^0_{(s)}} - m_{h^+} - m_{h'^-}$.
  In this thesis we quote only branching fraction ratios, like $\mathcal{B}(B^0 \to \pi^+\pi^-)/\mathcal{B}(B^0 \to K^+\pi^-)$, and we are interested only in the line shape of the distribution and not in the absolute normalization of the soft photon emission.

- We assumed the direction of the photon as collinear (50% of cases) or anti-collinear (50% of cases) with P_1^+ momentum direction in H^0 rest frame (see sec. 5.4.1). This violates the total momentum conservation, but it works fine for practical purposes. The 50% probability to be collinear/anticollinear is accurate for the decay modes with same particles in the final state, but it is still a good approximation also in the other cases, like $B^0 \to K^+\pi^-$ and $B_s^0 \to K^-\pi^+$.

- We preserved conservation of total energy. If $(E'^*_{1(2)}, \vec{p}\,'^*_{1(2)})$ is the particle four-momentum after the photon emission in the H^0 rest frame, and the particle 1 is emitting, we can write:
  - $E'^*_1 = E^*_1 - E_\gamma$;
  - $p'^*_1 = \sqrt{(E'^*_1)^2 - m_1^2}$;
  - $\hat{p}'^*_1 = \hat{p}^*_1$;
  - $E'^*_2 = E^*_2 \quad \text{and} \quad \vec{p}\,'^*_2 = \vec{p}^*_2$

  where $\hat{p} = \vec{p}/|\vec{p}|$ and $p = |\vec{p}|$.

To obtain all kinematic distributions of the generic $H^0 \to P_1^+ P_2^-$ decay with the soft photon emission, it is sufficient to boost the four-momenta of the particles $(E'^*_{1(2)}, \vec{p}\,'^*_{1(2)}) \to (E'_{1(2)}, \vec{p}\,'_{1(2)})$ in the laboratory frame with the same prescription described in sec. 5.3.

5.5 Testing the model with real data

Having included a detailed model of the CDF II detector resolution, and an accurate description of the soft photon emission effects in our FMC simulation, we are ready to compare it to data in order to check its accuracy. To this purpose, we used a real data sample of $D^0 \to K^-\pi^+$ decays, collected by the `B_CHARM` trigger (see sec. 3.2.2), and reconstructed in the decay chain $D^{*+} \to D^0\pi^+ \to [K^-\pi^+]\pi^+$.

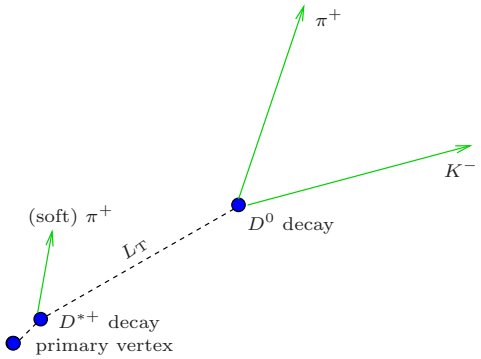


Figure 5.12: Schematic sketch of the $D^{*+} \to D^0\pi^+ \to [K^-\pi^+]\pi^+$ decay chain in the plane transverse to the proton beam direction.

Following Ref. [122], signal reconstruction (see fig. 5.12) was based solely on tracking and on the information of the identity of D^0 decay-products provided by the charge of the soft pion. One $D^0 \to K^-\pi^+$ and one $\overline{D}^0 \to K^+\pi^-$ candidate were formed for each pair of oppositely-curved tracks found in the XFT fiducial region ($|\eta| < 1$). Further requirements on the product of the track impact parameters ($d_0(K) \times d_0(\pi) < 0$ cm^2), on the D^0 candidate transverse momentum ($p_T(D^0) > 5.5$ GeV/c), on its transverse decay-length ($L_T(D^0) > 300$ μm), and on its impact parameter ($|d_0(D^0)| < 140$ μm) were applied to suppress a 10% contribution [127] from non-prompt D^{*+} decays. Candidates with

reconstructed invariant mass within 200 MeV/c^2 of the world–average D^0 mass [32] were combined with a third charged particle with $p_{\rm T} > 0.4$ GeV/c (soft pion) to form a $D^{*+} \to D^0\pi^+$ candidate. The charged pion mass is assigned to the like-sign pair of particles. The difference between the reconstructed D^{*+} and D^0 masses was required to be within $[0.1435, 0.1472]$ GeV/c^2 corresponding to an interval of $\pm 3\sigma$ from the nominal value of 0.1454 GeV/c^2 to reduce backgrounds (combinations of true D^0 decays with random tracks, random three-track combinations that satisfy the selection requirements, etc.). The selection results in about 1.5×10^6 signal decays. The invariant $K\pi$-mass

Quantity of the track	Units	Requirement
$p_{\rm T}(\pi)$, $p_{\rm T}(K)$	GeV/c	> 2.0
$p_{\rm T}(\pi_s)$	GeV/c	> 0.4
$\lvert\eta(\pi)\rvert$, $\lvert\eta(K)\rvert$	–	< 1.0
$\lvert d_0(\pi)\rvert$, $\lvert d_0(K)\rvert$	μm	[120, 1000]
Quantity of the candidate		
$q(\pi) \times q(K)$	e^2	-1
$d_0(\pi) \times d_0(K)$	μm^2	< 0
$p_{\rm T}(D^0)$	GeV/c	> 6
$L_{\rm T}(D^0)$	μm	> 300
$\sum p_{\rm T}(K, \pi)$	GeV/c	> 5.5
$\lvert d_0(D^0)\rvert$	μm	< 140
$\lvert d_0(D^{*+})\rvert$	μm	< 80
$\chi^2_{r\phi}$	–	< 20
$\Delta\varphi_0(K, \pi)$	Degrees	[2°, 90°]
$m_{D^{*+}} - m_{D^0}$	GeV/c^2	[0.1435, 0.1472]

Table 5.4: The $D^{*+} \to D^0\pi^+ \to [K^-\pi^+]\pi^+$ selection. To distinguish the "soft" pion originated from the D^{*+} decay from the pion originated from the D^0 decay, they are labeled respectively as π_s and π in the table.

distribution is shown in fig. 5.15.

To perform an accurate comparison between data and FMC even in the tails, we used tight selection cuts. We chose a tight D^0 mass window ($1.820 < m_{K\pi} < 1.900$ GeV/c^2) to avoid the contamination from mis-reconstructed decays in other modes (see fig. 5.13). At lower masses, there are $D^0 \to K^+K^-$ decays ($\mathcal{B} \simeq 3.9 \times 10^{-3}$) in which a kaon is mis-assigned the pion mass, and $D^0 \to K^-\pi^+\pi^0$ ($\mathcal{B} \simeq 13\%$) decays in which a π^0 is not reconstructed. At higher masses the situation is different, since the radiative tail of the $D^0 \to \pi^+\pi^-$ decays ($\mathcal{B} \simeq 1.4 \times 10^{-3}$), in which a pion is mis-assigned the kaon mass [122], contaminates almost uniformly the mass region chosen to perform the test.

To verify the accuracy of our mass line shape model, we used the FMC simulation to parameterize the invariant $K\pi$-mass distribution of the $D^0 \to K^-\pi^+$ decays. We generated a sample of $D^{*+} \to D^0\pi^+ \to [K^-\pi^+]\pi^+$ events, corresponding to about 700,000 candidates after the selection described in tab. 5.4. To have similar kinematics and to perform an identical kinematic selection we extended the two-body FMC simulation described in sec. 5.3, to a three-body FMC simulation, which is, in this case, a sequential chain of two two-body decays $D^{*+} \to D^0\pi^+$ plus $D^0 \to K^-\pi^+$.

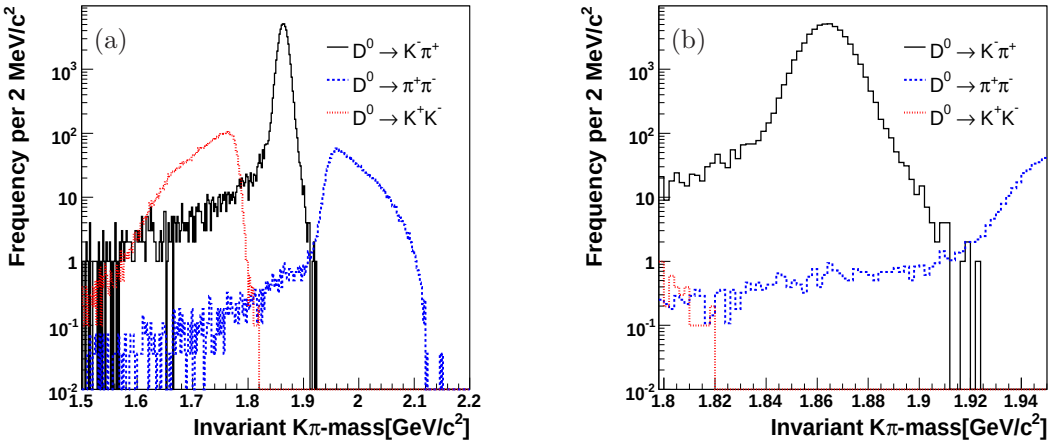


Figure 5.13: Invariant $K\pi$-mass distribution of simulated $D^0 \to h^+h^{'-}$ modes using the FMC simulation. $1.500 < m_{K\pi} < 2.100$ GeV/c^2 (a), $1.800 < m_{K\pi} < 1.950$ GeV/c^2 (b). In the figure we assumed $\frac{\mathcal{B}(D^0\to\pi^+\pi^-)}{\mathcal{B}(D^0\to K^-\pi^+)} = 0.03594$ and $\frac{\mathcal{B}(D^0\to K^+K^-)}{\mathcal{B}(D^0\to K^-\pi^+)} = 0.0992$ from Ref. [122].

The mass line shape of the $D^0 \to K^-\pi^+$ signal mode was parameterized from FMC using the following p.d.f.:

$$\begin{aligned}\wp_s(m;\vec{\theta}) &= f_{\rm bulk}[f_1\mathscr{G}(m;m_{D^0}+\delta_1,\sigma_1)+(1-f_1)\mathscr{G}(m;m_{D^0}+\delta_2,\sigma_2)] \\ &\quad +(1-f_{\rm bulk})\mathscr{T}(m;b,c,m_{D^0}+\delta_1),\end{aligned} \tag{5.21}$$

where:

$$\mathscr{G}(m;\mu,\sigma) = \frac{1}{\sqrt{2\pi}\sigma}e^{-\frac{1}{2}\left(\frac{m-\mu}{\sigma}\right)^2}, \tag{5.22}$$

$$\mathscr{T}(m;b,c,\mu) = \frac{1}{K}e^{b(m-\mu)}\cdot{\rm Erfc}(c(m-\mu)), \tag{5.23}$$

$$K = \int_{m_1}^{m_2} e^{b(m-\mu)}\cdot{\rm Erfc}(c(m-\mu))dm, \tag{5.24}$$

$${\rm Erfc}(x) = 1-{\rm Erf}(x) = \frac{2}{\sqrt{\pi}}\int_x^{+\infty} e^{-t^2}dt. \tag{5.25}$$

We used a sum of two Gaussians to parameterize the bulk of the distribution, while the long lower-mass tail due to the soft photon emission was parameterized with the function $\mathscr{T}(m;b,c,\mu)$. $f_{\rm bulk}$ is the relative fraction of the double Gaussian bulk with respect the total (bulk plus tail), while $1-f_{\rm bulk}$ is the fraction of the tail term. f_1 is the relative fraction of the more abundant Gaussian, labeled with the index 1, with respect to the sum of two Gaussians, while $\sigma_{1(2)}$ is the the width of the Gaussian 1(2). $\delta_{1(2)}$ is the mass shift from the input mass value of the D^0 ($m_{D^0} = 1.8646$ GeV/c^2) in the FMC simulation. The soft photon emission makes the mass distribution asymmetric, and the means of the Gaussians cannot be considered as being the same. For this reasons m_{D^0} is fixed in the parameterization while $\delta_{1(2)}$ is free to vary. In particular the parameterization returned similar

values for δ_1 and δ_2, so we used a single parameter $\delta = \delta_1 = \delta_2$. The parameters vector is defined as $\vec{\theta} \equiv \{f_{\rm bulk}, f_1, \sigma_1, \sigma_2, \delta_1, \delta_2, b, c\}$ and it is extracted by fitting the FMC simulated invariant mass distribution. Figure 5.14 shows the parameterization of the invariant mass distribution simulated using the FMC while the parameters are reported in tab. 5.5.

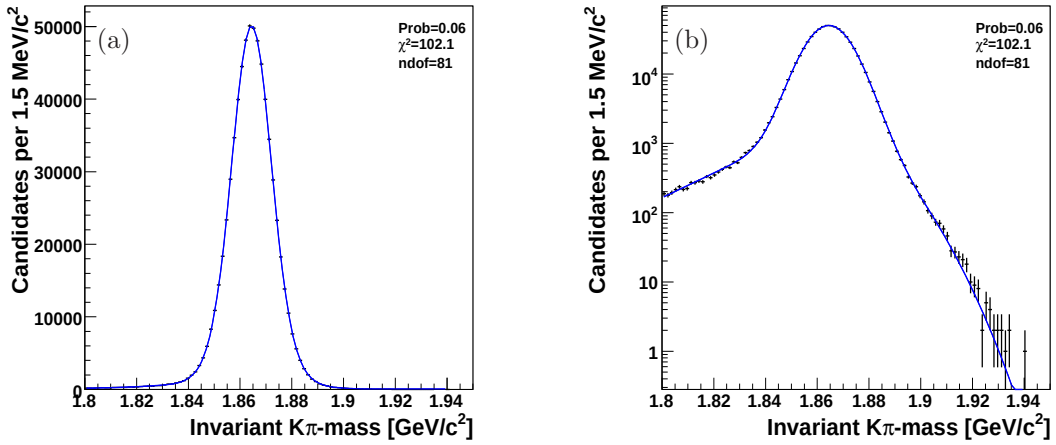


Figure 5.14: Mass template of the $D^0 \to K^-\pi^+$ decays. Parameterization of the invariant $K\pi$-mass distribution for the $D^0 \to K^-\pi^+$ decays using the Fast Monte Carlo. Linear scale on y-axis (a), logarithmic scale on y-axis (b).

Parameter	Units	Value
$f_{\rm bulk}$	–	0.918 ± 0.005
f_1	–	0.490 ± 0.051
σ_1	$[\mathrm{MeV}/c^2]$	6.88 ± 0.10
σ_2	$[\mathrm{MeV}/c^2]$	9.02 ± 0.15
$\delta = \delta_1 = \delta_2$	$[\mathrm{MeV}/c^2]$	-0.61 ± 0.13
b	$[\mathrm{GeV}/c^2]^{-1}$	52.8 ± 2.1
c	$[\mathrm{GeV}/c^2]^{-1}$	49.9 ± 1.1

Table 5.5: Parameterization of the invariant $K\pi$-mass of the $D^0 \to K^-\pi^+$ simulated events. See fig. 5.14.

After extracting the parameterization of the $D^0 \to K^-\pi^+$ signal from the FMC we performed a binned-χ^2 fit of the data in invariant $K\pi$-mass with the following p.d.f.:

$$N \cdot \wp(m_{K\pi}; N, f_s, a_0) = N \cdot \Big(f_s \; \wp_s(m_{K\pi}; \vec{\theta}) \; + \; f_d \; \wp_d(m_{K\pi}; \mu_d, \sigma_d) \; + \; (1 - f_s - f_d) \; \wp_b(m_{K\pi}; a_0) \Big) , \tag{5.26}$$

where the absolute normalization N, the relative signal fraction f_s, the background shape a_0 were determined by the fit. $\wp_s(m_{K\pi}; \vec{\theta})$ is the signal p.d.f. correctly normalized in the mass fit domain

Parameter	Units	(I)	(II)	Δ [%]
$f_{\rm bulk}$	–	0.918	0.910 ± 0.032	0.87
f_1	–	0.490	0.490	
σ_1	[MeV/c^2]	6.88	6.71 ± 0.02	2.47
σ_2	[MeV/c^2]	9.02	9.63 ± 0.02	6.76
$\delta = \delta_1 = \delta_2$	[MeV/c^2]	-0.61	-0.61	
b	[GeV/c^2]$^{-1}$	52.8	52.8	
c	[GeV/c^2]$^{-1}$	49.9	49.9	
f_s	–	0.9719 ± 0.0003	0.9824 ± 0.0004	1.08
a_0	–	-2.4 ± 0.3	-4.7 ± 0.4	48
Δ_m	[MeV/c^2]	0.798 ± 0.008	0.804 ± 0.008	0.74
χ^2/ndof	–	1254.3/50	60.7/47	

Table 5.6: Fit on $D^0 \to K^-\pi^+$ data. (I) The signal shape is completely fixed from the FMC, we fitted only parameters f_s, a_0, δ_m. (II) Some parameters of the signal shape are free to vary: f_s, a_0, δ_m plus $f_{\rm bulk}$, σ_1, σ_2 (II). $\Delta = \frac{\text{(I)}-\text{(II)}}{\text{(I)}}$. See fig. 5.15.

$[1.820, 1.900]$ GeV/c^2 and it was completely determined from the FMC (see above eq. (5.21)). The functions $\wp_d$ and $\wp_b$ are

- $\wp_d(m_{K\pi}; \mu_d, \sigma_d) = \frac{1}{\int_{1.820}^{1.900} \frac{1}{\sqrt{2\pi}\sigma_d} e^{-\frac{1}{2}(\frac{m_{K\pi}-\mu_d}{\sigma_d})^2} dm_{K\pi}} (\frac{1}{\sqrt{2\pi}\sigma_d} e^{-\frac{1}{2}(\frac{m_{K\pi}-\mu_d}{\sigma_d})^2})$,
- $\wp_b(m_{K\pi}; a_0) = \frac{1}{\int_{1.820}^{1.900}(1+a_0 m_{K\pi}) dm_{K\pi}} (1 + a_0 m_{K\pi})$.

$\wp_d(m_{K\pi}; \mu, \sigma)$ parameterizes the $\mathcal{O}(10^{-3})$ contamination of the doubly-Cabibbo-suppressed mode $D^0 \to K^+\pi^-$ [128]. The uncorrected mass assignment to the decay products inflates the width of the mass distribution by about a factor ten, with respect to the Cabibbo-favored mode $D^0 \to K^-\pi^+$ reconstructed with the correct mass assignment. μ_d and σ_d were extracted from the simulation and are fixed in the fit. f_d is defined as

$$f_d = f_s R_d \int_{1.820}^{1.900} \frac{1}{\sqrt{2\pi}\sigma_d} e^{-\frac{1}{2}(\frac{m_{K\pi}-\mu_d}{\sigma_d})^2} dm_{K\pi}, \tag{5.27}$$

where $R_d = \mathcal{B}(D^0 \to K^+\pi^-)/\mathcal{B}(D^0 \to K^-\pi^+) = 4.05 \cdot 10^{-3}$ was measured by CDF [128]. $\wp_b(m_{K\pi}|a_0)$ is the background parameterization (linear function), correctly normalized in the mass fit domain. To keep into account the global mass scale shift we fitted an additional parameter Δ_m by substituting $m_{K\pi} \to m_{K\pi} + \Delta_m$.

We start by fitting the invariant $K\pi$-mass distribution of the $D^0 \to K^-\pi^+$ decays, by using a signal shape completely fixed by the parameterization extracted from the FMC (tab. 5.5). Only the parameters N, f_s, a_0 and the global mass scale Δ_m were allowed to vary. The results of this fit are reported in column (I) of tab. 5.6 while in figs. 5.15(a) and (b) the fit function is superimposed on data. Due to the very high statistics $\chi^2/\text{ndof} = 1254.3/50$ of this fit is poor, but the curve describes the data with a precision unprecedented in previous CDF comparisons between data and simulation

MC. There is no evidence of any presence of an additional tail in the data, a long standing discrepancy. These observations seem to suggest that previously observed mismatches were due to the lack of a good model of soft photon radiation. The large sample of about 1.5M of candidates, provides large sensitivity even to small deviations from the expected mass shape. We performed a second fit, in which we left free to vary three additional parameters related to the signal shape $f_{\rm bulk}$, σ_1, σ_2. The results are reported in column (II) of tab. 5.6 while in figs. 5.15(c) and (d) the fit function is superimposed on the data. The $\chi^2/\text{ndof} = 60.7/47$ of this fit is now very good and the agreement between the FMC and the data is satisfactory. The parameters of the signal shape $f_{\rm bulk}$, σ_1, σ_2 differ from those extracted from FMC of just a few percents (see column Δ of tab. 5.6).

When we allow the additional parameters of the signal shape to vary the background level changes. It is difficult to extract better parameters without a greater knowledge of the background. However the discrepancies of the nominal FMC parameters are so small that it does not appear worthwhile to attempt any tuning unless one needs to model samples containing order $10^5 - 10^6$ signal events, while the samples we are interested in are just order 10^3.

Since our FMC simulates the entire decay chain $D^{*+} \to D^0\pi^+ \to [K^-\pi^+]\pi^+$ we repeated same checks performed on $D^0 \to K^-\pi^+$ also on $D^{*+} \to D^0\pi^+$ decay. These confirmed our accurate understanding of the D^{*+} mass line shape with approximately the same precision found on the D^0 mass [129]. In this case ($H^\pm \to P_1^\pm P_2^0 + n\gamma$), the formulas used to simulate the FSR are similar, but not equal to those used in this thesis ($H^0 \to P_1^+ P_2^- + n\gamma$) and can be found in Ref. [124].

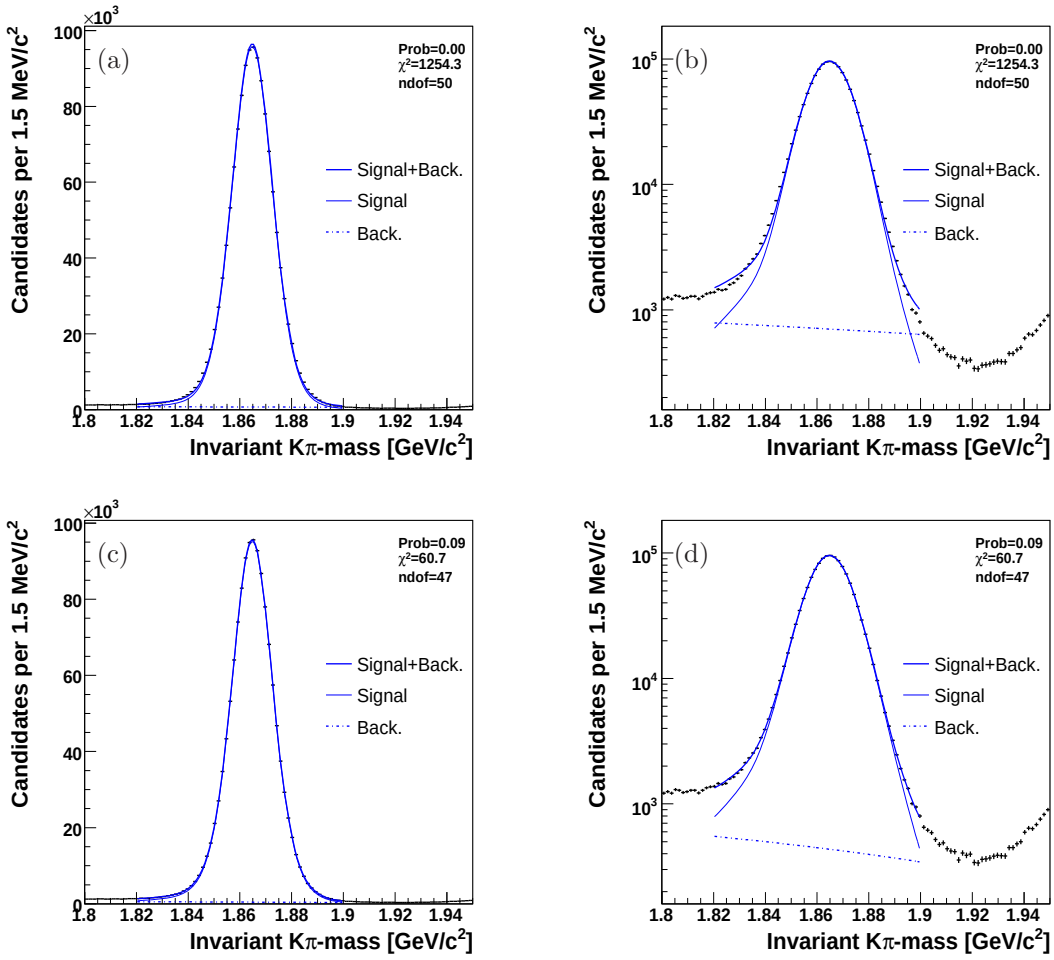


Figure 5.15: Check of the mass line shape template using a data sample of $D^0 \to K^-\pi^+$ decays from reconstructed $D^{*+} \to D^0\pi^+ \to [K^-\pi^+]\pi^+$. Invariant $K\pi$-mass distribution. The signal p.d.f. $\wp_s(m_{K\pi};\vec{\theta})$ is completely fixed from FMC in (a,b), the parameters σ_1, σ_2, $f_{\rm bulk}$ of $\wp_s(m_{K\pi};\vec{\theta})$ are free to vary in the fit in (c,d). Linear scale on y-axis (a,c), logarithmic scale on y-axis (b,d).

Chapter 6

Fit of composition

This chapter describes how the kinematic and PID information, discussed in previous chapters was combined in a maximum Likelihood fit to statistically determine the composition of the $B^0_{(s)} \to h^+h'^-$ sample.

6.1 Discriminating observables

A good choice of the discriminating observables is crucial to fully exploit the available information and to keep a simple analytic expression of the Likelihood. The goal is to get most of the available information using the minimum number of observables. In addition, the more independent the chosen observables are, the simpler is factorizing and modeling the joint probability density.

We represent the kinematic and PID information using the following five discriminating observables:

1. $\boldsymbol{m_{\pi\pi}}$ – invariant mass of the pair of final state particles with pion mass assignments;
2. $\boldsymbol{\alpha}$ – signed momentum imbalance between the two particles;
3. $\boldsymbol{p_{\mathrm{tot}}}$ – scalar sum of the particle momenta;
4. $\boldsymbol{\kappa_1}$ – kaonness (function of the dE/dx) of the lower-momentum particle;
5. $\boldsymbol{\kappa_2}$ – kaonness of the higher-momentum particle.

Particle identification information was summarized with one observable for each charged particle, the "kaonness" κ, defined as (see also sec. 4.4.7)

$$\kappa = \frac{dE/dx_{\mathrm{obs}} - dE/dx_{\pi}}{dE/dx_{K} - dE/dx_{\pi}}. \tag{6.1}$$

6.2 Likelihood function

The Likelihood function $\mathscr{L}$ is the product of the Likelihoods $\mathscr{L}_i$ of all events:

$$\mathscr{L}(\vec{\theta}) = \prod_{i=1}^{N} \mathscr{L}_i(\vec{\theta}|\vec{x}_i) \tag{6.2}$$

where the index i runs over the events. N is the total number of events passing the final selection, $\vec{\theta}$ is the vector of parameters that we want to estimate, $\vec{x}$ is the vector of the discriminating observables $\vec{x}_i = \{m_{\pi\pi}, \alpha, p_{\rm tot}, \kappa_1, \kappa_2\}_i$.
The Likelihood of each event is written as the sum of a signal term and a background term:

$$\mathscr{L}_i = b \cdot \mathscr{L}_i^{\rm bck} + (1-b) \cdot \mathscr{L}_i^{\rm sig}. \tag{6.3}$$

The index sig (bck) labels the part of the function that describes the signal (background) term; b is the fraction of background events and $1-b$ is the fraction of the $B^0_{(s)} \to h^+h^{'-}$ plus $\Lambda^0_b \to ph^-$ events ($(b \in \vec{\theta})$). The Likelihood of the signal events is factorized as a product of three p.d.f.'s:

$$\mathscr{L}^{\rm sig} = \sum_{j=1}^{s} f_j \cdot \wp_j^m(m_{\pi\pi}|\alpha, p_{tot}) \cdot \wp_j^p(\alpha, p_{\rm tot}) \cdot \wp_j^{\rm PID}(\kappa_1, \kappa_2|\alpha, p_{\rm tot}), \tag{6.4}$$

in which the index j runs over the twelve expected components: $B^0 \to \pi^+\pi^-$, $B^0 \to K^+\pi^-$, $\overline{B}^0 \to K^-\pi^+$, $B^0_s \to K^-\pi^+$, $\overline{B}^0_s \to K^+\pi^-$, $B^0_s \to K^+K^-$, $B^0 \to K^+K^-$, $B^0_s \to \pi^+\pi^-$, $\Lambda^0_b \to p\pi^-$, $\overline{\Lambda}^0_b \to \overline{p}\pi^+$, $\Lambda^0_b \to pK^-$, $\overline{\Lambda}^0_b \to \overline{p}K^+$ [1]. The parameters f_j are their fractions (of the total signal), and are determined by the fit. From the $(s-1)$ independent fractions resulting by the normalization condition,

$$f_s = 1 - \sum_{j=1}^{s-1} f_j, \tag{6.5}$$

we determined the yield of each mode. We conventionally label as $\wp^m$ the term that describes the invariant-mass distributions ("mass term"), $\wp^p$ the term that describes the momentum distributions ("momentum term"), and $\wp^{\rm PID}$ the term that models the dE/dx density ("PID term"). This factorization is not trivial since the three terms of the p.d.f. are inter-related by the dependencies between mass, momentum, and dE/dx observables.

The Likelihood of the background factorizes in a similar way to the signal term, and it consists of the sum of two contributions:

$$\mathscr{L}^{\rm back} = \sum_{l={\rm A,E}} f_l \cdot \wp_l^m(m_{\pi\pi}|\alpha, p_{\rm tot}) \cdot \wp_l^p(\alpha, p_{\rm tot}) \cdot \wp_l^{\rm PID}(\kappa_1, \kappa_2|p_{\rm tot}, \alpha), \tag{6.6}$$

where the index l runs over the different kinds of background, combinatorial ($l = E$) and physics ($l = A$) background. The parameters f_l are their fractions (of the total background) and are determined by the fit. From the normalization condition results $f_{\rm E} = 1 - f_{\rm A}$.

In Equations (6.3)–(6.6) the functional dependence on the vector $\vec{\theta}$ was omitted, since in the equations we wrote explicitly some terms of this vector, as f_i, $f_{\rm A}$ and b.

[1] C-conjugate modes are considered distinct for decays in $K\pi$, $p\pi$ and pK final states that are distinguishable on the basis of the final particle types.

6.3 Probability density function of the signal mass term

As studied in the previous chapters the invariant $\pi\pi$-mass distribution of the non-$\pi\pi$ components depends on the mass shift, which is a function of the momentum imbalance α and of the scalar sum of the momenta $p_{\rm tot}$ of the decay products. It is due to mis-assigned masses of the outgoing particles, as discussed in sec. 4.3. We accounted for this effect by writing a $\pi\pi$-mass p.d.f. which is conditional for a given momentum imbalance and scalar sum of the momenta. An other fundamental aspect is the effect of the finite momentum resolution of the detector which includes also the soft photon emission in the final state, as discussed in chap. 5.

Following the same strategy as in sec. 5.5, we parameterized the invariant mass distribution m_j, computed with the correct mass assignment ($j = B^0 \to \pi^+\pi^- \Longrightarrow m_j = m_{\pi\pi}$; $j = B^0 \to K^+\pi^- \Longrightarrow m_j = m_{K\pi}$; etc.), using the following p.d.f. (see eq. (5.21)):

$$\begin{aligned}\wp_j^m(m_j) &= f^j_{\rm bulk}\left[f_1^j \mathscr{G}(m_j; m_{H_j^0}+\delta_1^j, \sigma_1^j) + (1-f_1^j)\mathscr{G}(m_j; m_{H_j^0}+\delta_2^j, \sigma_2^j)\right] \\ &\quad +(1-f^j_{\rm bulk})\mathscr{T}(m_j; b^j, c^j, m_{H_j^0}+\delta_1^j) \end{aligned} \tag{6.7}$$

where:

$$\mathscr{G}(m;\mu,\sigma) = \frac{1}{\sqrt{2\pi}\sigma} e^{-\frac{1}{2}\left(\frac{m-\mu}{\sigma}\right)^2} \tag{6.8}$$

$$\mathscr{T}(m;b,c,\mu) = \frac{1}{K} e^{b(m-\mu)} \cdot \mathrm{Erfc}(c(m-\mu)) \tag{6.9}$$

$$K = \int_{m_1}^{m_2} e^{b(m-\mu)} \cdot \mathrm{Erfc}(c(m-\mu))dm \tag{6.10}$$

$$\mathrm{Erfc}(x) = 1 - \mathrm{Erf}(x) = \frac{2}{\sqrt{\pi}} \int_x^{+\infty} e^{-t^2} dt. \tag{6.11}$$

in which the index j runs over all components. We used a sum of two Gaussians to parameterize the bulk of the distribution, while the long lower-mass tail due to the soft photon emission is parameterized with the function in eq. (6.9). $f^j_{\rm bulk}$ is the relative fraction of the double-Gaussian bulk with respect to the total (bulk plus tail), while $1 - f^j_{\rm bulk}$ is the fraction of the tail term. f_1^j is the relative fraction of the more abundant Gaussian labeled with the index 1 with respect to the sum of two Gaussians, while $\sigma^j_{1(2)}$ is the the width of the Gaussian 1(2). $\delta^j_{1(2)}$ is the mass shift from the mass value of the hadron H_j^0 ($j = B^0 \to \pi^+\pi^- \Longrightarrow m_{H_j^0} = m_{B^0}$; $j = B_s^0 \to K^+K^- \Longrightarrow m_{H_j^0} = m_{B_s^0}$; etc.). The values of the parameters $\{f_{\rm bulk}, f_1, \sigma_1, \sigma_2, \delta_1, \delta_2, b, c\}_j$ are fixed in the fit; they were extracted from the FMC simulation (chap. 5) which accurately accounts all resolution effects.

We simulated each decay component j and we parameterized the invariant mass distribution. The probability density function in eq. (6.7) is correctly normalized to one in the mass interval $[m_1, m_2]$ for each component. Figures 6.1–6.4 show the invariant mass kinematic templates for all the $B^0_{(s)} \to h^+h'^-$ and $\Lambda_b^0 \to ph^-$ decay modes. For the $\Lambda_b^0 \to ph^-$ modes we turned off the soft photon emission because of the presence of a proton in the final state. The theoretical equations of sec. 5.4.1 used to include the Final State Radiation in the FMC simulation are valid only if the final state of the decay is composed by two pseudo-scalar particles. The expected yield of $\Lambda_b^0 \to ph^-$ decays are about a factor 10 smaller than the $B^0 \to \pi^+\pi^-$ yield, thus we neglect the effect of the FSR (already small) for these rare modes.

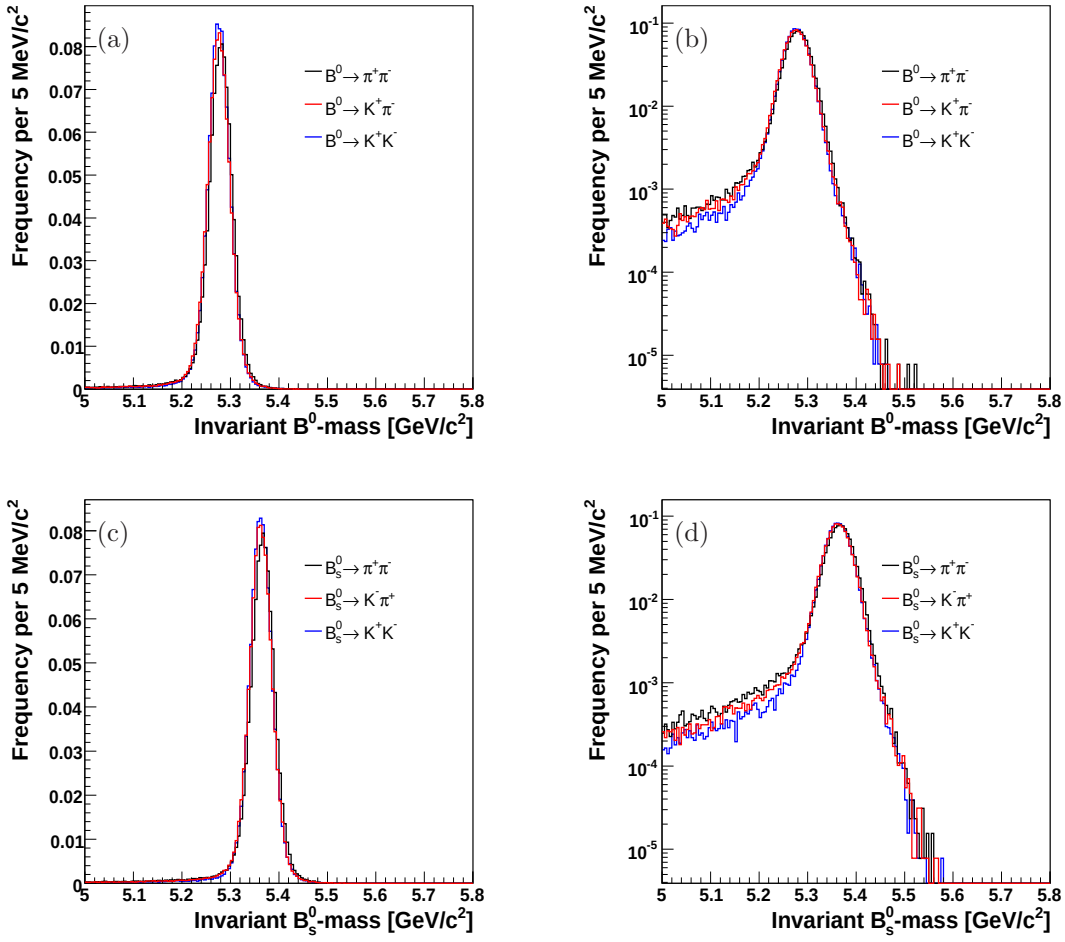


Figure 6.1: Invariant mass distribution of the simulated $B^0_{(s)} \to \pi^+\pi^-$ (black), $B^0 \to K^+\pi^-$ and $B^0_s \to K^-\pi^+$ (red), $B^0_{(s)} \to K^+K^-$ (blue) histograms. On the left linear scale, on the right logarithmic scale.

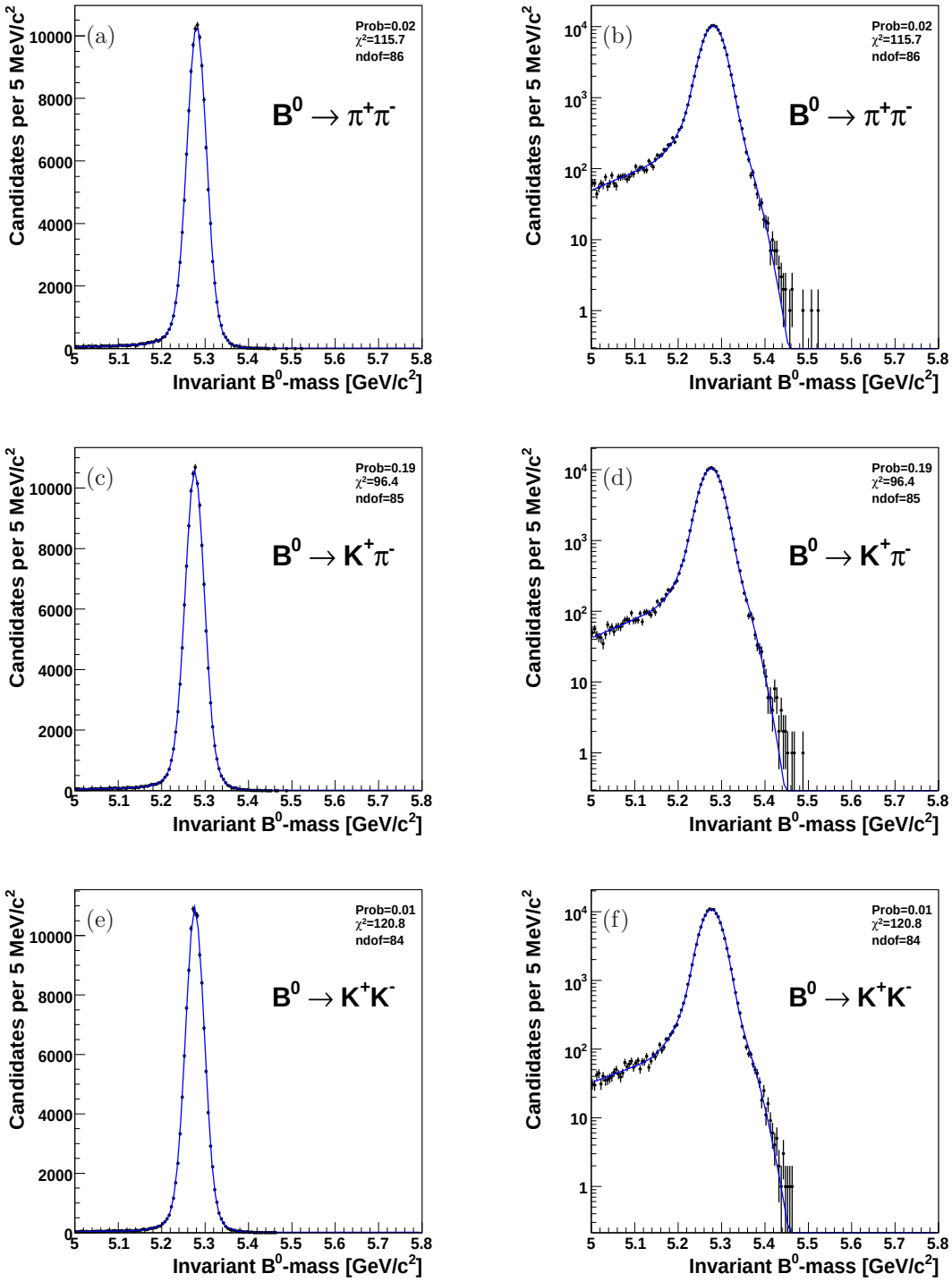


Figure 6.2: Invariant mass distribution of the simulated $B^0 \to h^+h'^-$ decays . On the left linear scale, on the right logarithmic scale. The template is overlaid.

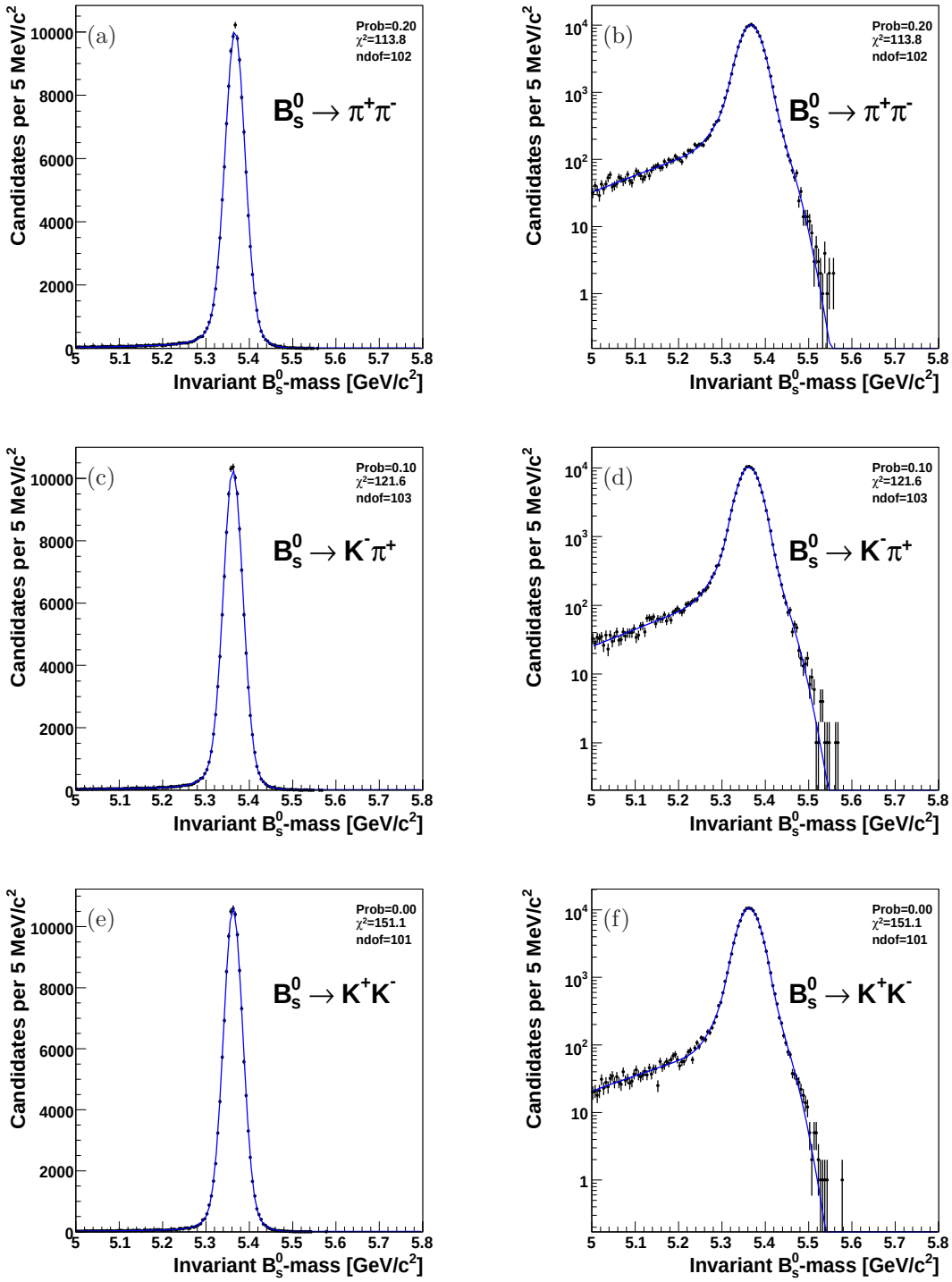


Figure 6.3: Invariant mass distribution of simulated $B_s^0 \to h^+h'^-$ decays . On the left linear scale, on the right logarithmic scale. The template is overlaid.

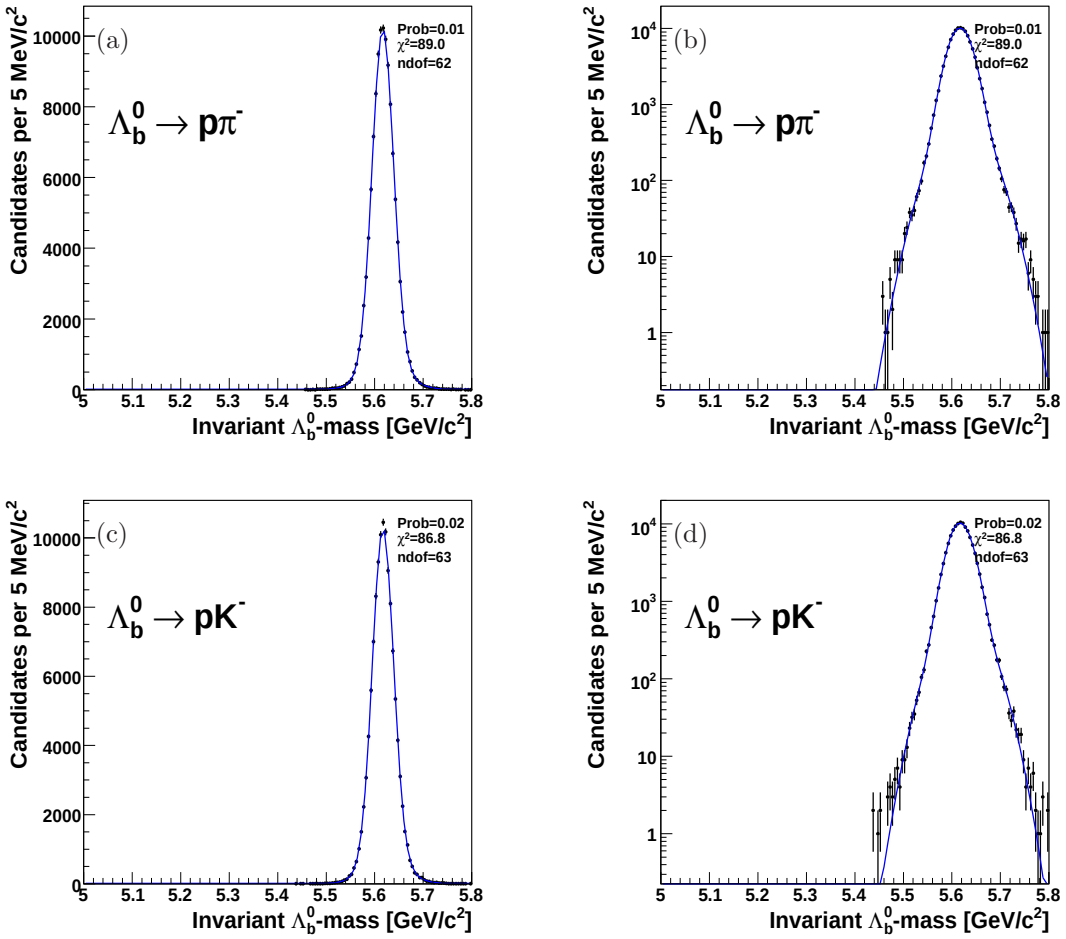


Figure 6.4: Invariant mass distribution of the simulated $\Lambda_b^0 \to ph^-$ decays . On the left linear scale, on the right logarithmic scale. The template is overlaid.

The p.d.f of the signal mass term $\wp_j^m(m_j)$ was written, in eq. (6.7), as a function of different mass observables m_j, for each decay mode (j) we have a different invariant mass variable. In sec. 4.3 we discussed how to write the different mass assignments m_j as a function of a single invariant mass observable $m_{\pi\pi}$ and the momenta observables α and $p_{\rm tot}$. For each component jth we can compute the correct invariant mass m_j but also the invariant $\pi\pi$-mass $m_{\pi\pi}$, and then we can write:

$$\begin{aligned} m_j - \langle m_j \rangle &= m_{\pi\pi} - \langle m_{\pi\pi} \rangle, \\ m_j - M_{H_j^0} &= m_{\pi\pi} - \mathcal{M}_j(\alpha, p_{\rm tot}), \end{aligned} \tag{6.12}$$

where $\mathcal{M}_j(\alpha, p_{\rm tot})$ is the expected average-value of the invariant mass computed with the pion hypothesis for both particles at any given momentum imbalance α and scalar sum of momenta $p_{\rm tot}$ (see tab. 4.1 in sec. 4.3). With this substitution we can write the probability density of the signal mass term as follows:

$$\begin{aligned} \wp_j^m(m_{\pi\pi}|\alpha, p_{\rm tot}) &= f^j_{\rm bulk} \Big[f_1^j \mathscr{G}(m_{\pi\pi}; \mathcal{M}_j(\alpha, p_{\rm tot}; m_{H_j^0} + \delta_1^j), \sigma_1^j) \\ &\qquad + (1 - f_1^j) \mathscr{G}(m_{\pi\pi}; \mathcal{M}_j(\alpha, p_{\rm tot}; m_{H_j^0} + \delta_2^j), \sigma_2^j) \Big] \\ &\quad + (1 - f^j_{\rm bulk}) \mathscr{T}(m_{\pi\pi}; b^j, c^j, \mathcal{M}_j(\alpha, p_{\rm tot}; m_{H_j^0} + \delta_1^j)). \end{aligned} \tag{6.13}$$

For each observed value of invariant $\pi\pi$-mass, of momentum imbalance α, and of scalar sum of momenta $p_{\rm tot}$, we assumed the mass distributed with the function described in eq. (6.7) spread around the specific average-value expected at that momentum imbalance and scalar sum of momenta, $\mathcal{M}(\alpha, p_{\rm tot})$. Each candidate with an invariant $\pi\pi$-mass $m_{\pi\pi}$, momentum imbalance α and scalar sum of momenta $p_{\rm tot}$, contributes to the mass p.d.f. of the jth signal mode with the term reported in eq. (6.13).

Input masses

For each decay mode, we included the analytic expression of $\mathcal{M}_j(\alpha, p_{\rm tot})$ shown in tab. 4.1, which depends on the masses m_{B^0}, $m_{B_s^0}$, $m_{\Lambda_b^0}$, m_K, m_π and m_p as external inputs. We used the world average values [32] for the masses of charged pion and kaon and for the mass of the proton. For the $B^0_{(s)}$ mesons and Λ_b^0, we used the masses measured by CDF in Run II: $m_{B^0} = 5279.63 \pm 0.53$ (*stat.*) ± 0.33 (*syst.*) MeV/c^2, $m_{B_s^0} = 5366.01 \pm 0.73$ (*stat.*) ± 0.33 (*syst.*) MeV/c^2 and $m_{\Lambda_b^0} = 5619.7 \pm 1.2$ (*stat.*) ± 1.2 (*syst.*) MeV/c^2 [106]. Using the masses measured with the same apparatus and reconstruction code as for $B^0_{(s)} \to h^+ h'^-$ data allows to cancel common systematic uncertainties. Therefore, only the statistical uncertainty on the measurement of b-hadron masses of Ref. [106] contributes to the systematic uncertainty on our measurement (see sec. 12.3).

The input masses of the $B^0_{(s)}$ mesons and Λ_b^0 baryon cannot be used directly in the analytic expression of $\mathcal{M}_j(\alpha, p_{\rm tot})$ shown in tab. 4.1, but they have to be corrected for the bias introduced by the energy loss correction, occurring during the track reconstruction algorithm, see sec. 5.2. The official offline reconstruction code compensates for the energy losses of all tracks through the detector material using a standard pion mass hypothesis [2]. This step introduces a bias on the invariant mass when one or both final particles are not pions. We evaluated in sec. 5.2 the effect of this bias on the

[2] This is not the same thing as assigning the pion mass to tracks when computing the invariant mass of a system of particles.

invariant mass distribution. The invariant mass of each component j is shifted by a quantity $\delta^j_{\rm Kal}$, reported in tab. 5.3. Thus in the analytic expression of $\mathcal{M}_j(\alpha, p_{\rm tot})$ shown in tab. 4.1, we replaced $m_{H^0_j} \to m_{H^0_j} + \delta^j_{\rm Kal}$ where the index j runs over all the possible signal modes.

Momentum dependence of the mass resolution

Up to this point, we treated the invariant mass resolution as independent of the momentum observables, but in reality, the invariant mass resolution depends on the momentum of the mother particle and therefore, on the momenta of the decay products. We explicitly introduced this dependence to keep into account the changes of the mass resolution as a function of our momentum observables α and $p_{\rm tot}$ (about 2 MeV/c^2 as a function of α and about 5 MeV/c^2 as a function of $p_{\rm tot}$, spanning the range $5.5 \lesssim p_{\rm tot} \lesssim 35$ GeV/c).

The choice of α and $p_{\rm tot}$ as variables in the fit rather than equivalent p_1 and p_2 variables turns out to be very convenient in this case, because α and $p_{\rm tot}$ are almost independent observables, and this is reflected in the factorizability of the momenta mass resolution dependence. The mass resolution can be written as the product of two independent functions of α and $p_{\rm tot}$: $\sigma(\alpha, p_{\rm tot}) \approx \sigma_\alpha(\alpha) \cdot \sigma_{p_{\rm tot}}(p_{\rm tot})$.

In our case, the invariant mass distribution is not a simple Gaussian function. It is the sum of a double-Gaussian bulk ($\sigma^j_{1(2)}$ is the width of the Gaussian 1(2)) and a long lower-mass tail due to the soft photon emission $\mathscr{T}$ (see eq. (6.13)). To parameterize these effects we generated samples of $B^0_{(s)} \to h^+ h^{'-}$ and $\Lambda^0_b \to p h^-$ decays, using a modified Fast Monte Carlo Simulation (see sec. 5.3), in which the invariant mass distribution was generated as a Gaussian function and not like $\wp^m_j(m_j)$. This was achieved by turning off the soft photon emission in the final state and the non-Gaussian contribution to the curvature resolution, since we were interested in the global dependence of the mass resolution on α and $p_{\rm tot}$. Thus we fitted the invariant mass distribution slices as a function of α and $p_{\rm tot}$ respectively, with a Gaussian distribution, and then we fitted the α and $p_{\rm tot}$ shapes for each signal decay mode. Figure 6.5 shows the invariant mass resolution in the Gaussian approximation, respectively as a function of α and p_{tot} for $B^0 \to \pi^+\pi^-$ and $B^0 \to K^+\pi^-$ decay mode. The α dependence was parameterized with a fourth order degree polynomial while the $p_{\rm tot}$ dependence with a straight line. The two dependencies are factorizable to a good approximation.

The values σ^j_1 and σ^j_2 extracted in the parameterization of $\wp^m_j(m_j)$ (see eq. (6.7)) are averaged along all momenta: $\sigma^j_1 \to \sigma^j_{01}$ and $\sigma^j_2 \to \sigma^j_{02}$. Then we introduced the (α, p_{tot}) dependence in the fit and the new momentum dependent values for σ^j_1 and σ^j_2 to insert in eqs. (6.7) and (6.13) become:

$$\begin{aligned}
\sigma^j_1 &= \sigma^j_{01} \cdot \left(1 + \frac{a^j_1}{\sigma^j_{01}}\alpha + \frac{a^j_2}{\sigma^j_{01}}\alpha^2 + \frac{a^j_3}{\sigma^j_{01}}\alpha^3 + \frac{a^j_4}{\sigma^j_{01}}\alpha^4\right) \cdot \left(1 + \frac{b^j_1}{\sigma^j_{01}}(p_{\rm tot} - \langle p_{\rm tot}\rangle_{p_{\rm tot}})\right) \\
\sigma^j_2 &= \sigma^j_{02} \cdot \left(1 + \frac{a^j_1}{\sigma^j_{02}}\alpha + \frac{a^j_2}{\sigma^j_{02}}\alpha^2 + \frac{a^j_3}{\sigma^j_{02}}\alpha^3 + \frac{a^j_4}{\sigma^j_{02}}\alpha^4\right) \cdot \left(1 + \frac{b^j_1}{\sigma^j_{02}}(p_{\rm tot} - \langle p_{\rm tot}\rangle_{p_{\rm tot}})\right)
\end{aligned} \tag{6.14}$$

where the index j runs over all possible signal modes, pol4=$\sum_{i=0}^{4} a_i \cdot \alpha$, pol1=$\sum_{i=0}^{1} b_i \cdot p_{\rm tot}$, $\langle p_{\rm tot}\rangle_{p_{\rm tot}}$ is the average $p_{\rm tot}$ value.

All the possible effects related to a dependence of the Final State Radiation on α and $p_{\rm tot}$ were neglected since they are second order effects and much smaller than the momentum variation of the

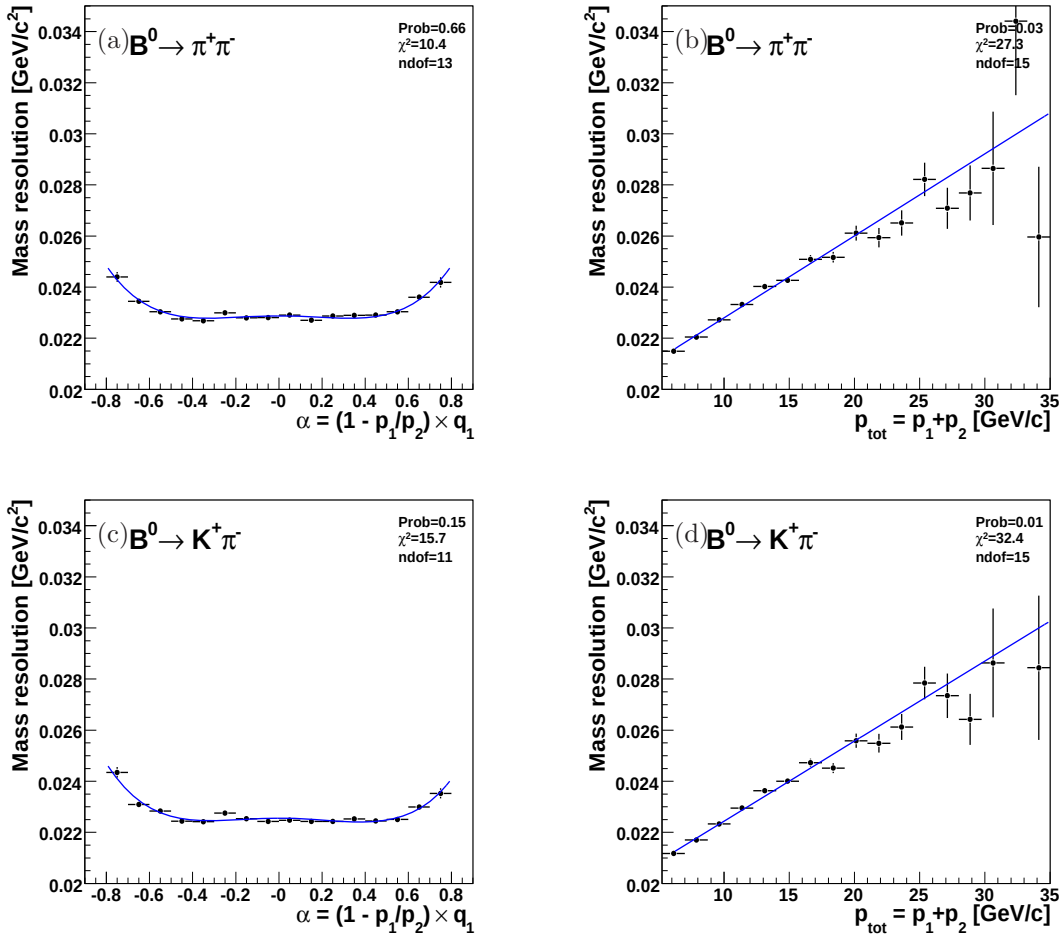


Figure 6.5: Dependence of the mass resolution on the momentum observables α and $p_{\rm tot}$ for the $B^0 \to \pi^+\pi^-$ and $B^0 \to K^+\pi^-$ decays. (a,c) mass resolution versus α parameterized with a fourth order degree polynomial (pol4), even terms are fixed to 0 for $B^0 \to \pi^+\pi^-$, $B^0 \to K^+K^-$, $B_s^0 \to \pi^+\pi^-$, $B_s^0 \to K^+K^-$. (b,d) mass resolution versus p_{tot} parameterized with a first order degree polynomial (pol1).

double Gaussian bulk of the invariant mass distribution.

6.4 Probability density function of the background mass term

In sec. 3.5 we described the main backgrounds which contribute to our data sample. We divided them in two different kinds: the combinatorial background (E) and physics background (A).

6.4.1 Combinatorial background (E)

In order to choose an appropriate functional form for the p.d.f of the combinatorial background, we studied samples of two generic random tracks extracted from the same $B^0_{(s)} \to h^+h'^-$ data. We looked at the distributions of the events passing the final selection (continuous line in fig. 6.6, labeled as "signal sample") and the corresponding distribution of the events with "opposite-χ^2_{3D}" requirement. The opposite-χ^2_{3D} sample contains events that pass the final selections of tab. 3.3 except for the requirement on the 3-D vertex quality, which is inverted to $\chi^2_{3D} > 35$ for the loose selection and inverted to $\chi^2_{3D} > 20$ for the tight selection (see fig. 6.6, dashed line). The opposite-χ^2_{3D} sample is enriched of "unphysical" decays, i. e., decays which have two tracks with an identical kinematics on the transverse plane to the $B^0_{(s)} \to h^+h'^-$ modes but coming from two distinct heavy-flavors in the event, which have sizable impact parameter but are separated along the z direction. These thresholds

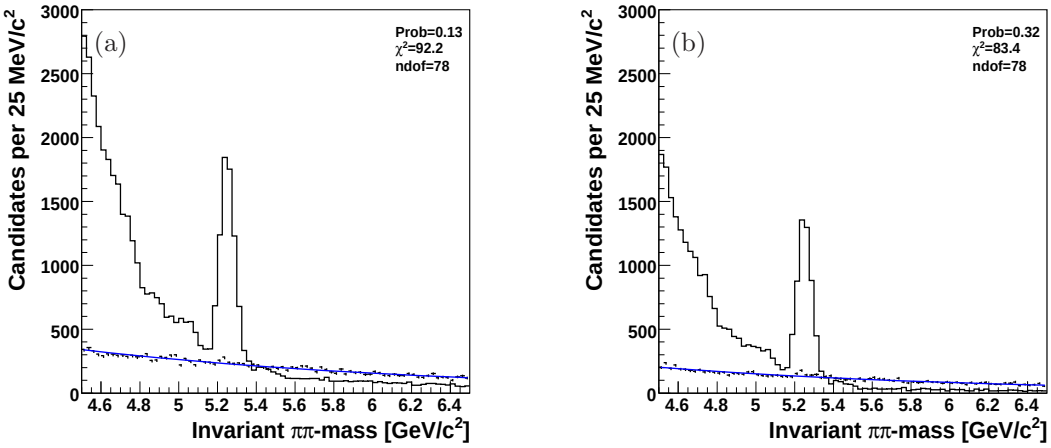


Figure 6.6: Invariant $m_{\pi\pi}$-mass distribution of the events passing the final optimized selection (continuous line). Loose cuts (a) and tight cuts (b). Invariant $m_{\pi\pi}$-mass distribution of events passing the final optimized selection with an opposite requirement on the 3-D vertex quality (point with error), $\chi^2_{3D} > 35$ (a), and $\chi^2_{3D} > 20$ (b). The exponential fit function is overlaid.

were chosen to remove as much as possible the contamination of $B^0_{(s)} \to h^+h'^-$ signal events and to obtain a reasonable statistics of background events. The invariant-mass shape of these random pairs of tracks is not completely independent of their χ^2_{3D}; thus, the opposite-χ^2_{3D} sample provides only an useful qualitative model (exponential) of the shape of the combinatorial background of the signal sample. For these reasons the invariant $m_{\pi\pi}$-mass of the combinatorial background was modeled with a decreasing exponential, whose slope is dominated by the events lying at higher masses than the peak (right-hand side of the signal):

$$\wp^m_E(m_{\pi\pi}|\alpha, p_{\rm tot}; c_{\rm E}) = \frac{1}{\int_a^b e^{c_{\rm E} m_{\pi\pi}} dm_{\pi\pi}} \cdot e^{c_{\rm E} m_{\pi\pi}}, \tag{6.15}$$

and in the central fit, the slope $c_{\rm E}$ of the combinatorial background mass shape is free to vary.

6.4.2 Physics background (A)

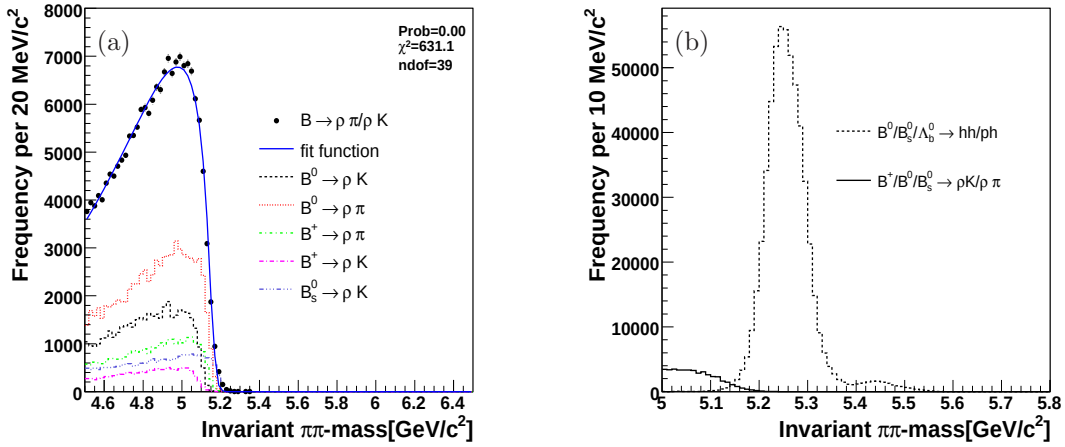


Figure 6.7: Invariant $\pi\pi$-mass distribution of simulated $B \to \rho\pi/\rho K$ decay modes and of the sum of all simulated $B \to \rho\pi/\rho K$ modes, the fit function (eq. (6.16)) is overlaid (a). Comparison of simulated $B \to \rho\pi/\rho K$ background modes and $B^0_{(s)} \to h^+h^{'-}(\Lambda^0_b \to ph^-)$ signal modes (b).

A change of the slope of the mass distribution of the signal sample, at masses just below the signal mass, clearly indicates an additional background source with an $L_{\rm T}$ distribution biased towards positive values. This contribution is readily interpreted as mis-reconstructed b-hadron decays. These are multi-body b-hadron decays, where only two tracks were reconstructed, resulting in the typical shoulder-shape, that is suppressed around 5.15 GeV/c^2, because their contribution is limited to the $m_{\pi\pi} < m_{B^0_{(s)}} - m_\pi$ region for kinematic reasons.

The main contribution to the partially-reconstructed heavy flavor decays is due to the coming from decay modes $B^+ \to h_1^+h_2^-h_3^+$, $B^0 \to h_1^+h_2^-h_3^0$ and $B_s^0 \to h_1^+h_2^-h_3^0$, where $h = \pi$ or K. In particular, they include also all the decay modes involving an intermediate resonance as a ρ or a K^* meson plus a pion or a kaon: $B^+ \to \rho^-\pi^+$, $B^+ \to \rho^0K^+$, $B^0 \to \rho^\mp\pi^\pm$, $B^0 \to \rho^-K^+$, $B_s^0 \to \rho^\mp\pi^\pm$, $B_s^0 \to \rho^+K^-$ (where $\rho \to \pi\pi$) and $B^+ \to K^{*0}\pi^+$, $B^+ \to K^{*+}\pi^0$, $B^0 \to K^{*+}\pi^-$, $B^0 \to K^{*0}\pi^0$ (where $K^* \to K\pi$) and many others. Many branching fractions of the decays involving the B^+ and B^0 mesons were measured at the B-Factories [48] while those of the B_s^0 mesons are still unknown with large theoretical uncertainties. A huge amount of computing power would be needed to generate physics background samples of adequate size for analyses like ours, with $\mathcal{O}(10^9)$ rejection factors on background. Hence we chose the simpler, and more reliable, approach of extracting the information on physics background from data, fitting its invariant mass distribution in the fit of composition.

In order to choose an appropriate functional form for the p.d.f of the physics background, we simulated some of the decays listed above, in particular those involving the ρ meson resonance which represent about 50% of the low-mass bump (see fig. 3.4). The invariant $\pi\pi$-mass distribution of the simulated events is shown in fig. 6.7. We summed the contributions according to their relative

branching fractions. For the B^+ and B^0 we used the measured values from [48], for the yet unmeasured B_s^0 modes we used the theoretical predictions [15] and for f_s and f_d we used the latest measurements from [48].

- $\mathcal{B}(B^+ \to \rho^- \pi^+) = (8.7^{+1.0}_{-1.1}) \times 10^{-6}$;
- $\mathcal{B}(B^+ \to \rho^0 K^+) = (4.25^{+0.55}_{-0.56}) \times 10^{-6}$;
- $\mathcal{B}(B^0 \to \rho^\mp \pi^\pm) = (24.0 \pm 2.5) \times 10^{-6}$;
- $\mathcal{B}(B^0 \to \rho^- K^+) = (15.3^{+3.7}_{-3.5}) \times 10^{-6}$;
- $\mathcal{B}(B_s^0 \to \rho^\mp \pi^\pm) = (0.002 - 0.015) \times 10^{-6}$;
- $\mathcal{B}(B_s^0 \to \rho^+ K^-) = (24.5^{+15.2}_{-12.9}) \times 10^{-6}$.

The $m_{\pi\pi}$ distribution of $B \to \rho\pi/\rho K$ was modeled with the convolution of a resolution function, a Gaussian centered in zero with the width of an individual signal mode ($\sigma_{\rm exp} \approx 22$ MeV/c^2), and an Argus function [109], whose cut-off falls just on the left-hand side of the $B^0_{(s)} \to h^+ h^{'-}$ peak:

$$\wp^m_{\rm A}(m_{\pi\pi}|\alpha, p_{\rm tot}; m_{\rm A}, c_{\rm A}) = \mathscr{G}(m_{\pi\pi}; 0, \sigma_{\rm exp}) * \mathscr{A}(m_{\pi\pi}; m_{\rm A}, c_{\rm A}), \tag{6.16}$$

$$\mathscr{A}(m_{\pi\pi}; m_{\rm A}, c_{\rm A}) = \begin{cases} \frac{1}{K_{\rm A}} \cdot \left[m_{\pi\pi} \cdot \sqrt{1 - \left(\frac{m_{\pi\pi}}{m_{\rm A}}\right)^2} \cdot e^{-c_{\rm A} \cdot \left(\frac{m_{\pi\pi}}{m_{\rm A}}\right)^2} \right] & \text{if } m_{\pi\pi} < m_{\rm A}, \\ 0 \quad \text{if } m_{\pi\pi} > m_{\rm A}, \end{cases} \tag{6.17}$$

where the normalization $K_{\rm A}$ is:

$$K_{\rm A} = \int_a^{m_{\rm A}} m_{\pi\pi} \cdot \sqrt{1 - \left(\frac{m_{\pi\pi}}{m_{\rm A}}\right)^2} \cdot e^{-c_{\rm A} \cdot \left(\frac{m_{\pi\pi}}{m_{\rm A}}\right)^2} dm_{\pi\pi} \quad \text{with} \quad a \leq m_{\rm A}. \tag{6.18}$$

Since we expect a similar distribution for all the partially-reconstructed heavy flavor decays which contribute to the physics background, we decided to use the p.d.f reported in eq. (6.16) to model the physics background with the parameters $m_{\rm A}$, $c_{\rm A}$ free to vary. As a further cross-check, we verified that a simple one-dimensional fit of just the mass shape of the $B^0_{(s)} \to h^+ h^{'-}$ candidates yields, for the Argus function, similar estimated parameters as the full composition fit.

6.5 Probability density function of the momentum term

6.5.1 Signal momentum term

The momentum p.d.f. is extracted from the simulated signal samples described in sec. 4.1. Since the signed momentum-imbalance (α) and the scalar sum of momenta ($p_{\rm tot}$) are not independent observables, we used a joint p.d.f., $\wp^p_j(\alpha, p_{\rm tot}; \vec{\theta})$, to model their distribution. Selection requirements and kinematic correlations between the outgoing particles cause the domain and shape of the α distribution to vary as a function of $p_{\rm tot}$. In fact, both momenta (p_1 and p_2) are necessarily larger

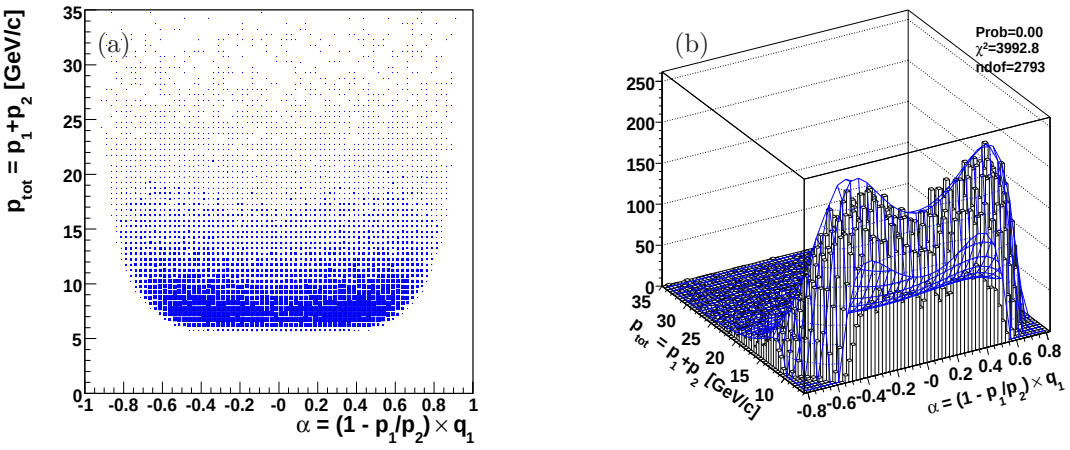


Figure 6.8: Distribution of the scalar sum of the momenta as a function of the signed momentum imbalance in the $B^0 \to \pi^+\pi^-$ simulated decays (a). The joint $(\alpha, p_{\rm tot})$ template is overlaid (b).

than 2 GeV/c, and their sum is larger than 5.5 GeV/c, because of the trigger requirements on their transverse momenta. This translates into the following conditions on α and $p_{\rm tot}$:

$$p_1 = p_{\rm tot}\left(\frac{1-|\alpha|}{2-|\alpha|}\right) > 2 \text{ GeV}/c \quad \text{and} \quad p_{\rm tot} > 5.5 \text{ GeV}/c. \tag{6.19}$$

The other constraint on momentum, $p_2 = p_{\rm tot}/(2-|\alpha|) > 2$ GeV/c, is automatically satisfied if eq. (6.19) holds. The domain of the joint p.d.f. is defined by the requirements of relation (6.19) and it is shown in fig. 6.8(a). The joint p.d.f. is written as the probability density of the scalar sum of momenta, $\wp(p_{\rm tot})$, times the conditional probability density of the signed momentum-imbalance at given $p_{\rm tot}$, $\wp(\alpha|p_{\rm tot})$. We empirically chose a parameterization of both densities, whose parameters were determined by means of a two-dimensional, binned, maximum Likelihood fit of the simulated distributions. An event, whose candidate has an observed scalar sum of momenta $p_{\rm tot}$ and an observed momentum-imbalance α, contributes to the momentum p.d.f. of the $j^{\rm th}$ signal mode with the term:

$$\begin{aligned} \wp_j^p(\alpha, p_{\rm tot}) &= \wp_j(p_{\rm tot}) \times \wp_j(\alpha|p_{\rm tot}) \\ &= \frac{1}{K_j}\left(e^{c_j p_{\rm tot}} \sum_{l=0}^{4} a_{l,j} p_{\rm tot}^l\right) \times \left[\sum_{m=0}^{6} b_{m,j}\alpha^m \left(\frac{p_{\rm tot}-2}{p_{\rm tot}-4}\right)^m\right], \end{aligned} \tag{6.20}$$

where the $p_{\rm tot}$ density is the product of an exponential function times a 4th-degree polynomial, whereas the conditional p.d.f. of α is a 6th-degree polynomial in α scaled by a factor $(p_{\rm tot}-2)/(p_{\rm tot}-4)$ deriving from the constraint on the domain of α given by eq. (6.19). The index j of the a, b, and c parameters denotes their dependence on the decay mode. The odd b terms are set to zero for decays into $\pi^+\pi^-$ and K^+K^- final states, where the α distributions are symmetric because the two outgoing particles have the same mass. The normalization factor K_j for each mode is calculated with a numerical two-dimensional integration of the p.d.f. in the appropriate domain of α and $p_{\rm tot}$.

Figure 6.8(b) shows the distribution of the scalar sum of momenta as a function of the momentum imbalance of the simulated $B^0 \to \pi^+\pi^-$ mode. Similar distributions are obtained for all signal modes. These are fit to the functions of eq. (6.20) to obtain the momentum templates. We checked the agreement between the model the and data by overlaying the templates to the α-distributions of simulated data, sampled in different $p_{\rm tot}$ ranges and viceversa.

6.5.2 Background momentum term

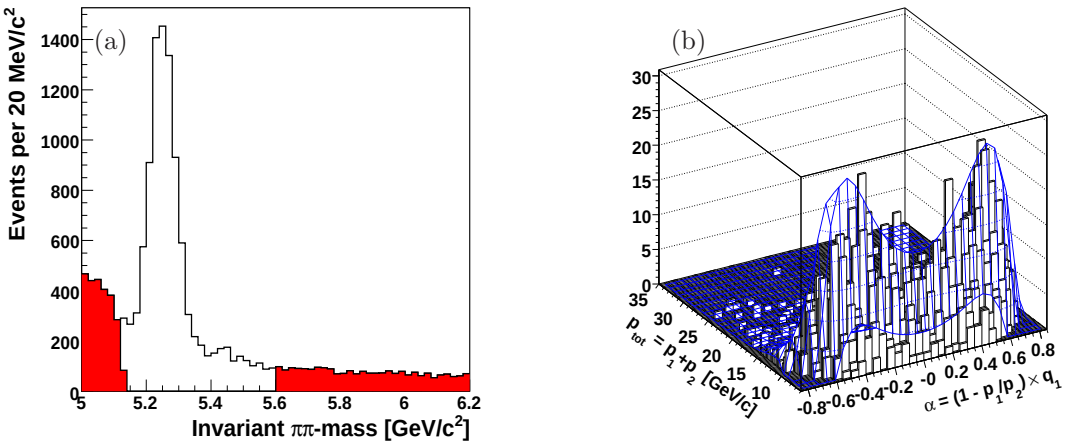


Figure 6.9: Invariant $\pi\pi$-mass sidebands (red) used to parameterize the momentum mass term (a). Distribution of the scalar sum of momenta as a function of the signed momentum imbalance of the background decays. Joint $(\alpha, p_{\rm tot})$ template as determined for background is overlaid (b).

As for the signal, we used a joint p.d.f. that parameterizes simultaneously the distribution of momentum imbalance (α) and of the scalar sum of momenta ($p_{\rm tot}$). The p.d.f. is further split in the density of the scalar sum, $\wp(p_{\rm tot})$, times the conditional density of the momentum imbalance, $\wp(\alpha|p_{\rm tot})$. We empirically chose the shapes of both densities, whose parameters were determined from data with a binned, two-dimensional binned fit of the distributions for candidates from the mass sidebands. For the combinatorial background we used the higher mass sideband to extract the momentum p.d.f., while for the physics component the situation is more complicate, since in the lower mass sideband there is an unknown mixture of two components. The contamination of the physics background under the $B^0_{(s)} \to h^+h^{'-}$ mass region is only a few %, then we decided to use the same p.d.f to parameterize both background components: $\wp^p_{\rm A}(\alpha, p_{\rm tot}) = \wp^p_{\rm E}(\alpha, p_{\rm tot}) = \wp^p_{\rm bck}(\alpha, p_{\rm tot})$. We parameterized the joint distribution $\wp^p_{\rm bck}(\alpha, p_{\rm tot})$ using the selections reported in tab. 3.3 and the data mass sidebands are defined in $m_{\pi\pi} \in [5.000, 5.125] \cup [5.600, 6.200]$ GeV/c^2 where the signal mass region $m_{\pi\pi} \in [5.120, 5.600]$ GeV/c^2 was removed. The relative weight between the combinatorial and physics background was preserved since the mass range fit is $m_{\pi\pi} \in [5.000, 5.800]$ GeV/c^2.

An event with an observed scalar sum of momenta $p_{\rm tot}$ and an observed momentum-imbalance α

contributes to the momentum p.d.f. of the background with the following term:

$$\wp^{p}_{\rm bck}(\alpha, p_{\rm tot}) = \wp(p_{\rm tot}) \times \wp(\alpha|p_{\rm tot}) = \frac{1}{K}\left[1+\left(\frac{p_{\rm tot}-\lambda}{a}\right)^2\right]^{-s} e^{\left[-\nu\ \tan^{-1}\left(\frac{p_{\rm tot}-\lambda}{a}\right)\right]} \times \sum_{m=0}^{6} b_m \alpha^m \left(\frac{p_{\rm tot}-2}{p_{\rm tot}-4}\right)^m, \quad (6.21)$$

where the $p_{\rm tot}$ density is a Pearson type-IV distribution [131], while the α conditional density is a 6th-degree polynomial of the α variable scaled by the usual factor $(p_{\rm tot}-2)/(p_{\rm tot}-4)$.[3] Since the momentum distribution of background is not expected to vary between positively and negatively-charged particles, the shape of the α distribution was forced to be symmetric by setting the odd b terms to zero. The normalization factor K is calculated through a numerical two-dimensional integration of the p.d.f. in the appropriate domain of α and $p_{\rm tot}$.

Figure 6.9(b) shows the distribution of the scalar sum of momenta as a function of the momentum imbalance of background events. The fit function of eq. (6.21) is overlaid. We checked the agreement between model and data by overlaying the template to the α-distribution of the background events, sampled in different $p_{\rm tot}$ ranges.

6.6 Probability density function of the PID term

6.6.1 Signal PID term

The p.d.f. of the PID information can not be factorized in the probability densities of the two particles, because of the correlation between the observed dE/dx values (see sec. 4.4.4). We therefore wrote a two-particle, joint p.d.f. that incorporates the probability densities of the intrinsic dE/dx observables of each particle, and of the correlation function.

We used the shapes of the intrinsic residuals and correlation determined in sec. 4.4.5 to write the p.d.f., which results from a convolution integral plus a transformation of variables. The convolution combines the intrinsic dE/dx residuals of both particles in the final state l and m (δ_l and δ_m) through the p.d.f. of correlation, $\wp_c(c)$, yielding the following p.d.f. for the jth mode:

$$\wp_j(\delta_l^{\rm obs}, \delta_m^{\rm obs}) = \wp_{H\to lm}(\delta_l^{\rm obs}, \delta_m^{\rm obs}) = [\wp_l(\delta_l) \times \wp_m(\delta_m)] * \wp_c(c) = \int_{-\infty}^{+\infty} \wp_l(\delta_l - c)\wp_m(\delta_m - c)\wp_c(c)dc, \quad (6.22)$$

which, at this stage, is independent of momenta. The index j, which runs over all components, is splitted in three indices $H \to lm$ because the PID term depends only on the identity of particles in the final states of the jth mode and not on the initial mother particle $H = B^0, B_s^0$ or Λ_b^0. The indices $l, m = K^\pm$, $\pi^\pm$, p or $\bar{p}$ determine the choice of the shapes for intrinsic residuals within the integral The p.d.f. in eq. (6.22) is function of a different set of observables for each mode, e. g., if $\alpha > 0$: $(\delta_{\pi^+}, \delta_{\pi^-})$[4] for the $B^0 \to \pi^+\pi^-$ case, $(\delta_{K^+}, \delta_{\pi^-})$ for the $B^0 \to K^+\pi^-$ case; if $\alpha < 0$: $(\delta_{\pi^-}, \delta_{\pi^+})$ for the $B^0 \to \pi^+\pi^-$ case, $(\delta_{\pi^-}, \delta_{K^+})$ for the $B^0 \to K^+\pi^-$ case and so on.

[3] The Pearson type-IV distribution is useful to approximate a broad class of asymmetric distributions with extensive tails.

[4] δ_A is the dE/dx residual in m_A mass hypothesis, see sec. 4.4.2.

To avoid possible biases related to using different sets of observables in different terms of the Likelihood function δ_l and δ_m [113], we rewrote the Likelihood in terms of a single observable, the kaonness κ, see sec. 4.4.7. Changing variable from residual to kaonness induces an additional dependence on momentum in the PID term. In fact, for each particle type, the following relation holds:

$$\delta = (\kappa - \langle\kappa\rangle)\left(\frac{dE}{dx}_K - \frac{dE}{dx}_\pi\right) \equiv (\kappa - \langle\kappa\rangle)\,\Delta \tag{6.23}$$

where Δ indicates the difference between the expected dE/dx values evaluated in kaon and pion mass-hypothesis, which is function of momentum. The advantage to use the kaonness in lieu of the residuals in different hypothesis is that the kaonness is defined for all kind of particles in the same way. In fact the residuals in all mass hypothesis are function of kaonness and momentum particle. The joint p.d.f. as a function of κ is

$$\wp_{lm}(\kappa_1^{\rm obs}, \kappa_2^{\rm obs}) = \int_{-\infty}^{+\infty} \wp(\delta_l - c)\wp(\delta_m - c)\left|\frac{\partial(\delta_l, \delta_m)}{\partial(\kappa_1, \kappa_2)}\right|\wp_c(c)dc, \tag{6.24}$$

where $\delta \equiv \delta(\kappa)$ and the notation $\kappa_1^{\rm obs}$, $\kappa_2^{\rm obs}$ to indicate the particles is described in sec. 6.1. After writing out the Jacobian, the above equation becomes

$$\wp_{lm}(\kappa_1^{\rm obs}, \kappa_2^{\rm obs}) = \int_{-\infty}^{+\infty} \wp(\delta_l - c)\wp(\delta_m - c)\Delta_1\Delta_2\wp_c(c)dc. \tag{6.25}$$

The transformation from residual to kaonness brings the momenta into the probability density through the differences of expected dE/dx values, $\Delta_1(\alpha, p_{\rm tot})$ and $\Delta_2(\alpha, p_{\rm tot})$. Hence, the correct expression of the joint p.d.f. function of κ becomes a conditional probability density at given momenta: $\wp_{lm}(\kappa_1^{\rm obs}, \kappa_2^{\rm obs}) \longrightarrow \wp_{lm}(\kappa_1^{\rm obs}, \kappa_2^{\rm obs}|\alpha, p_{\rm tot})$.

An event in which δ_l and δ_m are the observed dE/dx residuals of the particle pair, contributes to the jth signal mode of the PID p.d.f. with the following term:

$$\wp_j^{\rm PID}(\kappa_1^{\rm obs}, \kappa_2^{\rm obs}|\alpha, p_{\rm tot}) = \wp_{l,m}^{\rm PID}(\kappa_1^{\rm obs}, \kappa_2^{\rm obs}|\alpha, p_{\rm tot}) = \frac{1}{K_j}\int_{-\infty}^{+\infty} \wp_l(\delta_l - c)\wp_m(\delta_m - c)\Delta_1\Delta_2\wp_c(c)dc, \tag{6.26}$$

which includes $K_j = 1/\int_{-\infty}^{+\infty} \wp_j(\kappa_1^{\rm obs}, \kappa_2^{\rm obs}|\alpha, p_{\rm tot})d\kappa_1^{\rm obs}d\kappa_2^{\rm obs}$ as a normalization factor. The explicit expression of the p.d.f. was evaluated analytically; we omit here its explicit expression because of its length and lack of visually intelligible features.

6.6.2 Background PID term

The PID p.d.f. for background uses the same joint two-particle p.d.f. as for the signal. The term corresponding to each possible pair of particle types (l, m) in background, is weighed by a factor $w_l w_m$. Each weight w_l is proportional to the fractional contribution of particles of type l to the background, and it is a free parameter in the fit. We allowed for independent kaon, proton, electron and pion (or muon) contributions, and for positive and negative particles for the combinatorial background, while, for physics background, we allowed for independent kaon and pion contributions, averaging on the particle charge, since in this case we do not expect electrons and protons in the final state and any asymmetry between positive and negative particles. Muons and pions were not differentiated since

their contributions are indistinguishable; the ≈ 1.5 ns dE/dx resolution is insufficient to resolve the difference between their ionization rates, which is inappreciable because of the small difference in mass $m_{\pi^\pm} - m_\mu \simeq 34\text{MeV}/c^2$. This does not affect the signal composition, since muon contamination in the signal peak is negligible, if any, due to the small rates expected for $B^0_{(s)}$ meson decays in muon pairs [132], and muons from semileptonic heavy-flavor decays do not have a peaking distribution in mass. We used the model of residuals and correlation for kaons and pions and protons described in sec. 4.4.5. A candidate decaying to particles with κ_1^{obs} and κ_2^{obs} observed "kaonnesses", sum of observed scalar momenta p_{tot}, and observed momentum imbalance α, contributes to the PID term of the Likelihood of background with the following probability density function:

$$\wp^{\text{PID}}_{\text{A(E)}} = \sum_{l,m} w_l^{\text{A(E)}} w_m^{\text{A(E)}} [\wp_{l,m}(\kappa_1^{\text{obs}}, \kappa_2^{\text{obs}}|\alpha, p_{\text{tot}}) + \wp_{m,l}(\kappa_1^{\text{obs}}, \kappa_2^{\text{obs}}|\alpha, p_{\text{tot}})]. \tag{6.27}$$

The explicit expression of $\wp_{l,m}(\kappa_1^{\text{obs}}, \kappa_2^{\text{obs}}|\alpha, p_{\text{tot}})$ is shown in eq. (6.26). While in the signal case the l, m indices run over kaons, pions and protons ($K^\pm$, $\pi^\pm$, p and $\bar{p}$) according to the decay of $B^0_{(s)} \to h^+ h^{'-}$ and $\Lambda_b^0 \to p h^-$, in the above equation they include also electrons ($e^\pm$) for the combinatorial background (E), while for physics background l, m indexes run over kaons, pions (K, π) only, where $w^{\text{A}}_{K^+} = w^{\text{A}}_{K^-}$ and $w^{\text{A}}_{\pi^+} = w^{\text{A}}_{\pi^-}$.

6.6.3 $B^0_{(s)} \to h^+ h^{'-}$ correlation

We have observed in a few occasions that the probability density function of the correlation is sample dependent (see sec. 4.4.6), while the probability density function of the intrinsic residuals are expected to be the same by construction for the different data samples. We decided to use the templates of the intrinsic residuals unchanged and to let the correlation p.d.f. to be determined by the fit of composition, by letting the corresponding five parameters of the Gaussian correlation functions free to vary, rather than using the nominal value extracted from the $D^0 \to K^-\pi^+$ decays reconstructed from $D^{*+} \to D^0\pi^+ \to [K^-\pi^+]\pi^+$ decays (see sec. 4.4).

Although the disagreements between the correlations shape of different samples were within the systematics associated to the PID templates (see sec. 12.7), we preferred to take advantage of the large statistics available in the current $B^0_{(s)} \to h^+ h^{'-}$ sample to better estimate the correlation, yielding a reduction of the systematic uncertainty in exchange for a modest increase of statistical uncertainty ($\approx 2\%$).

Hence the PID p.d.f. in eq. (6.26) is a function of 5 fit parameters:

$$\wp_{l,m}(\kappa_1^{\text{obs}}, \kappa_2^{\text{obs}}|\alpha, p_{\text{tot}}) \to \wp_{l,m}(\kappa_1^{\text{obs}}, \kappa_2^{\text{obs}}|\alpha, p_{\text{tot}}; d_1^c, \mu_1^c, \sigma_1^c, \mu_2^c, \sigma_2^c) \tag{6.28}$$

where $d_1^c, \mu_1^c, \sigma_1^c, \mu_2^c, \sigma_2^c$ are the parameters which describe the double Gaussian of the correlation p.d.f. of eq. (4.25). d_1^c is the relative fraction of the Gaussian 1 ($d_2^c = 1 - d_1^c$), while $\mu^c_{1(2)}, \sigma^c_{1(2)}$ are respectively the mean and the width of the Gaussian 1(2).

Chapter 7

Isolation of B^0 and B_s^0 mesons

This chapter is devoted to the measurement of the distribution for the B^0 and B_s^0, as a function of momentum, of the isolation variable. This is a fundamental handle to enhance the signal-to-background ratio in the off-line selection. This, however, implies an additional amount of work since the Monte Carlo physics generators do not reproduce accurately its features. We need to evaluate how the isolation requirement modifies the transverse momentum distribution of the $B_{(s)}^0$ meson for an accurate parameterization of kinematic templates. We need to estimate the efficiency for the optimization selection process and to convert the fit results into a measurement of branching fraction. We focused our attention on the study of the control data sample of $B_{(s)}^0 \to J/\psi X$ decays to probe the characteristics and peculiarities of this variable.

7.1 Isolation

One of the most powerful variables to improve the $B_{(s)}^0 \to h^+ h'^-$ purity in the off-line selection is the "isolation". Given the hard fragmentation, b-hadrons tend to carry a larger fraction of the transverse momentum than the particles produced in the fragmentation [108]. The "isolation of the B candidate" is an estimator of the fraction of momentum, available from the b-quark fragmentation, carried by the b-meson:

$$I|_{R=1}(B) = \frac{p_{\mathrm{T}}(B)}{p_{\mathrm{T}}(B) + \sum\limits_{i \neq j : B \to j}^{R} p_{\mathrm{T}}(i)}, \tag{7.1}$$

where the sum in the right-hand term of the denominator runs over all tracks (other than those of the B candidate decay-chain) satisfying standard quality requirements and found in a local region around the flight direction of the B candidate. Such region is chosen to be a cone in the $(\eta - \phi)$ space, unitary in radius ($R = \sqrt{\phi^2 + \eta^2} = 1$), whose apex is the primary vertex and the axis is collinear with $\vec{p}_{\mathrm{T}}(B)$ (see fig. 7.1). When the decay products of the b-meson are contained in the cone, $I(B)$ is just the fraction of transverse momentum within the cone carried by the b-meson.[1] Candidates with large values of the isolation are more likely to be a real b-mesons than candidates with a low isolation.

[1] Since we use $R = 1$ all through this thesis, we henceforth simply write $I(B) \equiv I|_{R=1}(B)$.

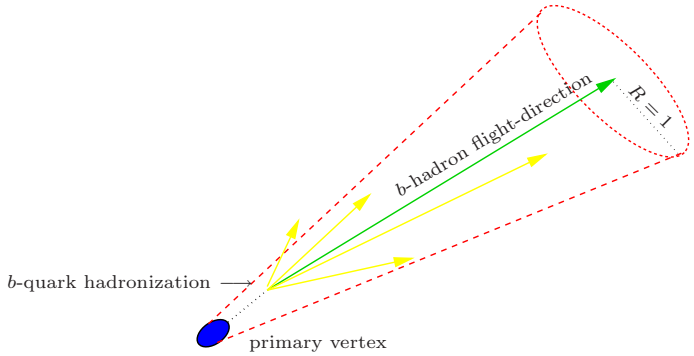


Figure 7.1: Illustration of the fragmentation of a b-quark into a b-hadron. The isolation cone is shown in red, the directions of the charged particles produced in the fragmentation are shown in yellow. Nothing is to scale.

The introduction of the isolation adds further complexity to the analysis: its distribution depends on the mechanism of hadronization of the b-quark, which is not described by the signal-only simulation discussed in sec. 4.1. The isolation depends on: 1) the multiplicity and momenta of the charged-particles not belonging to the b-meson decay-chain and produced in the b-quark fragmentation, or in the underlying event, or in possible pile-up events; 2) the transverse momentum of the b-meson, since the sharing of transverse momentum between the b-meson and its neighboring particles depends on the energy of the b-meson itself.[2] This has some consequences. First, the isolation is independent of the decay mode of the b-meson, but it depends on its production mechanism. We therefore expect different isolation distributions for the B^0 and B_s^0 mesons, which are produced through different fragmentation processes. A second consequence is the need to study the isolation using real data, since typical $p\bar{p}$ collision simulators, as PYTHIA, cannot reproduce reliably the details of the b-quark fragmentation. In addition, the dependence on the transverse momentum of the b-meson needs to be considered.

In the next sections we will analyse the characteristics and peculiarities of the isolation using fully reconstructed $B_{(s)}^0$ meson decays available in CDF data. We will measure the efficiencies $\varepsilon_{\rm iso}(B^0)$ and $\varepsilon_{\rm iso}(B_s^0)$ as a function of the transverse momentum $p_{\rm T}(B)$ and as a function of different set of requirements. In particular, we will focus on the requirements used in the present analysis $I(B) > 0.5$ and $I(B) > 0.525$.

7.2 Choice of the control samples

We chose fully reconstructed decays since we need to determine the transverse momentum and the direction of the $B_{(s)}^0$ meson. Samples collected by the same trigger as the $B_{(s)}^0 \to h^+h^{'-}$ decays, and with similar final states, like the exclusive $B_{(s)}^0 \to D_{(s)}^-\pi^+$ decays, would be desirable. However, common thresholds on transverse momentum between the `B_PIPI` (which collects $B_{(s)}^0 \to h^+h^{'-}$ decays) and the `B_CHARM` (which collects $B_{(s)}^0 \to D_{(s)}^-\pi^+$ decays) trigger paths are responsible of an

[2] QCD measurements show that the fraction of energy carried by a charged particle in a jet does not depend linearly on the energy of the jet itself.

higher turn-on point of the $p_{\rm T}(B)$ distribution of the $B^0_{(s)} \to D^-_{(s)}\pi^+$ with respect to the $B^0_{(s)} \to h^+h'^-$ modes. A two-body decay-product carries a larger average-fraction of the momentum of the decaying particle than the product of a multi-body decay. Thus, b-mesons in the `B_PIPI` path typically had lower transverse momenta than in the `B_CHARM` path. While a $\approx 40\%$ (30% after the isolation requirement) fraction of the $B^0_{(s)} \to h^+h'^-$ candidates have transverse momenta below 6 GeV/c, the $B^0_{(s)} \to D^-_{(s)}\pi^+$ candidates are removed from this region of the spectrum by the trigger bias.

We therefore used the fully reconstructed $B^0_{(s)} \to J/\psi X$ decays in the data collected by the di-muon trigger. This trigger selects events enriched in $J/\psi \to \mu^+\mu^-$ decays by requiring azimuthal matching between two oppositely-curved XFT-tracks with $p_{\rm T} > 1.5$ GeV/c and two non-adjacent track-segments in the CMU detectors. The lower threshold on the transverse momenta of the muons allows to reconstruct $B^0_{(s)}$ meson with transverse momenta distributions extending down to $p_{\rm T}(B) \approx 2{-}3$ GeV/c (see figs. 7.2(a) and (b)). The decays used to measure the isolation efficiency are:

- $\boldsymbol{B^0 \to J/\psi K^*(892)^0 \to [\mu^+\mu^-][K^+\pi^-]}$,
  with approximate total branching fraction 7.7×10^{-5};
- $\boldsymbol{B^0_s \to J/\psi\phi(1020) \to [\mu^+\mu^-][K^+K^-]}$,
  with approximate total branching fraction 2.6×10^{-5}.

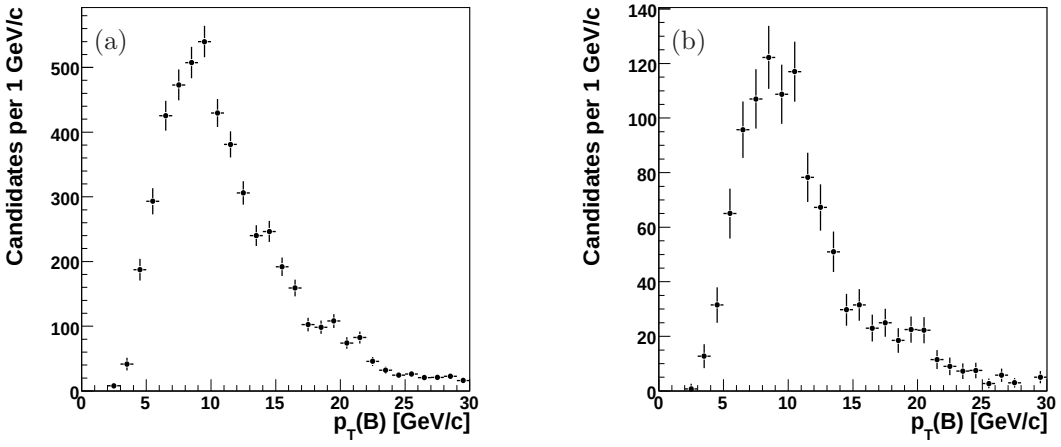


Figure 7.2: Background-subtracted $p_{\rm T}(B)$-distributions of the $B^0 \to J/\psi K^{*0}$ (a) and $B^0_s \to J/\psi\phi$ decays (b).

$B^0 \to J/\psi K^{*0}$ and $B^0_s \to J/\psi\phi$ modes (see fig. 7.3) were reconstructed in data collected by the di-muon trigger, following a standard CDF procedure [106, 144]. We relaxed only the requirement on the transverse momentum of $B^0_{(s)}$ mesons ($p_{\rm T}(B) > 2$ GeV/c) and we compensated the degradation of the signal purity by tightening the $p_{\rm T}$ requirements on the K^{*0} and ϕ. Table 7.1 summarizes the selection criteria. Of the two possible mass assignments in the K^{*0} reconstruction, $K^+\pi^-$ and $K^-\pi^+$, we chose the one yielding the invariant mass closer to the K^{*0} mass [32]. This choice is wrong in about 36% of the cases (see tab. 7.2) and it produces the long visible tails in the invariant mass distribution

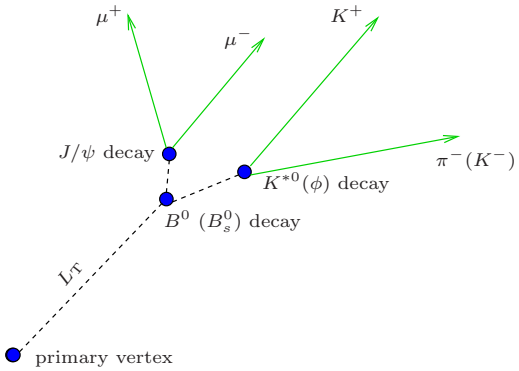


Figure 7.3: Illustration of the $B^0 \to J/\psi K^{*0} \to [\mu^+\mu^-][K^+\pi^-]$ ($B_s^0 \to J/\psi\phi \to [\mu^+\mu^-][K^+K^-]$) decay topology in the transverse plane.

of the $B^0 \to J/\psi K^{*0}$ candidates (see fig. 7.4(a)). This is not a real problem for the study of the isolation and will be discussed in sec. 7.3.1.

Figures 7.4(a) and (b) show the invariant-mass distribution resulting from the selection of tab. 7.1. We reconstructed about 7,800 $B^0 \to J/\psi K^{*0}$ decays with a signal-to-noise ratio ≈ 12 at the peak, and about 1,100 $B_s^0 \to J/\psi\phi$ decays with a signal-to-noise ratio ≈ 20 at the peak. The background is almost uniform and is dominated by random four-track combinations that accidentally satisfy the selection requirements and random two-track combinations associated with a real J/ψ meson.

Variable	Units	$B^0 \to J/\psi K^{*0}$	$B_s^0 \to J/\psi\phi$
$p_{\rm T}(\mu)$	GeV/c	> 1.5	> 1.5
$p_{\rm T}$ of non-ψ daughter	GeV/c	$p_{\rm T}(K),\ p_T(\pi) > 0.4$	$p_{\rm T}(K),\ p_{\rm T}(K) > 0.4$
$p_{\rm T}$(non-ψ)	GeV/c	$p_{\rm T}(K^{*0}) > 2.0$	$p_{\rm T}(\phi) > 2.0$
$p_{\rm T}(B)$	GeV/c	> 2.0	> 2.0
$L_{\rm T}(B)/\sigma_{L_{\rm T}(B)}$	–	> 4.5	> 4.5
$\sigma_{L_{\rm T}(B)}$	μm	< 400	> 400
J/ψ mass	GeV/c^2	$3.017 < m_{\mu\mu} < 3.177$	$3.017 < m_{\mu\mu} < 3.177$
Non-ψ mass	GeV/c^2	$0.842 < m_{K\pi} < 0.942$	$1.010 < m_{KK} < 1.030$
$\chi^2_{\rm T}(B)$	–	< 225	< 225
$\mathcal{P}(B_{vertex})$	–	$> 10^{-4}$	$< 10^{-4}$

Table 7.1: The $B^0_{(s)} \to J/\psi X$ selection. "Non-ψ" denotes the K^{*0} (ϕ) resonance in the B^0 (B_s^0) decays.

7.3 Measurement of the isolation efficiency

If we have a sample of N b-mesons decays where $N_{s(b)} = N \cdot f_{s(b)}$ is the total number of the signal (background) events and $f_{s(b)}$ is the fraction of the signal (background) events with respect to N, we

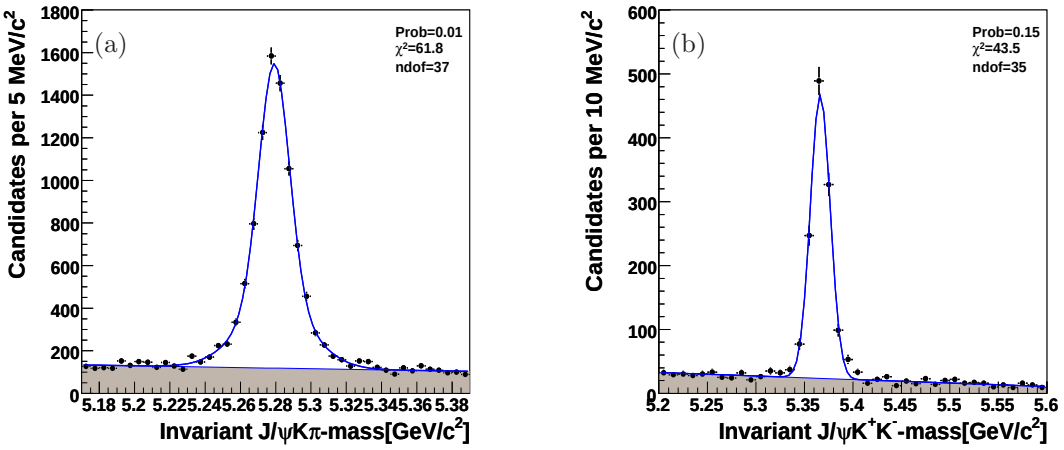


Figure 7.4: Invariant $J/\psi K\pi$-mass distribution of the $B^0 \to J/\psi K^{*0}$ candidates (a); invariant $J/\psi K^+K^-$-mass distribution of the $B_s^0 \to J/\psi\phi$ candidates (b).

define the efficiency of the $I(B) > 0.5$ (or 0.525) cut as

$$\varepsilon_{\rm iso}(B) = \frac{N_s^{\rm iso}}{N_s} = \frac{f_s^{\rm iso}}{f_s}, \tag{7.2}$$

where $N_s^{\rm iso} \leq N_s$ ($f_s^{\rm iso} \leq f_s$) is the number (fraction) of decays in which the isolation of the b-meson is larger than 0.5 (or 0.525). We extracted $\varepsilon_{\rm iso}(B)$ with a joint fit of the mass distribution of events passing the isolation cut ($f_s^{\rm iso}$), and failing the same cut ($f_s - f_s^{\rm iso}$). This was done both for the $B^0 \to J/\psi K^{*0}$ and the $B_s^0 \to J/\psi\phi$ decay mode separately.

The yields were fit by maximizing a Likelihood function that uses the information contained in two observables: the invariant mass of the B candidate (m_B, see fig. 7.5), and a boolean variable ("flag") that is true if the candidate satisfies the isolation requirement $I(B) > 0.5$ (or 0.525). The Likelihood $\mathscr{L}$ is a function of the vector $\vec{\theta} = (\theta_1, \ldots, \theta_n)$ of n unknown parameters, and is written as follows:

$$\mathscr{L}(\vec{\theta}) = \prod_{i=1}^{N} \mathscr{L}_i(\vec{\theta}) = \prod_{i=1}^{N} \begin{cases} f_s \varepsilon_{\rm iso}^s \mathscr{L}_i^{\rm sig} + f_b \varepsilon_{\rm iso}^b \mathscr{L}_i^{\rm bck-iso} & I(B) > I_{\rm cut}; \\ f_s (1-\varepsilon_{\rm iso}^s) \mathscr{L}_i^{\rm sig} + f_b (1-\varepsilon_{\rm iso}^b) \mathscr{L}_i^{\rm bck-noiso} & I(B) \leq I_{\rm cut}. \end{cases} \tag{7.3}$$

For each mode, the two-variate (m_B and flag) fit was implemented by minimizing the quantity $-2\ln(\mathscr{L})$. For each event passing (failing) the requirement, the first (second) branch of the above Likelihood function was used. In eq. (7.3), the product runs over the observed number of events N. The expected fractions of signal (f_s) and background ($f_b = 1 - f_s$) events, and the isolation efficiencies on signal ($\varepsilon_{\rm iso}^s$) and on background ($\varepsilon_{\rm iso}^b$) were determined by the fit. The p.d.f. used in the Likelihood that describe signal ($\mathscr{L}_i^{\rm sig}$) and background ($\mathscr{L}_i^{\rm bck-iso}$ and $\mathscr{L}_i^{\rm bck-noiso}$) distributions are described in next sections.

7.3.1 Probability density functions

The invariant-mass distribution of $B^0 \to J/\psi K^{*0}$ is described by the sum of two Gaussian probability distributions with the same mean and different standard deviations:

$$\mathscr{L}^{\rm sig} = \wp(m_B;\vec{\theta}) = \frac{f_1}{K_1} e^{-\frac{1}{2}(\frac{m_B-\mu}{\sigma_1})^2} + \frac{1-f_1}{K_2} e^{-\frac{1}{2}(\frac{m_B-\mu}{\sigma_2})^2}, \tag{7.4}$$

where the mean of the two Gaussians, μ, the standard deviations, σ_1 and σ_2, the relative fraction of the first Gaussian with respect to the second one, f_1, are parameters determined by the fit, and the normalization constants, $K_i = \int_a^b e^{-\frac{1}{2}(\frac{m_B-\mu}{\sigma_i})^2} dm_B$, depend on the mass-range of the fit, $a < m_B < b$. The use of a double Gaussian model to parameterize the invariant mass distribution of the $B^0 \to J/\psi K^{*0}$ decays was necessary to keep into account the non negligible fraction of *swapped* $K^{*0} \to K\pi$ decays, where the kaon mass was assigned to the pion and the pion mass was assigned to the kaon in the reconstruction of the K^{*0}. The fraction of swapped candidates was studied accurately using the full simulation in the standard CDF analysis and it depends strongly on the selection. Ref. [106] estimates a 10% of swapped component while Ref. [144] using a different off-line selection estimates a 20% for this fraction. However these values cannot be compared directly with the fraction returned by our fit (about 37% (see tab. 7.2)) since our selection is looser than the ones in Refs. [106, 144] because we need to reach low transverse momentum values. Moreover our simple model absorbs in the second wider Gaussian the non Gaussian tails of the mass distribution due to the resolution effects. These effects are reproduced precisely by the full simulation and they are included in the standard CDF analysis.
Improving the mass distribution model with the generation of a large Monte Carlo sample of $B^0 \to J/\psi K^{*0}$, knowing exactly the fraction of swapped candidates and the precise parameterization of the invariant mass distribution does not provide any improvement on the measurement of the isolation efficiency. In fact any isolation independent systematic effect is canceled out in the ratio of signal fractions, since it contributes equally to numerator and denominator.

The invariant-mass distribution of the $B_s^0 \to J/\psi\phi$ candidates is described with a Gaussian probability distribution:

$$\mathscr{L}^{\rm sig} = \wp(m_B;\vec{\theta}) = \frac{1}{K} e^{-\frac{1}{2}(\frac{m_B-\mu}{\sigma})^2}, \tag{7.5}$$

where the mean, μ, and the standard deviation, σ, are parameters determined by the fit, and the normalization constant, $K = \int_a^b e^{-\frac{1}{2}(\frac{m_B-\mu}{\sigma})^2} dm_B$, depends on the mass-range of the fit, $a < m_B < b$.

We described the background shape with a linear function as empirical probability distribution. Since the invariant-mass distribution of background events may depend on the isolation (see fig. 7.5), we used two different probability functions:

$$\mathscr{L}^{\rm bck-iso} = \wp(m_B;\vec{\theta}) = \frac{1}{K_1}(1+c_1 m_B) \quad \text{and} \quad \mathscr{L}^{\rm bck-noiso} = \wp(m_B;\vec{\theta}) = \frac{1}{K_2}(1+c_2 m_B), \tag{7.6}$$

where $\mathscr{L}^{\rm bck-iso}$ is used for candidates with $I(B) > 0.5$ (or 0.525) and $\mathscr{L}^{\rm bck-noiso}$ for candidates with $I(B) < 0.5$ (or 0.525).

7.3.2 Likelihood fit

The vector of the unknown parameters, $\vec{\theta}$, was estimated for each mode, independently, to determine

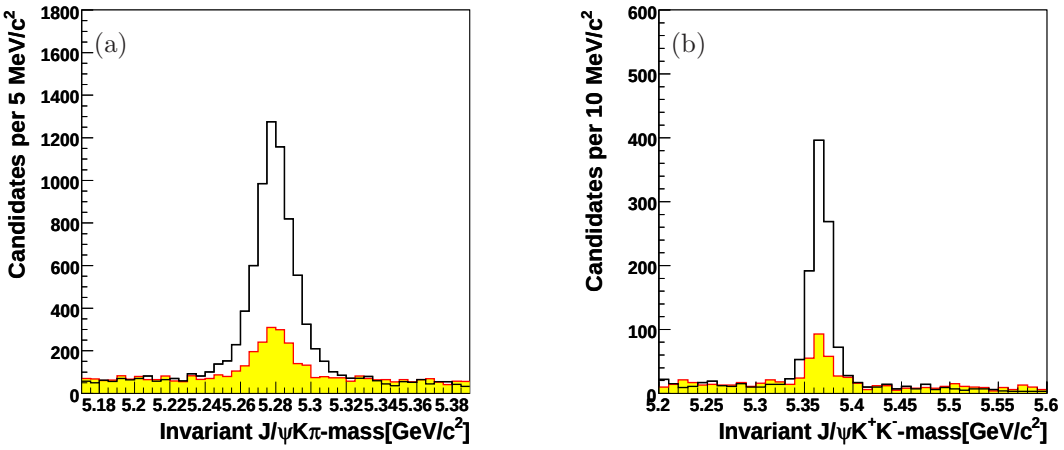


Figure 7.5: Invariant $J/\psi K\pi$-mass distribution of the $B^0 \to J/\psi K^{*0}$ candidates passing (black histogram), and failing (red filled histogram), the $I(B) > 0.5$ cut (a). Invariant $J/\psi K^+K^-$-mass distributions of the $B_s^0 \to J/\psi\phi$ candidates passing (black histogram), and failing (red filled histogram) the $I(B) > 0.5$ cut (b).

$\boldsymbol{f_s}$ – the estimate of the signal fraction in the sample, $f_b = 1 - f_s$;

$\boldsymbol{f_1, \mu, \sigma_1}$ and $\boldsymbol{\sigma_2}$ (or $\boldsymbol{\mu}$ and $\boldsymbol{\sigma}$) – the estimate of mass distribution of signal in $B^0 \to J/\psi K^{*0}$ (or $B_s^0 \to J/\psi\phi$) mode;

$\boldsymbol{\varepsilon^s_{\rm iso}}$ – the estimate of the efficiency of the $I(B) > I_{\rm cut}$ requirement on signal events;

$\boldsymbol{\varepsilon^b_{\rm iso}}$ – the estimate of the efficiency of the $I(B) > I_{\rm cut}$ requirement on background events;

$\boldsymbol{c_1}$ and $\boldsymbol{c_2}$ – the estimate of the parameters of the mass distribution of background.

Using the simultaneous fit of eq. (7.3) is convenient. Since several parameters (f_s, $\varepsilon^s_{\rm iso}$, $\varepsilon^b_{\rm iso}$, f_1, μ, σ_1, σ_2, c_1, and c_2) are shared between the two branches of the Likelihood, optimal use of the available information is achieved by determining these parameters simultaneously. In addition, using common parameters helps the convergence of the maximization of the Likelihood in a condition of low statistics and low purity subsamples of candidates failing the isolation requirement. Lastly, several systematic effects cancel out in the ratio of signal yields between the two samples.

Figures 7.6 and 7.7 show the invariant-mass distributions of the $B^0_{(s)} \to J/\psi X$ samples, with the fit functions overlaid. Table 7.2 contains the results of the fits for the requirement $I(B) > 0.5$ and $I(B) > 0.525$ respectively.

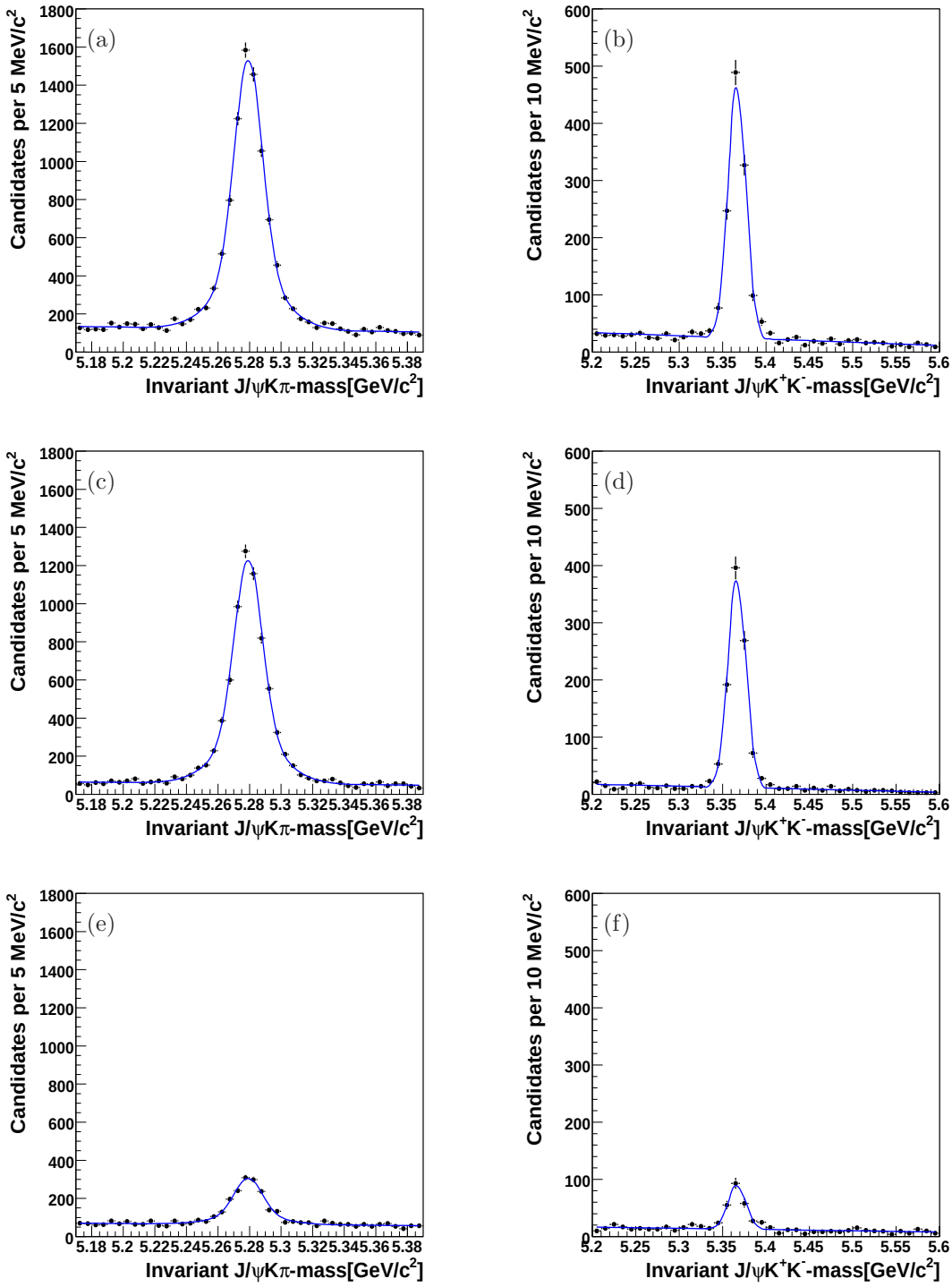


Figure 7.6: Invariant mass distributions of $B^0_{(s)} \to J/\psi X$ candidates without (a, b), passing (c, d), and failing (e, f) the isolation requirement $I(B) > 0.5$. $B^0 \to J/\psi K^{*0}$ (a, c, e), $B^0_s \to J/\psi\phi$ (b, d, f). Fit functions are overlaid (blue, solid line).

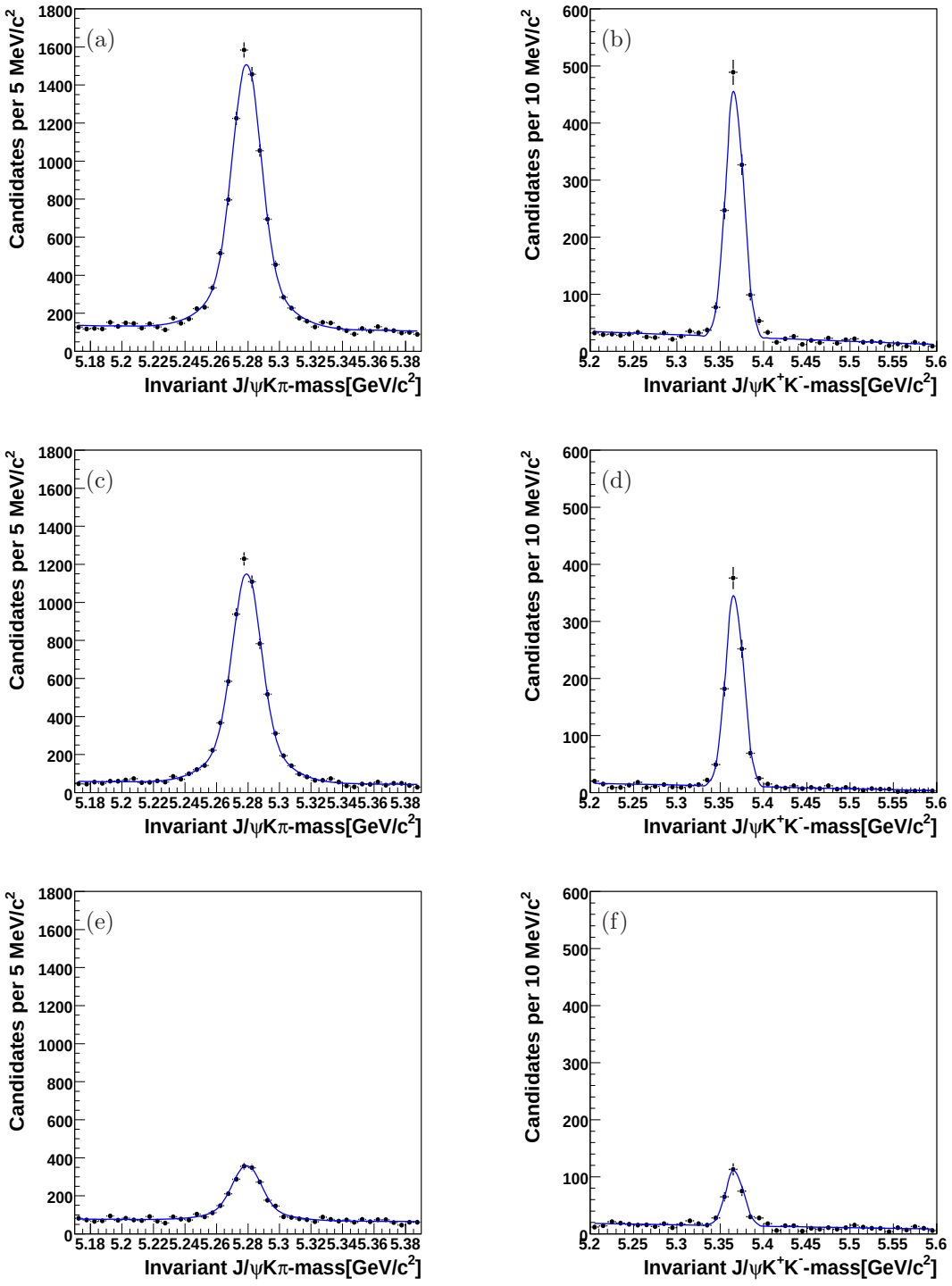


Figure 7.7: Invariant mass distributions of $B^0_{(s)} \to J/\psi X$ candidates without (a, b), passing (c, d), and failing (e, f) the isolation requirement $I(B) > 0.525$. $B^0 \to J/\psi K^{*0}$ (a, c, e), $B^0_s \to J/\psi\phi$ (b, d, f). Fit functions are overlaid (blue, solid line).

	$B^0 \to J/\psi K^{*0}$	$B_s^0 \to J/\psi\phi$
$\varepsilon_{\rm iso}^s$ [%]	82.9 ± 0.5	82.7 ± 1.3
$\varepsilon_{\rm iso}^b$ [%]	46.8 ± 0.9	46.6 ± 1.8
f_s [%]	59.7 ± 0.7	55.3 ± 1.3
f_1 [%]	64 ± 5	–
μ [MeV/c^2]	5279.2 ± 0.2	5366.6 ± 0.3
σ_1 [MeV/c^2]	8.6 ± 0.4	–
σ_2 [MeV/c^2]	20.2 ± 1.7	–
σ [MeV/c^2]	–	9.7 ± 0.3

	$B^0 \to J/\psi K^{*0}$	$B_s^0 \to J/\psi\phi$
$\varepsilon_{\rm iso}^s$ [%]	79.8 ± 0.6	78.3 ± 1.4
$\varepsilon_{\rm iso}^b$ [%]	41.1 ± 0.9	42.2 ± 1.8
f_s [%]	59.9 ± 0.7	55.4 ± 1.3
f_1 [%]	66 ± 5	–
μ [MeV/c^2]	5279.2 ± 0.2	5366.6 ± 0.3
σ_1 [MeV/c^2]	8.7 ± 0.4	–
σ_2 [MeV/c^2]	21.1 ± 1.8	–
σ [MeV/c^2]	–	9.8 ± 0.3

Table 7.2: Fit results for $I(B) > 0.5$ on the left, for $I(B) > 0.525$ on the right. $N = 13064$ events of $B^0 \to J/\psi K^{*0}$ and $N = 2041$ events $B_s^0 \to J/\psi\phi$ have been fitted.

7.4 $p_{\rm T}$-dependent effects

To study the dependence of the isolation efficiency on the transverse momentum of the $B_{(s)}^0$ mesons we performed additional fits in different $p_{\rm T}(B)$ bins. The results are reported in tab. 7.3. The current statistics of the $B_s^0 \to J/\psi\phi$ decays is limited and it does not allow to further refine the bins range. In particular the range of the first bin, $p_{\rm T}(B) \in [2, 6]$ GeV/c, useful to extract the isolation efficiency at low transverse momentum, cannot further be reduced with the current statistics. The situation will improve as the data samples increase in size (today CDF already recorded on tape $\approx 2.5{\rm fb}^{-1}$). In the last column of tab. 7.3 we reported the ratio between the isolation efficiencies of the B^0 and B_s^0 mesons as a function of the transverse momentum. While the single $\varepsilon_{\rm iso}(B_{(s)}^0)$ efficiency is strongly $p_{\rm T}(B)$ dependent, the ratio $\varepsilon_{\rm iso}(B^0)/\varepsilon_{\rm iso}(B_s^0)$ is a constant compatible with the unit. High $p_{\rm T}(B)$

$p_{\rm T}$ range [GeV/c]	$\varepsilon_{\rm iso}(B^0 \to J/\psi K^{*0})$ [%]	$\varepsilon_{\rm iso}(B_s^0 \to J/\psi\phi)$[%]	$\varepsilon_{\rm iso}(B^0)/\varepsilon_{\rm iso}(B_s^0)$
$2 < p_{\rm T}(B) < 6$	62.4 ± 2.4	59.6 ± 5.3	1.05 ± 0.10
$6 < p_{\rm T}(B) < 10$	75.9 ± 0.9	76.8 ± 2.2	0.99 ± 0.03
$10 < p_{\rm T}(B) < 14$	89.6 ± 0.8	88.6 ± 1.8	1.01 ± 0.02
$14 < p_{\rm T}(B) < 18$	94.9 ± 0.7	97.0 ± 1.6	0.98 ± 0.02
$18 < p_{\rm T}(B) < 30$	97.4 ± 0.8	97.8 ± 1.9	0.99 ± 0.02

Table 7.3: Isolation efficiency ($I(B) > 0.5$) as a function of $p_{\rm T}(B)$ from $B_{(s)}^0 \to J/\psi X$ decays.

values correspond to high isolation efficiency values.

Since the $p_{\rm T}(B)$-distribution of the $B_{(s)}^0 \to J/\psi X$ decays is harder than the $p_{\rm T}(B)$-distribution of the $B_{(s)}^0 \to h^+ h^{'-}$ decays (see fig. 7.8(a)), we expect different efficiency values and we cannot use the numbers of sec. 7.3 to extrapolate the acceptance corrections. We could choose to measure the quantity of interest in different $p_{\rm T}(B)$-bins as we did already in tab. 7.3, and then to average those with the new $p_{\rm T}(B)$-distribution. This strategy, however, requires samples with high statistics in order to refine the $p_{\rm T}(B)$ granularity and to obtain bins in the $p_{\rm T}(B)$-distribution can be considered

constant.

Though CDF II collected the second largest $B_s^0 \to J/\psi\phi$ sample in the world, this statistics is insufficient to refine adequately the $p_T(B)$ spectrum for our purpose. In particular the statistics at low transverse momentum $p_T(B) < 6$ GeV/c is limited. For this reason we used an alternative approach for measuring the isolation efficiency. We reweighted the $p_T(B)$ distribution of the $B^0_{(s)} \to J/\psi X$ decays to the $p_T(B)$ distribution of the $B^0_{(s)} \to h^+h^{'-}$ decays and we fitted the reweighted $B^0_{(s)} \to J/\psi X$ data directly to determine the average isolation efficiency for the $B^0_{(s)} \to h^+h^{'-}$ decays.

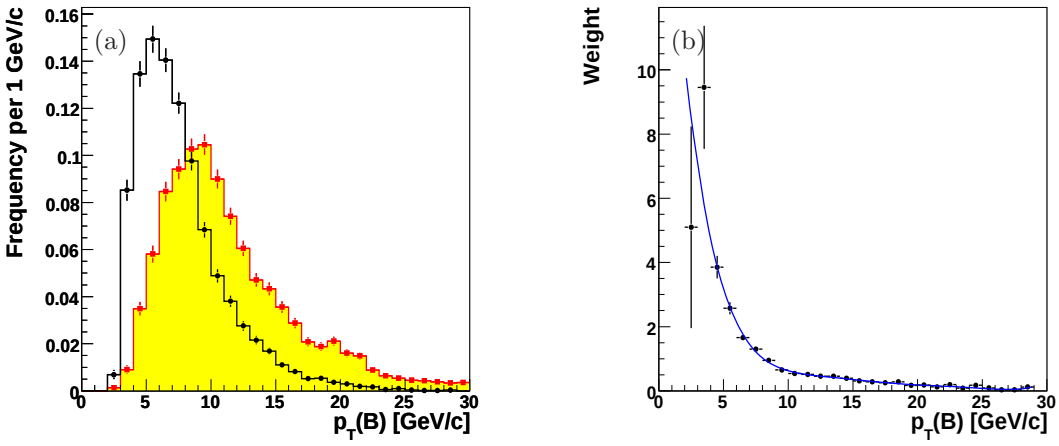


Figure 7.8: Background-subtracted $p_T(B)$-distribution of $B^0_{(s)} \to h^+h^{'-}$ decays (black points) is compared with $p_T(B)$-distribution of $B^0_{(s)} \to J/\psi X$ decays (red squares of the filled histogram) (a). Reweighting function between the two distributions (b).

To parameterize the weight-function that transforms the $p_T(B)$-spectrum of the $B^0_{(s)} \to J/\psi X$ decays into the $p_T(B)$-spectrum of the $B^0_{(s)} \to h^+h^{'-}$decays, we used a mixture of $B^0 \to J/\psi K^{*0}$ (fig. 7.2(a)) and $B_s^0 \to J/\psi\phi$ (fig. 7.2(b)) decays with the same fraction of $B^0(B_s^0)$ mesons observed in the $B^0_{(s)} \to h^+h^{'-}$ decays [1] corresponding to about 74%(26%). Figure 7.8(a) shows the comparison between the two spectra, the black histogram is the side-band subtracted $p_T(B)$-spectrum of the $B^0_{(s)} \to h^+h^{'-}$ decays while the filled yellow histogram is the side-band subtracted $p_T(B)$-spectrum of the $B^0_{(s)} \to J/\psi X$ decays with the same composition of the $B^0_{(s)} \to h^+h^{'-}$ in terms of the B^0 and B_s^0 fractions. Figure 7.8(b) shows the result of the ratio between the two histograms parameterized using a polynomial function. This weight-function $w(p_T(B))$ can be evaluated for each i^{th} event:

$$w_i = w(p_T(B)_i). \tag{7.7}$$

Section 7.3 describes the standard Likelihood function (eq. (7.3)) used to measure the isolation efficiency in a sample of known composition (see eqs. (7.4)–(7.6)). To perform a reweighted Likelihood fit the Likelihood has to be modified. The weight-function has to be normalized to the total number N of decays to avoid a bias of the estimate of the parameter errors. We define the normalized

weight-function:

$$W_i = W(p_{\mathrm{T}}(B)_i) = w_i \frac{N}{\sum_{j=1}^{N} w_j} \tag{7.8}$$

where the index $i(j)$ runs over the observed number of events in our sample of N candidates. Then we can reformulate the Likelihood keeping into account the $p_{\mathrm{T}}(B)$ reweighting:

$$\mathscr{L}(\vec{\theta}) = \prod_{i=1}^{N} [\mathscr{L}_i(\vec{\theta})]^{W_i} \tag{7.9}$$

where $\mathscr{L}_i$ is the same as in eq. (7.3).

7.4.1 Fit of the reweighted $B^0_{(s)} \to J/\psi X$ samples

Figures 7.9 and 7.10 show the invariant-mass distributions of the reweighted $B^0_{(s)} \to J/\psi X$ samples, with the fit functions overlaid. Table 7.4 contains the results of the fits applied to the reweighted samples of the different $B^0_{(s)} \to J/\psi X$ modes respectively for $I(B) > 0.5$ and $I(B) > 0.525$.

	$B^0 \to J/\psi K^{*0}$	$B_s^0 \to J/\psi\phi$
$\varepsilon^s_{\mathrm{iso}}$ [%]	72.4 ± 0.8	72.4 ± 1.9
$\varepsilon^b_{\mathrm{iso}}$ [%]	30.9 ± 0.7	29.2 ± 1.4
f_s [%]	42.1 ± 0.7	40.0 ± 1.3
f_1 [%]	49 ± 14	–
μ [MeV/c^2]	5278.9 ± 0.2	5366.2 ± 0.4
σ_1 [MeV/c^2]	7.7 ± 1.0	–
σ_2 [MeV/c^2]	16.0 ± 2.2	–
σ [MeV/c^2]	–	10.3 ± 0.4

	$B^0 \to J/\psi K^{*0}$	$B_s^0 \to J/\psi\phi$
$\varepsilon^s_{\mathrm{iso}}$ [%]	68.7 ± 0.8	66.7 ± 1.9
$\varepsilon^b_{\mathrm{iso}}$ [%]	26.0 ± 0.7	25.4 ± 1.4
f_s [%]	42.6 ± 0.8	40.1 ± 1.3
f_1 [%]	62 ± 11	–
μ [MeV/c^2]	5279.0 ± 0.2	5366.2 ± 0.4
σ_1 [MeV/c^2]	8.5 ± 0.7	–
σ_2 [MeV/c^2]	18.8 ± 3.1	–
σ [MeV/c^2]	–	10.3 ± 0.4

Table 7.4: Isolation efficiencies ($I(B) > 0.5$ on the left, $I(B) > 0.5$ on the right) estimated from the $B^0_{(s)} \to J/\psi X$ samples. The $p_{\mathrm{T}}(B)$-spectrum of $B^0_{(s)} \to J/\psi X$ decays has been reweighted to the $p_{\mathrm{T}}(B)$-spectrum of the $B^0_{(s)} \to h^+ h^{'-}$ decays. $N = 13064$ events of $B^0 \to J/\psi K^{*0}$ and $N = 2041$ events $B_s^0 \to J/\psi\phi$ have been fitted.

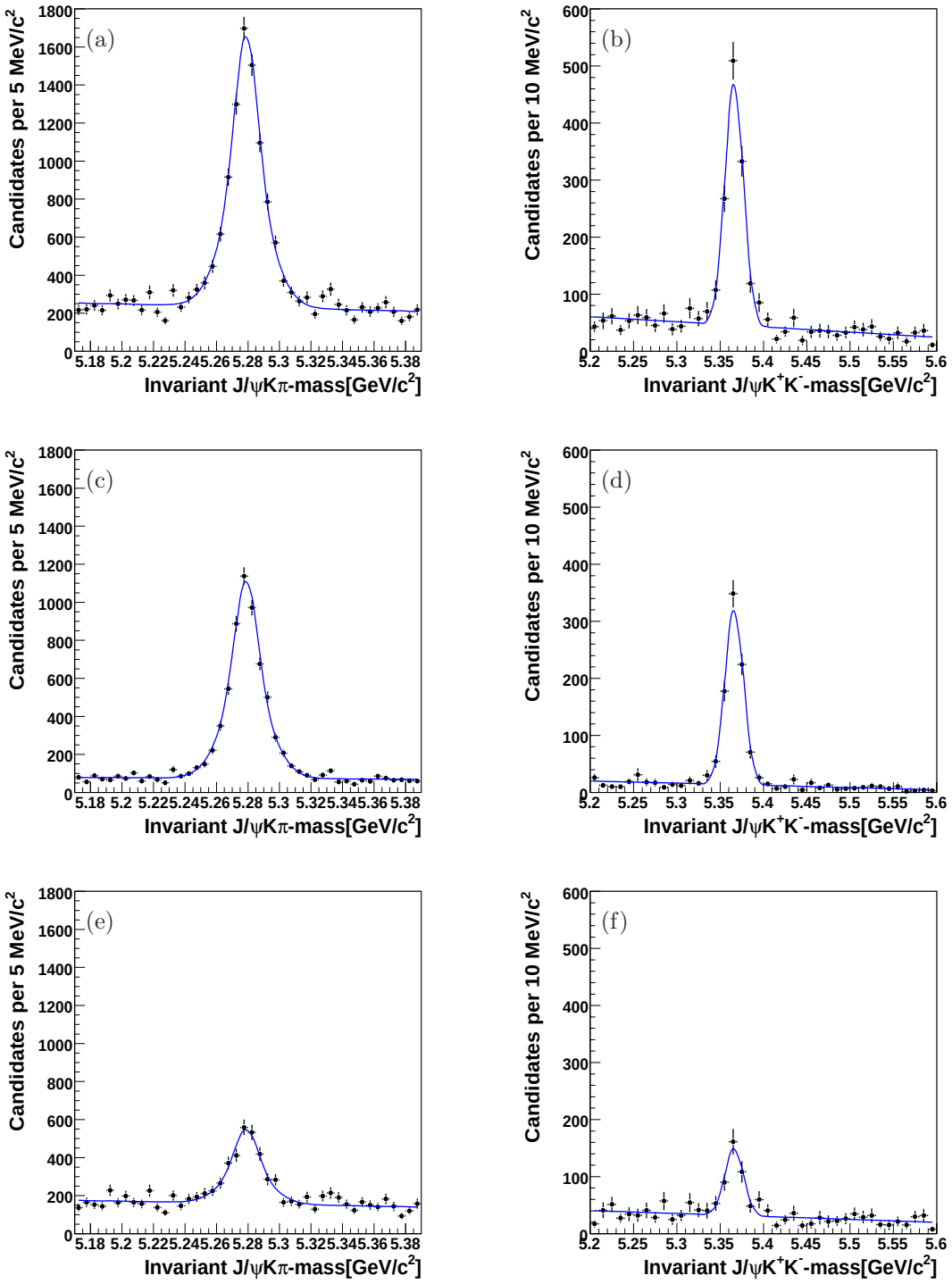


Figure 7.9: Invariant mass distributions of the $B^0_{(s)} \to J/\psi X$ candidates without (a, b), passing (c, d), and failing (e, f) the isolation requirement $I(B) > 0.5$. $B^0 \to J/\psi K^{*0}$ (a, c, e), $B^0_s \to J/\psi\phi$(b, d, f). The $p_{\mathrm{T}}(B)$-spectrum of $B^0_{(s)} \to J/\psi X$ decays has been reweighted to the $p_{\mathrm{T}}(B)$-spectrum of the $B^0_{(s)} \to h^+h'^-$ decays. Fit functions are overlaid (blue, solid line).

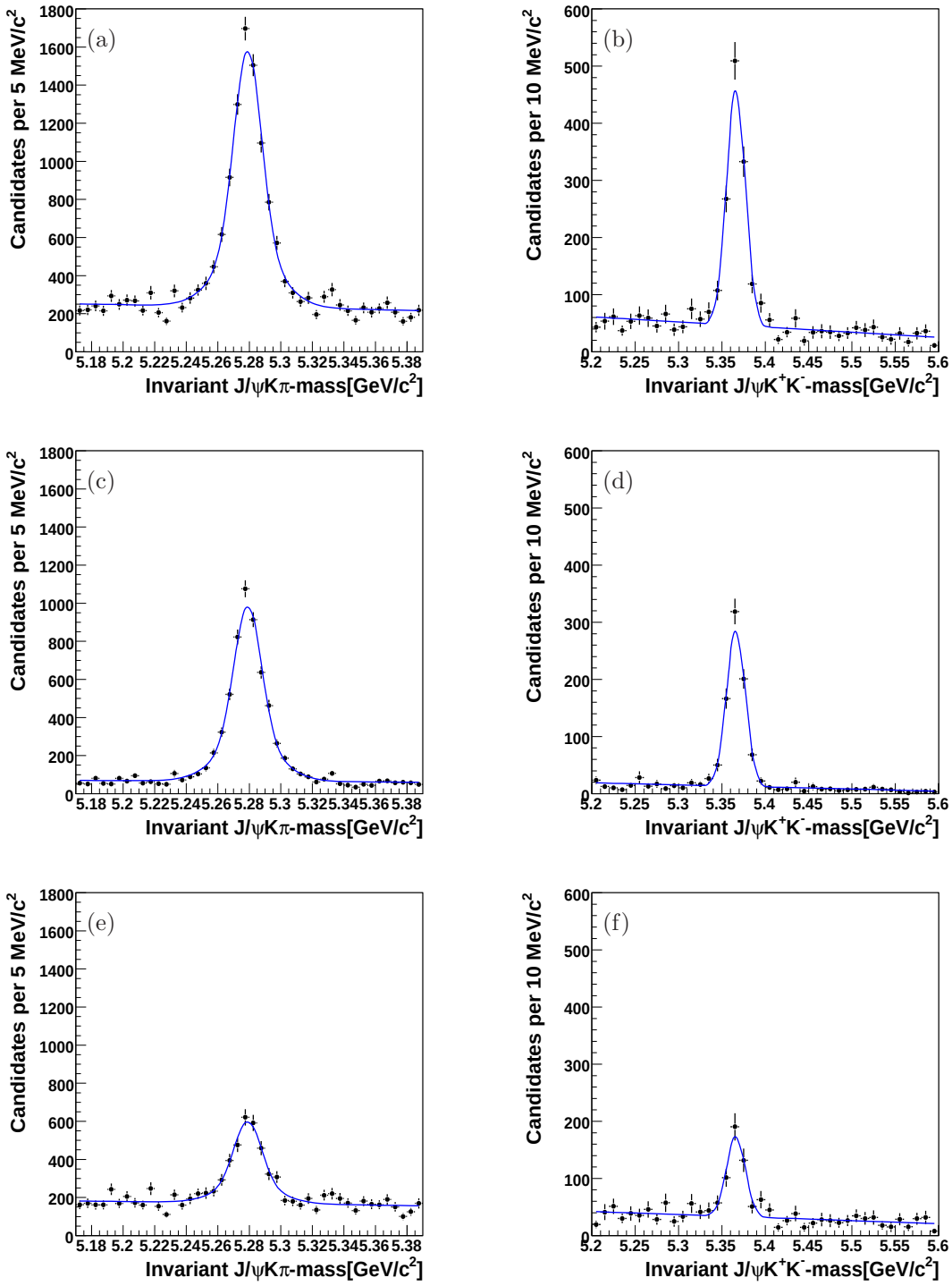


Figure 7.10: Invariant mass distributions of the $B^0_{(s)} \to J/\psi X$ candidates without (a, b), passing (c, d), and failing (e, f) the isolation requirement $I(B) > 0.525$. $B^0 \to J/\psi K^{*0}$ (a, c, e), $B^0_s \to J/\psi\phi$(b, d, f). The $p_{\mathrm{T}}(B)$-spectrum of $B^0_{(s)} \to J/\psi X$ decays has been reweighted to the $p_{\mathrm{T}}(B)$-spectrum of the $B^0_{(s)} \to h^+h^{'-}$ decays. Fit functions are overlaid (blue, solid line).

7.4.2 Isolation efficiency ratio $\frac{\varepsilon_{\mathrm{iso}}(B^0)}{\varepsilon_{\mathrm{iso}}(B_s^0)}$

The results of the fit of composition have to be corrected using the isolation efficiency, $\varepsilon_{\mathrm{iso}}$, averaged over the transverse momentum of the $B^0_{(s)}$ meson. We extracted $\varepsilon_{\mathrm{iso}}$ from the results of tab. 7.4 ($p_{\mathrm{T}}(B)$-spectrum of $B^0_{(s)} \to h^+h^{'-}$ decays), separately for the B^0 and B_s^0 meson decays. The resulting relative isolation efficiency with its statistical uncertainty is:

$$\left.\frac{\varepsilon_{\mathrm{iso}}(B^0)}{\varepsilon_{\mathrm{iso}}(B_s^0)}\right|^{I(B)>0.5}_{B^0_{(s)}\to h^+h'^-} = 1.000 \pm 0.028 \quad \text{and} \quad \left.\frac{\varepsilon_{\mathrm{iso}}(B^0)}{\varepsilon_{\mathrm{iso}}(B_s^0)}\right|^{I(B)>0.525}_{B^0_{(s)}\to h^+h'^-} = 1.030 \pm 0.032. \tag{7.10}$$

These values are statistically compatible with 1 and, along with other relative efficiency corrections described in chap. 10, will be used to translate the uncorrected fit parameters into physics measurements.

In addition, from the results of tab. 7.2 ($p_{\mathrm{T}}(B)$-spectrum of $B^0_{(s)} \to J/\psi X$ decays) we also extracted the relative isolation efficiency:

$$\left.\frac{\varepsilon_{\mathrm{iso}}(B^0)}{\varepsilon_{\mathrm{iso}}(B_s^0)}\right|^{I(B)>0.5}_{B^0_{(s)}\to J/\psi X} = 1.003 \pm 0.016 \quad \text{and} \quad \left.\frac{\varepsilon_{\mathrm{iso}}(B^0)}{\varepsilon_{\mathrm{iso}}(B_s^0)}\right|^{I(B)>0.525}_{B^0_{(s)}\to J/\psi X} = 1.019 \pm 0.019. \tag{7.11}$$

The degradation of the statistical uncertainty from (7.11) to (7.10) is expected. This is due to the effect of the reweighting from the $p_{\mathrm{T}}(B)$-spectrum of the $B^0_{(s)} \to J/\psi X$ decays to the one of $B^0_{(s)} \to h^+h^{'-}$ decays. As far as I know, this is the most accurate measurement of its kind. It will be interesting to repeat this measurement with the larger data samples already available at CDF ≈ 2.5 fb^{-1} (5–6 fb^{-1} by year 2009) to measure a possible discrepancy from unit and, in particular, a possible dependence on the $p_{\mathrm{T}}(B)$ distribution of this efficiency ratio.

7.4.3 $p_{\mathrm{T}}(B)$ dependence of the isolation

Using the large sample of $B^0 \to J/\psi K^{*0}$ we performed additional studies on the isolation variable. So far we studied only the efficiency ratio between the B^0 and B_s^0 mesons and we extracted the acceptance correction averaging on the whole transverse momentum domain. But another important issue cannot be neglected. This is directly related to the strong dependence of the isolation efficiency when a cut is applied: the $p_{\mathrm{T}}(B)$ distribution is sculpted (see fig. 7.11).

We measured the efficiency ratio between B^0 and B_s^0 in two different configurations of $p_{\mathrm{T}}(B)$ spectrum and we did not find any significant difference from the unit (also in different $p_{\mathrm{T}}(B)$-bins, see tab. 7.3). Moreover we observed that the $p_{\mathrm{T}}(B)$-spectra of $B^0 \to J/\psi K^{*0}$ and $B_s^0 \to J/\psi\phi$ decays do not show any significant differences (see fig. 7.12). This justifies the extraction of the efficiency curve as a function of the transverse momentum using only the large sample of $B^0 \to J/\psi K^{*0}$ decays and to assume this efficiency curve identical to the one of B_s^0 case. Using the technique of the reweighted Likelihood fit, we measured the isolation efficiency in different $p_{\mathrm{T}}(B)$-bins and we reported the results in tab. 7.5 for the isolation requirement $I(B) > 0.5$ (or 0.525). Since the fits have been performed in bins of momentum, in the table we also reported the average value $\langle p_{\mathrm{T}}(B)\rangle$ of each momentum bin. Figure 7.13 shows the measured values as function of transverse momentum. They were fitted to the following function:

$$a_0 \cdot \mathrm{Erf}(\mathrm{a_1}(\mathrm{p_T(B)} - \mathrm{a_2})) + \mathrm{a_3} \tag{7.12}$$

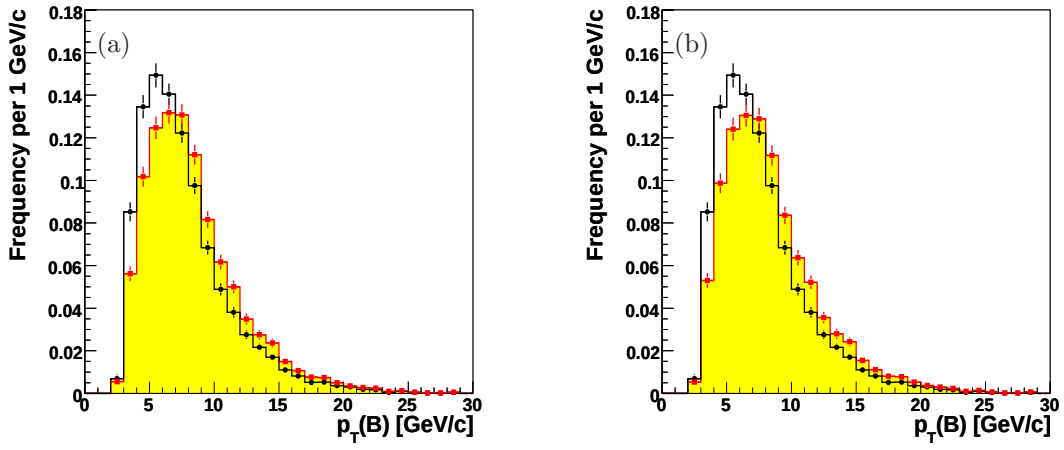


Figure 7.11: Background-subtracted $p_{\mathrm{T}}(B)$-distribution in $B^0_{(s)} \to h^+h'^-$ decays with (black points with error bars) and without (red squares with error bars of the filled yellow histogram) isolation requirement $I(B) > 0.5$ (a) and $I(B) > 0.525$ (b).

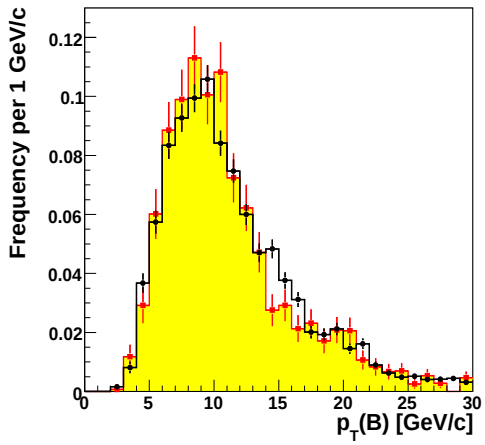


Figure 7.12: Background-subtracted $p_{\mathrm{T}}(B)$-distribution in $B^0_{(s)} \to J/\psi X$ decays. $p_{\mathrm{T}}(B)$-spectrum of $B^0 \to J/\psi K^{*0}$ (black points) is compared with $p_{\mathrm{T}}(B)$-spectrum of $B^0_s \to J/\psi\phi$ (red squares of the filled histogram).

where a_0, a_1, a_2, a_3 are free parameters in the fit and $\mathrm{Erf(x)} = \frac{2}{\sqrt{\pi}} \int_0^{\mathrm{x}} \mathrm{e}^{-\mathrm{t}^2} \mathrm{dt}$ is an error function. This function describes well the shape of the efficiency observed in the data. For large values of the transverse momentum it reaches a plateau of approximately 95%, while at low transverse momentum values it decreases quickly towards zero. Since the statistics at low transverse momentum is limited also in the $B^0 \to J/\psi K^{*0}$ decays, we cannot refine the first large bin $p_{\mathrm{T}}(B) \in [2, 6]$ GeV/c.

p_{T} range [GeV/c]	$\langle p_{\mathrm{T}}(B)\rangle$ [GeV/c]	$\varepsilon_{\mathrm{iso}}^{0.5}$ [%]	$\varepsilon_{\mathrm{iso}}^{0.525}$[%]
$2 < p_{\mathrm{T}}(B) < 6$	4.63	60.4 ± 2.6	56.0 ± 2.5
$6 < p_{\mathrm{T}}(B) < 7$	6.48	65.8 ± 2.0	63.0 ± 2.2
$7 < p_{\mathrm{T}}(B) < 8$	7.5	75.3 ± 2.0	70.5 ± 2.1
$8 < p_{\mathrm{T}}(B) < 9$	8.5	79.5 ± 1.7	74.9 ± 1.8
$9 < p_{\mathrm{T}}(B) < 10$	9.5	81.7 ± 1.6	77.8 ± 1.7
$10 < p_{\mathrm{T}}(B) < 11$	10.5	87.4 ± 1.6	84.7 ± 1.7
$11 < p_{\mathrm{T}}(B) < 12$	11.5	89.2 ± 1.4	85.3 ± 1.6
$12 < p_{\mathrm{T}}(B) < 13$	12.5	92.3 ± 1.4	89.2 ± 1.6
$13 < p_{\mathrm{T}}(B) < 14$	13.5	90.6 ± 1.5	89.2 ± 1.8
$14 < p_{\mathrm{T}}(B) < 15$	14.5	94.2 ± 1.4	93.5 ± 1.5
$15 < p_{\mathrm{T}}(B) < 20$	18.2	95.3 ± 0.8	93.6 ± 0.9

Table 7.5: Isolation efficiency as a function of $p_{\mathrm{T}}(B)$ from $B^0 \to J/\psi K^{*0}$ data with the $p_{\mathrm{T}}(B)$-spectrum reweighted to the $B^0_{(s)} \to h^+h^{'-}$ one. The efficiency has been measured for $I(B) > 0.5$ and $I(B) > 0.525$

With the efficiency curves extracted from the data, we reweighted the $p_{\mathrm{T}}(B)$-spectrum of the simulation to reproduce the effect of the isolation requirement. Figure 7.14 shows the agreement between the $p_{\mathrm{T}}(B)$ distribution of the side-band subtracted data with the isolation requirement applied and the Monte Carlo simulation reweighted to account for the isolation effect. The agreement is satisfactory for our purpose.

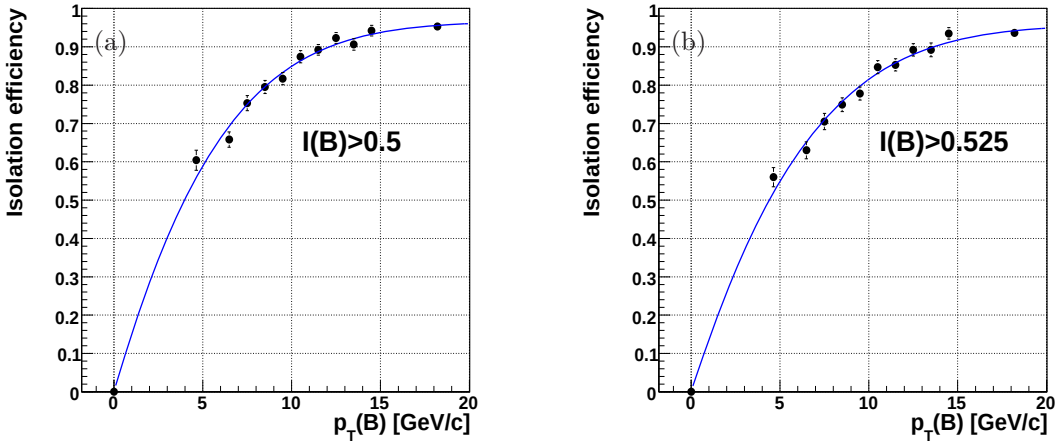


Figure 7.13: Isolation efficiency as a function of $p_{\mathrm{T}}(B)$ extracted from $B^0 \to J/\psi K^{*0}$ decays with the $p_{\mathrm{T}}(B)$-spectrum reweighted. $I(B) > 0.5$ (a) and $I(B) > 0.525$ (b). Fit functions are overlaid (blue, solid line) (See tab. 7.5).

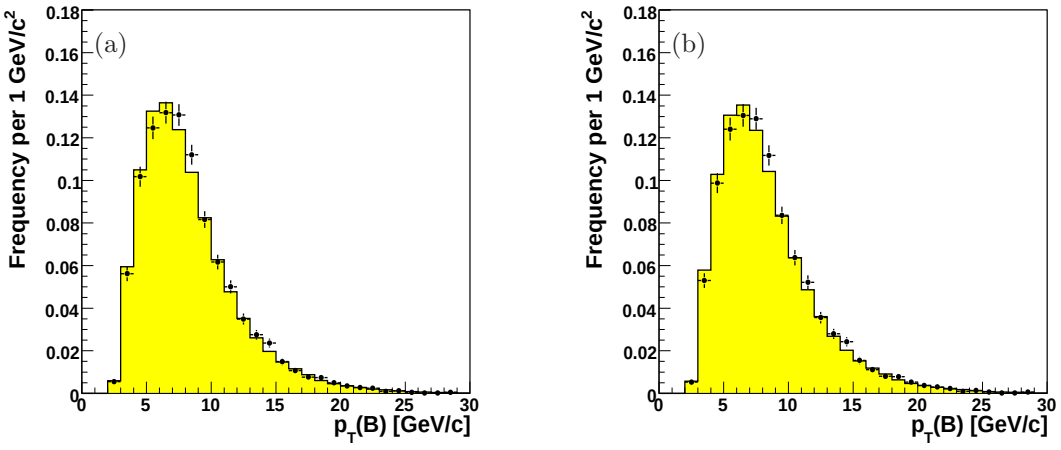


Figure 7.14: Background-subtracted $p_{\mathrm{T}}(B)$-distribution in $B^0_{(s)} \to h^+h'^-$ decays with isolation requirement $I(B) > 0.5$ (a), $I(B) > 0.525$ (b). Data (points with error bars) are compared with Monte Carlo simulation (filled histogram). The efficiency isolation as a function of $p_{\mathrm{T}}(B)$ has been extracted by the $B^0 \to J/\psi K^{*0}$ decays, see fig. 7.13.

7.4.4 Isolation efficiency vs I_{cut}

Another fundamental information concerns the isolation efficiency for different values of the requirement, since it is a necessary ingredient of the cuts selection optimization process (see chap. 8). The isolation cut has been chosen to minimize the statistical uncertainty on the measurement $\mathcal{A}_{\mathrm{CP}}(B^0 \to K^+\pi^-)$ (loose cuts) and to observe the $B_s^0 \to K^-\pi^+$ mode (tight cuts) and its efficiency has to be extracted from the real data. Using the same technique of the reweighted Likelihood fit we measured the isolation efficiency for different values of the cut in a range from 0.1 to 0.9. We reported the results in tab. 7.6 while in fig. 7.15(a) we plotted the values measured interpolated with a smooth curve. In the region between $I(B) > 0.4$ and $I(B) > 0.6$, where we expect to find the optimal point from the previous published version of this analysis [1], we refine the steps. In fig. 7.15(b), instead, we extracted the isolation efficiency directly from the $B^0_{(s)} \to h^+h'^-$ data (for signal and background). We performed the one-dimensional fits (as described in sec. 3.5) of the invariant $\pi\pi$-mass distribution at different values of the cut I_{cut}. We verify that the procedure described in this chapter is in agreement with what we observed in our data.

I_{cut}	ε_{iso} [%]
0.1	98.7 ± 0.2
0.2	98.6 ± 0.3
0.3	93.6 ± 0.5
0.4	86.5 ± 0.7
0.45	79.4 ± 0.7
0.5	72.4 ± 0.8
0.525	68.7 ± 0.8
0.55	64.3 ± 0.8
0.575	59.4 ± 0.8
0.6	54.7 ± 0.8
0.65	44.2 ± 0.8
0.7	34.4 ± 0.7
0.8	17.7 ± 0.6
0.9	5.6 ± 0.3

Table 7.6: Isolation efficiency from $B^0 \to J/\psi K^{*0}$ data with the $p_T(B)$-spectrum reweighted to the $B^0_{(s)} \to h^+h'^-$ one.

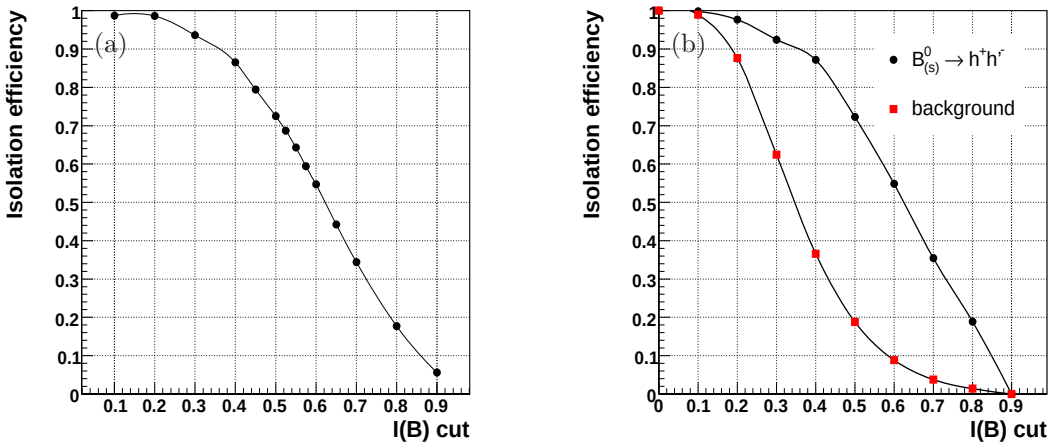


Figure 7.15: Isolation efficiency as a function of isolation cut $I(B) > X$ extracted from $B^0 \to J/\psi K^{*0}$ decays with the $p_T(B)$-spectrum reweighted (see tab. 7.6) (a) and extracted directly from the $B^0_{(s)} \to h^+h'^-$ data sample (b).

Chapter 8

Fit-based cuts optimization

In this chapter we describe the procedure used to optimize the selection of the data sample. This is aimed at minimizing the statistical uncertainty on the quantity we wish to measure. The procedure is based on the fit of composition described in chap. 6, and provides two different selections. One is optimized for the measurement of the direct CP asymmetry $\mathcal{A}_{\rm CP}(B^0 \to K^+\pi^-)$ and the other one for the sensitivity for either discovery or limit setting for the still unobserved $B_s^0 \to K^-\pi^+$ decay mode.

8.1 Unbiased selection optimization

Given a sample, an optimization of the selection is a procedure that selects a subsample. This procedure minimizes (or maximizes) a given parameter (*score function*), whose value depends on the selection. For example, when we perform a measurement of some physics quantity, a standard optimization of the selection should provide the smallest (expected) statistical uncertainty on that quantity. The optimization procedure must be performed in an unbiased way, i. e., it must not influence the value obtained from the measurement, it must be free from arbitrary choices.

In principle, to perform an unbiased optimization of our measurement, we should repeat the entire complex measurement procedure for all possible configurations of selection requirements. The optimal selection should be that one minimizes the uncertainty on the measurement of interest. In practice, the number of the possible selections is so large that this strategy can not be applied. It is therefore necessary to find some convenient parameterization of the resolution as a function of different sets of cuts. Thus, we can use this parameterization to predict the resolution on a given measurement for many different sets of cuts without having to perform a full fit. We will describe the procedure in the following

8.2 Minimum Variance Bound

A standard method used to estimate the expected resolution on a parameter determined with a maximum Likelihood fit is the Minimum Variance Bound [133]. If $\mathscr{L}(\vec{\theta})$ is a Likelihood function and

$\vec{\theta} = (\theta_1, \ldots, \theta_m)$ is the vector of parameters estimated by the fit, the In element $\mathrm{Cov}(\hat{\theta}_i, \hat{\theta}_j)$ ($\equiv \sigma_i^2$ if $i = j$) of the covariance matrix can be written as:

$$\mathrm{Cov}(\hat{\theta}_i, \hat{\theta}_j) \approx \frac{1}{-E\left[\frac{\partial^2 \ln \mathscr{L}(\vec{\theta})}{\partial\theta_i \partial\theta_j}\right]_{\vec{\theta}=\hat{\vec{\theta}}}}, \tag{8.1}$$

where N is the total number of events, $E[x]$ indicates the expectation value of x and $\hat{\theta}_i$ is the expected value of the ith parameter. Equation (8.1) is useful because, under fairly mild conditions of regularity of the problem, the MVB provides a convenient analytical calculation of the statistical power of an estimator, before carrying out the measurement. Since relation (8.1) involves an expectation value, i. e., an integration over the multi-dimensional observables space ($\vec{x}$, in the $B^0_{(s)} \to h^+h^{'-}$ case $\vec{x} = (m_{\pi\pi}, \alpha, p_{\mathrm{tot}}, \kappa 1, \kappa 2)$), its evaluation may be impractical. For this reason before discussing the $B^0_{(s)} \to h^+h^{'-}$ case, we will analyse in the next sections a simplified case: the measurement of the relative fraction of a Gaussian signal peak over a flat background This simple case allows us to study the MVB behavior as a function of the number S of signal events and of the number B of background events.

8.3 Gaussian peak (S) over a flat background (B)

Suppose we want to measure the relative fraction of a single signal distributed with a Gaussian p.d.f. over a flat background (see illustration in fig. 8.1(a)). If $S(B)$ is the number of signal(background) events, $f = S/(S+B)$ is the signal fraction, $1 - f = B/(S+B)$ is the background fraction, the Likelihood function can be written as:

$$\mathscr{L}(f) = f\ \mathscr{G}(x; 0, \sigma)\ +\ (1-f)\ \frac{1}{2c} \tag{8.2}$$

where $\mathscr{G}(x; \mu, \sigma) = \frac{1}{\sigma\sqrt{2\pi}} e^{-\frac{(x-\mu)^2}{2\sigma^2}}$, $2c$ is the range of the x observable. We define also the parameter b which denotes the height of the flat background: i. e., is the number of the background events per unit of x ($B = 2cb$). In this simple case it is possible to write a simple expression for the MVB. By substituting the Likelihood function of eq. (8.2) in the relation (8.1), and dividing by the fraction f, we obtain the expected relative resolution for the parameter f:

$$\frac{\sigma_f}{f} = \frac{1}{\sqrt{S}} \frac{1}{\sqrt{\int_{-\infty}^{+\infty} \left[2\pi\sigma^2(\frac{b}{S}) e^{\frac{x^2}{\sigma^2}} + \sqrt{2\pi}\sigma e^{\frac{x^2}{2\sigma^2}}\right]^{-1} dx}}. \tag{8.3}$$

$\frac{\sigma_f}{f}$ depends on the number of signal events S and on the ratio $\frac{b}{S}$ and it is a function of the cuts applied to the sample. Equation (8.3) depends only on well defined quantities like the height of the background and not on the arbitrary window in x of the chosen variable. If the signal-to-background ratio b/S is fixed, the relative resolution is proportional to depends as expected $\frac{1}{\sqrt{S}}$, as expected on general grounds. The integral in eq. (8.3) cannot be computed analytically, but it is simple to estimate its behavior in two cases, when $\frac{b}{S} \to 0$ and when $\frac{b}{S} \to \infty$:

$$\begin{cases} \frac{b}{S} \to 0 & \frac{\sigma_f}{f} \propto \frac{1}{\sqrt{S}}, \\ \frac{b}{S} \to \infty & \frac{\sigma_f}{f} \propto \frac{1}{\sqrt{S}} \cdot \sqrt{\frac{b}{S}}. \end{cases} \tag{8.4}$$

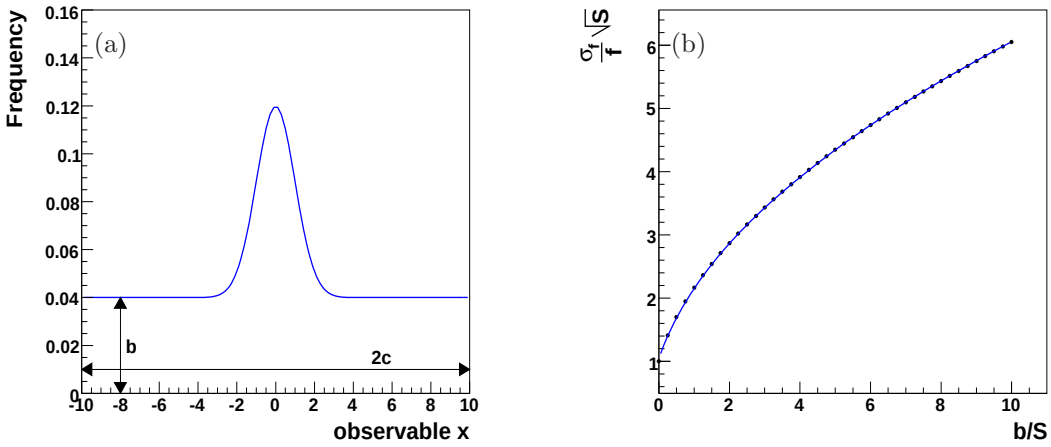


Figure 8.1: Illustration of a Gaussian signal peak over a flat background (a). Comparison between the points calculated numerically using the $\frac{\sigma_f}{f}$ expression from MVB for different values of $\frac{b}{S}$ and the approximated expression $\frac{\sigma_f}{f} = \frac{1}{\sqrt{S}}\sqrt{z + w'\frac{b}{S}}$ (solid line), where the constants z and w' are determined with an interpolation of the black points (b)

A simple function of S and $\frac{b}{S}$ with the same asymptotic behavior of eq. (8.3) is:

$$\frac{\sigma_f}{f} = \frac{1}{\sqrt{S}}\sqrt{z + w'\frac{b}{S}}, \tag{8.5}$$

where z and w' are constants to be determined. To verify that the relation (8.5) describes correctly the relation (8.3), we calculated numerically the value of $\frac{\sigma_f}{f}\sqrt{S}$ assuming $\sigma = 1$ for different values of $\frac{b}{S}$ and we interpolated these points with the approximated relation (8.5). Figure 8.1(b) shows that the approximation (blue line) interpolates well the points evaluated numerically with the exact formula as a function of $\frac{b}{S}$ (black points).

Relation (8.5) can be written as a function of the total number of background events in a given range. We remind that b is the number of events in a unit range in the x window. It is sufficient to define $w = \frac{w'}{2c}$, where $2c$ is the width of the domain of the x variable (see fig. 8.1(a)). Equation (8.5) becomes:

$$\frac{\sigma_f}{f} = \frac{1}{\sqrt{S}}\sqrt{z + w\frac{B}{S}}. \tag{8.6}$$

For this simple case we calculated the MVB and we found a functional form of S and $\frac{B}{S}$ which parameterizes accurately the MVB. This function has some interesting properties and it is worth describing them:

- it is optimal because it was extracted from the MVB which is the better statistical uncertainty estimate we can obtain performing an unbinned maximum Likelihood fit;
- it does not require an arbitrary choice of a range to define S and B. In fact if αS and βB are respectively the number of the signal events and of the background events relative to another

range we can write:

$$\frac{1}{\sqrt{S}}\sqrt{z+w\frac{B}{S}} \Longrightarrow \frac{1}{\sqrt{\alpha S}}\sqrt{z+w\frac{\beta B}{\alpha S}} = \frac{1}{\sqrt{S}}\sqrt{t+k\frac{B}{S}} \tag{8.7}$$

where $t = \frac{z}{\alpha}$ and $k = w\frac{\beta}{\alpha^2}$. If we vary the definition range for S and B we find a different set of cuts to apply to our sample but the optimal point remains unchanged;

- the optimal set of cuts does not change if we consider as background only combinatorial background or the sum of the combinatorial background plus other signals different from the signal we want to optimize. The reason is similar to the previous case:

$$\frac{1}{\sqrt{S}}\sqrt{z+w\frac{B}{S}} \Longrightarrow \frac{1}{\sqrt{S}}\sqrt{z+w\frac{B+\alpha S}{S}} = \frac{1}{\sqrt{S}}\sqrt{(z+w\alpha)+w\frac{B}{S}} = \frac{1}{\sqrt{S}}\sqrt{t+w\frac{B}{S}} \tag{8.8}$$

  where the additional background is supposed to come from another mode, proportional to our signal ($S' = \alpha S$);

- different measurements will have different values of z and w, we can therefore determine the optimal set of cuts for each specific measurement.

We assume that this same functional form should adequately describe the behavior of the resolution also in our measurement, where the background slope is more complicated and there are several signals. In this approximation, for each individual case we just need to estimate the parameters z and w. These can be extracted by performing a finite number of pseudo-experiments of the full analysis. It is possible to generate some simulated samples of the data we want to measure, for different values of $\frac{B}{S}$, and to plot $\frac{\sigma_f}{f}$ versus $\frac{B}{S}$ at fixed S, since the dependence of S of eq. (8.6) is known. From the interpolation of these points we can extract z and w. At this point an optimization procedure would simply need to evaluate the quantity S and B for all the combinations of the selection requirements. The optimal selection would be the one that minimizes $\frac{\sigma_f}{f}$, because this gives the best resolution on the measurement of relative branching fraction.

8.3.1 Search for a rare decay ($S \to 0$) over a flat background (B)

The above discussion apply to the measurement of a large fraction f, in which we want to minimize $\frac{\sigma_f}{f}$. In the case one wants to optimize the selection to maximize the sensitivity for the discovery or rate limit setting for a rare decay mode the situation is different. In this analysis we followed the general approach described in Ref. [134] where a frequentist definition of sensitivity of a search for new phenomena is discussed. This is particularly suitable for optimization, being independent of a-priori expectations about the presence of a signal, thus allowing the determination of a single set of cuts that is optimal both for setting limits and for making a discovery. Ref. [134] suggests to characterize the sensitivity of an experiment in the following way.

A test of the current best theory H_0 in favor of an alternative theory H_m, where m indicates the free parameters of the new theory (masses, coupling constants, cross sections, branching fractions, etc.), is specified by defining the set of values of the experimental observables X that will make us decide that H_0 must be rejected ("critical region"); the *significance level* of the test, indicated by α, is

the probability of rejecting H_0 when it is indeed true; that is to say, α is the probability for X to fall within the critical region, calculated under the assumption that H_0 is true. α is a "small number", common practice for new physics discovery being to require α to correspond to the 5σ single tail of a Gaussian distribution. The other element to be considered in a test is the probability that a discovery is made. The classical way to express this is by the *power function* $1-\beta(m)$, that is, the probability that X will fall in the critical region (=the probability that a discovery will be claimed) assuming H_m is true, as a function of the parameters m. It is clearly desirable to have the greatest possible power. A correct statistical practice requires to decide before the experiment the values of α and CL (Confidence Level). Then one can proceed by quoting the region of the parameters m for which the power of the chosen test is greater or equal to the Confidence Level chosen for the limits in case there is no discovery:

$$1-\beta_\alpha(m) > \text{CL}. \tag{8.9}$$

This region of m can be thought of as a region of parameters to which the experiment is "sufficiently sensitive".

Ref. [134] treats in detail the common problem of a counting experiment in presence of background using this generic approach. Here we have a similar problem, but we perform an unbinned maximum Likelihood fit to search for a rare decay as the $B_s^0 \to K^-\pi^+$. In this case the observable of interest m is the branching fraction ($\mathcal{B}$) of a rare mode. We measure it using an unbinned maximum Likelihood fit. One of the parameters returned from the fit is the number of signal events N, distributed with a known p.d.f. in which the mean is determined by B, the expected number of background events (supposed known), and the possible contribution of signal events $S_\mathcal{B}$:

$$\wp(N|H_0) = f(N,0,B), \tag{8.10}$$

$$\wp(N|H_\mathcal{B}) = f(N,S_\mathcal{B},B). \tag{8.11}$$

For this problem, the definition of a critical region for the presence of non-zero signal $S_\mathcal{B}$ takes the form of a condition like

$$N > N_{\min}. \tag{8.12}$$

Therefore, the test is completely defined once the desired significance level α is chosen. We can now evaluate its power as a function of $\mathcal{B}$, and determine the set of values for $\mathcal{B}$ such that eq. (8.9) holds. Since the power of a test of the form $N > N_{\min}$ grows monotonically with $S_\mathcal{B}$, eq. (8.9) leads to simple inequalities of the form:

$$S_\mathcal{B} > S_{\min} \tag{8.13}$$

Therefore, all is needed to completely characterize the solution of our problem is the value of $S_{\min}$, that is in general a function of α, β, and B. We know from pseudo-experiments that the parameters returned by our fit have Gaussian distributions. Therefore, condition (8.9) translates into the following equation for $S_{\min}$:

$$S_{\min} = a\ \sigma_N(B,0) + b\ \sigma_N(B,S_{\min}), \tag{8.14}$$

where $\sigma_N(B,0)$ and $\sigma_N(B,S_{\min})$ are the statistical uncertainties of N returned from the fit with no signal hypothesis ($S_\mathcal{B}=0$) or signal hypothesis ($S_\mathcal{B}$). a and b are the number of standard deviations corresponding to the one-sided Gaussian tests at significance α and β respectively. Since in the fit

the statistical uncertainty is dominated by the number of background events for small signal, we approximated $\sigma_N(B, S_{\min}) \approx \sigma_N(B, 0)$, then eq. (8.14) becomes:

$$S_{\min} = (a + b)\ \sigma_N(B, 0). \tag{8.15}$$

This expression holds for one specific set of selection criteria. Now, consider the common situation where one has to decide on the set of cuts to be used in the analysis. In this case both the background B and the number of expected signal events $S_{\mathcal{B}}$ depend on the cuts (let us indicate the whole set of cuts with the symbol t). In general, in order to decide which set of cuts t is best, one needs to determine for every t the set of values $\tilde{\mathcal{B}}$ to which the experiment is sensitive, by solving for $\tilde{\mathcal{B}}$ the inequality:

$$S_{\tilde{\mathcal{B}}}(t) \geq (a + b)\ \sigma_N(B(t), 0) \tag{8.16}$$

and then to choose the cuts t yielding the most extended region. If ε is the efficiency of the chosen set of cuts on the signal we can write:

$$S_{\mathcal{B}}(t) = \varepsilon(t) \cdot \mathcal{L}_{\text{int}} \cdot \sigma_{\text{prod}} \cdot \mathcal{B}, \tag{8.17}$$

where $\mathcal{L}_{\text{int}}$ is the integrated luminosity, σ_{prod} is the production cross section of the process and $\mathcal{B}$ is the branching fraction being determined. In this case one can simply invert the above equation to write down the minimum "detectable" (according to our criteria) branching fraction:

$$\mathcal{B}_{\min} = \frac{(a + b)\ \sigma_N(B(t), 0)}{\varepsilon(t) \cdot \mathcal{L}\ \cdot \sigma_{\text{prod}}} = K \cdot \frac{\sigma_N(B(t), 0)}{\varepsilon(t)} \tag{8.18}$$

Obviously, the maximum sensitivity is obtained when $\mathcal{B}_{\min}$ is smallest. The optimal choice of cuts does not depend on the assumed branching fraction $\mathcal{B}$. This is a very useful feature, since this parameter is often unknown.

If we consider the simple case of the measurement of the yield of a rare signal distributed with a Gaussian over a large background using a maximum Likelihood fit discussed in the previous section we can extract the analytical expression for $\sigma_N(B(t), 0)$. Using the same procedure and notation we calculated the expected resolution σ_S on the number of signal events S when $S \to 0$:

$$\sigma_N(B(t), 0) = \sigma_{S\to 0} = \sqrt{2\pi\sigma}\sqrt{b} \tag{8.19}$$

in which b denotes the height of the flat background. The resolution $\sigma_{S\to 0}$ depends only on b and, as in the previous section, the relation (8.19) can be written as a function of the total number of background events in a given x window $2c$-wide:

$$\sigma_{S\to 0} = \sqrt{\frac{\pi\sigma}{c}}\sqrt{B}. \tag{8.20}$$

$\sigma_{S\to 0}$ is the expected resolution on the measurement of the number of signal events when S is very small, and, as expected, it is function only of the background level B.
By substituting $\sigma_N(B(t), 0)$ in eq. (8.18) in this simple case we obtain:

$$\sigma_{\mathcal{B}} \propto \mathcal{B}_{\min} = K' \cdot \frac{\sqrt{B}}{\varepsilon(t)} \tag{8.21}$$

where $\sigma_{\mathcal{B}}$ is the statistical uncertainty on the measurement of $\mathcal{B}$ (proportional to $\mathcal{B}_{\rm min}$) which is the quantity to minimize to obtain the best set of cuts to discover and setting the limit on the branching fraction $\mathcal{B}$ of a new process. Equation (8.21) is valid only in Gaussian approximation, this means in the limit of high statistics, namely in the limit of large B.

8.4 Optimization for $B^0_{(s)} \to h^+h^{'-}$

The measurement of the branching fractions and of the direct CP asymmetries in the $B^0_{(s)} \to h^+h^{'-}$ decay modes is a more complex version of the same kind of problem. If we look, for example, at the invariant $\pi\pi$-mass observable, the $B^0_{(s)} \to h^+h^{'-}$ signal is not distributed like a Gaussian, but it is the sum of different contributions that are not even individually distributed as a Gaussian. Moreover the background is the sum of two contributions: combinatorial (exponential function) and physics background (convolution between an Argus function and a Gaussian). The Likelihood function described in the chap. 6 is a complex function depending on 5 observables ($\vec{x} = (m_{\pi\pi}, \alpha, p_{\rm tot}, \kappa 1, \kappa 2)$). Hence the analytical calculation of the MVB in this case is impractical. However, the simple expressions of eqs. (8.6) and (8.21), extracted from the analysis of the MVB of a Gaussian peak over a flat background in two limiting cases of large S and $S \to 0$, suggest the possibility of a similar simpler approximated parameterization. In general, we assumed that for the cases in which the analytical calculation of the MVB is impractical, it is possible to parameterize it with an expression which preserves the same dependence on S and $\frac{B}{S}$ as we found in the case of a Gaussian signal peak over a flat background. For this reason, to approximate the resolution in the $B^0_{(s)} \to h^+h^{'-}$ case we decided to use two similar relations inspired to eqs. (8.6) and (8.21). We verify a posteriori their validity with pseudo-experiments.

For the measurement of quantities related to the abundant modes (like $B^0 \to \pi^+\pi^-$, $B^0 \to K^+\pi^-$, $B^0_s \to K^+K^-$) we parameterized the resolution σ_m (where m is the observable we wish to measure, for example, $\mathcal{A}_{\rm CP}(B^0 \to K^+\pi^-)$, $\mathcal{B}(B^0 \to \pi^+\pi^-)/\mathcal{B}(B^0 \to K^+\pi^-)$, etc.) with the following relation:

$$\sigma_m = \frac{1}{\sqrt{S}}\sqrt{z_m + w_m \frac{B}{S}}, \tag{8.22}$$

where z_m e w_m are constants to be determined from case to case according to the observable we want to measure. S is the number of signal events, while B is the estimate of the background level. S and B can be defined as the number of signal and background events in a well defined invariant $\pi\pi$-mass window. S and B can be normalized in an arbitrary way since z_m e w_m are arbitrary constants which can reabsorb any such definition change (see sec. **??**).

For the observables relative to a rare decay (like the branching fraction of $B^0_s \to K^-\pi^+$, $B^0_s \to \pi^+\pi^-$, $B^0 \to K^+K^-$ and $\Lambda^0_b \to ph^-$) we used, instead, a parameterization of the MVB inspired to eq. (8.21):

$$\sigma_m = \frac{1}{\varepsilon(t)}\sqrt{z_m + w_m B}. \tag{8.23}$$

Also in this case z_m e w_m are the constants to be determined and they depend on the measurement m we want to perform. S and B are defined as in relation (8.22) while $\varepsilon(t)$ is the total signal efficiency for the selection t. This functional form is different from eq. (8.21) since the parameter z_m can be

different from 0. In the relation (8.21) $\sigma_{\mathcal{B}} \to 0$ when $B \to 0$, and this is an obvious consequence since also $S \to 0$. In the $B^0_{(s)} \to h^+h^{'-}$ case, B indicates the number of background events of all the $B^0_{(s)} \to h^+h^{'-}$ signal modes. If we consider the rare $B^0_s \to K^-\pi^+$ signal mode and if we optimize the statistical uncertainty on the measurement of its branching fraction, the "background" from other $B^0_{(s)} \to h^+h^{'-}$ modes ($B^0 \to \pi^+\pi^-$, $B^0 \to K^+\pi^-$, $B^0_s \to K^+K^-$) is proportional to the $B^0_s \to K^-\pi^+$ fraction which can not be eliminated. Then also if $B \to 0$, a residual background remains and $z_m \neq 0$. This makes it necessary to absorb this additional background in the score function.

To verify these assumptions and to extract the constants z_m and w_m for each measurement m we performed several pseudo-experiments of the full analysis. Using the same p.d.f.s described in chap. 6 we simulated the $B^0_{(s)} \to h^+h^{'-}$ data with an admixture of the expected dominant modes in the proportions resulting from the experimental knowledge at the time of the analysis: $B^0 \to \pi^+\pi^-$ (17%), $B^0 \to K^+\pi^-$ (63%) $B^0_s \to K^+K^-$ (20%). For each observable m, we extracted the statistical uncertainty σ_m by varying $\frac{B}{S}$ and keeping fixed S, performing the complete unbinned maximum Likelihood fit described in the chap. 6 to the simulated samples. Then we interpolated these points using the function described above and we extracted the constants z_m e w_m. Figures 8.2(a) and (b) show the agreement between the points and the score functions respectively for the measurement of the direct CP asymmetry $\mathcal{A}_{\rm CP}(B^0 \to K^+\pi^-)$ and for the discovery of the $B^0_s \to K^-\pi^+$ mode. The expressions of eqs. (8.22) and (8.23) describe well the shape of the statistical uncertainty returned from the full maximum Likelihood fit as a function of $\frac{S}{B}$. We checked that also the $\frac{1}{\sqrt{S}}$ dependence is well approximated. We repeated a similar procedure generating samples with different numbers of signal events S and the values found for z_m and w_m are resulted to be compatible with the $\frac{1}{\sqrt{S}}$ shape.

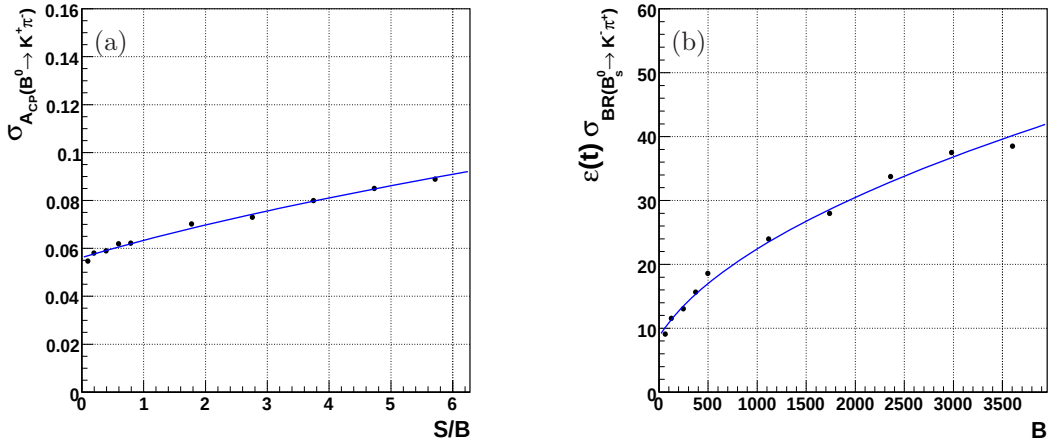


Figure 8.2: Statistical uncertainty on the measurement of the direct CP asymmetry $\mathcal{A}_{\rm CP}(B^0 \to K^+\pi^-)$ as function of $\frac{B}{S}$ at fixed $S = 630$ ($N_{B^0 \to K^+\pi^-} = 630$). Points are interpolated with the function $\sigma_{\mathcal{A}_{\rm CP}}$ of eq. (8.22) (a). Statistical uncertainty on the measurement of the branching fraction $\mathcal{B}(B^0_s \to K^-\pi^+)$ times the efficiency $\varepsilon(t)$ of the selection t as function of B ($N_{B^0_{(s)} \to h^+h'^-} = 1000$ and $N_{B^0_s \to K^-\pi^+} = 0$). Points are interpolated with function $\varepsilon(t)\sigma_{\mathcal{B}} = \sqrt{z_{\mathcal{B}} + w_{\mathcal{B}} B}$ (b).

In general, one should optimize the selection for each measurement he wants to perform. In our analysis there are several measurements related to the individual modes which contribute to the $B^0_{(s)} \to h^+h^{'-}$ peak. However, changing the selection for each measurement implies changing the efficiency values of the decays and then for each selection all templates of the Likelihood fit have to be re-parameterized. Every time we modify the selection to optimize a measurement we need to repeat the entire analysis process (templates parameterization, checks, systematics calculation, etc.) and that is very impractical. We decided to use just two different sets of cuts, respectively optimized to minimize the statistical uncertainty on the measurement of the direct CP asymmetry $\mathcal{A}_{\rm CP}(B^0 \to K^+\pi^-)$ and to optimize the sensitivity for discovery and limit setting (see sec. 8.3.1) for the rare decay mode $B^0_s \to K^-\pi^+$. We verified that the former set of cuts is also adequate to measure other decay rates of the larger yield modes ($B^0 \to \pi^+\pi^-$, $B^0_s \to K^+K^-$), while the latter is well suited to measure the decay rates and CP asymmetries related to rare modes ($B^0_s \to \pi^+\pi^-$, $B^0 \to K^+K^-$, $\Lambda^0_b \to p\pi^-$ and $\Lambda^0_b \to pK^-$).

8.5 Optimized selection

In the optimization we varied the thresholds on the following discriminating quantities: d_0 of the two tracks descending from the candidate, $L_{\rm T}(B)$, $|d_0(B)|$, $I(B)$ and $\chi^2_{3D}(B)$. We avoided using signal events from data to keep the optimization unbiased; for each jth configuration of the selection requirements we evaluated the following quantities:

$$\mathcal{S}^j_{\mathcal{A}_{\rm CP}} = \frac{1}{\sqrt{S_j}}\sqrt{z_{\mathcal{A}_{\rm CP}} + w_{\mathcal{A}_{\rm CP}}\frac{B_j}{S_j}} \tag{8.24}$$

$$\mathcal{S}^j_{\mathcal{B}} = \frac{1}{\varepsilon(t_j)}\sqrt{z_{\mathcal{B}} + w_{\mathcal{B}}B_j}. \tag{8.25}$$

respectively for the measurement of $\mathcal{A}_{\rm CP}(B^0 \to K^+\pi^-)$ and the discovery of $B^0_s \to K^-\pi^+$. The constants z and w were extracted from full pseudo-experiments as described in sec. 8.4. $\mathcal{S}^j_{\mathcal{A}_{\rm CP}(\mathcal{B})}$ are function of the expected number of signal (S_j), background (B_j) events, and the total reconstruction efficiency of the selection t_j ($\varepsilon(t_j)$) defined as follows:

- $\boldsymbol{S_j}$ – the number of simulated $B^0 \to K^+\pi^-$ decays that passed the jth configuration of the selection requirements in the invariant $\pi\pi$-mass window $[5.140 \div 5.320]$ GeV/c^2, normalized to the $B^0 \to K^+\pi^-$ ($N_{B^0\to K^+\pi^-} \approx 0.63\ N_{B^0_{(s)}\to h^+h'^-}$) decays observed in data after the baseline selection (see tab. 3.2). This guarantees that, in each step of the optimization, signal and background yields are correctly normalized. The chosen interval corresponds approximately to a window size of $\pm 2\sigma$ if we approximate the signal invariant $\pi\pi$-mass distribution of the $B^0 \to K^+\pi^-$ mode with a Gaussian.

- $\boldsymbol{B_j}$ – the number of background events passing the jth configuration of the selection requirements, in the same $m_{\pi\pi}$ window defined for the signal yields S_j, underneath the signal peak. For each jth configuration of the selection requirements B_j was estimated by fitting (one-dimensional χ^2-binned fit) the invariant $\pi\pi$-mass distribution. We used a single Gaussian function to model the total $B^0_{(s)} \to h^+h^{'-}$ signal and an exponential function to model the background. B_j was

the integral of the latter function in the invariant $\pi\pi$-mass window $[5.140 \div 5.320]$ GeV/c^2 for the $B^0 \to K^+\pi^-$ decays (eq. (8.24)) and $[5.230 \div 5.410]$ GeV/c^2 for the $B_s^0 \to K^-\pi^+$ decays (eq. (8.25)).

$\varepsilon(t_j)$ – the total reconstruction efficiency (trigger plus offline selection) of the signal events passing the jth configuration of the selection requirements t_j in the same $\pi\pi$-mass window defined for the $B_s^0 \to K^-\pi^+$ decays $[5.230 \div 5.410]$ GeV/c^2. $\varepsilon(t_j)$ was estimated using the simulation.

Starting from the baseline selection listed in tab. 3.2, each requirement was tightened independently of the others, scanning an adequate range of values. Table 8.1 shows the chosen ranges and step widths for each requirement, which resulted in 293,000 total selections. The effectiveness of the procedure relies on the capability to reproduce the real efficiency, for background and for signal, corresponding to each selection. Reliable efficiencies for background were ensured by our choice of using real $B^0_{(s)} \to h^+h^{'-}$ data. For the signal, the validation of sec. 4.1.1 guarantees that the simulation reproduces with sufficient accuracy the efficiencies used in the optimization, except for the isolation. The efficiency of the isolation cut was extracted separately and assumed factorizable with the other efficiencies. We extracted it from a control sample of real $B^+ \to J/\psi K^+$ decays reconstructed with the method described in chap. 7. At the time of the optimization of the selection only a limited data sample of $B^+ \to J/\psi K^+$ decays was available, about 5574 ± 91 candidates corresponding to the first 360 pb^{-1} of integrated luminosity collected by CDF II. For the purpose of optimization of the selection we neglected possible differences between the B^+, B^0 and B_s^0 isolation distributions.

The optimal selections are reported in the last two columns in tab. 8.1.

Quantity	Units	Lower edge	Higher edge	Step width	(I)	(II)
Minimum $L_{\rm T}$	μm	200	650	50	300	350
Min($\lvert d_0(1)\rvert$, $\lvert d_0(2)\rvert$)	μm	100	250	10	100	120
Maximum $\lvert d_0(B)\rvert$	μm	140	50	10	80	60
Minimum $I(B)$*	–	0.4	1.0	0.1	0.5	0.525
Maximum $\chi^2_{3D}(B)$	–	17	3	1.	7	5

Table 8.1: Quantities used in the optimization of the selection and ranges in which they were varied. Results of the optimization procedure: optimum selection for the measurement of $\mathcal{A}_{\rm CP}(B^0 \to K^+\pi^-)$ (I) and for the measurement of $\mathcal{B}(B_s^0 \to K^-\pi^+)$ (II). *Since we expect the optimal point of the isolation requirement $I(B) > 0.5$ the zone around this value was refined with the following steps: $I(B) > 0.475, 0.525, 0.55, 0.575, 0.625$.

8.6 Performance of the optimization procedure

The procedure described in this chapter represents the standard technique one should use to optimize the selection when the estimate of the physics observable of interest is performed with a maximum Likelihood fit. In sec. 8.3 we summarized all properties of the score function extracted from the MVB which makes it optimal for the purpose of optimizing the selection.

In the first published step of this analysis [1], performed using the first part of CDF II data corresponding to 180 pb^{-1} of integrated luminosity, the selection was optimized using the score function $\frac{\sqrt{S+B}}{S}$. This is optimal for a typical "*counting experiment*" since it is proportional to the statistical uncertainty on the measurement of the signal yield σ_S. By the comparison of the selection optimization procedure performed using $\frac{\sqrt{S+B}}{S}$ and the score functions described in this thesis, a sizeable improvement of the statistical uncertainty was obtained: the resolution on $\mathcal{A}_{\text{CP}}(B^0 \to K^+\pi^-)$ improved by 4% while the resolution on $\mathcal{B}(B_s^0 \to K^-\pi^+)$ improved by 12%.

In this analysis we used an additional variable ($\chi^2_{3D}(B)$) in the optimization procedure with respect to the published analysis, so the statistical uncertainty improvement is actually larger: the resolution on $\mathcal{A}_{\text{CP}}(B^0 \to K^+\pi^-)$ improved by 10% while the resolution on $\mathcal{B}(B_s^0 \to K^-\pi^+)$ improved by 27%.

Chapter 9

Fit results and cross-checks

In this chapter we report the results returned from the fit of composition, not yet corrected for the efficiency factors. We fit separately the sample selected with loose cuts and the one selected with tight cuts. We also describe also the checks performed to test the fitting code.

9.1 Fit results

The fit of composition was applied to two $B^0_{(s)} \to h^+h^{'-}$ samples: the sample selected for the measurement of $\mathcal{A}_{\rm CP}(B^0 \to K^+\pi^-)$ (loose cuts) and the one selected to measure the rare modes (tight cuts) (see tab. 3.3). The sample selected with tight cuts is a subsample of the one selected with loose cuts. We performed two individual fits of composition of the $B^0_{(s)} \to h^+h^{'-}$ data. All templates of the p.d.f.s and checks are performed independently, like two independent analyses. In both cases we used only candidates whose discriminating observables satisfied the following conditions.

- $5.000 < m_{\pi\pi} < 5.800$ GeV/c^2: this mass range contains the whole $B^0_{(s)} \to h^+h^{'-}$ and $\Lambda^0_b \to ph^-$ signal, and it allows a proper extrapolation of the background shape below the signal;
- $-0.8 < \alpha < 0.8$: this range excludes boundary regions where the model of the corresponding p.d.f. becomes inaccurate and may lead to undesired biases. This requirement removed just a few events;
- $p_{\rm tot} > 6.1$ GeV/c: we excluded a few candidates with lower $p_{\rm tot}$ values because of the difficulty of describing accurately the steep turn-on of the $p_{\rm tot}$ p.d.f.;
- $-5 < \kappa_1, \kappa_2 < 5$: candidates with extremely unlikely values of the observed dE/dx are excluded to reduce the of contamination from fake tracks or tracks with corrupted dE/dx information.

The total number of events is $N = 13502$ for the loose selection and $N = 8286$ for the tight selection.

From the current expectations on production fractions and branching fractions involved, we expect sizable contributions from three known modes, $B^0 \to \pi^+\pi^-$, $B^0 \to K^+\pi^-$ and $B^0_s \to K^+K^-$ and possibly small contributions from five still unobserved modes, $B^0 \to K^+K^-$, $B^0_s \to \pi^+\pi^-$, $B^0_s \to$

$K^-\pi^+$, $\Lambda_b^0 \to p\pi^-$and $\Lambda_b^0 \to pK^-$. Their fractions with respect to the total signal were left free to vary in the fit. Observation of the annihilation decay modes $B^0 \to K^+K^-$ and $B_s^0 \to \pi^+\pi^-$ is less likely because the typical theoretical predictions $\mathcal{B}(B^0 \to K^+K^-) = (0.01\text{–}0.21) \times 10^{-6}$ and $\mathcal{B}(B_s^0 \to \pi^+\pi^-) = (0.027\text{–}0.155) \times 10^{-6}$ [15] are small.

The physics observables related to the abundant modes ($B^0 \to \pi^+\pi^-$, $B^0 \to K^+\pi^-$ and $B_s^0 \to K^+K^-$) are quoted from the fit of the sample selected with the loose cuts, while those of the rare modes ($B_s^0 \to K^-\pi^+$, $B_s^0 \to \pi^+\pi^-$, $B^0 \to K^+K^-$, $\Lambda_b^0 \to p\pi^-$, $\Lambda_b^0 \to pK^-$) are quoted from the fit of the sample selected with the tight cuts. Both fits have the same number of free parameters except for those modeling the shape of the dE/dx correlation (see sec. 6.6.3). Since in the same sample and for the same kinematics we expect an identical correlation between the dE/dx response of both particles, we first extracted the parameters $d_1^c, \mu_1^c, \sigma_1^c, \mu_2^c, \sigma_2^c$ from the fit of composition on the sample selected with the loose cuts. In a second step, we fixed them in the fit of composition on the sample selected with the tight cuts at the values previously estimated.

We minimized the quantity $-2\ln(\mathscr{L})$ defined as described in the previous chapter using the MINUIT numerical minimization package [130]. The results of the fit are shown in tab. 9.1, and the corresponding correlation matrix is shown in sec. 9.2. Tables 9.2 and 9.3 summarize the most relevant physics quantities and yields determined by the parameters returned from the fit. The statistical uncertainties on these quantities have been calculated using the covariance matrix returned from the fit.

The results determined by the fit of composition for loose and tight selections are in agreement with the values obtained in the previous published version of this analysis, performed on a data sample corresponding to 180 pb^{-1} [1, 4]. The statistical uncertainty of physics observables is significantly decreased. With respect to the improvement given by the statistics we gained in resolution an additional 16% for $\hat{\mathcal{A}}_{\rm CP}(B^0 \to K^+\pi^-)$, 26% for the relative fraction of $B^0 \to \pi^+\pi^-$, and 21% for the relative fraction of $B_s^0 \to K^+K^-$. This remarkable result is due to the several crucial improvements introduced in the current version of the analysis: a new discriminating variable (χ^2_{3D}) in the selection (chap. 8), a new optimization of the selection (chap. 8), more accurate mass templates (chap. 5), more accurate PID model (chap. 4), etc..

Table 9.2 reports a significant result for the uncorrected direct CP asymmetry fit parameter $\hat{\mathcal{A}}_{\rm CP}(B^0 \to K^+\pi^-)$. The 2.3% statistical uncertainty is small and it is comparable with the best existing measurements (chap. 13). In the next chapters we will evaluate the efficiency corrections and the systematic uncertainties to confirm and quantify this significant result.

Table 9.2 also gives a clear hint of three new rare decay modes: $B_s^0 \to K^-\pi^+$, $\Lambda_b^0 \to pK^-$, $\Lambda_b^0 \to p\pi^-$. The significance of these modes will be estimated in chap. 12 where we will verify that our results remain significant after adding the systematic uncertainty in the evaluation of the total significance.

Table 9.2 also reports the fit results for the uncorrected direct CP asymmetries $\hat{\mathcal{A}}_{\rm CP}(\Lambda_b^0 \to pK^-)$ and $\hat{\mathcal{A}}_{\rm CP}(\Lambda_b^0 \to p\pi^-)$. The statistical uncertainties are promising for a future extension of the analysis. To translate these numbers into physics measurements we need to evaluate the efficiency corrections. The presence of the proton in the final state requires further additional studies which are outside the scope of the present analysis, and are the subject of a separate work.

parameter	loose	tight	parameter(#)
$\hat{f}_{B^0\to\pi^+\pi^-}$	0.160 ± 0.009	0.152 ± 0.008	1
$\hat{f}_{B^0\to K^+\pi^-}$	0.577 ± 0.010	0.567 ± 0.011	2
$\frac{\hat{f}_{\overline{B}^0\to K^-\pi^+} - \hat{f}_{B^0\to K^+\pi^-}}{\hat{f}_{\overline{B}^0\to K^-\pi^+} + \hat{f}_{B^0\to K^+\pi^-}}$	−0.092 ± 0.023	-0.089 ± 0.025	3
$\hat{f}_{B_s^0\to K^-\pi^+}$	0.035 ± 0.006	0.040 ± 0.006	4
$\frac{\hat{f}_{\overline{B}_s^0\to K^+\pi^-} - \hat{f}_{B_s^0\to K^-\pi^+}}{\hat{f}_{\overline{B}_s^0\to K^+\pi^-} + \hat{f}_{B_s^0\to K^-\pi^+}}$	0.48 ± 0.19	0.39 ± 0.15	5
$\hat{f}_{B_s^0\to K^+K^-}$	0.186 ± 0.009	0.179 ± 0.008	–
$\hat{f}_{B_s^0\to\pi^+\pi^-}$	0.0004 ± 0.003	0.004 ± 0.003	6
$\hat{f}_{B^0\to K^+K^-}$	0.003 ± 0.004	0.011 ± 0.004	7
$\hat{f}_{\Lambda_b^0\to pK^-}$	0.022 ± 0.003	0.027 ± 0.003	8
$\frac{\hat{f}_{\overline{\Lambda}_b^0\to\overline{p}K^+} - \hat{f}_{\Lambda_b^0\to pK^-}}{\hat{f}_{\overline{\Lambda}_b^0\to\overline{p}K^+} + \hat{f}_{\Lambda_b^0\to pK^-}}$	−0.29 ± 0.19	-0.36 ± 0.15	9
$\hat{f}_{\Lambda_b^0\to p\pi^-}$	0.015 ± 0.003	0.019 ± 0.003	10
$\frac{\hat{f}_{\overline{\Lambda}_b^0\to\overline{p}\pi^+} - \hat{f}_{\Lambda_b^0\to p\pi^-}}{\hat{f}_{\overline{\Lambda}_b^0\to\overline{p}\pi^+} + \hat{f}_{\Lambda_b^0\to p\pi^-}}$	0.06 ± 0.21	-0.02 ± 0.16	11
$\hat{b}$	0.481 ± 0.008	0.307 ± 0.008	12
$\hat{c}_{\rm E}$	-1.221 ± 0.124	-0.675 ± 0.109	14
$\hat{w}^{\rm E}_{\pi^+}$	0.545 ± 0.017	0.506 ± 0.037	–
$\hat{w}^{\rm E}_{e^+}$	0.036 ± 0.005	0.048 ± 0.012	–
$\hat{w}^{\rm E}_{p}$	0.080 ± 0.025	0.095 ± 0.057	16
$\hat{w}^{\rm E}_{K^+}$	0.337 ± 0.031	0.350 ± 0.072	–
$\hat{w}^{\rm E}_{\pi^-}$	0.533 ± 0.018	0.492 ± 0.036	–
$\hat{w}^{\rm E}_{e^-}$	0.030 ± 0.005	0.034 ± 0.010	–
$\hat{w}^{\rm E}_{\overline{p}}$	0.132 ± 0.027	0.226 ± 0.064	17
$\hat{w}^{\rm E}_{K^-}$	0.304 ± 0.033	0.248 ± 0.075	–
$\hat{f}_{\rm A}$	0.197 ± 0.016	0.502 ± 0.033	22
$\hat{m}_{\rm A}$ [GeV/c^2]	5.135 ± 0.001	5.158 ± 0.001	23
$\hat{c}_{\rm A}$	8.467 ± 3.45	0.429 ± 2.383	24
$\hat{w}^{\rm A}_{\pi}$	0.728 ± 0.027	0.717 ± 0.019	27
$\hat{w}^{\rm A}_{K}$	0.272 ± 0.027	0.282 ± 0.020	–
$\hat{d}^c_1$	0.993 ± 0.005	0.993 (fixed)	32
$\hat{\mu}^c_1$ [ns]	-0.171 ± 0.020	-0.171 (fixed)	33
$\hat{\sigma}^c_1$ [ns]	0.087 ± 0.138	0.087 (fixed)	34
$\hat{\mu}^c_2$ [ns]	2.481 ± 0.055	2.481 (fixed)	35
$\hat{\sigma}^c_2$ [ns]	0.0002 ± 10.	0.0002 (fixed)	36

Table 9.1: Results of fit of composition. Signal (background) related quantities are reported in the upper (lower) section. The last column reports the legend to convert the parameter number into physics quantity for interpreting the correlation matrix shown at pag. 188; the missing codes refer to parameters which are not part of the set of primary fit parameters ($\vec{\theta}$). C-conjugate modes are implied except for the parameter in the third, fifth, tenth and twelveth row.

observable	loose	tight
$\hat{\mathcal{A}}_{\rm CP}(B^0 \to K^+\pi^-) = \frac{\hat{f}_{\overline{B}^0\to K^-\pi^+} - \hat{f}_{B^0\to K^+\pi^-}}{\hat{f}_{\overline{B}^0\to K^-\pi^+} + \hat{f}_{B^0\to K^+\pi^-}}$	$\mathbf{-0.092 \pm 0.023}$	-0.089 ± 0.025
$\hat{\mathcal{A}}_{\rm CP}(B^0_s \to K^-\pi^+) = \frac{\hat{f}_{\overline{B}^0_s\to K^+\pi^-} - \hat{f}_{B^0_s\to K^-\pi^+}}{\hat{f}_{\overline{B}^0_s\to K^+\pi^-} + \hat{f}_{B^0_s\to K^-\pi^+}}$	0.48 ± 0.19	$\mathbf{0.39 \pm 0.15}$
$\hat{\mathcal{A}}_{\rm CP}(\Lambda^0_b \to p\pi^-) = \frac{\hat{f}_{\overline{\Lambda}^0_b\to \overline{p}\pi^+} - \hat{f}_{\Lambda^0_b\to p\pi^-}}{\hat{f}_{\overline{\Lambda}^0_b\to \overline{p}\pi^+} + \hat{f}_{\Lambda^0_b\to p\pi^-}}$	0.06 ± 0.21	-0.026 ± 0.16
$\hat{\mathcal{A}}_{\rm CP}(\Lambda^0_b \to pK^-) = \frac{\hat{f}_{\overline{\Lambda}^0_b\to \overline{p}K^+} - \hat{f}_{\Lambda^0_b\to pK^-}}{\hat{f}_{\overline{\Lambda}^0_b\to \overline{p}K^+} + \hat{f}_{\Lambda^0_b\to pK^-}}$	-0.29 ± 0.19	-0.36 ± 0.15
$\frac{\hat{f}_{\overline{B}^0\to K^-\pi^+} - \hat{f}_{B^0\to K^+\pi^-}}{\hat{f}_{\overline{B}^0_s\to K^+\pi^-} + \hat{f}_{B^0_s\to K^-\pi^+}}$	-3.13 ± 1.43	$\mathbf{-3.21 \pm 1.53}$
$\frac{\hat{f}_{B^0_s\to K^-\pi^+}}{\hat{f}_{B^0\to K^+\pi^-}}$	0.061 ± 0.011	$\mathbf{0.070 \pm 0.010}$
$\frac{\hat{f}_{B^0\to \pi^+\pi^-}}{\hat{f}_{B^0\to K^+\pi^-}}$	$\mathbf{0.277 \pm 0.018}$	0.269 ± 0.017
$\frac{\hat{f}_{B^0_s\to K^+K^-}}{\hat{f}_{B^0\to K^+\pi^-}}$	$\mathbf{0.323 \pm 0.019}$	0.316 ± 0.018
$\frac{\hat{f}_{B^0_s\to \pi^+\pi^-}}{\hat{f}_{B^0\to K^+\pi^-}}$	0.0007 ± 0.005	$\mathbf{0.008 \pm 0.005}$
$\frac{\hat{f}_{B^0\to K^+K^-}}{\hat{f}_{B^0\to K^+\pi^-}}$	0.005 ± 0.008	$\mathbf{0.019 \pm 0.008}$
$\frac{\hat{f}_{\Lambda^0_b\to pK^-}}{\hat{f}_{B^0\to K^+\pi^-}}$	0.039 ± 0.006	$\mathbf{0.049 \pm 0.006}$
$\frac{\hat{f}_{\Lambda^0_b\to p\pi^-}}{\hat{f}_{B^0\to K^+\pi^-}}$	0.027 ± 0.006	$\mathbf{0.034 \pm 0.005}$
$\frac{\hat{f}_{\Lambda^0_b\to p\pi^-}}{\hat{f}_{\Lambda^0_b\to pK^-}}$	0.69 ± 0.19	$\mathbf{0.71 \pm 0.15}$

Table 9.2: Physics observables. The quantities reported in boldface are used to evaluate the final measurements. C-conjugate modes are implied in the lower section of the table.

mode			loose	tight
$\mathcal{N}(B^0 \to \pi^+\pi^-)$	+	$\mathcal{N}(\overline{B}^0 \to \pi^+\pi^-)$	1121 ± 63	875 ± 46
$\mathcal{N}(B^0 \to K^+\pi^-)$	+	$\mathcal{N}(\overline{B}^0 \to K^-\pi^+)$	4045 ± 84	3256 ± 66
$\mathcal{N}(B^0 \to K^+\pi^-)$			2209 ± 64	1773 ± 52
$\mathcal{N}(\overline{B}^0 \to K^-\pi^+)$			1836 ± 61	1483 ± 51
$\mathcal{N}(B_s^0 \to K^-\pi^+)$	+	$\mathcal{N}(\overline{B}_s^0 \to K^+\pi^-)$	247 ± 45	230 ± 34
$\mathcal{N}(B_s^0 \to K^-\pi^+)$			64 ± 30	70 ± 22
$\mathcal{N}(\overline{B}_s^0 \to K^+\pi^-)$			183 ± 34	160 ± 26
$\mathcal{N}(B_s^0 \to K^+K^-)$	+	$\mathcal{N}(\overline{B}_s^0 \to K^+K^-)$	1307 ± 64	1028 ± 47
$\mathcal{N}(B_s^0 \to \pi^+\pi^-)$	+	$\mathcal{N}(\overline{B}_s^0 \to \pi^+\pi^-)$	3 ± 22	26 ± 16
$\mathcal{N}(B^0 \to K^+K^-)$	+	$\mathcal{N}(\overline{B}^0 \to K^+K^-)$	22 ± 31	61 ± 25
$\mathcal{N}(\Lambda_b^0 \to pK^-)$	+	$\mathcal{N}(\overline{\Lambda}_b^0 \to \overline{p}K^+)$	156 ± 24	156 ± 20
$\mathcal{N}(\Lambda_b^0 \to p\pi^-)$	+	$\mathcal{N}(\overline{\Lambda}_b^0 \to \overline{p}\pi^+)$	109 ± 23	110 ± 18

Table 9.3: Yields returned from the fit of composition.

Table 9.2 is rich in physics. In the next chapters we will evaluate the relative efficiency corrections and systematic uncertainties to translate them into physics measurements. In the next sections of this chapter, we will look at the covariance matrix, fit projections, and other checks of the fitting code.

9.2 Correlation matrix

The correlation matrices corresponding to the fits of composition are shown in this section. The matrix reports the correlation coefficients, defined as $\rho_{ij} = \mathrm{Cov}(\hat{\theta}_i, \hat{\theta}_j)/\hat{\sigma}_{\hat{\theta}_i}\hat{\sigma}_{\hat{\theta}_j}$, where $\mathrm{Cov}(\hat{\theta}_i, \hat{\theta}_j)$ is the off-diagonal element of the estimated covariance matrix of the fit. The legend for the fit parameters is in third column of tab. 9.1. The correlation matrix is similar for the two fits. We looked at this matrix to search for possible large correlations that may suggest a better choice of the fit parameters.

PARAMETER CORRELATION COEFFICIENTS ACP(B0->Kpi)

NO.	1	2	3	4	5	6	7	8	9	10	11	12	14	16	17	18	19	20	21	22	23	24	27	32	33	34	35	36
1	1.000																											
2	-0.336	1.000																										
3	-0.019	0.025	1.000																									
4	-0.281	-0.078	0.012	1.000																								
5	0.116	0.019	0.002	-0.358	1.000																							
6	-0.021	-0.110	0.005	-0.271	0.096	1.000																						
7	-0.102	-0.456	-0.009	0.057	-0.030	0.035	1.000																					
8	-0.085	-0.181	0.003	-0.028	-0.002	-0.040	0.104	1.000																				
9	-0.022	-0.032	0.010	-0.002	-0.025	-0.003	0.030	0.140	1.000																			
10	-0.065	-0.142	0.007	0.027	-0.024	-0.021	0.023	-0.188	0.006	1.000																		
11	0.003	0.004	0.049	-0.009	-0.050	0.005	-0.001	0.040	-0.110	-0.079	1.000																	
12	0.134	0.239	-0.026	-0.219	0.111	-0.212	-0.318	-0.181	-0.058	-0.199	0.018	1.000																
14	-0.111	-0.157	0.023	0.174	-0.085	0.151	0.307	0.091	0.035	0.037	-0.010	-0.556	1.000															
16	-0.056	-0.078	0.007	-0.027	0.007	0.061	0.116	-0.011	0.075	-0.089	0.093	-0.040	0.083	1.000														
17	-0.042	-0.065	-0.027	-0.024	0.027	0.075	0.082	-0.015	-0.072	-0.069	-0.065	-0.044	0.092	0.111	1.000													
18	-0.007	-0.077	-0.073	0.026	0.095	-0.078	0.134	0.094	0.062	-0.050	-0.052	-0.052	0.055	0.675	0.016	1.000												
19	0.072	-0.076	0.006	0.019	-0.022	0.054	0.067	0.039	0.029	0.018	0.026	-0.123	0.133	0.105	0.007	-0.123	1.000											
20	0.004	-0.063	0.054	0.011	-0.088	-0.060	0.096	0.088	-0.032	-0.036	0.056	-0.036	0.040	0.020	0.708	0.064	0.049	1.000										
21	0.082	-0.068	0.007	0.002	-0.007	0.053	0.054	0.034	-0.006	0.008	-0.009	-0.098	0.113	0.012	0.119	0.039	0.134	-0.098	1.000									
22	-0.125	-0.203	0.025	0.203	-0.100	0.192	0.305	0.137	0.046	0.120	-0.015	-0.616	0.814	0.074	0.089	0.050	0.150	0.039	0.127	1.000								
23	-0.004	-0.009	0.001	0.011	-0.006	0.012	0.007	0.006	0.002	0.007	0.000	-0.030	0.048	0.002	0.007	-0.002	0.010	0.004	0.007	0.060	1.000							
24	-0.014	-0.044	0.006	0.044	-0.022	0.068	0.035	0.017	0.008	0.029	-0.003	-0.127	0.196	0.032	0.041	-0.017	0.045	-0.013	0.045	0.267	-0.201	1.000						
27	0.195	0.131	-0.009	-0.118	0.053	0.011	-0.227	-0.159	-0.040	-0.053	0.006	0.292	-0.373	-0.038	-0.021	-0.164	-0.047	-0.136	-0.027	-0.412	-0.021	-0.021	1.000					
32	-0.006	0.010	0.004	0.021	-0.004	-0.012	-0.023	0.015	0.013	0.016	0.002	-0.018	0.010	-0.080	-0.070	-0.065	0.116	-0.055	0.102	0.014	0.000	-0.005	-0.032	1.000				
33	-0.424	-0.069	-0.004	0.036	-0.014	0.021	0.167	0.044	0.023	-0.006	0.007	-0.093	0.099	0.161	0.142	-0.105	-0.084	-0.107	-0.088	0.101	0.002	0.014	-0.231	0.446	1.000			
34	-0.172	0.168	0.015	0.156	-0.057	-0.059	-0.111	-0.017	0.012	0.076	-0.020	-0.076	0.067	-0.243	-0.204	-0.161	-0.072	-0.155	-0.074	0.077	0.004	0.002	-0.082	0.606	0.368	1.000		
35	-0.018	0.010	0.000	0.019	-0.004	-0.007	-0.018	0.007	0.009	0.009	0.000	-0.015	0.010	-0.049	-0.044	-0.034	0.003	-0.034	-0.008	0.012	0.000	-0.001	-0.019	0.839	0.390	0.467	1.000	
36	0.000	0.000	0.000	0.000	0.000	0.000	0.000	0.000	0.000	0.000	0.000	0.000	0.000	0.000	0.000	0.000	0.000	0.000	0.000	0.000	0.000	0.000	0.000	-0.002	-0.001	0.000	-0.006	1.000

PARAMETER CORRELATION COEFFICIENTS BR(B0s->Kpi)

NO.	1	2	3	4	5	6	7	8	9	10	11	12	14	16	17	18	19	20	21	22	23	24	27
1	1.000																						
2	-0.436	1.000																					
3	-0.021	0.018	1.000																				
4	-0.260	-0.089	0.009	1.000																			
5	0.077	0.017	0.026	-0.248	1.000																		
6	-0.048	-0.089	0.009	-0.256	0.064	1.000																	
7	-0.005	-0.424	-0.010	0.051	-0.026	0.035	1.000																
8	-0.059	-0.171	0.007	-0.029	-0.003	-0.013	0.076	1.000															
9	-0.014	-0.038	0.010	0.004	-0.035	0.011	0.038	0.143	1.000														
10	-0.062	-0.154	0.009	0.024	-0.022	-0.011	0.041	-0.194	0.008	1.000													
11	-0.005	-0.008	0.034	0.003	-0.043	0.011	0.005	0.039	-0.111	-0.006	1.000												
12	0.083	0.214	-0.029	-0.157	0.077	-0.217	-0.266	-0.199	-0.092	-0.199	-0.026	1.000											
14	-0.076	-0.202	0.032	0.166	-0.078	0.218	0.266	0.175	0.087	0.124	0.021	-0.639	1.000										
16	-0.003	-0.018	0.017	0.027	-0.009	0.049	0.039	0.000	0.080	-0.026	0.067	-0.081	0.123	1.000									
17	0.022	0.016	-0.032	-0.013	0.040	0.033	-0.032	-0.029	-0.065	-0.031	-0.074	0.015	0.004	-0.031	1.000								
18	-0.041	-0.043	-0.042	0.041	0.077	-0.060	0.091	0.083	0.070	-0.037	-0.075	-0.068	0.079	0.731	-0.012	1.000							
19	-0.037	-0.075	0.011	0.064	-0.039	0.079	0.089	0.069	0.057	0.060	0.039	-0.221	0.257	0.211	-0.025	-0.089	1.000						
20	-0.025	-0.010	0.021	0.006	-0.050	-0.064	0.023	0.053	-0.024	-0.022	0.039	0.005	-0.012	-0.029	0.781	-0.006	-0.002	1.000					
21	-0.014	-0.048	0.007	0.027	-0.013	0.065	0.049	0.047	0.003	0.029	-0.006	-0.135	0.160	0.025	0.194	0.020	0.054	-0.061	1.000				
22	-0.087	-0.233	0.033	0.181	-0.086	0.246	0.256	0.214	0.100	0.193	0.027	-0.676	0.874	0.113	-0.003	0.074	0.270	-0.013	0.169	1.000			
23	0.001	-0.001	0.000	0.001	-0.001	0.002	-0.008	0.001	0.000	0.001	0.000	0.000	0.006	0.001	0.001	-0.001	0.002	0.000	0.002	0.008	1.000		
24	-0.020	-0.062	0.008	0.059	-0.025	0.089	-0.013	0.060	0.026	0.063	0.006	-0.146	0.288	0.033	0.019	-0.002	0.078	-0.018	0.069	0.339	-0.133	1.000	
27	0.043	0.105	-0.017	-0.087	0.041	-0.049	-0.104	-0.142	-0.058	-0.075	-0.011	0.286	-0.397	-0.018	0.072	-0.123	-0.130	-0.049	-0.060	-0.414	-0.003	-0.116	1.000

Amongst the physics parameters $(1 - 11)$, we found the largest correlation coefficients: $\rho_{12} \approx -33\%$ between the fraction of $B^0 \to \pi^+\pi^-$ and $B^0 \to K^+\pi^-$, $\rho_{14} \approx -28\%$ between the fraction of $B^0 \to \pi^+\pi^-$ and $B^0 \to K^+K^-$, $\rho_{27} \approx -45\%$ between the fraction of $B^0 \to K^+\pi^-$ and $B^0 \to K^+K^-$. These values can be explained with the limited separation power of the fit for those decays having very similar kinematics and PID information and the constrain that the sum of all fractions must be equal to one: the $B^0 \to K^+\pi^-$ differs from $B^0 \to \pi^+\pi^-$ and $B^0 \to K^+K^-$ only for one pion/kaon in

the final state. A similar explanation holds for $\rho_{46} \approx -27\%$, the correlation coefficient between the fraction of $B_s^0 \to K^-\pi^+$ and $B_s^0 \to \pi^+\pi^-$ modes. In addition, we found a large correlation (about 20%) between the fraction of background b (par. 12) and almost all the fractions of $B_{(s)}^0 \to h^+h^{'-}$ and $\Lambda_b^0 \to ph^-$ decay modes, since a background fluctuation can influence the fractions of all modes, in particular the fraction of the rare modes. This is connected to the fact that, as we will see in sec. 12.6, the systematics associated to the background shape is dominant. We also notice a large correlation between the parameters describing the combinatorial and the physics background. A change of the combinatorial background obviously influences the shape and the normalization of the physics background. All other correlations are small.

9.3 Fit projections

In order to test the goodness of our fit[1] we compare the distributions of data with the joint p.d.f. corresponding to the Likelihood function evaluated with the maximizing set of parameters $\vec{\theta} = \hat{\vec{\theta}}$. If $\vec{x} = x_1, ..., x_n$ is a generic vector of observables and $\wp(\vec{x}|\vec{\theta})$ is the probability density function of the observables $\vec{x}$ we can define the *projection* onto the observable x_i as the following one-dimensional function:

$$\wp_i(x_i; \vec{\theta}) = \int \wp(\vec{x}|\vec{\theta}) dx_1 ... dx_{i-1} dx_{i+1} ... dx_n, \tag{9.1}$$

which is the predicted distribution for x_i under the assumed values for the fit parameters, and can be overlaid to the experimental data.This allows a way of detecting possible discrepancies between the observed distributions and the model. Distributions of the discriminating observables with fit projections overlaid are shown in figs. 9.1–9.6. The fit reproduces well all the observed distributions. The distributions of individual components are also shown.

To better visualize the agreement between the PID discriminating observables and the data we complemented the projections of κ_1 and κ_2 with the projections of their linear combination $\kappa_1+\kappa_2$ and $\kappa_1 - \kappa_2$. This allows to check if the fit reproduces well the shape of the correlation function between the dE/dx response of the two particles. We find that the fit reproduces accurately the data both in the central part of the distribution, where the signal is present, and in the tails at lower (higher) values of κ, where electrons (protons) due to background contribute.

Figures 9.4 and 9.5 report the distributions of the discriminating observables for candidates in the signal region only ($5.190 < m_{\pi\pi} < 5.310$ GeV/c^2) for a further check on whether the fit properly determines the sample composition below the signal peak. The same kind of check was repeated in the $\Lambda_b^0 \to ph^-$ mass region only ($5.350 < m_{\pi\pi} < 5.600$ GeV/c^2) in fig. 9.6.

[1] There is no a direct method for testing the goodness-of-fit of an unbinned maximum Likelihood fit. Different approaches have been proposed in literature for this purpose, but none is rigorously correct [135].

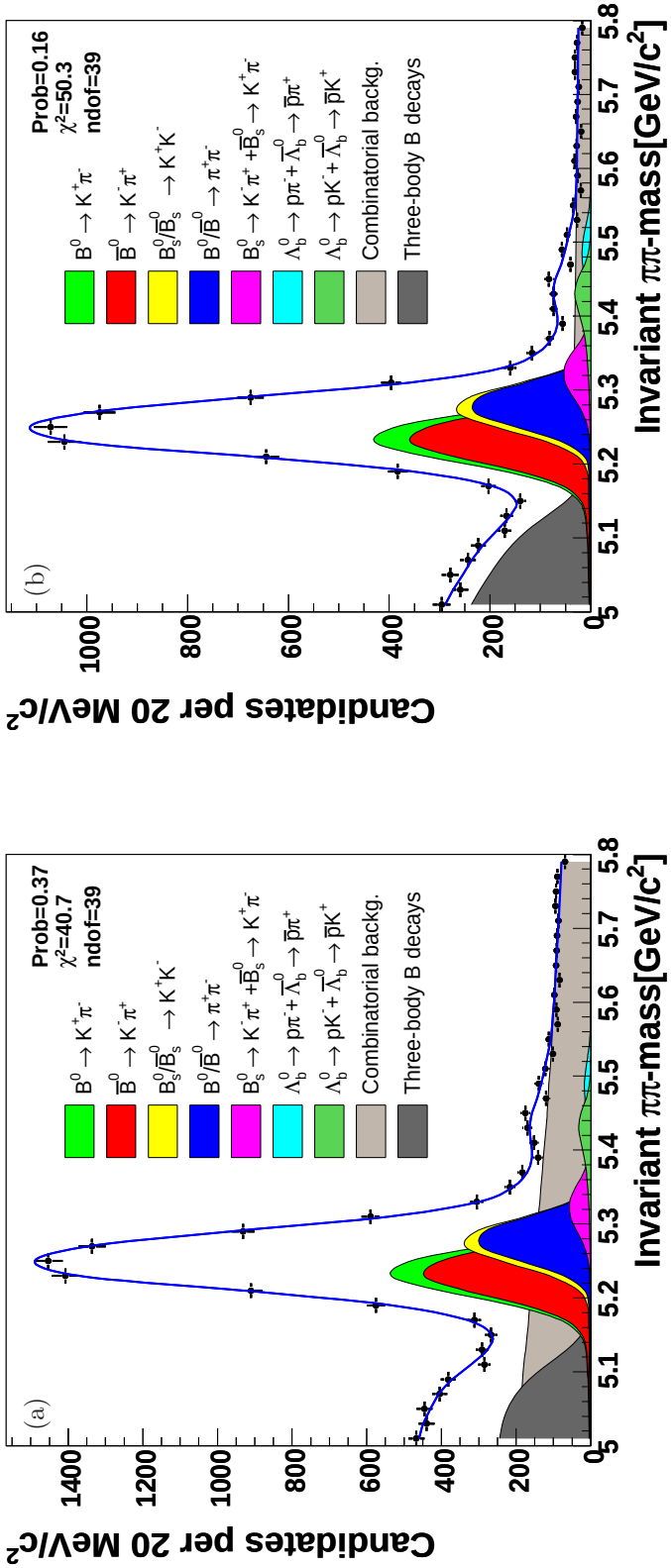


Figure 9.1: Fit projections onto the variable $m_{\pi\pi}$. Loose cuts (a), tight cuts (b).

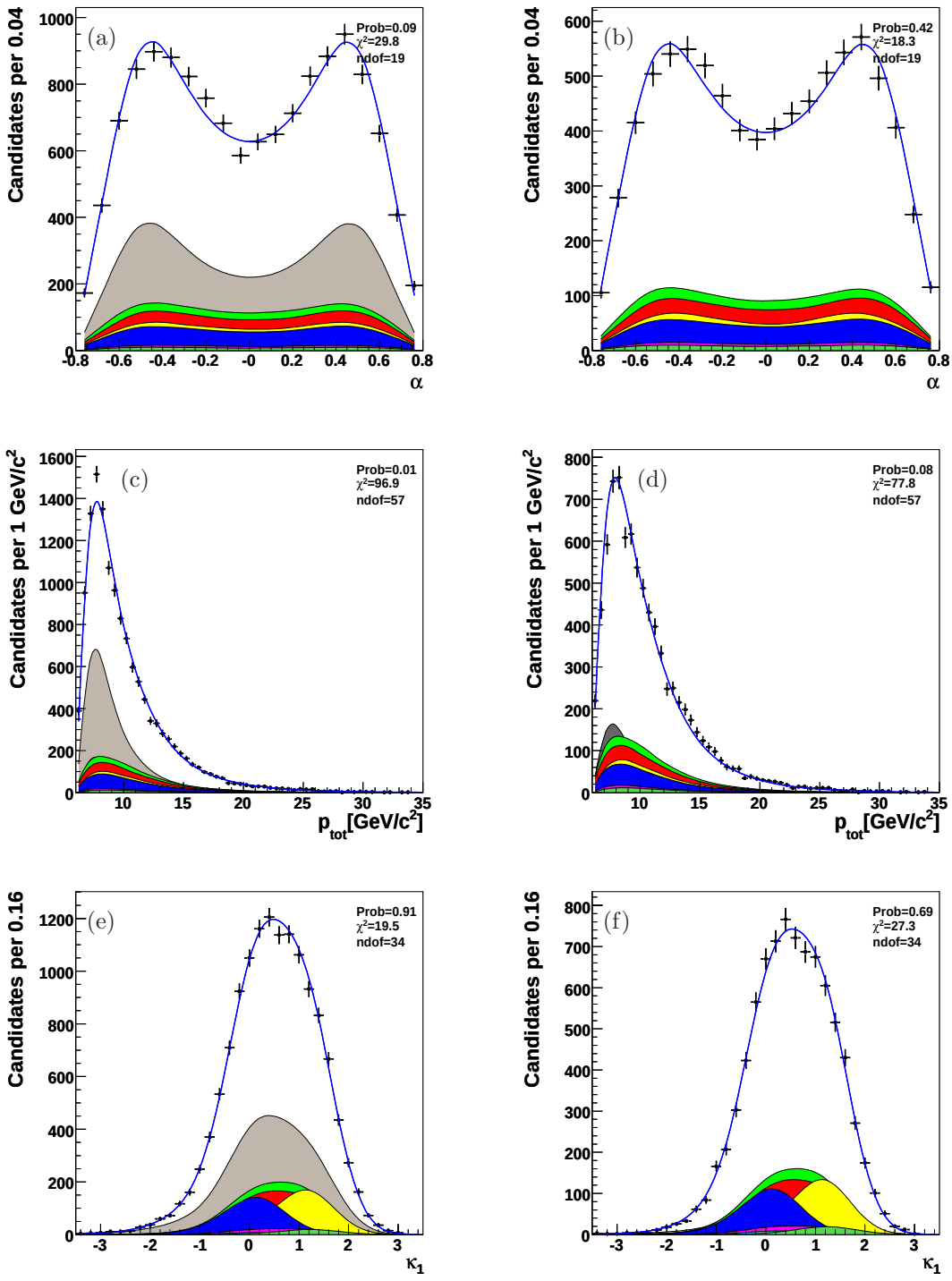


Figure 9.2: Fit projections onto the variables α, p_{tot}, κ_1 in all fit $m_{\pi\pi}$ range $[5.000, 5.800]$ GeV/c^2. Loose cuts (a, c, e), tight cuts (b, d, f). See fig. 9.1 for the legend.

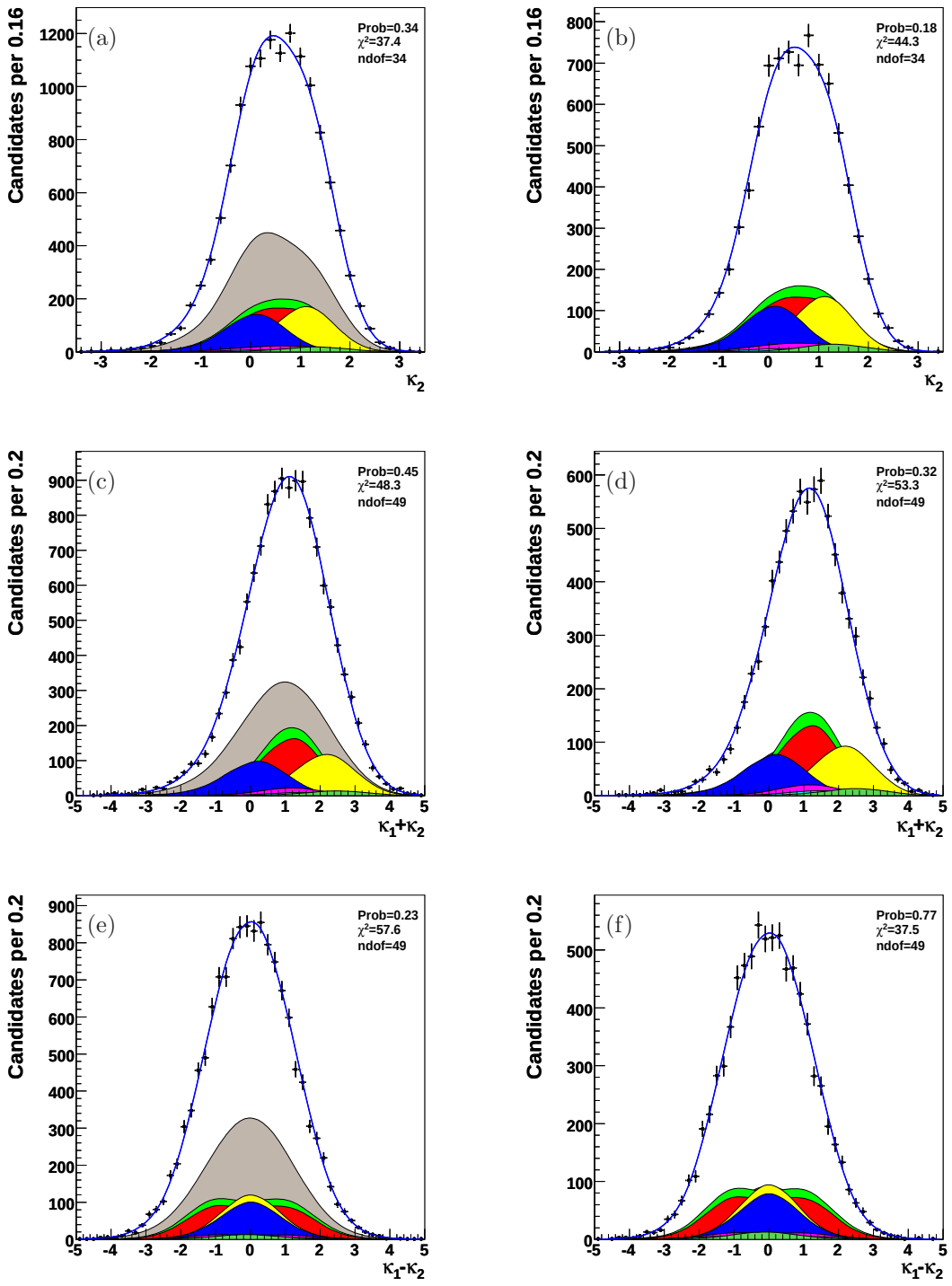


Figure 9.3: Fit projections onto the variables κ_2, $\kappa_1 + \kappa_2$, $\kappa_1 - \kappa_2$ in all fit $m_{\pi\pi}$ range $[5.000, 5.800]$ GeV/c^2. Loose cuts (a, c, e), tight cuts (b, d, f). See fig. 9.1 for the legend.

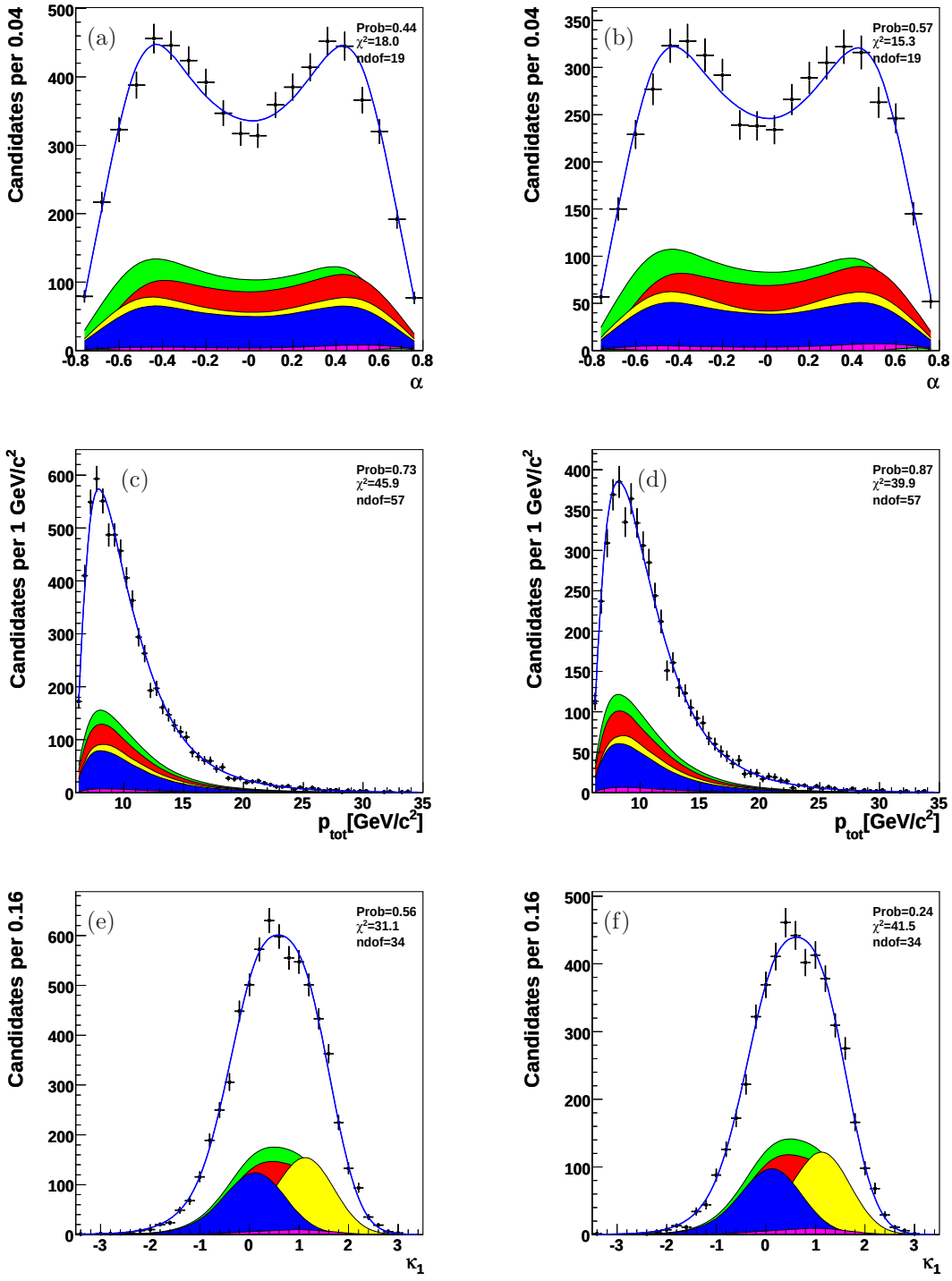


Figure 9.4: Fit projections onto the variables α, $p_{\rm tot}$, κ_1 in the signal $m_{\pi\pi}$ range $[5.190, 5.310]$ GeV/c^2. Loose cuts (a, c, e), tight cuts (b, d, f). See fig. 9.1 for the legend.

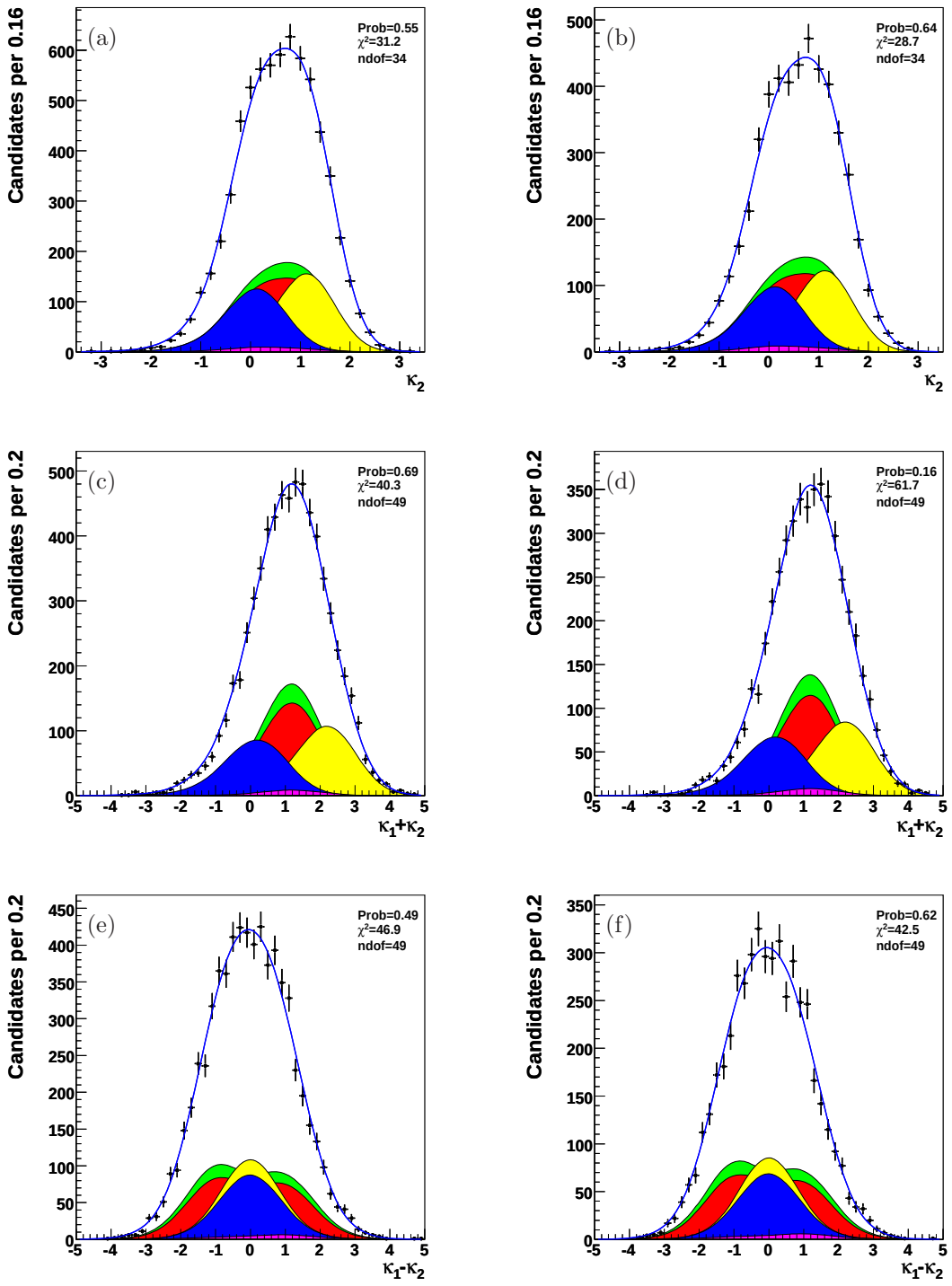


Figure 9.5: Fit projections onto the variables κ_2, $\kappa_1+\kappa_2$, $\kappa_1-\kappa_2$ in the signal $m_{\pi\pi}$ range $[5.190, 5.310]$ GeV/c^2. Loose cuts (a, c, e), tight cuts (b, d, f). See fig. 9.1 for the legend.

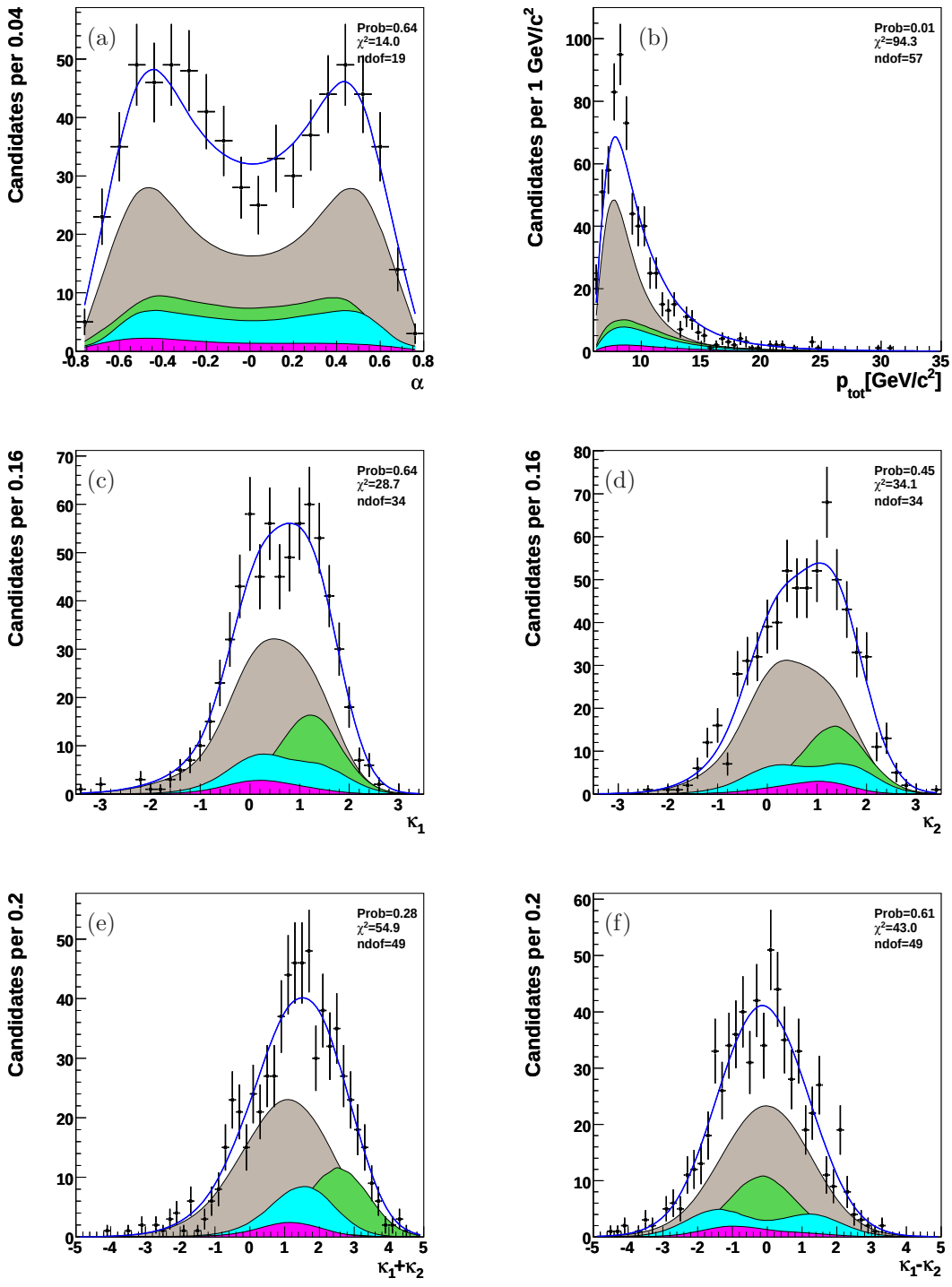


Figure 9.6: Fit projections onto the variables α, $p_{\rm tot}$, κ_1, κ_2, $\kappa_1+\kappa_2$, $\kappa_1-\kappa_2$ in the $\Lambda_b^0 \to ph^-$ $m_{\pi\pi}$ range $[5.350, 5.600]$ GeV/c^2. Tight cuts. See fig. 9.1 for the legend.

9.4 Checks

The fitting code was extensively tested on ensembles of simulated pseudo-experiments of variable size. We studied the fit under several configurations of the most critical parameters, such as the contamination of background, absolute scale of the masses, kinematics and PID performance. An exhaustive description of all these tests can be found in [3, 4]. Here we show only the distributions of the "pulls" for the physics fit parameters where the pseudo-experiments were generated in the same conditions of the current data samples. Some additional checks were performed using the data to gain more confidence in our results.

9.4.1 Pulls

Fit parameter	Pull mean	Pull standard deviation	χ^2/d.o.f.
$f_{B^0\to\pi^+\pi^-}/f_{B^0\to K^+\pi^-}$	-0.13 ± 0.05	0.92 ± 0.04	17.4/11
$\mathcal{A}_{\rm CP}(B^0 \to K^+\pi^-)$	0.01 ± 0.05	1.01 ± 0.04	6.3/10
$f_{B^0_s\to K^+K^-}/f_{B^0\to K^+\pi^-}$	-0.06 ± 0.05	1.05 ± 0.05	9.8/10
$f_{B^0_s\to K^-\pi^+}/f_{B^0\to K^+\pi^-}$	-0.09 ± 0.05	1.01 ± 0.05	15.9/10
$N_{B^0_s\to K^-\pi^+}$	-0.09 ± 0.05	1.01 ± 0.05	15.9/10
$N_{B^0_s\to\pi^+\pi^-}$	-0.14 ± 0.05	1.03 ± 0.05	4.5/8
$N_{B^0\to K^+K^-}$	-0.17 ± 0.05	1.00 ± 0.05	9.9/9
$N_{\Lambda^0_b\to p\pi^-}$	-0.21 ± 0.06	1.03 ± 0.06	15.6/12
$N_{\Lambda^0_b\to pK^-}$	-0.15 ± 0.05	1.03 ± 0.04	12.4/10

Table 9.4: Results of the Gaussian fit of the pull distributions. C-conjugate modes are implied except for the parameter in the second row.

To investigate the presence of a possible estimation bias, and the stability of the minimization code we studied the distributions of the pulls of the fit. The pull of each fit parameter θ_i is defined as:

$$\mathcal{P}(\theta_i) = \frac{\hat{\theta}_i - \theta_i}{\hat{\sigma}_{\hat{\theta}_i}}, \tag{9.2}$$

where $\hat{\theta}_i$ is the estimate of the parameter, and $\hat{\sigma}_{\hat{\theta}_i}$ is the estimate of its uncertainty. We evaluated the pulls using an ensemble of 400 pseudo-experiments that simulated the experimental circumstance of the fit on $B^0_{(s)} \to h^+h^{'-}$ data. Each pseudo-experiment consisted of the simulated distributions of the five discriminating observables (mass, momentum imbalance, scalar sum of momenta, and dE/dx of both tracks) corresponding to 8286 total events. The distributions of each signal mode and background component were generated according to the corresponding Likelihood term, using a pseudo-random number generator. The fractions of each signal mode and of background fluctuated from sample to sample according to a multinomial distribution with mean the set at true parameters $\vec{\theta}$. This properly accounts for the statistical fluctuations of signal and background fractions among the different samples, while keeping the total number of events constrained. We fit the composition of all pseudo-experiments using the same Likelihood function used for the data; we then derived the

pull distributions of the relevant physics quantities from the estimated parameters and uncertainties (see fig. 9.7).

The pulls are Gaussian-distributed with approximately unit variance and negligible bias (see tab. 9.4) for each estimated parameter, which is not obvious with finite samples and complicated probability densities. This ensures that the estimated uncertainty of each parameter $\hat{\sigma}_{\hat{\theta}_i}$ to be such that the range $[\hat{\theta}_i - \hat{\sigma}_{\hat{\theta}_i}, \hat{\theta}_i + \hat{\sigma}_{\hat{\theta}_i}]$ contains the true value θ_i with about 68% probability. Note that the pulls corresponding to ratios of fractions are not necessarily Gaussian-distributed because such ratios are not primary fit parameters. Since the distribution of the ratio of two Gaussian-distributed quantities has infinite variance, the Gaussian assumption for the pull distribution of ratios can only be approximate.

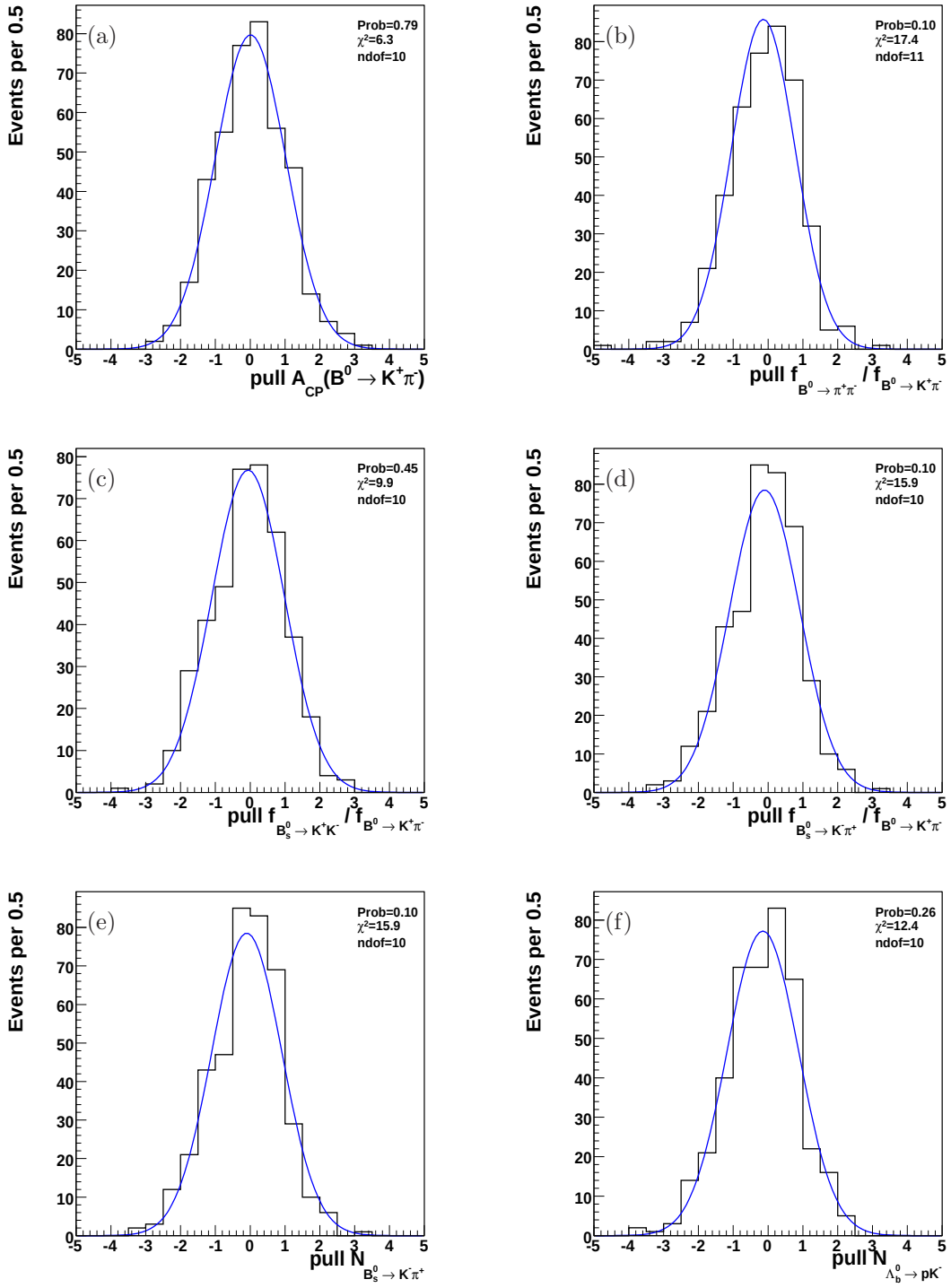


Figure 9.7: Distribution of the pulls of the most relevant fit parameters: (a) $f_{B^0\to\pi^+\pi^-}/f_{B^0\to K^+\pi^-}$, (b) $\mathcal{A}_{\rm CP}(B^0\to K^+\pi^-)$, (c) $f_{B^0_s\to K^+K^-}/f_{B^0\to K^+\pi^-}$, and (d) $f_{B^0_s\to K^-\pi^+}/f_{B^0\to K^+\pi^-}$. Results of χ^2-fits to Gaussian functions are overlaid in red.

9.4.2 Probability ratio plots

The fit of composition disentangles the individual signal components by combining kinematics ($m_{\pi\pi}$, α, $p_{\rm tot}$) and PID (κ_1, κ_2) information (see chap. 4). It is useful to visualize the effective total separation power of the fit. This can be done by looking at the *probability ratio* variable:

$$\mathcal{PR} = \frac{\wp_{B^0\to K^+\pi^-}}{\wp_{B^0\to K^+\pi^-} + \wp_{\overline{B}^0\to K^-\pi^+}}, \tag{9.3}$$

where $\wp_{B^0\to K^+\pi^-}$ and $\wp_{\overline{B}^0\to K^-\pi^+}$ are the total p.d.f. respectively for the $B^0 \to K^+\pi^-$ and $\overline{B}^0 \to K^-\pi^+$ modes, and they are functions of the complete set of observables $(m_{\pi\pi}, \alpha, p_{\rm tot}, \kappa_1, \kappa_2)$. $\mathcal{PR}$ takes values within the interval $[0, 1]$. If we evaluate this variable with an event of $B^0 \to K^+\pi^-$ $\mathcal{PR}$ has an high probability to be close to 1, while if we take an event of $\overline{B}^0 \to K^-\pi^+$ $\mathcal{PR}$ tends to 0. Any other event is distributed between 0 and 1. The probability ratio is a function of the discriminating observables, then we can plot its distribution obtained using the fitted data sample and also the distribution obtained by generating signals and background events directly from the total p.d.f.s of the fit of composition. Figure 9.8(a) shows the comparison between the distribution of $\mathcal{PR}$ obtained from the data (point with error bars) ad the distribution of $\mathcal{PR}$ obtained by generating events with the p.d.f.s of the fit of composition. The different colors of the histogram show how the events of $B^0 \to K^+\pi^-$ (red), $\overline{B}^0 \to K^-\pi^+$ (blue), other signals and background (yellow) are distributed in the variable $\mathcal{PR}$. The agreement between data distribution and projection is satisfactory. In addition it is possible to visualize the sizeable effective separation power between $B^0 \to K^+\pi^-$ and $\overline{B}^0 \to K^-\pi^+$ which allows to perform a precision measurement of the direct CP asymmetry $\mathcal{A}_{\rm CP}(B^0 \to K^+\pi^-)$.

The same procedure can be repeated for any two signal components S_1 and S_2, or between an individual signal S_1 and all the other signals $S_2, S_3, ..., S_N$ plus all backgrounds, that we will indicate with the label "rest". In particular we can write:

$$\mathcal{PR}_{S_1S_2} = \frac{\wp_{S_1}}{\wp_{S_1} + \wp_{S_2}} \tag{9.4}$$

$$\mathcal{PR}_{S_1\,\rm rest} = \frac{\wp_{S_1}}{\wp_{S_1} + \wp_{\rm rest}}. \tag{9.5}$$

$\wp_{S_1}$ and $\wp_{S_2}$ are the total p.d.f.s respectively for the signal component S_1 and S_2. Instead $\wp_{\rm rest}$ is the sum of the total p.d.f.s of all other signals except S_1 plus the total p.d.f.s of all backgrounds. Each term of the $\wp_{\rm rest}$ sum is weighted with the relative fraction estimated by the fit of composition without the contribution of the signal S_1. Figures 9.8 and 9.9 show the comparison between the data distribution and the projection of the probability ratio in different cases. The agreement obtained is satisfactory. By the comparison between a rare decay (like the $B_s^0 \to K^-\pi^+$, $\Lambda_b^0 \to p\pi^-$, $\Lambda_b^0 \to pK^-$) and the background (in this case all other signals plus backgrounds) it is possible to visualize the separation power of the fit in disentangling such decay from the rest.

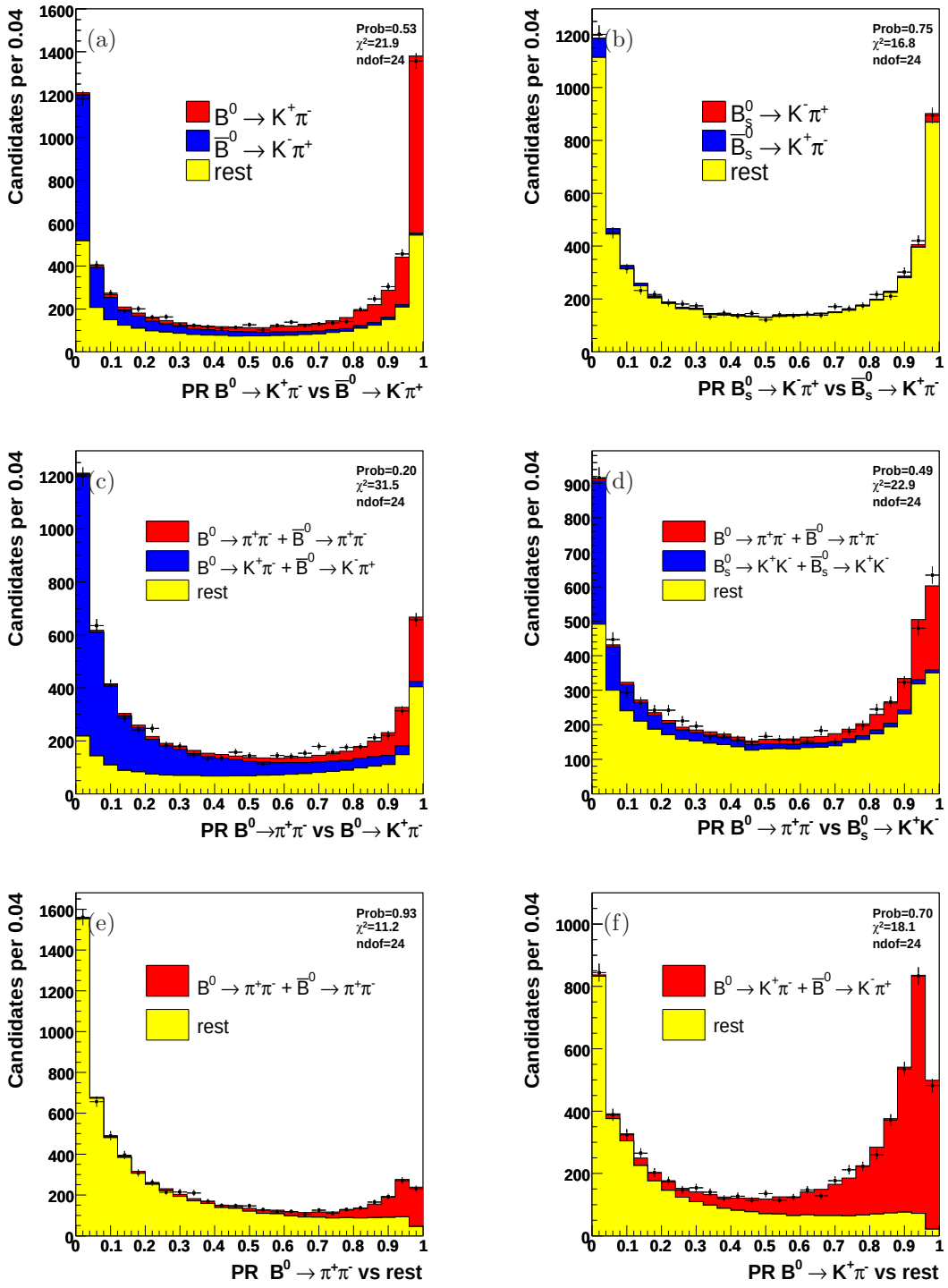


Figure 9.8: Distribution of the probability ratio ($\mathcal{PR}$) in the signal mass region ($5.1 < m_{\pi\pi} < 5.6$ GeV/c^2). Distribution of $\frac{\wp_{S_1}}{\wp_{S_1}+\wp_{S_2}}$ (a,b,c,d) and of $\frac{\wp_{S_1}}{\wp_{S_1}+\wp_{\rm rest}}$ (e,f) where $\wp_{S_1(S_2)}$ is the probability for each event to be a signal $S_1(S_2)$ and $\wp_{\rm rest}$ is the probability for each event to be all except the signal S_1 (other signals and backgrounds weighted with the measured relative fractions). The point with the error bars show the distribution obtained on the fitted data sample while the histogram shows the distributions obtained by generating signals and background events directly from the total p.d.f.s of the fit of composition.

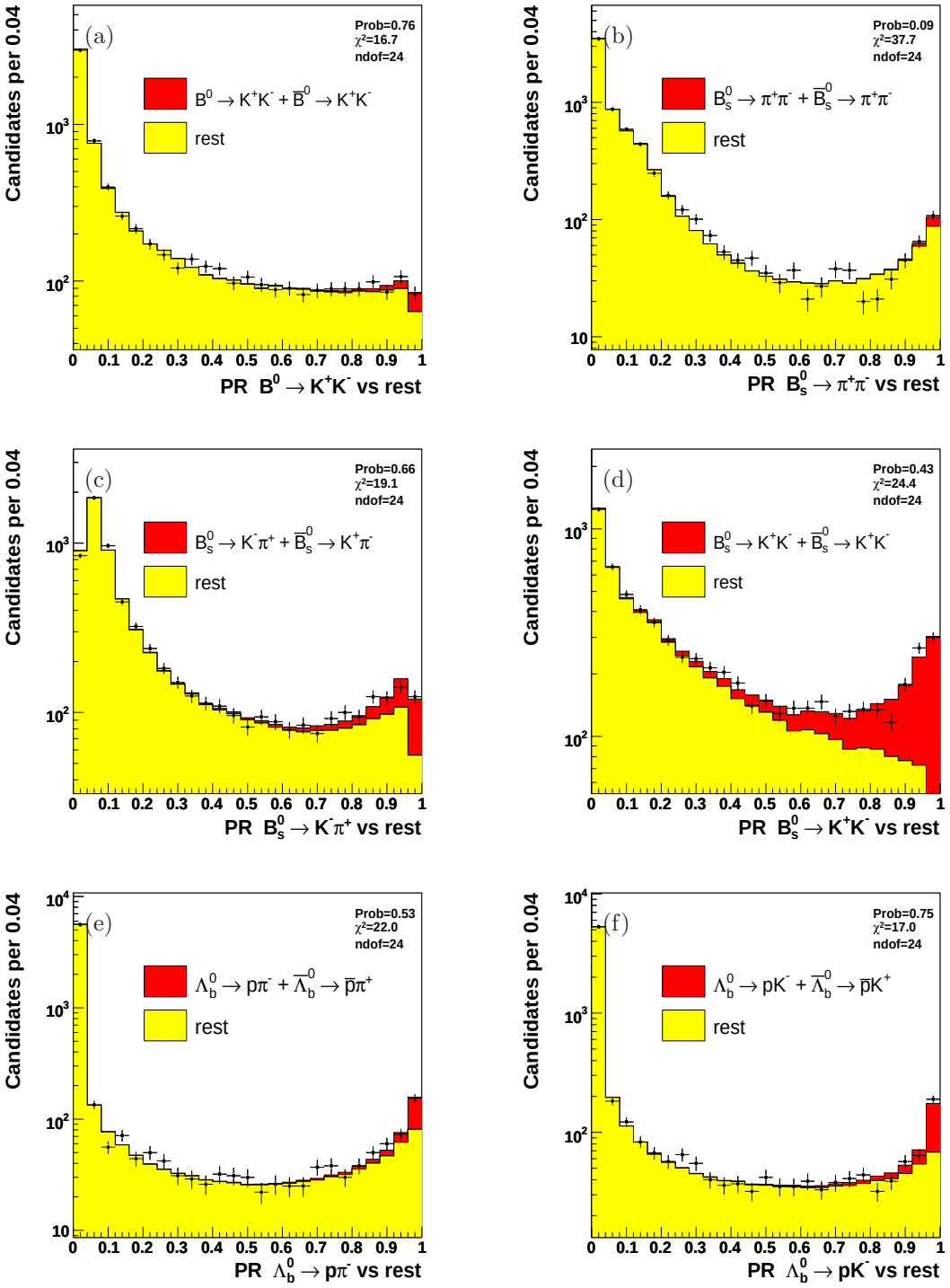


Figure 9.9: Distribution of the probability ratio ($\mathcal{PR}$) in the signal mass region ($5.1 < m_{\pi\pi} < 5.6$ GeV/c^2). Distribution of $\frac{\wp_{S_1}}{\wp_{S_1}+\wp_{\rm rest}}$ where $\wp_{S_1}$ is the probability for each event to be a signal S_1 and $\wp_{\rm rest}$ is the probability for each event to be all except the signal S_1 (other signals and backgrounds weighted with the measured relative fractions). The point with the error bars show the distribution obtained on the fitted data sample while the histogram shows the distributions obtained by generating signals and background events directly from the total p.d.f.s of the fit of composition.

9.4.3 Additional fits

We performed some additional fits of the $B^0_{(s)} \to h^+h'^-$ data sample, and we compared them with our central results of tab. 9.1 using the following expression:

$$\mathcal{C}_{\rm add} = \frac{|\hat{\theta}_{\rm cen} - \hat{\theta}_{\rm add}|}{\hat{\sigma}_{\rm max}} \tag{9.6}$$

where $\hat{\theta}_{\rm cen}$ and $\hat{\theta}_{\rm add}$ are respectively the values of the parameter determined by the central fit (loose selection) and by the additional fit. $\sigma_{\rm max}$ is the largest error between those returned by the two fits $\sigma_{\rm max} = \max(\sigma_{\rm cen}, \sigma_{\rm add})$. This is used as a conservative estimate of the uncertainty on the difference between the two fits, because the correlation is positive (generally large) and one of the two fits exploits only a portion of the information used by the other.

	$\mathcal{C}_{\rm kine}$	$\mathcal{C}_{\rm mass}$
$\hat{f}_{B^0\to\pi^+\pi^-}$	1.9	0.1
$\hat{f}_{B^0\to K^+\pi^-}$	2.1	0.2
$\frac{\hat{f}_{\overline{B}^0\to K^-\pi^+} - \hat{f}_{B^0\to K^+\pi^-}}{\hat{f}_{\overline{B}^0\to K^-\pi^+} + \hat{f}_{B^0\to K^+\pi^-}}$	0.07	0.02
$\hat{f}_{B^0\to K^+K^-}$	–	0.1
$\hat{f}_{B^0_s\to\pi^+\pi^-}$	–	0.04
$\hat{f}_{B^0_s\to K^-\pi^+}$	0.4	0.1
$\frac{\hat{f}_{\overline{B}^0_s\to K^+\pi^-} - \hat{f}_{B^0_s\to K^-\pi^+}}{\hat{f}_{\overline{B}^0_s\to K^+\pi^-} + \hat{f}_{B^0_s\to K^-\pi^+}}$	0.7	0.05
$\hat{f}_{B^0_s\to K^+K^-}$	2.1	0.1
$\hat{f}_{\Lambda^0_b\to p\pi^-}$	2.0	0.03
$\frac{\hat{f}_{\overline{\Lambda}^0_b\to \overline{p}\pi^+} - \hat{f}_{\Lambda^0_b\to p\pi^-}}{\hat{f}_{\overline{\Lambda}^0_b\to \overline{p}\pi^+} + \hat{f}_{\Lambda^0_b\to p\pi^-}}$	0.2	0.02
$\hat{f}_{\Lambda^0_b\to pK^-}$	0.8	0.002
$\frac{\hat{f}_{\overline{\Lambda}^0_b\to \overline{p}K^+} - \hat{f}_{\Lambda^0_b\to pK^-}}{\hat{f}_{\overline{\Lambda}^0_b\to \overline{p}K^+} + \hat{f}_{\Lambda^0_b\to pK^-}}$	0.3	0.01

Table 9.5: Comparisons between the central fit (loose selection), the equivalent fit that uses only the kinematic information ($\mathcal{C}_{\rm kine}$), and the equivalent fit where we leave the global mass scale free ($\mathcal{C}_{\rm mass}$). The $\mathcal{C}_{\rm add}$ quantity is defined in the text. Similar results are obtained for the tight selection.

Kinematic-only fit

We performed a fit of composition using only the kinematic information, by turning off the PID information in the Likelihood function: we used only the information from the variables $m_{\pi\pi}$, α and $p_{\rm tot}$. Since the PID information (contained in κ_1 and κ_2 variables) and kinematics are crucial independent ingredients of the analysis, we want to check for possible disagreements between these two informations. Table 9.5 reports the comparison between the fits with the method explained above, and the agreement obtained is satisfactory. Without the PID information the fit of composition loses much separation power in disentangling among the signal components. In particular, using only the

kinematic information it is very difficult to separate the $B^0 \to \pi^+\pi^-$ and $B_s^0 \to K^+K^-$ modes, which are very similar kinematically.

Global mass scale

Table 9.5 reports also the comparison between the central fit (loose selection) and a fit performed by letting the global mass scale completely free in the fit. We added a new parameter δ_m to the fit by making the substitution:

$$\begin{aligned} m_{B^0} &\to m_{B^0} + \delta_m \\ m_{B_s^0} &\to m_{B_s^0} + \delta_m \\ m_{\Lambda_b^0} &\to m_{\Lambda_b^0} + \delta_m \end{aligned}$$

where m_{B^0}, $m_{B_s^0}$, $m_{\Lambda_b^0}$ are the masses measured by CDF in Run II [106] and they are external inputs of the analytic expression of $\mathcal{M}_j(\alpha, p_{\rm tot})$ (see sec. 6.3). The agreement between fits is satisfactory, and the fitted value of the mass shift is compatible with zero within a small uncertainty $\delta_m = -0.3 \pm 0.6$ MeV/c^2. This guarantees that the chosen global mass scale is accurate and that the fit of composition measures it with a precision comparable to the current world best mass measurements of the b-mesons. The systematic uncertainty associated to our limited knowledge of the global mass scale will be evaluated in sec. 12.2 using this additional fit.

Chapter 10

Relative efficiency corrections

In order to translate the parameters returned from the fit of composition into physics measurements of branching fractions we need to apply the corrections for different efficiency of the selection for the various decay modes. This chapter is devoted to the evaluation of these efficiency corrections which were extracted from real data, whenever possible. The charge asymmetry correction for the CP asymmetry measurements is described in chap. 11.

10.1 Definitions

In order to translate the results returned from the fit of composition into measurements of relative branching fractions and CP asymmetries we need to apply corrections for the relative efficiencies of the selection between the various decay modes. For each channel, the fraction output by the fit must be corrected by an efficiency factor ε. Below we show how the efficiency corrections are applied to the results determined by the fit. We divided the observables in two categories, depending on the selection from which they were extracted. For the loose cuts we have:

$$\begin{aligned} \frac{\mathcal{B}(B^0 \to \pi^+\pi^-)}{\mathcal{B}(B^0 \to K^+\pi^-)} &= \frac{\hat{f}_{B^0\to\pi^+\pi^-}}{\hat{f}_{B^0\to K^+\pi^-}} \cdot \frac{\varepsilon(B^0 \to K\pi)}{\varepsilon(B^0 \to \pi\pi)} \\ \frac{f_s}{f_d} \times \frac{\mathcal{B}(B^0_s \to K^+K^-)}{\mathcal{B}(B^0 \to K^+\pi^-)} &= \frac{\hat{f}_{B^0_s\to K^+K^-}}{\hat{f}_{B^0\to K^+\pi^-}} \cdot \frac{\varepsilon(B^0 \to K\pi)}{\varepsilon(B^0_s \to KK)}. \end{aligned}$$

and for tight cuts we have:

$$\begin{aligned}
\frac{f_s}{f_d} \times \frac{\mathcal{B}(B_s^0 \to K^-\pi^+)}{\mathcal{B}(B^0 \to K^+\pi^-)} &= \frac{\hat{f}_{B_s^0 \to K^-\pi^+}}{\hat{f}_{B^0 \to K^+\pi^-}} \cdot \frac{\varepsilon(B^0 \to K\pi)}{\varepsilon(B_s^0 \to K\pi)} \\
\frac{\mathcal{B}(B^0 \to K^+K^-)}{\mathcal{B}(B^0 \to K^+\pi^-)} &= \frac{\hat{f}_{B^0 \to K^+K^-}}{\hat{f}_{B^0 \to K^+\pi^-}} \cdot \frac{\varepsilon(B^0 \to K\pi)}{\varepsilon(B^0 \to KK)} \\
\frac{f_s}{f_d} \times \frac{\mathcal{B}(B_s^0 \to \pi^+\pi^-)}{\mathcal{B}(B^0 \to K^+\pi^-)} &= \frac{\hat{f}_{B_s^0 \to \pi^+\pi^-}}{\hat{f}_{B^0 \to K^+\pi^-}} \cdot \frac{\varepsilon(B^0 \to K\pi)}{\varepsilon(B_s^0 \to \pi\pi)} \\
\frac{\mathcal{B}(\Lambda_b^0 \to p\pi^-)}{\mathcal{B}(\Lambda_b^0 \to pK^-)} &= \frac{\hat{f}_{\Lambda_b^0 \to p\pi^-}}{\hat{f}_{\Lambda_b^0 \to pK^-}} \cdot \frac{\varepsilon(\Lambda_b^0 \to pK)}{\varepsilon(\Lambda_b^0 \to p\pi)}.
\end{aligned}$$

The notation $\varepsilon(B^0_{(s)} \to hh')$, where the particles in the final state are labeled without the charge, indicates the CP-averaged efficiency for the decay $B^0_{(s)} \to h^+h^{'-}$. Conversely the notation $\varepsilon(B^0_{(s)} \to h^+h^{'-})$ indicates the non CP-averaged efficiency and it will be used in chap. 11, where the charge asymmetry efficiency correction will be treated. The total reconstruction efficiency ε used in the above relations factorizes as the product of four terms:

$$\varepsilon = \varepsilon_{\rm kin} \cdot c_{\rm XFT} \cdot c_{\rm FSR} \cdot \varepsilon_{\rm iso}. \tag{10.1}$$

$\varepsilon_{\rm kin}$ — this is the reconstruction efficiency (trigger and offline cuts). This term mostly accounts for the acceptance effects. It includes the trigger efficiency and the efficiency of the off-line reconstruction and selection. We extract the kinematic efficiency from Monte Carlo simulation. Any geometric acceptance effect is properly taken into account, since the simulation reproduces the kinematic distributions of the decays and it includes an accurate description of the detector geometry. This term does not include the contribution of the isolation requirement and of tracking efficiency which are treated separately.

$c_{\rm XFT}$ — this correction takes into account the relative efficiency of the XFT trigger on charged kaons and pions. This is not simulated in the Monte Carlo and it was extracted from real data.

$c_{\rm FSR}$ — this correction takes into account the kinematic acceptance efficiency due to the presence of the Final State Radiation. It is not simulated in the standard Monte Carlo and it was extracted from a specialized FMC simulation (chap. 5).

$\varepsilon_{\rm iso}$ — this is the efficiency that a signal event satisfies the isolation cut. It was determined from real data and it depends only on the initial meson type $\varepsilon_{\rm iso}(B^0_{(s)} \to h^+h'^-) = \varepsilon_{\rm iso}(B^0_{(s)})$.

10.2 Kinematic efficiencies

In order to evaluate the total reconstruction efficiency $\varepsilon_{\rm kin}$ we used the realistic simulation described in sec. 4.1. The CP-averaged kinematic efficiency, for each signal mode $B^0_{(s)} \to h^+h^{'-}$, is defined

as the ratio between the number of events passing the selection ($N_{\rm passing}$) and the number of events initially generated by the simulation ($N_{\rm generation}$):

$$\varepsilon_{\rm kin} = \frac{N_{\rm passing}}{N_{\rm generation}}. \tag{10.2}$$

Using simulated samples is reliable for this purpose. The effects contributing to the kinematic efficiency are well reproduced by the simulation and are similar among all the signal modes. Any possible small systematic discrepancy between real data and the simulation vanishes in the efficiency ratio between two different modes. Additional contributions arise from the different probability of interaction with matter among positively-charged kaons(pions), and negatively-charged kaons(pions). Although several CDF measurements confirm that the GEANT package reproduces accurately these effects, we measured directly from real data the ratio of kinematic efficiency between the final states $K^+\pi^-$ and $K^-\pi^+$ (see sec. 11.6.1 and chap. 11) due to the sensitivity of the direct CP asymmetry to this effect.

10.2.1 Lifetimes in the Monte Carlo

Since the signal selection relies on both impact parameter and transverse decay length cuts, the assumed B lifetimes in the Monte Carlo have an impact on the kinematic efficiencies. We used the PDG 2005 [32] value of $c\tau(B^0) = 460 \pm 4$ μm for the B^0 meson, and $c\tau(\Lambda_b^0) = 368 \pm 24$ μm for the Λ_b^0 baryon. For the lifetime of the B_s^0 going in the flavor specific $K^-\pi^+$ mode we used the PDG 2005 [32] value measured on semileptonic decays: $c\tau(B_s^0) = 438 \pm 17$ μm. The choice of the $c\tau(B_s^0 \to K^+K^-)$ is less straightforward because it depends both on the CP content of this mode and on the value of $\Delta\Gamma_s/\Gamma_s$, which are not well known. We can write:

$$\Gamma(B_s^0(t) \to K^+K^-) + \Gamma(\overline{B}_s^0(t) \to K^+K^-) \propto R_{\rm H} e^{-\Gamma_{\rm H}^{(s)} t} + R_{\rm L} e^{-\Gamma_{\rm L}^{(s)} t}, \tag{10.3}$$

where $R_{\rm H}$ ($R_{\rm L}$) is the relative fraction of "heavy" ("light") mass eigenstate of this mode. However, the $B_s^0 \to K^+K^-$ mode is expected in Standard Model [68] to be dominated by the "short" eigenstate ($B_s^{\rm L}$ CP-even), with a "long"eigenstate ($B_s^{\rm H}$ CP-odd) contribution smaller than 5%. Therefore we evaluated the value of $c\tau(B_s^0 \to K^+K^-)$ used in our analysis using the following assumptions:

- the $B_s^0 \to K^+K^-$ decay mode is a 100% "short" eigenstate ($B_s^{\rm L}$ CP-even);
- $\Delta\Gamma_s/\Gamma_s = 0.12 \pm 0.06$ from Standard Model expectation [52];
- according to the Standard Model the widths for B_s^0 and B^0 mesons are equal, $\Gamma_s = \Gamma_d$.

From these assumptions we obtain:

$$\begin{aligned} c\tau(B_s^0 \to K^+K^-) &= \frac{c}{\Gamma_s^{\rm short}} = \frac{c}{\Gamma_s + \Delta\Gamma_s/2} = \frac{c}{\Gamma_d + 0.12 \cdot \Gamma_d/2} & (10.4) \\ &= [434 \pm 4\ (\Gamma_d) \pm 12\ (\Delta\Gamma_s^{\rm SM})]\ \mu m. & (10.5) \end{aligned}$$

We split the uncertainty on $c\tau(B_s^0 \to K^+K^-)$ into the part due to the uncertainty on Γ_d, which contributes 1%, and the part due to the 0.06 uncertainty on $\Delta\Gamma_s/\Gamma_s$ expected from the Standard Model. The systematics on our results coming from the first source of uncertainty is discussed in sec. 12.9.1,

the systematics related to the $\Delta\Gamma_s/\Gamma_s$ uncertainty is evaluated in sec. 12.9.2. The $B_s^0 \to \pi^+\pi^-$ lifetime was extracted under the same assumptions used for the $B_s^0 \to K^+K^-$, therefore we assumed equal $c\tau(B_s^0 \to K^+K^-) = c\tau(B_s^0 \to \pi^+\pi^-)$.

Recently, both the CDF and DØ Collaborations [54, 53] measured $\Delta\Gamma_s/\Gamma_s$ using samples of fully exclusive $B_s^0 \to J/\psi\phi$ decays. The experimental results for Γ_s and $\Delta\Gamma_s$ are in agreement with the Standard Model expectations but the uncertainties are still larger than theoretical ones. Since there is no reason to think that the Standard Model expectations for Γ_s and $\Delta\Gamma_s$ are wrong, we consider our assumption still valid, to use the expected value for Γ_s and $\Delta\Gamma_s/\Gamma_s$ instead of the current experimental value to evaluate the lifetime of $B_s^0 \to \pi^+\pi^-$ and $B_s^0 \to K^+K^-$ modes.

Table 10.1 reports the input lifetimes used to generate the simulated samples.

mode	$c\tau$ $[\mu m]$
B^+	501
B^0	460
$B_s^0 \to \pi^+\pi^-$	434
$B_s^0 \to K^-\pi^+$	438
$B_s^0 \to K^+K^-$	434
Λ_b^0	368

Table 10.1: Summary of the input lifetimes in the simulation.

10.2.2 Kinematic efficiency corrections

The kinematic efficiency corrections extracted from the simulation are divided in two groups, according to the two different selections. For the loose cuts we have:

$$\frac{\varepsilon_{\rm kin}(B^0 \to K\pi)}{\varepsilon_{\rm kin}(B^0 \to \pi\pi)} = 0.978 \pm 0.004 \text{ (MC)} \quad (10.6)$$

$$\frac{\varepsilon_{\rm kin}(B^0 \to K\pi)}{\varepsilon_{\rm kin}(B_s^0 \to KK)} = 1.032 \pm 0.004 \text{ (MC)}. \quad (10.7)$$

For the tight cuts we have:

$$\frac{\varepsilon_{\rm kin}(B^0 \to K\pi)}{\varepsilon_{\rm kin}(B^0 \to KK)} = 1.023 \pm 0.004 \text{ (MC)} \quad (10.8)$$

$$\frac{\varepsilon_{\rm kin}(B^0 \to K\pi)}{\varepsilon_{\rm kin}(B_s^0 \to K\pi)} = 1.008 \pm 0.004 \text{ (MC)} \quad (10.9)$$

$$\frac{\varepsilon_{\rm kin}(B^0 \to K\pi)}{\varepsilon_{\rm kin}(B_s^0 \to \pi\pi)} = 0.971 \pm 0.004 \text{ (MC)} \quad (10.10)$$

$$\frac{\varepsilon_{\rm kin}(\Lambda_b^0 \to pK)}{\varepsilon_{\rm kin}(\Lambda_b^0 \to p\pi)} = 0.982 \pm 0.004 \text{ (MC)}. \quad (10.11)$$

The uncertainty referred as (MC) is due to the finite statistics of the simulated samples used to estimate the kinematic efficiency $\varepsilon_{\rm kin}$ and it corresponds to the Poisson fluctuation of the number of events passing the selection. This uncertainty will be used to evaluate the relative associated systematics (see sec. 12.8.1).

10.2.3 Trigger bias corrections

A separate correction is needed to account for the different XFT efficiency to reconstruct charged kaons and pions. This is due to the different specific ionization of pions and kaons in the COT volume [122, 136]. In the typical momentum range of the $B^0_{(s)} \to h^+h^{'-}$ decay products, charged pions (with typical Lorentz boost $\beta\gamma \approx 15$) ionize more than charged kaons ($\beta\gamma \approx 4$). The consequence is a larger pulse width of pions than of kaons and, as a consequence a larger hit multiplicity of the pions in the COT. The requirement of the XFT on the minimum number of axial COT hits reflects in a different trigger efficiency for kaons than for pions. This introduces different relative efficiencies between the $B^0_{(s)} \to h^+h^{'-}$ modes with different number of kaons and pions in the final state. This effect is not reproduced by the CDF II simulation, and was instead measured by a study on XFT-unbiased prong in three-body $D^+_{(s)}$ meson decays ($D^+ \to K^-\pi^+\pi^+$, $D^+ \to K^+K^-\pi^+$and $D^+_s \to K^+K^-\pi^+$) triggered on two tracks [122]. Using the XFT information associated to the non-triggered kaon (or pion), the ratio between the number of kaons (pions) reconstructed off-line that would have passed the XFT requirements $N_{\rm XFT}$ and the total number of kaons (pions) reconstructed off-line $N_{\rm off}$ was measured as a function of the transverse momentum:

$$\varepsilon_{\rm XFT} = \frac{N_{\rm XFT}}{N_{\rm off}}. \tag{10.12}$$

For each charged particle having transverse momentum $p_{\rm T}$, the ratio of the XFT efficiency between data and Monte Carlo simulation ($c_{\rm XFT}$) was fitted to a straight-line function of $1/p_{\rm T}$:

$$c_{\rm XFT}(p_{\rm T}) = \frac{\varepsilon^{\rm data}_{\rm XFT}}{\varepsilon^{\rm MC}_{\rm XFT}} = k_0 + \frac{k_1}{p_{\rm T}}, \tag{10.13}$$

where $\varepsilon^{\rm data}_{\rm XFT}$ is the XFT-efficiency measured on real data, and $\varepsilon^{\rm MC}_{\rm XFT}$ is the XFT efficiency extracted from simulation. The parameters of the above formula are determined from binned χ^2-fits as a function of time (in terms of runs). Following Ref. [122], we applied the correction to the simulated samples. The contribution to the final yield of each simulated $B^0_{(s)} \to h^+h^{'-}$ event was reweighed by the product $c_{\rm XFT}[p_{\rm T}(h)] \times c_{\rm XFT}[p_{\rm T}(h^{'})]$ and the two factors were evaluated using the proper set of k_i parameters and the specific value of transverse momentum of the particle. The kinematic efficiencies reweighted with the XFT-corrections with their uncertainties for the observables quoted using the loose selection are:

$$\begin{aligned}
\frac{\varepsilon_{\rm kin}(B^0 \to K\pi)}{\varepsilon_{\rm kin}(B^0 \to \pi\pi)} \cdot \frac{c_{\rm XFT}(B^0 \to K\pi)}{c_{\rm XFT}(B^0 \to \pi\pi)} &= 0.934 \pm 0.004\ ({\rm MC})\ ^{+0.016}_{-0.019}\ ({\rm XFT}) \\
\frac{\varepsilon_{\rm kin}(B^0 \to K\pi)}{\varepsilon_{\rm kin}(B^0_s \to KK)} \cdot \frac{c_{\rm XFT}(B^0 \to K\pi)}{c_{\rm XFT}(B^0_s \to KK)} &= 1.080 \pm 0.004\ ({\rm MC})\ ^{+0.027}_{-0.013}\ ({\rm XFT}).
\end{aligned}$$

Those for the tight selection are:

$$\begin{aligned}
\frac{\varepsilon_{\rm kin}(B^0 \to K\pi)}{\varepsilon_{\rm kin}(B^0 \to KK)} \cdot \frac{c_{\rm XFT}(B^0 \to K\pi)}{c_{\rm XFT}(B^0 \to KK)} &= 1.072 \pm 0.004\ ({\rm MC}) \pm 0.020\ ({\rm XFT}) \\
\frac{\varepsilon_{\rm kin}(B^0 \to K\pi)}{\varepsilon_{\rm kin}(B^0_s \to K\pi)} \cdot \frac{c_{\rm XFT}(B^0 \to K\pi)}{c_{\rm XFT}(B^0_s \to K\pi)} &= 1.008 \pm 0.004\ ({\rm MC})\ ^{+0.000}_{-0.017}\ ({\rm XFT}) \\
\frac{\varepsilon_{\rm kin}(B^0 \to K\pi)}{\varepsilon_{\rm kin}(B^0_s \to \pi\pi)} \cdot \frac{c_{\rm XFT}(B^0 \to K\pi)}{c_{\rm XFT}(B^0_s \to \pi\pi)} &= 0.927 \pm 0.004\ ({\rm MC}) \pm 0.017\ ({\rm XFT}) \\
\frac{\varepsilon_{\rm kin}(\Lambda^0_b \to pK)}{\varepsilon_{\rm kin}(\Lambda^0_b \to p\pi)} \cdot \frac{c_{\rm XFT}(\Lambda^0_b \to pK)}{c_{\rm XFT}(\Lambda^0_b \to p\pi)} &= 0.929 \pm 0.004\ ({\rm MC}) \pm 0.017\ ({\rm XFT}).
\end{aligned}$$

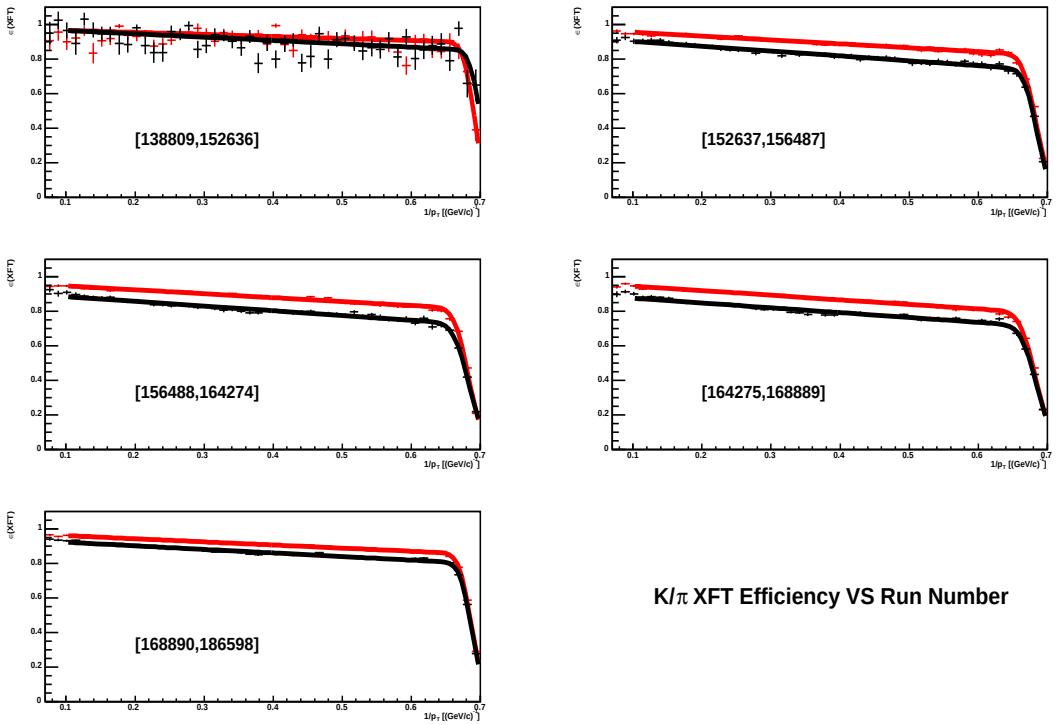


Figure 10.1: XFT efficiency of positively-charged kaons (black points) and pions (red points) as a function of $1/p_{\mathrm{T}}$, as measured in $D^{+}_{(s)}$ meson decays [122]. Fit functions are overlaid (solid lines).

The uncertainty referred as (XFT), is due to the statistical and systematic uncertainty on the measurement of the parameters k_i of eq. (10.13). This uncertainty will be used to evaluate the relative associated systematics (sec. 12.8.2).

10.2.4 FSR correction

The invariant mass template of each signal mode was extracted from an accurate study described in chap. 5 where we kept into account also the effect due to the soft photon emission in the final state (FSR). The mass template is defined only when an energy cut-off[1] is given (see sec. 5.4.1 and sec. 5.4.2) and for the present analysis we chose $E_{\mathrm{max}} = 0.5$ GeV. Since in the fit of composition we use only the invariant $\pi\pi$-mass, the lower boundary $m_{\pi\pi} > 5$ GeV/c^2 has an asymmetric effect on the radiative tails of each signal mode. In other words, in the invariant $\pi\pi$-mass the signal peaks are shifted from the position computed with the correct mass assignment towards the lower mass boundary (see fig. 4.9), then, the radiative tail is long as a function of this shift in the mass window fit $5 < m_{\pi\pi} < 5.8$ GeV/c^2. To keep into account this effect we simulated 10^7 events for all signal modes with and without the FSR using the FMC simulation described in sec. 5.3. The correction due to the

[1]The cut-off E_{max} is the maximum energy of the photon emitted in the rest frame of the B meson.

FSR ($c_{\rm FSR}$) is defined as the ratio between the number of events passing the selection including the FSR ($N^{\rm on}_{\rm FSR}$) and the number of events passing the selection excluding FSR ($N^{\rm off}_{\rm FSR}$):

$$c_{\rm FSR} = \frac{N^{\rm on}_{\rm FSR}}{N^{\rm off}_{\rm FSR}}. \tag{10.14}$$

The kinematic efficiencies reweighted with the XFT-corrections and corrected for the FSR factors are:

$$\frac{\varepsilon_{\rm kin}(B^0\to K\pi)}{\varepsilon_{\rm kin}(B^0\to\pi\pi)}\cdot\frac{c_{\rm XFT}(B^0\to K\pi)}{c_{\rm XFT}(B^0\to\pi\pi)}\cdot\frac{c_{\rm FSR}(B^0\to K\pi)}{c_{\rm FSR}(B^0\to\pi\pi)} = 0.936\pm0.004\ ({\rm MC})\ ^{+0.016}_{-0.019}\ ({\rm XFT}) \tag{10.15}$$

$$\frac{\varepsilon_{\rm kin}(B^0\to K\pi)}{\varepsilon_{\rm kin}(B^0_s\to KK)}\cdot\frac{c_{\rm XFT}(B^0\to K\pi)}{c_{\rm XFT}(B^0_s\to KK)}\cdot\frac{c_{\rm FSR}(B^0\to K\pi)}{c_{\rm FSR}(B^0_s\to KK)} = 1.074\pm0.004\ ({\rm MC})\ ^{+0.027}_{-0.013}\ ({\rm XFT}) \tag{10.16}$$

Those for the tight cuts are:

$$\frac{\varepsilon_{\rm kin}(B^0\to K\pi)}{\varepsilon_{\rm kin}(B^0\to KK)}\cdot\frac{c_{\rm XFT}(B^0\to K\pi)}{c_{\rm XFT}(B^0\to KK)}\cdot\frac{c_{\rm FSR}(B^0\to K\pi)}{c_{\rm FSR}(B^0\to KK)} = 1.074\pm0.004\ ({\rm MC})\pm0.020\ ({\rm XFT}) \tag{10.17}$$

$$\frac{\varepsilon_{\rm kin}(B^0\to K\pi)}{\varepsilon_{\rm kin}(B^0_s\to K\pi)}\cdot\frac{c_{\rm XFT}(B^0\to K\pi)}{c_{\rm XFT}(B^0_s\to K\pi)}\cdot\frac{c_{\rm FSR}(B^0\to K\pi)}{c_{\rm FSR}(B^0_s\to K\pi)} = 1.008\pm0.004\ ({\rm MC})\ ^{+0.000}_{-0.017}\ ({\rm XFT}) \tag{10.18}$$

$$\frac{\varepsilon_{\rm kin}(B^0\to K\pi)}{\varepsilon_{\rm kin}(B^0_s\to\pi\pi)}\cdot\frac{c_{\rm XFT}(B^0\to K\pi)}{c_{\rm XFT}(B^0_s\to\pi\pi)}\cdot\frac{c_{\rm FSR}(B^0\to K\pi)}{c_{\rm FSR}(B^0_s\to\pi\pi)} = 0.927\pm0.004\ ({\rm MC})\pm0.017\ ({\rm XFT}) \tag{10.19}$$

$$\frac{\varepsilon_{\rm kin}(\Lambda^0_b\to pK)}{\varepsilon_{\rm kin}(\Lambda^0_b\to p\pi)}\cdot\frac{c_{\rm XFT}(\Lambda^0_b\to pK)}{c_{\rm XFT}(\Lambda^0_b\to p\pi)} = 0.929\pm0.004\ ({\rm MC})\pm0.017\ ({\rm XFT}) \tag{10.20}$$

The uncertainty due to the additional FSR correction is negligible with respect to the uncertainty due to the finite statistics of simulation and due to the XFT effects, then we do not evaluate any additional systematics associated to this correction.

The efficiency ratio corrections described above do not take into account the different efficiency of the isolation on B^0 and on B^0_s. This additional correction affects only the observables related to a B^0_s meson decay mode normalized to a B^0 meson decay mode and it was measured with fully reconstructed B decays. Chapter 7 describes in detail the procedure to measure from real data the efficiency correction due to the isolation requirement while sec. 10.4 reports only the results of that work.

10.3 Results (not involving isolation efficiency and charge asymmetry correction)

We now have all the corrections to the ratios of branching fractions which do not need the isolation efficiency and charge asymmetry correction. We can extract the corresponding measurements. All the associated uncertainties account for the statistical fluctuations due to finite samples only. The corrections for the remaining measurements are treated in the rest of this chapter.

10.3.1 Ratio $\mathcal{B}(B^0\to\pi^+\pi^-)/\mathcal{B}(B^0\to K^+\pi^-)$

Using the kinematic, XFT and FSR efficiencies $\frac{\varepsilon(B^0\to K\pi)}{\varepsilon(B^0\to\pi\pi)}\simeq 0.936$ (see eq. (10.15)), we corrected the fit results to extract the following measurement of relative branching fraction:

$$\frac{\mathcal{B}(B^0\to\pi^+\pi^-)}{\mathcal{B}(B^0\to K^+\pi^-)} = 0.259\pm0.017\ (stat.). \tag{10.21}$$

10.3.2 Ratio $\mathcal{B}(B^0 \to K^+K^-)/\mathcal{B}(B^0 \to K^+\pi^-)$

Using the kinematic, XFT and FSR efficiencies, $\frac{\varepsilon(B^0\to K\pi)}{\varepsilon(B^0\to KK)} \simeq 1.074$ (see eq. (10.17)), we corrected the fit results to extract the following measurement of relative branching fraction:

$$\frac{\mathcal{B}(B^0 \to K^+K^-)}{\mathcal{B}(B^0 \to K^+\pi^-)} = 0.020 \pm 0.008\ (stat.). \tag{10.22}$$

10.3.3 Ratio $\mathcal{B}(\Lambda_b^0 \to p\pi^-)/\mathcal{B}(\Lambda_b^0 \to pK^-)$

Using the kinematic, XFT and FSR efficiencies, $\frac{\varepsilon(\Lambda_b^0\to pK)}{\varepsilon(\Lambda_b^0\to p\pi)} \simeq 0.929$ (see eq. (10.20)), we corrected the fit results to extract the following measurement of relative branching fraction:

$$\frac{\mathcal{B}(\Lambda_b^0 \to p\pi^-)}{\mathcal{B}(\Lambda_b^0 \to pK^-)} = 0.66 \pm 0.14\ (stat.). \tag{10.23}$$

10.4 Efficiency of the B-isolation cut

The isolation of B meson depends on the multiplicity and momenta of the tracks produced in the b-quark fragmentation, which is not described by the signal-only simulation discussed in sec. 4.1. We therefore had to use real data to characterize this observable. Chapter 7 describes the measurement of the isolation efficiency for the values of the cut used in the present analysis using fully reconstructed $B^0_{(s)} \to J/\psi X$ decays. The results are summarized in sec. 7.4.2, here we reports only the efficiency ratio values averaged on the transverse momentum distribution of the $B^0_{(s)} \to h^+h^{'-}$ decays:

$$\left.\frac{\varepsilon_{\rm iso}(B^0)}{\varepsilon_{\rm iso}(B_s^0)}\right|^{I(B)>0.5} = 1.000 \pm 0.028, \tag{10.24}$$

$$\left.\frac{\varepsilon_{\rm iso}(B^0)}{\varepsilon_{\rm iso}(B_s^0)}\right|^{I(B)>0.525} = 1.030 \pm 0.032. \tag{10.25}$$

Since we do not expect any difference for this efficiency ratio when we move from $I(B) > 0.5$ to $I(B) > 0.525$ and since the measurements in eqs. (10.24) and (10.25) are strongly correlated (we can not take the average), we corrected the results using the value with smaller statistical uncertainty:

$$\frac{\varepsilon_{\rm iso}(B^0)}{\varepsilon_{\rm iso}(B_s^0)} = 1.000 \pm 0.028. \tag{10.26}$$

This statistical uncertainty will be used to evaluate the relative associated systematics (see sec. 12.8.3).

10.5 Results (involving isolation efficiency)

The isolation efficiency, along with the kinematic, XFT and FSR efficiencies of sec. 10.2.4, completes the set of corrections used to obtain the remaining ratios of branching fractions. All the uncertainties account only for the statistical fluctuations due to finite samples.

10.5.1 Ratio $(f_s/f_d) \times \mathcal{B}(B_s^0 \to K^-\pi^+)/\mathcal{B}(B^0 \to K^+\pi^-)$

Following eqs. (10.18) and (10.26), we corrected the fit results for the kinematic, XFT, FSR and the isolation efficiencies, $\frac{\varepsilon(B^0 \to K\pi)}{\varepsilon(B_s^0 \to Kpi)} \simeq 1.008$, to extract the following measurement of relative branching fraction:

$$\frac{f_s}{f_d} \times \frac{\mathcal{B}(B_s^0 \to K^-\pi^+)}{\mathcal{B}(B^0 \to K^+\pi^-)} = 0.071 \pm 0.010\ (stat.). \tag{10.27}$$

10.5.2 Ratio $(f_s/f_d) \times \mathcal{B}(B_s^0 \to K^+K^-)/\mathcal{B}(B^0 \to K^+\pi^-)$

Following eqs. (10.16) and (10.26), we corrected the fit results for the kinematic, XFT, FSR and the isolation efficiencies, $\frac{\varepsilon(B^0 \to k\pi)}{\varepsilon(B_s^0 \to KK)} \simeq 1.074$, to extract the following measurement of relative branching fraction:

$$\frac{f_s}{f_d} \times \frac{\mathcal{B}(B_s^0 \to K^+K^-)}{\mathcal{B}(B^0 \to K^+\pi^-)} = 0.347 \pm 0.020\ (stat.). \tag{10.28}$$

10.5.3 Ratio $(f_s/f_d) \times \mathcal{B}(B_s^0 \to \pi^+\pi^-)/\mathcal{B}(B^0 \to K^+\pi^-)$

Following eqs. (10.19) and (10.26), we corrected the fit results for the kinematic, XFT, FSR and the isolation efficiencies, $\frac{\varepsilon(B^0 \to K\pi)}{\varepsilon(B_s^0 \to \pi\pi)} \simeq 0.927$, to extract the following measurement of relative branching fraction:

$$\frac{f_s}{f_d} \times \frac{\mathcal{B}(B_s^0 \to \pi^+\pi^-)}{\mathcal{B}(B^0 \to K^+\pi^-)} = 0.007 \pm 0.004\ (stat.). \tag{10.29}$$

10.6 Further considerations

The corrections described in this chapter were extracted from real data when it was possible and from simulation when it was strictly necessary. For this analysis we used the data-driven approach and we used the simulation only to extract the kinematic efficiencies. These depend on differences in geometric acceptance among the $B_{(s)}^0 \to h^+h^{'-}$ modes and the simulation properly reproduces these effects. In addition every small systematic effects cancel out in the ratio of branching fractions where these corrections are involved. The resulting input from simulation is modest: the largest kinematic correction amounts to a factor of about 3.2% (see eqs. (10.6)–(10.11)).

Chapter 11

Charge asymmetry

In this chapter we describe the measurement of the detector-induced charge asymmetry between positively and negatively charged kaons and pions, due to their different probability of strong interaction in the tracker material. This allows to extract the correction factor for the CP asymmetry measurement directly from real data. Due to the high precision of the measurement, we extracted this correction from data, performing a complete analysis on a large sample of $D^0 \to K^-\pi^+$ decays.

11.1 Introduction

In the measurement of CP asymmetry the only relevant acceptance effect is the detector-induced charge asymmetry between positively and negatively charged kaons and pions, due to their different probability of strong interaction with the tracker material. All other inefficiencies, such as the $\mathcal{O}(1\%)$ asymmetry between positively and negatively-charged particles induced by the COT cell-geometry, cancel out in the ratio which defines the expression of the CP asymmetry. The terms related to the detector-induced charge asymmetry are the ratios:

$$\frac{\varepsilon(B^0 \to K^+\pi^-)}{\varepsilon(\overline{B}^0 \to K^-\pi^+)} \quad \text{and} \quad \frac{\varepsilon(\overline{B}^0_s \to K^+\pi^-)}{\varepsilon(B^0_s \to K^-\pi^+)}. \tag{11.1}$$

Below we show how the efficiency corrections in eq. (11.1) are applied to the results determined by the fit. We divided the observables in two categories, depending on the selection from which they were extracted. For the loose cuts we have:

$$\mathcal{A}_{\rm CP}(B^0 \to K^+\pi^-) = \frac{\mathcal{B}(\overline{B}^0 \to K^-\pi^+) - \mathcal{B}(B^0 \to K^+\pi^-)}{\mathcal{B}(\overline{B}^0 \to K^-\pi^+) + \mathcal{B}(B^0 \to K^+\pi^-)} = \frac{\hat{f}_{\overline{B}^0 \to K^-\pi^+} \cdot \frac{\varepsilon(B^0 \to K^+\pi^-)}{\varepsilon(\overline{B}^0 \to K^-\pi^+)} - \hat{f}_{B^0 \to K^+\pi^-}}{\hat{f}_{\overline{B}^0 \to K^-\pi^+} \cdot \frac{\varepsilon(B^0 \to K^+\pi^-)}{\varepsilon(\overline{B}^0 \to K^-\pi^+)} + \hat{f}_{B^0 \to K^+\pi^-}}$$

and for the tight cuts we have:

$$\mathcal{A}_{\rm CP}(B^0_s \to K^-\pi^+) = \frac{\mathcal{B}(\overline{B}^0_s \to K^+\pi^-) - \mathcal{B}(B^0_s \to K^-\pi^+)}{\mathcal{B}(\overline{B}^0_s \to K^+\pi^-) + \mathcal{B}(B^0_s \to K^-\pi^+)} = \frac{\hat{f}_{\overline{B}^0_s \to K^+\pi^-} \cdot \frac{\varepsilon(B^0_s \to K^-\pi^+)}{\varepsilon(\overline{B}^0_s \to K^+\pi^-)} - \hat{f}_{B^0_s \to K^-\pi^+}}{\hat{f}_{\overline{B}^0_s \to K^+\pi^-} \cdot \frac{\varepsilon(B^0_s \to K^-\pi^+)}{\varepsilon(\overline{B}^0_s \to K^+\pi^-)} + \hat{f}_{B^0_s \to K^-\pi^+}}$$

Although some CDF measurements confirm that the GEANT [103] package reproduces accurately these effects [122] we preferred to measure it directly from real data, to achieve the best precision and

the confidence in the result needed for this delicate measurement. We measured the efficiency ratios in eq. (11.1) using an *unbiased* sample of $D^0 \to K^-\pi^+$. By unbiased we mean that the $D^0 \to K^-\pi^+$ decays were reconstructed without requiring they were produced in the decay of a D^{*+}, which is usual in CDF when a clean D^0 sample is desired. The request of an additional charged pion in the final state and of the explicit reconstruction of the $D^{*+} \to D^0\pi^+ \to [K^-\pi^+]\pi^+$ decay chain, would generate an artificial asymmetry, since the CDF II tracking has a different efficiency for reconstructing the tracks associated to π^+ and π^- with low momentum, which would introduce extra uncertainties. For this reason we selected for our purpose about 10^6 *prompt* $D^0 \to K^-\pi^+$ decays and analysed them with the same methods used for the $B^0_{(s)} \to h^+h^{'-}$ decays and described in this thesis. This is a powerful check of all the analysis since we actually used the same reconstruction and fitting code of the $B^0_{(s)} \to h^+h^{'-}$ analysis. In this way, we are at same time eliminating possible spurious effects hidden in our procedure.

Since the Standard Model predicts a very small $\mathcal{O}(10^{-6})$ [142] direct CP asymmetry in the $D^0 \to K^-\pi^+$ decay, and since the current experimental measurements[1] [32] do not show any indication of a deviation from this prediction, we assume that:

$$\frac{\mathcal{B}(\overline{D}^0 \to K^+\pi^-) - \mathcal{B}(D^0 \to K^-\pi^+)}{\mathcal{B}(\overline{D}^0 \to K^+\pi^-) + \mathcal{B}(D^0 \to K^-\pi^+)} \ll 10^{-3}. \tag{11.2}$$

If we write relation (11.2) in terms of the measured relative fractions of $D^0 \to K^-\pi^+$ and $\overline{D}^0 \to K^+\pi^-$ and efficiency correction, we obtain:

$$\frac{\mathcal{B}(\overline{D}^0 \to K^+\pi^-) - \mathcal{B}(D^0 \to K^-\pi^+)}{\mathcal{B}(\overline{D}^0 \to K^+\pi^-) + \mathcal{B}(D^0 \to K^-\pi^+)} = \frac{\hat{f}_{\overline{D}^0\to K^+\pi^-} \cdot \frac{\varepsilon(D^0\to K^-\pi^+)}{\varepsilon(\overline{D}^0\to K^+\pi^-)} - \hat{f}_{D^0\to K^-\pi^+}}{\hat{f}_{\overline{D}^0\to K^+\pi^-} \cdot \frac{\varepsilon(D^0\to K^-\pi^+)}{\varepsilon(\overline{D}^0\to K^+\pi^-)} + \hat{f}_{D^0\to K^-\pi^+}} \ll 10^{-3} \tag{11.3}$$

from which we can extract the desired ratio $\frac{\varepsilon(\overline{D}^0\to K^+\pi^-)}{\varepsilon(D^0\to K^-\pi^+)}$ with an uncertainty smaller than 10^{-3}. To keep into account the different momentum spectrum of decay products of a D^0 meson with respect to a $B^0_{(s)}$ meson, to extract $\frac{\varepsilon(B^0\to K^+\pi^-)}{\varepsilon(\overline{B}^0\to K^-\pi^+)}$ and $\frac{\varepsilon(\overline{B}^0_s\to K^+\pi^-)}{\varepsilon(B^0_s\to K^-\pi^+)}$, we need to re-weigh the two-dimensional distribution of both particle momenta.

11.2 Reconstruction of the prompt $D^0 \to h^+h^{'-}$ sample

The sample of prompt $D^0 \to h^+h^{'-}$ decays used to study the charge asymmetry effects was collected between February 2002 (run 138809) and March 2006 (run 212133), as $B^0_{(s)} \to h^+h^{'-}$ decays, by the `B_CHARM` and `B_CHARM_HIGHPT` triggers (see sec. 3.2.2), paths that belong, along with the `B_PIPI` and `B_PIPI_HIGHPT` paths, to the Displaced-Tracks Trigger. Therefore a large fraction of trigger requirements is common to these two paths and most trigger-dependent effects are automatically taken into account in the reconstruction and selection of the events. Prompt $D^0 \to h^+h^{'-}$ decays have the same kinematic topology and the same final state as $B^0_{(s)} \to h^+h^{'-}$ decays.
The expected yield of prompt $D^0 \to h^+h^{'-}$ decays is very large, about 15×10^6 of $D^0 \to K^-\pi^+$ decays in a sample of integrated luminosity of $\int \mathcal{L}dt \simeq 1$ fb^{-1}. Handling such a large sample implies

[1] The current experimental sensitivity is $\mathcal{O}(10^{-2})$.

practical difficulties, however a sufficient satisfactory precision on the measured asymmetry can be obtained by processing only a limited amount of data. Therefore we processed only 15% of the available data, sampling uniformly the runs over the whole range to keep into account possible time dependent changes of the detector.

Quantity of the track	Units	Requirement
Axial Si hits	–	≥ 3
$90° - z$ Si hits	–	≥ 2
Axial COT SL (hits/SL)	–	≥ 2 (≥ 5)
Stereo COT SL (hits/SL)	–	≥ 2 (≥ 5)
Total COT hits	–	≥ 42
Reco. algorithm	–	OIZ
p_{T}	GeV/c	> 2.0
$\lvert\eta\rvert$	–	< 1.0
$\lvert d_0\rvert$	μm	[120, 1000]
Quantity of the candidate		
$q(1) \times q(2)$	e^2	-1
$d_0(1) \times d_0(2)$	$\mu\mathrm{m}^2$	< 0
L_{T}	μm	> 300
$\sum p_{\mathrm{T}}$	GeV/c	> 5.5
$\lvert d_0\rvert$	μm	< 80
I	–	> 0.5
χ^2_{3D}	–	< 7
$\lvert\eta\rvert$	–	< 1.0
$\Delta\varphi_0$	Degrees	[2°, 90°]
$m_{\pi\pi}$	GeV/c^2	[0.8, 2.2]

Table 11.1: Summary of the selection for $D^0 \to h^+h'^-$ decays.

To reconstruct the $D^0 \to h^+h'^-$ decays we applied the same prescription and we processed the data using the same executable used to reconstruct the $B^0_{(s)} \to h^+h'^-$ decays (see chap. 3). The requirements applied to select the $D^0 \to h^+h'^-$ decays are summarized in tab. 11.1. The selection is the same used for the measurement of the direct CP asymmetry in $B^0 \to K^+\pi^-$ mode (loose cuts, see tab. 3.3), except for the small differences between the `B_PIPI` and the `B_CHARM` trigger paths. The requirement on the minimum impact parameter for both tracks is $d_0 > 120$ μm instead of $d_0 > 100$ μm, the azimuthal opening angle $\Delta\varphi_0$ is within [2°, 90°] instead of [20°, 135°], and obviously the requirement on the invariant $\pi\pi$-mass $m_{\pi\pi}$ is within [0.8, 2.2] instead of [4.0, 7.0] GeV/c^2. Since we cannot distinguish pions from kaons event by event, we computed the invariant mass of each candidate with different mass assignments. Figure 11.1 reports the invariant $\pi\pi$-mass and KK-mass distribution of the candidates passing the selection cuts listed in tab. 11.1. Three signals are clearly visible: on the left (low masses) the $D^0 \to K^+K^-$ signal, at the center the $D^0 \to K^-\pi^+$ signal, on the right (high masses) the $D^0 \to \pi^+\pi^-$ signal. These are better resolved in mass than the $B^0_{(s)} \to h^+h'^-$ decays. In fact the D^0 meson has a smaller mass than neutral B mesons and is reconstructed with

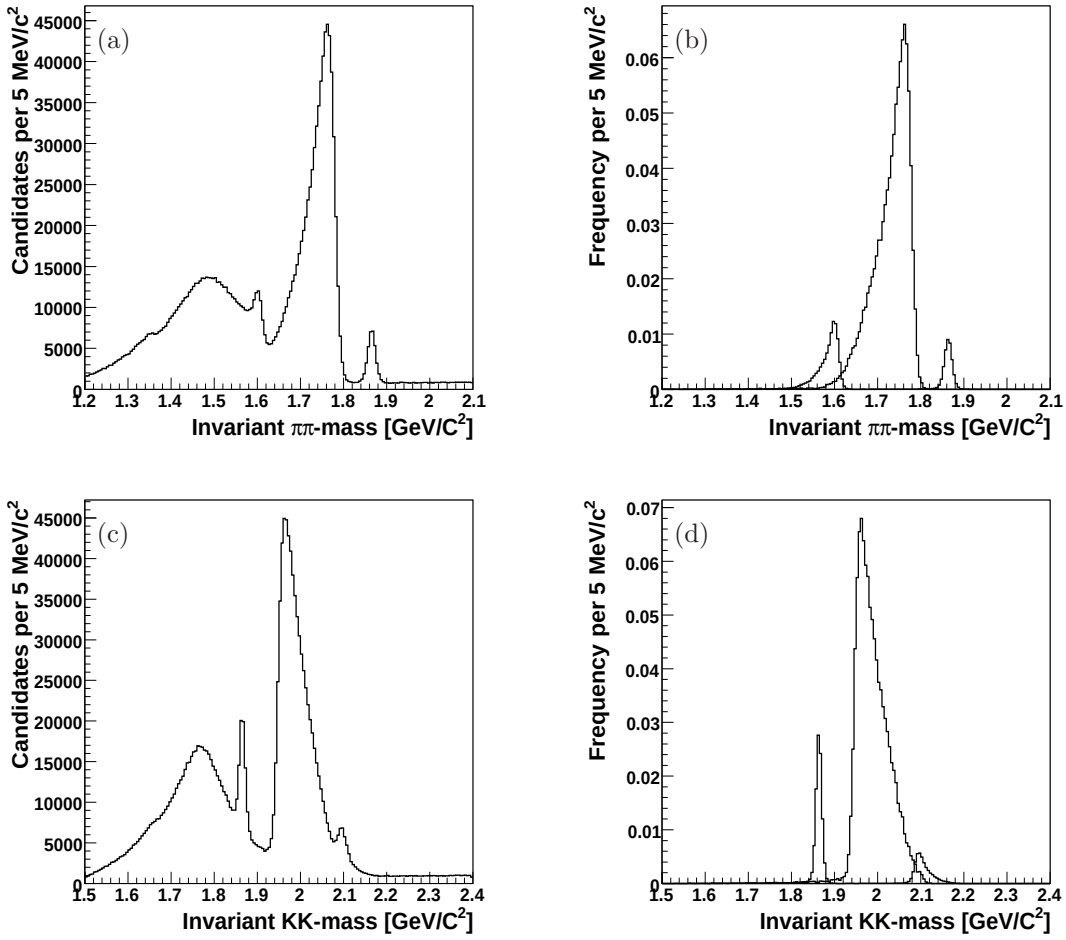


Figure 11.1: Invariant $\pi\pi$-mass and KK-mass distribution of prompt $D^0 \to h^+h^{'-}$ candidates. Data (a,c) and simulation (b,d).

a better mass resolution (about 8 MeV/c^2 rather than 22 MeV/c^2). In addition, the mass shift due to the erroneous mass assignment is larger than in the $B^0_{(s)} \to h^+h^{'-}$ case. As in the $B^0_{(s)} \to h^+h^{'-}$ case, two different background components are clearly visible. At higher masses ($m_{\pi\pi} > 1.9$ GeV/c^2 or $m_{KK} > 2.2$ GeV/c^2) one can see a combinatorial component, which contributes uniformly in all mass region, while at lower masses, in addition to the combinatorial component, a large bump due to partially-reconstructed multibody D^0 and/or D^+ decays is also visible .

We introduce two requirements to separate the $D^0 \to K^-\pi^+$ decays from other $D^0 \to \pi^+\pi^-$ and $D^0 \to K^+K^-$ decays and from the partially-reconstructed background. We apply the cut $m_{KK} > 1.93$ GeV/c^2, where m_{KK} is the invariant mass of the track pair computed by assigning the kaon mass to both tracks (see figs. 11.1(c) and (d)). This cut removes all the $D^0 \to K^+K^-$ decays, in addition to removing almost all background due to partially-reconstructed D^0 or D^+ multibody decays. To

remove the $D^0 \to \pi^+\pi^-$ contribution, we require $m_{\pi\pi} < 1.82$ GeV/c^2. Figure 11.2 shows the invariant $\pi\pi$-mass distribution obtained after applying the selection listed in tab. 11.1 plus the two additional mass requirements.

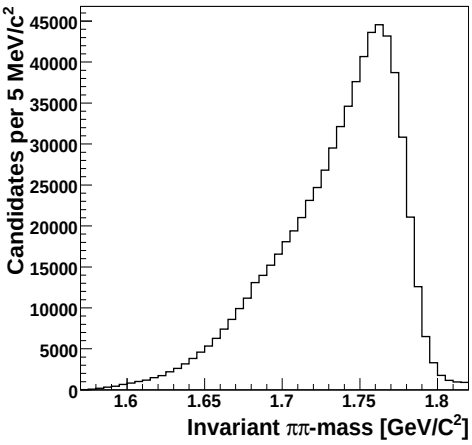


Figure 11.2: Invariant $\pi\pi$-mass distribution of prompt $D^0 \to h^+h'^-$ candidates with the additional requirement $m_{KK} > 1.93$ GeV/c^2 and $m_{\pi\pi} < 1.82$ GeV/c^2.

11.2.1 Checking the content of non-prompt D^0

A significant fraction of D^0 in our sample may come from the decay of B mesons. The CP asymmetry in the $D^0 \to K^-\pi^+$ decays could thus be biased by a possible CP asymmetry of B meson decays from which the D^0 originated [140, 141]. To evaluate the contamination of non-prompt $D^0 \to K^-\pi^+$ decays, we studied the distribution of the impact parameter d_0 of the D^0 candidates. Figure 11.3(b) reports the simulated (we used the FMC described in sec. 5.3) distribution of the prompt $D^0 \to K^-\pi^+$ decays, fitted with a Gaussian function. The fit determined $\mu = 0.14 \pm 0.11$ μm and $\sigma = 24.5 \pm 0.1$ μm. A deviation from a Gaussian distribution on real data implies that our sample contains a component of non-prompt D^0 decays. We fitted the background-subtracted $d_0(D^0)$ distribution of the data with a sum of two Gaussian distributions, as shown fig. 11.3(a). The fit returns a contamination of non-prompt decays $f_2 = 0.17 \pm 0.01$, a mean $\mu_1 = \mu_2 = 0.87 \pm 0.05$ μm, and standard deviations $\sigma_1 = 30.2 \pm 0.1$ μm and $\sigma_2 = 54.3 \pm 0.7$ μm. The resolution of the dominant Gaussian resulting from the fit performed on data is larger than the value returned from the simulation by $\approx 23\%$: 30.2 μm with respect to 24.5 μm from simulation. For the purpose to estimate the contribution of the non-prompt D^0 this discrepancy is not relevant, the only relevant thing is that the distribution of the simulated prompt $D^0 \to K^-\pi^+$ decays is a Gaussian with good approximation.

The Standard Model prediction of CP asymmetry in the B-meson system is much smaller than 0.5%, and this is confirmed by the current experimental measurements [138, 139]. The DØ Collabo-

ration measured a dimuon asymmetry [140]:

$$\frac{\mathcal{N}(b\bar{b} \to \mu^+\mu^+X) - \mathcal{N}(b\bar{b} \to \mu^-\mu^-X)}{\mathcal{N}(b\bar{b} \to \mu^+\mu^+X) + \mathcal{N}(b\bar{b} \to \mu^+\mu^+X)} = -0.0028 \pm 0.0013\ (stat.) \pm 0.0009\ (syst.)$$

and the direct CP asymmetry [141]

$$\frac{\mathcal{B}(B^- \to J/\psi K^-) - \mathcal{B}(B^+ \to J/\psi K^+)}{\mathcal{B}(B^- \to J/\psi K^-) + \mathcal{B}(B^+ \to J/\psi K^+)} = 0.0067 \pm 0.0074\ (stat.) \pm 0.0026\ (syst.).$$

If we assume a conservative value of CP asymmetry in the B-mesons of 0.5%, the expected effect on the $D^0 \to K^-\pi^+$ direct CP asymmetry is the product $17\% \times 0.5\%$ which is less than 0.1%. Since we expect an uncorrected CP asymmetry of the prompt $D^0 \to K^-\pi^+$ decays $\mathcal{O}(1\%)$ we neglect the effect of a possible CP asymmetry in the B-mesons system of the non-prompt D^0 component.

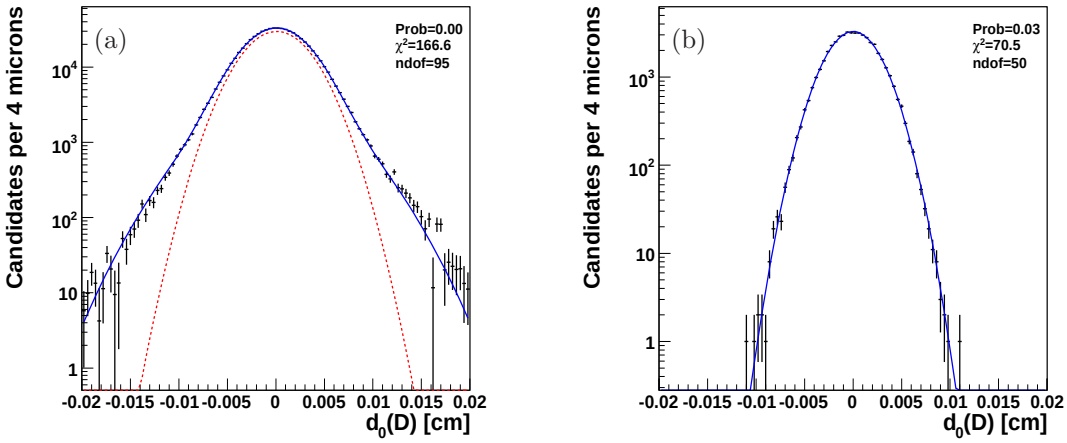


Figure 11.3: Impact parameter distribution of D^0 candidates. The background-subtracted distribution reconstructed from real data (a) was fitted with a sum of two Gaussian distributions (blue continuous line). Red dotted line is the non-prompt component returned from the fit. The distribution obtained from the simulated sample (b) was fitted with a single Gaussian distribution.

11.3 Measurement of the charge asymmetry

We performed an unbinned, maximum Likelihood fit, to statistically determine the relative fractions of $D^0 \to K^-\pi^+$ and $\overline{D}^0 \to K^+\pi^-$ decays. The fitting technique has been described in detail in chap. 6, in this section we will just outline some minor changes needed to adapt the fit to the $D^0 \to h^+h^{'-}$ case. One important difference between the $D^0 \to h^+h^{'-}$ and the $B^0_{(s)} \to h^+h^{'-}$ case is the relative rôle of PID and kinematics. While in the $B^0_{(s)} \to h^+h^{'-}$ case the two contribute almost equally, for the $D^0 \to h^+h^{'-}$ the kinematics is dominant. In order to perform a thorough check of our $B^0_{(s)} \to h^+h^{'-}$ analysis, we decided to perform on the $D^0 \to K^-\pi^+$ two separate fits, a kinematic-only fit and a

PID-only fit. The kinematic fit is taken as our measurement of the efficiency correction, due to its lack of sensitivity to systematic uncertainties in the PID parameterization, while the PID-only fit is used for comparison, to check that there are no significant asymmetries in the PID parameterization that might affect the $B^0_{(s)} \to h^+h^{'-}$ fit.

We use the same kinematic observables of the $B^0_{(s)} \to h^+h^{'-}$ fit (see sec. 6.1): $m_{\pi\pi}$, α and $p_{\rm tot}$. The kinematic-only fit disentangles very well the $D^0 \to K^-\pi^+$ and $\overline{D}^0 \to K^+\pi^-$ signals, as can be easily seen from fig. 11.5 where the two-dimensional plot of $m_{\pi\pi}$ vs α is shown. The PID fit id described separately in sec. 11.5.

The Likelihood function $\mathscr{L}$ is expressed as the product of the Likelihood of each event $\mathscr{L}_i$:

$$\mathscr{L}(\vec{\theta}) = \prod_{i=1}^{N} \mathscr{L}_i(\vec{\theta}|\vec{x}_i), \tag{11.4}$$

where the index i runs over the events, N is the total number of events passing the final selection, $\vec{\theta}$ is the vector of parameters to be determined, $\vec{x}$ is the vector of the discriminating observables $\vec{x}_i = \{m_{\pi\pi}, \alpha, p_{\rm tot}\}_i$. The Likelihood of each event is written as the sum of a signal term and a background term:

$$\mathscr{L}_i = b \cdot \mathscr{L}_i^{\rm bck} + (1-b) \cdot \mathscr{L}_i^{\rm sig}. \tag{11.5}$$

The index sig (bck) labels the part of the function that describes the signal (background) term; b is the fraction of background events and $1-b$ is the fraction of the $D^0 \to K^-\pi^+$ plus $\overline{D}^0 \to K^+\pi^-$ events ($(b \in \vec{\theta})$). In terms of p.d.f. the Likelihood of the signal events is factorized as:

$$\begin{aligned} \mathscr{L}^{\rm sig} = \quad & f_{D^0\to K^-\pi^+} \cdot \wp^m_{D^0\to K^-\pi^+}(m_{\pi\pi}|\alpha, p_{tot}) \cdot \wp^p_{D^0\to K^-\pi^+}(\alpha, p_{\rm tot}) \\ + \quad & f_{\overline{D}^0\to K^+\pi^-} \cdot \wp^m_{\overline{D}^0\to K^+\pi^-}(m_{\pi\pi}|\alpha, p_{tot}) \cdot \wp^p_{\overline{D}^0\to K^+\pi^-}(\alpha, p_{\rm tot}). \end{aligned} \tag{11.6}$$

where the parameter $f_{D^0\to K^-\pi^+}$ is the fraction with respect to the total signal of $D^0 \to K^-\pi^+$ mode determined by the fit, while $f_{\overline{D}^0\to K^+\pi^-} = 1 - f_{D^0\to K^-\pi^+}$. The Likelihood of the background has a similar factorization of the signal term, in this case there is only the contribution of the combinatorial background:

$$\mathscr{L}^{\rm bck} = \wp^m_{\rm bck}(m_{\pi\pi}|\alpha, p_{\rm tot}) \cdot \wp^p_{\rm bck}(\alpha, p_{\rm tot}). \tag{11.7}$$

11.3.1 Probability density function of the signal mass term

When charged pion mass is assigned to both tracks the resulting invariant mass for the $D^0 \to K^-\pi^+$ and $\overline{D}^0 \to K^+\pi^-$ decay modes is shifted to lower values than the true D^0 mass. If the momenta of both tracks are known, it is possible to calculate analytically this shift on a event-by-event basis. The situation is identical to the $B^0_{(s)} \to h^+h^{'-}$ case, therefore we wrote the probability density function for the mass term following the steps described in sec. 6.3. We parameterized the invariant mass distribution $m_{K^-\pi^+}$ and $m_{K^+\pi^-}$, computed with the correct mass assignment (i. e., $m_{K^-\pi^+}$ for the $D^0 \to K^-\pi^+$ mode), using the p.d.f. of eq. (6.7) by substituting m_{H^0} with m_{D^0} (see also eq. (5.21) in chap. 5). Figure 11.4 shows the invariant mass kinematic templates for $D^0 \to K^-\pi^+$ decay mode, valid also for $\overline{D}^0 \to K^+\pi^-$. To move from $\wp^m_{D^0\to K^-\pi^+}(m_{K^-\pi^+})$ and $\wp^m_{\overline{D}^0\to K^+\pi^-}(m_{K^+\pi^-})$ computed

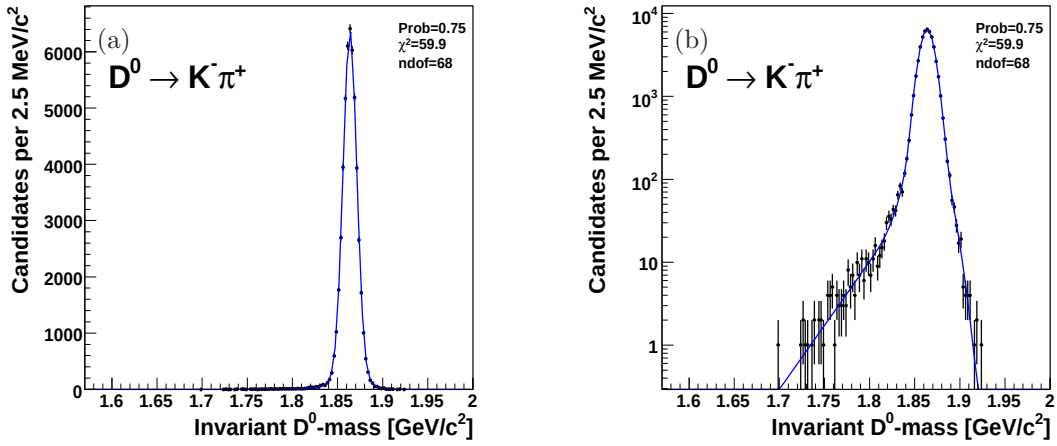


Figure 11.4: Invariant D^0-mass distribution of simulated $D^0 \to K^-\pi^+$ decays with the additional requirement $m_{KK} > 1.93$ GeV/c^2. Linear scale (a), logarithmic scale (b).

with the correct mass assignment to the probability density functions of the invariant $\pi\pi$-mass, we perform the substitution described in eq. (6.12):

$$\begin{aligned} m_{K^-\pi^+} - M_{D^0} &= m_{\pi\pi} - \mathcal{M}_{D^0\to K^-\pi^+}(\alpha, p_{\rm tot}) \\ m_{K^+\pi^-} - M_{D^0} &= m_{\pi\pi} - \mathcal{M}_{\overline{D}^0\to K^+\pi^-}(\alpha, p_{\rm tot}), \end{aligned} \tag{11.8}$$

where $\mathcal{M}_{D^0\to K^-\pi^+}(\alpha, p_{\rm tot})$ and $\mathcal{M}_{\overline{D}^0\to K^+\pi^-}(\alpha, p_{\rm tot})$ are the expected average-value of the invariant mass computed with the pion hypothesis for both particles at given momentum imbalance α and scalar sum of momenta $p_{\rm tot}$, see tab. 11.2 (see also tab. 4.1 of sec. 4.3). Using this substitution we can write the probability density for the signal mass term $\wp^m_{D^0\to K^-\pi^+}(m_{\pi\pi}|\alpha, p_{tot})$ and $\wp^m_{\overline{D}^0\to K^+\pi^-}(m_{\pi\pi}|\alpha, p_{tot})$.

The distributions of invariant $\pi\pi$-mass as a function of the signed momentum-imbalance for simulated $D^0 \to h^+h'^-$ decays are shown in fig. 11.5. As in the $B^0_{(s)} \to h^+h'^-$ case, different trends for the different decay modes are visible, but the differences, in this case, are larger and allow to better disentangle the different contributions. The opposite slope between $D^0 \to K^-\pi^+$ and $\overline{D}^0 \to K^+\pi^-$ decays is evident. This is used to measure the CP-violating decay-rate asymmetry in these modes. This large separation power provided by the kinematic information makes the use of PID information unnecessary in this measurement.

11.3.2 Probability density function of the background mass term

We found that the empirical functional form that describes the invariant $\pi\pi$-mass distribution of the background candidates in the mass window centered on the signal region is an error function multiplied by an exponential function. The exponential function parameterizes the shape of the combinatorial background coming from pairs of random tracks accidentally satisfying the selection requirements,

mode	$\mathcal{M}^2[p_1(\alpha, p_{\rm tot}), p_2(\alpha, p_{\rm tot})] \quad \alpha < 0$
$\overline{D}^0 \to \pi^- K^+$	$m^2_{D^0} + (m^2_\pi - m^2_K) + 2 \cdot \sqrt{p_1^2 + m^2_\pi} \cdot \left(\sqrt{p_2^2 + m^2_\pi} - \sqrt{p_2^2 + m^2_K} \right)$
$D^0 \to K^- \pi^+$	$m^2_{D^0} + (m^2_\pi - m^2_K) + 2 \cdot \sqrt{p_2^2 + m^2_\pi} \cdot \left(\sqrt{p_1^2 + m^2_\pi} - \sqrt{p_1^2 + m^2_K} \right)$
$D^0/\overline{D}^0 \to K^- K^+$	$m^2_{D^0} + 2 \cdot (m^2_\pi - m^2_K) + 2 \cdot \left(\sqrt{p_1^2 + m^2_\pi} \cdot \sqrt{p_2^2 + m^2_\pi} - \sqrt{p_1^2 + m^2_K} \cdot \sqrt{p_2^2 + m^2_K} \right)$
$D^0/\overline{D}^0 \to \pi^- \pi^+$	$m^2_{D^0}$
mode	$\mathcal{M}^2[p_1(\alpha, p_{\rm tot}), p_2(\alpha, p_{\rm tot})] \quad \alpha > 0$
$D^0 \to \pi^+ K^-$	$m^2_{D^0} + (m^2_\pi - m^2_K) + 2 \cdot \sqrt{p_1^2 + m^2_\pi} \cdot \left(\sqrt{p_2^2 + m^2_\pi} - \sqrt{p_2^2 + m^2_K} \right)$
$\overline{D}^0 \to K^+ \pi^-$	$m^2_{D^0} + (m^2_\pi - m^2_K) + 2 \cdot \sqrt{p_2^2 + m^2_\pi} \cdot \left(\sqrt{p_1^2 + m^2_\pi} - \sqrt{p_1^2 + m^2_K} \right)$
$D^0/\overline{D}^0 \to K^+ K^-$	$m^2_{D^0} + 2 \cdot (m^2_\pi - m^2_K) + 2 \cdot \left(\sqrt{p_1^2 + m^2_\pi} \cdot \sqrt{p_2^2 + m^2_\pi} - \sqrt{p_1^2 + m^2_K} \cdot \sqrt{p_2^2 + m^2_K} \right)$
$D^0/\overline{D}^0 \to \pi^+ \pi^-$	$m^2_{D^0}$

Table 11.2: Mass expressions for $D^0 \to h^+ h^{'-}$ decays. Upper table: $\mathcal{M}^2(\alpha, p_{\rm tot})$ for $\alpha < 0$ (i.e. the negative particle carries smaller momentum). Lower table: $\alpha > 0$ (i.e. the positive particle carries smaller momentum). For simplicity, the formulas in the tables are written as functions of p_1 and p_2, instead of α and $p_{\rm tot}$.

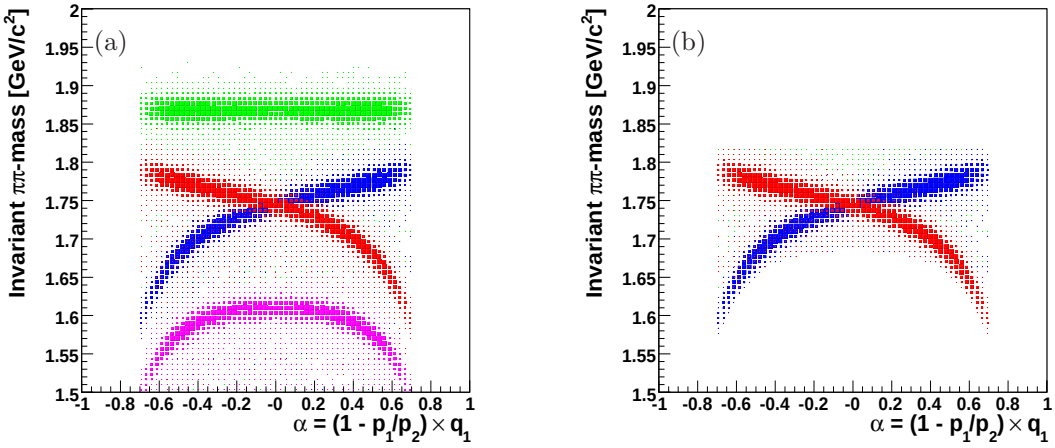


Figure 11.5: Invariant $\pi\pi$-mass distribution for a sample of simulated prompt $D^0 \to h^+ h^{'-}$ as a function of momentum imbalance α (a). Additional requirements $m_{KK} > 1.93$ GeV/c^2 and $m_{\pi\pi} < 1.82$ GeV/c^2 (b). $D^0 \to \pi^+\pi^-$ green, $D^0 \to K^-\pi^+$ blue, $\overline{D}^0 \to K^+\pi^-$ red, $D^0 \to K^+K^-$ pink.

while the error function accounts for the effect of the requirement $m_{KK} > 1.93$ GeV/c^2 in invariant $\pi\pi$-mass:

$$\wp^m_{\rm back}(m_{\pi\pi}|\alpha, p_{\rm tot}; c_1, c_2, m_0) = \frac{1}{K} \cdot e^{-c_1(m_{\pi\pi} - m_0)} \cdot {\rm Erf}(c_2(m_{\pi\pi} - m_0) + 1) \quad (11.9)$$

$${\rm Erf}(x) = \frac{2}{\sqrt{\pi}} \int_0^x e^{-t^2} dt \quad (11.10)$$

$$K = \int_{m_1}^{m_2} e^{-c_1(m_{\pi\pi} - m_0)} \cdot {\rm Erf}(c_2(m_{\pi\pi} - m_0) + 1) dm_{\pi\pi}. \quad (11.11)$$

The parameters c_1, c_2 and m_0 are free to vary in the fit.

11.3.3 Probability density function of the momentum term

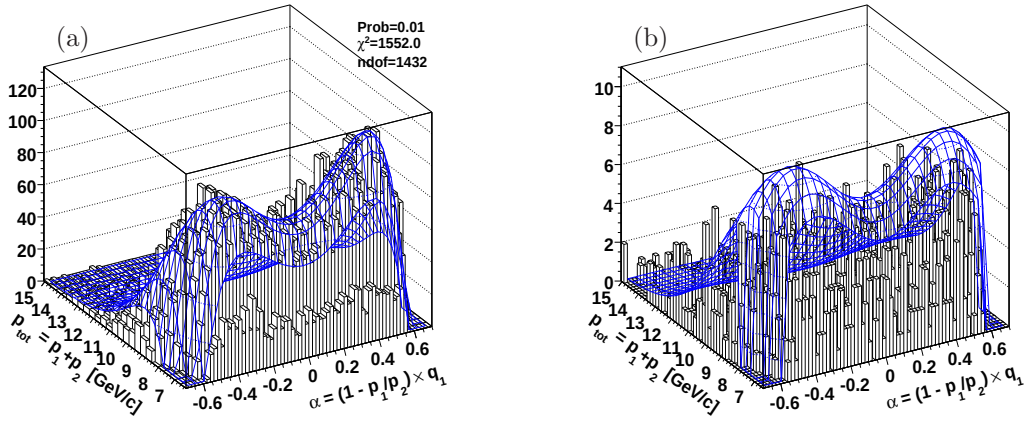


Figure 11.6: Distribution of the scalar sum of momenta as a function of the signed momentum imbalance in the simulated $D^0 \to K^-\pi^+$ decays (a) and background (b). Joint $(\alpha, p_{\rm tot})$ template is overlaid (b).

The momentum p.d.f.s relative to $D^0 \to K^-\pi^+$ and $\overline{D}^0 \to K^+\pi^-$ signals are extracted from the simulated samples while the momentum p.d.f. for background is extracted from real data, using the high-mass sideband ($m_{\pi\pi} > 1.9$ GeV/c^2 in fig. 11.1(a)). To extract the templates we used the same functional forms described in sec. 6.5.2. Figure 11.6 shows the distribution of the scalar sum of momenta as a function of the momentum imbalance for signal events (a) and for background events (b). The fit functions of eqs. (6.20) and (6.21), respectively for signal and background are overlaid.

11.4 Fit results

The fit was applied to $D^0 \to K^-\pi^+$ sample passing the selection summarized in tab. 11.1 plus the mass requirements $m_{KK} > 1.93$ GeV/c^2 and $m_{\pi\pi} < 1.82$ GeV/c^2. In addition, we imposed the following conditions:

- $1.57 < m_{\pi\pi} < 1.82$ GeV/c^2: this mass range contains the whole $D^0 \to K^-\pi^+$ and $\overline{D}^0 \to K^+\pi^-$ signals, and it allows a proper extrapolation of the background shape below the signal;
- $-0.7 < \alpha < 0.7$: this range excludes boundary regions where the model of the corresponding p.d.f. becomes inaccurate and may lead to undesired biases. This requirement removed just a few events;

- $p_{\rm tot} > 6.5$ GeV/c: we excluded a few candidates with lower $p_{\rm tot}$ values because of the difficulty of describing accurately the steep turn-on of the $p_{\rm tot}$ p.d.f..

Since the total number of events used in this fit is large, $N = 730575$, we divided the sample in three subsamples with approximately the same size and we performed three separate fits. To divide the sample we used the natural division given by the off-line production which processed the data in three different datasets corresponding respectively to $N_{0d} = 191060$, $N_{0h} = 313973$ and $N_{0i} = 225542$ events. The final results are the average on the individual fit results. Table 11.3 reports the results returned of the fits performed on the three subsamples.

parameter	0d	0h	0i
$\mathcal{N}(D^0 \to K^-\pi^+) + \mathcal{N}(\overline{D}^0 \to K^+\pi^-)$	176887 ± 192	292915 ± 236	210699 ± 199
$\hat{f}_{D^0\to K^-\pi^+}$	0.4957 ± 0.0013	0.4957 ± 0.0010	0.4963 ± 0.0012
$\hat{f}_{\overline{D}^0\to K^+\pi^-}$	0.5043 ± 0.0013	0.5043 ± 0.0010	0.5036 ± 0.0012
$\frac{\hat{f}_{\overline{D}^0\to K^+\pi^-} - \hat{f}_{D^0\to K^-\pi^+}}{\hat{f}_{\overline{D}^0\to K^+\pi^-} + \hat{f}_{D^0\to K^-\pi^+}}$	0.00862 ±0.00268	0.00865 ± 0.00208	0.00730 ± 0.00245

Table 11.3: Results of kinematic-pnly fits on prompt $D^0 \to K^-\pi^+$.

For each subsample the uncorrected direct CP asymmetries, reported in the last line of tab. 11.3, are compatible with an effect $\approx 0.8\%$, as expected. The statistical uncertainty for each subsample is $\approx 0.25\%$. Averaging over the subsamples we obtain: is:

$$\frac{\hat{f}_{\overline{D}^0\to K^+\pi^-} - \hat{f}_{D^0\to K^-\pi^+}}{\hat{f}_{\overline{D}^0\to K^+\pi^-} + \hat{f}_{D^0\to K^-\pi^+}} = 0.00823 \pm 0.00136\ (stat.). \tag{11.12}$$

As we will see in sec. 11.6 this resolution allows to measure this charge asymmetry with a better precision than the previous CDF estimate performed using large samples of simulated events.

11.4.1 Fit projections

The distributions of the discriminating observables with the fit projections overlaid are shown in fig. 11.7. The projections on the invariant $\pi\pi$-mass distribution are satisfactory, while the projections on the momenta discriminating observables α and $p_{\rm tot}$ do not reproduce accurately the observed distributions. The model used to parameterize the joint probability $\wp^p(\alpha, p_{\rm tot})$ for signal and background is simply not adequate for an high-statistics fit like this. The data sample fitted is much larger than Monte Carlo sample used to parameterize the templates and, also, the functional forms used do not describe well the shapes observed on data. The data distribution of α shows a cusp for $\alpha \to 0$, while the function used to parameterize the α shape has a continuous first derivative in $\alpha = 0$. However, for the measurement of charge asymmetry the approximate model of the joint probability of momentum

variables is a negligible problem, since all Likelihood momentum terms under charge conjugation (particle $\leftrightarrow$ anti-particle) are invariant except for a change variable $\alpha \leftrightarrow -\alpha$. This can be translated as $\wp^p_{D^0\to K^-\pi^+}(\alpha, p_{\rm tot}) = \wp^p_{\overline{D}^0\to K^+\pi^-}(-\alpha, p_{\rm tot})$. Therefore, the imperfections in the kinematic templates do not affect the asymmetry returned by the fit.

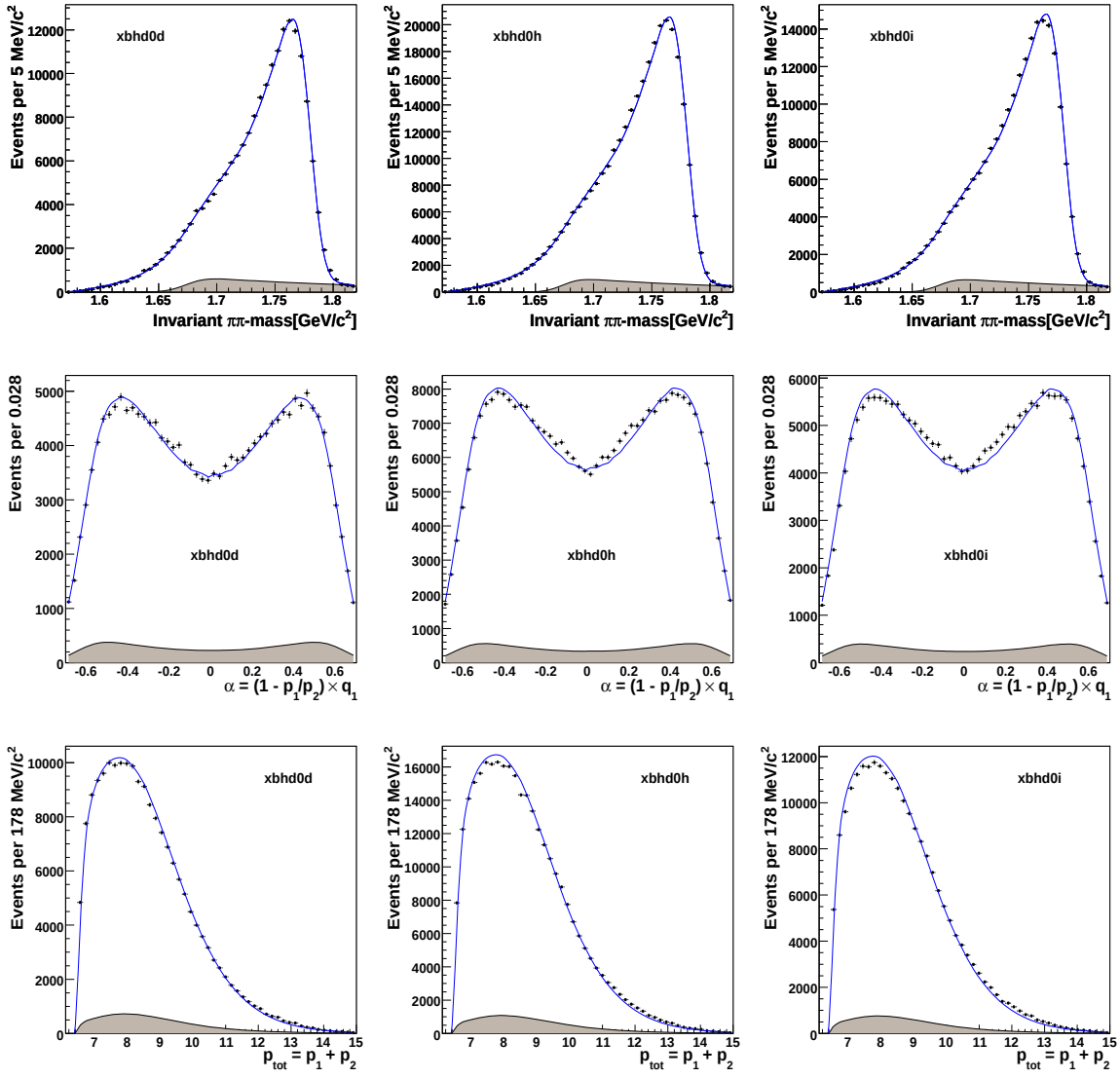


Figure 11.7: Fit projection onto $m_{\pi\pi}$, α and $p_{\rm tot}$ variables for different subsamples. Grey region is the background contribution.

11.5 Cross-check: PID-only fit

As a cross check of the result obtained in the previous section, we performed an alternative fit of the same quantity on the same data sample of prompt $D^0 \to K^-\pi^+$ decays, using only the PID information. The dE/dx templates were individually parameterized for positively and negatively charged kaons and pions (sec. 4.4) and this might introduce a bias in the measurement of the charge asymmetry. In the fit of composition of $B^0_{(s)} \to h^+h^{'-}$ we used both kinematic and dE/dx information, and it is therefore desirable to check that the possible charge asymmetry due to the dE/dx templates is contained within the associated systematic uncertainty (sec. 12.7).

We used the same PID observables used in the $B^0_{(s)} \to h^+h^{'-}$ fit (see sec. 6.1): κ_1, κ_2, α and $p_{\rm tot}$. The dE/dx-only fit needs also the information of the momentum of both particles. As in the previous fit the Likelihood function $\mathscr{L}$ is expressed as the product of the Likelihood of each event $\mathscr{L}_i$:

$$\mathscr{L}(\vec{\theta}) = \prod_{i=1}^{N} \mathscr{L}_i(\vec{\theta}|\vec{x}_i), \tag{11.13}$$

where the index i runs over the events, N is the total number of events passing the final selection, $\vec{\theta}$ is the vector of parameters to be determined, $\vec{x}$ is the vector of the discriminating observables $\vec{x}_i = \{\kappa_1, \kappa_2, \alpha, p_{\rm tot}\}_i$. The Likelihood of each event is written as the sum of a signal term and a background term:

$$\mathscr{L}_i = b \cdot \mathscr{L}_i^{\rm bck} + (1-b) \cdot \mathscr{L}_i^{\rm sig}. \tag{11.14}$$

The index sig (bck) labels the part of the function that describes the signal (background) term; b is the fraction of background events and $1-b$ is the fraction of the $D^0 \to K^-\pi^+$ plus $\overline{D}^0 \to K^+\pi^-$ events ($(b \in \vec{\theta})$). In terms of p.d.f. the Likelihood of the signal events is factorized as:

$$\begin{aligned} \mathscr{L}^{\rm sig} = \quad & f_{D^0\to K^-\pi^+} \cdot \wp^p_{D^0\to K^-\pi^+}(\alpha, p_{\rm tot}) \cdot \wp^{\rm PID}_{D^0\to K^-\pi^+}(\kappa_1, \kappa_2|\alpha, p_{tot}) \\ + \quad & f_{\overline{D}^0\to K^+\pi^-} \cdot \wp^p_{\overline{D}^0\to K^+\pi^-}(\alpha, p_{\rm tot}) \cdot \wp^{\rm PID}_{\overline{D}^0\to K^+\pi^-}(\kappa_1, id_2|\alpha, p_{tot}). \end{aligned} \tag{11.15}$$

where the parameter $f_{D^0\to K^-\pi^+}$ is the fraction with respect to the total signal of $D^0 \to K^-\pi^+$ mode determined by the fit, while $f_{\overline{D}^0\to K^+\pi^-} = 1 - f_{D^0\to K^-\pi^+}$. The Likelihood of the background has a similar factorization of the signal term, in this case there is only the contribution of the combinatorial background:

$$\mathscr{L}^{\rm bck} = \wp^p_{\rm bck}(\alpha, p_{\rm tot}) \cdot \wp^{\rm PID}_{\rm bck}(\kappa_1, \kappa_2|\alpha, p_{\rm tot}). \tag{11.16}$$

The PID p.d.f.s are exactly the same of those used for the $B^0_{(s)} \to h^+h^{'-}$ fit, and from this point of view the $D^0 \to K^-\pi^+$ decay mode is strictly similar to the $B^0_s \to K^-\pi^+$ decay mode. They are extensively explained in sec. 6.6.1 and 6.6.2.

11.5.1 Fit results for the dE/dx-only fit

We repeated the same procedure described in sec. 11.4 using the Likelihood described above. We fitted the three subsamples, and in each fit we fixed the background fraction b to the value found in the kinematic-only fit, because the separation power signal-background is mainly based on kinematics. We fitted the relative fractions of $D^0 \to K^-\pi^+$ and $\overline{D}^0 \to K^+\pi^-$ decay modes and the particle

parameter	0d	0h	0i
$\frac{\hat{f}_{\overline{D}^0\to K^+\pi^-} - \hat{f}_{D^0\to K^-\pi^+}}{\hat{f}_{\overline{D}^0\to K^+\pi^-} + \hat{f}_{D^0\to K^-\pi^+}}$	0.0018 ± 0.0031	0.0034 ± 0.0024	0.0009 ± 0.0028

Table 11.4: Results of PID-only fits on prompt $D^0 \to K^-\pi^+$.

composition of the background. The results are shown in tab. 11.4. The three results are in agreement, and the average uncorrected value of the direct CP asymmetry is:

$$\left.\frac{\hat{f}_{\overline{D}^0\to K^+\pi^-} - \hat{f}_{D^0\to K^-\pi^+}}{\hat{f}_{\overline{D}^0\to K^+\pi^-} + \hat{f}_{D^0\to K^-\pi^+}}\right|_{dE/dx} = 0.00207 \pm 0.00157\ (stat.). \tag{11.17}$$

This alternative measurement of the uncorrected direct CP asymmetry must be compared with the result extracted using only the kinematic information (eq. (11.12)). The difference between the central values of the two fits is equal to 0.006 ± 0.002 (about 3σ) assuming independent errors. However, the systematic uncertainty associated to the statistical uncertainty of the dE/dx templates parameterization is dominant over this statistical uncertainty. We can see from tab. 12.1 that the effect of dE/dx systematics on the measurement of $\mathcal{A}_{\rm CP}(B^0 \to K^+\pi^-)$ is equal to 0.0064. This value is already larger than the difference between the kinematic- and PID-only fits presented in this section. This is a powerful cross check of the entire procedure used to parameterize the dE/dx templates. Since this fit is completely unconstrained by the kinematics, it will be even more sensitive than the $B^0_{(s)} \to h^+h^{'-}$ fit to the dE/dx systematics. The study described in this chapter shows the possibility to control possible dE/dx bias with a great accuracy and therefore to produce even more accurate $\mathcal{A}_{\rm CP}$ measurements with larger samples in the future.

11.6 Charge asymmetry

In order to convert the asymmetry results determined by the fit into a measurement of CP asymmetry, we need to apply a correction for the different relative efficiency between the $D^0 \to K^-\pi^+$ and $\overline{D}^0 \to K^+\pi^-$decay modes:

$$\frac{\mathcal{B}(\overline{D}^0 \to K^+\pi^-) - \mathcal{B}(D^0 \to K^-\pi^+)}{\mathcal{B}(\overline{D}^0 \to K^+\pi^-) + \mathcal{B}(D^0 \to K^-\pi^+)} = \frac{\hat{f}_{\overline{D}^0\to K^+\pi^-} \cdot \frac{\varepsilon(D^0\to K^-\pi^+)}{\varepsilon(\overline{D}^0\to K^+\pi^-)} - \hat{f}_{D^0\to K^-\pi^+}}{\hat{f}_{\overline{D}^0\to K^+\pi^-} \cdot \frac{\varepsilon(D^0\to K^-\pi^+)}{\varepsilon(\overline{D}^0\to K^+\pi^-)} + \hat{f}_{D^0\to K^-\pi^+}}. \tag{11.18}$$

The only detector effect that can influence the asymmetry result is the different interaction probability of the particle pairs $K^+\pi^-$ and $K^-\pi^+$ with the detector material. This is mainly due to the larger hadronic cross section of the K^- with respect to the K^+.

If we assume the Standard Model expectation $\mathcal{O}(10^{-6})$ [142] for the direct CP asymmetry in $D^0 \to K^-\pi^+$ decays, we can write:

$$\frac{\hat{f}_{\overline{D}^0\to K^+\pi^-} \cdot \frac{\varepsilon(D^0\to K^-\pi^+)}{\varepsilon(\overline{D}^0\to K^+\pi^-)} - \hat{f}_{D^0\to K^-\pi^+}}{\hat{f}_{\overline{D}^0\to K^+\pi^-} \cdot \frac{\varepsilon(D^0\to K^-\pi^+)}{\varepsilon(\overline{D}^0\to K^+\pi^-)} + \hat{f}_{D^0\to K^-\pi^+}} \ll 10^{-3}. \tag{11.19}$$

From this relation we can extract the value of efficiency ratio $\frac{\varepsilon(D^0\to K^-\pi^+)}{\varepsilon(\overline{D}^0\to K^+\pi^-)}$ directly from real data without any Monte Carlo input using the fraction $\hat{f}$ measured in the fit. The resulting value, averaged over the subsamples `0d`, `0h` and `0i`, is:

$$\frac{\varepsilon(D^0 \to K^-\pi^+)}{\varepsilon(\overline{D}^0 \to K^+\pi^-)} = 0.9837 \pm 0.0027 \tag{11.20}$$

$$\frac{\varepsilon(\overline{D}^0 \to K^+\pi^-)}{\varepsilon(D^0 \to K^-\pi^+)} = 1.0166 \pm 0.0028. \tag{11.21}$$

We quote only the statistical uncertainty returned from the fit, because all systematic uncertainties due to the fit parameterization are expected to be much smaller than the statistical uncertainty. They cancel out in the ratio between relative fractions. We neglect also the systematic uncertainty coming from the Standard Model assumption $A_{\mathsf{CP}}(D^0 \to K^-\pi^+) = \mathcal{O}(10^{-6})$, since our statistical uncertainty is $\mathcal{O}(10^{-3})$.

It is interesting to note that this value is in perfect agreement with a previous evaluation of the same effect entirely based on Monte Carlo [122, 136]:

$$\left.\frac{\varepsilon(D^0 \to K^-\pi^+)}{\varepsilon(\overline{D}^0 \to K^+\pi^-)}\right|_{\mathrm{MC}} = 0.9825 \pm\ 0.0014\ (stat.) \pm\ 0.0045(syst.). \tag{11.22}$$

The statistical uncertainty of Monte Carlo based estimate is due to limited statistics of simulated sample, while the systematic uncertainty is related to the capability of GEANT [103] in reproducing the the detector-induced charge asymmetry. Using only a small subsample of prompt $D^0 \to K^-\pi^+$ decays we measured the efficiency ratio $\frac{\varepsilon(D^0\to K^-\pi^+)}{\varepsilon(\overline{D}^0\to K^+\pi^-)}$ with more precision than the Monte Carlo based estimate obtaining an excellent agreement.

11.6.1 Momentum correction

To keep into account the different momentum distribution of the D^0 and $B^0_{(s)}$ decays we reweighted the joint distribution of $(\alpha, p_{\rm tot})$ using the $B^0_{(s)} \to h^+h^{'-}$ Monte Carlo. We first evaluated the efficiency ratio $\frac{\varepsilon(B^0_s \to K^-\pi^+)}{\varepsilon(\overline{B}^0_s \to K^+\pi^-)}$ without any reweighting, and second reweighting the $(\alpha, p_{\rm tot})$ distribution of $B^0_s \to K^-\pi^+$ to that of $D^0 \to K^-\pi^+$. The ratio of these two quantities is applied as a multiplicative correction to the values of eq. (11.20) and eq. (11.21), to account for the different D^0 and $B^0_{(s)}$ meson momentum spectrum. The small difference in the momentum $(\alpha,p_{\rm tot})$ distribution between $B^0 \to K^+\pi^-$ and $B^0_s \to K^-\pi^+$ has a negligible effect. Thus we obtain the final acceptance corrections:

$$\frac{\varepsilon(\overline{B}^0 \to K^-\pi^+)}{\varepsilon(B^0 \to K^+\pi^-)} = \frac{\varepsilon(B^0_s \to K^-\pi^+)}{\varepsilon(\overline{B}^0_s \to K^+\pi^-)} = 0.9871 \pm 0.0027\ (stat.) \tag{11.23}$$

$$\frac{\varepsilon(B^0 \to K^+\pi^-)}{\varepsilon(\overline{B}^0 \to K^-\pi^+)} = \frac{\varepsilon(\overline{B}^0_s \to K^+\pi^-)}{\varepsilon(B^0_s \to K^-\pi^+)} = 1.0131 \pm 0.0028\ (stat.). \tag{11.24}$$

11.7 Results (involving charge asymmetry correction)

At this point we have all the corrections for those measurements involving the charge asymmetry correction. We can extract the corresponding CP asymmetry measurements . All the associated uncertainties account for the statistical fluctuations due to finite samples only.

11.7.1 Direct CP asymmetry in the $B^0 \to K^+\pi^-$ and $B^0_s \to K^-\pi^+$ decay

Following eqs. (11.23) and (11.24), we corrected the fit results for the charge-asymmetry factor, $\frac{\varepsilon(B^0 \to K^+\pi^-)}{\varepsilon(\overline{B}^0 \to K^-\pi^+)} = \frac{\varepsilon(\overline{B}^0_s \to K^+\pi^-)}{\varepsilon(B^0_s \to K^-\pi^+)} \simeq 1.0131$, to extract the direct CP asymmetries:

$$\mathcal{A}_{\rm CP}(B^0 \to K^+\pi^-) = \frac{\mathcal{B}(\overline{B}^0 \to K^-\pi^+) - \mathcal{B}(B^0 \to K^+\pi^-)}{\mathcal{B}(\overline{B}^0 \to K^-\pi^+) + \mathcal{B}(B^0 \to K^+\pi^-)} = -0.086 \pm 0.023\ (stat.) \tag{11.25}$$

$$\mathcal{A}_{\rm CP}(B^0_s \to K^-\pi^+) = \frac{\mathcal{B}(\overline{B}^0_s \to K^+\pi^-) - \mathcal{B}(B^0_s \to K^-\pi^+)}{\mathcal{B}(\overline{B}^0_s \to K^+\pi^-) + \mathcal{B}(B^0_s \to K^-\pi^+)} = 0.39 \pm 0.15\ (stat.). \tag{11.26}$$

11.7.2 Ratio $\frac{f_d}{f_s} \times \frac{\Gamma(\overline{B}^0 \to K^-\pi^+) - \Gamma(B^0 \to K^+\pi^-)}{\Gamma(\overline{B}^0_s \to K^+\pi^-) - \Gamma(B^0_s \to K^-\pi^+)}$

As mentioned in sec. 1.7.5 it is also important to quote the following quantity:

$$\frac{f_d}{f_s} \times \frac{\Gamma(\overline{B}^0 \to K^-\pi^+) - \Gamma(B^0 \to K^+\pi^-)}{\Gamma(\overline{B}^0_s \to K^+\pi^-) - \Gamma(B^0_s \to K^-\pi^+)} = \frac{\hat{f}_{\overline{B}^0 \to K^-\pi^+} \cdot \frac{\varepsilon(B^0 \to K^+\pi^-)}{\varepsilon(\overline{B}^0 \to K^-\pi^+)} - \hat{f}_{B^0 \to K^+\pi^-}}{\hat{f}_{\overline{B}^0_s \to K^+\pi^-} \cdot \frac{\varepsilon(B^0_s \to K^-\pi^+)}{\varepsilon(\overline{B}^0_s \to K^+\pi^-)} - \hat{f}_{B^0_s \to K^-\pi^+}} \cdot \frac{\varepsilon(B^0_s \to K^-\pi^+)}{\varepsilon(B^0 \to K^+\pi^-)}.$$

This quantity needs an additional correction, which can be factorized in the following way:

$$\frac{\varepsilon(B^0_s \to K^-\pi^+)}{\varepsilon(B^0 \to K^+\pi^-)} = \frac{\varepsilon(B^0_s \to K\pi)}{\varepsilon(B^0 \to K\pi)} \times \frac{\varepsilon^{\rm c}(B^0_s \to K^-\pi^+)}{\varepsilon^{\rm c}(B^0 \to K^+\pi^-)}, \tag{11.27}$$

where $\varepsilon(B^0_{(s)} \to hh')$ indicates the CP-averaged efficiency for the $B^0_{(s)} \to h^+h^{'-}$ decay extracted in sec. 10.2.4, and $\varepsilon^{\rm c}(B^0_{(s)} \to h^+h^{'-})$ factorizes the terms depending on the detector-induced charge asymmetry. Since the difference in the momentum (α,$p_{\rm tot}$) distribution between $B^0 \to K^+\pi^-$ and $B^0_s \to K^-\pi^+$ is negligible we can write:

$$\frac{\varepsilon^{\rm c}(B^0_s \to K^-\pi^+)}{\varepsilon^{\rm c}(B^0 \to K^+\pi^-)} = \frac{\varepsilon(\overline{B}^0 \to K^-\pi^+)}{\varepsilon(B^0 \to K^+\pi^-)} = \frac{\varepsilon(B^0_s \to K^-\pi^+)}{\varepsilon(\overline{B}^0_s \to K^+\pi^-)}. \tag{11.28}$$

Following eqs. (10.18) and (10.26) and eqs. (11.23) and (11.24), we corrected the fit results for the kinematic, XFT, FSR and the isolation efficiencies, $\frac{\varepsilon(B^0_s \to K\pi)}{\varepsilon(B^0 \to K\pi)} \simeq 0.992$ and $\frac{\varepsilon(B^0 \to K^+\pi^-)}{\varepsilon(\overline{B}^0 \to K^-\pi^+)} = \frac{\varepsilon(\overline{B}^0_s \to K^+\pi^-)}{\varepsilon(B^0_s \to K^-\pi^+)} \simeq 1.0131$, to extract the following ratio:

$$\frac{f_d}{f_s} \times \frac{\Gamma(\overline{B}^0 \to K^-\pi^+) - \Gamma(B^0 \to K^+\pi^-)}{\Gamma(\overline{B}^0_s \to K^+\pi^-) - \Gamma(B^0_s \to K^-\pi^+)} = -3.00 \pm 1.50\ (stat.). \tag{11.29}$$

Chapter 12

Systematic uncertainties and significance

This chapter describes the main sources of systematic uncertainty and the method used to evaluate the significance of the results on rare decay modes.

12.1 Systematic uncertainties

The measurements described in this thesis focus on ratios of branching fractions of kinematically similar decay modes. We expect that most systematic effects related to the individual modes, e. g., the uncertainty on the integrated luminosity of the sample, cancel in the ratio, thus resulting in a smaller systematic uncertainty on the measured ratios. Only systematic effects with a different impact on different modes were therefore considered. Furthermore, we ignored the systematic effects inducing uncertainties significantly, i. e., a factor $\mathcal{O}(10)$, smaller than their largest counterparts, because their contribution to the total systematic uncertainty is negligible.

To evaluate the systematic effects we used different strategies. In most cases, we adopted the pseudo-experiment technique. For each is source of systematic effects s[1] we generated different sets of pseudo-experiments using the complete Likelihood function described in chap. 6 and the set of parameters determined by the fit of composition. One set of pseudo-experiments assumes, for the parameter s, the nominal value s_0 used in the analysis ("central" analysis), while the other sets use alternative configurations, in which s is varied within a realistic range, e. g., $\pm 1\sigma_s$ when the source of systematic uncertainty is the statistical uncertainty σ_s on the parameter s. The resulting systematic uncertainty associated to s is the largest difference between the results of the analysis of the samples with alternative configurations, and the results of the sample with the nominal configuration. The number of pseudo-experiments used for each parameter s is around 100, unless otherwise specified.

Sections 12.2–12.9 contain the discussion on the dominant systematic uncertainties, while sec. 12.10 summarizes the effect of each measurement.

[1] The symbol s may indicate either a single parameter of a multidimensional parameter.

12.2 Uncertainty on the global mass scale (mass scale)

The central analysis is performed by assuming a known global mass scale, in which we assigned to the B^0, B_s^0 and Λ_b^0 masses the values measured by CDF in Run II [106] (see sec. 6.3). Since the invariant mass is used in separating signal modes, it is interesting to check how the fit behaves when the mass scale is allowed to float and to evaluate the systematic uncertainty associated to this effect. Section 9.4.3 describes an additional fit of composition performed on data with the global mass scale left completely free to vary. We added a new parameter δ_m to the fit with the substitution:

$$\begin{aligned} m_{B^0} &\rightarrow m_{B^0} + \delta_m \\ m_{B_s^0} &\rightarrow m_{B_s^0} + \delta_m \\ m_{\Lambda_b^0} &\rightarrow m_{\Lambda_b^0} + \delta_m \end{aligned}$$

where m_{B^0}, $m_{B_s^0}$, $m_{\Lambda_b^0}$ are the masses measured by CDF [106] and they are external inputs of the analytic expression of $\mathcal{M}_j(\alpha, p_{\rm tot})$ (see sec. 6.3). The global scale of the masses is determined to be $\delta_m = -0.3 \pm 0.6$ MeV/c^2 for the loose selection and $\delta_m = -0.7 \pm 0.7$ MeV/c^2 for the tight selection. The difference of $-2\ln(\mathscr{L})$ obtained between the fit with floating mass scale and the central fit is $-2\Delta\ln(\mathscr{L}) \simeq -0.2$ for the loose selection and $-2\Delta\ln(\mathscr{L}) \simeq -1.02$ for the tight selection. The estimated value of δ_m is just $0.5\sigma(1\sigma)$ different from zero for the loose(tight) selection. This indicates no statistical evidence for a shift of the mass scale in data.[2] The results with floating mass scale are consistent with those of the central fit with $\delta_m = 0$.

To evaluate the systematic uncertainty associated to our limited knowledge of the global mass scale we generated an ensemble of pseudo-experiments where the global mass scale is shifted by the quantity $\pm\sigma_{\delta_m}$ in either direction, extracted from the fit of composition performed on real data with the mass scale δ_m floating. The systematic uncertainty associated to the global mass scale is the largest difference between the results of the analysis of the samples with alternative configurations $\delta_m = +\sigma_{\delta_m}$ and $\delta_m = -\sigma_{\delta_m}$, and the results of the sample with the nominal configuration $\delta_m = 0$.

12.3 Uncertainty on the nominal b-hadron masses (nominal masses)

The B^0, B_s^0 and Λ_b^0 masses are external inputs to the analytic expression of $\mathcal{M}_j(\alpha, p_{\rm tot})$ (see sec. 6.3). In the central analysis they are fixed to the masses measured by CDF [106]. To evaluate the systematic uncertainty associated to our limited experimental knowledge of nominal input masses we generated ensembles of pseudo-experiments in which we independently varied the B^0, B_s^0 and Λ_b^0 input masses measured by CDF within $\pm1\sigma$ statistical uncertainty (see sec. 6.3). We included this effect considering only the *statistical* uncertainty on the input values of masses, rather than the *total* uncertainty (sum in quadrature of statistical and systematic uncertainty) since the CDF masses were measured using the same apparatus and reconstruction code used in this analysis, and then all common systematic

[2] A fundamental property of the Likelihood ratio test-statistics prescribes that, for sufficiently regular Likelihoods and in the asymptotic limit, the quantity $-2\Delta\ln(\mathscr{L})$ between two ML estimators with a difference n in dimensionality, is distributed as a χ^2 with n degrees of freedom [146].

uncertainties cancel out. In fact the dominant systematic effects (tracker mis-alignments and incorrect absolute-scale of the momentum) are independent of the details of the considered decay-mode, since they are related only to the tracker performance. Thus, only the statistical uncertainties on the input masses contribute to the systematic uncertainty of our analysis.

The eight possible combinations of B^0, B_s^0 and Λ_b^0 masses were simulated by independently increasing (decreasing) by one statistical standard deviation the masses measured in Ref. [106]: $m_{B^0} = 5279.63 \pm 0.53$ (*stat.*) MeV/c^2, $m_{B_s^0} = 5366.01 \pm 0.73$ (*stat.*) MeV/c^2 and $m_{\Lambda_b^0} = 5619.7 \pm 1.2$ (*stat.*) MeV/c^2. The largest discrepancy between the results of the analysis of the samples with alternative masses configurations and the results of the sample with the nominal configuration was taken as the systematic uncertainty.

12.4 Charge asymmetries of momentum p.d.f. (asymm. $\wp^p$)

The momentum probability density functions ($\wp_j^p(\alpha, p_{\rm tot})$ and $\wp_{\rm bck}^p(\alpha, p_{\rm tot})$) were extracted from simulated samples for all signal modes and from data mass sidebands for the background (see sec. 6.5). Since the signed momentum-imbalance (α) and the scalar sum of the momenta ($p_{\rm tot}$) are not independent observables, we used a joint p.d.f. to model their distributions. Section 6.5 describes all the details of the parameterization. The b coefficients of eqs. (6.20) and (6.21) characterize the factorized $\alpha\frac{p_{\rm tot}-2}{p_{\rm tot}-4}$ terms. In the parameterization we assumed that $\wp^p(\alpha, p_{\rm tot}) = \wp^p(-\alpha, p_{\rm tot})$ for decays into $\pi^+\pi^-$ and K^+K^- final states, where the α distributions are symmetric because the two outgoing particles have the same mass, and for background. Technically this was done by setting the odd b coefficients to zero in the parameterization of the central analysis. In order to take into account possible hidden asymmetries in the distributions due to any possible detector asymmetries reproduced by the simulation, we repeated the analysis using an ensemble of pseudo-experiments in which we re-parameterized the momentum probability density functions with asymmetric fit functions for all signal modes and for background (i. e., leaving free to vary also the odd b coefficients). The systematic uncertainty associated is the difference between the results with the asymmetric configurations for $\wp_j^p(\alpha, p_{\rm tot})$ and $\wp_{\rm bck}^p(\alpha, p_{\rm tot})$ and the results with the symmetric nominal configuration.

12.5 Momentum p.d.f. of background ($\wp_{\rm bck}^p$ model)

The momentum probability density function of background $\wp_{\rm bck}^p(\alpha, p_{\rm tot})$ was extracted from the data mass sidebands (see sec. 6.5.2). In the central analysis we used the high mass sideband to extract the momentum p.d.f. of the combinatorial background. For the physics background the situation is more complicated, since in the low mass sideband there is an unknown mixture of these two components. The contamination from physics background in the $B_{(s)}^0 \to h^+h'^-$ mass region is only a few%. Therefore we decided to use the same p.d.f to parameterize both background components. We parameterized the joint distribution $\wp_{\rm bck}^p(\alpha, p_{\rm tot})$ using the selections reported in tab. 3.3 with data mass sidebands defined within the region $m_{\pi\pi} \in [5.000, 5.125] \cup [5.600, 6.200]$ GeV/c^2 where the signal mass region $m_{\pi\pi} \in [5.125, 5.600]$ GeV/c^2 was removed. The relative weight between the combinatorial and physics backgrounds was preserved since the mass window fit is within the mass

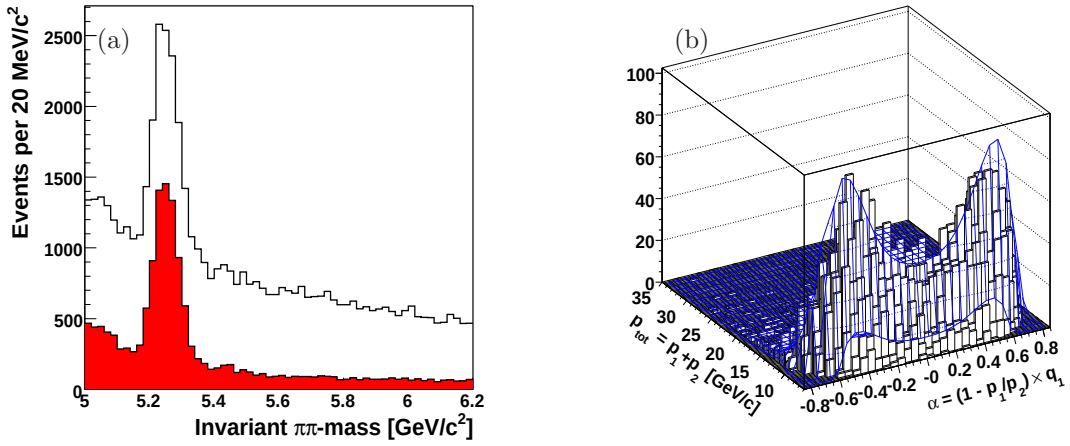


Figure 12.1: Invariant $\pi\pi$-mass distribution for candidates passing the loose selection (filled red), passing the loose selection except the requirement on isolation $I(B) > 0.5$ and on 3-D vertex quality $\chi^2_{3D}(B) < 7$ (not filled black) (a). Distribution of the scalar sum of momenta as a function of the signed momentum imbalance for the background decays. Joint $(\alpha, p_{\rm tot})$ templates as determined for alternative background is overlaid (b).

interval $m_{\pi\pi} \in [5.000, 5.800]$ GeV/c^2 (see sec. 6.5.2) and because we assumed an approximately flat combinatorial background distribution. This strategy, used in the central analysis, may not be very accurate because of the low statistics used in the parameterization (due to the very selective criteria used to isolate the final samples). In order to assess a systematic uncertainty due to our limited knowledge of the real distribution of the background momentum, we parameterized $\wp^p_{\rm bck}(\alpha, p_{\rm tot})$ in an alternative way. We removed the requirements on isolation $I(B)$ and 3-D vertex quality $\chi^2_{3D}(B)$ to increase the statistics of the mass sidebands. Since the dominant background under the signal peak is combinatorial we parameterized only the right sideband $m_{\pi\pi} \in [5.600, 5.800]$ GeV/c^2. Since the isolation requirement sculpts the distribution of transverse momentum of the B candidates, and the distribution of scalar sum of momenta $p_{\rm tot}$, the data-distributions without isolation requirement are reweighted with the functions extracted in sec. 4.1.1 (see also chap. 7 for more details). The associated systematic uncertainty is the difference between the results of the analysis of the samples generated with this alternative configuration for $\wp^p_{\rm bck}(\alpha, p_{\rm tot})$ and the results of the sample with the nominal configuration.

12.6 Uncertainty on the combinatorial background mass term ($\wp^m_E$ model)

Since our central analysis assumed empirically an invariant $\pi\pi$-mass model of the combinatorial background (E) distributed as an exponential function (see sec. 6.4) we assessed a systematic uncertainty

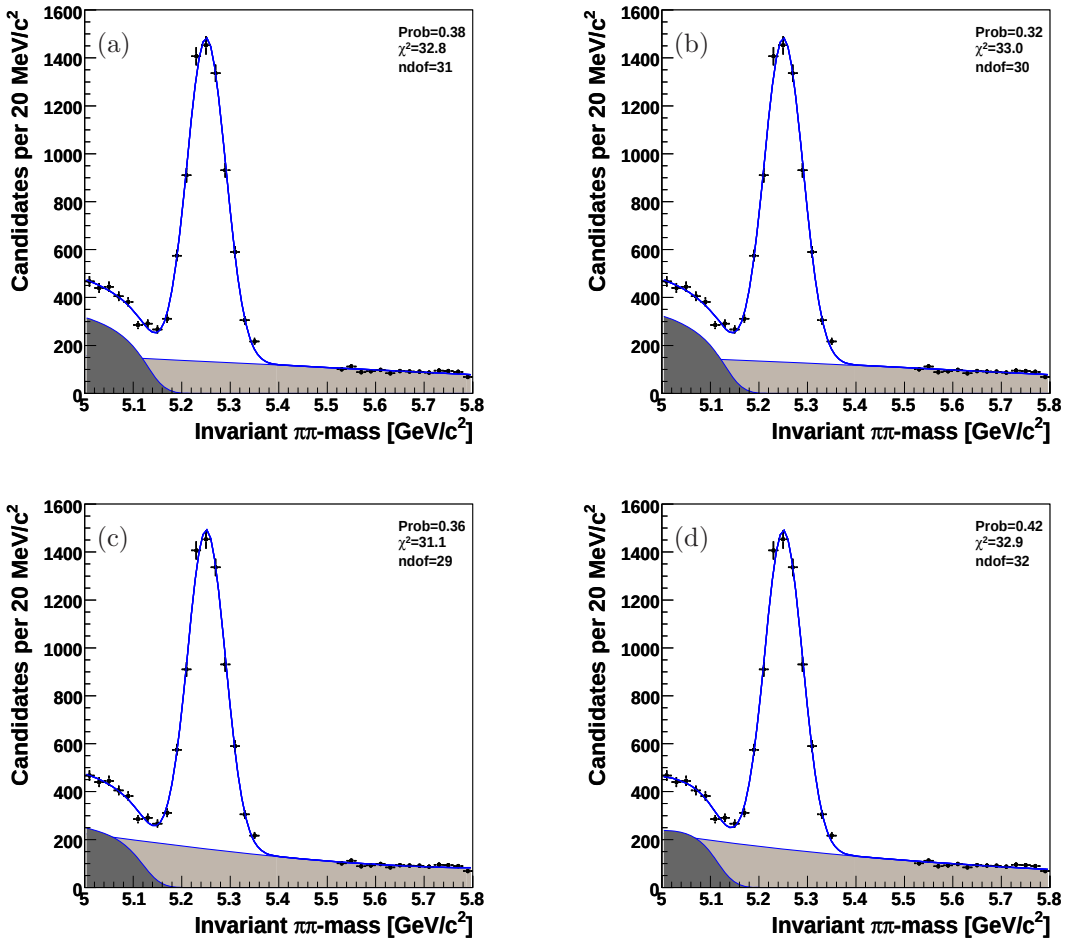


Figure 12.2: Invariant $\pi\pi$-mass distribution of the events passing the loose selection. A Gaussian (signal) plus pol1 (a), pol2 (b), pol3 (b) and exponential (d) (combinatoric background, light Grey) plus a smeared Argus (physics background, dark Grey) fit function is overlaid.

due to our limited knowledge of the real distribution. We repeated the fit of composition on ensembles of pseudo-experiments where the exponential function $\wp_E^m$ (see sec. 6.4) was substituted with different polynomial shapes of increasing degree, up to the third one. The choice of these alternative shapes has been dictated by the ability to provide good quality one-dimensional fits (χ^2-test) to the invariant $\pi\pi$-mass mass distribution of real data. Figures 12.2 and 12.3 show these one-dimensional fits respectively for the the sample selected with the loose cuts and the tight cuts. The largest difference between the fit results obtained with the samples generated with these alternative models and those obtained with the standard exponential model was quoted as systematic uncertainty.

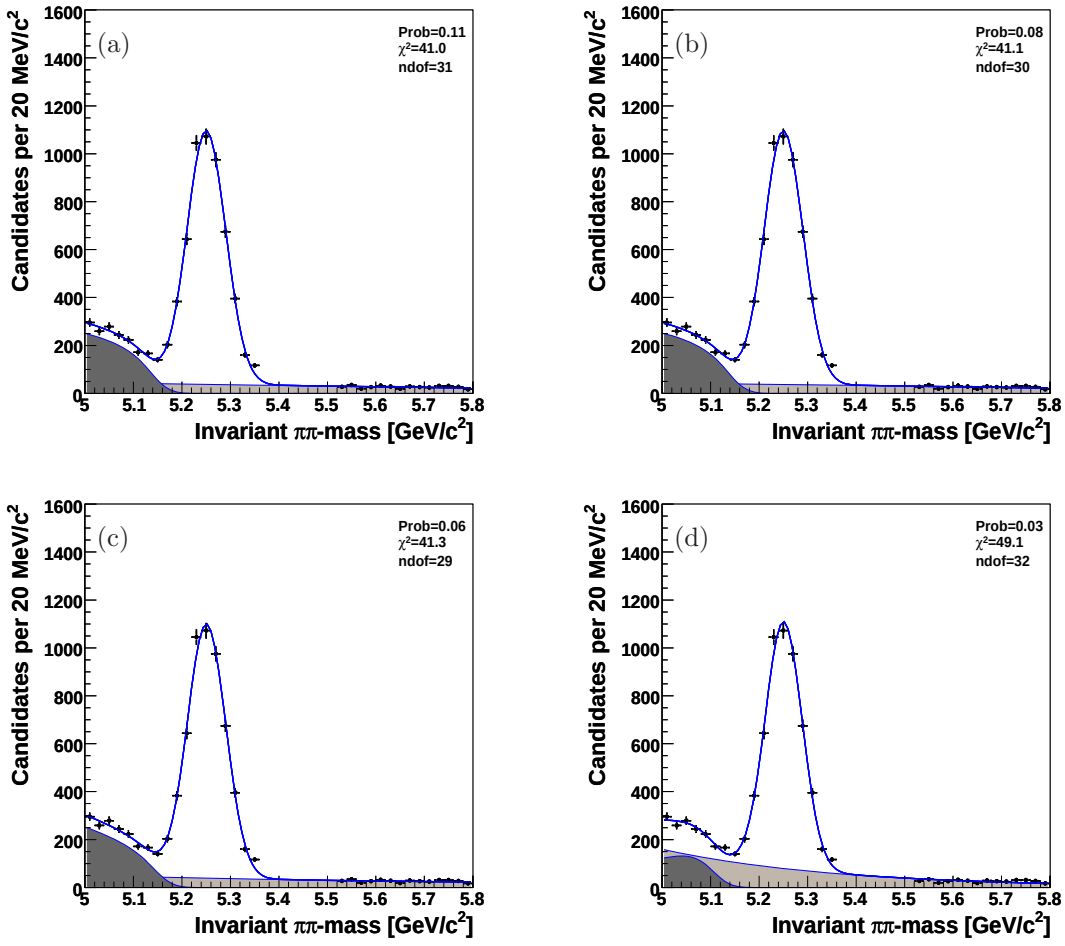


Figure 12.3: Invariant $\pi\pi$-mass distribution of the events passing the tight selection. A Gaussian (signal) plus pol1 (a), pol2 (b), pol3 (b) and exponential (d) (combinatoric background, light Grey) plus a smeared Argus (physics background, dark Grey) fit function is overlaid.

12.7 dE/dx related systematics (dE/dx)

Sections 4.4 and 6.6 summarize how the fit of composition exploits the PID information in separating the different signal modes and background. The model used to introduce this information in the Likelihood is sophisticated, needing a large number of parameters. For example, the probability density function which describes the $B^0 \to K^+\pi^-$ signal mode results from a convolution integral that combines the intrinsic dE/dx residuals of both particles (δ_{K^+} and δ_{π^-}) through the p.d.f. of correlation, $\wp_c(c)$, yielding the following p.d.f. (see sec. 6.6):

$$\begin{aligned} \alpha > 0 \quad &\to \quad \wp_{B^0\to K^+\pi^-}(\delta^{\rm obs}_{K^+}, \delta^{\rm obs}_{\pi^-}) = [\wp_{K^+}(\delta_{K^+}) \times \wp_{\pi^-}(\delta_{\pi^-})] * \wp_c(c) \\ \alpha < 0 \quad &\to \quad \wp_{B^0\to \pi^- K^+}(\delta^{\rm obs}_{\pi^-}, \delta^{\rm obs}_{K^+}) = [\wp_{\pi^-}(\delta_{\pi^-}) \times \wp_{K^+}(\delta_{K^+})] * \wp_c(c). \end{aligned}$$

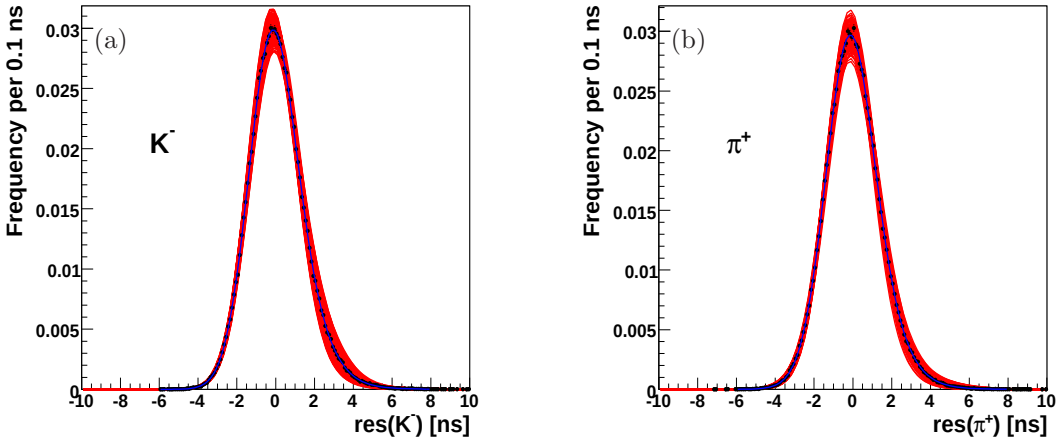


Figure 12.4: Distribution of observed dE/dx residual ($\wp(\delta^{\rm obs}) = \wp(\delta + c) = \wp(\delta) * \wp(c)$), for negatively charged kaons (with kaon mass hypothesis) (a), for positively charged pions (with pion mass hypothesis) (b). The results of the fit to the functions in eq. (4.27) and eq. (4.26) are overlaid (blue, solid line). The red band results from the overlapping of different curves generating with 100 different seed values x_0 from the template used in the standard analysis using the technique described in sec. 12.7.

Just this term of the Likelihood needs eight parameters for the three Gaussians of $\wp_{K^+}$, eight parameters for the three Gaussians of $\wp_{\pi^-}$ and five parameters for the two Gaussians of correlation $\wp_c(c)$, for a total of 21 parameters. If we consider all kind of particles adding the parameters to model the distribution of intrinsic residual of K^-, π^+, p and $\bar{p}$ we obtain a total number of 53 parameters. All these parameters have a statistical uncertainty which contributes to the systematic uncertainty on our final measurements. In reality in our analysis the parameters which model the correlation are free parameters in the fit of composition, therefore the total number is $53 - 5 = 48$, because each free parameter already contributes to the statistical uncertainty.

The systematic uncertainty related to the statistical uncertainty on the determination of PID probability density functions was assessed by repeating the fit of composition in which all PID parameters, described above, are randomly varied in a 1σ-radius multidimensional sphere. We varied the parameters of the PID templates in all the possible *directions* generating randomly shifts in the parameters multi-dimensional space. In order to statistically sample a sufficient number of directions in this large dimensions space, we repeated the analysis for various seed values. For each seed value the PID functions change in a different way and we can obtain a measurement of the effect of systematic uncertainties on the analysis results.

If we indicate the PID parameter vector with $\theta_i \pm \Delta_{\theta_i}$ where $i = 0, 1, ..., N$ (N is the total number of parameters) we varied θ_i:

$$\theta_i = \theta_i + \Delta_{\theta_i} \cdot s_{i+1} \tag{12.1}$$

where s_{i+1} is the ith random shift. To generate randomly a list of shifts s_{i+1} we used the congruence

method [145].

$$s_{i+1} = \frac{\sqrt{N} \cdot x_{i+1} \cdot n}{\sqrt{\sum_{i=0}^{N-1} x_{i+1}^2}} \tag{12.2}$$

where $n = 1, 2, 3, ...$ is the number of statistical uncertainty Δ_{θ_i} we want to use to evaluate the total systematic uncertainty (in our case we assumed $n = 1$) and

$$x_{i+1} = -1 + 2\frac{(a \cdot x_i + c)\%m}{m - 1} \tag{12.3}$$

where a, c and m are fixed by choosing one of the most used tern for the congruence method, $a = 40$, $c = 3641$ and $m = 729$ [145]. x_0 is the seed value. The generated numbers x_i are included within the interval $[-1, 1]$.

Figure 12.4 shows the distribution of the observed residuals for the negatively charged kaons and the positively charged pions (we obtain similar distributions for the other particles). The blue solid line is the template used in the central analysis while the red band, centered around data distribution, is the overlap of 100 templates generating with 100 different x_0 seeds with the technique described above, in which all PID parameters are randomly varied in a 1σ-radius multidimensional sphere. We repeated the fit of composition using this 100 different PID probability density functions. The systematic uncertainty on the physics observables associated to the statistical uncertainty of the templates parameterization is given by the r.m.s. of the distribution of the observables returned from the fits of composition performed with different seeds. In other words if we consider, for instance, the measurement of the direct CP asymmetry in the $B^0 \to K^+\pi^-$ decay mode, for each PID seed $(x_0)_j$ we can perform a fit of composition on data and obtain a different result for this measurement $\mathcal{A}_{\rm CP}(B^0 \to K^+\pi^-)_j$. The r.m.s. of distribution of $\mathcal{A}_{\rm CP}(B^0 \to K^+\pi^-)_j$ is the systematic uncertainty associated to our non perfect knowledge of the real distribution of PID templates on the measurement.

In this procedure we neglect the correlations between the PID parameters since the covariance matrix of PID parameters is hard to extract. They are determined through an iterative procedure (see sec. 4.4.5) and not using a single fit. Adding the correlations would imply a reduction of the final systematic uncertainty since the correlations tend to compensate the uncertainty of one parameter with respect to another one. The dE/dx related systematic uncertainty is one of the dominant in our measurements (see tabs. 12.1–12.4 and figs. 12.5–12.7), but it is still smaller than the statistical uncertainty, therefore we decide to do not include the correlations in the procedure and to quote a conservative value for now.

12.8 Efficiency-related systematic effects

12.8.1 Effect of Poisson fluctuations in simulated samples (MC stat.)

The relative kinematic efficiency ratios (see sec. 10.2) used to convert the ratios of event yields in ratios of branching fractions, were determined within $\mathcal{O}(0.4\%)$ statistical uncertainties (see sec. 10.2.4). This uncertainty is indicated with the symbol (MC) in eqs. (10.15)–(10.20). We re-evaluated each ratio of branching fractions by using acceptance corrections fluctuated by one standard deviation in either

direction. The difference between the resulting branching fraction and the central result was taken as systematic uncertainty. See tabs. 12.1–12.4.

12.8.2 Uncertainty on the XFT-bias correction (XFT bias)

The functions used to correct the mismatch between data and Monte Carlo in reproducing the different XFT triggering-efficiency for pions and kaons are extracted from data (see sec. 10.2.3). The statistical uncertainty on the parameterization of these functions introduces a systematic uncertainty on our final results. This uncertainty is indicated with the symbol (XFT) in eqs. (10.15)–(10.20). We re-evaluated each ratio of branching fractions by using acceptance corrections fluctuated by one standard deviation in either directions. The difference between the resulting branching fraction and the central result was used as systematic uncertainty. See tabs. 12.1–12.4.

12.8.3 Uncertainty on the B-isolation efficiency (B-isol.)

The efficiency of the isolation requirement was measured with real data (see sec. 10.4 and chap. 7) with a statistical uncertainty $\approx 2.8\%$ and it contributes to a systematic uncertainty on the measurements of ratios of branching fractions between B_s^0 and B^0 decays. We re-evaluated the ratios of branching fractions after fluctuating the relative isolation efficiency by one standard deviation in either directions. The difference between the resulting branching fraction and the central result was used as systematic uncertainty. See tabs. 12.1–12.4.

12.8.4 Charge asymmetry correction (charge asymmetry)

The efficiency ratio $\frac{\varepsilon(B^0\to K^+\pi^-)}{\varepsilon(\overline{B}^0\to K^-\pi^+)} = \frac{\varepsilon(\overline{B}_s^0\to K^+\pi^-)}{\varepsilon(B_s^0\to K^-\pi^+)}$ was measured with real data (see sec. 11.6.1 and chap. 11) with a statistical uncertainty $\approx 0.3\%$ and it contributes to a systematic uncertainty on the related CP-asymmetry measurements. We re-evaluated the CP related measurements after fluctuating this efficiency ratio by one standard deviation in either direction. The difference between the resulting branching fraction and the central result was used as systematic uncertainty. See tabs. 12.1–12.4.

12.9 Lifetime-related systematic effects

12.9.1 Uncertainty on the nominal $B_{(s)}^0$ meson lifetimes ($B_{(s)}^0$ lifetime)

The selection of the samples used in this analysis relies on cuts on the impact parameter (d_0) of both tracks and on the transverse decay length of the B candidate ($L_{\rm T}$). Therefore we assessed a systematic uncertainty due to the experimental uncertainty of the B^0 and B_s^0 lifetime measurements. This affects also the estimate of $c\tau(B_s^0 \to K^+K^-)$ and $c\tau(B_s^0 \to \pi^+\pi^-)$ since they were extracted from Γ_d and $\Delta\Gamma_s/\Gamma_s$ in the central analysis (see sec. 10.2.1). The additional systematics due to the uncertainty on $\Delta\Gamma_s/\Gamma_s$ was evaluated separately in sec. 12.9.2.

To evaluate the systematic uncertainty we generated two simulated samples, one where the B^0 lifetime is increased by a factor 1σ [32] ($c\tau(B^0) = 460 + 4 = 464$ μm) and the B_s^0 lifetime is decreased

by a factor 1σ [32] ($c\tau(B_s^0) = 438 - 17 = 421$ μm) and another one where the B^0 lifetime is decreased by a factor 1σ [32] ($c\tau(B^0) = 460 - 4 = 458$ μm) and the B_s^0 lifetime is increased by a factor 1σ [32] ($c\tau(B^0) = 438 + 17 = 455$ μm). We re-evaluated the efficiency correction factors by using these modified simulated samples. The largest difference between the resulting branching fraction obtained and the central result was used as systematic uncertainty. See tabs. 12.1–12.4.

12.9.2 Uncertainty on $\Delta\Gamma_s/\Gamma_s$ ($\Delta\Gamma_s/\Gamma_s$)

The measurements involving the $B_s^0 \to K^+K^-$ and $B_s^0 \to \pi^+\pi^-$ decays suffer from the additional systematic uncertainty due to the limited experimental and theoretical knowledge of $\Delta\Gamma_s/\Gamma_s$. To quote the results in the central analysis we assumed the Standard Model expectation for the lifetime-difference which has a 50% relative uncertainty ($\Delta\Gamma_s/\Gamma_s = 0.12 \pm 0.06$, see sec. 10.2.1). Such uncertainty introduces an uncertainty of ± 12 μm in $c\tau(B_s^0 \to K^+K^-)$ and $c\tau(B_s^0 \to \pi^+\pi^-)$. We re-evaluated the efficiency correction factors by using additional simulated samples in which we fluctuated the lifetime of the $B_s^0 \to K^+K^-$ and $B_s^0 \to \pi^+\pi^-$ modes by one standard deviation in either direction ($c\tau(B_s^0 \to K^+K^-) = c\tau(B_s^0 \to \pi^+\pi^-) = 446$ μm and $c\tau(B_s^0 \to K^+K^-) = c\tau(B_s^0 \to \pi^+\pi^-) = 422$ μm). The difference between the resulting branching fraction obtained and the central result was used as systematic uncertainty. See tabs. 12.1–12.4.

12.10 Total systematic uncertainties

A synopsis of all the systematic uncertainties is reported in tabs. 12.1–12.4. The total systematic uncertainty on each measurement has been determined as the sum in quadrature of the single systematic uncertainties. When the systematic uncertainty is asymmetric, the largest value has been used in the squared sum. In order to visualize the magnitude of systematic uncertainties (σ_i) contributing to each measurement we represented them with circular charts, reported in figs. 12.5–12.7, in which the area of each sector is proportional to σ_i^2.

source	$\mathcal{A}_{\rm CP}(B^0 \to K^+\pi^-)$	$\frac{\mathcal{B}(B^0\to\pi^+\pi^-)}{\mathcal{B}(B^0\to K^+\pi^-)}$	$\frac{f_s}{f_d} \times \frac{\mathcal{B}(B_s^0\to K^+K^-)}{\mathcal{B}(B^0\to K^+\pi^-)}$
mass scale	0.0004	0.0036	0.0034
$\boldsymbol{\wp^p}$ **asymm.**	0.0001	0.0006	0.0030
$\boldsymbol{dE/dx}$	0.0064	0.0129	0.0107
nominal masses	0.0054	0.0050	0.0050
$\boldsymbol{\wp^m_E}$ **model**	0.0027	0.0020	0.0020
$\boldsymbol{\wp^p_{\rm bck}}$ **model**	0.0007	0.0010	0.0060
MC stat.	–	0.0011	0.0012
charge asymm.	0.0014	–	–
$\boldsymbol{\Delta\Gamma_s/\Gamma_s}$	–	–	0.0060
$\boldsymbol{B^0_{(s)}}$ **lifetime**	–	–	0.0060
$\boldsymbol{B}$**-isol.**	–	–	0.0097
XFT-bias	–	0.0050	0.0080
TOTAL	**0.009**	**0.0165**	**0.0208**

Table 12.1: Summary of the systematic uncertainties for observables extracted using the loose selection.

source	$\frac{f_s}{f_d} \times \frac{\mathcal{B}(B_s^0 \to K^-\pi^+)}{\mathcal{B}(B^0 \to K^+\pi^-)}$	$\mathcal{A}_{\rm CP}(B_s^0 \to K^-\pi^+)$	$\frac{f_d}{f_s} \times \frac{\Gamma(\overline{B}^0 \to K^-\pi^+) - \Gamma(B^0 \to K^+\pi^-)}{\Gamma(\overline{B}_s^0 \to K^+\pi^-) - \Gamma(B_s^0 \to K^-\pi^+)}$
mass scale	0.0017	0.009	0.009
$\boldsymbol{\wp^p}$ **asymm.**	0.0020	0.020	0.045
$\boldsymbol{dE/dx}$	0.0036	0.053	0.115
nominal masses	0.0029	0.020	0.060
$\boldsymbol{\wp_E^m}$ **model**	0.0040	0.034	0.040
$\boldsymbol{\wp_{\rm bck}^p}$ **model**	0.0024	0.040	0.116
MC stat.	0.0003	–	0.012
charge asymm.	–	0.001	0.042
$\boldsymbol{\Delta\Gamma_s/\Gamma_s}$	–	–	–
$\boldsymbol{B_{(s)}^0}$ **lifetime**	0.0001	–	0.065
$\boldsymbol{B}$**-isol.**	0.0020	–	0.084
XFT-bias	0.0011	–	0.054
TOTAL	**0.0074**	**0.080**	**0.224**

Table 12.2: Summary of the systematic uncertainties for observables related to the $B_s^0 \to K^-\pi^+$ mode extracted using the tight selection.

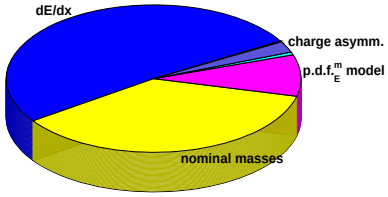
source	$\frac{\mathcal{B}(B^0\to K^+K^-)}{\mathcal{B}(B^0\to K^+\pi^-)}$	$\frac{f_s}{f_d}\times\frac{\mathcal{B}(B_s^0\to\pi^+\pi^-)}{\mathcal{B}(B^0\to K^+\pi^-)}$	$\frac{\mathcal{B}(\Lambda_b^0\to p\pi^-)}{\mathcal{B}(\Lambda_b^0\to pK^-)}$
mass scale	0.0009	0.0002	0.0040
$\boldsymbol{\wp^p}$ **asymm.**	0.0010	0.0022	0.0320
$\boldsymbol{dE/dx}$	0.0033	0.0007	0.0502
nominal masses	0.0016	0.0003	0.0180
$\boldsymbol{\wp_E^m}$ **model**	0.0030	0.0015	0.0468
$\boldsymbol{\wp_{\mathrm{bck}}^p}$ **model**	0.0040	0.0043	0.0060
MC stat.	0.	0.	0.0028
charge asymm.	–	–	–
$\boldsymbol{\Delta\Gamma_s/\Gamma_s}$	–	0.	–
$\boldsymbol{B^0_{(s)}}$ **lifetime**	–	0.0001	–
$\boldsymbol{B}$**-isol.**	–	0.0002	–
XFT-bias	0.0001	0.0001	0.0120
TOTAL	**0.0063**	**0.0052**	**0.0790**

Table 12.3: Summary of the systematic uncertainties for observables related to other rare modes extracted using the tight selection.

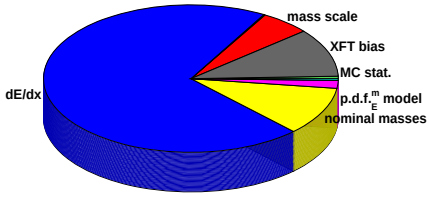
source	$\mathcal{N}(B^0 \to K^+K^-)$	$\mathcal{N}(B_s^0 \to \pi^+\pi^-)$	$\mathcal{N}(B_s^0 \to K^-\pi^+)$	$\mathcal{N}(\Lambda_b^0 \to p\pi^-)$	$\mathcal{N}(\Lambda_b^0 \to pK^-)$
mass scale	4	1	1	1	1
$\wp^p$ **asymm.**	4	9	6	6	1
dE/dx	13	2	7	7	7
nominal masses	6	3	3	3	2
$\wp_E^m$ **model**	27	8	12	12	6
$\wp_{\mathtt{bck}}^p$ **model**	17	7	4	4	6
TOTAL	**35**	**14**	**16**	**16**	**11**

Table 12.4: Summary of the systematic uncertainties for the yield measurements of rare modes. Tight selection.

$\mathcal{A}_{\rm CP}(B^0 \to K^+\pi^-)$



$\frac{\mathcal{B}(B^0\to\pi^+\pi^-)}{\mathcal{B}(B^0\to K^+\pi^-)}$



$\frac{f_s}{f_d} \times \frac{\mathcal{B}(B_s^0\to K^+K^-)}{\mathcal{B}(B^0\to K^+\pi^-)}$

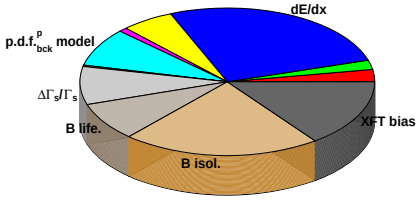
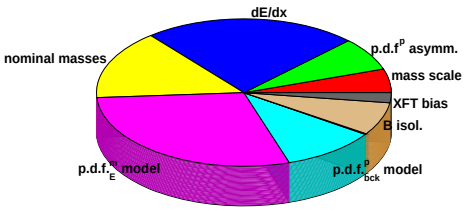
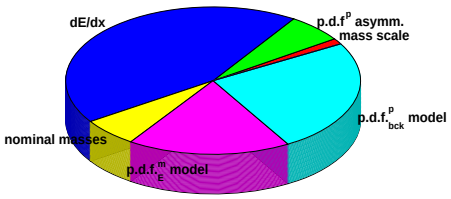


Figure 12.5: Circular chart of the systematic uncertainties (σ_i) contributing to the measurements extracted using the loose selection. The area of each sector is proportional to σ_i^2. Only the dominant systematic uncertainties are labeled.

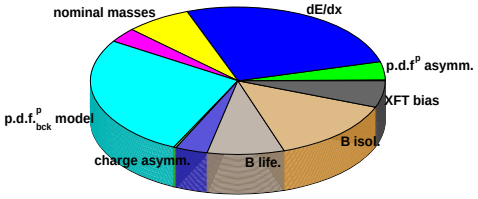
$\frac{f_s}{f_d} \times \frac{\mathcal{B}(B_s^0 \to K^-\pi^+)}{\mathcal{B}(B^0 \to K^+\pi^-)}$



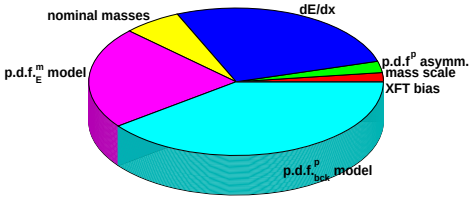
$\mathcal{A}_{\rm CP}(B_s^0 \to K^-\pi^+)$



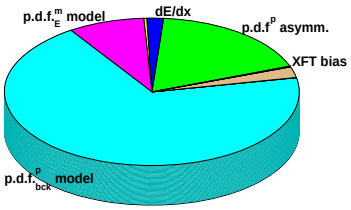
$\frac{f_d}{f_s} \times \frac{\Gamma(\overline{B}^0 \to K^-\pi^+) - \Gamma(B^0 \to K^+\pi^-)}{\Gamma(\overline{B}_s^0 \to K^+\pi^-) - \Gamma(B_s^0 \to K^-\pi^+)}$



$\frac{\mathcal{B}(B^0 \to K^+K^-)}{\mathcal{B}(B^0 \to K^+\pi^-)}$



$\frac{f_s}{f_d} \times \frac{\mathcal{B}(B_s^0 \to \pi^+\pi^-)}{\mathcal{B}(B^0 \to K^+\pi^-)}$



$\frac{\mathcal{B}(\Lambda_b^0 \to p\pi^-)}{\mathcal{B}(\Lambda_b^0 \to pK^-)}$

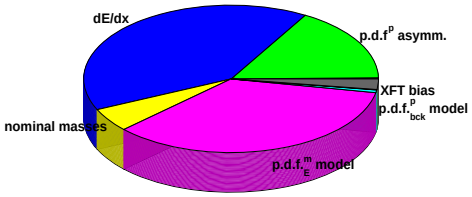
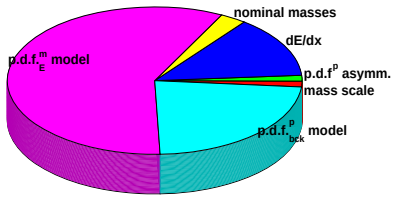
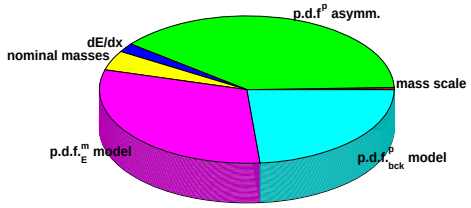


Figure 12.6: Circular chart of the systematic uncertainties (σ_i) contributing to the measurements extracted using the tight selection. The area of each sector is proportional to σ_i^2. Only the dominant systematic uncertainties are labeled.

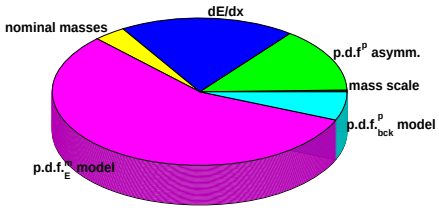
$\mathcal{N}(B^0 \to K^+K^-)$



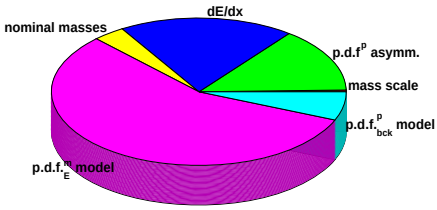
$\mathcal{N}(B^0_s \to \pi^+\pi^-)$



$\mathcal{N}(B^0_s \to K^-\pi^+)$



$\mathcal{N}(\Lambda^0_b \to p\pi^-)$



$\mathcal{N}(\Lambda^0_b \to pK^-)$

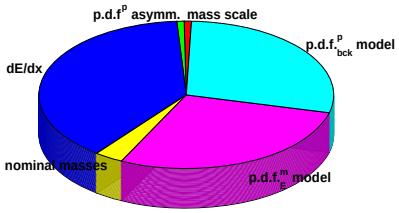


Figure 12.7: Circular chart of the systematic uncertainties (σ_i) contributing to the measurements of yield of rare modes. The area of each sector is proportional to σ_i^2. Only the dominant systematic uncertainties are labeled.

12.11 Significance of the rare modes

A test of the current best theory H_0 in favor of an alternative theory H_m, where m indicates the free parameters of the new theory (i. e., branching fractions), is specified by defining the set of values of the experimental observables X that will make us decide that H_0 must be rejected ("critical region"); the *significance level* of the test, indicated by α, is the probability of rejecting H_0 when it is indeed true. α is the probability for X to fall within the critical region, calculated under the assumption that H_0 is true. In the present thesis the significance level α is measured in Gaussian equivalent units ($n\sigma$ where $n = 1, 2, 3, ...$). The notation $\alpha = n\sigma$ correspond to $n\sigma$ single tail of a Gaussian distribution:

$$\alpha = \frac{1}{\sqrt{2\pi}\sigma} \int_{n\sigma}^{+\infty} e^{-\frac{1}{2}\frac{t^2}{\sigma^2}} dt. \tag{12.4}$$

The common practice for claiming new physics discoveries is to require α larger than 5σ. For more details see sec. 8.3.1.

In the present analysis we searched for five rare modes still unobserved: $B^0 \to K^+K^-$, $B_s^0 \to K^-\pi^+$, $B_s^0 \to \pi^+\pi^-$, $\Lambda_b^0 \to p\pi^-$, $\Lambda_b^0 \to pK^-$. We estimated the significance of new rare modes by performing additional fits of composition on real data. For each rare mode ($B^0 \to K^+K^-$, $B_s^0 \to K^-\pi^+$,$B_s^0 \to \pi^+\pi^-$, $\Lambda_b^0 \to p\pi^-$, $\Lambda_b^0 \to pK^-$) we repeated the fit by fixing its relative fraction to zero. Table 12.5 reports the values of $-2\ln(\mathscr{L})$ of each fits and its difference $-2\Delta\ln(\mathscr{L})$, referred as *Likelihood Ratio*, with the central fit performed with all relative fractions of rare modes free to vary. Since the the distribution of statistical uncertainty for each fit parameter are distributed very

fit	$-2\ln(\mathscr{L})$	$-2\Delta\ln(\mathscr{L})$	α
central fit	71413.19	0	–
$f_{B^0\to K^+K^-} = 0$	71420.02	7.83	2.6σ
$f_{B_s^0\to \pi^+\pi^-} = 0$	71416.39	3.2	1.8σ
$f_{B_s^0\to K^-\pi^+} = 0$	71479.14	66.95	8.1σ
$f_{\Lambda_b^0\to p\pi^-} = 0$	71478.95	65.76	8.1σ
$f_{\Lambda_b^0\to pK^-} = 0$	71520.46	107.27	10.3σ

Table 12.5: Significance of rare modes computed by performing additional fits of composition on real data. For each rare mode ($B^0 \to K^+K^-$, $B_s^0 \to K^-\pi^+$,$B_s^0 \to \pi^+\pi^-$, $\Lambda_b^0 \to p\pi^-$, $\Lambda_b^0 \to pK^-$) we repeated the fit by fixing its relative fraction to zero.

closely as a Gaussian distribution (see sec. 9.4.1) the distribution of $-2\Delta\ln(\mathscr{L})$ is distributed with good approximation as a χ^2 distribution with 1 degree of freedom. In fact for sufficiently regular Likelihoods and in the asymptotic limit, the quantity $-2\Delta\ln(\mathscr{L})$ between two Maximum Likelihood estimators with a difference n in dimensionality, is distributed as a χ^2 with n degrees of freedom [146]. Table 12.5 reports the significance values found for each rare mode and the relative values for $-2\ln(\mathscr{L})$ and the Likelihood Ratio $-2\Delta\ln(\mathscr{L})$. Significance values for $B_s^0 \to K^-\pi^+$, $\Lambda_b^0 \to p\pi^-$, $\Lambda_b^0 \to pK^-$ are found larger than 5σ, 8.1σ, 8.1σ and 10.3σ, respectively.
We verified that the distribution of the Likelihood Ratio $-2\Delta\ln(\mathscr{L})$ for each rare mode is regular for values comparable with those reported in the third column of tab. 12.5. We generated about

500 pseudo-experiments for each fit of composition reported in tab. 12.5 and fig. 12.8 shows the distribution of $-2\Delta\ln(\mathscr{L})$. The limited number of pseudo-experiments allows to explore only regions close approximately to significances of 3σ. Higher significance values are hard to explore, since they require a large computing time considering such a sophisticated maximum Likelihood fit.

The method described above is a standard technique, however it does not keep into account the systematic uncertainty in quoting the significance value. For this reason we used also an other approach, which combines statistical and systematic uncertainty of each measurement, to evaluate the significance. From the statistical point of wiew this approach is equivalent to that one described above.

The statistical uncertainty to evaluate the significance in this new approach was estimated using an ensemble of 500 pseudo-experiments in which no contribution from the rare signals ($B^0 \to K^+K^-$, $B_s^0 \to K^-\pi^+$,$B_s^0 \to \pi^+\pi^-$, $\Lambda_b^0 \to p\pi^-$, $\Lambda_b^0 \to pK^-$) was generated, while the relative fraction of all rare modes was left free to vary in each fit of composition. Figure 12.9 shows the distributions of yield determined by the fits of pseudo-experiments. The distributions were fitted with a Gaussian distribution. The mean is centered at zero within the fit resolution while the width is the statistical uncertainty on the yield measurement ($\sigma_0^{stat.}$) with the hypothesis of no rare signal modes in our sample. If N is the yield measured on real data with the complete analysis, $\sigma_N^{stat.}$ is its statistical uncertainty and $\sigma_N^{syst.}$ is its systematic uncertainty (we assume the systematic uncertainty is distributed as a Gaussian) we evaluated the significance, in Gaussian equivalent σ, in the following way:

$$\alpha = \frac{N}{\sqrt{(\sigma_0^{stat.})^2 + (\sigma_N^{syst.})^2}}\sigma. \tag{12.5}$$

Table 12.6 reports (last column) the significance values obtained using this approach that combines statistical and systematic uncertainty. Table 12.6 also reports the values of $\sigma_0^{stat.}$ extracted from the pseudo-experiments with no contributions due to the rare signals and the measurement of yield $N \pm \sigma_N^{stat.} \pm \sigma_N^{syst.}$ for each rare signal modes performed in the present analysis.

We obtained three rare signal modes with significance larger than 5σ, $B_s^0 \to K^-\pi^+$, $\Lambda_b^0 \to p\pi^-$, $\Lambda_b^0 \to pK^-$ with significances 8.2σ, 6.0σ and 11.5σ respectively.

mode	$N \pm \sigma_N^{stat.} \pm \sigma_N^{syst.}$	$\sigma_0^{stat.}$	α
$B^0 \to K^+K^-$	$61 \pm 25 \pm 35$	21	1.5σ
$B_s^0 \to \pi^+\pi^-$	$26 \pm 16 \pm 14$	11	1.5σ
$B_s^0 \to K^-\pi^+$	$230 \pm 34 \pm 16$	23	8.2σ
$\Lambda_b^0 \to p\pi^-$	$110 \pm 18 \pm 16$	9	6.0σ
$\Lambda_b^0 \to pK^-$	$156 \pm 20 \pm 11$	8	11.5σ

Table 12.6: Significance of the rare modes. The significance was estimated by combining the statistical uncertainty on the measurement of each rare mode using an ensemble of pseudo-experiments with no contributions from rare signal modes $\sigma_0^{stat.}$ and the systematic uncertainty $\sigma_N^{syst.}$. See text for details.

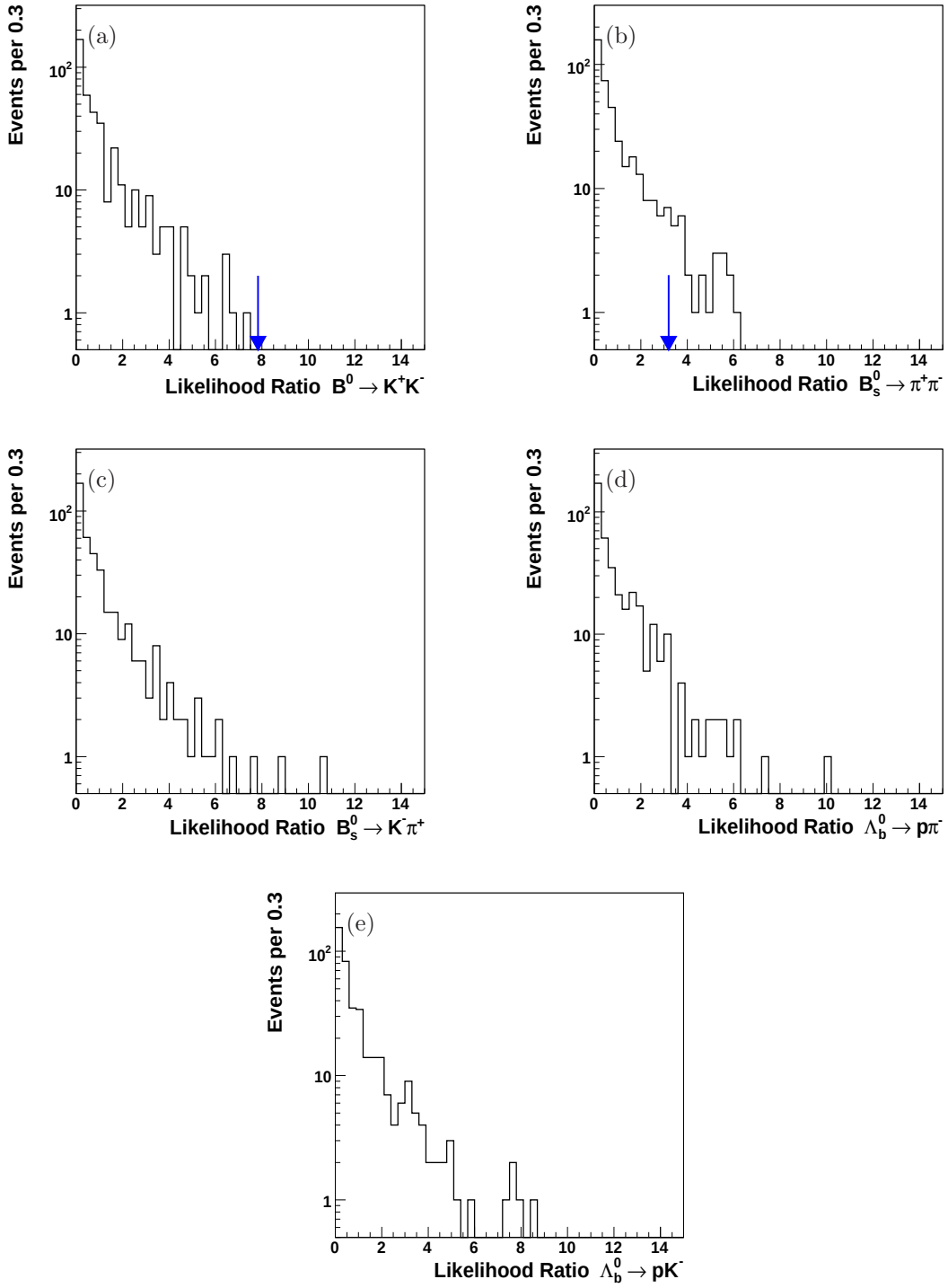


Figure 12.8: Likelihood Ratio distribution for $B^0 \to K^+K^-$ (a), $B_s^0 \to \pi^+\pi^-$ (b), $B_s^0 \to K^-\pi^+$ (c), $\Lambda_b^0 \to p\pi^-$ (d), $\Lambda_b^0 \to pK^-$ (e) mode. We 500 pseudo-experiments. The blue arrow shows the value of the Likelihood Ratio $-2\Delta\ln(\mathscr{L})$ determined with data (see third column of tab. 12.5). The Likelihood Ratio value for $B_s^0 \to K^-\pi^+$, $\Lambda_b^0 \to p\pi^-$ and $\Lambda_b^0 \to pK^-$ is out of the plot range.

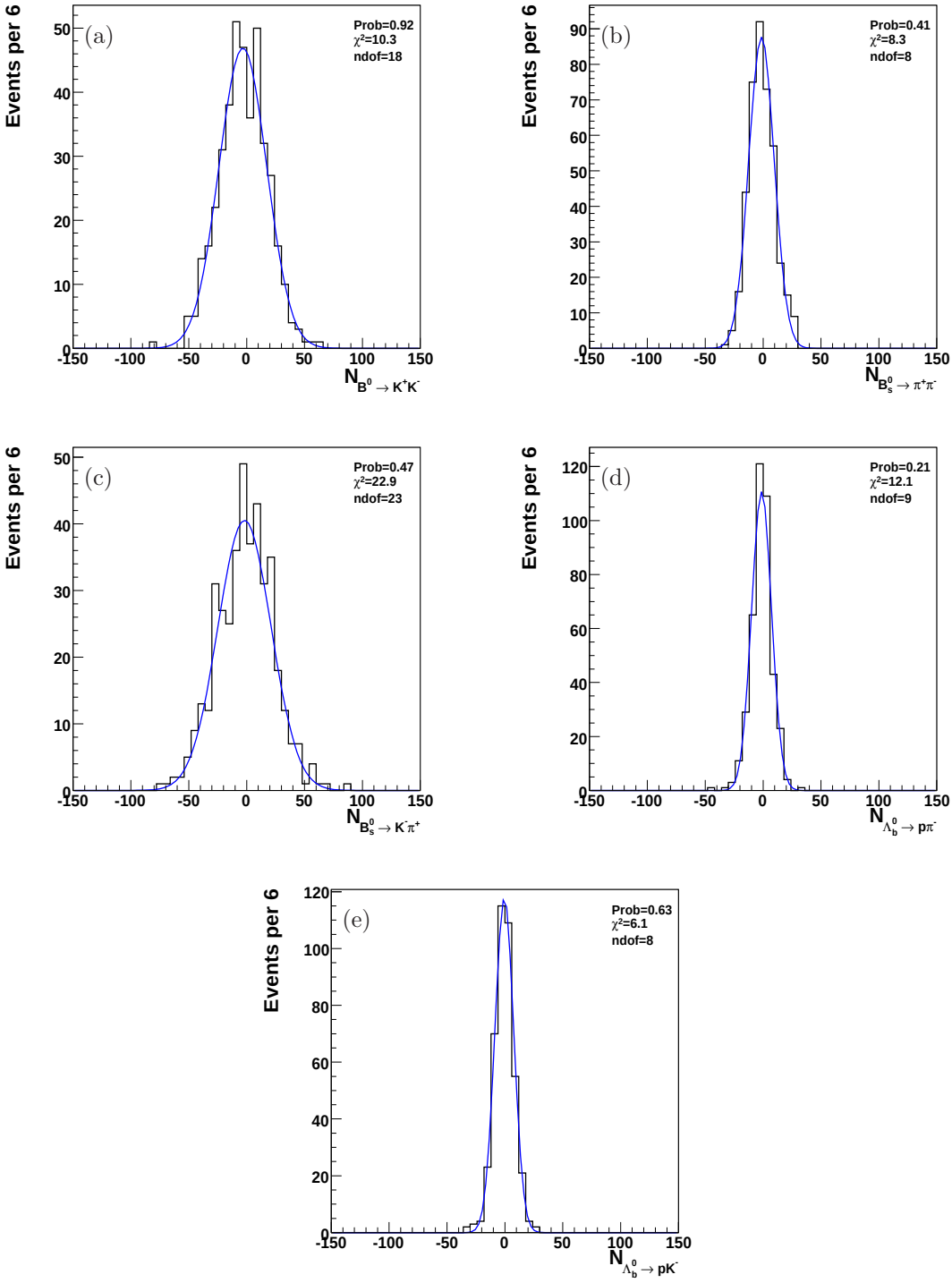


Figure 12.9: Distribution of the number of events for $B^0 \to K^+K^-$ (a), $B_s^0 \to \pi^+\pi^-$ (b), $B_s^0 \to K^-\pi^+$ (c), $\Lambda_b^0 \to p\pi^-$ (d), $\Lambda_b^0 \to pK^-$ (e) mode. We used an ensemble of 500 pseudo-experiments in which no contribution from rare signal modes was generated while the relative fraction of all the rare modes was left free to vary in each fit of composition.

Chapter 13

Results and discussion

This chapter presents the final results of this thesis and a discussion of their impact in the current experimental and theoretical picture.

13.1 Final results

Using the fit results from chap. 9, the efficiency corrections from chap. 10 and the systematic uncertainties from chap. 12 we obtain the measurements of branching fractions and time-integrated direct CP asymmetries of two-body $B^0_{(s)}$ decays into charmless, charged pseudo-scalar mesons at CDF with 1 fb^{-1} of data. The results are summarized in tab. 13.1.

The results include the first observation of the $B^0_s \to K^-\pi^+$ decay mode and a measurement of its branching fraction and of its direct CP asymmetry. This is the first direct CP measurement performed in the B^0_s meson system. Charmless decays of a b-baryon are also observed for the first time in the two modes $\Lambda^0_b \to p\pi^-$ and $\Lambda^0_b \to pK^-$. Interesting results are also obtained for the B^0 modes, including a word-class measurement of the direct CP asymmetry of $B^0 \to K^+\pi^-$.

In the next sections we discuss each measurement in detail. A discussion on the prospects for the future measurements at CDF is also included. For a better understanding we present the measurements divided in three groups: 1) measurements of rare decays modes with a focus on $B^0_s \to K^-\pi^+$; 2) measurements of the direct CP asymmetry in $B^0 \to K^+\pi^-$ and $B^0_s \to K^-\pi^+$, with a discussion about their comparison; 3) precise measurements of branching fractions of the $B^0 \to \pi^+\pi^-$ and $B^0_s \to K^+K^-$ decay modes.

13.2 Search for rare decay modes

The search for rare decay modes was performed using the tight selection (see chap. 8), optimized to maximize the probability of discovery and rate limit setting of the $B^0_s \to K^-\pi^+$ mode. The fit of composition allowed for the presence of any component of the form $B^0_{(s)} \to h^+h^{'-}$ and $\Lambda^0_b \to ph^-$ with the relative fraction as a free parameter. In the next sub-sections we present the results obtained from

Mode	$\mathcal{N}$	Quantity	Measurement	$\mathcal{B}(10^{-6})$
$B^0 \to K^+\pi^-$	4045 ± 84	$\frac{\mathcal{B}(\overline{B}^0\to K^-\pi^+)-\mathcal{B}(B^0\to K^+\pi^-)}{\mathcal{B}(\overline{B}^0\to K^-\pi^+)+\mathcal{B}(B^0\to K^+\pi^-)}$	-0.086 ± 0.023 ± 0.009	
$B^0 \to \pi^+\pi^-$	1121 ± 63	$\frac{\mathcal{B}(B^0\to\pi^+\pi^-)}{\mathcal{B}(B^0\to K^+\pi^-)}$	0.259 ± 0.017 ± 0.016	5.02 ± 0.33 ± 0.35
$B_s^0 \to K^+K^-$	1307 ± 64	$\frac{f_s}{f_d}\times\frac{\mathcal{B}(B_s^0\to K^+K^-)}{\mathcal{B}(B^0\to K^+\pi^-)}$	0.347 ± 0.020 ± 0.021	25.8 ± 1.5 ± 3.9
$B_s^0 \to K^-\pi^+$	230 ± 34 ± 16	$\frac{f_s}{f_d}\times\frac{\mathcal{B}(B_s^0\to K^-\pi^+)}{\mathcal{B}(B^0\to K^+\pi^-)}$	0.071 ± 0.010 ± 0.007	5.27 ± 0.74 ± 0.90
		$\frac{\mathcal{B}(\overline{B}_s^0\to K^+\pi^-)-\mathcal{B}(B_s^0\to K^-\pi^+)}{\mathcal{B}(\overline{B}_s^0\to K^+\pi^-)+\mathcal{B}(B_s^0\to K^-\pi^+)}$	0.39 ± 0.15 ± 0.08	
		$\frac{f_d}{f_s}\times\frac{\Gamma(\overline{B}^0\to K^-\pi^+)-\Gamma(B^0\to K^+\pi^-)}{\Gamma(\overline{B}_s^0\to K^+\pi^-)-\Gamma(B_s^0\to K^-\pi^+)}$	-3.00 ± 1.50 ± 0.22	
$B_s^0 \to \pi^+\pi^-$	26 ± 16 ± 14	$\frac{f_s}{f_d}\times\frac{\mathcal{B}(B_s^0\to\pi^+\pi^-)}{\mathcal{B}(B^0\to K^+\pi^-)}$	0.007 ± 0.004 ± 0.005	0.52 ± 0.29 ± 0.38 (< 1.3 @ 90% CL)
$B^0 \to K^+K^-$	61 ± 25 ± 35	$\frac{\mathcal{B}(B^0\to K^+K^-)}{\mathcal{B}(B^0\to K^+\pi^-)}$	0.020 ± 0.008 ± 0.006	0.39 ± 0.16 ± 0.12 (< 0.7 @ 90% CL)
$\Lambda_b^0 \to pK^-$	156 ± 20 ± 11	$\frac{\mathcal{B}(\Lambda_b^0\to p\pi^-)}{\mathcal{B}(\Lambda_b^0\to pK^-)}$	0.66 ± 0.14 ± 0.08	
$\Lambda_b^0 \to p\pi^-$	110 ± 18 ± 16			

Table 13.1: Results on data sample selected with loose cuts (top) and with tight cuts (bottom). Absolute branching fractions are normalized to the the world–average values $\mathcal{B}(B^0 \to K^+\pi^-) = (19.4 \pm 0.6) \times 10^{-6}$ and $f_s = (10.4 \pm 1.4)\%$ and $f_d = (39.8 \pm 1.0)\%$ [48]. The first quoted uncertainty is statistical, the second is systematic. $\mathcal{N}$ is the CP–averaged number of fitted events for each mode. For rare modes both systematic and statistical uncertainty on $\mathcal{N}$ was quoted while for abundant modes only statistical one.

the search for the rare modes: $B_s^0 \to K^-\pi^+$, $B_s^0 \to \pi^+\pi^-$, $B^0 \to K^+K^-$, $\Lambda_b^0 \to pK^-$ and $\Lambda_b^0 \to p\pi^-$.

13.2.1 $B_s^0 \to K^-\pi^+$

We report the first observation of the decay mode $B_s^0 \to K^-\pi^+$, with a yield:

$$\mathcal{N}(B_s^0 \to K^-\pi^+) = 230 \pm 34\ (stat.) \pm 16\ (syst.), \tag{13.1}$$

with a significance level 8.2σ. This corresponds to a relative branching fraction:

$$\frac{f_s}{f_d} \times \frac{\mathcal{B}(B_s^0 \to K^-\pi^+)}{\mathcal{B}(B^0 \to K^+\pi^-)} = 0.071 \pm 0.010\ (stat.) \pm 0.007\ (syst.), \tag{13.2}$$

where f_s/f_d is the ratio of production fractions of B_s^0 and B^0 mesons from the hadronization of a b-quark in $p\bar{p}$ collisions. Using the world-average values $\mathcal{B}(B^0 \to K^+\pi^-) = (19.4 \pm 0.6) \times 10^{-6}$ [48] and assuming for f_s/f_d the world-average value from $p\bar{p}$ and e^+e^- collisions, $f_s = (10.4 \pm 1.4)\%$, $f_d = (39.8 \pm 1.0)\%$ [48], we extract the following absolute branching fraction:

$$\mathcal{B}(B_s^0 \to K^-\pi^+) = (5.27 \pm 0.74\ (stat.) \pm 0.90\ (syst.)) \times 10^{-6}, \tag{13.3}$$

which is just below the current best limit, obtained from the previous version of the present analysis $\mathcal{B}(B_s^0 \to K^-\pi^+) < 5.6 \times 10^{-6}$ @ 90%CL [1].

Our result for $\mathcal{B}(B_s^0 \to K^-\pi^+)$ is at the lower end of current theoretical expectations from QCDF and pQCD approach, while the SCET approach shows a better agreement (see tab. 1.2). Beneke and Neubert [15] predict $\mathcal{B}(B_s^0 \to K^-\pi^+) = (10.2^{+6.0}_{-5.2}) \times 10^{-6}$ using the QCDF approach, in agreement

with the results of Sun, Zhu, and Du, who include further power corrections and contributions from electroweak annihilation [148]. Chiang and Zhou predict $\mathcal{B}(B_s^0 \to K^-\pi^+) = (5 \pm 1) \times 10^{-6}$, based on SU(3) flavor symmetries [149]. Similar values are predicted also by calculations based on pQCD, Ali et al. predict $\mathcal{B}(B_s^0 \to K^-\pi^+) = (7.6^{+3.3}_{-2.4}) \times 10^{-6}$ [16]. Yu, Li, and Lu expect $\mathcal{B}(B_s^0 \to K^-\pi^+) =$ (6.2–8.1) $\times 10^{-6}$, assuming the $70^\circ < \alpha < 130^\circ$ range for the CKM phase α [19]. Williamson and Zupan, using SCET, obtain $\mathcal{B}(B_s^0 \to K^-\pi^+) = (4.9 \pm 1.8) \times 10^{-6}$ [17] in agreement with our result.

A sizable reduction of the systematic uncertainty is expected, along with the statistical, as the data samples increase in size: the dominant sources of systematic uncertainty include the uncertainty on the kinematic templates of the combinatorial background, the uncertainty in the determination of dE/dx templates, the statistical uncertainty on the nominal values of $B^0_{(s)}$ meson masses used in the Likelihood, and the statistical uncertainty on the isolation efficiency (see fig. 12.6). These contributions are of statistical origin, thus expected to decrease as the size of calibration samples used to determine them increases.

With the full statistics expected in CDF Run II (5–6 fb^{-1} by year 2009) the branching fraction of $B_s^0 \to K^-\pi^+$ mode will provide relevant input for tuning of phenomenological models relative to the $B^0_{(s)} \to h^+h'^-$ decays. See also sec. 13.3.2 and 13.5.

13.2.2 $B_s^0 \to \pi^+\pi^-$

From the observed yield of $\mathcal{N}(B_s^0 \to \pi^+\pi^-) = 26 \pm 16\ (stat.)\ \pm 14\ (syst.)$ events, no evidence for the pure-annihilation decay $B_s^0 \to \pi^+\pi^-$ was found. We obtain the measurement of relative branching fraction:

$$\frac{f_s}{f_d} \times \frac{\mathcal{B}(B_s^0 \to \pi^+\pi^-)}{\mathcal{B}(B^0 \to K^+\pi^-)} = 0.007 \pm 0.004\ (stat.)\ \pm 0.005\ (syst.). \tag{13.4}$$

By normalizing the above result to the $B^0 \to K^+\pi^-$ branching fraction by using the world-average value $\mathcal{B}(B^0 \to K^+\pi^-) = (19.4 \pm 0.6) \times 10^{-6}$ [48], and by assuming for f_s/f_d the world-average value from $p\bar{p}$ and e^+e^- collisions, $f_s = (10.4 \pm 1.4)\%$, $f_d = (39.8 \pm 1.0)\%$ [48], we obtain the following absolute branching fraction:

$$\mathcal{B}(B_s^0 \to \pi^+\pi^-) = (0.52 \pm 0.29\ (stat.) \pm 0.38\ (syst.)) \times 10^{-6}. \tag{13.5}$$

Since the result is compatible with zero, we set a frequentist upper limit on the corresponding branching fraction based on Gaussian distributions of the fit pulls (see sec. 9.4.1) and the Likelihood-Ratio (LR) ordering, following Ref. [150]. Systematic uncertainties were added in quadrature to the statistical uncertainty for a proper inclusion of systematic effects in the extraction of the upper limit. The resulting 90% confidence level (CL) upper limit on the branching fraction of $B_s^0 \to \pi^+\pi^-$ mode is:

$$\mathcal{B}(B_s^0 \to \pi^+\pi^-) < 1.3 \cdot 10^{-6}\ @\ 90\%\ \text{CL}. \tag{13.6}$$

This result represents an improvement of approximately 20% with respect to the world-best limit, coming from the previous version of this analysis $\mathcal{B}(B_s^0 \to \pi^+\pi^-) < 1.7 \times 10^{-6}$ at 90% CL [1] and an improvement by more than two orders of magnitude with respect to the previous best limit $\mathcal{B}(B_s^0 \to \pi^+\pi^-) < 1.7 \times 10^{-4}$ at 90% CL [151]. The small change from the previous limit is due to the observed slight excess ($\approx 2\sigma\ (stat.)$).

Our central value is close to the expectations from recent calculations. Ali et al. predict $\mathcal{B}(B_s^0 \to \pi^+\pi^-) = (0.57^{+0.18}_{-0.16}) \times 10^{-6}$ within the PQCD approach [16], in the same approach Li, Lu, Xiao, and Yu calculate $\mathcal{B}(B_s^0 \to \pi^+\pi^-) = (0.42 \pm 0.06) \times 10^{-6}$, but with Sudakov resummation, and including contributions from electroweak and QCD penguin amplitudes [80]. Conversely, Beneke and Neubert, using QCDF, predict smaller values, $\mathcal{B}(B_s^0 \to \pi^+\pi^-) = (0.024^{+0.165}_{-0.024}) \times 10^{-6}$ [15], in agreement with Yang et al., that also used QCDF but with a different solution to avoid end-point divergences, obtaining $\mathcal{B}(B_s^0 \to \pi^+\pi^-) = (0.124 \pm 0.028) \times 10^{-6}$ [81].

The CDF experiment is currently the only one capable to search for this decay mode. With the continuous increase of the collected data sample it has the unique opportunity to obtain the first observation of a decay proceeding exclusively through annihilation topology. The prospects for the future are very interesting, with the statistics already available at CDF ≈ 2.5 fb^{-1} we will soon be able to to explore the region predicted by the pQCD approach.

13.2.3 $B^0 \to K^+K^-$

From the observed yield of $\mathcal{N}(B^0 \to K^+K^-) = 61 \pm 25\ (stat.)\ \pm 35\ (syst.)$ events, no evidence for the pure-annihilation $B^0 \to K^+K^-$ decay was found. We obtain the measurement of relative branching fraction:

$$\frac{\mathcal{B}(B^0 \to K^+K^-)}{\mathcal{B}(B^0 \to K^+\pi^-)} = 0.020 \pm 0.008\ (stat.)\ \pm 0.006\ (syst.). \tag{13.7}$$

By normalizing the above result to the world-average value $\mathcal{B}(B^0 \to K^+\pi^-) = (19.4 \pm 0.6) \times 10^{-6}$ [48], we obtain the following absolute branching fraction:

$$\mathcal{B}(B^0 \to K^+K^-) = (0.39 \pm 0.16\ (stat.) \pm 0.12\ (syst.)) \times 10^{-6}. \tag{13.8}$$

The precision and the central value of our result is comparable with the current measurements of B-Factories:

$$\mathcal{B}(B^0 \to K^+K^-) = \begin{cases} (0.04 \pm 0.15\ (stat.) \pm 0.08\ (syst.)) \times 10^{-6} & \textit{BABAR}\ (227\text{M}\ B\bar{B})\ [63] \\ (0.09^{+0.18}_{-0.13}\ (stat.) \pm 0.01\ (syst.)) \times 10^{-6} & \text{Belle}\ (449\text{M}\ B\bar{B})\ [65]. \end{cases} \tag{13.9}$$

Since the result is compatible with zero, we set a frequentist upper limit on the corresponding branching fraction following the procedure detailed for the $B_s^0 \to \pi^+\pi^-$ limit (see sec. 13.2.2). The resulting 90% CL upper limit on the branching fractions of $B^0 \to K^+K^-$ mode is

$$\mathcal{B}(B^0 \to K^+K^-) < 0.7 \cdot 10^{-6}\ @\ 90\%\ \text{CL}. \tag{13.10}$$

This result represents an improvement of approximately 60% with respect to the upper limit, coming from the previous version of this analysis $\mathcal{B}(B^0 \to K^+K^-) < 1.8 \times 10^{-6}$ at 90% CL [1]. It is close to B-Factories upper limits, $\mathcal{B}(B^0 \to K^+K^-) < 0.50 \times 10^{-6}$ at 90% CL from *BABAR* [63]. and $\mathcal{B}(B^0 \to K^+K^-) < 0.41 \times 10^{-6}$ at 90%CL from Belle [65].

The expected sensitivities are still far from probing the full range of theoretical expectations, which, however, are affected by large uncertainties: Beneke and Neubert, for instance, predict $\mathcal{B}(B^0 \to K^+K^-) = (0.013^{+0.087}_{-0.013}) \times 10^{-6}$ [15]. It is possible that the $B_s^0 \to \pi^+\pi^-$ decay mode will become visible in advance of the $B^0 \to K^+K^-$ mode.

13.2.4 $\Lambda_b^0 \to pK^-$ and $\Lambda_b^0 \to p\pi^-$

We report the first observation of decay modes $\Lambda_b^0 \to pK^-$ and $\Lambda_b^0 \to p\pi^-$, with yields:

$$\mathcal{N}(\Lambda_b^0 \to pK^-) = 156 \pm 20\ (stat.) \pm 11\ (syst.), \tag{13.11}$$

$$\mathcal{N}(\Lambda_b^0 \to p\pi^-) = 110 \pm 18\ (stat.) \pm 16\ (syst.), \tag{13.12}$$

with a significance level of 11.5σ for $\Lambda_b^0 \to pK^-$ mode and of 6σ for $\Lambda_b^0 \to p\pi^-$. The measurements of branching fractions and direct CP asymmetries need additional work: the $p_{\rm T}$ spectrum of Λ_b^0 baryon is different from the $p_{\rm T}$ spectrum of $B_{(s)}^0$ mesons, and a possible Λ_b^0 polarization could modify the efficiency factors and then the kinematic templates; the Λ_b^0 isolation efficiency is likely to be different from the $B_{(s)}^0$ efficiency; XFT efficiency for protons needs to be determined, as the detector-induced charge asymmetry between positively and negatively charged protons. This work is outside the scope of this analysis and it is the subject of a separate analysis. However we can easily extract from the current analysis the measurement of relative branching fraction, where all these effects cancel in the ratio:

$$\frac{\mathcal{B}(\Lambda_b^0 \to p\pi^-)}{\mathcal{B}(\Lambda_b^0 \to pK^-)} = 0.66 \pm 0.14\ (stat.) \pm 0.08\ (syst.). \tag{13.13}$$

This is in agreement with the prediction in [153].

CDF is currently the only experiment capable to perform the measurements of these decay modes. Future measurement of the branching fractions and direct CP asymmetries of $\Lambda_b^0 \to pK^-$ and $\Lambda_b^0 \to p\pi^-$ will provide relevant input for tuning phenomenological models and probing the CKM mechanism in the charmless decays of a b-baryon.

13.3 CP asymmetries

The measurement of the time-integrated direct CP asymmetries in the $B_{(s)}^0 \to h^+h'^-$ decays was one of the main goals of the present analysis since they offer an unique opportunity to probe the source of CP violation mechanism in the Standard Model. The direct CP asymmetry in the $B^0 \to K^+\pi^-$ decay mode was measured using the 'loose' selection which was specifically optimized for this purpose. The measurement of direct CP asymmetry in the $B_s^0 \to K^-\pi^+$ decay mode, instead, was performed using the 'tight' selection since the $B_s^0 \to K^-\pi^+$ was observed for the first time in this way. Below we present the results.

13.3.1 Direct CP asymmetry of $B^0 \to K^+\pi^-$

From the partial rate asymmetry between $\overline{B}^0 \to K^-\pi^+$ and $B^0 \to K^+\pi^-$ decays we obtain the direct CP asymmetry. In this measurement the flavor of the meson was not identified. We assumed that all $K^+\pi^-$ final states originate from B^0 decays, and all $K^-\pi^+$ final states originate from $\overline{B}^0$ decays and that they are initially produced in equal numbers. We therefore neglect a possible contribution from the doubly-Cabibbo-suppressed (DCS) decays ($B^0 \to K^-\pi^+$ and $\overline{B}^0 \to K^+\pi^-$), of possible asymmetries in flavor mixing ($B^0 \to \overline{B}^0 \to K^-\pi^+$ and $\overline{B}^0 \to B^0 \to K^+\pi^-$), and of their combined effect, since their size is not appreciable at the current level of experimental accuracy. The measured

asymmetry is:

$$\mathcal{A}_{\rm CP}(B^0 \to K^+\pi^-) = \frac{\mathcal{B}(\overline{B}^0 \to K^-\pi^+) - \mathcal{B}(B^0 \to K^+\pi^-)}{\mathcal{B}(\overline{B}^0 \to K^-\pi^+) + \mathcal{B}(B^0 \to K^+\pi^-)} = -0.086 \pm 0.023\ (stat.) \pm 0.009\ (syst.). \tag{13.14}$$

Our measurement is different from 0 by 3.5σ (statistical and systematic uncertainties added in quadrature) and it is compatible with the current world average (see fig. 13.1). The latest update of HFAG [48] reports the most recent results:

$$\mathcal{A}_{\rm CP}(B^0 \to K^+\pi^-) = \begin{cases} -0.107 \pm 0.018\ (stat.)^{+0.007}_{-0.004}\ (syst.) & \textit{BABAR}\ (383\text{M}\ B\bar{B})\ [155] \\ -0.093 \pm 0.018\ (stat.) \pm 0.008\ (syst.) & \text{Belle}\ (532\text{M}\ B\bar{B})\ [156]. \end{cases} \tag{13.15}$$

The precision of our measurement is very close.

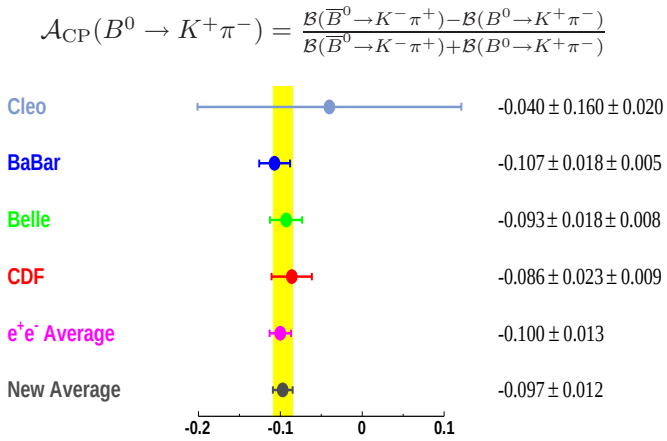


Figure 13.1: Current measurements of $\mathcal{A}_{\rm CP}(B^0 \to K^+\pi^-)$ reported on HFAG [48]. The yellow band is the world average.

The systematic uncertainty is promising for future extension of this measurement to the new large samples already being accumulated by CDF. In fact, the main contributions to the systematics are the uncertainty in the determination of dE/dx templates and the uncertainty associated to our limited knowledge of nominal input masses of the b-hadrons (see fig. 12.5). Their impact is already less than $\mathcal{O}(1\%)$, which is at the same level of the current measurements at the B-Factories, and can be reduced with a larger calibration samples for the dE/dx templates and with an improved measurements of the nominal input masses. The statistical uncertainty, which currently is still the dominant uncertainty in this measurement, is expected to decrease by a factor of at least 2.5 with the full Run II sample (5–6 fb^{-1}).

Our measurement strengthens the statistical significance of the deviation with respect to the direct CP asymmetry in the its charged partner $\mathcal{A}_{\rm CP}(B^+ \to K^+\pi^0) = +0.047 \pm 0.026$ [48]. In the past, several authors argued that the asymmetries in these two modes should be equal in the Standard Model due to isospin symmetry [12, 13, 14], but today there are proposed explanations within the Standard Model

[70, 71, 72] (see sec. 1.7.3). Explaining these direct CP asymmetries in the Standard Model is still difficult and subject to sizeable uncertainties. The question about the possible non-Standard Model origin of this large direct CP violation asymmetry observed in $B^0 \to K^+\pi^-$ decay is still open. At present, the most promising way to probe the source of this CP violation seems to be the comparison of this asymmetry with the same measurement in its U-spin partner $B_s^0 \to K^-\pi^+$. We report below the measurement of this quantity.

13.3.2 Direct CP asymmetry of $B_s^0 \to K^-\pi^+$

From the partial rate asymmetry between $\overline{B}_s^0 \to K^+\pi^-$ and $B_s^0 \to K^-\pi^+$ decays we obtain the first measurement of the direct CP asymmetry in a B_s^0 meson decay. As in the measurement of $\mathcal{A}_{\rm CP}(B^0 \to K^+\pi^-)$ we neglected the contribution of doubly-Cabibbo-suppressed (DCS) decays ($B_s^0 \to K^+\pi^-$ and $\overline{B}_s^0 \to K^-\pi^+$), of possible asymmetries in flavor mixing ($B_s^0 \to \overline{B}_s^0 \to K^+\pi^-$ and $\overline{B}_s^0 \to B_s^0 \to K^-\pi^+$), and of their combined effect. The measured asymmetry is

$$\mathcal{A}_{\rm CP}(B_s^0 \to K^-\pi^+) = \frac{\mathcal{B}(\overline{B}_s^0 \to K^+\pi^-) - \mathcal{B}(B_s^0 \to K^-\pi^+)}{\mathcal{B}(\overline{B}_s^0 \to K^+\pi^-) + \mathcal{B}(B_s^0 \to K^-\pi^+)} = 0.39 \pm 0.15\ (stat.)\ \pm 0.08\ (syst.). \tag{13.16}$$

Our measurement is compatible with 0 at 2.3σ (taking into account statistical and systematic uncertainties), but it is also compatible with the large positive CP asymmetry predicted by several models. Because of the current large uncertainty both of measurement and the expectations, the measured $\mathcal{A}_{\rm CP}(B_s^0 \to K^-\pi^+)$ is in agreement with the values predicted by several and different approaches. Ali et al. predict $\mathcal{A}_{\rm CP}(B_s^0 \to K^-\pi^+) = (+24.1^{+3.6+3.0+1.2}_{-3.9-3.3-2.3})\%$ [16] in the pQCD framework. Williamson and Zupan estimate $\mathcal{A}_{\rm CP}(B_s^0 \to K^-\pi^+) = (+20 \pm 17 \pm 19 \pm 5)\%$ [17] in the SCET approach. Although the QCDF prediction from Beneke and Neubert [15] $\mathcal{A}_{\rm CP}(B_s^0 \to K^-\pi^+) = (-6.7^{+2.2+2.9+0.4+15.2}_{-2.1-3.1-0.2-15.5})\%$ gives a central value with a negative sign, the prediction and the experimental measurement are marginally compatible because of large uncertainties.

The comparison of $\mathcal{A}_{\rm CP}(B_s^0 \to K^-\pi^+)$ with other measured CP-asymmetries in $B_{(s)}^0 \to h^+h'^-$ decays is more stringent in performing tests of Standard Model or in probing New Physics effects because of reduced uncertainties. For example, if we neglect the W-exchange and penguin-annihilation diagrams contributing to $B_{(s)}^0 \to h^+h'^-$ decays (see sec. 1.7.1), the decay rates and CP-asymmetries in the $B_s^0 \to K^-\pi^+$ and $B^0 \to \pi^+\pi^-$ decays are related by SU(3) symmetry. In this limit [7, 74] we expect:

$$\mathcal{A}_{\rm CP}(B_s^0 \to K^-\pi^+) = \mathcal{A}_{\rm CP}^{\rm dir}(B^0 \to \pi^+\pi^-), \tag{13.17}$$

where $\mathcal{A}_{\rm CP}^{\rm dir}(B^0 \to \pi^+\pi^-)$ is the direct CP asymmetry of the $B^0 \to \pi^+\pi^-$ decay. Deviations from eq. (13.17) are expected to be of the size of U-spin symmetry breaking. The current experimental measurements of $\mathcal{A}_{\rm CP}^{\rm dir}(B^0 \to \pi^+\pi^-)$ are not fully in agreement (see also sec. 1.7.2):

$$\mathcal{A}_{\rm CP}^{\rm dir}(B^0 \to \pi^+\pi^-) = \begin{cases} +0.21 \pm 0.09\ (stat.) \pm 0.02\ (syst.) & \textit{BABAR}\ [61] \\ +0.55 \pm 0.08\ (stat.) \pm 0.05\ (syst.) & \text{Belle}\ [62]. \end{cases} \tag{13.18}$$

However, eq. (13.17) seems in agreement with currently available data. A more precise measurement of direct CP-asymmetry in $B_s^0 \to K^-\pi^+$ could shed more light on this controversial issue, possibly

together with a third measurement of $\mathcal{A}_{\rm CP}^{\rm dir}(B^0 \to \pi^+\pi^-)$ from CDF from a time-dependent extension of this analysis.

Gronau-Lipkin test

The $B^0 \to K^+\pi^-$ and $B_s^0 \to K^-\pi^+$ branching fractions are very different due to the different strong and weak phases entering in the tree and penguin amplitudes, as discussed in chap. 1. However, as shown by Gronau [7], the two relevant products of the CKM matrix elements entering in the expressions for the direct CP asymmetries in these decays are equal, and, as stressed by Lipkin [8] subsequently, the final states in these decays are charge conjugates, and the strong interactions being charge-conjugation invariant, the direct CP asymmetry in $B_s^0 \to K^-\pi^+$ can be related to the well-measured CP asymmetry in the decay $B^0 \to K^+\pi^-$ using U-spin symmetry. In this symmetry limit, we have [7, 8]:

$$\Gamma(B_s^0 \to K^-\pi^+) - \Gamma(\overline{B}_s^0 \to K^+\pi^-) = \Gamma(\overline{B}^0 \to K^-\pi^+) - \Gamma(B^0 \to K^+\pi^-), \tag{13.19}$$

$$\mathcal{A}_{\rm CP}(B_s^0 \to K^-\pi^+) = -\mathcal{A}_{\rm CP}(B^0 \to K^+\pi^-) \times \frac{\mathcal{B}(B^0 \to K^+\pi^-)}{\mathcal{B}(B_s^0 \to K^-\pi^+)} \times \frac{\tau(B_s^0)}{\tau(B^0)}. \tag{13.20}$$

Following suggestions in the literature, these equations can be tested to search for possible New Physics effects, which would very likely violate them. To that end, one can define the following two parameters (using eq. (1.57) for the definition of CP asymmetry):

$$R_3 \equiv \frac{\Gamma(\overline{B}^0 \to K^-\pi^+) - \Gamma(B^0 \to K^+\pi^-)}{\Gamma(\overline{B}_s^0 \to K^+\pi^-) - \Gamma(B_s^0 \to K^-\pi^+)}, \tag{13.21}$$

$$\Delta \equiv \frac{\mathcal{A}_{\rm CP}(B^0 \to K^+\pi^-)}{\mathcal{A}_{\rm CP}(B_s^0 \to K^-\pi^+)} + \frac{\mathcal{B}(B_s^0 \to K^-\pi^+)}{\mathcal{B}(B^0 \to K^+\pi^-)} \times \frac{\tau(B^0)}{\tau(B_s^0)}. \tag{13.22}$$

The Standard Model predicts $R_3 = -1$ and $\Delta = 0$ assuming U-spin symmetry. Both Lipkin and Gronau argue in their papers that the U-spin breaking has a small influence on these relations. In a very recent paper [16] Ali et al. confirm the Gronau-Lipkin relations using the pQCD approach. In fact, they predict how good quantitatively this symmetry is in the ratios R_3 and Δ, using a detailed dynamical theory of the U-spin symmetry violation. They found that these quantities are quite reliably calculable [16]:

$$R_3 = -1.00^{+0.10}_{-0.10}, \;\; \Delta = -0.00^{+0.07}_{-0.05}, \tag{13.23}$$

confirming the smallness of U-spin breaking effects.

We performed the test by measuring the R_3 quantity. From the partial rate $\overline{B}_s^0 \to K^+\pi^-$, $B_s^0 \to K^-\pi^+$, $\overline{B}^0 \to K^-\pi^+$ and $B^0 \to K^+\pi^-$decays, we extract the following measurement:

$$\frac{f_d}{f_s} \times \frac{\Gamma(\overline{B}^0 \to K^-\pi^+) - \Gamma(B^0 \to K^+\pi^-)}{\Gamma(\overline{B}_s^0 \to K^+\pi^-) - \Gamma(B_s^0 \to K^-\pi^+)} = -3.00 \pm 1.50 \; (\textit{stat.}) \; \pm 0.22 \; (\textit{syst.}), \tag{13.24}$$

where f_s/f_d is the ratio of production fractions of B_s^0 and B^0 mesons from the hadronization of a b-quark in $p\bar{p}$ collisions. Assuming for f_s/f_d the world-average value from $p\bar{p}$ and e^+e^- collisions, f_s

$= (10.4 \pm 1.4)\%$, $f_d = (39.8 \pm 1.0)\%$ [48], we obtain for R_3:

$$R_3 = \frac{\Gamma(\overline{B}^0 \to K^-\pi^+) - \Gamma(B^0 \to K^+\pi^-)}{\Gamma(\overline{B}^0_s \to K^+\pi^-) - \Gamma(B^0_s \to K^-\pi^+)} = -0.78 \pm 0.39\ (stat.) \pm 0.12\ (syst.). \tag{13.25}$$

The measured value for R_3 favors the Standard Model over New Physics scenarios, but the experimental uncertainty currently is too large to make a strong statement.

It is interesting to use eq. (13.22) to extract the Standard Model expectation for $\mathcal{A}_{\rm CP}(B^0_s \to K^-\pi^+)$. If we use the world average for $\mathcal{A}_{\rm CP}(B^0 \to K^+\pi^-) = -0.097 \pm 0.012$ [48] (including the measurement of this thesis), assume $\tau(B^0_s)/\tau(B^0) = 1$, and use the ratio of branching fractions measured in this thesis $\frac{\mathcal{B}(B^0_s \to K^-\pi^+)}{\mathcal{B}(B^0 \to K^+\pi^-)} = 0.272 \pm 0.038\ (stat.) \pm 0.046\ (syst.)$, and $\Delta = -0.00^{+0.07}_{-0.05}$ from eq. (13.23) (extracted from Ref. [16]) we obtain the prediction:

$$\mathcal{A}_{\rm CP}(B^0_s \to K^-\pi^+)|^{\rm SM} = 0.36^{+0.13}_{-0.11}, \tag{13.26}$$

which is compatible with our measurement.

The measurements of $\mathcal{B}(B^0_s \to K^-\pi^+)$ and of $\mathcal{A}_{\rm CP}(B^0_s \to K^-\pi^+)$ performed in this thesis seem to favor the Standard Model and in particular are in agreement with the Gronau-Lipkin relation which connect the branching fractions and direct CP asymmetries of $B^0_s \to K^-\pi^+$ and $B^0 \to K^+\pi^-$ decays.

Prospects

Although measurements are not extremely accurate at present, the situation will greatly improve with full CDF Run II samples (5–6 fb^{-1} by year 2009). In the assumption that the Gronau-Lipkin relation is true, we extracted the expectation of quantity $\sigma(\mathcal{A}_{\rm CP}(B^0_s \to K^-\pi^+))/\mathcal{A}_{\rm CP}(B^0_s \to K^-\pi^+)$ where $\sigma(\mathcal{A}_{\rm CP}(B^0_s \to K^-\pi^+))$ is the statistical uncertainty on the measurement of $\mathcal{A}_{\rm CP}(B^0_s \to K^-\pi^+)$, which is independent on the true value of this observable. Figure 13.2 reports this quantity as a function of the integrated luminosity. To observe a significant value of $\mathcal{A}_{\rm CP}(B^0_s \to K^-\pi^+)$ we do not need full Run II statistics. Using less than 4 fb^{-1} it will possible to observe at 5σ the CP asymmetry in $B^0_s \to K^-\pi^+$ in the Standard Model hypothesis. Conversely, observation of a ~ 0 asymmetry would be a signal of New Physics with high statistical significance.

13.4 Precision branching fractions

The sample selected with loose cuts, optimized for the measurement of $\mathcal{A}_{\rm CP}(B^0 \to K^+\pi^-)$, also provides good measurements of the branching fractions of the "large yield" modes $B^0 \to \pi^+\pi^-$ and $B^0_s \to K^+K^-$.

13.4.1 $B^0 \to \pi^+\pi^-$

From the observed yields of $\mathcal{N}(B^0 \to \pi^+\pi^-) + \mathcal{N}(\overline{B}^0 \to \pi^+\pi^-)$ 1121 ± 63 decays and $\mathcal{N}(B^0 \to K^+\pi^-) + \mathcal{N}(\overline{B}^0 \to K^-\pi^+) = 4045 \pm 84$ decays we measured the ratio of branching fractions:

$$\frac{\mathcal{B}(B^0 \to \pi^+\pi^-)}{\mathcal{B}(B^0 \to K^+\pi^-)} = 0.259 \pm 0.017\ (stat.) \pm 0.016\ (syst.). \tag{13.27}$$

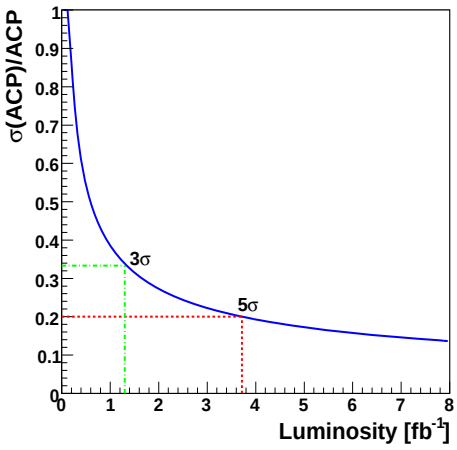


Figure 13.2: Expectation for the ratio between the statistical uncertainty $\sigma(\mathcal{A}_{\rm CP}(B_s^0 \to K^-\pi^+))$ and $\mathcal{A}_{\rm CP}(B_s^0 \to K^-\pi^+)$ as a function of integrated luminosity. This expectation is independent of the true value for $\mathcal{A}_{\rm CP}(B_s^0 \to K^-\pi^+)$ if we assume the Gronau-Lipkin relation true.

BABAR quotes only absolute branching fractions, while Belle complements its measurement also quoting the ratio of branching fractions $\frac{\mathcal{B}(B^0\to\pi^+\pi^-)}{\mathcal{B}(B^0\to K^+\pi^-)} = 0.26 \pm 0.01\ (stat.) \pm 0.01\ (syst.)$ [64] allowing a direct comparison with our measurement. Using the world-average value $\mathcal{B}(B^0 \to K^+\pi^-) = (19.4 \pm 0.6) \times 10^{-6}$ [48] we obtain the following absolute branching fraction:

$$\mathcal{B}(B^0 \to \pi^+\pi^-) = (5.02 \pm 0.33\ (stat.)\ \pm 0.35\ (syst.)) \times 10^{-6}. \tag{13.28}$$

This result is compatible with the other existing experiments (see also fig. 13.3):

$$\mathcal{B}(B^0 \to \pi^+\pi^-) \quad = \quad \begin{cases} (5.5 \pm 0.4\ (stat.)\ \pm 0.3\ (syst.)) \times 10^{-6} & \textit{BABAR}\ (227\text{M}\ B\bar{B})\ [63] \\ (5.1 \pm 0.2\ (stat.)\ \pm 0.2\ (syst.)) \times 10^{-6} & \text{Belle}\ (449\text{M}\ B\bar{B})\ [64]. \end{cases} \tag{13.29}$$

The agreement of this delicate measurement with the world average is a very important cross check of the validity of the entire analysis described in this thesis, providing a convincing evidence of the quality of the fit of composition used to disentangle the individual signal modes. It is worth noting that the invariant $\pi\pi$-mass distributions of the $B_s^0 \to K^+K^-$ and $B^0 \to \pi^+\pi^-$ modes overlap completely (see fig. 4.6). As a consequence, the relative fraction of $B^0 \to \pi^+\pi^-$ with respect to the one of $B_s^0 \to K^+K^-$ is entirely determined by the dE/dx information. Any spurious enhancement(reduction) of the estimated $B_s^0 \to K^+K^-$ contribution due to an improper use of the dE/dx information would decrease(increase) the $B^0 \to \pi^+\pi^-$ contribution, resulting in an incorrect result for the ratio (13.27).

Besides its rôle as cross-check, this result is interesting in itself, especially in perspective if future extension of the measurement to the full Run II statistics. We expect a reduction of a factor of three of the statistical uncertainty on this ratio. The main contributions to the systematics are the uncertainty in the determination of dE/dx templates and the uncertainty associated to our limited knowledge of nominal input masses of the b-hadrons (see fig. 12.5). Their impact can be reduced

with a larger calibration samples for the dE/dx templates and with an improved measurements of the nominal input masses. It is therefore likely that CDF will produce in the future the world's best measurement of $\frac{\mathcal{B}(B^0\to\pi^+\pi^-)}{\mathcal{B}(B^0\to K^+\pi^-)}$.

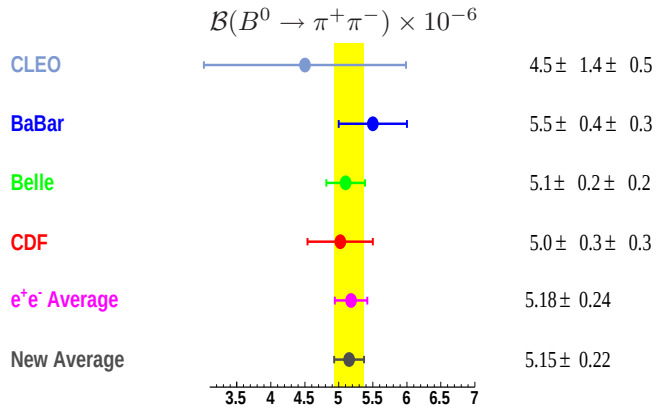


Figure 13.3: Current measurements of $\mathcal{B}(B^0 \to \pi^+\pi^-) \times 10^{-6}$ reported on HFAG [48]. The yellow band is the world average.

13.4.2 $B_s^0 \to K^+K^-$

From the observed yields of $\mathcal{N}(B_s^0 \to K^+K^-) + \mathcal{N}(\overline{B}_s^0 \to K^+K^-) = 1307 \pm 64$ decays and $\mathcal{N}(B^0 \to K^+\pi^-) + \mathcal{N}(\overline{B}^0 \to K^-\pi^+) = 4045 \pm 84$ decays we measured the following ratio of branching fractions:

$$\frac{f_s}{f_d} \times \frac{\mathcal{B}(B_s^0 \to K^+K^-)}{\mathcal{B}(B^0 \to K^+\pi^-)} = 0.347 \pm 0.020\ (stat.) \pm 0.021\ (syst.), \tag{13.30}$$

where f_s/f_d is the ratio of production fractions of B_s^0 and B^0 mesons from the hadronization of a b-quark in $p\bar{p}$ collisions. This measurement is based on the following assumptions (see sec. 10.2.1):

- the $B_s^0 \to K^+K^-$ mode is 100% "short" eigenstate ($B_s^{\rm L}$ CP-even);
- $\Delta\Gamma_s/\Gamma_s = 0.12 \pm 0.06$ as by Standard Model expectation [52];
- equal widths for B_s^0 and B^0 mesons $\Gamma_s = \Gamma_d$.

Using the world-average values $\mathcal{B}(B^0 \to K^+\pi^-) = (19.4 \pm 0.6) \times 10^{-6}$ [48] and assuming for f_s/f_d the world-average value from $p\bar{p}$ and e^+e^- collisions, $f_s = (10.4 \pm 1.4)\%$, $f_d = (39.8 \pm 1.0)\%$ [48], we obtain the absolute branching fraction:

$$\mathcal{B}(B_s^0 \to K^+K^-) = (25.8 \pm 1.5\ (stat.)\ \pm 3.9\ (syst.)) \times 10^{-6}, \tag{13.31}$$

in agreement with the determination from the first version of this analysis $\mathcal{B}(B_s^0 \to K^+K^-) = (33 \pm 5.7 \pm 6.7) \times 10^{-6}$ [1]. In the measurement of the absolute branching fraction the contribution of the

systematic component is larger than the statistical, due to the 14% uncertainty in the determination of $f_s/f_d = 0.261 \pm 0.036$ [48], which is the dominant source of uncertainty in the evaluation of this measurement. If we look at the measurement of the relative branching fraction of eq. (13.30) the systematic and statistical components have the same size and the total uncertainty is just 8%. In the relative measurement the dominant sources of systematic uncertainty include the statistical uncertainty in the determination of PID probability density functions, the statistical uncertainty on the isolation efficiency and the statistical uncertainty on the XFT-bias correction (see fig. 12.5). All these uncertainties are of statistical origin, thus expected to decrease as the size of calibration samples used to determine them increases.

This result for $\mathcal{B}(B_s^0 \to K^+K^-)$ is in agreement with the current theoretical expectations. Beneke and Neubert [15] predict $\mathcal{B}(B_s^0 \to K^+K^-) = (22.7^{+27.5}_{-12.9}) \times 10^{-6}$ in the QCDF approach. Chiang and Zhou predict $\mathcal{B}(B_s^0 \to K^+K^-) = (19 \pm 4) \times 10^{-6}$, based on SU(3) flavor symmetries [149]. Similar values are predicted also by calculations based on pQCD: Ali et al. predict $\mathcal{B}(B_s^0 \to K^+K^-) = (13.6^{+8.9}_{-6.8}) \times 10^{-6}$ [16]. Williamson and Zupan, using the SCET approach, claim the most accurate prediction $\mathcal{B}(B_s^0 \to K^+K^-) = (18.2 \pm 6.8) \times 10^{-6}$ [17], also in agreement with our result.
As mentioned also in sec. 1.7.6, Descotes-Genon, Matias, and Virto recently proposed a new calculation of $\mathcal{B}(B_s^0 \to K^+K^-)$ which complements the QCDF expansion with SU(3) symmetry relations to control, for the first time also the $1/m_b$ corrections [76]. The $B_s^0 \to K^+K^-$ decay rate is connected to the $B^0 \to K^0\bar{K}^0$ decay rate. The resulting prediction (in Standard Model assumptions) $\mathcal{B}(B_s^0 \to K^+K^-) = (20 \pm 9) \times 10^{-6}$ is also in good agreement with our result.

Extraction of γ from $B_s^0 \to K^+K^-$ and $B^0 \to \pi^+\pi^-$

Ref. [20] describes one of several examples in the literature of the importance of the measurement of the $B_s^0 \to K^+K^-$ branching fraction. In this section we will briefly summarize the discussion in [20]. Since the author used a slightly outdated result of this analysis for $\mathcal{B}(B_s^0 \to K^+K^-) = 24.4 \pm 1.4\ (stat.) \pm 4.6\ (syst.)$ [2], all numbers in this section, estimated with the experimental input of $\mathcal{B}(B_s^0 \to K^+K^-)$, refer to this outdated measurement, but for the purpose of illustrating the consequence of the result of this thesis, this is completely equivalent to the available result.

In the Standard Model, using the unitarity of the CKM matrix, the transition amplitude of the $B^0 \to \pi^+\pi^-$ decay can be written as in eq. (1.104), as a function of γ, λ, $\mathcal{C}$, ϕ_d and $de^{i\theta}$. γ is the corresponding angle of the UT, λ the parameter of the Wolfenstein expansion of the CKM matrix, $\mathcal{C}$ denotes a CP-conserving strong amplitude governed by the tree contributions, while the CP-conserving hadronic parameter $de^{i\theta}$ measures the ratio of penguin to tree amplitudes. The CP asymmetries using the same notation as a functions of these parameters take the following form:

$$\mathcal{A}_{\rm CP}^{\rm dir}(B_d \to \pi^+\pi^-) = G_1(d, \theta; \gamma) \tag{13.32}$$

$$\mathcal{A}_{\rm CP}^{\rm mix}(B_d \to \pi^+\pi^-) = G_2(d, \theta; \gamma, \phi_d); \tag{13.33}$$

where ϕ_d is the CP-violating B^0–$\bar{B}^0$ mixing phase, which is given by 2β in the SM, with β denoting another UT angle. This phase has been measured at the B-Factories with the help of the "golden" decay mode $B^0 \to J/\psi K_{\rm S}$ [48]:

$$\phi_d = (42.6 \pm 2)^\circ. \tag{13.34}$$

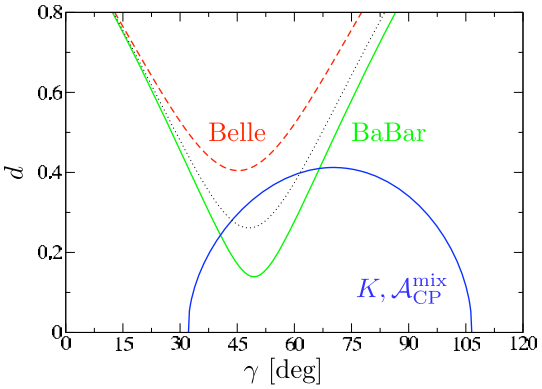


Figure 13.4: The contours in the γ–d plane that follow from the central values of the *BABAR* and Belle measurements of the CP asymmetries of the $B^0 \to \pi^+\pi^-$ channel and the ratio of the CP-averaged $B^0 \to \pi^+\pi^-$, $B_s^0 \to K^+K^-$ branching fractions. The dotted line corresponds to the HFAG average for the direct CP violation in $B^0 \to \pi^+\pi^-$. The figure has been extracted from Ref. [20].

The general expressions in eq. (13.32) and eq. (13.33) allow to eliminate the strong phase θ, and to evaluate d as a function of γ. Figure 13.4 from Ref. [20], shows the corresponding contours for the central values of the *BABAR* and Belle results in eq. (1.111) and eq. (1.112). In order to guide the eye, the figure also includes the contour (dotted line) representing the central value of the HFAG average $\mathcal{A}_{CP}^{dir}(B_d \to \pi^+\pi^-) = +0.38 \pm 0.07$ for the direct CP violation in $B^0 \to \pi^+\pi^-$ [48]. These contours are exactly valid in the Standard Model.

In analogy to eq. (1.104), the corresponding decay amplitude for $B_s^0 \to K^+K^-$ decays can be written as a function of a second set of parameters γ, λ, $\mathcal{C}'$, ϕ_s and $d'e^{i\theta'}$ (see eq. (1.124). $\mathcal{C}'$ and $d'e^{i\theta'}$ are the $B_s^0 \to K^+K^-$ counterparts of the $B^0 \to \pi^+\pi^-$ parameters $\mathcal{C}$ and $de^{i\theta}$, respectively. In analogy to $B^0 \to \pi^+\pi^-$, the CP-asymmetries are function of these parameters:

$$\mathcal{A}_{CP}^{dir}(B_s^0 \to K^+K^-) = G_1'(d', \theta'; \gamma) \tag{13.35}$$

$$\mathcal{A}_{CP}^{mix}(B_s^0 \to K^+K^-) = G_2'(d', \theta'; \gamma, \phi_s), \tag{13.36}$$

ϕ_s in the Standard Model is expected to be small (see sec. 1.7.6) and then it is assumed equal to 0 in eq. (13.36). If we apply the U-spin symmetry, we obtain the following relations [5]:

$$d' = d, \quad \theta' = \theta. \tag{13.37}$$

As was also pointed out in Ref. [5], these relations are not affected by factorizable U-spin-breaking corrections, i. e., the relevant form factors and decay constants cancel. Since the CP asymmetries of the $B_s^0 \to K^+K^-$ decay have not yet been measured, Ref. [20] used the CP-averaged branching fractions ratio between $B_s^0 \to K^+K^-$ and $B^0 \to \pi^+\pi^-$ decay modes for the determination of γ, in place of (13.35) and (13.36). This implies the presence of additional uncertainties due to the limited knowledge of form factors and decay constants in the extraction of the additional contour in the γ–d plane to solve the system. These quantities can be extracted from the theory and allows to extract γ.

For this purpose it is useful to introduce the quantity

$$K = \frac{1}{\epsilon}\left|\frac{\mathcal{C}}{\mathcal{C}'}\right|^2\left[\frac{m_{B_s^0}}{m_{B^0}}\,\frac{\Phi(m_\pi/m_{B^0}, m_\pi/m_{B^0})}{\Phi(m_K/m_{B_s^0}, m_K/m_{B_s^0})}\,\frac{\tau_{B^0}}{\tau_{B_s^0}}\right]\left[\frac{\mathcal{B}(B_s^0\to K^+K^-)}{\mathcal{B}(B^0\to\pi^+\pi^-)}\right], \tag{13.38}$$

where $\epsilon \equiv \frac{\lambda^2}{1-\lambda^2} = 0.05$, and where

$$\Phi(x,y) \equiv \sqrt{[1-(x+y)^2]\,[1-(x-y)^2]}, \tag{13.39}$$

is the $B \to PP$ phase-space function, and the $\tau_{B^0_{(s)}}$ are the $B^0_{(s)}$ lifetimes. Applying the relations in eq. (13.37), K becomes

$$K = \frac{1}{\epsilon^2}\left[\frac{\epsilon^2 + 2\epsilon d\cos\theta\cos\gamma + d^2}{1 - 2d\cos\theta\cos\gamma + d^2}\right]. \tag{13.40}$$

Combining K with $\mathcal{A}_{\rm CP}^{\rm mix}(B^0\to\pi^+\pi^-)$, which both depend on $d\cos\theta$, Ref. [20] obtains another contour in the γ–d plane. The intersection of this contour with the previous one allows to determine γ. In order to determine K from the CP-averaged branching ratios, the U-spin-breaking corrections to the ratio $|\mathcal{C}'/\mathcal{C}|$ (which equals 1 in the strict U-spin limit) must be determined. In contrast to the U-spin relations in eq. (13.37), $|\mathcal{C}'/\mathcal{C}|$ involves hadronic form factors in the factorization approximation:

$$\left|\frac{\mathcal{C}'}{\mathcal{C}}\right|_{\rm fact} = \frac{f_K}{f_\pi}\,\frac{F_{B_s^0K}(m_K^2;0^+)}{F_{B^0\pi}(m_\pi^2;0^+)}\left(\frac{m_{B_s^0}^2 - m_K^2}{m_{B^0}^2 - m_\pi^2}\right), \tag{13.41}$$

where f_K and f_π denote the kaon and pion decay constants, and $F_{B_s^0K}(M_K^2;0^+)$ and $F_{B^0\pi}(m_\pi^2;0^+)$ parameterize the hadronic quark-current matrix elements. These quantities were analyzed using QCD sum-rule techniques [59], yielding

$$\left|\frac{\mathcal{C}'}{\mathcal{C}}\right|_{\rm fact}^{\rm QCDSR} = 1.52^{+0.18}_{-0.14}. \tag{13.42}$$

Using the experimental value of $\mathcal{B}(B^0\to\pi^+\pi^-)$ and $\mathcal{B}(B_s^0\to K^+K^-)$ with eq. (13.42) and adding errors in quadrature, the numerical value for K is

$$K = 41.0 \pm 10.3. \tag{13.43}$$

Figure 13.4 also includes the contour obtained from the central values of K and $\mathcal{A}_{\rm CP}^{\rm mix}(B^0\to\pi^+\pi^-)$. We see that the intersections with the $\mathcal{A}_{\rm CP}^{\rm dir}(B^0\to\pi^+\pi^-)$–$\mathcal{A}_{\rm CP}^{\rm mix}(B^0\to\pi^+\pi^-)$ contour following from the *BABAR* data give a twofold solution for γ (around 41° and 67°), whereas we obtain no intersection with the corresponding Belle curve. Consequently, the measured $B_s^0\to K^+K^-$ branching fraction somewhat disfavors the Belle result for the direct CP violation in $B^0\to\pi^+\pi^-$. Using this approach the numerical system can be solved and one obtains [20] the Standard Model solution $\gamma = (66.6^{+4.3}_{-5.0})^\circ$. It is also possible to explore the impact of non-factorizable U-spin-breaking corrections to eq. (13.37) by introducing the following parameters:

$$\xi \equiv d'/d, \quad \Delta\theta \equiv \theta' - \theta. \tag{13.44}$$

Assuming generous U-spin-breaking effects $\xi = 1 \pm 0.15$ and $\Delta\theta = \pm 20^\circ$ the impact on the numerical solution for γ is

$$\gamma = (66.6^{+4.3+4.0+0.1}_{-5.0-3.0-0.2})^\circ,$$

where the second and third errors refer to ξ and $\Delta\theta$, respectively. γ is only moderately affected by these uncertainties. This is a remarkable result and it is in good agreement with the UTfit and CKMfitter Collaborations [159, 158], yielding respectively $\gamma = (64.4 \pm 4.2)^\circ$ and $\gamma = (59.0^{+9.2}_{-3.7})^\circ$ from other inputs.

Prospects for time dependent measurements

The capability of collecting and reconstructing a large sample of $B_s^0 \to K^+K^-$ and $B^0 \to \pi^+\pi^-$ decays, demonstrated in this thesis, provides the opportunity to detect CP violation in these decays. With the measurement of the CP violation in the $B_s^0 \to K^+K^-$ the use of the U-spin symmetry can be minimized in the extraction of the angle γ, and internal consistency checks of the strategy become available [5]. The CP violation in the $B_s^0 \to K^+K^-$ decay mode is also a powerful probe of New Physics effects as described in [68, 82, 157]. In addition CDF can also access to the CP violation in the $B^0 \to \pi^+\pi^-$ decays, providing a useful third measurement to confirm the B-Factories measurements in a different experimental environment.

This challenging measurement is a long-term goal of the analysis described in this thesis, and it will need the full Run II statistics (5–6 fb^{-1} by year 2009). The recent measurement of B_s^0 flavor oscillations [147] shows that all the needed ingredients for this measurement are available: an excellent proper-time resolution of the CDF II tracker (between 70 and 100 fs^{-1}), necessary to resolve the sine and cosine terms of the $B_s^0 \to K^+K^-$ decay-rate asymmetry as a function of time; a good performance, $\epsilon D^2 \simeq 5.3\%$, in identifying the flavor of the b-meson at production, despite the difficult environment of hadron collisions; and a precise measurement of the mass-difference Δm_s, a necessary input parameter of the Fleischer strategy [5]. Assuming an effective signal to noise ratio S/B $\simeq 1$ (depending on the selection), with the full Run II statistics (≈ 6 fb^{-1}) we expect a measurement of CP-violating asymmetries in $B_s^0 \to K^+K^-$ decays with a resolution in the range $[0.15, 0.3]$. These asymmetries are sensitive to possible SUSY effects as described by Baek et al. in Ref. [157] and the expected resolution for these measurements is sufficient to identify hints of New Physics.

13.5 U-spin-breaking effects

The predictions within the Standard Model on decay rates and CP-violating asymmetries of $B^0_{(s)} \to h^+h'^-$ decays are dominated by large uncertainties due to non-exact phenomenological approaches which try to describe the hadronic interaction. To improve their predictive power, different approaches use several strategies, like the U-spin symmetry. The $B^0_{(s)} \to h^+h'^-$ decays are a privileged laboratory where it is possible to use this symmetry in the theoretical calculations advantageously: measurements of several of $B^0_{(s)} \to h^+h'^-$ observables allow to extract the parameters of interest and simultaneously allow to check the validity of U-spin assumptions used. Ref. [20] shows some examples of this strategy. As in sec. 13.4.2, we will briefly summarize the discussion in [20]. Since the author used a slightly outdated result of this analysis for $\mathcal{B}(B_s^0 \to K^-\pi^+) = 5.0 \pm 0.75\ (stat.) \pm 1.0\ (syst.)$ and $\mathcal{B}(B_s^0 \to K^+K^-) = 24.4 \pm 1.4\ (stat.) \pm 4.6\ (syst.)$ [2], all numbers in this section, estimated with the experimental input of $\mathcal{B}(B_s^0 \to K^-\pi^+)$ and $\mathcal{B}(B_s^0 \to K^+K^-)$, refer to these outdated measurements, but for the purpose of illustrating the consequence of the result of this thesis, this is completely

equivalent to the available result.

13.5.1 $B^0 \to K^+\pi^-$ vs $B_s^0 \to K^-\pi^+$ again

In analogy with the formalism of sec. 1.7.2 and 1.7.6 using the unitarity of the CKM matrix, the decay amplitudes of $B^0 \to K^+\pi^-$ and $B_s^0 \to K^-\pi^+$ can be written as follows:

$$A(B_d^0 \to \pi^- K^+) = -P\left[1 - re^{i\delta}e^{i\gamma}\right], \tag{13.45}$$

$$A(B_s^0 \to \pi^+ K^-) = P_s\sqrt{\epsilon}\left[1 + \frac{1}{\epsilon}r_s e^{i\delta_s}e^{i\gamma}\right], \tag{13.46}$$

where $P_{(s)}$ and $r_{(s)}e^{i\delta_{(s)}}$ are CP-conserving hadronic parameters, which describe penguin amplitudes and the ratio of trees to penguins, respectively. Using the U-spin flavour symmetry of strong interactions, in analogy to eq. (13.37) it is possible to write the following relations:

$$r_s = r, \quad \delta_s = \delta. \tag{13.47}$$

In the case of the relation between $|P_s|$ and $|P|$, factorizable U-spin breaking corrections arise, which are described by the following ratio of decay constants and form factors:

$$\left|\frac{P_s}{P}\right|_{\text{fact}} = \frac{f_\pi}{f_K}\frac{F_{B_s^0 K}(m_\pi^2;0^+)}{F_{B^0\pi}(m_K^2;0^+)}\left(\frac{m_{B_s^0}^2 - m_K^2}{m_{B^0}^2 - m_\pi^2}\right). \tag{13.48}$$

Using the recent QCD sum-rule results of Ref. [59] yields

$$\left|\frac{P_s}{P}\right|_{\text{fact}}^{\text{QCDSR}} = 1.02^{+0.11}_{-0.10}. \tag{13.49}$$

With the help of the U-spin symmetry one can write the following relation

$$\frac{\mathcal{A}_{\text{CP}}(B_s^0 \to K^-\pi^+)}{\mathcal{A}_{\text{CP}}(B^0 \to K^+\pi^-)} = -\left|\frac{P_s}{P}\right|^2\left[\frac{m_{B^0}}{m_{B_s^0}}\frac{\Phi(m_\pi/m_{B_s^0}, m_K/m_{B_s^0})}{\Phi(m_\pi/m_{B^0}, m_K/m_{B^0})}\frac{\tau_{B_s^0}}{\tau_{B^0}}\right]\left[\frac{\mathcal{B}(B^0 \to K^+\pi^-)}{\mathcal{B}(B_s^0 \to K^-\pi^+)}\right]. \tag{13.50}$$

This relation allows to obtain experimental insights into U-spin-breaking effects with the help of the measurements of $\mathcal{A}_{\text{CP}}(B_s^0 \to K^-\pi^+)$ and $\mathcal{B}(B_s^0 \to K^-\pi^+)$ performed in this thesis. The HFAG world averages [48] have been used for $\mathcal{A}_{\text{CP}}(B^0 \to K^+\pi^-)$ and $\mathcal{B}(B^0 \to K^+\pi^-)$, in particular the measurement of $\mathcal{A}_{\text{CP}}(B^0 \to K^+\pi^-)$ performed in this thesis has been included. Adding the errors in quadrature, is possible to extract

$$\left|\frac{P_s}{P}\right|_{\text{exp}} = \left|\frac{P_s}{P}\right|\sqrt{\left[\frac{r_s}{r}\right]\left[\frac{\sin\delta_s}{\sin\delta}\right]} = 1.06 \pm 0.28, \tag{13.51}$$

where the non-factorizable U-spin-breaking effects to eq. (13.47) has been taken into account. An excellent agreement was obtained with eq. (13.49). The measurement of this quantity is rather imprecise at present, but the situation will greatly improve with CDF full Run II samples (5–6 fb^{-1}). When the precision of experimental measurements will improve, this quantity will give valuable insights into U-spin-breaking effects. Relation (13.50) is a different version of the Gronau-Lipkin relation of eq. (13.20) obtained with a different approach.

13.5.2 Ratio of branching fractions and SU(3)

If we replace the strange spectator quark of $B_s^0 \to K^+K^-$ by a down quark, we obtain the $B^0 \to K^+\pi^-$ decay, as mentioned in sec. 1.7.1. Consequently, the only difference between the corresponding hadronic matrix elements is due to processes involving these spectator quarks: penguin annihilation and exchange topologies, which contribute to $B_s^0 \to K^+K^-$, but are absent in the $B^0 \to K^+\pi^-$ channel. These contributions, expected to play a minor rôle, can be probed through the $B^0 \to K^+K^-$ and the $B_s^0 \to \pi^+\pi^-$ decays [46]. The measurement of the upper limit on the CP-averaged branching fraction of $B_s^0 \to \pi^+\pi^-$ from this thesis and CP-averaged branching fraction of $B^0 \to K^+K^-$ (world-average from this thesis and B-Factories measurement [48]) do not indicate any anomalous behavior of these topologies thus they will be neglected in the following discussion.

Applying SU(3) flavour symmetry, we may then identify the $B_s^0 \to K^+K^-$ and $B^0 \to K^+\pi^-$ decay amplitudes, and obtain the simple relation between the CP-averaged branching fractions [20]:

$$\frac{\mathcal{B}(B_s^0 \to K^+K^-)}{\mathcal{B}(B^0 \to K^+\pi^-)} = \left[\frac{m_{B^0}}{m_{B_s^0}} \frac{\Phi(m_K/m_{B_s^0}, m_K/m_{B_s^0})}{\Phi(m_\pi/m_{B^0}, m_K/m_{B^0})} \frac{\tau_{B_s^0}}{\tau_{B^0}}\right] \left(\frac{f_\pi}{f_K} \left|\frac{\mathcal{C}'}{\mathcal{C}}\right|_{\text{fact}}\right)^2. \tag{13.52}$$

This relation allows to extract:

$$\left|\frac{\mathcal{C}'}{\mathcal{C}}\right|_{\text{fact}}^{\text{exp}} = 1.42 \pm 0.14, \tag{13.53}$$

from the real data. Within the uncertainties, this number agrees remarkably well with eq. (13.42), and gives further confidence on the corresponding form factors and the smallness of non-factorizable SU(3)-breaking effects. In analogy to relation (13.52), it is also possible to write

$$\frac{\mathcal{B}(B_s^0 \to K^-\pi^+)}{\mathcal{B}(B^0 \to \pi^+\pi^-)} = \left[\frac{m_{B^0}}{m_{B_s^0}} \frac{\Phi(m_\pi/m_{B_s^0}, m_K/m_{B_s^0})}{\Phi(m_\pi/m_{B^0}, m_\pi/m_{B^0})} \frac{\tau_{B_s^0}}{\tau_{B^0}}\right] \left(\frac{f_K}{f_\pi} \left|\frac{P_s}{P}\right|_{\text{fact}}\right)^2. \tag{13.54}$$

Since the form-factor ratio

$$\frac{f_\pi}{f_K} \left|\frac{\mathcal{C}'}{\mathcal{C}}\right|_{\text{fact}} = \frac{F_{B_s^0 K}(m_K^2; 0^+)}{F_{B^0\pi}(m_\pi^2; 0^+)} \left(\frac{m_{B_s^0}^2 - m_K^2}{m_{B^0}^2 - m_\pi^2}\right) \tag{13.55}$$

is essentially equal to

$$\frac{f_K}{f_\pi} \left|\frac{P_s}{P}\right|_{\text{fact}} = \frac{F_{B_s^0 K}(m_\pi^2; 0^+)}{F_{B^0\pi}(m_K^2; 0^+)} \left(\frac{m_{B_s^0}^2 - m_K^2}{m_{B^0}^2 - m_\pi^2}\right), \tag{13.56}$$

it is possible to arrive at the following relation, which does not depend on the form-factor ratios:

$$\mathcal{B}(B_s^0 \to K^-\pi^+) = \left[\frac{\mathcal{B}(B_s^0 \to K^+K^-)}{\mathcal{B}(B^0 \to K^+\pi^-)}\right] \mathcal{B}(B^0 \to \pi^+\pi^-) = (6.5 \pm 1.3) \times 10^{-6}. \tag{13.57}$$

Instead of predicting this branching ratio, we can use eq. (13.57) to test for non-factorizable SU(3)-breaking effects:

$$\Delta_{\text{SU(3)}}^{\text{NF}} \equiv 1 - \left[\frac{\mathcal{B}(B_s^0 \to K^+K^-)}{\mathcal{B}(B_s^0 \to K^-\pi^+)}\right] \left[\frac{\mathcal{B}(B^0 \to \pi^+\pi^-)}{\mathcal{B}(B^0 \to K^+\pi^-)}\right] = -0.26 \pm 0.26^{1}. \tag{13.58}$$

[1] Ref. [20] reports $\Delta_{\text{SU(3)}}^{\text{NF}} = -0.3 \pm 0.4$. We re-evaluated this quantity using the current available measurements and canceling all common systematic uncertainties, thus obtaining a more precise result.

The result is compatible with zero within current uncertainties. This relation is free from additional systematic uncertainties like the uncertainty on the production fractions of the B_s^0 and B^0 mesons f_s and f_d, which is the dominant uncertainty in the current measurement of absolute branching fraction of $B_s^0 \to K^+K^-$. With full Run II samples, the extension of this analysis will therefore allow to check this relation with high precision and provide valuable insights into U-spin breaking.

13.6 Conclusions

In this thesis I described the analysis of $B^0_{(s)} \to h^+h'^-$ decays at CDF performed to measure the relative branching fractions of individual decay modes and the CP-violating asymmetry of $B^0 \to K^+\pi^-$ and $B_s^0 \to K^-\pi^+$ decays. This analysis provided several results. I summarize them below.

I report the first observation of the decay mode $B_s^0 \to K^-\pi^+$. This is the second decay of a B_s^0 meson into two pseudo-scalar mesons to be observed (the first one was the $B_s^0 \to K^+K^-$, in the previous version of this analysis [1]). The measurement of the $B_s^0 \to K^-\pi^+$ branching fraction and direct CP-asymmetry have interesting consequences, as discussed in the previous sections. The comparison of the measured branching fraction with theoretical predictions provides valuable information for tuning the phenomenological models of hadronic $B^0_{(s)}$ meson decays (SU(3) symmetries, QCDF, SCET, QCD sum-rules, etc.) and optimizing the choice of their input parameters, in particular this branching fraction is sensitive to CKM angle values of α and γ. Even more relevant is the measurement of its direct CP-asymmetry, since, as suggested from several authors with several and different approaches [7, 8, 16, 20], by the comparison with the CP asymmetry of its U-spin partner $B^0 \to K^+\pi^-$ is possible to perform a stringent test of Standard Model to probe hints of New Physics. We perform the Gronau-Lipkin test and we find that with the current statistical uncertainty we cannot establish a significant asymmetry, but the Standard Model prediction of large asymmetry is compatible with our data and is favored over the possibilities of no asymmetry. It will be very interesting to pursue the same check with more data, with ≈ 2.5 fb^{-1} that are already available at CDF, and in the next future with full Run II samples of 5–6 fb^{-1} by year 2009.

I report an accurate measurement of the branching fraction $B_s^0 \to K^+K^-$. As in the $B_s^0 \to K^-\pi^+$ mode, the comparison of this branching fraction with theoretical predictions provides valuable information for tuning the phenomenological models of hadronic B decays and in particular provides one the first experimental insight on the magnitude of the SU(3) breaking, a necessary test and ingredient for the U-spin-based method of extracting the CKM parameters, like γ angle [5, 20]. The CDF capability of collecting a large sample of $B_s^0 \to K^+K^-$, demonstrated in this thesis, provides the opportunity to measure time-dependent CP asymmetries in this mode in the near future. These measurements are only possible at hadrons collisions experiments and represent one of the most promising way to probe New Physics effects. The intermediate experimental goal between the currently available high-precision measurements of time-integrated rates and future time-dependent measurement of asymmetries, is the study of the time evolution of $B_s^0 \to K^+K^-$ decays. This provides crucial information on the lifetime difference in the B_s^0 meson system, $\Delta\Gamma_s/\Gamma_s$, as already demonstrated by a preliminary result obtained using the technique developed in this thesis to disentangle the $B_s^0 \to K^+K^-$ signal from other $B^0_{(s)} \to h^+h'^-$ modes [78].

I report the first observation of the $\Lambda_b^0 \to pK^-$ and $\Lambda_b^0 \to p\pi^-$ decay modes. They are the first charmless decays of a b-baryon to be observed and open a new interesting field of study in which there is little theoretical background.

The measurements on B_s^0 and Λ_b^0 decays are unique to CDF and this makes CDF a special place where it is possible to probe this physics. In this analysis I also performed interesting measurements on B^0 sector. They are not unique in the current experimental panorama, but have also a great relevance, since their contribution to the current world averages is comparable with that one of the already existing measurements. I report a precise measurement of direct CP-asymmetry in the $B^0 \to K^+\pi^-$ decays. This measurement along with the CP-asymmetry in the $B_s^0 \to K^-\pi^+$ are the first measurements of this kind in hadronic collisions environment. I also report a precise measurement of the relative branching fraction of $B^0 \to \pi^+\pi^-$ decay. The prospects for these measurements are very promising. In fact, using the methodology developed in this thesis we expect to perform soon the world best measurements with the current available data sample ≈ 2.5 fb^{-1}.

I also report improved upper limits on the branching fractions of $B^0 \to K^+K^-$ and $B_s^0 \to \pi^+\pi^-$ modes, which are determined by penguin-annihilation amplitudes. These measurements have implications for both the knowledge of CKM sector of the Standard Model and the phenomenology of non-perturbative hadronic contributions in non-leptonic $B_{(s)}^0$ meson decays. The $B_s^0 \to \pi^+\pi^-$ is unique to CDF, and this channel is likely to be observed sooner than $B^0 \to K^+K^-$.

An important consequence of this work is the demonstration that precision measurements on hadronic B decays are possible in hadronic environment, when good on-line and off-line tracking are available.

The Tevatron is planned to operate (at least) through September 2009, delivering a total integrated luminosity of 5–6 fb^{-1}. During this time, the CDF experiment will continue exploiting the physics opportunity of accessing jointly B^0 and B_s^0 decays into two-body charmless mesons. This opportunity is unique to CDF at least until the planned run of the KEKB collider at the center-of-mass energy of the Υ(5S) resonance or the LHCb data-taking (2008) will start.

Bibliography

[1] A. Abulencia et al. (CDF Collaboration), *Observation of $B_s^0 \to K^+K^-$ and Measurements of Branching Fractions of Charmless Two-Body Decays of B^0 and B_s^0 Mesons in $p\bar{p}$ Collisions at $\sqrt{s}$=1.96* TeV, Phys. Rev. Lett. **97**, 211802 (2006), [hep-ex/0607021].

[2] M. Morello, *Branching fractions and direct CP asymmetries of charmless decay modes at the Tevatron*, Nucl. Phys. **B** (Proc. Suppl.) **170**, 39-4 (2007), [hep-ph/0612018].

[3] M. Morello, *Decadimenti di mesoni B in due adroni charmless a CDF II*, Tesi di Laurea (Graduation thesis), University of Pisa (2003), in Italian, unpublished.

[4] D. Tonelli, *First observation of the $B_s^0 \to K^+K^-$ decay mode, and measurement of the B^0 and B_s^0 mesons decay-rates into two-body charmless final states at CDF.*, Ph. D. thesis, Scuola Normale Superiore, Pisa, FERMILAB-THESIS-2006-23 (2006).

[5] R. Fleischer, *New Strategies to extract β and γ from $B_d \to \pi^+\pi^-$ and $B_s \to K^+K^-$*, Phys. Lett. **B459**, 306 (1999), [hep-ph/9903456].

[6] A. Soni and D.A. Suprun, *Determination of γ from charmless $B \to M_1M_2$ decays using U-spin*, Phys. Rev. D **75**, 054006 (2006), [hep-ph/0609089].

[7] M. Gronau, *U-spin symmetry in Charmless B Decays*, Phys. Lett. **B492**, 297 (2000), [hep-ph/0008292].

[8] H. J. Lipkin, *Is observed direct CP violation in $B_d \to K^+\pi^-$ due to new physics? Check standard model prediction of equal violation in $B_s \to K^-\pi^+$*, Phys. Lett. **B621**, 126 (2005), [hep-ph/0503022].

[9] M. Gronau and D. Wyler, *On determining a weak phase from CP asymmetries in charged B decays*, Phys. Lett. **B265**, 172 (1991).

[10] D. Atwood, I. Dunietz, and A. Soni, *Enhanced CP violation with $B \to KD^0(\overline{D}^0)$ modes and extraction of the CKM angle gamma*, Phys. Rev. Lett. **78**, 3257 (1997), [hep-ph/9612433]; D. Atwood, I. Dunietz, and A. Soni, *Improved methods for observing CP violation in $B^\pm \to KD$ and measuring the CKM phase gamma*, Phys. Rev. D **63**, 036005 (2001), [hep-ph/0008090].

[11] B. Aubert et al. (*BABAR* Collaboration), *Direct* CP *Violating Asymmetry in* $B^0 \to K^+\pi^-$ *Decays*, Phys. Rev. Lett. **93**, 131801 (2004), [hep-ex/0407057];
Y. Chao et al. (Belle Collaboration), *Evidence for direct* CP *Violation in* $B^0 \to K^+\pi^-$ *Decays*, Phys. Rev. Lett. **93**, 191802 (2004), [hep-ex/0408100].

[12] Y.Y. Keum and A.I. Sanda, *Possible large direct* CP *violations in charmless B decays: Summary report on the pQCD method*, Phys. Rev. D **67**, 054009 (2003), [hep-ph/0209014].

[13] M. Beneke et al., *QCD factorization in* $B \to \pi K, \pi\pi$ *decays and extraction of Wolfenstein parameters*, Nucl. Phys. **B 606**, 245-321 (2001), [hep-ph/0104110]

[14] M. Gronau and J.L. Rosner, *The* $b \to s$ *penguin amplitude in charmless* $B \to PP$ *decays*, Phys. Rev. D **71**, 074019 (2005), [hep-ph/0503131].

[15] QCD Factorization was first proposed in,
M. Beneke et al., *QCD Factorization in* $B \to \pi\pi$ *Decays: Strong Phases and CP Violation in the Heavy Quark Limit*, Phys. Rev. Lett. **83**, 1914 (1999), [hep-ph/9905312] and
———, *QCD Factorization for exclusive non-leptonic B-meson Decays: General arguments and the case for heavy-light final states*, Nucl. Phys. **B 591**, 313 (2000), [hep-ph/0006124];
the most recent update is
M. Beneke and M. Neubert, *QCD factorization for* $B \to PP$ *and* $B \to PV$ *decays*, Nucl. Phys. **B 675**, 333 (2003), [hep-ph/0308039].

[16] A. Ali et al., *Charmless non-leptonic* B_s *decays to* PP, PV *and* VV *final states in the pQCD approach*, [hep-ph/0703162].

[17] A. Williamson and J. Zupan, *Two body B decays with isosinglet final states in SCET*, Phys. Rev. D **74**, 014003 (2006) erratum-ibidem Phys. Rev. D **74**, 03901 (2006) [hep-ph/0601214].

[18] A. Buras et al., *Anatomy of prominent B and K Decays and Signatures of CP-Violating New Physics in the Electroweak Penguin Sector*, Nucl. Phys. **B 697**, 133 (2004), [hep-ph/0402112].

[19] X.-Q. Yu, Y. Li, and C.-D. Lü, *Branching ratio and CP asymmetry of* $B_s \to \pi K$ *decays in the perturbative QCD approach*, Phys. Rev. D **71**, 074026 (2005), erratum-ibidem Phys. Rev. D **72**, 119903 (2005), [hep-ph/0501152].

[20] $B_{s,d} \to \pi\pi, \pi K, KK$*: Status and Prospects*, R. Fleischer, Eur. Phys. J. **C52**, 267-281 (2007). [hep-ph/0705.1121]

[21] R. Fleischer, *Flavour Physics and CP Violation*, Lectures given at the 2005 European School of High-Energy Physics, Kitzbuehel, Austria, 21 August - 3 September 2005, CERN-PH-TH/2006-152, [hep-ph/0608010].

[22] J. H. Christenson et al., *Evidence for the* 2π *Decay of the* K_2^0 *Meson*, Phys. Rev. Lett. **13**, 138 (1964);
A. Abashian et al., *Search for CP nonconservation in* K_2^0 *decays*, Phys. Rev. Lett. **13**, 243 (1964).

[23] A. Alavi-Harati et al. (KTeV Collaboration), *Observation of Direct* CP *Violation in* $K_{S,L} \to \pi\pi$ *Decays*, Phys. Rev. Lett. **83**, 22 (1999), [hep-ex/9905060];
V. Fanti et al. (NA48 Collaboration), *A new measurement of direct CP violation in two pion decays of the neutral kaon*, Phys. Lett. **B465**, 335 (1999), [hep-ex/9909022].

[24] J.R. Batley et al. (NA48 Collaboration), *A precision measurement of direct CP violation in the decay of neutral kaons into two pions*, Phys. Lett. **B544**, 97 (2002), [hep-ex/0208009];

[25] A. Alavi-Harati et al. (KTeV Collaboration), *Measurements of direct CP violation, CPT symmetry, and other parameters in the neutral kaon system*, Phys. Rev. D **67**, 2003 (012005), [hep-ex/0208007];

[26] A. D. Sakharov, *Violation Of CP Invariance, C Asymmetry, And Baryon Asymmetry Of The Universe*, Pisma Zh. Exp. Theor. Fiz. **5**, 32 (1967), English translation in JETP Lett. **5**, 24 (1967), reprinted in Sov. Phys. Usp. **34**, 392 (1991).

[27] N. Cabibbo, *Unitary Symmetry and Leptonic Decays*, Phys. Rev. Lett. **10**, 531 (1963);
M. Gell-Mann, *A Schematic Model for Baryons and Mesons*, Phys. Lett. **8**, 214 (1964);
G. Zweig, *An SU(3) Model for Strong Interaction Symmetry and Its Breaking. 2.*, CERN-TH-412.

[28] M. Kobayashi and T. Maskawa, *CP-Violation in the Renormalizable Theory of Weak Interaction*, Prog. Theor. Phys. **49**, 652 (1973).

[29] B. Aubert et al. (*BABAR* Collaboration), *Observation of* CP *Violation in the* B^0 *Meson System*, Phys. Rev. Lett. **87**, 091801 (2001), [hep-ex/0107013];
K. Abe et al. (Belle Collaboration), *Observation of large* CP *Violation in the Neutral B Meson System*, Phys. Rev. Lett. **87**, 091802 (2001), [hep-ex/0107061].

[30] S. L. Glashow, J. Iliopoulos, and L. Maiani, *Weak Interactions with Lepton-Hadron Symmetry*, Phys. Rev. D **2**, 1285 (1970).

[31] C. Jarlskog, *Commutator of the Quark Mass Matrices in the Standard Electroweak Model and a Measure of Maximal* CP *Nonconservation*, Phys. Rev. Lett. **55**, 1039 (1985);
———, *A basis independent formulation of the connection between quark mass matrices,* CP *violation and experiment*, Z. Phys. C **29**, 491 (1985);
I. Dunietz, O. W. Greenberg, and D.-D. Wu, A priori *definition of maximal CP nonconservation*, Phys. Rev. Lett. **55**, 29351 (1985).

[32] S. Eidelman et al. (Particle Data Group), *Review of particle physics*, Phys. Lett. **B592**, 1 (2004).

[33] L. Wolfenstein, *Parameterization of the Kobayashi-Maskawa Matrix*, Phys. Rev. Lett. **51**, 1945 (1983).

[34] A.J. Buras, *Weak Hamiltonian, CP violation and rare decays*, Lectures given at Summer School on Theoretical Physics: Probing the Standard Model of Particle Interactions, Les Houches, France, 28 July − 5 September 1997. [hep-ph/9806471]

[35] G. Buchalla, A.J. Buras, and M.E. Lautenbacher, *Weak Decays Beyond Leading Logarithms*, Rev. Mod. Phys. **68**, 1125 (1996), [hep-ph/9512380].

[36] A.J. Buras and R. Fleischer, *Limitations in measuring the angle β by using SU(3) relations for B meson decay amplitudes*, Phys. Lett. **B341**, 379 (1995), [hep-ph/9409244].

[37] M. Ciuchini et al., *Charming penguins strike back*, Phys. Lett. **B515**, 33 (2001), [hep-ph/0104126].
C. Isola et al., *Charming penguin contributions to charmless B decays into two pseudoscalar mesons*, Phys. Rev. D **65**, 094005 (2002), [hep-ph/0110411].
C.W. Bauer et al., *$B \to M(1)M(2)$: Factorization, charming penguins, strong phases, and polarization*, Phys. Rev. D **70**, 054015 (2004), [hep-ph/0401188].

[38] N.G. Deshpande and X.-G. He, *Isospin structure of penguins and their consequences in B physics*, Phys. Rev. Lett. **74**, 26 (1995), [hep-ph/9408404],
M. Gronau et al., *Electroweak penguins and two-body B decays*, Phys. Rev. D **52**, 6374 (1995), [hep-ph/9504327].

[39] M. Neubert and B. Stech, *Non-leptonic weak decays of B mesons*, Adv. Ser. Direct. High Energy Phys. **15**, 294 (1998), and references therein. [hep-ph/9705292].

[40] J.D. Bjorken, Nucl. Phys. **B** (Proc. Suppl.) **11**, 325 (1989);
M. Dugan and B. Grinstein,, Phys. Lett. **B255**, 583 (1991);
H.D. Politzer and M.B. Wise, Phys. Lett. **B257**, 399 (1991);

[41] Y.-Y. Keum, H.-N. Li, and A. I. Sanda, *Fat penguins and imaginary penguins in perturbative QCD*, Phys. Lett. **B504**, 6 (2001), [hep-ph/0004004];
———, *Penguin enhancement and $B \to K\pi$ decays in perturbative QCD*, Phys. Rev. D **63**, 054008 (2001), [hep-ph/0004173].

[42] C. W. Bauer, S. Fleming, and M. E. Luke, *Summing Sudakov logarithms in $B \to X_s\gamma$ in effective field theory*, Phys. Rev. D **63**, 014006 (2001), [hep-ph/0005275];
C. W. Bauer et al., *An effective field theory for collinear and soft gluons: Heavy to light decays*, Phys. Rev. D **63**, 114020 (2001), [hep-ph/0011336];
C. W. Bauer and I. W. Steward, *Invariant operators in collinear effective theory*, Phys. Lett. **B516**, 134 (2001), [hep-ph/0107001].

[43] A. Khodjamirian, *$B \to \pi\pi$ decay in QCD*, Nucl. Phys. **B 605**, 558 (2001), [hep-ph/0012271];
A. Khodjamirian, T. Mannel, and B. Melic, *QCD light-cone sum rule estimate of charming penguin contributions in $B \to \pi\pi$*, Phys. Lett. **B571**, 75 (2003), [hep-ph/0304179].

[44] S. Baek et al., *Can one detect new physics in I=0 and/or I=2 contributions to the decays $B \to \pi\pi$?*, Phys. Rev. D **72**, 036004 (2005), [hep-ph/0506075].

[45] R. Fleischer and D. Wyler, *Exploring CP violation with B_c decays*, Phys. Rev. D **62**, 057503 (2000), [hep-ph/0004010].

[46] M. Gronau, J.L. Rosner, and D. London, *Weak coupling phase from decays of charged B mesons to πK and $\pi\pi$*, Phys. Rev. Lett. **73**, 21 (1994), [hep-ph/9404282];
M. Gronau, O.F. Hernandez, D. London, and J.L. Rosner, *Decays of B mesons to two light pseudoscalars*, Phys. Rev. D **50**, 4529 (1994), [hep-ph/9404283].

[47] A.B. Carter and A.I. Sanda, Phys. Rev. Lett. **45**, 952 (1980) and Phys. Rev. D **23**, 1567 (1981);
I.I. Bigi and A.I. Sanda, Nucl. Phys. **B 193**, 85 (1981).

[48] E. Barberio et al. (Heavy Flavor Averaging Group), *Averages of b-hadron Properties at the End of 2006*, [hep-ex/0704.3575v1].

[49] B Oscillations Working Group: `http://lepbosc.web.cern.ch/LEPBOSC/`.

[50] T. Inami and C.S. Lim, *Effects Of Superheavy Quarks And Leptons In Low-Energy Weak Processes $K_L \to \mu\overline{\mu}$, $K^+ \to \pi + \nu\overline{\nu}$ And $K^0 \leftrightarrow \overline{K}^0$*, Prog. Theor. Phys. **65** (1981) 297 , erratum-ibidem p. 1772.

[51] A.J. Buras, *CP violation in B and K decays: 2003*, Lectures given at 41^{st} International University School of Theoretical Physics: Flavour Physics (IUTP 41), Schladming, Styria, Austria, 22–28 February 2003. [hep-ph/0307203].

[52] M. Beneke et al., *Next-to-Leading Order QCD Corrections to the Lifetime Difference of B_s Mesons*, Phys. Lett. **B459**, 631 (1999), [hep-ph/9808385];
I. Dunietz, R. Fleischer, and U. Nierste, *In pursuit of new physics with B_s decays*, Phys. Rev. D **63**, 114015 (2001), [hep-ph/0012219];
A. Lenz, *Decay Rate Difference in the Neutral B-System: $\Delta\Gamma_{B_s}$ and $\Delta\Gamma_{B_d}$*, [hep-ph/0412007] and *Lifetimes and oscillations of heavy mesons*, [hep-ph/0612176].

[53] T. Aaltonen et al. (CDF Collaboration), *Measurement of $\Delta\Gamma_s$ and ϕ_s in $B_s^0 \to J/\psi\phi$ decays*, CDF Internal Note 8950 (2007), published
http://www-cdf.fnal.gov/physics/new/bottom/070809.blessed-DG-BsPsiPhi/public_note_Bs.pdf .

[54] V.M. Abazov et al. (DO Collaboration), *Lifetime Difference and CP-Violating Phase in the B_s^0 System*, Phys. Rev. Lett. **98**, 121801 (2007), [hep-ex/0701012].

[55] A.S. Dighe, I. Dunietz, and R. Fleischer, *Extracting CKM phases and $B_s - \overline{B}_s$ mixing parameters from angular distributions of non-leptonic B decays*, Eur. Phys. J. **C6**, 647 (1999), [hep-ph/9804253]

[56] I. Dunietz, *$B_s - \overline{B}_s$ mixing, CP violation and extraction of CKM phases from untagged B_s data samples*, Phys. Rev. D **52**, 3048 (1995),[hep-ph/9501287].

[57] I. Dunietz, R. Fleischer, and U. Nierste, *In pursuit of new physics with B_s decays*, Phys. Rev. D **63**, 114015 (2001), [hep-ph/0012219].

[58] A.J. Buras, *Waiting for clear signals of new physics in B and K decays*, Invited talk at 9th Adriatic Meeting, Dubrovnik, Croatia, 4-14 Sep 2003. Published in Springer Proc. Phys. 98:315-331. Also in *Dubrovnik 2003, Particle physics and the universe* 315-331, [hep-ph/0402191].

[59] A. Khodjamirian, T. Mannel, and M. Melcher, *Flavor SU(3) symmetry in Charmless B Decays*, Phys. Rev. D **68**, 114007 (2003), [hep-ph/0308297];
———, *Kaon distribution Amplitude from QCD Sum Rules*, Phys. Rev. D **70**, 094002 (2004), [hep-ph/0407226];
A. Khodjamirian, T. Mannel, and N. Offen, *Form Factors from Light-Cone Sum Rules with B-Meson Distribution Amplitudes*, [hep-ph/0611193].

[60] M. Gronau and D. London, *Isospin Analysis Of CP Asymmetries In B Decays*, Phys. Rev. Lett. **65**, 3381 (1990).

[61] B. Aubert et al. (*BABAR* Collaboration), *Observation of CP violation in $B^0 \to K^+\pi^-$ and $B^0 \to \pi^+\pi^-$*, Phys. Rev. Lett. **99**, 021603 (2007). [hep-ex/0703016].

[62] H. Ishino et al. (Belle Collaboration), *Observation of Direct CP-Violation in $B^0 \to \pi^+\pi^-$ Decays and Model-Independent Constraints on ϕ_2*, Phys. Rev. Lett. **98**, 211801 (2007), [0608035]

[63] B. Aubert et al. (*BABAR* Collaboration), *Improved Measurements of the Branching Fractions for $B^0 \to \pi^+\pi^-$ and $B^0 \to K^+\pi^-$, and a Search for $B^0 \to K^+K^-$*, Phys. Rev. D **75**, 012008 (2007), [hep-ex/0608003].

[64] K. Abe et al. (Belle Collaboration), *Improved measurements of branching fractions for $B \to K\pi$ and $B \to \pi\pi$ decays*, to appear in the proceedings of the XXXIII International Conference on High Energy Physics (ICHEP2006), Moscow, [hep-ex/0609015].

[65] K. Abe et al. (Belle Collaboration), *Observation of B decays to two kaons*, Phys. Rev. Lett. **98**, 181804 (2007), [hep-ex/0608049].

[66] A. Bornheim et al. (CLEO Collaboration), *Measurements of charmless hadronic two body B meson decays and the ratio $\mathcal{B}(B \to DK)/\mathcal{B}(B \to D\pi)$*, Phys. Rev. D **68**, 052002 (2003), Erratum-ibid.D75:119907,2007, [hep-ex/0302026]

[67] R. Fleischer, *Constraining penguin contributions and the CKM angle gamma through $B_d \to \pi^+\pi^-$*, Eur. Phys. J. **C16**, 87 (2000), [hep-ph/0001253].

[68] R. Fleischer and J. Matias, *Searching for New Physics in Non-Leptonic B Decays*, Phys. Rev. D **61**, 074004 (2000), [hep-ph/9906274];
———, *Exploring CP Violation through Correlations in $B \to \pi K$, $B_d \to \pi^+\pi^-$, $B_s \to K^+K^-$ Observable Space*, Phys. Rev. D **66**, 054009 (2002), [hep-ph/0204101].

[69] A.J. Buras, R. Fleischer, S. Recksiegel, and F. Schwab, *New Aspects of $B \to \pi\pi$, πK and their Implications for Rare Decays*, Eur. Phys. J. **C45**, 701 (2006), [hep-ph/0512032].

[70] M. Pierini, *An update on charming penguins in charmless B decays*, Talk given at 4th International Workshop on the CKM Unitarity Triangle (CKM 2006), Nagoya, Japan, 12-16 Dec 2006. Paper in preparation.

[71] S. Mishima, *Recent developments in the PQCD approach*, Talk given at 4th International Workshop on the CKM Unitarity Triangle (CKM 2006), Nagoya, Japan, 12-16 Dec 2006. [hep-ph/0703210]

[72] R. Fleischer, *The $B \to \pi K$ Puzzle: A Status Report*, Talk given at 4th International Workshop on the CKM Unitarity Triangle (CKM 2006), Nagoya, Japan, 12-16 Dec 2006. CERN-PH-TH-2007-017, [hep-ph/0701217]

[73] M. Gronau and J. L. Rosner, *Weak phase γ from the ratio of $B \to K\pi$ rates*, Phys. Rev. D **57**, 6843 (1998), [hep-ph/9711246].

[74] M. Gronau and J. L. Rosner, *The role of $B_s^0 \to K^-\pi^+$ in determining the weak phase γ*, Phys. Lett. **B482**, 71 (2000), [hep-ph/0003119].

[75] A.J. Buras, R. Fleischer, S. Recksiegel, and F. Schwab, *The $B \to \pi\pi$, πK Puzzles in the Light of New Data: Implications for the Standard Model, New Physics and Rare Decays*, Acta Phys. Polon. **B36** 2015, (2005), [hep-ph/0410407].

[76] S. Descotes-Genon, J. Matias, and J. Virto, *Exploring $B_{d,s} \to KK$ decays through flavour-symmetries and QCD factorisation*, Phys. Rev. Lett. **97**, 061801 (2006), [hep-ph/0603239].

[77] B. Aubert et al. (*BABAR* Collaboration), *Evidence for $B^+ \to \bar{K}^0 K^+$ and $B^0 \to K^0\bar{K}^0$, and Measurement of the Branching Fraction and Search for Direct CP Violation in $B^+ \to \bar{K}^0 K^+$*, Phys. Rev. Lett. **95**, 221801 (2005), [hep-ex/0507023].

[78] D. Tonelli, *CDF hot topics*, Talk presented at 4th Flavor Physics and CP Violation Conference (FPCP 2006), Vancouver, British Columbia, Canada, 9-12 Apr 2006, FERMILAB-CONF-06-116-E, [hep-ex/0605038]

[79] F. Su et al., *Large Strong Phases and CP Violation in the Annihilation Processes $\overline{B}^0 \to K^+K^-$, $K^{*\pm}K^{\mp}$, $K^{*+}K^{*-}$*, [hep-ph/0604082].

[80] Y. Li et al., *Branching ratio and CP asymmetry of $B_s \to \pi^+\pi^-$ decays in the perturbative QCD approach*, Phys. Rev. D **70**, 034009 (2004), [hep-ph/0404028].

[81] Y.-D. Yang et al., *Revisiting the annihilation decay $\bar{B}_s \to \pi^+\pi^-$.*, Eur. Phys. J. **C44**, 243 (2005), [hep-ph/0507326].

[82] D. London and J. Matias, *Testing the Standard Model with $B_s^0 \to K^+K^-$ Decays*, Phys. Rev. D **70**, 031502 (2004), [hep-ph/0404009].

[83] R. Blair et al. (CDF II Collaboration), *The CDF II Detector, Technical Design Report*, FERMILAB-Pub-96/390-E CDF (1996).

[84] D. P. McGinnis, *Fermilab Tevatron operational status*, in C. Horak (ed.), proceedings of the Particle Accelerator Conference (PAC 05), (2005); in addition, detailed and updated information on the Tevatron is available in the following web-pages:
`http://www-bd.fnal.gov/runII/index.html`
`http://www-bdnew.fnal.gov/operations/rookie_books/rbooks.html`.

[85] C. S. Hill, *Initial experience with the CDF layer 00 silicon detector*, Nucl. Instrum. Methods **A511**, 118 (2003).

[86] A. Sill, *CDF Run II silicon tracking projects*, Nucl. Instrum. Methods **A447**, 1 (2000).

[87] M. Bishai et al., *An SVX3D chip user's companion*, CDF Internal Note 5062 (1999), unpublished.

[88] A. Affolder et al., *Status report of the intermediate silicon layers detector at CDF II*, Nucl. Instrum. Methods **A485**, 6 (2002).

[89] T. Affolder et al., *CDF Central Outer Tracker*, Nucl. Instrum. Methods **A526**, 249 (2004).

[90] J. Marriner, *Secondary vertex fit with mass and pointing constraints (CTVMFT)*, CDF Internal Note 1996 (1993), unpublished.

[91] P. Gatti, *Performance of the new tracking system at CDF II*, Tesi di Dottorato (Ph. D. thesis), University of Padova, FERMILAB-THESIS-2001-23 (2001);
S. Menzemer, *TrackingCal - A tracking and alignment software package for the CDF II silicon detector*, Ph. D. thesis, University of Karlsruhe and CDF Internal Note 5968 (2002), unpublished.

[92] D. Acosta et al., *A Time-of-Flight detector in CDF-II*, Nucl. Instrum. Methods **A518**, 605 (2004).

[93] L. Balka et al., *The CDF central electromagnetic calorimeter*, Nucl. Instrum. Methods **A267**, 272 (1988);
S. R. Hahn et al., *Calibration systems for the CDF central electromagnetic calorimeter*, Nucl. Instrum. Methods **A267**, 351 (1988).

[94] M. Gallinaro, *A New Scintillator Tile/Fiber Preshower Detector for the CDF Central Calorimeter*, IEEE Trans. Nucl. Sci. **52**, 879 (2005), [physics/0411056].

[95] S. Bertolucci et al., *The CDF central and endwall hadron calorimeter*, Nucl. Instrum. Methods **A267**, 301 (1988).

[96] M. Albrow et al., *The CDF plug upgrade electromagnetic calorimeter: test beam results*, Nucl. Instrum. Methods **A480**, 524 (2002);
M. Albrow et al., *A preshower detector for the CDF Plug Upgrade: test beam results*, Nucl. Instrum. Methods **A431**, 104 (1999);
G. Apollinari et al., *Shower maximum detector for the CDF plug upgrade calorimeter*, Nucl. Instrum. Methods **A412**, 515 (1998).

[97] G. Ascoli et al., *CDF central muon detector*, Nucl. Instrum. Methods **A268**, 33 (1988);
C. M. Ginsburg, *CDF Run 2 Muon System*, Eur. Phys. J. **33**, S1002 (2004).

[98] C. Avila et al. (E811 Collaboration), *A measurement of the proton-antiproton total cross-section at $\sqrt{s}$=1.8* TeV, Phys. Lett. **B445**, 419 (1999);
F. Abe et al. (CDF Collaboration), *Measurement of the anti-proton proton total cross-section at $\sqrt{s}$=546* GeV *and 1800* GeV, Phys. Rev. D **50**, 5550 (1994).

[99] D. Acosta et al., *The performance of the CDF luminosity monitor*, Nucl. Instrum. Methods **A494**, 57 (2002).

[100] E. J. Thomson et al., *Online Track Processor for the CDF Upgrade*, IEEE Trans. Nucl. Sci. **49**, 1063 (2002).

[101] For more details on the SVT, see the following conference proceedings (and references therein):
B. Ashmanskas et al., *The CDF Silicon Vertex Trigger*, Nucl. Instrum. Methods **A518**, 532 (2004), [physics/0306169];
M. Dell'Orso, *The CDF Silicon Vertex Trigger*, Nucl. Phys. **B** (Proc. Suppl.) **156**, 139 (2006).

[102] J. Antos et al., *Data processing model for the CDF experiment*, submitted to IEEE Trans. Nucl. Sci., [physics/0606042] (2006).

[103] R. Brun et al., *GEANT: Simulation Program For Particle Physics Experiments. User Guide And Reference Manual*, CERN-DD-78-2-REV (1978).

[104] For an exact definition of the $\chi^2_{\rm SVT}$ quantity, see
S. Belforte et al., *Silicon Vertex Tracker Technical Design Report*, CDF Internal Note 3108 (1995), unpublished.

[105] For a simple introduction to the concepts of Kalman filtering, see
P. Maybeck, *Stochastic Models, Estimation, and Control*, Vol. 1, New York: Academic Press, 1979, and references therein.

[106] D. Acosta et al. (CDF Collaboration), *Measurement of Bottom-Quark Hadron Masses in Exclusive J/ψ Decays with the CDF Detector*, Phys. Rev. Lett. **96**, 202001 (2006), [hep-ex/0508022].

[107] M. Campanelli and E. Gerchtein, *Calibration of the momentum scale for Kalman refitter using $J\psi$ events*, CDF Internal Note 6905 (2004), unpublished;

[108] J. D. Bjorken, *Properties of hadron distributions in reactions containing very heavy quarks*, Phys. Rev. D **17**, 171 (1978);
M. Suzuki, *Fifth quark and dimuon production by Neutrinos*, Phys. Lett. **B68**, 164 (1977).

[109] H. Albrecht et al. (ARGUS Collaboration), *Search for hadronic $b \to u$ decays*, Phys. Lett. **B241**, 278 (1990).

[110] P. Sphicas, *A $b\bar{b}$ Monte Carlo Generator*, CDF Internal Note 2655 (1994), unpublished;
K. Anikeev, P. Murat, and Ch. Paus, *Description of Bgenerator II*, CDF Internal Note 5092 (1999), unpublished.

[111] D. Acosta et al. (CDF Collaboration), *Measurement of the J/ψ and b-Hadron Production Cross Sections in $p\bar{p}$ Collisions at $\sqrt{s}$ = 1960 GeV*, Phys. Rev. D **71**, 032001 (2005), [hep-ex/0412071].

[112] D. J. Lange, *The EvtGen particle decay simulation package*, Nucl. Instrum. Methods **A462**, 152 (2001);
W. Bell et al., *User Guide for EvtGen @ CDF*, CDF Internal Note 5618 (2003), unpublished.

[113] For a discussion on the bias related to the use of multiple variables in multi-component fits see G. Punzi, *Comments on Likelihood fits with variable resolution*, eConf. **C030908** WELT002 (2003), [physics/0401045].

[114] D. Ayres et al., *Design Report Of the Fermilab Collider Detector Facility (Cdf), August 1981*, Batavia, USA, Fermilab (1981);
F. Abe et al. (CDF Collaboration), *The CDF Detector: An Overview*, Nucl. Instrum. Methods **A271**, 387 (1988).

[115] H. A. Bethe, *Theory of passage of fast corpuscular rays through matter*, Annalen Phys. **5**, 325 (1930), in German;
———, *Scattering of electrons*, Z. Phys. **76**, 293 (1932);
F. Bloch, *Stopping power of atoms with several electrons*, Z. Phys. **81**, 363 (1933).

[116] S.-S. 'Eiko' Yu et al., *COT dE/dx Measurement and Corrections*, CDF Internal Note 6361 (2004), unpublished.

[117] S. D'Auria et al., *Track-based calibration of the COT specific ionization*, CDF Internal Note 6932 (2004), unpublished.

[118] M.A. Ciocci, G. Punzi, and P. Squillacioti, *Update of Combined PID in 6.1.4*, CDF Internal Note 8478 (2006), unpublished;
G. Punzi and P. Squillacioti, *Update of Combined PID in 5.3.4*, CDF Internal Note 7866 (2005), unpublished;
R.Carosi et al., *Particle Identification by combining TOF and dEdx information*, CDF Internal Note 7488 (2005), unpublished.

[119] P. Squillacioti, *Measurement of the branching fraction ratio $\mathcal{B}(B^+ \to \overline{D}^0 K^+)/\mathcal{B}(B^+ \to \overline{D}^0 \pi^+)$ with the CDF II detector.*, Ph. D. thesis, University of Siena, Siena, FERMILAB-THESIS-2006-27 (2006).

[120] M. Campanelli et al., *TOF performance studies with Λ^0 and K_s^0 decays*, CDF Internal Note 6757 (2004), unpublished.

[121] G. Punzi, *Useful formulas on statistical separation of classes of events*, [physics/0611219].

[122] D. Acosta et al. (CDF Collaboration), *Measurement of Partial Widths and Search for Direct CP Violation in D^0 Meson Decays to K^-K^+ and $\pi^-\pi^+$*, Phys. Rev. Lett. **94**, 122001 (2005), [hep-ex/0504006].

[123] V. Cirigliano, J. F. Donoghue, and E. Golowich, *$K \to \pi\pi$ phenomenology in the presence of electromagnetism*, Eur. Phys. J. **C**18, 83 (2000), [hep-ph/0008290].

[124] E. Baracchini and G. Isidori, *Electromagnetic corrections to non-leptonic two-body B and D decays*, Phys. Lett. **B633**, 309 (2006), [hep-ph/0508071].

[125] E. Baracchini, *Correzioni radiative ai decadimenti in due corpi del mesone B*, Tesi di Laurea (Graduation thesis), University of Rome "La Sapienza" (2005), in Italian, unpublished.

[126] E. Barberio, B. Van Eijk, and Z. Was, *PHOTOS: A Universal Monte Carlo for QED radiative corrections in decays*, Comput. Phys. Commun. **66**, 115 (1991);
E. Barberio and Z. Was, *PHOTOS: A Universal Monte Carlo for QED radiative corrections. Version 2.0*, Comput. Phys. Commun. **79**, 291 (1994).

[127] D. Acosta et al. (CDF Collaboration), *Measurement of Prompt Charm Meson Production Cross Sections in $p\bar{p}$ Collisions at $\sqrt{s} = 1.96$ TeV*, Phys. Rev. D **91**, 241804 (2003), [hep-ex/0307080].

[128] A. Abulencia et al. (CDF Collaboration), *Measurement of the Ratio of Branching Fractions $\mathcal{B}(D^0 \to K^-\pi^+)/\mathcal{B}(D^0 \to K^+\pi^-)$*, Phys. Rev. D **74**, 031109(R) (2006), [hep-ex/0605027].

[129] M. Morello, G. Punzi, and G. Volpi, *Fast Monte Carlo for generation of accurate kinematic templates of non-leptonic B and D decay*, CDF Internal Note 8800 (2007), unpublished.

[130] F. James and M. Roos, *'MINUIT' A system for Function Minimization And Analysis of the Parameter Errors and Correlations*, Comput. Phys. Commun. **10**, 343 (1975);
F. James, *MINUIT – Function Minimization and Error Analysis – Reference Manual*, CERN Program Library **D506** (1998).

[131] K. Pearson, *Contributions to the Mathematical Theory of Evolution – II. Skew Variation in Homogeneous Material*, Philos. Trans. Roy. Soc. London A **186**, 343 (1895);
———, *Contributions to the Mathematical Theory of Evolution – X. Supplement to a Memoir on Skew Variation*, Philos. Trans. Roy. Soc. London A **197**, 443 (1901);
———, *Contributions to the Mathematical Theory of Evolution – XIX. Second Supplement to a Memoir on Skew Variation*, Philos. Trans. Roy. Soc. London A **216**, 429 (1916).

[132] A. Abulencia et al. (CDF Collaboration), *Search for $B_s^0 \to \mu^+\mu^-$ and $B^0 \to \mu^+\mu^-$ Decays in $p\bar{p}$ Collisions with CDF II*, Phys. Rev. Lett. **95**, 221805 (2005), erratum-ibidem Phys. Rev. Lett. **95**, 249905 (2005), [hep-ex/0508036].

[133] Although the inequality was first (implicitly) derived by Aitken and Silverstone, it is generally referred to as Cramér-Rao (or Fréchet) inequality, following the papers below:
C. R. Rao, *Information and accuracy attainable in the estimation of statistical parameters*,

Bull. Calcutta Math. Soc., **37**, 81 (1945);
H. Cramér, *Mathematical Methods of Statistics*, Princeton University Press (1946).

[134] G. Punzi, *Sensitivity of searches for new signals and its optimization*, eConf. **C030908** MODT002 (2003), [physics/0308063].

[135] J. Heinrich, *Pitfalls of Goodness-of-fit from Likelihood*, eConf. **C030908** MOcT001 (2003), [physics/0310167].

[136] R. Carosi et al., *Relative branching fractions and CP-violating decay rate asymmeteries in Cabibbo supressed decays of the D^0 meson*, CDF Internal Note 6391 (2004), unpublished.

[137] M. Casarsa et al., *Measurement of isolation efficiency in low $p_{\rm T}$ B mesons*, CDF Internal Note 7049 (2004), unpublished.

[138] M. Ciuchini et al., *Lifetime differences and CP violation parameters of neutral B mesons at the next-to-leading order in QCD*, JHEP 0308:031 (2003), [hep-ph/0308029].

[139] I. Dunietz et al., *CP violation in $b \to (c\bar{c})$ without tagging*, Phys. Lett. **B316**, 561 (1993).

[140] V.M. Abazov et al. (D0 Collaboration), *Measurement of the CP-violation parameter of B^0 mixing and decay with $p\bar{p} \to \mu\mu X$ data*, Phys. Rev. D **74**, 092001 (2006), [hep-ex/0609014].

[141] V.M. Abazov et al. (D0 Collaboration), *Measurement of direct CP violation in $B^+ \to J/\psi K^+$ decay*, Conference Note 5405-CONF,
http://www-d0.fnal.gov/Run2Physics/WWW/results/prelim/B/B49/B49.pdf.

[142] L. Benussi et al., *Discoveries in flavour physics at e^+e^- colliders*, prepared for International Workshop on Discoveries in Flavour Physics at e^+e^- Colliders (DIF 06), Frascati, Rome, Italy, 28 Feb - 3 Mar 2006. Published in Frascati physics series 41. `http://www.lnf.infn.it/sis/frascatiseries/Volume41/volume41.pdf`.

[143] D. Acosta et al. (CDF Collaboration), *Measurement of the Lifetime Difference between B_s Mass Eigenstates*, Phys. Rev. Lett. **94**, 101803 (2005), [hep-ex/0412057].

[144] A. Belloni et al., *Same Side Kaon Tagging Studies in Fully Reconstructed*, CDF Internal Note 7979 (2006), unpublished.

[145] See, for istance,
D. Brunner and A. Uhl, *Optimal Multipliers for Linear Congruential Pseudo Random Number Generators with Prime Moduli: Parallel Computation and Properties*, BIT. Numer. Math. **39**, 193-209, (1999);
E.W. Weisstein, *Linear Congruence Method*, From MathWorld–A Wolfram Web Resource. `http://mathworld.wolfram.com/LinearCongruenceMethod.html`

[146] S. S. Wilks, *The large-sample distribution of the likelihood ratio for testing composite hypotheses*, Ann. Math. Statist. **9**, 60 (1938).

[147] A. Abulencia et al. (CDF Collaboration), *Measurement of the $B_s^0 - \overline{B}_s^0$ Oscillation Frequency*, Phys. Rev. Lett. **97**, 062003 (2006), [hep-ex/0606027] and
———, *Observation of $B_s^0 - \overline{B}_s^0$ Oscillations*, Phys. Rev. Lett. **97**, 242003 (2006), [hep-ex/0609040].

[148] J. Sun, G. Zhu, and D. Du, *Phenomenological Analysis of Charmless Decays $B_s \to PP, PV$ with QCD Factorization*, Phys. Rev. D **68**, 054003 (2003), [hep-ph/0211154].

[149] C.-W. Chiang and Y-F. Zhou, *Flavor SU(3) analysis of charmless B meson decays to two pseudoscalar mesons*, [hep-ph/0609128].

[150] G. J. Feldman and R. D. Cousins, *Unified approach to the classical statistical analysis of small signals*, Phys. Rev. D **57**, 3873 (1998), [hep-physics/9711021].

[151] D. Buskulic et al. (ALEPH Collaboration), *Observation of charmless hadronic B decays*, Phys. Lett. **B384**, 471 (1996).

[152] D. Acosta et al. (CDF Collaboration), *Search for $\Lambda_b^0 \to p\pi^-$ and $\Lambda_b^0 \to pK^-$ decays in $p\bar{p}$ collisions at $\sqrt{s} = 1.96$ TeV*, Phys. Rev. D **72**, 051104(R) (2005), [hep-ph/0507067].

[153] R. Mohanta, A. K. Giri, and M. P. Khanna, *Charmless two body hadronic decays of the Λ_b baryon*, Phys. Rev. D **63**, 074001 (2001), [hep-ph/0006109].

[154] S. Chen et al. (CLEO Collaboration), *Measurement of Charge Asymmetries in Charmless Hadronic B Meson Decays*, Phys. Rev. Lett. **85**, 525 (2000), [hep-ex/0001009].

[155] B. Aubert et al. (*BABAR* Collaboration), *Observation of CP violation in $B^0 \to K^+\pi^-$ and $B^0 \to \pi^+\pi^-$*, Phys. Rev. Lett. **99**, 021603 (2007). [hep-ex/0703016].

[156] Y. Unno for the Belle Collaboration, presented at the XXXIII International Conference on High Energy Physics (ICHEP2006), Moscow.

[157] S. Baek et al., *$B_s^0 \to K^+K^-$ and $B^0 \to K^0\bar{K}^0$ Decays within Supersymmetry*, JHEP **0612**, 19 (2006), [hep-ph/0610109].

[158] J. Charles et al. (CKMfitter Group), *CP Violation and the CKM Matrix: Assessing the Impact of the Asymmetric B Factories*, Eur. Phys. J. **C41**, 1 (2005), [hep-ph/0406184] and web-updates at `http://ckmfitter.in2p3.fr`.

[159] M. Bona et al. (UTfit Group), *Model-independent constraints on Delta F=2 operators and the scale of New Physics*, JHEP **0507**, 28 (2005), [hep-ph/0707.0636] and web-updates at `http://utfit.roma1.infn.it`.